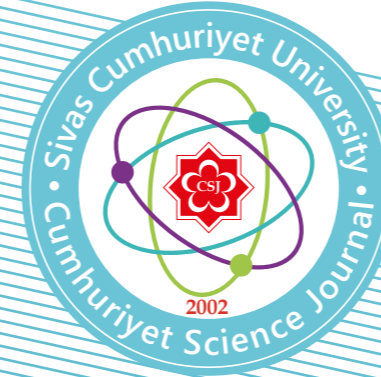




Cumhuriyet Science Journal
Faculty of Science, Cumhuriyet University
58140 - Sivas - Türkiye
Phone: +90(346) 487 13 72
Fax: +90(346) 219 11 86
e-mail: csj@cumhuriyet.edu.tr
<http://csj.cumhuriyet.edu.tr/en>
<http://dergipark.org.tr/en/pub/csaj>

Cumhuriyet Science Journal Vol: 45 No: 1 Year 2024

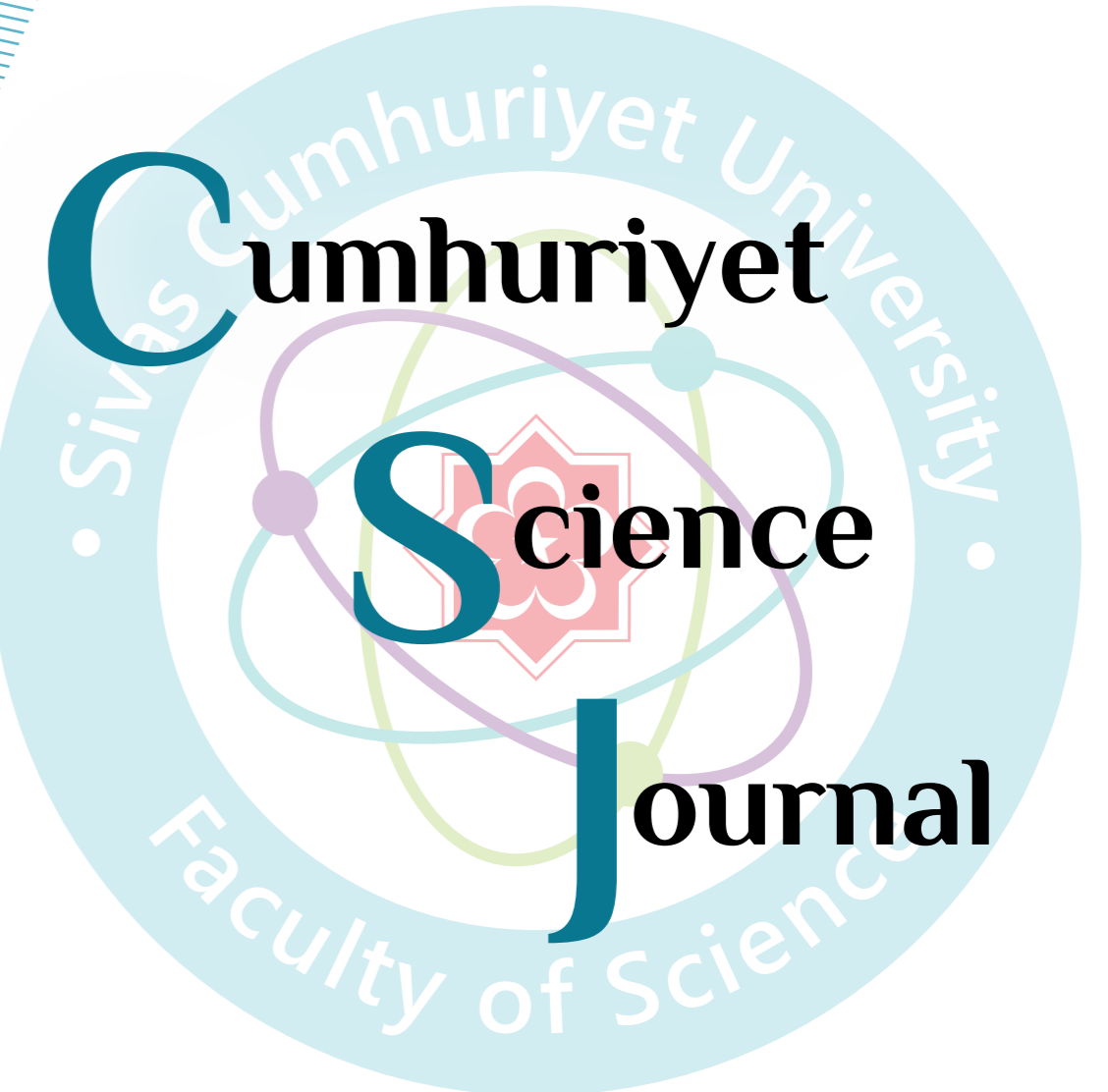


Sivas Cumhuriyet University

ISSN : 2680-2587

e-ISSN : 246-2587X

dergipark.org.tr/tr/pub/csaj
e-mail: csj@cumhuriyet.edu.tr



Cumhuriyet Science Journal (CSJ) is an official publication of Sivas Cumhuriyet University, Science Faculty. The high quality research papers related to the natural sciences are published as online four times a year. CSJ is an open access, free of charge journal and all articles in CSJ have undergone peer review and upon acceptance are immediately and permanently free for everyone to read and download.

Volume: 45

Number: 1

Year: 2024



ISSN: 2587-2680
e-ISSN: 2587-246X
Period: Quarterly
Founded: 2002

Publisher: Sivas Cumhuriyet University

Cumhuriyet Science Journal (CSJ)

Journal Previous Name: Cumhuriyet Üniversitesi Fen-Edebiyat Fakültesi Fen Bilimleri Dergisi

Old ISSN: 1300-1949

Owner on behalf of the Sivas Cumhuriyet University, Faculty of Science

Prof. Dr. İdris ZORLUTUNA (Sivas Cumhuriyet University)

Editor in Chief

Prof. Dr. İdris ZORLUTUNA (Sivas Cumhuriyet University)

Managing Editor

Prof. Dr. Adil ELİK (Sivas Cumhuriyet University)

Editors

Prof. Dr. Baki KESKİN

bkeskin@cumhuriyet.edu.tr

Subjects: Mathematics and Statistics

Institution: Sivas Cumhuriyet University

Prof. Dr. Adil ELİK

elik@cumhuriyet.edu.tr

Subjects: Chemistry and Chemical Engineering,
Environmental Sciences, Basic Sciences (General)

Institution: Sivas Cumhuriyet University

Prof. Dr. Nilüfer TOPSAKAL

ntopsakal@cumhuriyet.edu.tr

Subjects: Applied Mathematics

Institution: Sivas Cumhuriyet University

Prof. Dr. Serkan AKKOYUN

sakkoyun@cumhuriyet.edu.tr

Subjects: Physics and Physical Engineering

Institution: Sivas Cumhuriyet University

Prof. Dr. Halil İbrahim ULUSOY

hiulusoy@cumhuriyet.edu.tr

Subjects: Chemistry, Analytical Chemistry, Drug Analysis, Pharmacy

Institution: Sivas Cumhuriyet University

Prof. Dr. Fatih UNGAN

funghan@cumhuriyet.edu.tr

Subjects: Optics, Phonotics and Fiber optics

Institution: Sivas Cumhuriyet University

Prof. Dr. Nail ALTUNAY

naltunay@cumhuriyet.edu.tr

Subjects: Bioanalytical Chemistry, Chemometric Analysis

Institution: Sivas Cumhuriyet University

Section Editors

Prof. Dr. Natalia BONDARENKO

bondarenkonp@info.sgu.ru

Subjects: Applied Mathematics and Physics

Institution: Samara University

Prof. Dr. Marcello LOCATELLI

marcello.locatelli@unich.it

Subjects: Analytical Chemistry

Institution: University "G. d'Annunzio" of Chieti-Pescara

Prof. Dr. Konstantin P. KATIN

kpkatin@yandex.ru

Subjects: Theoretical Chemistry, Computational design of nanostructures, nanodevices and nanotechnologies

Institution: National Research Nuclear University

Prof. Dr. Duran KARAKAŞ

dkarakas@cumhuriyet.edu.tr

Subjects: Inorganic Chemistry, Theoretical Chemistry

Institution: Sivas Cumhuriyet University

Assoc. Prof. Dr. Yaşar ÇAKMAK

ycakmak@cumhuriyet.edu.tr

Subjects: Applied Mathematics

Institution: Sivas Cumhuriyet University

Prof. Dr. Sevgi DURNA DAŞTAN

sdurna@cumhuriyet.edu.tr

Subjects: Molecular Biology

Institution: Sivas Cumhuriyet University

Assist. Prof. Dr. Yener ÜNAL

uyener@cumhuriyet.edu.tr

Subjects: Statistics

Institution: Sivas Cumhuriyet University

Abstracted&Indexing

ULAKBİM TR-Dizin

Index Copernicus (ICI Journals Master List)

Clarivate Analytics Zoological Record

Crossref

WorldCat

Akademik Dizin

Arastirmax Bilimsel Yayın İndeksi

Bielefeld Academic Search Engine (BASE)

Directory of Research Journal Indexing (DRJI)

Google Scholar

Research Gate

Idealonline

Editorial Board

Prof. Dr. Sezai ELAGÖZ (ASELSAN)
Prof. Dr. Mustafa SOYLAK (Erciyes University)
Prof. Dr. Chuan Fu Yang (Nanjing University of Science and Technology)
Prof. Dr. Münevver SÖKMEN (KGTU)
Prof. Dr. Hüseyin MERDAN (TOBB ETU)
Prof. Dr. Mehmet AKKURT (Erciyes University)
Prof. Dr. Mustafa KAVUTÇU (Gazi University)
Prof. Dr. Francois VOS (The University of Queensland)
Prof. Dr. Abuzar KABIR (International Forensic Research Institute)
Prof. Dr. Mustafa TÜZEN (GOP University)
Prof. Dr. Songül KAYA MERDAN (METU)
Prof. Dr. Jose Javier Valiente-Dobon (INFN-LNL, Padova University)
Prof. Dr. Yeşim SAĞ AÇIKEL (Hacettepe University)
Prof. Dr. Mehmet ŞİMŞİR (Sivas Cumhuriyet University)
Prof. Dr. Atalay SÖKMEN (KGTU)
Prof. Dr. Ricardo I. JELDRES (Universitat de Antofagasta)
Prof. Dr. Mustafa YILDIRIM (Sivas Cumhuriyet University)
Prof. Dr. Ali DELİCEOĞLU (Erciyes University)
Prof. Dr. Tuncay BAYRAM (Karadeniz Technical University)
Prof. Dr. Gökhan KOÇAK (Erciyes University)
Prof. Dr. Nadjet Laouet (Freres Mentouri Constantine-1 University)
Assoc. Prof. Dr. Savaş KAYA (Sivas Cumhuriyet University)

Layout Editors:

Assist. Prof. Dr. Yener ÜNAL
Lecturer Aykut HASBEK

Copyeditors:

Assist. Prof. Dr. Doğa Can SERTBAŞ
Assist. Prof. Dr. Hacı Ahmet KARADAŞ
Research Assistant Özgür İNCE

Proofreader:

Lecturer Aykut HASBEK

Publication Type: Peer Reviewed Journal

Cite Type: Cumhuriyet Sci. J.

Contact Information

Faculty of Science Cumhuriyet University
58140 Sivas- TURKEY
Phone: +90 (346) 487 13 72
Fax: +90 (346) 219 11 86
e-mail: csj@cumhuriyet.edu.tr
<http://dergipark.gov.tr/csj>

CONTENTS		PAGES
1	The Strain-Dependent Antimicrobial and Antibiofilm effect of Cis and Trans-Vaccenic Acid against Pseudomonas Aeruginosa Ayşenur YAZICI	<i>Research Article</i> 1 - 7
2	Cytotoxic Effects of Theranekron D6 on HepG2 Hepatocellular Carcinoma Cells Deniz ŞUMNULU	<i>Research Article</i> 8 – 14
3	The Anti-proliferative Effect of Caffeic Acid and Dactolisib on Human Cervical Carcinoma HeLa Cell Line Zeynep Büşra BOLAT	<i>Research Article</i> 15 – 19
4	Comparison of Characteristics and Antimicrobial Activity of Synthesized Zinc Oxide And Magnetite Iron Oxide Nanoparticles Using Four Different Plant Extracts Burcu AYDOĞDU Mehmet AYTAZ İlkey ÜNAL	<i>Research Article</i> 20 - 28
5	Evaluation of Antibiofilm and Antimicrobial Activities of N-heterocyclic Carbene Complexes Uğur TUTAR Cem ÇELİK Mehmet ATAŞ	<i>Research Article</i> 29 - 34
6	Crocus Officinalis (L.) Extract on Human Colorectal Cancer Cell Line (HT-22): Investigation in Vitro Sinan SOYLU	<i>Research Article</i> 35 - 39
7	Aloe vera Gel Extract Prolongs Lifespan in Caenorhabditis elegans Şeyda BERK	<i>Research Article</i> 40 - 46
8	Chemometric Determination of Parkinson's Drugs Containing Multiple Active Substances Ayşe Merve ARSLAN Güzide PEKCAN	<i>Research Article</i> 47 - 53
9	Synthesis of Gum Arabic-Based Biopolymer Network and Determination of Its Toxicity Properties in In Vitro - In Vivo Model Systems İdil Karaca AÇARI Duygu ÖZHAN Turhan Ali KURUÇAY Süleyman KÖYTEPE Burhan ATEŞ	<i>Research Article</i> 54 - 63
10	Removal of Bromophenol Blue from Aqueous Solution Using Bentonite, Zeolite and Graphene Oxide Nuket KARTAL TEMEL İbrahim Gökçe ERDEM	<i>Research Article</i> 64 - 72
11	Fluorescence Cell Imaging by Carbon Quantum Dots Derived from the Medicinal Plant Malva Sylvestris Layth Shakir MAHMOOD Gulsin ARSLAN Idris SARGIN Serdar KARAKURT	<i>Research Article</i> 73 - 79
12	Synthesis, Cytotoxic Activity Evaluation and Molecular Docking Studies of Some Benzimidazole Derivatives Aybüke Züleyha KAYA Derya OSMANIYE Asaf Evrim EVREN Leyla YURTTAŞ Şeref DEMIRAYAK	<i>Research Article</i> 80 - 87
13	Electrospun Poly(ϵ -caprolactone) Nanofibers Containing Pomegranate Peel Extract and Bioactive Glass as Potential Wound Dressings Ayşen AKTÜRK	<i>Research Article</i> 88 - 93
14	Production and Characterization of Ni _{0.50} Al _{0.50} and Ni _{0.55} Al _{0.45} Powders by Volume Combustion Synthesis Gülizar SARIYER Hasan Erdem ÇAMURLU	<i>Research Article</i> 94 - 99
15	Treatment of Sugar Industry Wastewater via Fenton Oxidation with Zero-Valent Iron Ceren ORAK	<i>Research Article</i> 100 - 104
16	Cytotoxicity Analysis of the Effects of Heterobasidion Annosum Mycelia and Cisplatin on Colon Adenocarcinoma (CACO-2) Cell Line Çiğdem SEVİM Sabri ÜNAL Temel Kan BAKIR Mertcan KARADENİZ Ali TAGHIZADEH TGZD	<i>Research Article</i> 105 - 110

17	Some Sums Involving Generalized Harmonic and r-Derangement Numbers Sibel KOPARAL	<i>Research Article</i>	111 - 116
18	Dynamics Of A Conformable Fractional Order Generalized Richards Growth Model On Star Network With N=20 Nodes Neriman KARTAL	<i>Research Article</i>	117 - 124
19	A Note on the Trace of Generalized Permuting Tri-Derivations Süleyman ZORTAŞ Hasret YAZARLI	<i>Research Article</i>	125 - 129
20	Solvability of an Inverse Problem for an Elliptic-Type Equation Özlem KAYTMAZ Mustafa YILDIZ	<i>Research Article</i>	130 - 134
21	On Almost $C(\alpha)$ -Manifold Satisfying Certain Curvature Conditions Tuğba MERT Mehmet ATÇEKEN Pakize UYGUN	<i>Research Article</i>	135 - 146
22	Kähler Magnetic Curves in Conformally Euclidean Schwarzschild Space Özgür KELEKÇİ	<i>Research Article</i>	147 - 152
23	Evaluation of the Central Copper Contact Pin Effect in High-Energy Region in Gamma-ray Spectrometry Esra UYAR	<i>Research Article</i>	153- 159
24	Machine Learning Based Classification of the Halos in Light Nuclei Region Serkan AKKOYUN	<i>Research Article</i>	160 - 163
25	Asymptotic Relative Efficiency Comparison for some Fit Indices in Structural Equation Modeling İlkay DOĞAN İsmet DOĞAN Nurhan DOĞAN	<i>Research Article</i>	164 - 167
26	Functional Analysis of Variance: An Application to Stock Exchange Selin ÖĞÜTCÜ Nuri ÇELİK	<i>Research Article</i>	168 - 174
27	Row and Column Effects Modelling of Elderly Age Groups and Chronic Health Problem on COVID-19 Gokcen ALTUN Serpil AKTAŞ	<i>Research Article</i>	175 - 181

The Strain-Dependent Antimicrobial and Antibiofilm effect of *Cis* and *Trans*-Vaccenic Acid against *Pseudomonas Aeruginosa*

Ayşenur Yazıcı^{1,2,a,*}

¹Department of Molecular Biology and Genetics, Faculty of Science, Erzurum Technical University, Erzurum, Türkiye.

²High Technology Research and Application Centre (YUTAM), Molecular Microbiology Laboratory, Erzurum Technical University, Erzurum, Türkiye.

*Corresponding author

Research Article

History

Received: 11/08/2023

Accepted: 31/01/2024



This article is licensed under a Creative Commons Attribution-NonCommercial 4.0 International License (CC BY-NC 4.0)

ABSTRACT

This study, it was aimed to investigate the antibacterial and antibiofilm activity of *cis* and *trans*-vaccenic acid against *Pseudomonas aeruginosa*. In the study, four different *P. aeruginosa* strains were used. Antibacterial activity was determined by microdilution and growth curve. The antibiofilm activity was determined by crystal violet assay. In addition, the effect of vaccenic acids on pyocyanin production was investigated. The minimum inhibitory concentration (MIC) of *cis* and *trans*-vaccenic acid against all strains was determined as 128-256 µg/mL, and the minimum biofilm inhibitory concentration (MBIC) value was 8-512 µg/mL. While vaccenic acids reduced cell growth in three strains, they also significantly inhibited pyocyanin production. In one strain, it inhibited biofilm formation without affecting cell growth. As a result, the presence of antibacterial and antibiofilm activity of *cis* and *trans*-vaccenic acid against *P. aeruginosa* was determined as potential agents in the fight against this bacteria.

Keywords: Vaccenic acid, *Pseudomonas aeruginosa*, Antibiotic resistance, Biofilm, Pyocyanin

^aaysenur.ozdemir@erzurum.edu.tr  <https://orcid.org/0000-0002-3369-6791>

Introduction

Nowadays, antibiotic resistance is a major public health threat all over the world. Although resistance is a natural evolutionary process of bacteria, many factors contribute to its acceleration. Misuse and unnecessary usage of antibiotics by humans and their excessive usage in agriculture can be given as examples [1,2]. Biofilms, on the other hand, are a type of bacterial life. It consists of polysaccharides, e-DNA and proteins produced by bacteria [3]. Biofilms formed by quorum sensing (QS) mechanisms prevent antibiotics from penetrating into cells. It is 10-1000 folds more resistant to antibiotics compared to planktonic cells [4]. It is estimated that more than 80% of infections are caused by biofilm [5]. Therefore, the discovery of molecules with antibiofilm properties is quite significant.

P. aeruginosa is an opportunistic pathogen classified by the World Health Organization (WHO) as critical [6]. *P. aeruginosa* is a Gram-negative, non-spore-forming bacteria. It is the main cause of many diseases, especially cystic fibrosis, wound and urinary tract infections [7]. *P. aeruginosa* is highly resistant to antibiotics due to its biofilm-forming properties. Nowadays, its incidence is also increasing rapidly. Due to the rapid development of resistance, the number of effective antibiotics is also decreasing. Therefore, the development of new antibiotics or synergy studies is urgently needed [8].

Vaccenic acid, naturally found in human milk and yogurt, is a natural omega-7 fatty acid [9]. Previous studies have suggested that *trans*-vaccenic acid has a significant effect in reducing the incidence of cancer and obesity [10].

However, there are limited studies on the antimicrobial and antibiofilm activities of fatty acids. To the best of my knowledge, its effectiveness on *P. aeruginosa* is unknown.

For the first time, the efficacy of *cis* and *trans*-vaccenic acid against *P. aeruginosa* was assessed in this study. A reference strain (PAO1) and three different clinical isolates of *P. aeruginosa* were used in the study. As a result, *cis* and *trans*-vaccenic acid showed antibacterial and antibiofilm properties in *P. aeruginosa* and inhibited pyocyanin production.

Material and Methods

Reagents

Cis-vaccenic acid (Cas number: 506-17-2) and *trans*-vaccenic acid (Cas number: 693-72-1) were purchased from Sigma-Aldrich (St. Louis, MO, USA). Both of them were dissolved in dimethyl sulfoxide (DMSO, Isolab, Cas number: 67-68-5). All other chemicals used in this study were analytical grade.

P. aeruginosa Strains and Culture Conditions

In this study, four *P. aeruginosa* (PAO1, PA21, PA23 and PA41) were used. PA21, PA23 and PA41 are clinical isolates from our previous studies. (ETU, BAP: 2021/021). These isolates are in stocks of -80 °C in the Molecular Microbiology Laboratory, High Technology Research and Application Centre (YUTAM). Bacterial strains from the frozen stocks were inoculated on Mueller Hinton Agar (MHA, Across Bio) medium at 37 °C. Liquid cultures were

made in Mueller Hinton Broth (MHB, Across Bio) medium at 37 °C and 150 rpm.

Microdilution Assay

The microdilution test was performed to determine the minimum inhibitory concentration (MIC) value [11,12]. The amounts of the *cis* and *trans*-vaccenic acid were used in 1-512 µg/mL concentrations. Briefly, the overnight growing bacterial culture in MHB medium was diluted until the optical density at 600 nm was between 0,08 and 0,1. This value was accepted as 0,5 McFarland concentration in further experiments and 100 µL of these cells were dispensed into the wells. Subsequently, increasing concentrations of *cis* and *trans*-vaccenic acids were dispersed and the total volume was made up to 200 µL with MHB medium. The plates were incubated at 37°C for 24 hours. The concentrations without growth after 24 hours were recorded as the MIC value.

Growth Curve Pattern

The effect of *cis* and *trans*-vaccenic acids on the growth of *P. aeruginosa* was observed [13]. Briefly, the overnight growing bacterial culture was diluted to 0,5 McFarland concentration into 20 mL MHB medium containing ½ MIC and ¼ MIC concentrations of *cis* and *trans*-vaccenic acids. These tubes were incubated at 37°C and 150 rpm. Then, the growth curve was measured for each *P. aeruginosa* strain at 600 nm optical density. Measurements were taken at 1, 2, 4, 6, 12 and 24 hours. Bacterial culture without *cis* and *trans*-vaccenic acids was used as a control.

Biofilm Inhibition Assay

The effect of *cis* and *trans*-vaccenic acids on biofilm formation in *P. aeruginosa* was determined by the crystal violet test [14,15]. First, bacterial cells grown overnight were adjusted to a 0,5 McFarland concentration. A medium containing *cis* and *trans*-vaccenic acid at a concentration of 1-512 µg/mL and 100 µL of diluted cells were then added to the 96-well plates. The plate was statically incubated at 37°C for 48 hours. At the end of the incubation, non-adherent cells were discarded and all wells were washed with sterile water. After, wells were stained with 0,5% crystal violet for 20 minutes in the dark. At the end of the period, the dye was removed and the biofilm layers were dissolved with 30% acetic acid. Measurements were taken at 590 nm optical density with the spectrophotometer (Multiscan Go, Thermo Scientific, USA).

Pyocyanin Detection Assay

Pyocyanin is one of the virulence compounds produced by *P. aeruginosa*. It is secreted out of the cell. The effect of vaccenic acid on pyocyanin production was evaluated [16,17]. Briefly, a single colony of *P. aeruginosa* was inoculated in a 4 mL MHB medium containing ½ MIC and ¼ MIC concentrations of *cis* and *trans*-vaccenic acids into the 12-well plate. Medium without vaccenic acid was used to control. All tube was incubated at 37°C for 24

hours. After that, culture was obtained with a centrifuge at 12.000 rpm for 5 min. Then, 500 µL chloroform was added and mixed vigorously. The chloroform layer was taken with a centrifuge at 12.000 rpm for 2 min and transferred new tube and 200 µL 0,2 M HCl was added and mixed. The obtained supernatant was taken and measured at 520 nm optical density in the spectrophotometer.

Statistical Analysis

All experiments were performed in three or four replicates. All data were evaluated using the program GraphPad Prism, version 8.4. ANOVA was used for the comparison of data obtained from the pyocyanin inhibition assay.

Results

Antimicrobial Activity of Vaccenic Acid

The antimicrobial effect of vaccenic acids was determined against four different *P. aeruginosa* strains by microdilution assay. The results indicated that *cis* and *trans*-vaccenic acids have antimicrobial activity in increasing concentrations against *P. aeruginosa* tested references and clinic strains. Table 1 shows MIC values of *cis* and *trans*-vaccenic acids. The MIC values were similar between isolates.

Table 1. MIC value of *cis* and *trans*-vaccenic acid against *P. aeruginosa* (The results are an average of three independent experiments).

Strains	MIC (µg/mL)		MBIC (µg/mL)	
	<i>cis</i> -vaccenic acid	<i>trans</i> -vaccenic acid	<i>cis</i> -vaccenic acid	<i>trans</i> -vaccenic acid
PAO1	128	256	256	256
PA21	256	>256	256	256
PA23	256	256	512	512
PA41	256	256	8	32

Growth Curve Pattern

Understanding the interaction between planktonic cells and vaccenic acid is definitely important. Therefore, 24-hour growth curves of bacteria were determined in the presence of vaccenic acids. Figure 1 describes the growth curve of *P. aeruginosa* with *cis* and *trans*-vaccenic acids. In PAO1, PA21 and PA23 strains, 1/2 MIC value decreased cell growth compared to the control group. However, in the PA41 strain, there was no significant difference between 1/2 MIC, 1/4MIC treatments and control groups.

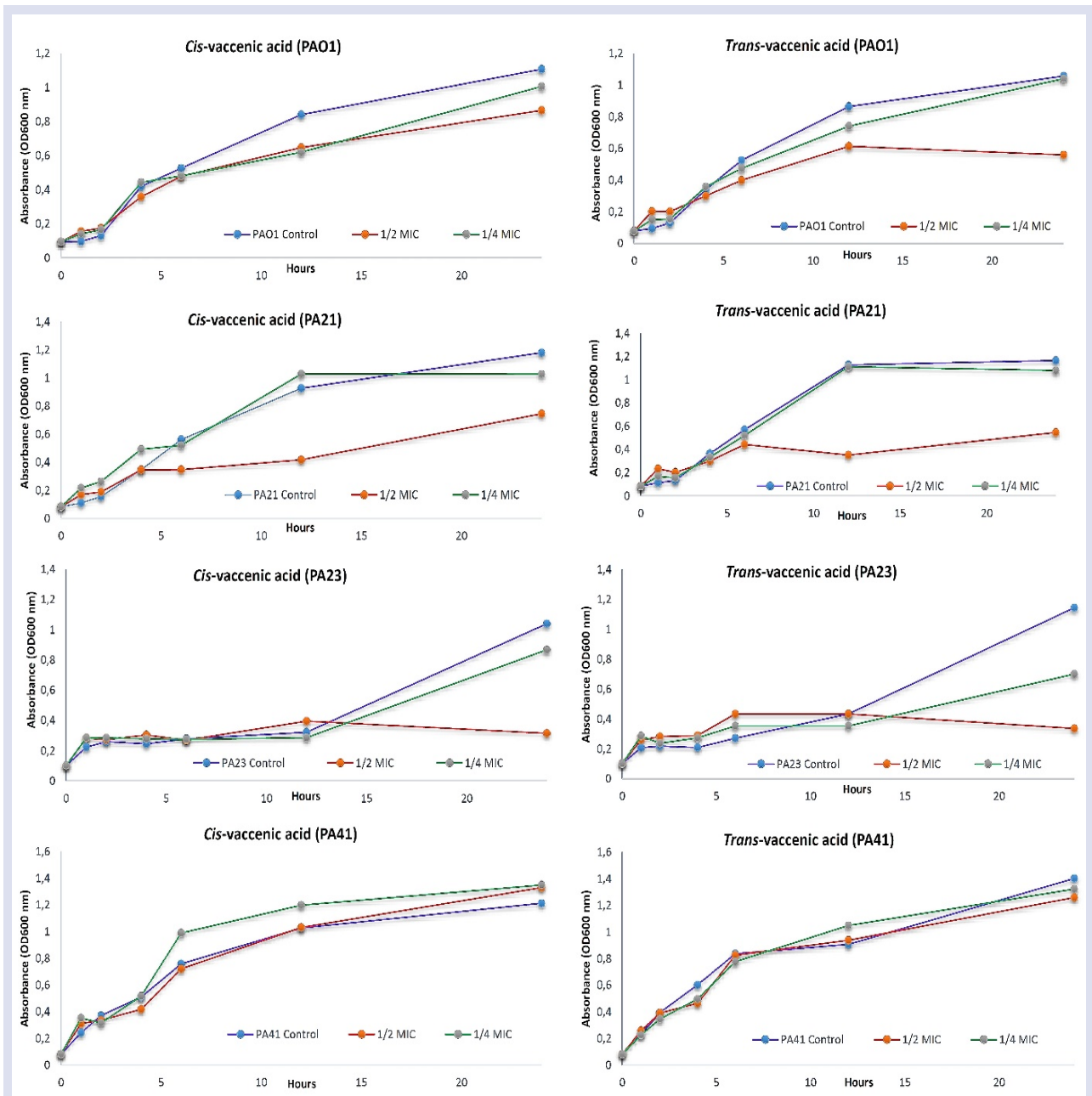


Figure 1. Growth curves of four *P. aeruginosa* strains in the presence of *cis* and *trans*-vaccenic acid at 1/2 MIC and 1/4 MIC concentrations.

The antibacterial compounds may be inhibiting cell growth or killing cells [18]. Antibacterial compounds that inhibit growth may contribute to biofilm formation. Biofilms, on the other hand, are more robust assemblages than free-growing cells due to the complexity of their structures. They also create a tremendous environment for the spread of antibiotic resistance genes [18,19,20]. Therefore, inhibition of biofilm formation should be performed without affecting cell growth [21]. Synergistic effective antibiofilm molecules and antibiotics should be used together as a different approach. In a second approach, newly developed antibiotics should have dual effects, antibacterial and antibiofilm.

In the current study, the relationship between antibiofilm activity and cell growth of *cis* and *trans*-

vaccenic acid was revealed by comparing the results of the crystal violet.

Antibiofilm Activity of Vaccenic Acids

The effect of *cis* and *trans*-vaccenic acid on biofilm formation was investigated by the crystal violet test. *Cis* and *trans*-vaccenic acid showed antibiofilm activity at increasing concentrations (Figure 2). MIC and MBIC values were found to be similar for PAO1, PA21 and PA23 strains. On the other hand, in PA41 isolate, the MBIC value was found to be much smaller than the MIC value (Table 1).

According to these results, *cis* and *trans*-vaccenic acids showed both antibacterial and antibiofilm activity. However, this activity altered depending on the strain. The higher antibiofilm activity was recorded in PA41 isolates.

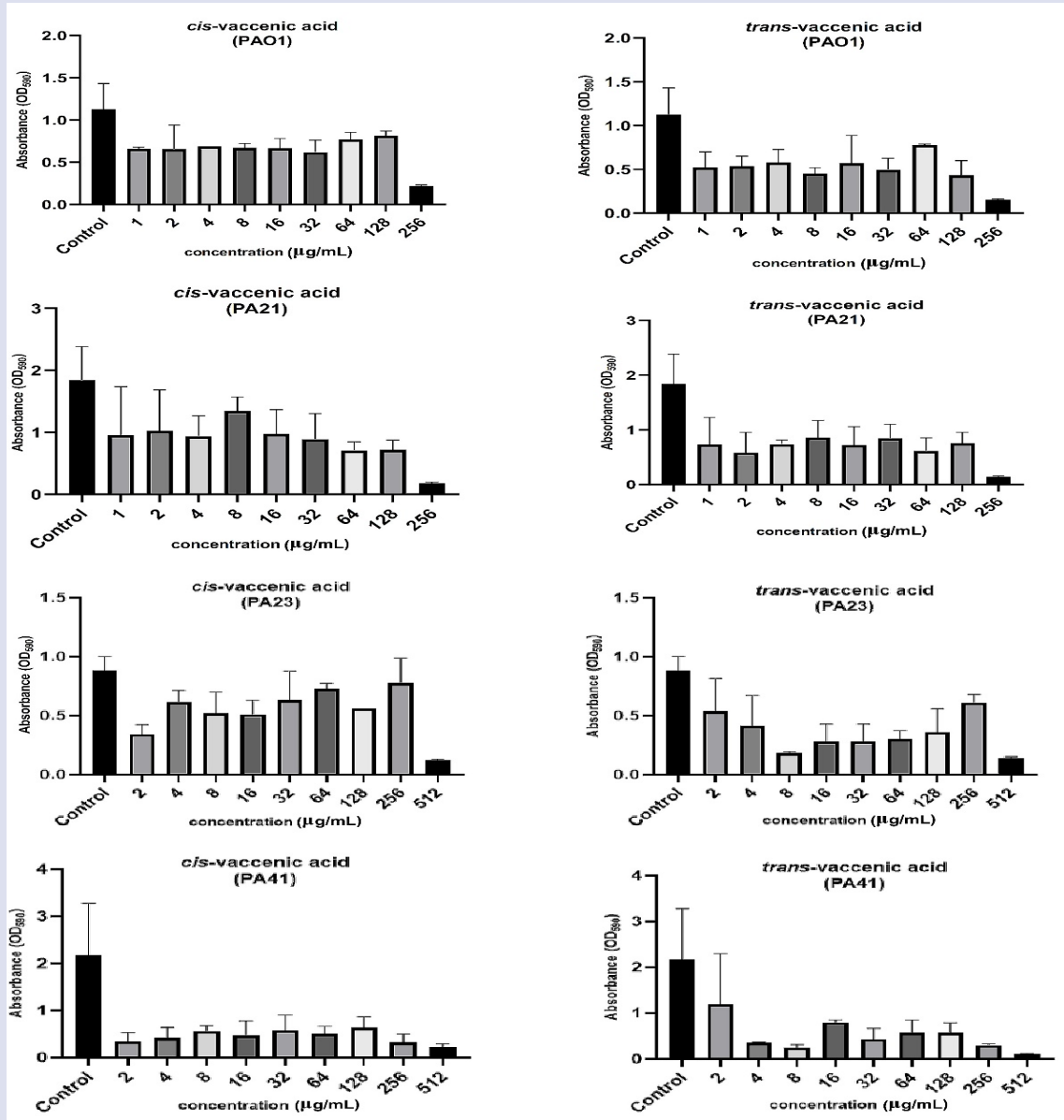


Figure 2. Crystal violet assay for the effect of cis and trans-vaccenic acid on biofilm formation in four *P. aeruginosa* strains. (The results are an average of four independent experiments).

Pyocyanin Detection Assay

Pyocyanin is a blue-greenish color pigment produced by *P. aeruginosa*. This pigment contributes to the virulence properties of *P. aeruginosa* [16]. Pyocyanin, which is strongly blue in neutral and basic pH values, turns red color under acidic conditions [17]. In this study, the change in pyocyanin production in the presence of *cis* and *trans*-vaccenic acid was measured (Figure 3). *Trans*-vaccenic acid was found to inhibit pyocyanin production in all studied isolates. *Cis*-vaccenic acid inhibited pyocyanin production in clinical isolates except in PAO1 and PA41 isolates. PA41 isolate, on the other hand, produces pyocyanin at a very low rate. *Cis*-vaccenic acid had no effect on PA41 pyocyanin production like PAO1.

Pyocyanin helps QS mechanisms, biofilm formation and bacteria survival in an oxygen-free environment [35]. Inhibiting the production of this pigment, which contributes to virulence characteristics, is quite significant in reducing the ability of *P. aeruginosa* to cause infection.

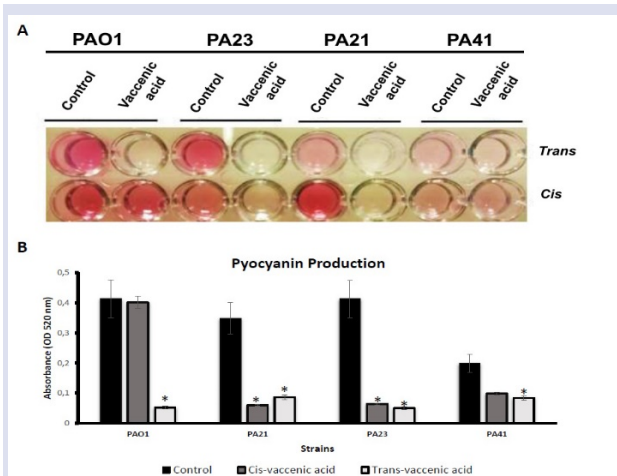


Figure 3. Pyocyanin detection assay plate images (A) of cis and trans-vaccenic acid on four *P. aeruginosa* strains. (B) Optical density readings at 520 nm. “*” indicates statistically significant differences at $p < 0,05$.

Trans-vaccenic acid inhibited pyocyanin production in all isolates studied. *Cis*-vaccenic acid, on the other hand, showed an isolate-dependent inhibition effect. As a result, inhibition of pyocyanin production gave more effective results in *trans*-vaccenic acid.

Discussion

The spread of antibiotic resistance has been assessed as a severe hazard to public health globally [22]. Drug resistance is seen in almost all known bacteria. Not only the inaccurate and excessive use of antibiotics by people but also the use of antibiotics in agriculture and animal husbandry causes the development of resistance [23].

In the current investigation, *cis* and *trans*-vaccenic acid was assessed for antimicrobial and antibiofilm activity against *P. aeruginosa*. This bacteria has been classified among critical pathogens by the WHO [6,24]. Moreover, according to the Centers for Disease Control and Prevention's 2022 report, an increase in multi-drug-resistant (MDR) *P. aeruginosa* infections was observed in hospitals in 2020 [25]. The most important reason for this may be secondary infections developing after Covid-19 disease [39]. Other reasons may be that MDR *P. aeruginosa* infections are prevalent in people with lung disease and weakened immunity. Notwithstanding, the rate of discovery of new antibiotics and antimicrobial agents against MDR strains of *P. aeruginosa* is relatively slow [1,2].

Fatty acids have many biological properties, such as joining the membrane structure, forming phospholipids, and storing energy [26,27,28]. In addition to these features, they have properties such as antibacterial, antifungal, antiviral, anti-algal and anti-protozoan. It performs these activities by inhibiting growth or killing the pathogen [29]. On the other hand, these properties may vary depending on the natural structure of fatty acids [30]. Furthermore, some studies have reported that fatty acids are more effective against Gram-positive bacteria [31]. There are a lot of studies about fatty acids of antibacterial activity against Gram-positive; even so, few studies have shown their effect against Gram-negative bacteria such as *Helicobacter pylori* and *Escherichia coli* [32,33].

Vaccenic acid is a type of fatty acid naturally found in human milk [9]. *Trans*-vaccenic acid (11-*trans*-Octadecenoic acid) is a positional and geometric isomer of oleic acid [10]. The anticancer effect of them and down-regulating the protein expression of Bcl-2 and procaspase-9 has been shown [10]. In addition, it has a beneficial effect on heart disease and obesity [10].

The antibacterial activity against Gram-positive and negative of the methanolic extract of *Quercus leucotrichophora*, which was found to contain *cis*-vaccenic acid by GC-MS [34], shows that further studies on vaccenic

acid are needed. In addition, a recently published study demonstrated that *cis*-vaccenic acid has anti-QS activity against *Chromobacterium violaceum* and methicillin-resistant *Staphylococcus aureus* [9]. Similarly, in the current study, the both antimicrobial, and antibiofilm activity of vaccenic acid was demonstrated against four *P. aeruginosa* strains. The *cis* and *trans* isomers of vaccenic acid were used separately. It was determined that both isomers showed strain-dependent activity.

The antimicrobial activity of amphipathic fatty acids is intended to disrupt cell membrane integrity. It also blocks energy metabolism and nutrient intake of cells [29]. On the other hand, Kumar et al. suggested that fatty acids have an antibiofilm effect at sub-MIC values, and show non-specific antimicrobial effects at high concentrations [36]. The reason why concentration is so important is not obvious. However, in recent studies, it was understood that fatty acids behave as diffusible signal factor [37]. For instance, *cis*-11-metil-2-dodecenoic acid and *cis*-2-decenoic acid act as a diffusible signal factor and disrupted preformed biofilm [37,38].

In the current study, when the studied *P. aeruginosa* isolates were compared, it was observed that *cis* and *trans* vaccenic acids had different effects. For instance, in the PA41 isolate, both *cis* and *trans*-vaccenic acid inhibited biofilm formation at 32 and 8-fold lower MIC, respectively. Comparing this result with a growth curve test for PA41 isolate, it seems that antibiofilm activity does not occur by inhibiting cell growth. One possible reason may be that the antibiofilm activity disrupts the QS mechanisms. Other reasons may be reducing extracellular polymeric matrix (EPS) production, decreasing mobility, acting as a diffusible signal factor, and changing cell membrane fluidity [36]. In light of these results, the mechanism of action and molecular response of the vaccenic acid should be investigated.

Conclusion

Fatty acids are being studied as potential antimicrobial agents. One of them is vaccenic acid which is a natural omega-7 fatty acid. In this study, the antibacterial activity of *cis* and *trans*-vaccenic acid on *P. aeruginosa* was shown, and it was also shown that it has an isolate-dependent strong antibiofilm activity. It is thought to inhibit the formation of virulence properties by suppressing the production of pyocyanin. Therefore, it may be suitable for *P. aeruginosa* treatment. However, further genetic analysis is needed.

Conflict of interest

The author declare no competing interests.

Acknowledgment

This study has not received financial support.

References

- [1] Majumder A., Rahman S., Cohall D., Bharatha A., Singh K., Haqu, M., Gittens Hilaire M., Antimicrobial stewardship: Fighting antimicrobial resistance and protecting global public health, *Infect Drug Resist.*, 13 (2020) 4713.
- [2] Hernando-Amado S., Coque M., Baquero F., Martínez L., Defining and combating antibiotic resistance from One Health and Global Health perspectives, *Nat. Microbiol.*, 4 (9) (2019) 1432-1442.
- [3] Sharahi Y., Azimi T., Shariati A., Safari H., Tehrani K., Hashemi A., Advanced strategies for combating bacterial biofilms, *J. Cell. Physiol.*, 234 (9) (2019) 14689-14708.
- [4] Wu H., Moser C., Wang Z., Høiby N., Song J., Strategies for combating bacterial biofilm infections, *Int. J. Oral Sci.*, 7 (1) (2015) 1-7.
- [5] Pani A., Lucini V., Dugnani S., Scaglione F., Erdosteine enhances antibiotic activity against bacteria within biofilm, *Int. J. Antimicrob. Agents.*, 59 (3) (2022) 106529.
- [6] Whole health organization, WHO publishes list of bacteria for which new antibiotics are urgently needed, Available at: <https://www.who.int/en/news-room/detail/27-02-2017-who-publishes-list-of-bacteria-for-which-new-antibiotics-are-urgently-needed> Retrieved: 07.01.2023
- [7] Abadi A., Rizvanov A., Haertlé T., Blatt L., World Health Organization report: current crisis of antibiotic resistance, *BioNanoScience.*, 9 (4) (2019) 778-788.
- [8] Bassetti S., Tschudin-Sutter S., Egli A., Osthoff M., Optimizing antibiotic therapies to reduce the risk of bacterial resistance, *Eur. J. Intern. Med.*, 99 (2022) 7-12.
- [9] Karuppiyah V., Seralathan M. Quorum sensing inhibitory potential of vaccenic acid against *Chromobacterium violaceum* and methicillin-resistant *Staphylococcus aureus*, *World J. Microbiol. Biotechnol.*, 38 (8) (2022) 1-10.
- [10] Lim N., Oh J., Wang T., Lee S., Kim H., Kim J., Lee G., Trans-11 18:1 vaccenic acid (TVA) has a direct anti-carcinogenic effect on MCF-7 human mammary adenocarcinoma cells, *Nutrients.*, 6 (2) (2014) 627-36.
- [11] Kowalska-Krochmal B., Dudek-Wicher R., The Minimum Inhibitory Concentration of Antibiotics: Methods, Interpretation, Clinical Relevance, *Pathogens.*, 10 (2) (2021) 165.
- [12] European Committee for Antimicrobial Susceptibility Testing (EUCAST) of the European Society of Clinical Microbiology and Infectious Diseases (ESCMID), Discussion Document Determination of minimum inhibitory concentrations (MICs) of antibacterial agents by broth dilution, *Clin Microbiol Infect.*, 9 (8) (2003) ix-xv.
- [13] Sterniša M., Sabotič J., Klančnik A., A novel approach using growth curve analysis to distinguish between antimicrobial and anti-biofilm activities against Salmonella, *Int. J. Food Microbiol.*, 364 (2022) 109520.
- [14] Xu Z., Liang Y., Lin S., Chen D., Li B., Li L., Deng Y., Crystal violet and XTT assays on *Staphylococcus aureus* biofilm quantification, *Curr. Microbiol.*, 73 (4) (2016) 474-482.
- [15] Çobanoğlu Ş., Yazıcı A., Isolation, Characterization, and Antibiofilm Activity of Pigments Synthesized by *Rhodococcus sp.* SC1. *Curr. Microbiol.*, 79 (1) (2022) 1-10.
- [16] Ganesh S., Rai V., Inhibition of quorum-sensing-controlled virulence factors of *Pseudomonas aeruginosa* by Murraya koenigii essential oil: a study in a *Caenorhabditis elegans* infectious model, *J. Med. Microbiol.*, 65 (12) (2016) 1528-1535.
- [17] El Feghali R., Nawas T., Extraction and purification of pyocyanin: A simpler and more reliable method, *MOJ Toxicol.*, 4 (2018) 417-422.
- [18] Bernier P., Surette G., Concentration-dependent activity of antibiotics in natural environments, *Front Microbiol.*, 4 (2013) 20.
- [19] Karygianni L., Ren Z., Koo H., Thurnheer T., Biofilm matrixome: extracellular components in structured microbial communities, *Trends Microbiol.*, 28 (8) (2020) 668-681.
- [20] Donlan M., Biofilms: microbial life on surfaces, *Emerg. Infect. Dis.*, 8 (9) (2002) 881.
- [21] Dieltjens L., Appermans K., Lissens M., Lories B., Kim W., Van der Eycken V., Steenackers P., Inhibiting bacterial cooperation is an evolutionarily robust anti-biofilm strategy, *Nat. Commun.*, 11 (1) (2020) 1-11.
- [22] Manyi-Loh C., Mamphweli S., Meyer E., Okoh A., Antibiotic use in agriculture and its consequential resistance in environmental sources: potential public health implications, *Molecules.*, 23 (4) (2018) 795.
- [23] Ventola L., The antibiotic resistance crisis: part 1: causes and threats, *Clin. Pharmacol. Ther.*, 40 (4) (2015) 277.
- [24] Qin S., Xiao W., Zhou C., Pu Q., Deng X., Lan L., Wu M., *Pseudomonas aeruginosa*: pathogenesis, virulence factors, antibiotic resistance, interaction with host, technology advances and emerging therapeutics, *Signal Transduct Target Ther.*, 7 (1) (2022) 1-27.
- [25] Centers for Disease Control and Prevention, COVID-19: U.S. Impact on Antimicrobial Resistance, Special Report 2022. Atlanta, GA: U.S. Department of Health and Human Services, CDC; (2022). Available at: <https://www.cdc.gov/drugresistance/covid19.html>
- [26] Hamazaki K., Suzuki N., Kitamura I., Hattori A., Nagasawa T., Itomura M., Hamazaki T., Is vaccenic acid (18:1t n-7) associated with an increased incidence of hip fracture? An explanation for the calcium paradox, *Prostaglandins Leukot. Essent.*, 109 (2016) 8-12.
- [27] Stanley-Samuelson W., Jurenka A., Cripps C., Blomquist J., de Renobales M., Fatty acids in insects: composition, metabolism, and biological significance, *Arch. Insect Biochem. Physiol.*, 9 (1) (1988) 1-33.
- [28] Ibarguren M., López J., Escribá V., The effect of natural and synthetic fatty acids on membrane structure, microdomain organization, cellular functions and human health, *Biochim Biophys Acta Biomembr BBA.*, 1838 (6) (2014) 1518-1528.
- [29] Desbois P., Smith J., Antibacterial free fatty acids: activities, mechanisms of action and biotechnological potential, *Appl. Microbiol. Biotechnol.*, 85 (6) (2010) 1629-1642.

- [30] Karlova T., Polakova L., Šmidrkal J., Filip V., Antimicrobial effects of fatty acid fructose esters, *Czech J. Food Sci.*, 28 (2) (2010) 146-149.
- [31] Casillas-Vargas G., Ocasio-Malavé C., Medina S., Morales-Guzmán C., Del Valle G., Carballeira M., Sanabria-Ríos J., Antibacterial fatty acids: An update of possible mechanisms of action and implications in the development of the next generation of antibacterial agents, *Prog. Lipid Res.*, 82 (2021) 101093.
- [32] Petschow W., Batema P., Ford L., Susceptibility of *Helicobacter pylori* to bactericidal properties of medium-chain monoglycerides and free fatty acids, *Antimicrob Agents Chemother.*, 40 (2) (1996) 302-306.
- [33] Petschow W., Batema P., Talbott D., Ford L., Impact of medium-chain monoglycerides on intestinal colonisation by *Vibrio cholerae* or enterotoxigenic *Escherichia coli*, *J. Med. Microbiol.*, 47 (5) (1998) 383-389.
- [34] Semwal P., Painuli S., Badoni H., Bacheti K., Screening of phytoconstituents and antibacterial activity of leaves and bark of *Quercus leucotrichophora* A. Camus from Uttarakhand Himalaya, *Clin. Phytoscience.*, 4 (1) (2018) 1-6.
- [35] Hassett J., Charniga L., Bean K., Ohman E., Cohen S., Response of *Pseudomonas aeruginosa* to pyocyanin: mechanisms of resistance, antioxidant defenses, and demonstration of a manganese-cofactored superoxide dismutase, *Infect. Immun.*, 60 (2) (1992) 328-336.
- [36] Kumar P., Lee H., Beyenal H., Lee J., Fatty acids as antibiofilm and antivirulence agents, *Trends Microbiol.*, 28 (9) (2020) 753-768.
- [37] Ryan P., An Q., Allan H., McCarth Y., Dow M., The DSF family of cell-cell signals: an expanding class of bacterial virulence regulators, *PLoS Pathog.*, 11 (7) (2015) e1004986.
- [38] Zhou L., Zhang H., Cámara M., He W., The DSF family of quorum sensing signals: diversity, biosynthesis, and turnover, *Trends Microbiol.*, 25 (4) (2017) 293-303.
- [39] De Bruyn A., Verellen S., Bruckers L., Geebelen L., Callebaut I., De Pauw I., Dubois J., Secondary infection in COVID-19 critically ill patients: a retrospective single-center evaluation, *BMC Infect. Dis.*, 22 (1) (2022) 207.

Cytotoxic Effects of Theranekron D6 on HepG2 Hepatocellular Carcinoma Cells

Deniz Şumnu 1,a,*

¹ Technology Research Development Application and Research Center, Trakya University, Edirne, Türkiye.

*Corresponding author

Research Article

History

Received: 20/09/2023

Accepted: 25/02/2024



This article is licensed under a Creative Commons Attribution-NonCommercial 4.0 International License (CC BY-NC 4.0)

ABSTRACT

Theranekron D6 is an alcoholic extract of *Tarantula cubensis*. In this study, the cytotoxic effects of Theranekron D6 on HepG2 and on AML12 cells were investigated by MTT analyses. Gene expression analyses were performed by qRT-PCR. Apoptotic, necrotic, and healthy cells were viewed by a fluorescent microscope, and they were counted by a flow cytometry device. 143 µg/mL Theranekron D6 was calculated as an IC₅₀ value for HepG2 cells, and it was applied to both cell lines. No significant increase in the amount of apoptotic and necrotic cells was observed at the AML12 cells, while both of them increased by 31.04% at the HepG2 cells by Theranekron D6 application. The accuracy of flow cytometry data was confirmed through fluorescence microscope analyses. At the HepG2 cells, significant increases were observed at the expression levels of Bax (5.61 ± 0.34), Cas3 (2.74 ± 0.34), APAF1 (3.64 ± 0.44), and p53 (2.10 ± 0.3) genes, but at the AML12 cells, the expression levels of the same genes 1.14 ± 0.14, 0.54 ± 0.17, 0.71 ± 0.17, and 0.93 ± 0.3 not increased. Based on these data, it was concluded that Theranekron D6 may be a chemotherapy candidate for HepG2 cells.

Keywords: AML12, Anticancer, Cytotoxicity, HepG2, *Tarantula cubensis* D6.✉ denizsumnu@trakya.edu.trORCID: <https://orcid.org/0009-0009-0693-3569>

Introduction

Hepatocellular carcinoma (HCC) has an incidence of 90% among all types of liver cancer and ranks first in terms of death among all cancer types [1, 2]. HCC ranks 5th among all cancer types in men and 9th in women and is the second deadliest type of cancer worldwide [3]. In the triggering of HCC, cirrhosis due to chronic liver damage caused by fibrosis, hepatitis B (HBV) and hepatitis C (HCV) virus infection, alcohol addiction, and metabolic syndrome are stated to be risk factors [4]. Apart from these, the consumption of tobacco products and the intake of aflatoxin B1 (a cancer-triggering fungus found in foods) have also been primarily associated with HCC [2, 5]. More than 850,000 individuals are diagnosed with HCC each year [2].

The fact that the diagnosis of HCC is usually made once the cancer has reached advanced stages limits the possible methods of treatment. Because of this, the life expectancy of patients with HCC is usually between six and twenty months once they are diagnosed. According to studies conducted on American individuals, there is less than a 50% chance of a two-year and less than a 10% chance of a five-year life expectancy after diagnosis for all HCC cases [6, 7]. In the fight against advanced HCC, chemotherapeutic drugs such as sorafenib, regorafenib, and lenvatinib are frequently used to prolong the quality and duration of life in patients [8].

For many years, scientists have been researching the possible benefits of the venoms of various living species to treat many types of cancer. Especially in ancient Greek, Indian, and Chinese medicine, many kinds of animal

venoms are frequently used in the fight against various cancer types [9]. According to some studies on breast cancer, the venoms of the Chinese Red Scorpion (*Buthus martensi*), the Yellow Persian Scorpion (*Odontobuthus doriae*), the Arabian Thicktail Scorpion (*Androctonus crassicauda*), the Chinese Scorpion (*Buthus matensii Karsch*), Venezuelan Scorpion (*Tityus discrepans*) have been reported to induce apoptosis of MDA 435, MCF-7, and SKBR3 cell lines [10-14]. In addition, the apoptotic effects of Brazilian Yellow Scorpion (*Tityus serrulatus*) venom on SiHa and HeLa cervical adenocarcinoma cell lines have been demonstrated [15].

Although snake venom has positive effects on cancer, it has been revealed that the antineoplastic effects of scorpion venom are much more promising than snake venom [16, 17]. Similar to these studies, in this study the apoptotic effects of Theranekron D6 (TD6) on HepG2 cell lines were investigated. TD6 is an alcoholic extract of *Tarantula cubensis* D6. Although it has long been known that TD6 has anti-inflammatory, demarcative, necrotizing, and resorptive effects and has been used in wound healing [18], the main purpose of its application in animal health is to treat oral, skin, and nipple papillomatosis [19-21]. It is also used to treat animal diseases such as panaritium, laminitis, foot rot, and arthritis [22]. Recently, the anticancer activity of TD6 has been reported in canine mammary tumors [23].

Apoptosis is the controlled cell death mechanism used to fight many cancer types. Reactive oxygen species (ROS) cause upregulation of apoptosis via mitochondrial apoptotic pathway genes. Some studies showed that snake venom toxins enhance ROS in mitochondria and cause inhibition of cancer cell growth by mitochondrial apoptotic signaling pathway genes [24-26]. The apoptotic effect of TD6 in HCC cells has not been thoroughly investigated. The present study describes the mitochondrial apoptotic effect of TD6 in the HepG2 cell line via oxidative stress mechanisms.

Materials and Methods

Cell Culture

Human hepatocellular carcinoma (HepG2) (ATCC, USA) and human healthy liver cell line (AML12) (ATCC) were maintained in "Dulbecco's Modified Eagle's Medium/Nutrient F-12 Raw", 10% fetal bovine serum (SIGMA-ALDRICH, USA), 2 mM L-Glutamine (Thermo-Fisher, USA), and 100 IU/ml penicillin-streptomycin (Thermo-Fisher). Theranekron D6 was purchased from Richter Pharma (Germany). Cells were cultured in a humidified incubator at 37°C and 5% carbon dioxide.

3-(4,5-dimethylthiazol-2-yl)-2,5-diphenyl tetrazolium bromide (MTT) analyzes

AML12 and HepG2 cell lines were separately seeded in 180 µl volumes with approximately 5×10^3 cells in each well on 96-well spectrophotometric plates (NEST, USA). Cells were treated with 8.9, 17.8, 35.75, 71.5, 143, 286 µg/mL concentrations of TD6 for 24 h. After treatments, 20 µl of MTT (5 mg/ml) solution was applied to each well, and plates were incubated at 37°C for 3 h in 95% humidity and 5% CO₂. At the end of the incubation, all the liquid phase on the cells was removed, and 180 µl dimethyl sulfoxide (DMSO) was applied for 20 min to each well. The viability of the cells was calculated by reading the absorbance value at 570 nm wavelength in the Thermo Scientific Multiskan GO spectrophotometer device (USA).

Cell Fluorescent Staining

AML12 and HepG2 cells were separately seeded in 4 wells of 6-well plates (NEST) with 5×10^4 cells per well. No substance was applied to two wells, and they were used as AML12 and HepG2 controls. 143 µg/mL TD6 was applied to the other two wells of both cell lines for 24 h. At the end of 24 h, each cell line was stained with both Annexin V-FITC/PI Apoptosis Kit (Elabscience, USA) and Hoechst 34580 (Cayman Chemical, USA) fluorescent dyes,

and microscope images were taken. For the Annexin V/PI application, at the end of 24 h, the medium on the cells was removed and washed with 1× PBS. In 2 ml 1× Annexin V binding buffer, 5 µl of Annexin V-FITC and 5 µL of PI were mixed and applied to each well for 20 min at room temperature in the dark. Images were taken on a 5× objective using the FITC channel of the Zeiss Observer Z1 fluorescent microscope. For the application of Hoechst 34580, 25 µg of Hoechst 34580 was dissolved in 50 ml of 1× PBS. After removing the medium from the cells, 2 ml of Hoechst 34580 solution was applied to each well in the dark at room temperature for 20 min. At the end of the application, cells were visualized using a 5× objective and the DAPI channel.

Flow Cytometry-Based Quantitative Apoptosis Analyses

AML12 and HepG2 cells were separately seeded into two 6-well plates, with 5×10^4 cells in each well. After 24 h of cells adhering to the plate, 3 wells of AML12 cells and 3 wells of HepG2 cells were treated with 143 µg/mL TD6 for 24 h. Other cells in both three wells were used as AML12 and HepG2 control cells. At the end of 24 h, cells in all wells were trypsinized and removed into 1.5 ml collection tubes (Eppendorf, Germany). All tubes were centrifuged in a centrifuge device (Hermle, Germany) at 300 g for 5 minutes to remove trypsin from the cells. At the end of 5 minutes, the supernatants were removed from the pellet, and the cells were resuspended in 500 µl 1× PBS. 200 µl 1× Annexin V binding buffer, 2.5 µl Annexin V-FITC, and 2.5 µl PI were mixed with the 500 µl 1× PBS and cell mixture for each sample and incubated in the dark at room temperature for 15 min. Annexin V-stained cells were counted for the BL1-A channel, PI-stained cells were counted for the BL2-A channel, and both Annexin V and PI-stained cells were counted for the BL1-A and BL2-A channels together in an Applied Biosystems Attune acoustic focusing cytometer flow cytometry device (Applied Biosystems, USA).

Total RNA Isolation, cDNA Synthesis, and RT-PCR Analyses

Total RNAs were extracted from cells using the Column Pure RNA Miniprep Kit (ABM, USA), and the OneScript Plus cDNA Synthesis Kit (ABM) was used for cDNA synthesis according to the manufacturer's protocols. RT-qPCR was performed using BlasTaq 2× qPCR MasterMix (ABM). RT-qPCR analysis is applied to the QuantStudio 6 Flex (Applied Biosystems) RT-PCR device. The primer sequences of the genes and RT-qPCR conditions are shown in Table 1.

Table 1. Gene codes with GenBank ID, primer base sequences of genes, and RT-PCR conditions.

Gene Codes and GenBank ID	Primer Base Sequences	Real Time PCR Conditions	
Gapdh	F: CAATGCCTCCTGCACCACCA R: GATGTTCTGGAGAGCCCGC	Hold Stage: 1 Cycle 50°C 2 minute 95°C 10 minute	
NM_002046	F: GTCACCATACATGGAATGGCA R: CTGATCCAACCGTGTGCAAA		
APAF-1	F: TCCCCCTCAGATGATCTCTCCA R: CGGAAAGGTTAAGCGTCGAAAA		
NM_001160	F: GGAGGATTGTGGCCTTCTTT R: GCCCAATACGACCAATCCGTTGA		
Akt	F: CCCGAGAGGTCTTTTCCGAG R: CCAGCCCATGATGGTTCTGAT		
NM_005163	F: TGGTAACTGGTCTTAAACCGGAATC R: GGCGGTGAGTGCAGGATAGG		
BCL-2	F: GGAAGCGAATCAATGGACTCTGG R: GCATCGACATCTGTACCAGACC		PCR Stage: 40 Cycle 95°C 15 second 60°C 1 minute
NM_000657.2	F: ACCTGAAAGTTACATCCACAGAA R: GGGTGTATCCAAAACCCGGA		
Bax	F: TCTACACCCGACAACTCCATCCG R: TCTGGCATTTTGGAGAGGAAGTG		
NM_138761	F: TCACTGTGGCTGTACCAAGGTG R: CCAGGAAGTAAAAGCATTCCAGC		
CAT	F: GGGCATGACTAATCCCCTACTGA R: GCCCAATCCTAGACGGCAAC		
NM_001752.3	F: CCTCTGACGTCCATCATCTC R: ATCTTCTGCTGCCGCTCGCTT		
Cas3	F: CCTGGAACCTCACATCAACG R: CCAACGCCTCCTGGTACTTC	Melt Curve Stage: 1 Cycle 95°C 15 second 60°C 1 minute 95°C 15 second	
NM_004346	F: AGATGGACTTCAACCTGCTAGTG R: GTCAAAGAGACGAGCGGTAAG		
CD133	F: GAGATGGCAGGGATCCTGTACG R: ATTCTGGAATTCGTCTACGATGATGACC		
NM_006017.2	F: TTGTCTGTCACACTTCTGTAGTT R: AACAGTCCCATTGGATTCAACA		
CycD1	F: TATGTGAGCCGCTGAATGCCA R: CACTGACCTTATTGTGGGCTTG		
NM_053056	F: GAGGTTGGCTCTGACTGTACC R: TCCGTCAGTAGATTACCAC		
CuZn-SOD	F: GCTACTGCCATCCAATCGAG R: TGGTGATGTTGGACTCCTCA		
NM_000454.4			
EGF			
NM_001945.3			
ErbB2			
NM_001005862.2			
Mn-SOD			
NM_001322819.2			
GS			
NM_000178.2			
GSR			
NM_000637.5			
PI3K			
NM_006218.2			
GSR			
NM_000637.5			
p53			
NM_001126118			
VEGF			
NM_001033756			

Statistical Analyses

In MTT analyses, cells without substance were considered 100% viable. The percentage of cell viability was calculated using the following formula:

Cell viability = (absorbance value of the TD6 applied wells / absorbance value of the control wells) × 100.

Three consecutive TD6 applications were calculated with the $2^{-\Delta\Delta CT}$ formula. The relative gene expression levels were normalized to the glyceraldehyde 3-phosphate dehydrogenase (GAPDH) gene. Statistical significance was assessed for both RT-PCR and flow cytometry analyses using the SPSS Paired-Samples T test. $P < 0.05$ values were considered statistically significant.

Results

3-(4, 5-dimethylthiazol-2-yl)-2, 5-diphenyl tetrazolium bromide (MTT) Analyses

In the AML12 cell line, 98.54% and 80.96% viabilities were determined for the lowest (8.9 µg/mL) and highest (286 µg/mL) doses of TD6 application, respectively. Contrary to the AML12 cell line, 86.25%, 49.93%, and

45.92% viabilities were determined for the lowest (8.9 µg/mL), IC_{50} (143 µg/mL), and highest (286 µg/mL) doses of TD6 application in HepG2 cells, respectively. For a 143 µg/mL TD6 application, 89.41% viability was determined in AML12 cells. TD6 exhibited selective toxicity in AML12 and HepG2 cells, and 143 µg/mL TD6 was chosen as an application dose for both cell lines (Figure 1).

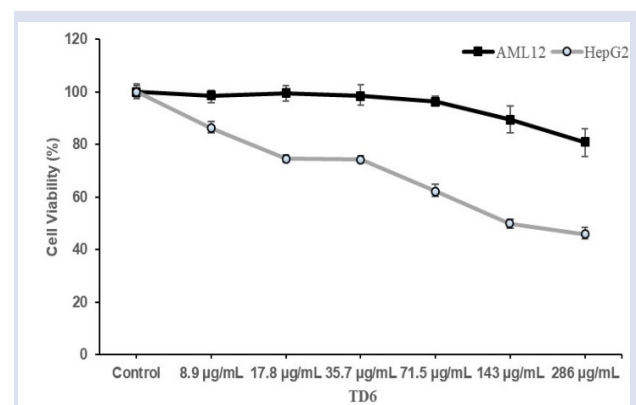


Figure 1. MTT cell viability (%) assay on the control and TD6-treated AML12 and HepG2 cells for 24 h (mean ± SD).

Gene Expression Analyses

In the AML12 cell line, statistically significant increases at gene expression levels of PI3K, Akt, EGF, VEGF (angiogenesis pathway genes), CD133 oncogene, and CycD1 cell cycle/proliferation gene were determined. Conversely, decreases were observed in the Cas3 gene expression level, and no significant changes were determined at the gene expression levels of BCL-2, Bax, APAF-1, p53 (mitochondrial apoptotic pathway genes), Mn-SOD, and GS (mitochondrial oxidative stress regulator genes). Contrary to the AML12 cell line, the expression level of CycD1 decreased, while BCL-2, Bax, APAF-1, Cas3, p53, Mn-SOD, and GS, significantly increased in the HepG2 cell line. PI3K, Akt, EGF, VEGF, and ErbB2 gene expression levels remained stable due to the TD6 application in the HepG2 cell line ($p < 0.05$) (Table 2).

Table 2. mRNA expression level changes of angiogenesis, cell cycle, apoptotic, oxidative stress, and oncogenes in AML12 and HepG2 cells due to the TD6 application (mean \pm SD) (relative to the control group; $p < 0.05$).

Genes	AML12		HepG2	
	Relative Fold Changes	P Values	Relative Fold Changes	P Values
PI3K	2.34 \pm 0.18	0.006	0.65 \pm 0.07	0.012
ErbB2	1.65 \pm 0.28	0.059	0.79 \pm 0.03	0.006
Akt	2.17 \pm 0.14	0.005	0.80 \pm 0.06	0.027
VEGF	2.35 \pm 0.28	0.022	0.78 \pm 0.16	0.128
EGF	2.76 \pm 0.29	0.009	0.75 \pm 0.21	0.162
CD133	2.85 \pm 0.11	0.001	1.07 \pm 0.25	0.765
CycD1	2.11 \pm 0.15	0.007	0.26 \pm 0.18	0.018
BCL2	0.92 \pm 0.13	0.356	4.17 \pm 0.17	0.001
Bax	1.14 \pm 0.14	0.248	5.61 \pm 0.34	0.002
Cas3	0.54 \pm 0.17	0.042	2.74 \pm 0.34	0.013
APAF1	0.71 \pm 0.17	0.094	3.64 \pm 0.44	0.009
p53	0.93 \pm 0.3	0.668	2.10 \pm 0.3	0.024
Mn-SOD	0.83 \pm 0.19	0.242	3.71 \pm 0.14	0.001
GS	0.79 \pm 0.2	0.204	6.72 \pm 0.16	0.000

Flow Cytometry-Based Quantitative Apoptosis Analyses

In the AML12 cell line, no statistically significant change in apoptotic cell quantity was observed between the control (1.84% \pm 0.97) and TD6-treated (1.23% \pm 0.41) cells. In the HepG2 cell line, the levels of early apoptosis significantly increased in the TD6-treated group (25.34% \pm 2.79) compared with the control group (3.65% \pm 2.95). Also, late apoptosis was assessed. The levels of late apoptosis were significantly higher in the TD6-applied group (9.96% \pm 5.11) compared with the control group (0.61% \pm 0.54) (Fig. 2A). The average of three repeats of the control total apoptotic cells was calculated as 4.26% \pm 2.01, while the TD6-treated apoptotic HepG2 cells were 35.3% \pm 2.52. This difference (31.04%) between the control and TD6-treated HepG2 cells was assessed as statistically significant ($p = 0.001$) (Figure 2).

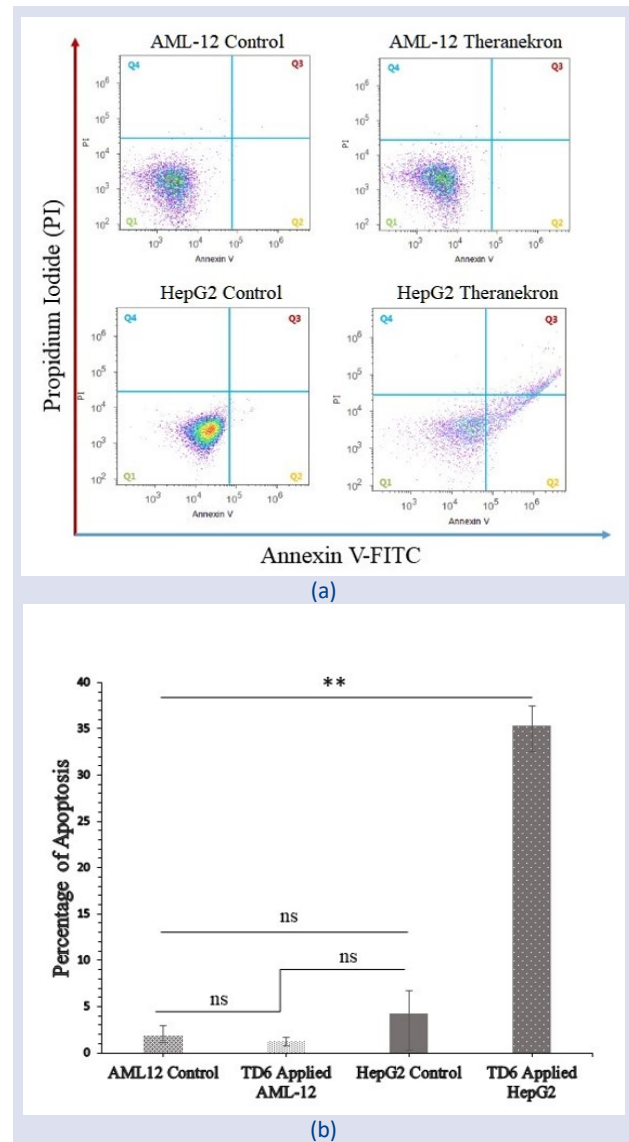


Figure 2. (a) Lower-left quadrant: viable cells unlabeled by Annexin V and PI; lower-right quadrant: early-apoptotic cells labeled by Annexin V only; upper-left quadrant: early-necrotic cells labeled by PI only; upper-right quadrant: late-apoptotic/necrotic cells labeled by both Annexin V and PI. The data are representative of three independent measurements. (b) Apoptotic rates of control and TD6-treated AML12 and HepG2 cells using Annexin V and PI double staining (mean \pm SD.) (relative to the control group; SPSS Paired-Samples T test applied; ^{ns} $p > 0.05$, ^{*} $p < 0.05$, ^{**} $p < 0.01$).

Fluorescent Staining

In the TD6-treated HepG2 cell line, the interior of some cell membranes is stained with Annexin V (bright green), which is a marker of early apoptosis, and the nuclei of many cells are stained with PI (red), which is a marker of late apoptosis. In addition, degraded nuclei have been seen that are stained with Hoechst 34580 in the TD6-applied HepG2 cell line. Contrary to these findings, neither early nor late apoptosis markers were observed in the TD6-treated AML12 cell line (Figure 3).

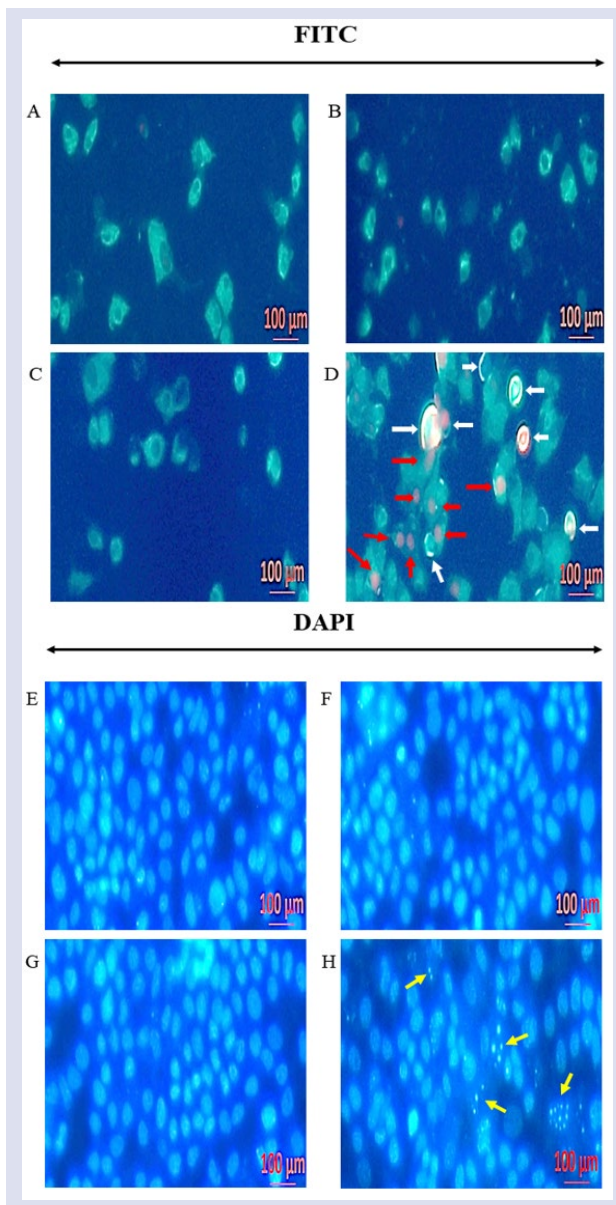


Figure 3. Fluorescence staining images of (A) and (E) control, (B) and (F) TD6-treated AML12, and (C) and (G) control, (D) and (H) TD6-treated HepG2 cells (white arrows: Annexin V-labeled early apoptotic cells; red arrows: PI-labeled late apoptotic cells; and yellow arrows: Hoechst 34580-stained nuclei degraded cells).

Discussion

In the present study, the oxidative, cytotoxic, and apoptotic effects of TD6 on the HCC HepG2 cell line and the healthy liver cell line AML12 have been investigated. Mitochondrial oxidative stress has an important role in activating the mitochondrial apoptotic pathway. Especially enhancing Mn-SOD and GS in mitochondria causes apoptosis through the mitochondrial apoptotic cascade [27]. In line with this strategy, many chemotherapy agents are being used in the fight against cancer. In a study about the induction of oxidative stress by anticancer drugs, it has been shown that doxorubicin, actinomycin D, mitomycin C, mercaptopurine, carmofur,

vinorelbine, vinblastine, camptothecin, and paclitaxel have oxidant activities that trigger apoptosis in DLD-1 human colorectal cancer cells [28]. However, some of these chemotherapeutic agents also have cytotoxic effects on healthy cells and tissues. Therefore, in this study, the cytotoxic effect of TD6 was investigated by applying 8.9-286 µg/mL doses to both the carcinoma cell line HepG2 and the healthy cell line AML12 for 24 h. It was determined from MTT analysis that the highest dose of 286 µg/mL suppressed only 19.04% cell proliferation in the AML12 cell line, whereas 143 µg/mL suppressed 50.07% cell proliferation in the HepG2 cell line. In a study, the human embryonic kidney cell line (HEK-293), human breast cancer cell line (MCF-7), human small cell lung cancer cell line with multidrug-resistant variant (H69AR), and human prostate cancer cell line (PC3), the most appropriate IC_{50} values of TD6 were investigated depending on the application doses range of 10-100 µg/mL for 24, 48, and 72 hours. In this study, IC_{50} values based on 72 hours of application time for HEK-293, MC-7, H69AR, and PC3 cell lines were calculated as 88.3 µg/mL, 94.7 µg/mL, 295 µg/mL, and 118.9 µg/mL. Remarkably, in this study, the IC_{50} value for the healthy HEK-293 cell line is lower than the IC_{50} value determined for cancerous cell lines, which shows that, TD6 has a more cytotoxic effect on the healthy cell line than on cancerous cell lines [29]. In another study, prostate (PC3), breast (MDA-MB-231), lung (H69), and ovarian (OVCAR-3) cancer cell lines and a non-cancerous epithelial (MCF-10A) cell line were treated with another *Tarantula cubensis* product called "Tarantula-Logoplex" (Richter Pharma) with a dose range of 10-500 µg/mL for 24, 48, and 72 hours, and the IC_{50} values were investigated. In this study, IC_{50} values for the cell lines in the order specified, depending on the 72-hour application time of Tarantula-Logoplex (TL), were calculated as 40.2 ± 1.2 , 159.3 ± 2.1 , 498.3 ± 1.2 , 48.9 ± 1.8 , and 217.8 ± 2.0 µg/mL [30]. From this study, the IC_{50} value determined for the healthy epithelial cell line (MCF-10A) is higher than those determined for prostate (PC3), breast (MDA-MB-231), and uterine (OVCAR-3) cancer cell lines, showing that the cytotoxic effect of TL is higher for these three cancerous cell lines than for the healthy epithelial cell line. However, the IC_{50} value for the lung cancer (H69) cell line is more than twice the IC_{50} value of the healthy epithelial cell line, indicating that TL has a more cytotoxic effect on MCF-10A than H69. As seen from these studies, the acholic extract of *Tarantula cubensis* has a selective cytotoxic effect on different cancer cell lines. According to the MTT analysis performed in the present study, depending on the application dose of 8.9-286 µg/mL TD6 to the healthy liver cell line (AML12) and hepatocellular carcinoma cell line (HepG2), the proliferation was suppressed by 50.07% in the HepG2 cell line for 143 µg/mL TD6, while in the AML12 cell line only 10.59% of suppression was observed by the same dose of TD6. In order to investigate this selective effect of TD6 on cytotoxicity, 143 µg/mL of TD6 (the IC_{50} value of the cancerous cell line HepG2) was chosen as the reference application dose for both cell lines.

RT-PCR analysis showed that 143 µg/mL of TD6 promoted mitochondrial apoptosis by increasing mitochondrial oxidative stress in HepG2 cells via significant increases in expression levels of Mn-SOD, GS, BCL-2, Bax, Apaf-1, Cas3, and p53 genes ($p < 0.05$). Mitochondria are the source of cellular ROS. Excessive production of ROS causes oxidative stress, and if oxidative stress is not normalized in the mitochondria by scavenger enzyme genes (Mn-SOD and GS), the mitochondrial apoptotic pathway induces apoptosis [31]. The enhancement of BCL-2, Bax, APAF-1, Cas3, and p53 gene expression levels indicates that oxidative stress genes were not able to scavenge ROS in HepG2 cells. In addition, a significant decrease in the expression level of the CycD1 gene indicates that the HepG2 cell line could not pass the G0/ G1 phase in the cell cycle, and HepG2 cells went into apoptosis. Contrary to HepG2 cells, it was determined that TD6 has not stimulated apoptosis due to the significant increase in the expression levels of CycD1 and PI3K/ Akt/ EGF/ VEGF angiogenesis pathway genes in the AML12 cell line ($p < 0.05$) and also that oxidative stress gene expression levels remain stable.

The other important apoptosis indicators are Annexin V and PI stains. Annexin V exerts high affinity to phosphatidyl serine (PS) residues via Ca^{2+} cations. PS are translocated to the inner membrane of the cells, both in the apoptotic and necrotic stages, but initial of the apoptosis the cell membrane remains intact, while late stage of apoptosis and necrosis the cell membrane loses its integrity and becomes leaky. Annexin V is a little molecule, so at the initiation of apoptosis, only Annexin V passes through into the cell membrane, but at the late stage of apoptosis and necrosis, PI, which is the bigger molecule than Annexin V, passes through the membrane and reaches the nuclei of the cell and binds to it. Under the fluorescent microscope using both the FITC and PI channels, the early stage of apoptotic cells is seen as bright green due to the FITC channel, but at the late stage of apoptosis and necrosis, the cell nuclei are seen as red due to the PI channel of the fluorescent microscope [32]. In this study, both early and late apoptosis were demonstrated in TD6-applied HepG2 cells via Annexin V and PI staining methods in the fluorescence microscope, but there was no apoptotic sign in the AML12 cell line by the same application. Moreover, flow cytometry analysis provided numerical support for demonstrating these apoptotic events. Hoechst 34580 and its derivatives (Hoechst 33258 and Hoechst 33342) have a high affinity for DNA, and they are frequently used in anti-cancer drug studies to view both the nuclei of live and apoptotic or necrotic cells [33]. In this study, the result of the Hoechst 34580 staining assay showed that some nuclei degraded cells in the HepG2 cell line, but no apoptotic sign was detected by the same application in the AML12 cell line.

Conclusion

TD6 causes apoptosis via enhanced reactive oxidative species and trigger to mitochondrial apoptotic pathway in

the HepG2 cell line. However, there is less cytotoxic effect in the healthy AML12 cell line. This selective feature indicates the importance of Theranekron D6 in cancer studies. However, further in vitro and in vivo researches are needed to use TD6 in HCC and other types of cancer treatments, and more effective results can be obtained by combining it with currently used cancer drugs.

Conflicts of interest

There are no conflicts of interest in this work.

Acknowledgement

Thanks for all laboratory equipment supplied by Trakya University Technology Research Development Application and Research Center (TUTAGEM) and Apotherapy Zeynep Meral Şahin, who was suggested to Theranekron D6 in cancer application.

References

- [1] Ferlay J., Soerjomataram I., Dikshit R., Eser S., Mathers C., Rebelo M., Parkin D.M., Forman D., Bray F., Cancer incidence and mortality worldwide: sources, methods and major patterns in GLOBOCAN 2012, *Int J Cancer*, 136(5) (2015) E359–86.
- [2] Torre L., Global cancer statistics, 2012, *CA-CANCER J CLIN*, 65(2) (2015) 87–108.
- [3] Park J.W., Chen M., Colombo M., Global patterns of hepatocellular carcinoma management from diagnosis to death: the BRIDGE Study, *LIVER INT*, 35(9) (2015) 2155–2166.
- [4] EASL-EORTC clinical practice guidelines: management of hepatocellular carcinoma, *J Hepatol.*, 56(4) (2012) 908–43.
- [5] Laursen L., A preventable cancer, *Nature*, 516(7529) (2014) S2–3.
- [6] McGlynn KA, London W.T., “The global epidemiology of hepatocellular carcinoma: present and future”, *Clin Liver Dis.*, 15(2) (2011) 223–x.
- [7] McGlynn K.A., Petrick J.L., London W.T., “Global epidemiology of hepatocellular carcinoma: an emphasis on demographic and regional variability”, *Clin Liver Dis.*, 19(2) (2015) 223–38.
- [8] Sim H.W., Knox J., Hepatocellular carcinoma in the era of immunotherapy, *Curr Probl Cancer*, 42(1) (2018) 40–48.
- [9] Gomes A., Bhattacharjee P., Mishra R., Biswas A.K., Dasgupta S.C., Giri B., Anticancer potential of animal venoms and toxins, *Indian J Exp Biol.*, 48(2) (2010) 93-103.
- [10] Chang N.S., Transforming growth factor-beta protection of cancer cells against tumor necrosis factor cytotoxicity is counteracted by hyaluronidase (review), *Int J Mol Med*, 2(6) (1998) 653-9.
- [11] Zargan J., Sajad M., Umar S., Naime M., Ali S., Khan H.A., Scorpion (*Odontobuthus doriae*) venom induces apoptosis and inhibits DNA synthesis in human neuroblastoma cells, *Mol Cell Biochem.*, 348(1-2) (2011) 173-81.
- [12] Caliskan F., Garcia B.I., Coronas F.I., Batista C.V., Zamudio F.Z., Possani L.D., Characterization of venom components

- from the scorpion *Androctonus crassicauda* of Turkey: peptides and genes, *Toxicon*, 48(1) (2006) 12-22.
- [13] D'Suze G., Rosales A., Salazar V., Sevcik C., Apoptogenic peptides from *Tityus discrepans* scorpion venom acting against the SKBR3 breast cancer cell line, *Toxicon*, 56(8) (2010) 1497-505.
- [14] Li H.M., Wang D.C., Zeng Z.H., Jin L., Hu R.Q., Crystal structure of an acidic neurotoxin from scorpion *Buthus martensii* Karsch at 1.85 Å resolution, *J Mol Biol.*, 261(3) (1996) 415-31.
- [15] Oliveira E.B., Farias K.J.S., Gomes D.L., de Araújo J.M.G., da Silva W.D., Rocha H.A.O., Donadi E.A., Fernandes-Pedrosa M.F., Crispim J.C.O., *Tityus serrulatus* Scorpion Venom Induces Apoptosis in Cervical Cancer Cell Lines. *Evid Based Complement Alternat Med.*, 2019: 5131042.
- [16] Fu Y.J., Yin L.T., Liang A.H., Zhang C.F., Wang W., Chai B.F., Fan X.J., Therapeutic potential of chlorotoxin-like neurotoxin from the Chinese scorpion for humangiomas, *Neurosci Lett.*, 412(1) (2007) 62-7.
- [17] Mamelak A.N., Jacoby D.B., Targeted Delivery of Antitumoral Therapy to Glioma and Other Malignancies with Synthetic Chlorotoxin (TM-601), *Expert Opin Drug Deliv.*, 4(2) (2007) 175-86.
- [18] Stampa S., A field trial comparing the efficacy of sulphamonomethoxine, penicillin, and tarantula poison in the treatment of pododermatitis circumspecta of cattle, *J S Afr Vet Assoc.*, 57(2) (1986) 91-3.
- [19] Cam Y., Kibar M., Atasever A., Atalay O., Beyaz L., Efficacy of levamisole and *Tarantula cubensis* venom for the treatment of bovine cutaneous papillomatosis, *Vet Rec.*, 160(14) (2007) 486-8.
- [20] Icen H., Sekin S., Simsek A., Kochan A., Tunik S., The efficacy of *Tarantula cubensis* extract (Theranekron) in treatment of canine oral papillomatosis, *Asian J Anim Vet Adv.*, 6(7) (2011) 744-749.
- [21] Paksoy Z., Gülesci N., Kandemir F.M., Dinçel G.Ç., Effectiveness of levamisole and tarantula *cubensis* extract in the treatment of teat Papillomatosis of cows, *Indian J Anim Res.*, 49(5) (2015) 704-8.
- [22] Sardari K., Kakhki E.G., Mohri M., Evaluation of wound contraction and epithelialization after subcutaneous administration of TheranekronR in cows, *Comp Clin Path.*, 16(3) (2007) 197-200.
- [23] Gultiken N., Guvenc T., Kaya D., Agaoglu A.R., Ay S.S., Kucukaslan I., Emre B., Findik M., Schafer-Somi S., Aslan S., *Tarantula cubensis* extract alters the degree of apoptosis and mitosis in canine mammary adenocarcinomas, *J Vet Sci.*, 16(2) (2015) 213-9.
- [24] Al-Asmari A.K., Riyasdeen A., Al-Shahrani M.H., Islam M., Snake venom causes apoptosis by increasing the reactive oxygen species in colorectal and breast cancer cell lines, *Onco Targets Ther.*, 15 (2022) 1289.
- [25] Akhtar B., Muhammad F., Sharif A., Anwar M.I., Mechanistic insights of snake venom disintegrins in cancer treatment, *Eur J Pharmacol.*, 899 (2021) 174022.
- [26] Chong H.P., Tan K.Y., Tan C.H., Cytotoxicity of snake venoms and cytotoxins from two southeast Asian cobras (*Naja sumatrana*, *Naja kaouthia*): exploration of anticancer potential, selectivity, and cell death mechanism, *Front Mol Biosci.*, 7 (2020) 583587.
- [27] Orrenius S., Gogvadze V., Zhivotovsky B., Mitochondrial Oxidative Stress: Implications for Cell Death, *Annu Rev Pharmacol Toxicol.*, 47 (2007) 143-183.
- [28] Yokoyama C., Sueyoshi Y., Ema M., Mori Y., Takaishi K., Hisatomi H., Induction of oxidative stress by anticancer drugs in the presence and absence of cells, *Oncol Lett.*, 14(5) (2017) 6066-70.
- [29] Çamlı Pulat Ç., In vitro cytotoxic activity of *Tarantula cubensis* alcoholic extract on different human cell lines. *Cumhuriyet Sci. J.*, 42(2) (2021) 252-259.
- [30] İlhan S., Can a Veterinary Drug be Repurposed for Human Cancers?: Cytotoxic Effect of *Tarantula cubensis* Venom on Human Cancer Cells. *Journal of the Institute of Science and Technology*, 11(3) (2021) 1763-1769.
- [31] Andreyev A.Y., Kushnareva Y.E., Starkov A.A., Mitochondrial metabolism of reactive oxygen species, *Biochemistry*, 70 (2005) 200-214.
- [32] Vermes I., Haanen C., Steffens-Nakken H., Reutelingsperger C., A novel assay for apoptosis Flow cytometric detection of phosphatidylserine early apoptotic cells using fluorescein labelled expression on Annexin V. *Journal of Immunological Methods*, 184 (1995) 39-51
- [33] Dasari M., Acharya A.P., Kim D., Lee S., Lee S., Rhea J., Molinaro R., Murthy N., H-gemcitabine: A new gemcitabine prodrug for treating cancer, *Bioconjugate Chem.*, 24 (2013) 4-8.

The Anti-proliferative Effect of Caffeic Acid and Dactolisib on Human Cervical Carcinoma HeLa Cell Line

Zeynep Büşra Bolat^{1,2,3,a,*}

¹ Department of Molecular Biology and Genetics, Faculty of Engineering and Natural Sciences, Istanbul Sabahattin Zaim University, İstanbul, 34303 Türkiye.

² Molecular Biology and Genetics Department, Hamidiye Institute of Health Sciences, University of Health Sciences-Turkey, İstanbul, 34668, Türkiye.

³ Experimental Medicine Research and Application Center, University of Health Sciences-Turkey, İstanbul, 34662, Türkiye.

*Corresponding author

Research Article

History

Received: 23/11/2023

Accepted: 27/02/2024



This article is licensed under a Creative Commons Attribution-NonCommercial 4.0 International License (CC BY-NC 4.0)

ABSTRACT

Cervical carcinoma is a common gynecological cancer with high mortality rate among women worldwide. Caffeic acid exerts an antiproliferative effect against cervical carcinoma. Dactolisib is a dual PI3K and mTOR inhibitor that has a therapeutic potential for cervical carcinoma. This study aimed to reveal the anti-proliferative effect of combination treatment of caffeic acid and Dactolisib on cervical carcinoma HeLa cell line. Cytotoxicity of caffeic acid and Dactolisib on HeLa cell line was assessed by MTS assay. Colony formation of HeLa cells treated with caffeic acid and Dactolisib was determined by staining colonies with crystal violet and visualizing under light microscope. Dactolisib decreased cell proliferation of HeLa cells in time and dose dependent manner. 5 μ M caffeic acid did not show any significant change in cell viability of HeLa cells. Combination treatment of 5 μ M caffeic acid and 0.5 μ M Dactolisib showed decrease in cell viability of HeLa cells when compared to Dactolisib treated cells. Combination of caffeic acid and Dactolisib decreased colony diameter of HeLa cells significantly when compared to control group. Caffeic acid and Dactolisib shows anti-proliferative effect on human cervical carcinoma HeLa cell line, so further studies should be performed to reveal the mechanism of action.

Keywords: Cervical carcinoma, Dactolisib, Caffeic acid, Anti-proliferative effect.

^a zeynepbusra.bolat@sbu.edu.tr  <https://orcid.org/0000-0002-9216-6336>

Introduction

Cervical carcinoma, a common gynecological cancer, is the fourth most diagnosed cancer with high morbidity and mortality rate among women worldwide. Despite the successful smear screening and advanced treatment programs, each year new cervical carcinoma cases are being reported [1]. Current treatment modalities include radiotherapy, chemotherapy and surgery applied alone or in combination [2]. Platinum-based compounds are used as a first line chemotherapy to treat cervical carcinoma; however, drug resistance is seen in patients [3]. Thus, novel strategies such as natural anticancer compounds and conventional chemotherapeutics are used as combination cancer therapy to optimize the efficacy of chemotherapy regimens [4].

Caffeic acid (CA), a member of phenolic acid family of polyphenols, shows significant therapeutic and biological activities in disease treatment [5]. CA demonstrates anti-inflammatory, anti-bacterial, anti-oxidant and antiproliferative properties [6]. CA shows antitumor effect on hepatocarcinoma [7], melanoma [8], prostate [9], breast [10], ovarian [11] and cervical cancer [12]. CA can affect cancer cells alone or in combination with chemotherapeutic drug, to decrease the drugs dose and overcome resistance against those drugs [13]. Previous studies show that combination of cisplatin and CA significantly increased apoptosis in cervical carcinoma when compared to cisplatin administered alone [14].

Thus, new combination treatment strategies targeting key pathways is crucial for cervical carcinoma therapy.

The phosphatidylinositol 3-kinase/protein kinase B/mammalian target of rapamycin (PI3K/Akt/mTOR) is a key pathway that plays a role in wide range of normal cellular functions. In various cancers, somatic mutations in genes related with PI3K or mTOR pathway lead to constitutive activation of pathway which lead to dysregulation of tumor cell proliferation and cell survival [15]. Studies show that HPV oncogenes can activate the PI3K/Akt/mTOR signaling pathway to modulate tumor progression and initiation [16]. PI3K is amplified and activated in HPV-induced cervical cancers [17]. Dactolisib (NVP-BE2235), an imidazo [4, 5-c] quinoline derivative, is a dual inhibitor of PI3K and mTOR kinases that is in phase I/II clinical trials for solid tumors. Dactolisib inhibits by binding to the ATP-binding cleft of PI3K and mTOR kinases [18]. Dactolisib suppressed HeLa cell invasiveness and metastasis by inhibiting the PI3K/Akt pathway. PI3K/Akt/mTOR signaling pathway activation promotes tumorigenesis of cervical carcinoma, thus inhibiting this pathway may be a strategy for targeting therapies [19]. Furthermore, a recent study shows that HeLa cell line was more sensitive to Dactolisib compared to other key pathway inhibitors, suggesting that this PI3K/mTOR inhibitor therapy may be a potential benefit to cervical cancer patient [20].

The purpose of this study was to identify the anti-proliferative effect of CA and Dactolisib on cervical carcinoma HeLa cell line. Cell viability of HeLa cell line was investigated under the treatment of CA, Dactolisib or their combination. The growth inhibition of HeLa cell line was assessed through colony formation assay. The present study suggests that combination therapy of CA and Dactolisib for treatment of cervical carcinoma may be a potential therapy. However, further studies are needed to reveal the mechanism of action of this combination therapy.

Material and Method

Reagents

Dactolisib was obtained by Selleck chemicals and dissolved in DMSO to obtain stock concentration of 2.12 mM. CA was purchased from Sigma-Aldrich and dissolved in DMSO to obtain stock concentration of 20 mM. The final concentration of DMSO was less than 0.1% in all cell cultures. MTS (3-(4,5-di-methyl-thiazol-2-yl)-5-(3-carboxy-methoxy-phenyl)-2-(4-sulfo-phenyl)-2H-tetrazolium) was purchased from Promega and crystal violet was obtained by Sigma-Aldrich.

Cell culture

The human cervical carcinoma HeLa cell lines were maintained in Dulbecco's Modified Eagle Medium (DMEM, Gibco) supplemented with 100 U/mL penicillin, 0.1 mg/mL streptomycin and amphotericin (1% PSA, Gibco) solution and 10% fetal bovine serum (FBS, Sigma-Aldrich). Cells were maintained in a humidified incubator with 5% CO₂ at 37 °C conditions.

Cell Viability Assay

Cell viability was determined using MTS colorimetric assay. In 96-well plates, HeLa cells were seeded with a density of 5×10^3 cells/well. After 24 h, cells were treated with Dactolisib, CA or their combination for 24 h and 48 h. After incubation period, cells were subjected to a mixture of MTS reagent and DMEM medium and the absorbance value was measured using a microplate reader (Bio-tek ELx800, USA) at 490 nm. Cell viability (%) was calculated by setting non-treated control cells to 100%.

Colony Forming Assay

HeLa cells were seeded at a density of 300 cells/ well in 6-well plates and incubated overnight to allow attachment of cells. The following day, HeLa cells were treated with Dactolisib, CA or combination of both and incubated for 14 days. Following incubation time, each well was fixed with 100% methanol at 4 °C for 20 minutes and stained with crystal violet for 5 minutes. The number

of colonies were counted under an inverted light microscope at 4× magnification (DMI1, Leica Microsystems) combined with a digital camera.

Statistical Analysis

All experiments were performed (n=3) and results are expressed as the mean ± SD. Free trial version of GraphPad Prism 8.0 was used to draw graphics and t-test or two-way ANOVA was used as statistical analysis. $P < 0.05$ (*), $p < 0.01$ (**), $p < 0.001$ (***) and $p < 0.0001$ (****) were considered statistically significant.

Results

Combination treatment of CA and Dactolisib induces anti-proliferative effect in HeLa cells

Cell proliferation MTS assay was used to determine the cytotoxic effect of Dactolisib, CA or a combination of both on HeLa cell lines. Dactolisib demonstrated significant cytotoxicity on HeLa cell lines in time and dose-dependent manner. At 24 h, there was a significant decrease in cell viability of HeLa cells to 83.6%, 85.5%, 83.8%, 66.0% and 62.5% when treated with 0.25, 0.5, 1, 2 and 4 μM Dactolisib, respectively. A decrease to 64.7%, 65.8%, 60.9%, 60.0%, and 57.4% was detected in HeLa cells when treated with 0.25, 0.5, 1, 2 and 4 μM Dactolisib, respectively at 48 h (Fig. 1).

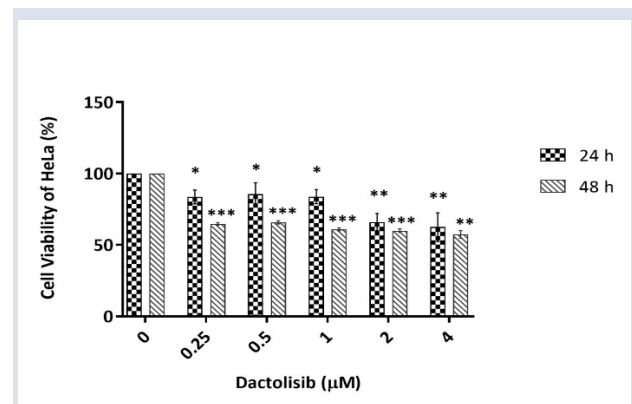


Figure 1. Cell viability of HeLa cells after exposure to 0.25 - 4 μM Dactolisib for 24 h and 48 h. The control group represents cells with no treatment. Data represents average of three independent experiments ± SD ($p < 0.05$ (*), $p < 0.01$ (**), and $p < 0.001$ (***)).

HeLa cells treated with 5 μM CA did not show any change ($p > 0.05$) in cell viability at 24h and 48h. CA demonstrated significant cytotoxicity on HeLa cell lines only at high dosage (40 μM). At 24 h, there was no significant change in cell viability of HeLa cells when treated with 5, 10 and 20 μM CA, showing a slight decrease of 3%, 2% and 7%, respectively. Similarly at 48 h, a slight ($p > 0.05$) decrease of 1% and 8% was detected when HeLa cells were treated with 10 and 20 μM CA, respectively. On the contrary, significant decrease in cell

viability of HeLa cells were detected when treated with 40 μM CA at 24h and 48 h (Fig. 2).

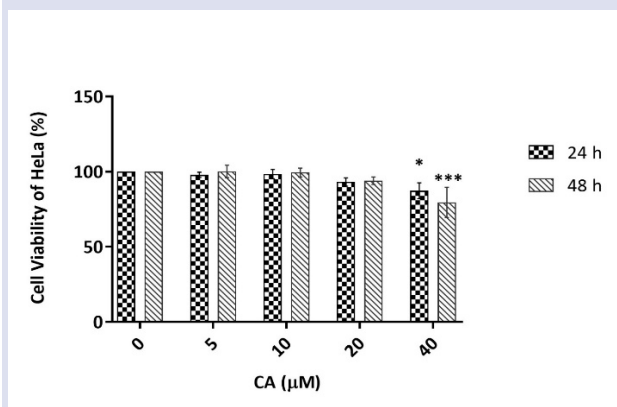


Figure 2. Cell viability of HeLa cells after exposure to 5- 40 μM CA for 24 h and 48 h. The control group represents cells with no treatment. Data represents average of three independent experiments \pm SD ($p < 0.05$ (*)) and $p < 0.001$ (***)).

As shown in Figure 3, cell viability of HeLa cells when treated with low doses of Dactolisib (0.25 μM and 0.5 μM) alone and in combination with CA was evaluated using MTS assay. There was no significant decrease in CA and control group at all time points. A significant decrease was observed in cell viability of HeLa cells treated with 0.25 μM Dactolisib alone and in combination (CA and Dactolisib) group when compared to CA group at all time points. No significant change ($p > 0.05$) was detected between 0.25 μM Dactolisib alone and in combination group (Figure 3A).

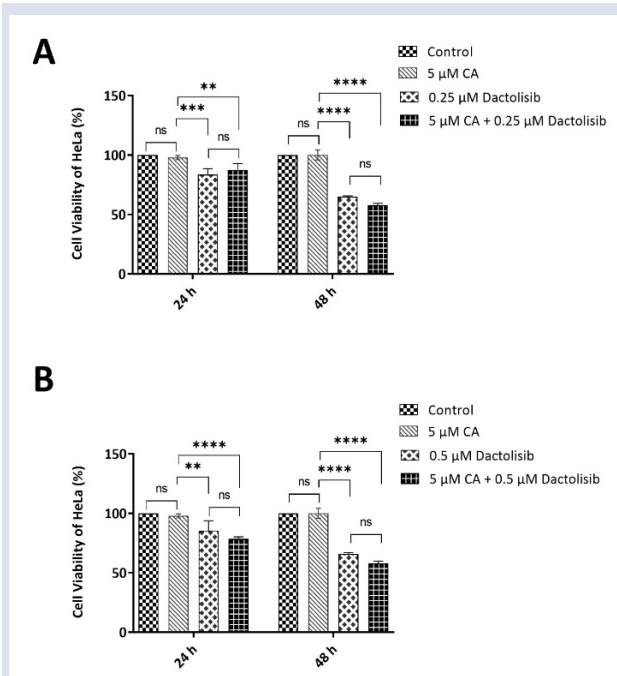


Figure 3. Cell viability of HeLa cells after exposure to (A) combination of 5 μM CA and 0.25 μM Dactolisib and (B) combination of 5 μM CA and 0.5 μM Dactolisib for 24 h and 48 h. The control group represents cells with no treatment. Data represents average of three independent experiments \pm SD ($p < 0.01$ (**), $P < 0.001$ (***) and $P < 0.0001$ (****)).

Similarly, HeLa cells treated with 0.5 μM Dactolisib alone and in combination with CA showed significant decrease in cell viability when compared to CA group at 24 and 48 h. No significant change ($p > 0.05$) was detected between 0.5 μM Dactolisib alone and in combination with CA group (Figure 3B).

Combination Treatment of CA and Dactolisib Inhibits Growth Formation of HeLa Cells

Cell colony formation assay was used to determine the effect of CA and Dactolisib HeLa cells were incubated with Dactolisib, CA or combination of both for 14 days. The number of colonies for each group was counted. The well images and colonies under light microscope show that the number of colonies was reduced in Dactolisib alone and in combination with CA groups compared to control group (Fig. 4A-B). The colony diameters of HeLa cells were nearly 1.504, 0.213 and 0.127 mm for CA, Dactolisib and combination group, respectively. For control (un-treated) group the colony diameter was 1.719 mm. Thus, there was no significant change in colony diameter of HeLa cells when treated with CA. The colony diameter of HeLa cells decreased significantly when treated with Dactolisib alone and in combination with CA. This indicates that Dactolisib has inhibitory effect in HeLa cell formation (Fig. 4C).

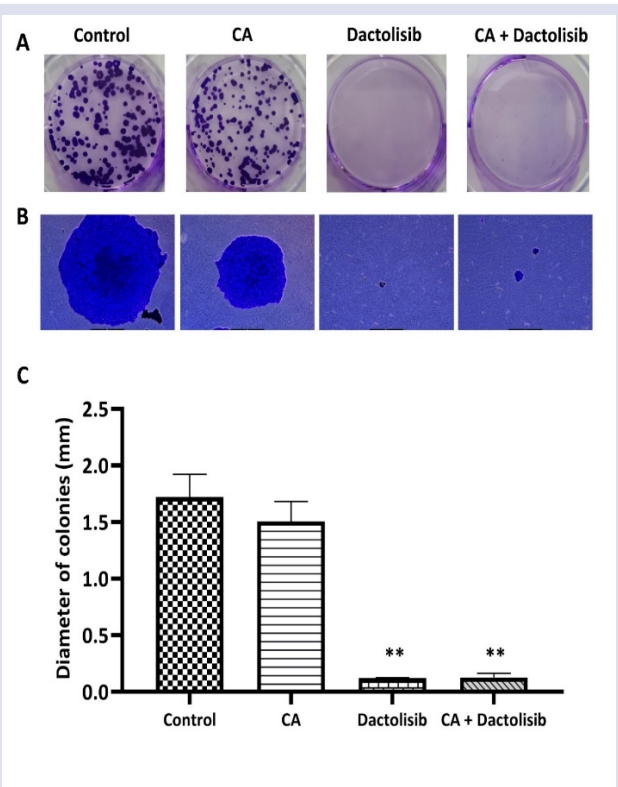


Figure 4. Colony formation of HeLa cells treated with 5 μM CA, 0.5 μM Dactolisib or a combination of both. (A) Representative images of colony formation in 6-well, (B) under light microscope and (C) the diameter of colonies observed in the HeLa cells after 14 days treatments with Dactolisib, CA or combination of both. Scale bar: 620 μm . $P < 0.01$ (**).

Discussion

Cervical carcinoma is one of the leading causes of cancer related deaths in females worldwide. Chemotherapy is the first line therapy in cervical carcinoma however, drug resistance is commonly seen [21]. PI3K/mTOR pathway is required for a wide range of normal cellular functions and is a major signaling pathway that modulate survival in cancer cells. Studies show that in various types of cancer, somatic mutations in genes related with PI3K or mTOR induces constitutive pathway activation; causing dysregulation of tumor cell growth, proliferation and apoptosis [15]. Activation of the PI3K/Akt/mTOR pathway promotes tumorigenesis of cervical carcinoma and this pathway may be a novel candidate for targeting this cancer [22]. Rapamycin is used by many researchers to inhibit the mTOR signaling pathway. This drug only inhibits mTOR complex (TORC) 1 causing it to induce Akt phosphorylation by feedback activation [23], which results in the reduction of the anti-cancer effect of rapamycin. Thus, more effective inhibitors targeting these pathways are needed.

Dactolisib is a dual PI3K and mTOR kinase inhibitor showing promise in preclinical mouse models for solid tumors [24]. A study conducted by Xie et. al., shows that Dactolisib has an anti-proliferative and anti-cancer effect on cervical carcinoma HeLa, SiHa and C33A cells and it has a potential in treatment of cervical carcinoma. 320 nM Dactolisib showed a significant decrease of cell viability in HeLa cells by reducing the cell viability to nearly 25% at 48 h using MTT assay [19]. In the current study, Dactolisib showed significant cytotoxicity on HeLa cell lines in time and dose-dependent manner (Figure 1). However, at highest dosage of 4 μ M Dactolisib there was only decrease of HeLa cell viability to 57%. Our results show that low doses of Dactolisib did not have effective anti-proliferative effect on HeLa cells as literature. The final concentration of DMSO for both studies were stated as being less than 0.1%, so these differences could be due to different cell viability assays. Even though both MTT and MTS are tetrazolium based assays, they could show differences in cell viability [25].

Combination treatment of phytochemicals and chemotherapeutic act as a novel approach to cancer therapy as it increase the cancer treatment efficacy and reduce adverse side effects [26]. CA is a polyphenol phytochemical which shows antitumor effect on cervical carcinoma [12]. In the present study, (5- 20 μ M) CA did have a significant effect on HeLa cells except when treated with 40 μ M CA (Figure 2). Thus, low doses of CA could not be used as an effective anti-cancer agent, however potential synergism of CA combining with anticancer drug should be evaluated. The combination treatment of CA and Dactolisib exhibit anti-proliferative effect on cervical carcinoma HeLa cell line. CA administered alone on HeLa cells did not have a significant effect (nearly 99% viable cells). Dactolisib administered alone and in combination with CA showed nearly 7% more decrease in cell viability of HeLa cells (Figure 3). Studies show that synergistic

effect was observed when CA was given in combination with other inhibitors suggesting a synergism [27]. Thus, CA could be a phytochemicals candidate for increasing efficacy of cancer treatment when administered with another drug.

Clonogenic cell survival assay determines the ability of a cell to proliferate and this assay shows antiproliferative effect of a drug. Dactolisib inhibits the colony formation of HeLa cells in 10 days, showing a dose dependent inhibition in HeLa cells [19]. In the present study, we have shown that Dactolisib alone or in combination with CA and Dactolisib inhibits the growth of colonies formed by HeLa cells at 14 days. The diameter of colonies significantly decreased in Dactolisib alone and in combination treated groups (Figure 4C). Interestingly, Dactolisib alone treated HeLa cells had slightly less colony number and diameter compared to combination group, but with no significant differences. Thus, these results confirm that CA and Dactolisib exert anti-proliferative effect on HeLa cells.

In conclusion, the PI3K/Akt/mTOR pathway is a key signaling pathway which promotes tumorigenesis of cervical carcinoma. Dactolisib is a potential anti-proliferative agent against cervical carcinoma. CA is a polyphenol that has an anticancer effect against cervical carcinoma. This is the first study in literature representing the anti-proliferative effect of combination treatment of CA and Dactolisib in cervical carcinoma. Dactolisib shows decrease of cell viability in HeLa cells in dose and time dependent manner, while CA did not show any significant differences in cell viability. The colony formation was inhibited significantly in HeLa cells when treated with CA and Dactolisib. Further studies are required to verify Dactolisib and CA to completely understand the anti-proliferative activity and mechanism of action in cervical carcinoma therapy.

Acknowledgement

The human cervical carcinoma HeLa cell lines was a kind gift of Prof. Aysegul Dogan at Yeditepe University.

Conflict of interest

The author declares no conflict of interest.

References

- [1] Podwika S.E., Duska L.R, Top advances of the year: Cervical cancer, *Cancer*, 129 (2023) 657–63.
- [2] Bahrami A., Hasanzadeh M., Hassanian S.M., ShahidSales S., Ghayour-Mobarhan M., Ferns G.A., Avan A., The Potential Value of the PI3K/Akt/mTOR Signaling Pathway for Assessing Prognosis in Cervical Cancer and as a Target for Therapy, *J of Cell. Biochem.*, 118 (2017) 4163–9.
- [3] Brown A., Kumar S., Tchounwou P.B., Cisplatin-Based Chemotherapy of Human Cancers, *J.Cancer Sci Ther*, 11(4) (2020).
- [4] Hussain Y., Islam L., Khan H., Filosa R., Aschner M., Javed S., Curcumin–cisplatin chemotherapy: A novel strategy in

- promoting chemotherapy efficacy and reducing side effects, *Phytother. Res.*, 35 (12) (2021) 6514–6529.
- [5] Mirzaei S., Gholami M.H., Zabolian A., Saleki H., Farahani M.V., Hamzehlou S., et al., Caffeic acid and its derivatives as potential modulators of oncogenic molecular pathways: New hope in the fight against cancer, *Pharmacol. Res.*, 171 (2021) 105759.
- [6] Alam M., Ashraf G.M., Sheikh K., Khan A., Ali S., Ansari MdM., Adnan M., Pasupuleti V.R., Hassan M.I., Potential Therapeutic Implications of Caffeic Acid in Cancer Signaling: Past, Present, and Future, *Front Pharmacol.*, 13 (2022) 845871.
- [7] Chung T., Moon S., Chang Y., Ko J., Lee Y.C., Cho G., Kim S.H., Kim J.G., Kim C.H., Novel and therapeutic effect of caffeic acid and caffeic acid phenyl ester on hepatocarcinoma cells: complete regression of hepatoma growth and metastasis by dual mechanism, *FASEB J.*, 18 (14) (2004) 1670–81.
- [8] Pelinson L.P., Assmann C.E., Palma T.V., Da Cruz IBM., Pillat M.M., Mânica A., et al., Antiproliferative and apoptotic effects of caffeic acid on SK-Mel-28 human melanoma cancer cells, *Mol Biol Rep*, 46 (2) (2019) 2085–92.
- [9] Sanderson J.T., Clabault H., Patton C., Lassalle-Claux G., Jean-François J., Paré A.F., Hébert M.J.G., Surette M.E., Touaibia M., Antiproliferative, antiandrogenic and cytotoxic effects of novel caffeic acid derivatives in LNCaP human androgen-dependent prostate cancer cells, *Bioorg Med Chem*, 21 (22) (2013) 7182–93.
- [10] Kabała-Dzik A., Rzepecka-Stojko A., Kubina R., Wojtyczka R.D., Buszman E., Stojko J., Caffeic Acid Versus Caffeic Acid Phenethyl Ester in the Treatment of Breast Cancer MCF-7 Cells: Migration Rate Inhibition, *Integr Cancer Ther*, 17 (4) (2018) 1247–1259.
- [11] Kleczka A., Kubina R., Dzik R., Jasik K., Stojko J., Cholewa K., Kabała-Dzik A., Caffeic Acid Phenethyl Ester (CAPE) Induced Apoptosis in Serous Ovarian Cancer OV7 Cells by Deregulation of BCL2/BAX Genes, *Molecules*, 25 (2020) 3514.
- [12] Teng Y.-N., Wang C.C.N., Liao W.-C., Lan Y.-H., Hung C.-C., Caffeic Acid Attenuates Multi-Drug Resistance in Cancer Cells by Inhibiting Efflux Function of Human P-Glycoprotein, *Molecules*, 25 (2020) 247.
- [13] Pavlíková N., Caffeic Acid and Diseases—Mechanisms of Action, *Int. J. Mol. Sci.*, 24 (1) (2022) 588.
- [14] Koraneekit A., Limpaboon T., Sangka A., Boonsiri P., Daduang S., Daduang J., Synergistic effects of cisplatin-caffeic acid induces apoptosis in human cervical cancer cells via the mitochondrial pathways, *Oncol. Lett.*, 15 (5) (2018) 7397-7402.
- [15] Polivka J., Janku F., Molecular targets for cancer therapy in the PI3K/AKT/mTOR pathway, *Pharmacol. Ther.*, 142 (2014) 164–75.
- [16] Zhang L., Wu J., Ling M.T., Zhao L., Zhao K.-N., The role of the PI3K/Akt/mTOR signalling pathway in human cancers induced by infection with human papillomaviruses, *Mol Cancer*, 14 (2015) 87.
- [17] Lee C.M., Fuhrman C.B., Planelles V., Peltier M.R., Gaffney D.K., Soisson A.P., Dodson M. K., Tolley H. D., Green C. L., Zempolich K. A., Phosphatidylinositol 3-Kinase Inhibition by LY294002 Radiosensitizes Human Cervical Cancer Cell Lines, *Clin. Cancer Res.*, 12 (1) (2006) 250–6.
- [18] Maira S.-M., Stauffer F., Brueggen J., Furet P., Schnell C., Fritsch C., et al., Identification and characterization of NVP-BEZ235, a new orally available dual phosphatidylinositol 3-kinase/mammalian target of rapamycin inhibitor with potent in vivo antitumor activity, *Mol Cancer Ther.*, 7 (7) (2008) 1851–63.
- [19] Xie G., Wang Z., Chen Y., Zhang S., Feng L., Meng F., Yu Z., Dual blocking of PI3K and mTOR signaling by NVP-BEZ235 inhibits proliferation in cervical carcinoma cells and enhances therapeutic response, *Cancer Lett.*, 388 (2017) 12–20.
- [20] Hamid M.B., Serafin A.M., Akudugu J.M., Selective therapeutic benefit of X-rays and inhibitors of EGFR, PI3K/mTOR, and Bcl-2 in breast, lung, and cervical cancer cells, *Eur. J. Pharmacol.*, 912 (2021) 174612.
- [21] Lando M., Holden M., Bergersen L.C., Svendsrud D.H., Stokke T., Sundfør K., Glad I. K., Kristensen G. B., Lyng H., Gene Dosage, Expression, and Ontology Analysis Identifies Driver Genes in the Carcinogenesis and Chemoradioresistance of Cervical Cancer, *PLoS Genet.*, 5 (2009) e1000719.
- [22] Feng T., Zheng L., Liu F., Xu X., Mao S., Wang X., Liu J., Lu Y., Zhao W., Yu X., Tang W., Growth factor progranulin promotes tumorigenesis of cervical cancer via PI3K/Akt/mTOR signaling pathway, *Oncotarget*, 7 (2016) 58381–58395.
- [23] O'Reilly K.E., Rojo F., She Q.-B., Solit D., Mills G.B., Smith D., Lane H., Hofmann F., Hicklin D. J., Ludwig D. L., Baselga J., Rosen N., mTOR Inhibition Induces Upstream Receptor Tyrosine Kinase Signaling and Activates Akt, *Cancer Res.*, 66 (3) (2006) 1500–8.
- [24] Gil Del Alcazar C.R., Hardebeck M.C., Mukherjee B., Tomimatsu N., Gao X., Yan J., Xie X. J., Bachoo R., Li L., Habib A. A., Burma S., Inhibition of DNA Double-Strand Break Repair by the Dual PI3K/mTOR Inhibitor NVP-BEZ235 as a Strategy for Radiosensitization of Glioblastoma, *Clin. Cancer Res.*, 20 (5) (2014) 1235–48.
- [25] Wang P., Henning S.M., Heber D., Limitations of MTT and MTS-Based Assays for Measurement of Antiproliferative Activity of Green Tea Polyphenols, *PLoS ONE*, 5 (4) (2010) e10202.
- [26] Gao Q., Feng J., Liu W., Wen C., Wu Y., Liao Q., Zou L., Sui X., Xie T., Zhang J., Hu Y., Opportunities and challenges for co-delivery nanomedicines based on combination of phytochemicals with chemotherapeutic drugs in cancer treatment, *Adv. Drug Deliv. Rev.*, 188 (2022) 114445.
- [27] Ialongo D., Tudino V., Arpacioğlu M., Messore A., Patacchini E., Costi R., Santo R. D., Madia V. N., Synergistic Effects of Caffeine in Combination with Conventional Drugs: Perspectives of a Drug That Never Ages, *Pharmaceuticals*, 16 (2023) 730.

Comparison of Characteristics and Antimicrobial Activity of Synthesized Zinc Oxide And Magnetite Iron Oxide Nanoparticles Using Four Different Plant Extracts

Burcu Aydođdu ^{1,a,*}, Mehmet Aytar ^{2,b}, İlky Ünal ^{3,c}

¹ Department of Mechanical Engineering, Faculty of Engineering, Munzur University, Tunceli, Türkiye.

² Department of Biology, Graduate School of Natural and Applied Sciences, Adnan Menderes University, Aydın, Türkiye.

³ Department of Gastronomy and Culinary Arts, Faculty of Fine Arts, Design and Architecture Education, Munzur University, Tunceli, Türkiye.

*Corresponding author

Research Article

History

Received: 03/10/2023

Accepted: 12/01/2024



This article is licensed under a Creative Commons Attribution-NonCommercial 4.0 International License (CC BY-NC 4.0)


ABSTRACT


The aim of this study was to synthesize Zinc oxide (ZnO) and magnetite iron oxide (Fe₃O₄) nanoparticles utilizing a precipitation method, employing plant extracts from *Ocimum basilica*(1), *Cinnamomum zeylanicum*(2), *Lactarius salmonicolor*(3) and *Paeonia kesrouanensis*(4) as reduction and stabilizing agents. Additionally, the antimicrobial activity of these nanoparticles against both gram-positive (*S. aureus*, ATCC 25923) and gram-negative (*E. coli*, ATCC 25922; *P. aeruginosa*, PAO1), bacteria as well as fungus (*C. albicans* 90028) was evaluated. The nanoparticles (NPs) were characterised by various analyses, including TEM, SEM, XRD, FTIR, DSL, and zeta potential. Based on the TEM image, the ZnONPs exhibited a cluster of flower-like structures, whereas the Fe₃O₄NPs displayed a spherical shape with a varying size distribution. The zeta potential values for ZnO NPs ranged from -5.35 to -16.9, while for Fe₃O₄NPs ranged from -7.43 to -20.7. All ZnO nanoparticles exhibited antimicrobial activity exclusively against the *S. aureus* strain, whereas Fe₃O₄NPs did not demonstrate any antibacterial effect.

Keywords: Antimicrobial activity, Green synthesis, Magnetite iron oxide, Zinc oxide

 burcuaydogdu@munzur.edu.tr

 <https://orcid.org/0000-0002-3309-1995>

 ilkayunal@munzur.edu.tr

 <https://orcid.org/0000-0002-1587-4187>

 maytar90@gmail.com

 <https://orcid.org/0000-0002-8083-7358>

Introduction

Nanoparticles (NPs) are particles in the nanoscale, typically ranging in size from 1 to 100 nanometers, and they exhibit distinctive characteristics and behaviours compared to their bulk counterparts, primarily because of their small size and high surface-to-volume ratio[1]. Overall, nanoparticles play an important role in advancing technology and have a wide range of applications in various industries including materials research, health, drug delivery, electronics, optics, environmental remediation, cosmetics, and sunscreens[2]. Their unique properties make them valuable building blocks for the development of innovative materials, devices and systems[3]. Zinc oxide nanoparticles are a widely used material in various applications such as electronics, antibacterial coatings, wound dressings and cosmetics due to their excellent high surface area to volume ratio, optical properties, semiconductor behavior, antibacterial and antifungal activity, photocatalytic activity, electrical conductivity and biocompatibility.[4]. Iron oxide nanoparticles, alternatively referred to as magnetic iron oxide nanoparticles or ferrite nanoparticles, have garnered substantial attention across multiple disciplines. superparamagnetism properties that make them valuable in a variety of applications like magnetic resonance imaging (MRI), drug delivery, and hyperthermia therapy[5]. Nanoparticles are typically synthesized using a

variety of techniques, including chemical, physical, and biological methods. Green synthesis refers to the production of nanoparticles using environmentally friendly and sustainable techniques using biomolecules, yeast, bacteria, plant or their extracts[6]. The green synthesis approach aims to minimize the use of hazardous chemicals and reduce the environmental impacts associated with conventional synthesis methods[7]. Plant extracts serve as natural sources of reducing and stabilizing agents. Other reasons for their use include the plant's easy availability, it's content of biocompatible bioactive compounds, and control of size and shape. It is important to note that the properties and characteristics of nanoparticles synthesized with plant extracts may vary depending on factors such as plant species, extract composition, synthesis conditions, and purification methods. *Aloe vera* and *neem* extracts have also been studied for the green synthesis of zinc oxide nanoparticles [8,9]. The choice of plant extract depends on factors such as availability, phytochemical composition, and desired nanoparticle properties[10]. Each plant extracts may contain additional bioactive components that impart specific properties to the synthesized nanoparticles. These components may include antioxidants, antimicrobial agents, anti-inflammatory compounds, and other bioactive molecules[11]. This offers the possibility

of imparting therapeutic or functional properties to nanoparticles, thus expanding their potential applications in biomedicine and healthcare. The type of plant used is important as the plant extract contains some proteins, enzymes and other phytochemicals that can act as different reducing and stabilizing agents during the synthesis of nanoparticles. *Ocimum basilicum* has been used to treat illnesses such as anxiety, fever, infections, arthropod stings, stomach aches, cough, headaches, and constipation [12]. The same time, Basil polysaccharides have anti-tumor, anti-oxidant, anti-bacterial effects as well as anti-aging activity, anti-atherosclerotic effects, immunity enhancing effect and are useful in the treatment of diabetes [13]. *Cinnamomum zeylanicum* was traditionally used to treat arthritis, diarrhea, allergies and ulcers [14]. *Paeonia kesrouanensis* is a plant frequently used in Chinese medicine and has been reported to have been used in various treatments for centuries [15]. When the antimicrobial activity of the plant against microorganisms was evaluated, it was seen that the extract of the plant was 3 times more effective than Vancomycin, Penicillin and Erythromycin and 2 times more effective than Tetracycline [16]. *Lactarius salmonicolor* has been found to have antitumor, antimicrobial, antiviral, antiallergic, immunomodulatory, anti-inflammatory, antiatherogenic, hypoglycemic, hepatoprotective and central nervous system activities [17].

The aim of this study is to realize the green synthesis of zinc and magnetite nanoparticles by using extracts of four different plants as reducing/stabilizing agents without using chemicals. In addition, the effects of the different plant extracts used on the morphological structures and antimicrobial activities of the 8 synthesized nanoparticles were comparatively evaluated. As a result, the usage area of nanoparticles can be determined according to their specific properties. Nanoparticles synthesized using four plant extracts were coded as ZnONPs-1 and Fe₃O₄NPs-1 (*Ocimum basilicum*), ZnONPs-2 and Fe₃O₄NPs-2 (*Cinnamomum zeylanicum*), ZnONPs-3 and Fe₃O₄NPs-3 (*Lactarius salmonicolor*), ZnONPs-4 and Fe₃O₄NPs-4 (*Paeonia kesrouanensis*). The ZnONPs and Fe₃O₄NPs were characterized by microscopic and spectroscopic methods. The antimicrobial activity was evaluated against *Staphylococcus aureus* (*S. aureus*, 25923), *Pseudomonas aeruginosa* (PAO1, *P. aeruginosa*), *Escherichia coli* (*E. coli* 25922), *Candida albicans* (*C. albicans* 90028) strains.

Materials and Methods

Reagents

Iron(II) chloride (FeCl₂), Iron(III) chloride (FeCl₃), Zinc acetate (Zn(CH₃CO₂)₂·2H₂O), Sodium hydroxide (NaOH), Potassium hydroxide (KOH) were purchased from Sigma-Aldrich. The plants were obtained from the local market.

Preparation of the Plant Extract

Ocimum basilicum, *Cinnamomum zeylanicum*, *Lactarius salmonicolor*, *Paeonia kesrouanensis* were

washed several times to remove dirt and dried in the shade. 1 g of the plant was weighed and incubated individually in 100 mL of distilled water at 40°C for 24 hours. After cooling, it was filtered with filter paper and the filtrate was stored at 4°C.

Preparation of Bio-synthesized ZnONPs and Fe₃O₄NPs

ZnONPs and Fe₃O₄NPs were synthesized using 4 different plant extracts. General synthesis procedure below:

Synthesis of ZnONPs: A 0.1 M 25 mL zinc acetate solution was prepared in a falcon tube and kept in a water bath at 50 °C for 1 hour. Then, 25 mL of plant extract was added. The pH was adjusted to 6 with KOH. The mixture was kept in a shaking water bath at 60 °C for 2 hours. After this time, the solution was centrifuged, washed and dried in an oven at 100 °C for 24 hours.

Synthesis of Fe₃O₄NPs: 50 mL 0.14 M FeCl₂ and 50 mL 0.17 M FeCl₃ solution were prepared in Falcon tubes and kept in a water bath at 70 °C for 1 hour. After reaching room temperature, the FeCl₂ and FeCl₃ solutions were mixed. The mixture was stirred for 1 hour. The pH was adjusted to 9 with NaOH. Then, 25 ml of plant extract was added. The mixture was again kept in a shaking water bath at 70 °C for 2 hours. After this time, the solution was centrifuged, washed and dried in an oven at 100 °C for 24 hours [18].

Characterization Analysis

The crystallinity and structure of all samples were determined using X-ray diffractometer (XRD) Rigaku Miniflex (Japan) over a range of 2θ angles from 20° to 80°. Fourier transform infrared spectroscopy (FT-IR) was used to determine chemical functional groups of the samples using ATR-FTIR 6700 Jasco (Japan) in the 4000–400 cm⁻¹ range. The morphology of the nanoparticles were observed using transmission electron microscopy (TEM) (JOEL Brand, JEM-1011). Particle size and zeta potential value were measured using a Malvern Zetasizer Nano ZSP.

Antimicrobial Activity

The agar well Diffusion method was used to test the antimicrobial activity of all ZnO NPs and Fe₃O₄NPs against gram-negative *Escherichia coli* (*E. coli*, ATCC 25922), *Pseudomonas aeruginosa* (*P. aeruginosa*, PAO1), gram-positive *Staphylococcus aureus* (*S. aureus*, ATCC 25923) and *Candida albicans* (*C. albicans* 90028) fungus. Gram-positive and gram-negative microorganisms were incubated overnight on Tryptic soy agar (TSA) at 37°C, while *C. albicans* fungus was set on Potato Dextrose Agar (PDA) at 28°C. After incubation, suspensions of microorganisms at 0.5 McFarland turbidity were prepared in physiological saline and standardized suspensions of each bacterium were placed on Mueller-Hinton agar plates. 8 mm diameter wells were punched in the petri using a sterile cork borer. 100 ml of each sample prepared at two different concentrations, 5 and 10 mg/mL, was

added to the wells. Gentamicin and fluconazole solutions were used as control antibiotics for bacteria and fungi, respectively. Antimicrobial activity was measured as a zone of inhibition (mm) around the sample discs using a standard steel ruler after 24 hours of incubation. The experiment was carried out in triplicate.

Results and Discussion

TEM Results

Shape and morphology of green synthesised ZnO NPs and Fe₃O₄NPs were evaluated by TEM analysis (Fig. 1).

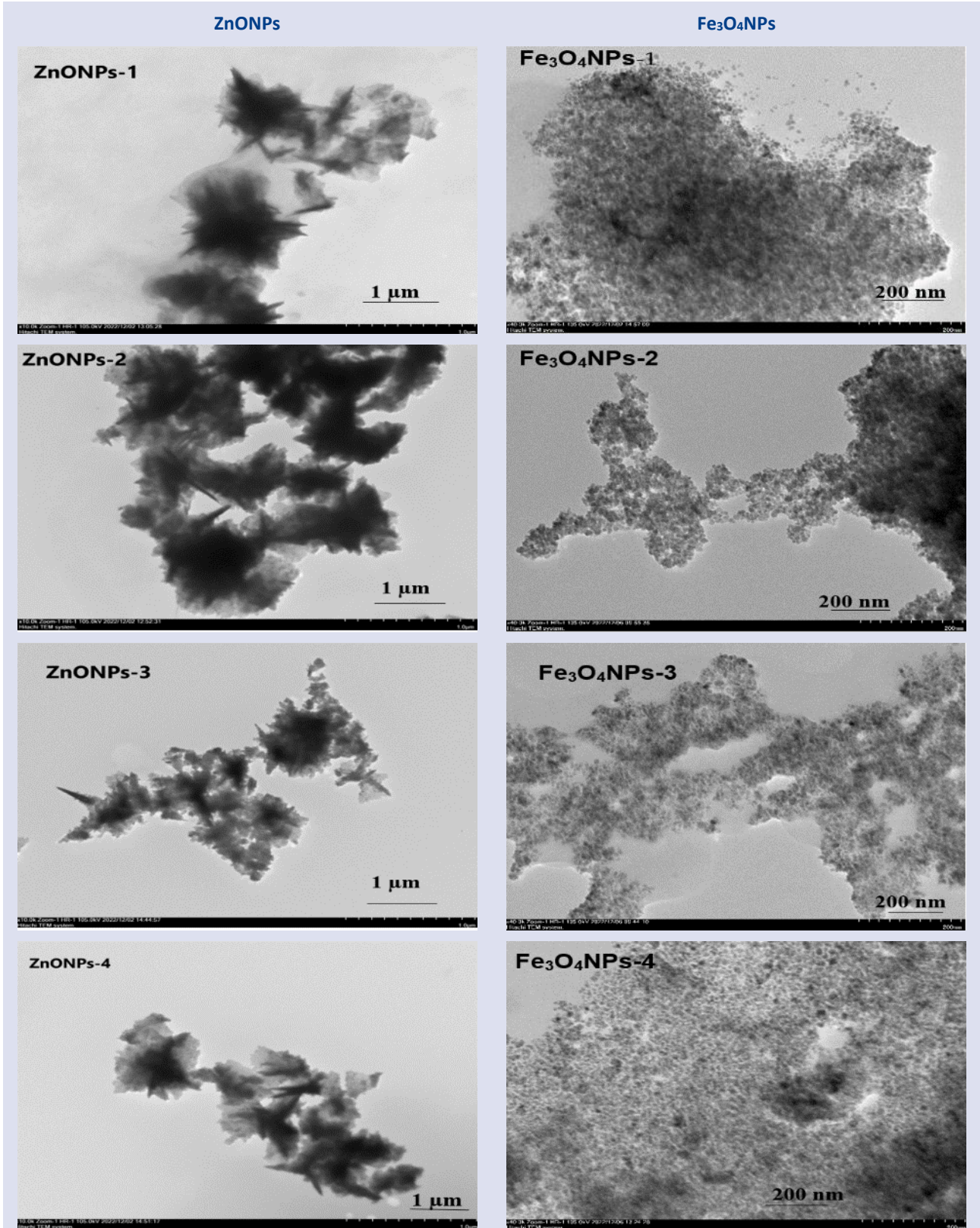


Figure 1. TEM image of ZnONPs and Fe₃O₄NPs

According to the TEM image, the ZnONPs showed a flower-like structure cluster, while the Fe₃O₄NPs had a spherical shape with different size distribution.

Among the synthesized NPs, ZnNPs-4 showed a smaller size distribution, while Fe₃O₄NPs-3 had a uniform and single-crystal. The size and shape of the NPs can be controlled according to experimental conditions, such as ratios of reactants, reducing/stabilizing agents, temperature, and time [19]. ZnONPs and Fe₃O₄NPs have different shapes such as rod-like, star-like, spherical, flower-like, cubes, triangles, or tetrapods, and isometric [20]. NP shapes are one of the most important factors influencing their areas of application. Mazitova et al. (2018) synthesized flower-like-ZnO nanoparticles by laser ablation of solid targets in a liquid [21].

XRD Results

The XRD results of synthesized ZnONPs and Fe₃O₄ NPs are given in Figure 2. The XRD spectrum of all Fe₃O₄NPs samples showed an intense diffraction peak at the 2θ regions corresponding to the crystal planes by Miller index (111), (220), (400), (422), (511), (440), and (531). The XRD pattern also showed that the particles have a face-centred cubic (FCC) crystal structure[22]. In addition, The miller index corresponding to the 100 plane shows that znO is hexagonal. (100), (002), (101), (102), (110), (103), (200), (112), (201), (004), and (202) planes of hexagonal ZnO nanoparticles (JCPDS 36-1451)[23].

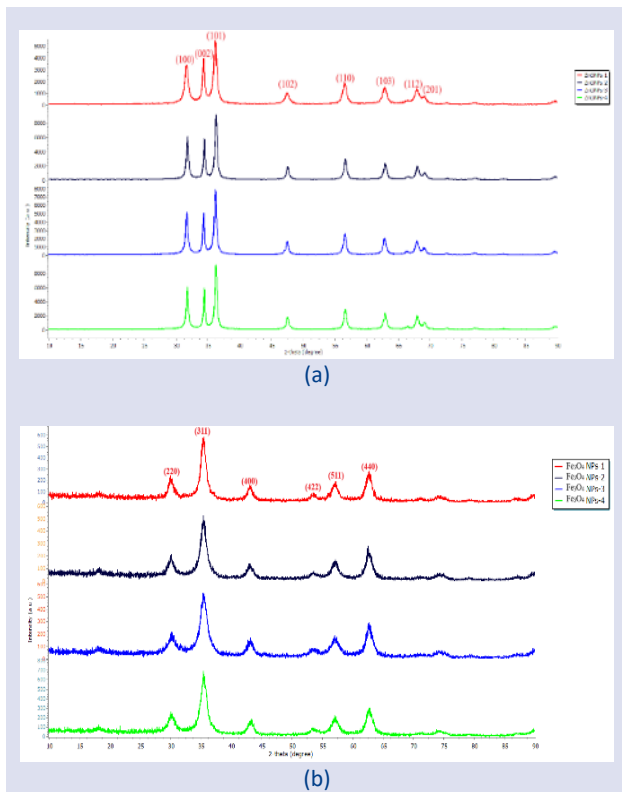


Figure 2. XRD graphs a) ZnONPs-1(red line), ZnONPs-2(navy blue line), ZnONPs-3 (blue line), ZnONPs-4 (green line) b)Fe₃O₄NP-1(red line), Fe₃O₄NP-2(navy blue line), Fe₃O₄NP-3 (blue line), Fe₃O₄NP-4 (green line)

ZnONPs exhibited more sharper and narrower XRD peaks, whereas Fe₃O₄NPs displayed broader peaks. This indicates that the phytochemicals present on the surface of the nanoparticles break the crystalline structure and make them amorphous. The average nanoparticle crystallite size was calculated from XRD peak broadening using the Debye-Scherrer equation for characteristic peaks.

$$D = K\lambda/\beta\cos\theta$$

where D represents the average diameter in nm, K presents the Scherrer constant (0.89), λ presents the wavelength of the X-ray (λ = 0.154056 nm), β presents the corresponding full width at half maximum (FWHM) of the peaks is the diffraction peak and θ represents the Bragg diffraction angle. The results are given in Tables 1-2. It was observed that the crystal size of Fe₃O₄NPs was lower than that of ZnONPs, which was compatible with the DLS results

Table 1. Average XRD crystallite size of the ZnONPs

Peak Number	Planes hkl	2θ			
		ZnONPs-1	ZnONPs-2	ZnONPs-3	ZnONPs-4
1	100	31.70	31.85	31.70	31.80
2	002	34.30	34.53	34.40	34.49
3	101	36.12	36.33	36.21	36.29
4	102	47.54	47.60	47.51	47.59
5	110	56.50	56.67	56.58	56.65
6	103	62.66	62.95	62.78	62.95
7	112	67.83	67.96	67.98	67.93
8	201	68.97	69.08	69.11	69.04
XRD Crystallite Size of The Samples		17.60 nm	20.11 nm	19.70 nm	21.52 nm

Table 2. Average XRD crystallite size of the Fe₃O₄NPs

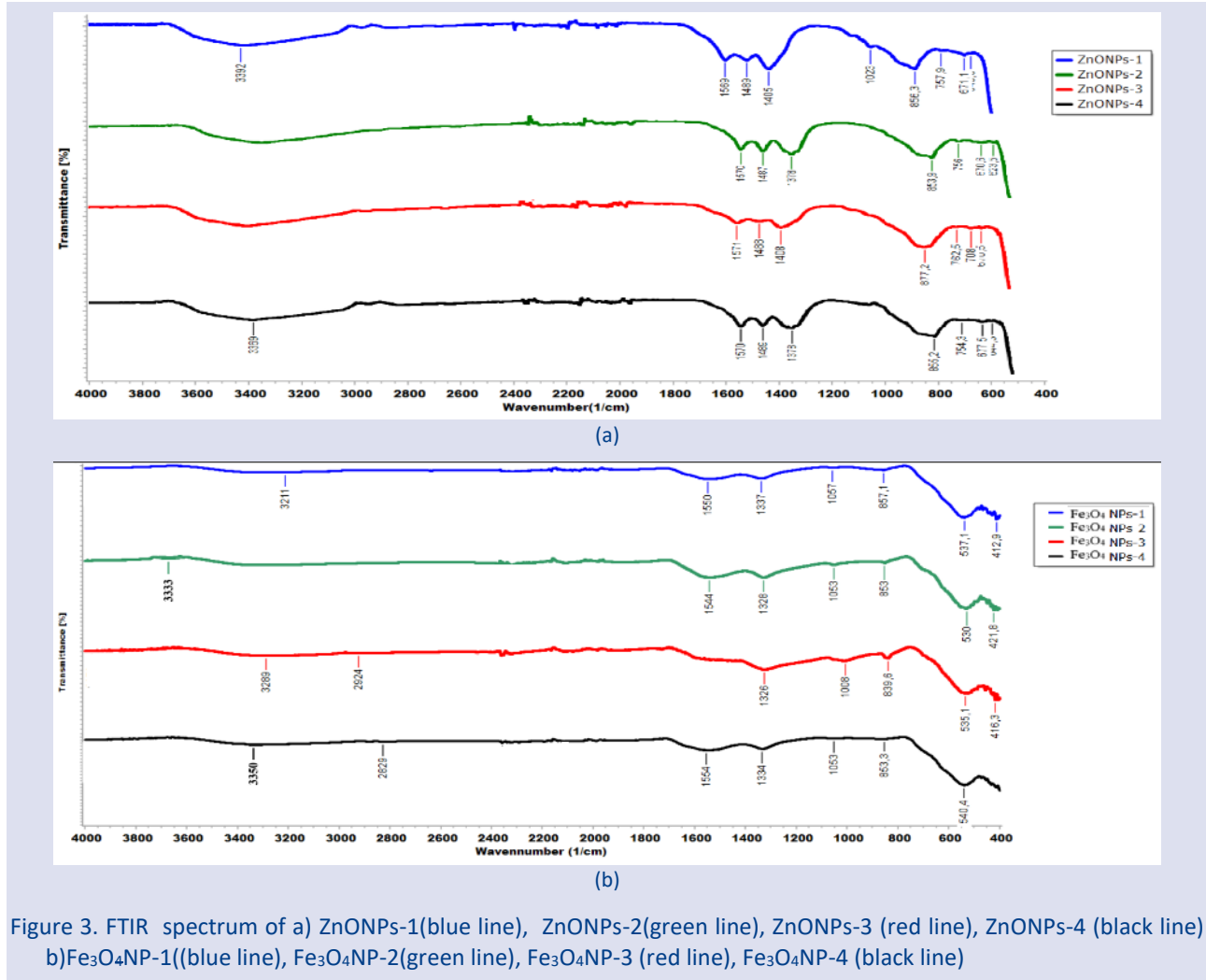
Peak Number	Planes hkl	2θ			
		Fe ₃ O ₄ NPs-1	Fe ₃ O ₄ NPs-2	Fe ₃ O ₄ NPs-3	Fe ₃ O ₄ NPs-4
1	220	29.80	30.13	30.32	30.16
2	311	35.41	35.38	35.30	35.47
3	400	43.09	43.03	43.22	43.18
4	422	53.54	53.80	53.71	53.82
5	511	57.07	57.12	57.20	57.13
6	440	62.61	62.48	62.57	62.55
XRD Crystallite Size of The Samples		7.93 nm	6.45 nm	5.84 nm	6.24 nm

FT-IR Results

FTIR was used to analyze the presence of possible functional groups responsible for nanoparticle reduction and capping (Fig.3). Phytochemicals such as alcohols, phenols, amines, carboxylic acids, and others present in plant extracts have the capability to interact with the surfaces of zinc and iron, thereby aiding in the stabilization of nanoparticles. The broad peak within the 3400-3300 cm⁻¹ range, a common occurrence in FTIR spectra,

provides confirmation of the existence of intermolecular hydrogen bonding[24]. The absorption peaks at approximately ~ 1570 and ~ 1400 cm^{-1} in both spectra, known to come from plant extracts and help particle synthesis, are assigned to C=C stretching and C-C stretching vibrations, respectively. The bands at approximately ~ 850 cm^{-1} and ~ 757 cm^{-1} are attributed to primary amine and N-H deformation bands. Metal-

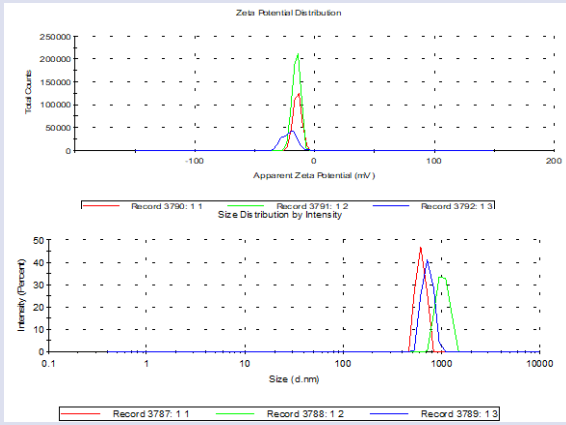
oxygen bond exhibits distinctive absorption bands within the wavenumber range of 400 to 600 cm^{-1} [25]. The absorption peaks around 535 cm^{-1} observed in the spectra of Fe_3O_4 NPs are attributed to Fe-O bending vibration[26][22]. Similarly, the peaks observed at approximately 600 cm^{-1} in the FTIR spectra of ZnONPs correspond to Zn-O stretching[23], respectively.



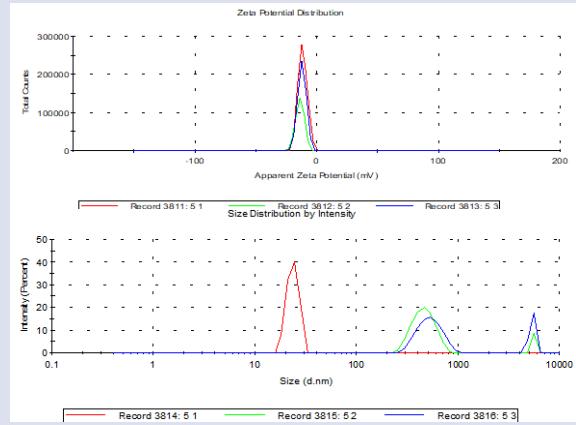
DLS and Zeta Potential Results

Dynamic light scattering (DLS) is a widely used technique for determining particle size in colloidal suspensions.[27] The parameter used to define the size range in the particle size distribution is called the "polydispersity index" (PDI). This index indicates that values less than 0.05 are essentially highly monodisperse, while PDI values greater than 0.7 indicate that the sample has a very broad particle size distribution[28]. The zeta potential is a very important parameter that provides information about the stability of particles. As the zeta potential increases, particles are prevented from coming together and forming aggregates due to the greater electrostatic repulsion between them, increasing the stability of the colloidal suspension.[29]. The zeta potential is closely related to the morphology of the

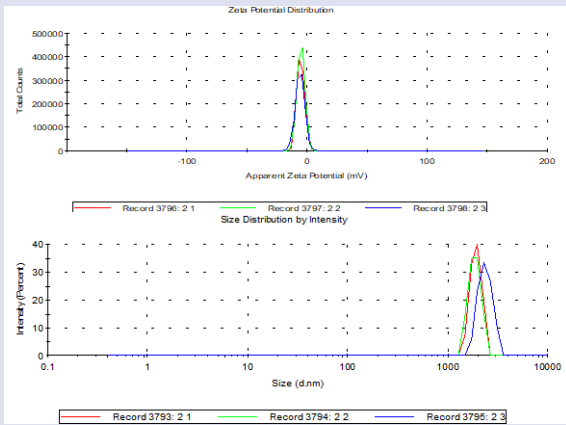
particle surface. The particle size distributions, PDI value and zeta potentials of the zinc and iron NPs are shown in Figure 4 and Table 3. ZnONP-3 and ZnONP-4, which have a low PDI value, showed a more homogeneous distribution while all Fe_3O_4 NPs with high PDI values showed a heterogeneous size distribution. All nanoparticles were found to have a high size distribution. Metal nanoparticles often tend to agglomerate by sticking together. This agglomeration process can result in larger differences in particle sizes. Nanoparticle agglomeration can occur during the drying process due to Van der Waals forces or chemical interactions[30]. The zeta potential values of the NPs differed according to the type of plant extract. While this value was between -5.35 and -16.9 for ZnONP's, it changed between -7.43 and -20.7 for Fe_3O_4 NPs.



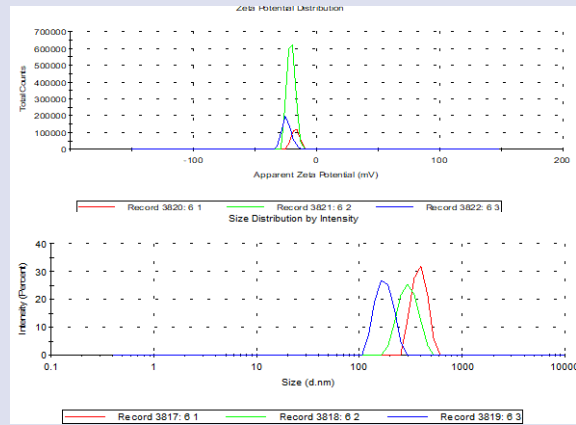
(a)



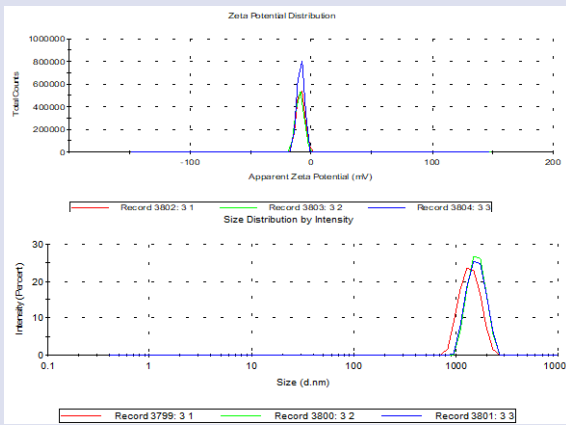
(e)



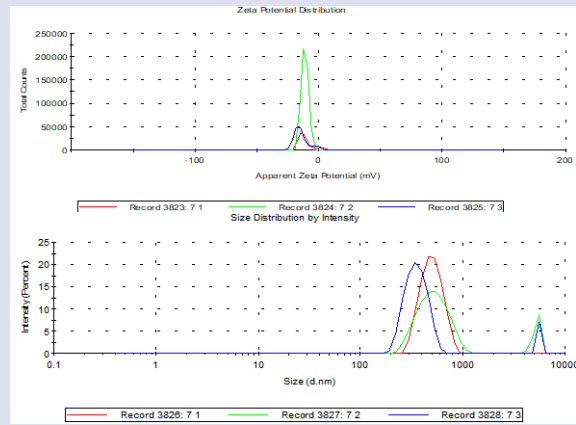
(b)



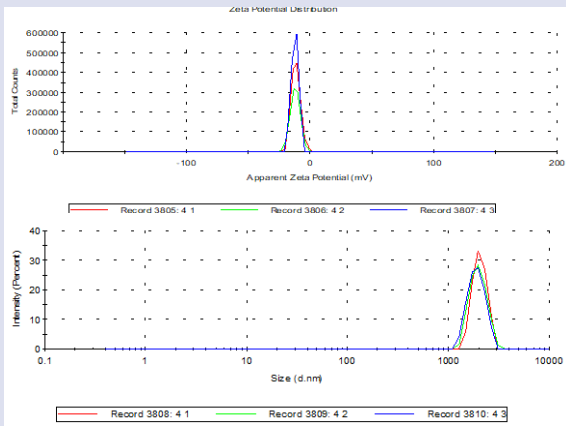
(f)



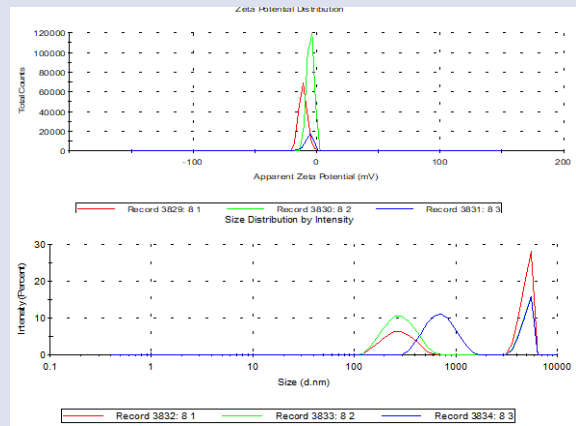
(c)



(g)



(d)



(h)

Figure 4. Zeta potential and size distribution graphs a) ZnONPs-1 b) ZnONPs-2 c) ZnONPs-3 d) ZnONPs-4 e) Fe₃O₄NP-1 f) Fe₃O₄NP-2 g) Fe₃O₄NP-3 h) Fe₃O₄NP-4

Table 3. Size distribution, PDI value, and zeta potential of ZnONPs and Fe₃O₄NPs synthesized from plant extracts

Samples	Z-Ave(d.nm)	Pdl	Zeta potential
ZnONPs-1	2453±285.7	0.75±0.16	-16.9±3.71
ZnONPs-2	3198±102.7	0.80±0.34	-5.35±0.49
ZnONPs-3	2204±165.9	0.30±0.10	-8.85±0.38
ZnONPs-4	2344±286.3	0.29±0,21	-11.9±0.47
Fe ₃ O ₄ NP-1	2537±1845	0.86±0.12	-12.5±1.18
Fe ₃ O ₄ NP-2	1417±286.3	0.85±0.12	-20.7±3.5
Fe ₃ O ₄ NP-3	1083±241.3	0.67±0.14	-12.1±1.85
Fe ₃ O ₄ NP-4	1341±529.	0.72±0.15	-7.43±3.1

Antimicrobial Activity

The antimicrobial activities of all ZnO and Fe₃O₄NP samples are shown in Figure 5 and Table 4.

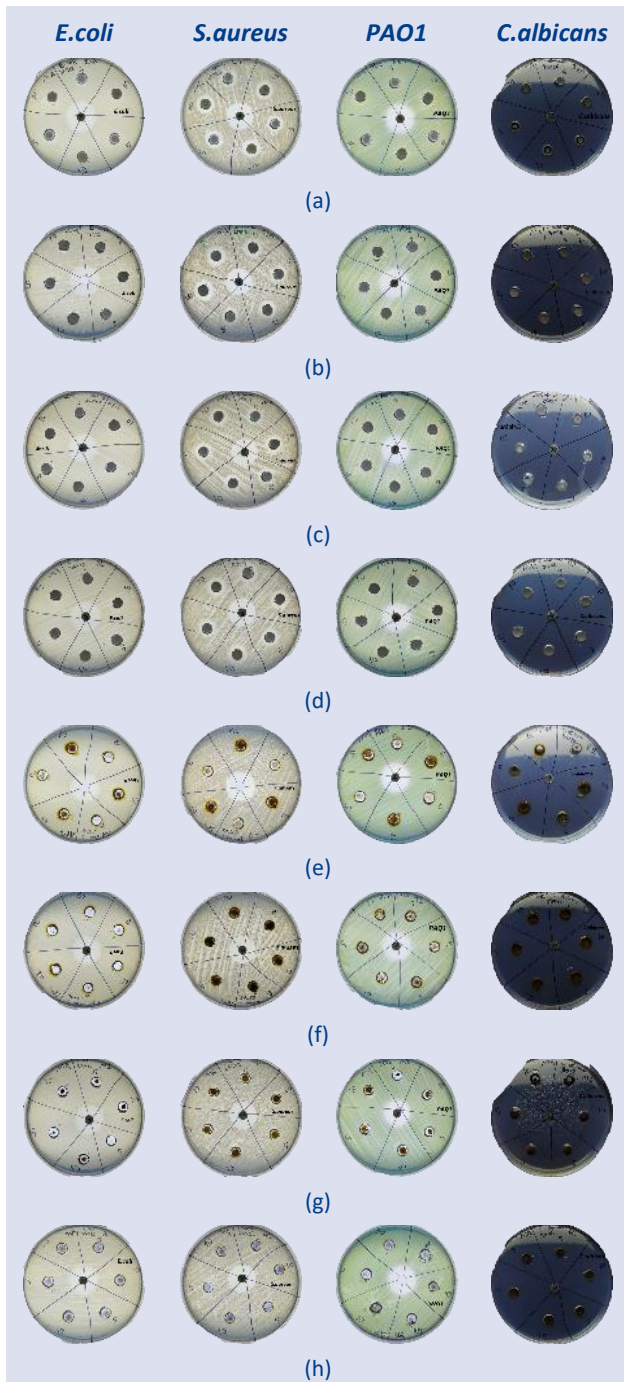


Figure 5. Antimicrobial effect of a) ZnONPs-1 b) ZnONPs-2 c) ZnONPs-3 d) ZnONPs-4 e) Fe₃O₄NPs-1 f) Fe₃O₄NPs -2 g) Fe₃O₄NPs -3 h) Fe₃O₄NPs -4

The results showed that all ZnO nanoparticles exhibited antimicrobial activity against the *S. aureus* strain alone (Figure 5). However, the Fe₃O₄NPs did not show any antibacterial effects against any strain. When the inhibition zone of ZnONPs was compared, no significant difference was observed in the inhibition zone of nanoparticles synthesized with different plant extracts. Furthermore, the inhibition diameters did not differ significantly at the 5 and 10 mg/mL concentrations. The size, shape, and concentration of the NPs may have been effective in preventing antimicrobial effects. Saqib et al (2018) reported that magnetic Fe₃O₄NPs (25-40 nm, spherical,) showed very low activity against both Gram-positive (*S. aureus*) and Gram-negative (*E. coli*) bacteria.[31].

Table 4. Inhibition zone diameter of ZnONPs and Fe₃O₄NP

<i>E. coli</i> 25922								
Component	ZnONPs-1	Fe ₃ O ₄ NPs-1	ZnONPs-2	Fe ₃ O ₄ NPs-2	ZnONPs-3	Fe ₃ O ₄ NPs-3	ZnONPs-4	Fe ₃ O ₄ NPs-4
5 mg/mL	-	-	-	-	-	-	-	-
10 mg/mL	-	-	-	-	-	-	-	-
Standard	18 ±0	18 ±0	18 ±0	18 ±0	18 ±0	18 ±0	18 ±0	18 ±0
<i>S. aureus</i> 25923								
Component	ZnONPs-1	Fe ₃ O ₄ NPs-1	ZnONPs-2	Fe ₃ O ₄ NPs-2	ZnONPs-3	Fe ₃ O ₄ NPs-3	ZnONPs-4	Fe ₃ O ₄ NPs-4
5 mg/mL	11 ±0	-	10 ±0	-	10 ±0	-	11 ±0	-
10 mg/mL	12 ±0	-	12 ±0	-	11 ±0	-	12 ±0	-
Standard	19 ±0	19 ±0	19 ±0	19 ±0	19 ±0	19 ±0	19 ±0	19 ±0
<i>P. aeruginosa</i> PAO1								
Component	ZnONPs-1	Fe ₃ O ₄ NPs-1	ZnONPs-2	Fe ₃ O ₄ NPs-2	ZnONPs-3	Fe ₃ O ₄ NPs-3	ZnONPs-4	Fe ₃ O ₄ NPs-4
5 mg/mL	-	-	-	-	-	-	-	-
10 mg/mL	-	-	-	-	-	-	-	-
Standard	18 ±0	18 ±0	18 ±0	18 ±0	18 ±0	18 ±0	18 ±0	18 ±0
<i>C. albicans</i> 90028								
Component	ZnONPs-1	Fe ₃ O ₄ NPs-1	ZnONPs-2	Fe ₃ O ₄ NPs-2	ZnONPs-3	Fe ₃ O ₄ NPs-3	ZnONPs-4	Fe ₃ O ₄ NPs-4
5 mg/mL	-	-	-	-	-	-	-	-
10 mg/mL	-	-	-	-	-	-	-	-
Standard	23 ±0	23 ±0	23 ±0	23 ±0	23 ±0	23 ±0	23 ±0	23 ±0

Conclusion

In essence, nanoparticle synthesis using plant extracts offers a sustainable, biocompatible, and versatile approach with a wide range of potential applications in fields ranging from healthcare to environmental science. This approach aligns with the growing emphasis on green and sustainable nanotechnology practices while providing tailored nanomaterials for specific needs. Hence, the study involved the assessment of various plant extracts and their impacts on nanoparticle synthesis. ZnO and magnetic Fe₃O₄ NPs were synthesised by using green synthesis method. Based on the TEM analysis results, different plant extracts had no discernible impact on nanoparticle shapes, but they did influence the size distribution. Specifically, ZnONP-1 exhibited a small crystalline size and exceptional stability. In contrast, Fe₃O₄NP-3 displayed a reduced crystallite size, while Fe₃O₄NP-2 possessed high stability according to XRD and zeta potential results. Upon examination of the antimicrobial activity results, it was found that only all ZnO nanoparticles displayed activity against the *S. aureus* strain. In conclusion, it is important to note that the choice of the plant in nanoparticle synthesis is a critical factor that can be tailored to achieve desired nanoparticle characteristics and biological activities, making it essential in designing nanoparticles for specific application.

Conflicts of interest

The authors report no conflicts of interest in this work.

Reference

- [1] N. Joudeh and D. Linke, Nanoparticle classification, physicochemical properties, characterization, and applications: a comprehensive review for biologists, *J Nanobiotechnology* 20 (1) (2022) 1–29.
- [2] Yusuf et al., Nanoparticles as Drug Delivery Systems: A Review of the Implication of Nanoparticles' Physicochemical Properties on Responses in Biological Systems, *Polymers (Basel)* 15 (7) (2023).
- [3] Khan, K. Saeed, and I. Khan, Nanoparticles: Properties, applications and toxicities, *Arabian Journal of Chemistry* 12 (7) (2019) 908–931.
- [4] J. Ali et al., Green synthesized zinc oxide nanostructures and their applications in dye-sensitized solar cells and photocatalysis: A review, *Mater Today Commun* 36 (August) (2023) 106840.
- [5] J.R. Vargas-Ortiz, C. Gonzalez, and K. Esquivel, Magnetic Iron Nanoparticles: Synthesis, Surface Enhancements, and Biological Challenges, *Processes* 10 (11) (2022).
- [6] H. Chopra et al., Green Metallic Nanoparticles: Biosynthesis to Applications, *Front Bioeng Biotechnol* 10 (April) (2022) 1–29.
- [7] Alayli et al., Synthesis of Nanoparticles by Green Synthesis Method, *International Journal of Innovative Research and Reviews* 1 (1) (2017) 6–9.
- [8] Chaudhary et al., Antimicrobial activity of zinc oxide nanoparticles synthesized from Aloe vera peel extract, *SN Appl Sci* 1 (1) (2019) 1–9.
- [9] M.F. Sohail et al., Green synthesis of zinc oxide nanoparticles by Neem extract as multi-facet therapeutic agents, *J Drug Deliv Sci Technol* 59 (June) (2020) 101911.
- [10] G.A. Naikoo et al., Bioinspired and green synthesis of nanoparticles from plant extracts with antiviral and antimicrobial properties: A critical review, *Journal of Saudi Chemical Society* 25 (9) (2021) 101304.
- [11] I.K. Siakavella et al., Effect of plant extracts on the characteristics of silver nanoparticles for topical application, *Pharmaceutics* 12 (12) (2020) 1–17.
- [12] P.D. Twilley, S. Rademan, and N. Lall, Are medicinal plants effective for skin cancer?, in *Medicinal Plants for Holistic Health and Well-Being*, Elsevier, (2017): pp. 13–75.
- [13] B. Feng et al., Basil polysaccharide inhibits hypoxia-induced hepatocellular carcinoma metastasis and progression through suppression of HIF-1 α -mediated epithelial-mesenchymal transition, *Int J Biol Macromol* 137 (2019) 32–44.
- [14] I. Rahayu, Casey Christiany, and Susana Elya Sudrajat, The Potency of Cinnamomum Zeylanicum to Prevent Diseases: a Review, *Eureka Herba Indonesia* 2 (1) (2021) 52–62.
- [15] Z. Wang et al., Origins, phytochemistry, pharmacology, analytical methods and safety of cortex moutan (*paenonia suffruticosa* Andrew): A systematic review, *Molecules* 22 (6) (2017).
- [16] A. Ozdemir, Antioxidant Capacity And Antimicrobial Activity of *Paeonia Peregrina* L [Usak-Itecik Tulip] Extracts and Its Phenolic and Flavonoid Compounds, *The Ulutas Medical Journal* 5 (4) (2019) 1.
- [17] G. Athanasakis et al., Antioxidant properties of the wild edible mushroom *Lactarius salmonicolor*, *J Med Food* 16 (8) (2013) 760–764.
- [18] B.O. Asimeng et al., Characterization and Inhibitory Effects of Magnetic Iron Oxide Nanoparticles Synthesized from Plant Extracts on HeLa Cells, *Int J Biomater* 2020 (2020) 15–18.
- [19] P. Sharma et al., Application of ZnO-based nanocomposites for vaccines and cancer immunotherapy, *Pharmaceutics* 11 (10) (2019) 6–10.
- [20] A. Naveed Ul Haq et al., Synthesis Approaches of Zinc Oxide Nanoparticles: The Dilemma of Ecotoxicity, *J Nanomater* 2017 (Table 1) (2017).
- [21] G.T. Mazitova et al., Synthesis and Properties of Zinc Oxide Nanoparticles: Advances and Prospects, *Rev J Chem* 9 (2) (2019) 127–152.
- [22] K. Parajuli, A.K. Sah, and H. Paudyal, Green Synthesis of Magnetite Nanoparticles Using Aqueous Leaves Extracts of *Azadirachta indica*; and Its Application for the Removal of As(V) from Water, *Green and Sustainable Chemistry* 10 (04) (2020) 117–132.
- [23] K. Handore et al., Novel green route of synthesis of ZnO nanoparticles by using natural biodegradable polymer and its application as a catalyst for oxidation of aldehydes, *Journal of Macromolecular Science, Part A: Pure and Applied Chemistry* 51 (12) (2014) 941–947.
- [24] R. Gomathi, H. Suhana, and D. Paradesi, Characterization Study of Cytotoxicity of Green Synthesized ZnO Nanoparticles Loaded with Anti-Cancer Doxorubicin Drug, *ChemistrySelect* 6 (18) (2021) 4533–4538.
- [25] M.B. Nayan et al., Comparative Study on the Effects of Surface Area, Conduction Band and Valence Band Positions on the Photocatalytic Activity of ZnO-M_xO_y Heterostructures, *J Water Resour Prot* 11 (03) (2019) 357–370.

- [26] F. Ahangaran, A. Hassanzadeh, and S. Nouri, Surface modification of Fe₃O₄@SiO₂ microsphere by silane coupling agent, *Int Nano Lett* 3 (1) (2013).
- [27] C.M. Hoo et al., A comparison of atomic force microscopy (AFM) and dynamic light scattering (DLS) methods to characterize nanoparticle size distributions, *Journal of Nanoparticle Research* 10 (SUPPL. 1) (2008) 89–96.
- [28] M. Danaei et al., Impact of particle size and polydispersity index on the clinical applications of lipidic nanocarrier systems, *Pharmaceutics* 10 (2) (2018) 1–17.
- [29] R. Xu, Progress in nanoparticles characterization: Sizing and zeta potential measurement, *Particuology* 6 (2) (2008) 112–115.
- [30] S.C. Endres, L.C. Ciacchi, and L. Mädler, A review of contact force models between nanoparticles in agglomerates, aggregates, and films, *J Aerosol Sci* 153 (November 2020) (2021).
- [31] S. Saqib et al., Synthesis, characterization and use of iron oxide nano particles for antibacterial activity, *Microsc Res Tech* 82 (4) (2019) 415–420.

Evaluation of Antibiofilm and Antimicrobial Activities of N-heterocyclic Carbene Complexes

Uğur Tutar ^{1,a,*}, Cem Çelik ^{2,b}, Mehmet Ataş ^{3,c}

¹ Department of Botanica, Faculty of Pharmacy, Sivas Cumhuriyet University, Sivas, Türkiye.

² Department of Medical Microbiology, Faculty of Medicine, Sivas Cumhuriyet University, Sivas, Türkiye.

³ Department of Pharmaceutical Microbiology, Faculty of Pharmacy, Sivas Cumhuriyet University, Sivas, Türkiye.

*Corresponding author

Research Article

History

Received: 13/11/2023

Accepted: 12/03/2024



This article is licensed under a Creative Commons Attribution-NonCommercial 4.0 International License (CC BY-NC 4.0)

ABSTRACT

In recent years, resistance to antimicrobials has become a global problem. Despite the need for new antibiotics with the increase of resistant bacteria, developing new antimicrobials is problematic. Biofilms formed by microorganisms play an essential role in the development of resistance. We aimed to investigate the antimicrobial and antibiofilm activities of N-heterocyclic carbene (NHC) complexes. In this study, previously synthesized and characterized NHC complexes on standard bacterial and fungal strains were investigated. The minimal inhibition concentration (MIC) test was used to determine the antimicrobial activities of the compounds, and the biofilm inhibition concentration test was used to determine the anti-biofilm activities. Compounds 2b and 2c showed potent antimicrobial activity on microorganisms between ≤ 1.9 and $7.8 \mu\text{g/mL}$. Antimicrobial activity in salts of compounds (1a-1c) was weaker than silver compounds (2a-2c). The antibiofilm activity was between 27 and 79%, especially in silver-bound compounds (2a-2c). Benzimidazole derivative NHC compounds that we evaluated in our study were found to have significant antimicrobial and antibiofilm effects on pathogenic microorganisms. These compounds, which we assessed in our study, may be antimicrobial drug candidates that can be used in different areas. It will be essential to conduct further in vitro and in vivo studies on this subject.

Keywords: N heterocyclic carbene, Benzimidazole, Antimicrobial activity, Antibiofilm activity.

^a ututar5@gmail.com

^c atasmehmet@gmail.com

^b <https://orcid.org/0000-0002-8058-0994>

^d <https://orcid.org/0000-0002-9425-0080>

^e cemcelik58@gmail.com

^f <https://orcid.org/0000-0002-7141-5874>

Introduction

Although microorganisms are indispensable elements of our world, they are also the cause of many negative aspects in the fields of food and industry, especially infections [1-3]. While the common effort of those dealing with health sciences is to provide the best conditions for the environment and all living things, microorganisms are one of the most important obstacles [4].

Antimicrobial substances are used extensively for human and animal health, for the protection of nutrients in the food industry, and protection from the harmful effects of microorganisms in the sector [5]. However, in recent years, the resistance developed by microorganisms against these substances has emerged as a global problem. Efforts such as reducing the overuse of antimicrobials, improving sanitation, and infection control have not solved this problem completely, and new antimicrobials are needed has been understood [4,6]. Although resistance to antimicrobial agents has increased rapidly, new antimicrobial agents have not been developed at the same rate [7]. One of the reasons for the lack of discoveries is the increasing consumption of natural structures with antimicrobial activity [8]. Therefore, synthetic chemistry plays a crucial role in developing new strategies and antimicrobials [9].

Biofilms are one of the essential causes of resistance to antimicrobial agents. Biofilms, formed from a complex process, cause significant health and economic losses due to their important role in infectious diseases, increasing metal biodegradation processes in industrial sectors, decreasing food quality in agriculture and food sectors, and contaminating water systems. Many antibiotics are not able to destroy dense biofilms. For this reason, it is necessary to find effective substances that can destroy biofilms or prevent the formation of biofilms [10-12]. NHCs are heterocyclic species containing a carbene carbon and at least one nitrogen atom in the ring structure. An increasing number of publications today have focused on the medical applications of NHCs. Especially metal complexes of NHCs are evaluated as metallopharmaceuticals with great promise to be antibacterial and anticancer agents [13]. The successful isolation and characterization of an N heterocyclic carbene (NHC) at the end of the twentieth century have opened a new class of organic compounds for research. To date, NHCs have been among the most powerful tools in organic chemistry with numerous commercially important applications and have found applications in various fields, including medical fields [14]. This study aimed to determine the antibiofilm and antimicrobial properties of

Benzimidazole derivative NHC compounds previously designed and synthesized. We think that our study will contribute to the literature on studies on new compounds that have the potential to be antimicrobial agents.

Materials and Methods

Compounds

In this study, previously synthesized and characterized benzimidazolium-based Ag(I)-NHC complexes; 1-allyl-3-(3-methylbenzyl) benzimidazolium chloride (1a), 1-allyl-3-(4-isopropylbenzyl) benzimidazolium chloride (1b), 1-allyl-3-(4-ter-butylbenzyl) benzimidazolium bromide (1c), chloro [1-allyl-3-(3-methylbenzyl) benzimidazole-2-ylidene] silver(I) (2a), chloro[1-allyl-3-(4-isopropylbenzyl) benzimidazole-2-ylidene] silver (I) (2b), bromo[1-allyl-3-(4-ter-butylbenzyl) benzimidazole-2-ylidene] silver(I) (2c), [15,16]. were evaluated in terms of antimicrobial and antibiofilm properties.

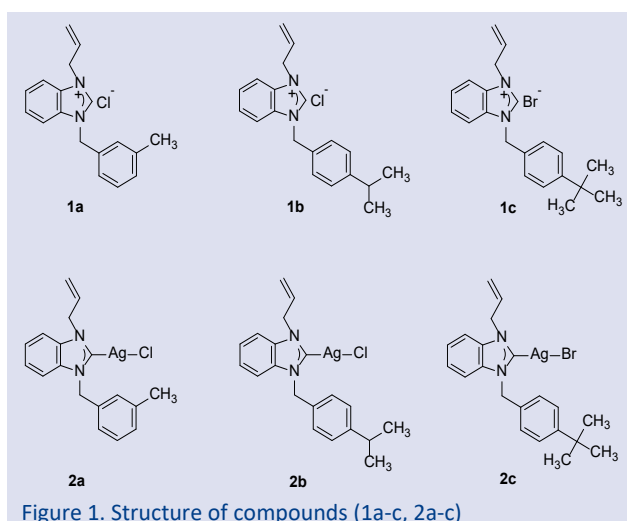


Figure 1. Structure of compounds (1a-c, 2a-c)

The minimal inhibition concentration (MIC) test was used to determine the compounds' antimicrobial activities, and the Biofilm inhibition concentration (BIC) test was used to determine their anti-biofilm activities.

Microorganism

In this study, ATCC 25922 *Escherichia coli*, ATCC 27853 *Pseudomonas aeruginosa*, ATCC 29213 *Staphylococcus aureus*, ATCC 29212 *Enterococcus faecalis*, and ATCC 10231 *Candida albicans* bacteria and yeast strains obtained from the standard strains of the American Type Culture Collection were used. Standard microorganisms were stored at -80 °C and revived at room temperature before the study.

Antimicrobial Activity, Determination of MICs

To determine the antimicrobial activities of the compounds, the broth microdilution method was used as applied by Şahin et al. [17]. Briefly, Overnight broth cultures were used to prepare inoculations of microorganisms and microorganism inoculations were adjusted to the standard turbidity of 0.5 McFarland (1×10^8

CFU/mL microorganism). Microorganism inoculations were adjusted to a final concentration of 5×10^5 CFU/ mL. Before starting the test, 2 mg of the compound was weighed and dissolved with 10% (v/v) DMSO in 4 mL of MHB to prepare a stock solution. Then, serial two-fold dilutions were prepared with MHB at concentrations ranging from 3.9 to 250 µg/ mL in 96-well plates. Ciprofloxacin and fluconazole were used as standard antibacterial and antifungal agents. Optical densities were measured after 24 hours of incubation at 37 °C. A microplate reader (SPECTROstar Nano, BMG LABTECH, Ortenberg/Germany) was used to measure the optical density at 620 nm. The lowest concentration that inhibits the growth of microorganisms was determined as MIC.

Biofilm Inhibition Concentration (BIC) Assay

The microtiter plate test was applied to evaluate the antibiofilm activities of the compounds against microorganisms, similar to the work of Şahin et al. with some modifications [18]. Overnight broth cultures were used to prepare inoculations of microorganisms. Briefly, 100 µL of Tryptic Soy Broth (TSB) containing 1% glucose (w/v) and microorganism at a density of 0.5 McFarland (1×10^8 CFU/ mL) was dispensed into 96-well U-bottom microplates. Then, 100 µL of different compound concentrations (1.9 - 250 µg/ mL) was dispensed into different wells. Only 200 µL of TSB solution was dispensed into the negative control well, and only 200 µL of the microorganism solution in the positive control well. The prepared microplates were incubated at 37 °C for 24 hours. At the end of the period, all wells were washed three times with 300 µL phosphate buffer solution (PBS), and planktonic cells were removed. Then, the biofilm in all wells was fixed with 95% methanol for 15 minutes. After fixation, 0.1% crystal violet (w/v) was added to the wells, dried at room temperature, and stained for 30 minutes. At the end of the period, the excess dye was removed with PBS 3 times and left to dry. A 33% acetic acid solution was added to dissolve the dye in the wells and evaluated at 570 nm in a microplate reader (SPECTROstar Nano, BMG LABTECH, Ortenberg/Germany). All experiments were repeated three times.

The percent biofilm inhibition was calculated using the formula given below.

$$\text{Biofilm inhibition (\%)} = \left\{ \frac{A_c - A_s}{A_c} \right\} \times 100$$

(A_c and A_s are the absorbance of the control and sample, respectively)

Results and Discussion

Compounds 2b and 2c showed strong antimicrobial activity against bacteria and yeast strains. These compounds were found to have inhibition concentrations close to the control antimicrobial agents (ciprofloxacin and fluconazole). Compound 2a showed moderate antimicrobial activity compared to other silver compounds in our study. Although antimicrobial activity was observed in the salts of the compounds (1a-1c), this effect was found to be weaker than in the silver compounds (2a-2c) (Table 1).

Table 1. Minimum-inhibitory concentrations (MIC, in µg/ mL) of compounds

Compounds	Microorganisms				
	ATCC 25922 <i>E.coli</i>	ATCC 27853 <i>Pseudomonas aeruginosa</i>	ATCC 29213 <i>Staphylococcus aureus</i>	ATCC 29212 <i>Enterococcus faecalis</i>	ATCC 10231 <i>Candida albicans</i>
1a	62.5	62.5	125	125	62.5
1b	125	125	125	125	125
1c	62.5	125	62.5	125	62.5
2a	15.6	31.25	62.5	31.25	31.25
2b	<=1.9	3.9	3.9	3.9	3.9
2c	3.9	3.9	7.8	<=1.9	3.9
Ciprofloxacin	<= 1.9	<=1.9	<= 1.9	<= 1.9	
Fluconazole					<= 1.9

When we evaluated the antibiofilm activities of the compounds we studied at concentrations sub-MIC, it was found that all compounds had this effect at different concentrations. The antibiofilm activity was found between 27 and 79% against microorganisms, especially silver-bound compounds (2a-2c). Other salt compounds (1a-1c) also inhibited biofilms of microorganisms at different rates at values sub-MIC. (Table 2).

Nowadays, the processes of discovering and producing new antibiotics are problematic. Therefore, there is an antimicrobial resistance crisis affecting the whole world. The process of developing a new antibiotic involves excellent difficulties. Traditional methods for finding antimicrobial agents have not produced a new antibiotic for a long time [19].

As a result, there has been a severe decrease in new antibacterial agents in recent years. However, new antibiotics are urgently needed due to the threat posed by increased highly resistant pathogenic bacteria [20].

Table 2. Reduction in biofilm formation on ½ MIC value of compounds (%)

Compounds	Microorganisms				
	ATCC 25922 <i>E.coli</i>	ATCC 27853 <i>Pseudomonas aeruginosa</i>	ATCC 29213 <i>Staphylococcus aureus</i>	ATCC 29212 <i>Enterococcus faecalis</i>	ATCC 10231 <i>Candida albicans</i>
1a	31.25/24±0.5	31.25/8±0.5	62.5/27±0.5	62.5/22±1.0	31.25/14±1.0
1b	62.5/45±0.5	62.5/14±1.0	62.5/29±0.5	62.5/39±0.5	62.5/42±2.0
1c	31.25/41±1.0	62.5/16±1.0	31.25/37±0.5	62.5/11±0.5	31.25/31±0.5
2a	7.8/68±0.5	15.6/27±0.5	31.25/44±0.5	15.6/49±0.5	15.6/47±0.5
2b	NT	1.9/38±1.0	1.9/68±1.0	1.9/62±0.5	1.9/70±1.0
2c	1.9/79±1.0	1.9/34±0.5	3.9/61±0.5	NT	1.9/66±1.0

NT: Non-tested (The biofilm inhibition test could not be studied because the MIC value was at the lowest concentration studied).

The main goal of medicinal chemistry is to design and synthesize bioactive compounds that can be safe and effective drugs [21]. Synthetic chemistry is critical for the discovery and development of new drugs. Chemical syntheses play an important role in pharmaceutical research and development. In the last century, many new synthesized compounds have led to the discovery and development of important life-changing drugs. Today, there is a critical need for new syntheses to develop new drugs that will guide future treatments [22].

Our study evaluated benzimidazole-derived Ag-NHC compounds' antimicrobial and antibiofilm activities and

their salts, which were previously synthesized but whose antimicrobial and antibiofilm properties were unknown. The results of our study showed antimicrobial and antibiofilm activities similar to those of the control antimicrobials (ciprofloxacin and fluconazole), especially in the silver-bound 2b and 2c compounds (Table 1, 2).

There are publications in the literature on the antimicrobial activities of NHC molecules. Sakamoto et al. [23]. demonstrated the antimicrobial activity of the Ag(I)-NHC compounds they synthesized in their study and reported that most of this effect was due to the Ag metal. Sarı et al. [24]. Showed the antimicrobial activities of

benzimidazolium-based Ag(I)-NHC compounds they synthesized on Gram-positive and Gram-negative bacteria and yeasts. It is understood that Ag(I)-NHC compounds, whose activities we evaluated in our study, are more effective on microorganisms than those reported in this study. Gök et al. [25]. Demonstrated the antimicrobial activities of the benzimidazolium-based Ag(I)-NHC compounds they synthesized on Gram-positive and Gram-negative bacteria and yeasts. Butorac et al. [26]. reported that silver and gold-bound NHC compounds showed antimicrobial activity on *S. aureus*, *Bacillus subtilis*, *E. coli*, and *P. aeruginosa*. Siegmund et al. [27]. Their study with NHC complexes reported that their synthesised compounds exhibited strong antimicrobial activity on Gram-positive bacterial strains at low concentrations. Researchers reported that these compounds are important for developing new metal-based antibiotic agents. The silver-bound NHC complexes that we evaluated in our study also showed strong antimicrobial activity at low concentrations on all microorganisms we studied. Therefore, we think these compounds, which we evaluated in our study, may be important for developing new metal-based antibiotics.

About 80% of human bacterial infections are related to biofilms [28]. Therefore, it is critically important to design and develop anti-biofilm molecules that can be used in the treatment of biofilm-related diseases [29]. Benzimidazole derivatives are widely used as antimicrobial, antihistamine, antiviral, antidiabetic, anticancer, antifungal, anti-inflammatory, analgesic, etc., due to their pharmacological activities; it has become very important in recent years in the field of medicinal chemistry. There are currently few benzimidazole derivatives on the market as drug candidates against various diseases. However, intensive studies show that benzimidazole-based drug candidates can increase rapidly [30]. The previous study reported benzimidazolium salts with methicillin-resistant *S. aureus* bacteria are potent antibiotic and anti-biofilm agents. In this study, the researchers reported that new drugs should be developed to combat resistant bacteria and that it is important that these drugs can prevent or destroy biofilms [31]. We think that benzimidazole-derived compounds, which we evaluated in our study, may be among the future antimicrobials against resistant microorganisms with their strong antibiofilm and antimicrobial effects.

Üstün et al. [32]. They studied the antimicrobial activity and antibiofilm activity in the synthesised benzimidazole derivative NHC compounds. Researchers found antimicrobial activity against microorganisms in salts between 31.25 -250 µg/ mL concentrations, while they found much higher effects in their silver-bound complexes at concentrations \leq 1.9-15.6 µg/ mL. Again, researchers reported that salts at sub-MIC concentrations inhibited microorganism biofilms by 8-51.6%, while silver-bound NHC compounds inhibited microorganism biofilms up to 77% at sub-MIC concentrations. While the salts of the compounds we evaluated in our study had antimicrobial and antibiofilm activity similar to the studies

of Üstün et al., much stronger activities were found in Ag(I)-NHC complexes, especially in compounds 2b and 2c. We think that these compounds should be included in further in vitro and in vivo studies to be future antimicrobials.

Sahin et al. [17]. They evaluated the newly synthesized NHC precursors and Ag(I)-NHC complexes regarding antibacterial, antifungal, and antibiofilm activities. Researchers compared the biological activities of the synthesised products in their studies with standard drugs, as in our study. Researchers who reported that the compounds have moderate antibacterial and antibiofilm activities reported that especially compound 2a inhibited *E. coli* biofilms, and compound 2d inhibited *C. albicans* biofilms at the highest rate. Bernardi et al. [33]. Investigated the antibiofilm properties of NHC compounds to which they bind different metals on Gram (+) and Gr (-) bacteria. This study reported that very strong antibiofilm activity was observed in Ag(I)-NHC compounds. The researchers stated that the results obtained in this study would open new perspectives in developing metal-based drugs that can be used to treat infections associated with biofilms. We also think that the strong antimicrobial and antibiofilm activity we obtained in our study may contribute to developing new antimicrobials with antibiofilm properties. O'Beirne et al. [34]. Their study with NHC compounds reported that the compounds showed excellent inhibition on *E. coli*, *P. aeruginosa*, and *K. pneumoniae*. The researchers reported that the compounds did not have an antibiofilm effect on *P.aeruginosa* but showed antibiofilm activity on Methicillin-resistant *S.aureus* (MRSA) and *C.parapsilosis*. The compounds we evaluated in our study also showed antibiofilm activity in *P.aeruginosa* biofilms. There are many studies on the antimicrobial properties of Ag(I)-NHCs in the literature. Kaloğlu et al [13] evaluated the antimicrobial activity of synthesised Ag-(I) NHC compounds on different microorganisms. They reported that these compounds showed strong activity.

The studies show that Ag(I)-NHC compounds have the potential to be applied in medicine due to their antimicrobial activity and low toxicity. The slow transport of silver ions across the cell membrane disrupts the cell's electron transport system and the structure of enzymes. The disadvantage of using silver compounds in pharmaceutical studies is that they quickly lose their effectiveness due to the rapid release of Ag⁺ ions. Therefore, the synthesis of silver complexes with strong coordinating ligands is crucial to prevent the rapid release of silver ions.

Conclusion

There is a great need for new antibiotics with the increase of highly resistant pathogenic bacteria. However, new antimicrobial agents have not been developed as needed in recent years. Benzimidazole derivative NHC compounds, whose antimicrobial and antibiofilm activities were evaluated in our study, were found to have

significant antimicrobial and antibiofilm effects on pathogenic microorganisms. Especially compounds 2b and 2c showed strong antimicrobial activity on microorganisms between ≤ 1.9 and $7.8 \mu\text{g}/\text{mL}$. The antibiofilm activity was found between 27 and 79%, especially in silver-bound compounds (2a-2c). In the literature, there are few studies on the antibiofilm activities of benzimidazole-derived NHC compounds. These compounds, which we evaluated in our study, can be drug candidates that can be used in different fields. It will be essential to conduct further in vitro and in vivo studies on this subject.

Acknowledgements

The authors would like to thank Neslihan Şahin for providing us with the compounds.

Conflict of interest

The authors declare no conflicts of interest.

References

- [1] Kowalchuk GA., Jones SE., Blackall LL., Microbes Orchestrate Life on Earth, *ISME J.*, 2(8) (2008) 795-796.
- [2] Lorenzo JM., Munekata PE., Dominguez R., Pateiro M., Saraiva JA., Franco D., Main Groups of Microorganisms of Relevance for Food Safety and Stability, *Innovative Technologies for Food Preservation.*, (2018) 53–107.
- [3] Lindahl JF., Grace D., The Consequences of Human Actions on Risks for Infectious Diseases: a Review, *Infect Ecol Epidemiol.*, (5) (2015) 30048.
- [4] McEwen SA., Collignon PJ., Antimicrobial Resistance: A One Health Perspective, *Microbiol Spectr.*, 6 (2) (2018) 10.1128.
- [5] Topal M., Uslu Şenel G., Arslan Topal EI., Öbek E., Antibiotics and Usage Areas, *Erciyes Üniversitesi Fen Bilimleri Enstitüsü Dergisi.*, 31(3) (2015) 121-127.
- [6] Ventola CL., The Antibiotic Resistance Crisis: Part 1: Causes and Threats, *P T.*, 40 (4) (2015) 277-283.
- [7] Conly J., Johnston B., Where Are All the New Antibiotics? The New Antibiotic Paradox, *Can J Infect Dis Med Microbiol.*, 16 (3) (2005) 159-160.
- [8] Chen CH., Lu TK., Development and Challenges of Antimicrobial Peptides for Therapeutic Applications, *Antibiotics (Basel)*, 9 (1) (2020) 24.
- [9] Konaklieva MI., Addressing Antimicrobial Resistance Through New Medicinal and Synthetic Chemistry Strategies, *SLAS Discov.*, 24 (4) (2019) 419-439.
- [10] Jain A., Gupta Y., Agrawal R., Khare P., Jain SK., Biofilms--A Microbial Life Perspective: A Critical Review, *Crit Rev Ther Drug Carrier Syst.*, 24 (5) (2007) 393-443.
- [11] Dumitru C., Bacterial Biofilms and Their Biological Significance, *Rev Rom Med Vet.*, 28 (2) (2018) 35-40.
- [12] Dincer S., Masume Uslu F., Delik A., Antibiotic Resistance in Biofilm. Bacterial Biofilms, London, UK: IntechOpen Limited, (2020).
- [13] Hopkinson MN., Richter C., Schedler M., Glorius F., An Overview of N-heterocyclic Carbenes, *Nature*, 510 (7506) (2014) 485-496.
- [14] Smith CA., Narouz MR., Lummis PA., Singh I., Nazemi A., Hung Li C., Crudden CM., N-heterocyclic Carbenes in Materials Chemistry, *Chem Rev.*, 119 (8) (2019) 4986-5056.
- [15] Şahin-Bölükbaşı S., Şahin N., Tahir MN., Arıcı C., Cevik E., Gürbüz N., Özdemir İ., Cummings BS., Novel N-heterocyclic Carbene Silver (I) Complexes: Synthesis, Structural Characterization, and Anticancer Activity, *Inorganica Chim Acta.*, 486 (2019) 711-718.
- [16] Şahin N., Şahin-Bölükbaşı S., Tahir MN., Arıcı C., Çevik E., Gürbüz N., Özdemir İ., Cummings BS., Synthesis, Characterization, and Anticancer Activity of Allyl Substituted N-heterocyclic Carbene Silver (I) Complexes, *J Mol Struct.*, 1179 (2019) 92-99.
- [17] Şahin N., Üstün E., Tutar U., Çelik C., Gürbüz N., Özdemir İ., Antimicrobial Activity, Inhibition of Biofilm Formation, and Molecular Docking Study of Novel Ag-NHC Complexes, *J Organomet Chem.*, 954–955 (2021) 122082.
- [18] Tutar U., Çelik C., Antibiofilm and Antimicrobial Properties of 1-allyl-3-(2-diisopropylaminoethyl) Benzimidazolium Chloride and Its Silver(I)-NHC Complex, *Cumhuriyet Sci J.*, 43 (3) (2022) 432-436.
- [19] Lewis K., The Science of Antibiotic Discovery, *Cell*, 181 (1) (2020) 29-45.
- [20] Wohlleben W., Mast Y., Stegmann E., Ziemert N., Antibiotic Drug Discovery, *Microb Biotechnol.*, 9 (5) (2016) 541-548.
- [21] Boström J., Brown DG., Young RJ., Keserü GM., Expanding the Medicinal Chemistry Synthetic Toolbox, *Nat Rev Drug Discov.*, 17 (10) (2018) 709-727.
- [22] Campos KR., Coleman PJ., Alvarez JC., Dreher SD., Garbaccio RM., Terrett NK., Tillyer RD., Truppo MD., Parmee ER., The Importance of Synthetic Chemistry in the Pharmaceutical Industry, *Science*, 363 (6424) (2019) eaat0805.
- [23] Sakamoto R., Morozumi S., Yanagawa Y., Toyama M., Takayama A., Kasuga NC., Nomiya K., Synthesis, Characterization, and Structure-Activity Relationship of the Antimicrobial Activities of Dinuclear N-heterocyclic Carbene (NHC)-Silver(I) Complexes, *J Inorg Biochem.*, 163 (2016) 110-117.
- [24] Sarı Y., Akkoç S., Gök Y., Sifniotis V., Özdemir İ., Günel S., Kayser V., Benzimidazolium-Based Novel Silver N-heterocyclic Carbene Complexes: Synthesis, Characterization and In Vitro Antimicrobial Activity, *J Enzyme Inhib Med Chem.*, 31 (6) (2016) 1527-1530.
- [25] Gök Y., Akkoç S., Erdoğan H., Albayrak S., In Vitro Antimicrobial Studies of New Benzimidazolium Salts and Silver N-heterocyclic Carbene Complexes, *J Enzyme Inhib Med Chem.*, 31 (6) (2016) 1322-1327.
- [26] Butorac RR., Al-Deyab SS., Cowley AH., Antimicrobial Properties of Some Bis(iminoacene)phthalene (BIAN)-Supported N-heterocyclic Carbene Complexes of Silver and Gold, *Molecules*, 16 (3) (2011) 2285-2292.
- [27] Siegmund D., Lorenz N., Gothe Y., Spies C., Geissler B., Prochnow P., Nuernberger P., Bandow JE., Metzler-Nolte N., Benzannulated Re(i)-NHC Complexes: Synthesis, Photophysical Properties and Antimicrobial Activity, *Dalton Trans.*, 46 (44) (2017) 15269-15279.
- [28] Jiang Y., Geng M., Bai L., Targeting Biofilms Therapy: Current Research Strategies and Development Hurdles, *Microorganisms*, 8 (8) (2020) 1222.
- [29] Roy R., Tiwari M., Donelli G., Tiwari V., Strategies for Combating Bacterial Biofilms: A Focus on Anti-biofilm Agents and Their Mechanisms of Action, *Virulence*, 9 (1) (2018) 522-554.
- [30] Vasava MS., Bhoi MN., Rathwa SK., Jethava DJ., Acharya PT., Patel DB., Patel HD., Benzimidazole: A Milestone in the Field of Medicinal Chemistry, *Mini Rev Med Chem.*, 20 (7) (2020) 532-565.

- [31] Tessier J., Schmitzer AR., Benzimidazolium Salts Prevent and Disrupt Methicillin-Resistant *Staphylococcus aureus* Biofilms, *RSC Adv.*, 10 (2020) 9420-9430.
- [32] Üstün E., Şahin N., Çelik C., Tutar U., Özdemir N., Gürbüz N., Özdemir İ., Synthesis, Characterization, Antimicrobial and Antibiofilm Activity, and Molecular Docking Analysis of NHC Precursors and Their Ag-NHC Complexes, *Dalton Trans.*, 50 (42) (2021) 15400-15412.
- [33] Bernardi T., Badel S., Mayer P., Groelly J., de Frémont P., Jacques B., Braunstein P., Teyssot ML., Gaulier C., Cisnetti F., Gautier A., Roland S., High-Throughput Screening of Metal-N-heterocyclic Carbene Complexes Against Biofilm Formation by Pathogenic Bacteria, *ChemMedChem.*, 9(6) (2014) 1140-1144.
- [34] O'Beirne C., Piatek ME., Fossen J., Müller-Bunz H., Andes DR., Kavanagh K., Patil SA., Baumann M., Tacke M., Continuous Flow Synthesis and Antimicrobial Evaluation of NHC* Silver Carboxylate Derivatives of SBC3 In Vitro and In Vivo, *Metallomics.*, 13 (2) (2021) mfaa011.
- [35] Kaloğlu N., Kaloğlu M., Özdemir İ., Günel S., Özdemir İ., Silver-N-heterocyclic carbene complexes: Synthesis, characterization, and antimicrobial properties, *J Chin Chem Soc.*, 64(4) (2017) 420-426.
- [36] Nayak S., Gaonkar, S L., Coinage Metal N-Heterocyclic Carbene Complexes: Recent Synthetic Strategies and Medicinal Applications, *ChemMedChem*, 16(9) (2021) 1360-1390.

Crocus Officinalis (L.) Extract on Human Colorectal Cancer Cell Line (HT-22): Investigation in Vitro

Sinan Soylu^{1,a,*}

¹ Department Of General Surgery, Faculty of Medicine, Sivas Cumhuriyet University, Sivas, Türkiye.

*Corresponding author

Research Article

History

Received: 14/01/2024

Accepted: 15/03/2024



This article is licensed under a Creative Commons Attribution-NonCommercial 4.0 International License (CC BY-NC 4.0)

ABSTRACT

Crocus sativus L. has been used as spice, food colouring and medicinal plant for thousands of years. In this study, antioxidant properties and cytotoxic effect of saffron extract were evaluated in HT-22 cell lines. Malignant and non-malignant cells (L929) were cultured in DMEM medium and incubated with different concentrations of saffron extract in different solvents (water, ethanol, ethyl-acetate, n-hexane). Cell viability was determined by MTT assay. Antioxidant parameters such as DPPH, FRAP, total polyphenol and flavonoid amounts were measured. The highest DPPH value was found as 15.90±0.12 µg/mL in ethyl acetate solvent. Total polyphenols were 89.06±0.02 mg GAE/g extract, flavonoids were 76.98±2.08 µg QE/g extract and FRAP was 67.93±0.98 mg/g extract in ethanol solvent. In colon cancer, IC50 value 94±1.37 µg/mL was found to be the highest value. This is thought to be due to the high antioxidant capacity in ethanol solvent. While antioxidant capacity was not found to be high, antiproliferation effect was found to be high. Saffron may also be considered as a promising chemotherapeutic agent in cancer treatment in the future.

Keywords: Antioxidant parameters, Crocus sativus L., HT-22 cell lines, Saffron.

^a ssoylu@cumhuriyet.edu.tr

^{id} <https://orcid.org/0000-0002-3911-3227>

Introduction

Cancer is increasingly becoming the biggest health problem all over the world. Natural products have long been used in the prevention and treatment of many diseases, including cancer, due to their low side effects. For this reason, studies on natural plants are increasing today and it is being investigated whether they are good drug candidates [1]. Colon cancer, which is among the top five cancer types in the world, occurs in the gastrointestinal system. According to the 2018 estimated data of the World Health Organization, colon cancer was found in 1.80 million cases and ranks second in the world with 862 thousand among cancer cases resulting in death [2].

Today, many additives such as preservatives, colourants and oxidation inhibitors are widely used in food. However, in recent years, there has been a very rapid increase in use and 200.000 tonnes of additives are used in food annually. Despite the increasing use of additives today, the awareness of consumers increases the use of additives obtained from natural sources. In line with these developing demands, manufacturers pay more attention to the use of additives obtained from natural sources in their production [3]. Saffron is a spice of natural origin used to give colour and flavour in food and is a natural substance that has proven to have positive effects on health.

Saffron is a plant used as a medicine in Anatolia since the Hittite period. It is known that saffron has been used

in herbal treatment since ancient times due to its antidepressant, sedative, anodyne, decongestant, antispasmodic, diaphoretic and expectorant properties [4]. Crocus sativus L. (saffron) is a 20-30 cm tall perennial cultivated plant of the crocus genus belonging to the Iridaceae (irises) family growing in Mediterranean and Asian countries [5]. Saffron (Crocus sativus L.) is widely cultivated in arid and semi-arid regions of Iran [6]. The stigmas and stigmas of the blue-purple coloured flower are called saffron [7]. Saffron is cultivated for flavouring food, for the production of cosmetics and perfumes, and for medicinal purposes. Carotenoids, phenolic groups and flavonoids in the structure of foods are the structures responsible for the antioxidant effect. Saffron (Crocus sativus L.) is an important plant that can be used in functional food production because it has high antioxidant capacity [8]. "Crocic" is a water-soluble natural dye among carotenoids with high colouring power and golden yellow colour. It also has a strong antioxidant and anticancer effect together with picroxin and safranal. In addition, picroxin and safranal are sought after special flavour and aroma substances. These compounds are also effective in determining the quality of saffron.

Saffron contains proteins, fats and carbohydrates, as well as some valuable compounds such as vitamin A, vitamin C and folic acid. Saffron is also a rich source of minerals such as iron, calcium, magnesium, copper, manganese, potassium, phosphorus and zinc. It also

contains some vital metabolites, monoterpenoids, flavonoids, carotenoids and anthocyanins. Saffron contains different chemical constituents that fluctuate greatly depending on growing conditions. Chemical composition analyses showed that saffron contains about 50%-63% sugar (dextrin, starch, pectin, gums and pentosans), 12%-13% protein, 10%-12% moisture, 5%-8% fat, 5%-7% minerals and 5%-10% crude fiber. According to the analysis, the essential oil of saffron tepals and tepals (one of the outer parts of the flower) differed in composition. The essential oil of tepals contains crocetin, crocin, picrocrocin and safranal as main components [9,10].

Studies conducted with saffron extract and its components have shown that they have anticarcinogenic [11], antigenotoxic [12], antioxidant [13], anti-inflammatory [14], antihypertensive [15], anti-obesity [16], liver protective [17] properties.

In this study, it is aimed to investigate the antioxidant and anticarcinogenic properties of saffron, which is also grown in Iran.

Materials and Methods

Preparation of Extracts

The collected *Crocus Officinalis* (L.) were collected Iranian. Iranian saffron was obtained from Bahraman company, which grows and supplies saffron to the market in Mashhad city, Khorasan Razavi province. *Crocus Officinalis* (L.) were washed with tap water, then distilled water and dried in the laboratory for 2 weeks. The dried samples were ground and 100 gram samples were extracted twice in 1000 mL of different solvents (water, ethanol, n-hexane and ethyl acetate solvents) at 45°C for 45 min in an ultrasonic bath. The extracts were filtered through Whatman No.1 filter paper and concentrated in vacuo to obtain the extracts. The extracts obtained were stored at -20 °C for use in experimental procedures.

Determination of Antioxidant Properties

Determination of radical scavenging activity (DPPH)

DPPH (2,2-diphenyl-1-picrylhydrazyl) assay was performed according to the procedure developed by Cuendet et al. Ascorbic acid was used as a reference standard. DPPH was dissolved in methanol solution (0.004 g/100mL). According to this method, the sample was mixed with DPPH radical, incubated in the dark for 30 minutes and the absorbance was measured at 517 nm in a spectrophotometer [18].

Determination of iron (Fe+3) reducing power in extracts

FRAP test developed by Benzie and Strain (1996) and modified by us was performed [19]. Reducing agents such as antioxidants cause the ferricyanide (Fe+3) complex to be reduced to Fe+2. In this method, this reduction property is utilised and the colour changes from yellow to

green depending on the reducing power of the sample tested. The resulting green colour gives maximum absorbance at 700 nm. increasing absorbance indicates an increase in the reducing power. According to this method, trolox was used as standard antioxidant compound.

Total flavonoid content determination

Total flavonoid content (TFC) of the extracts was determined by aluminium chloride method. The determination of total flavonoids using $AlCl_3$ is based on the formation of stable complexes of flavones and flavonols between $AlCl_3$, keto and hydroxyl groups. In addition, $AlCl_3$ also involves the formation of complexes with ortho-dihydroxyl groups of A- or B- rings of flavonoids. According to this method, quercetin was used as standard [20].

Estimation of Total Phenolic Content (TPC) Determination

Folin–Ciocalteu's assay and colorimetric method were used to evaluate the total phenolic content [21]. The *Crocus Officinalis* (L.) extract (1 mg/mL) was mixed with 1 mL Folin-Ciocalteu reagent and then 5 mL distilled water was added. After 5 minutes, 1 mL of sodium carbonate (10%) was then added. The final mixture was then incubated in the dark at room temperature for 60 min and the absorbance was measured against the blank at 725 nm using a UV-VIS spectrophotometer. The total phenolic content of the extract was calculated from the standard gallic acid (10-250 mg/L) calibration curve and expressed as mg gallic acid equivalent (GAE) per gram dry extract weight.

Cell Culture

Cells

In this study, colon cancer (HT-22-HTB-38™) cell lines and fibroblast cells (L-929) were grown in DMEM medium containing 10% (v/v) fetal bovine serum (FBS), 1% penicillin-streptomycin, in an incubator at 5% CO₂, 95% humidity and 37°C.

Cytotoxicity tests

The cytotoxic effects of *Crocus Officinalis* (L.) extract, which was found to be the most effective antioxidant, on colon and healthy cells were performed using MTT method. Firstly, cells were seeded in plates at 5×10^4 cells/well. All cells were treated with different concentrations (100, 50, 25, 12.5, 6.25, 3.125, 1.56 µg/mL) of the extracts and incubated for 24 hours. After incubation, MTT solution was added and incubated for 2-4 hours. After the plate was poured, 100 µL DMSO was added and formazone crystals were formed. Absorbance values were obtained by reading on an ELISA reader at 545 nm [22].

Results

Antioxidant Parameters

DPPH radical scavenging activity was determined for different concentrations of *Crocus Officinalis* (L.) extracts. For this purpose, the % inhibition values at each concentration were calculated from the absorption values obtained and plotted against the concentration. The following formula was used in the calculation.

$$I (\%) = \left[\frac{A_{blanc} - A_{sample}}{A_{blanc}} \right] \times 100$$

Table 1. DPPH values

	Water	Etanol	Ethyl acetate	n-hexane	Ascorbic Acid
µg/mL	23.04±0.02	31.67±0.30	15.90±0.12	22.03±0.06	4.94±0.06

** The values are given as mean ± standard deviation.

IC₅₀ value of *Crocus Officinalis* (L.) extract was 23.04±0.02 µg/mL water, 31.67±0.30 µg/mL ethanol, 15.90±0.12 µg/mL ethyl acetate, 22.03±0.06µg/mL n-hexane. The IC₅₀ value of ascorbic acid was found to be 4.94±0.06 µg/mL (Table 1).

Crocus Officinalis (L.) extract was analysed according to the method of Chang et al. The amount of total phenolic matter was calculated as gallic acid equivalent [19]. The concentrations of total flavanoid compounds in *Crocus Officinalis* (L.) extracts (200, 100, 50, 25, 12.5, 6.25, 3.125, 1.562 µg/mL) were calculated as quercetin equivalent from the equation obtained from the quercetin standard graph calibration curve given $y = 0.0032x + 0.0768$ (R²=0.9997) [18].

Table 2. Total phenolic and flavanoid content of different solvents extracts

	Water	Etanol	Ethyl acetate	n-hexane
Total phenolic content (mg GAE/g extract)	44.16±0.04	89.06±0.02	53.26±0.04	48.43±0.01
Total flavanoids content (µg QE/g extract)	31.09±1.08	76.98±2.08	56.98±1.46	60.98±2.04

** The values are given as mean ± standard deviation.

In the analysis of extracts according to Benzie and Strain method, the amounts of FRAP antioxidant power were calculated as trolox equivalents. The concentrations of iron reducing compounds (200, 100, 50, 25, 12.5, 6.25, 3.125, 1.562 µg/mL) in extract were calculated as equivalent to trolox from the equation obtained from the calibration curve of the trolox standard graph.. The obtained graph equation was found as $y = 0.0031x - 0.0012$ (R²=0.9999).

The results of FRAP antioxidant power of *Crocus Officinalis* (L.) extracts obtained from ethanol, water, ethyl acetate and n-hexane solvents are given in Table 3.

Table 3. FRAP values

	Water	Etanol	Ethyl acetate	n-hexane
(mg/g)	42.38±1.29	67.93±0.98	5.83±1.04	50.82±1.90

** The values are given as mean ± standard deviation.

Cell Culture

In the study, *Crocus Officinalis* (L.) extracts prepared in water, ethanol, ethyl acetate and n-hexane solvents were applied to colon cancer in cell culture with 24 hours incubation. IC₅₀ values were calculated and given below (Table 4 and Table 5).

Table 4. IC₅₀ values of *Crocus Officinalis* (L.) calculated in different solvents in colon cancer

	Water	Etanol	Ethyl acetate	n-hexane
(µg/mL)	178±1.73	94±1.37	157±2.09	143±1.03

** The values are given as mean ± standard deviation.

Table 5. IC₅₀ values of *Crocus Officinalis* (L.) calculated in different solvents in healthy cell line

	Water	Etanol	Ethyl acetate	n-hexane
(µg/mL)	318±2.91	159±2.65	230±1.09	258±1.78

** The values are given as mean ± standard deviation.

Discussion

C. sativus L. is a plant widely cultivated in different parts of the world for nutritional and economic purposes [23]. Different solvent extracts of *C. sativus* L. show different pharmacological effects [24]. As a result, in the present study, four different extracts of *C. sativus* L. were obtained and their antioxidant activities and anticancer effects were investigated.

Flavonoids are important because of their capacity to act as various antioxidants [25]. They are commonly found

in phenolic compounds and are reported to be potent antioxidants [25]. Recent studies have shown that phenolic compounds have a possible protective role against oxidative disorders [26].

Karimi et al. (2010) analysed the total phenolic content of Greek methanol saffron extracts by Folin-Ciocalteu method and found the phenolic content to be 6.5 mg GAE/g. This study, they were found that Total flavonoid content was measured as 5.8 mg /g (26). Makhoul et al. (2011) determined the total phenolic content of saffron flowers grown in Lebanon by Folin-Ciocalteu method and found 16 mg GAE/g. Havva et al. (2010) measured the total flavonoid content as 2.9 mg/g in a similar study on saffron extract. While Kariminin found the inhibition percentage of saffron extracts by DPPH method as 55% in his study, Hawa et al. (2010) found the inhibition percentage of ethanol and water extracts of saffron by DPPH method as 50% in pure ethanol and 59% in pure water [27,28,29].

IC50 value of *Crocus Officinalis* (L.) extract was found 23.04±0.02 µg/mL for water, 31.67±0.30 µg/mL for ethanol, 15.90±0.12 µg/mL for ethyl acetate, 22.03±0.06µg/mL for n-hexane. The IC50 value of ascorbic acid was found to be 4.94±0.06 µg/mL (Table 1).

Total phenolic different solvents extracts were found 44.16±0.04 mg GAE/g extract for water, 89.06±0.02 mg GAE/g extract for ethanol, 53.26±0.04 mg GAE/g extract for ethly acetat, 48.43±0.01 mg GAE/g extract for n-hexane. The flavonoid content were determined 31.09±1.08 µg QE/g extract for water, 76.98±2.08 µg QE/g extract for ethanol, 56.98±1.46 µg QE/g extract for ethly acetat, 60.98±2.04 µg QE/g extract for n-hexane. According to FRAP analyses were found 42.38±1.29 mg/g extract for water, 67.93±0.98 mg/g extract for ethanol, 45.83±1.04 mg/g extract for ethly acetat, 50.82±1.90 mg/g extract for n-hexane. The total phenolic, FRAP, and flavonoid content observed in our study showed that the antioxidant capacity of *C. sativus* was low. However, in our study, the highest antioxidant capacity was observed in the extract made with ethanol solvent.

In this study, the cytotoxic and apoptogenic effects of ethanolic saffron extract in HeLa and HepG2 cell lines were investigated. According to the data obtained, it was found that saffron extract had more cytotoxic activity against HeLa and HepG2 cell lines than non-malignant cells tested [30]. Studies from around the world have shown that polyphenols found in medicinal plants suppress cell proliferation and induce apoptosis [31]. A small number of cell line studies have proven the anti-cancer effect of *C. sativus* leaves. Saffron and crocetin have been reported to induce apoptosis in human breast cancer cells via p53-mediated apoptosis stimulation [32]. In our study, we applied saffron extracts to colon cancer cells. Our data showed that saffron extract had greater cytotoxic activity against HT-22 cell lines than against non-malignant cells tested, which is consistent with previous studies showing that saffron and its constituents have anti-tumour and anticarcinogenic activities.

Conflicts of interest

There are no conflicts of interest in this work.

References

- [1] Smith-Warner S.A., Elmer P.J., Tharp T.M., Fosdick L., Randall B., Gross M., Wood J., Potter J.D., Increasing vegetable and fruit intake: randomized intervention and monitoring in an at-risk population, *Cancer Epidemiol Biomar Prev.*, 9 (3) (2000) 307-317.
- [2] World Health Organization. 2018. Global Health Observatory. <http://www.who.int.-/data/gho> Erişim tarihi: 21.06.2018
- [3] Doğruyol H., Additives in Foods and Their Harm; Childhood Hyperactivity, *Current Pediatrics.*, 4 (2) (2006) 42-48.
- [4] Abdullaev F.I., Espinosa-Aguirre J.J., Biomedical properties of saffron and its potential use in cancer therapy and chemoprevention trials, *Cancer Detection and Prevention.*, 28 (6) (2004) 426-432.
- [5] Khazdair M.R., Boskabady M.H., Hosseini M., Rezaee R., Tsatsakis A.M., The effects of *Crocus sativus* (saffron) and its constituents on nervous system: A review, *Avicenna J Phytomed.*, 5 (5) (2015) 376-391.
- [6] Behzad S., Razavi M., Mahajeri M., The effect of mineral nutrients (N.P.K.) on saffron production, *Acta Hort.*, 306 (1992) 426-430.
- [7] Melnyk J.P., Wang S., Marcone M.F., Chemical and biological properties of the world's most expensive spice: Saffron, *Food Research International.*, 43 (8) (2010) 1981–1989.
- [8] Bolhassani A., Khavari A., Bathaie S.Z., Saffron and natural carotenoids: Biochemical activities and anti-tumor effects, *Biochimica et Biophysica Acta (BBA)-Reviews on Cancer.*, 1845 (1) (2014) 20-30.
- [9] Rios, J. L., Recio, M. C., Giner, R. M. ve Manez, S. (1996). An Update Review of Saffron and its Active Constituents. *Phytotherapy Research*, 10(3), 189-193.
- [10] Zararsız H. F., *Gastronomi Ve Mutfak Sanatları Anabilim Dalı*, master thesis, karabük of university, Lisansüstü Eğitim of institue, 2023.
- [11] Abdullaev F.I., Riverón-Negrete L., Caballero-Ortega H., Manuel Hernández J., Pérez-López I., Pereda-Miranda R., Espinosa-Aguirre J.J., Use of in vitro assays to assess the potential antigenotoxic and cytotoxic effects of saffron (*Crocus sativus* L.), *Toxicol In Vitro.*, 17 (5-6) (2003) 731-736.
- [12] Hosseinzadeh H., Abootorabi A., Sadeghnia H.R., Protective Effect of *Crocus sativus* Stigma Extract and Crocin (trans-crocin 4) on Methyl Methanesulfonate-Induced DNA Damage in Mice Organs, *Dna and Cell Biology.*, 27 (12) (2008) 1-8.
- [13] Assimopoulou A.N., Sinakos Z., Papageorgiou V.P., Radical scavenging activity of *Crocus sativus* L. extract and its bioactive constituents, *Phytother. Res.*, 19(11) (2005) 997-1000.
- [14] Hosseinzadeh H., Younesi H.M., Antinociceptive and antiinflammatory effects of *Crocus sativus* L. stigma and petal extracts in mice, *BMC Pharmacol.*, 2 (2002) 1-8.
- [15] Fatehi M., Rashidabady T., Fatehi-Hassanabad Z., Effects of *Crocus sativus* petals' extract on rat blood pressure, *J. Ethnopharmacol.*, 84 (2-3) (2003) 199-203.
- [16] Mashmoul M., Azlan A., Yusof B.N.M., Khaza'ai H., Mohtarrudin N., Boroushaki M.T., Effects of saffron extract and crocin on anthropometrical, nutritional and lipid

- profile parameters of rats fed a high fat diet, *Journal of Functional Foods*, 8 (2014) 180-187.
- [17] Omid A., Riahinia N., Montazer Torbati M.B., Behdani M.A., Hepatoprotective effect of Crocus sativus (saffron) petals extract against acetaminophen toxicity in male Wistar rats, *Avicenna J Phytomed.*, 4 (5) (2014) 330- 336.
- [18] Cuendet M., Hostettmann K., Potterat O., Iridoid glucosides with free radical scavenging properties from *Fagraea blumei*, *Helvetica Chimica Acta*, 80 (4) (1997) 1144-1152.
- [19] Benzie I. F., Strain J. J., The ferric reducing ability of plasma (FRAP) as a measure of "antioxidant power": the FRAP assay, *Analytical biochemistry.*, 239 (1) (1996) 70-76.
- [20] Joseph J., Paul D., Kavitha M.P., Dineshkumar B., Menon J.S., Bhat A.R. and Krishnakumar K., Preliminary phytochemical screening and in vitro antioxidant activity of Banana flower (*Musa paradisiaca* AAB Nendran variety), *Journal of Pharmacy Research*, 8 (2) (2014) 144 – 1519.
- [21] Chang C.C., Yang M.H., Wen H.M., Chern J.C., Estimation of total flavonoid content in propolis by two complementary colorimetric methods, *Journal of Food and Drug Analysis*, 10 (3) (2002) 178–182.
- [22] Gezezen H., Tutar U., Hepokur C., Ceylan M., Synthesis and biological evaluation of novel indenopyrazole derivatives, *J Biochem Mol Toxicol.*, 33(5) (2019) :e22285. doi: 10.1002/jbt.22285
- [23] Kaur C., Dalamu M., Singh S., Walia S., Joshi A.D., Variations in phenolics and antioxidants in Indian onions (*Allium cepa* L.) Genotype selection for breeding, *Nutr. Food Sci.*, 40 (1) (2004) 6–19
- [24] Mzabri I., Addi M., Berrichi A., Traditional and Modern Uses of Saffron (*Crocus Sativus*), *Cosmetics*, 6 (4) (2019) 63.
- [25] Somayeh R., Sohrab M., Maryam H., Seyed A.S., Evaluation of antioxidant activities of bioactive compounds and various extracts obtained from saffron (*Crocus sativus* L.): A review, *J. Food Sci. Technol.*, 52 (2015) 1881–1888.
- [26] Karimi E., Oskoueian E., Hendra R., Jaafar H.Z., Evaluation of *Crocus sativus* L. stigma phenolic and flavonoid compounds and its antioxidant activity, *Molecules*, 15 (9) (2010) 6244–6256.
- [27] Forni C., Facchiano F., Bartoli M., Beneficial Role of Phytochemicals on Oxidative Stress and Age-Related Diseases, *BioMed Res. Int.*, 7 (2019) 1-16.
- [28] Makhlof H., Saksouk M., Habib J., Chahine R., Determination of antioxidant activity of saffron taken from the flower of *Crocus sativus* grown in Lebanon., *African Journal of Biotechnology*, 10 (41) (2011) 8093-8100.
- [29] Hawa Z., Jaafari E., Bahtaei D., Evaluation of *Crocus sativus* L. Stigma Phenolic and Flavonoid Compounds and Its Antioxidant Activity, *Molecules*, 15 (9) (2010) 6244-6256.
- [30] Tavakkol-Afshari J., Brook A., Mousavi S. H., Study of cytotoxic and apoptogenic properties of saffron extract in human cancer cell lines, *Food and Chemical Toxicology*, 46 (11) (2018) 3443-3447.
- [31] Kondhare D., Lade H., Phytochemical profile, aldose reductase inhibitory, and antioxidant activities of indian traditional medicinal *Coccinia grandis* (L.) fruit extract, *Biotech.*, 7 (6) (2017) 378.
- [32] Wali A. F., Alchamat H. A. A., Hariri H. K., Hariri B. K., Menezes G. A., Zehra U., Ahmad, P., Antioxidant, antimicrobial, antidiabetic and cytotoxic activity of *Crocus sativus* L. Petals, *Applied Sciences.*, 10 (4) (2020) 1519.

Aloe vera Gel Extract Prolongs Lifespan in *Caenorhabditis elegans*

Şeyda Berk^{1,2,a,*}

¹ Department of Molecular Biology and Genetics, Faculty of Science, Sivas Cumhuriyet University, Sivas, Türkiye.

² Advanced Technology Research Center (CUTAM), Sivas Cumhuriyet University, Sivas, Türkiye.

*Corresponding author

Research Article

History

Received: 04/12/2023

Accepted: 12/03/2024



This article is licensed under a Creative Commons Attribution-NonCommercial 4.0 International License (CC BY-NC 4.0)

ABSTRACT

Caenorhabditis elegans (*C. elegans*), with its superiority and physiological aging properties, has become a widely recognized model system in research on aging, longevity mechanisms, age-related diseases, and drug screening. Lifespan-extending mutations in *C. elegans* are known to slow the aging process by interfering with a number of signaling pathways such as the AMP-activated protein kinase (AMPK), mechanistic target of rapamycin (mTOR) and insulin/IGF-1 signaling (IIS) pathways. We aimed to see how *Aloe vera* (*A. vera*) gel affects the fertilization and lifespan of *C. elegans*. In the presence of all *A. vera* gel concentrations (0.312 - 5 mg/mL), the fertilization capacity of N2 worms increased and extended their lifespan as well as increased their body size. We found that in N2 worms cultured with 2.5 mg/ml *A. vera* gel, *sgk-1*, *age-1*, and *let-363* mRNA expression was significantly increased, while *rsk-1* mRNA expression was significantly decreased. We therefore conclude that it may extend lifespan through a mechanism specifically dependent on mTOR signaling. All these observations will provide a new perspective on mammalian life extension through the model organism *C. elegans*.

Keywords: *Aloe vera*, *C. elegans*, Lifespan, Ageing, Fertilization.

^a sberk@cumhuriyet.edu.tr

^{id} <https://orcid.org/0000-0003-4687-0223>

Introduction

Anti-aging and living a long, healthy life free of illness have been goals since ancient times, despite the fact that aging is a complicated phenomenon that is still not fully understood. *C. elegans*, a small nematode, is now a popular model system for studies on aging. Research using *C. elegans* in multiple labs has greatly advanced our basic understanding of aging as a biological process regulated by cellular signaling pathways and gene expression programs [1]. The isolation of long-lived *C. elegans* mutants sparked a scientific journey that has yielded numerous insights into the mechanisms that regulate lifespan, with implications for human longevity [2]. The requirement for extended periods of time (months to years) in mammalian systems presents the largest obstacle to lifespan extension research. The adaptable, seemingly straightforward model organism *C. elegans*, which has a brief lifespan (measured in days), has been used to overcome this. Its fundamental systems and mechanisms are strikingly similar to those of mammals [3]. Furthermore, a number of investigations have demonstrated that the mechanisms for longevity found in *C. elegans* are also found in flies, mice, and humans in comparable patterns [4]. First observed in *C. elegans*, the positive correlation between extended healthy longevity and modulation of insulin/IGF-1 signaling was later confirmed in flies and mice [1]. This gives studies on the longevity of *C. elegans* greater context. It also requires less time and is simple to use [3]. The mTOR pathway is another important pathway that connects metabolism

and nutrient availability to longevity. This pathway regulates numerous downstream signaling pathways that control cell proliferation, growth, survival, motility, and protein synthesis [5]. Research on *C. elegans* has demonstrated that mTOR activity inhibition increases worm lifespan. The IIS pathway and the mTOR pathway are most likely separate pathways that contribute to longevity, though there may be some overlap [6].

The effects of bioactive secondary metabolites of plant foods on the prevention of oxidative stress-related diseases have received excessive attention. Many secondary metabolites, including polyphenols, ascorbic acid, and carotenoids, have been shown to reduce oxidative stress caused by reactive oxygen species (ROS) and this situation is described as oxidative damage (or oxidative stress) theory [7]. Free radicals, or ROS, are involved in oxidative stress-related illnesses and aging. In order to combat ROS damage, the antioxidant defense system and aerobic metabolism coevolved [8]. When ROS production is out of control relative to antioxidant activity, biomolecules such as DNA, lipids, and proteins can be damaged. Aging and other chronic illnesses like cancer, heart disease, atherosclerosis, myocardial infarction, diabetes, and other degenerative diseases in human can be mediated by these activities [9]. The relationship between aging and oxidative damage accumulation, as well as antioxidant defense levels, has been supported by oxidative damage theory [7]. *C. elegans* mutants with reduced insulin/IGF-1 signaling (IIS) are resistant to

oxidative stress, and *C. elegans* mutants with increased resistance to a ROS-producing compound (juglone) have been identified [10].

A. vera is a genus of perennial succulent or xerophyte that belongs to the Liliaceae family. It has elongated, peaked leaves that store a large amount of water in their tissue, and it can be stemless or have very short stems. Additionally, the inner leaf pulp, which makes up the majority of the plant volume, is composed of large thin-walled parenchymal cells containing *A. vera* gel and is also referred to as inner leaf, inner leaf fillet, or fillet [11]. Pharmacologically active components found in aloe have a variety of biological effects, such as fungicidal, immunomodulating, antiviral, antibacterial, anti-inflammatory, and anticancer properties [12].

In present study, we investigated the effects of *A. vera* gel extracts on the fertility and survival of *C. elegans* in N2 worms. Furthermore, we assessed variations in the mRNA expression of the insulin/IGF signaling (IIS) and rapamycin (TOR) signaling components, *sgk-1* (serine/threonine-protein kinase *sgk-1*), *age-1/PI3K* (phosphatidylinositol 3-kinase *age-1*), *let-363/TOR* (target of rapamycin homolog), and *rsk-1/S6K* (ribosomal protein S6 kinase beta), which are two important nutrient-sensing pathways in the most well-validated anti-aging research.

Materials and Methods

A. vera Gel Extract Preparation

Fresh, mature, healthy leaves of commercially purchased *A. vera* were thoroughly cleaned with water, then the spikes on the edges were removed and cut into transverse pieces. The dense epidermis was carefully separated from the parenchyma with a sharp knife. Before homogenization in a blender, the parenchyma was again gently washed with distilled water at ambient conditions to extract surface exudates. To remove fibers, the homogenized gel was centrifuged at 3000 rpm for 30 min. The supernatant was obtained by vacuum filtering through a filter paper (Whatman, Turkey) to obtain fresh *A. vera* gel. The resulting aqueous *A. vera* gel was used directly and a new batch of gel was prepared each time [13].

C. elegans and *Escherichia coli* Strains

For this investigation, the OP50 strain of *E. coli* and the wild-type *C. elegans* (N2 Bristol) were procured from the Caenorhabditis Genetics Centre (CGC) at the University of Minnesota (Minneapolis–St. Paul, MN 55455, USA).

Maintenance of *C. elegans*

Worms were maintained in accordance with Brenner's previously instruction [14]. Briefly, worms were grown at 20 °C on nematode growth medium (NGM) agar [Preparation of NGM agar plates: 3 g NaCl, 17 g agar and 2.5 g peptone 975 mL H₂O were added, mixed and autoclaved. After the autoclave mixture was cooled to 55 °C, 1 mL of 1 M CaCl₂, 1 mL of 5 mg/ml cholesterol in ethanol, 1 ml of 1 M MgSO₄ and 25 mL of 1 M KPO₄ (pH:6) buffer were added and the prepared NGM solution was dispensed into petri dishes (60x15mm)] seeded with *E. coli* OP50 (food).

Worms cultivated on NGM plates were transferred using the "chunking" technique. This method involved

taking a sterile scalpel or spatula and moving a piece of agar from one old plate to a new one. There were worm stock transfers every one to three generations. The method of controlling worms involved observing them through a dissecting microscope. Obtaining axenized *C. elegans* eggs and synchronous cultures of *C. elegans* were carried out according to the method previously described by Özdemir et al. [15]

Fertilization Assay

Age-matched adult worms (one worm per well) were cultured at 20°C in 24-well plates containing 1 mL/well S Medium [1L S Basal, 10 mL 1 M potassium citrate pH: 6, 10 mL trace metals solution (1.86 g disodium EDTA, 0.69 g FeSO₄ • 7 H₂O, 0.2 g MnCl₂ • 4 H₂O, 0.29 g ZnSO₄ • 7H₂O, 0.025 g CuSO₄ • 5 H₂O, dissolved in 1L H₂O), 3 mL 1 M CaCl₂, 3 mL 1 M MgSO₄] with 3L of *E. coli* OP50 and increasing concentrations of *A. vera* gel extract (0.312 mg/mL, 0.625 mg/mL, 1.250 mg/mL, 2.5 mg/mL, and 5 mg/mL). The number of eggs laid in each well over a seven-day period was counted under a microscope. The experiments were repeated twice, and each experiment was carried out in quadruplicate.

Lifespan Assay

The L4 stage worms were placed in 24-well plates with 1 mL/well S (about 12 worms per well). In medium containing 3µL of *E. coli* OP50, worms were cultured at 20°C for the lifespan assay while increasing concentrations of *A. vera* gel extract (0.312 - 5 mg/mL) were added. To prevent reproduction, 5-Fluoro-2'-deoxyuridine (FUDR), was utilized. Worms were counted under a microscope every day, and the medium was changed every seven days. After being gently prodded to move the plate, animals were considered dead if they did not move. In order to analyze the body size of worms, photomicrographs taken at 0, 7, and 14 days were obtained using the Zeiss Axiovert A1 in conjunction with the Zeiss Digital Microscope Camera (AxioCam ICc 5). Body size was determined using ImageJ software. GraphPad Prism was used to analyze the data. The experiments were repeated twice, with each experiment being carried out in duplicate.

RNA Isolation and cDNA Synthesis

Preparation of worm samples for RNA isolation was carried out according to the previously described method [15]. Total RNA was isolated using a commercially available kit according to the manufacturer's instructions (HibriGen Biotechnology, Istanbul, Turkey, Total RNA Isolation kit; Cat. No: MG-RNA-01-100). The cDNA synthesis has been performed using the iScript cDNA Synthesis Kit (Bio-Rad, Hercules, CA, USA; Cat. No: 1708891) for obtaining cDNA product with 500 ng/µL of RNA according to manufacturer's recommendations. The cDNA that was produced was either immediately examined by qPCR or was kept at +4°C for further use.

Quantitative Real-time PCR (RT-qPCR)

RT-qPCR was used to assess the expression *sgk-1*, *age-1*, *let-363* and *rsk-1* mRNA in N2 L4 stage worms. The SYBR green assay and the StepOnePlus™ Real Time PCR system (Applied Biosystems, USA) were used for quantitative PCR, which was done according to the manufacturer's instructions for real-time amplifications.

The assay was carried out in a total reaction volume of 20 μL with 10 μL of BlasTaqTM 2X qPCR Master Mix (Abm, Canada, USA), 0.5 μL of each primer, and 2 μL of cDNA template. Table 1 contains primer information. All reactions were carried out in 96-well plates. The PCR was carried out using the real-time instrument in accordance with the manufacturer's instructions. Typically, 3 minutes of initial denaturation at 95°C was followed by 40 cycles of 10 seconds denaturation at 95°C, 30 seconds annealing at 60°C, and 15 seconds extension at 72°C. For the purpose of melting curve analysis, a cycle of dissociation

steps (58°C for 1 minute followed by 0.5°C for 10 seconds up to 95°C) was added. At the end of each PCR experiment, a melting curve was generated to confirm the presence of a single peak and rule out the synthesis of primer dimers and non-specific products. For each gene, two biological samples were collected and measured twice. *act-1* and *cdc-42* reference genes were determined as the most stable genes for N2 strain in the study conducted by our research group [15]. Therefore, *act-1* and *cdc-42* were used to normalize mRNA levels using the method as previously described [16].

Table 1. Primer sequences and gene information for RT-qPCR

Gene symbol	Gene description	Sequence name	Function	Primer sequence	Reference
<i>act-1</i>	Actin-1	T04C12.6	Cytoskeletal structural protein	F: 5'-CTCTTGCCCATCAACCATG-3' R: 5'-CTTGCTGGAGATCCACATC-3'	[17]
<i>cdc-42</i>	Cell division control protein 42 homolog	R07G3.1	RHO GTPase	F: 5'-CTGCTGGACAGGAAGATTACG-3' R: 5'-CTCGGACATTCTCGAATGAAG-3'	[17]
<i>rsk-1</i>	Ribosomal protein S6 kinase beta	Y47D3A.16	ribosomal protein S6 kinase activity	F: 5'-CCGTTTGTGGGATTCACC-3' R: 5'-TGGCTTTCTCGGGCTCTT-3'	[18]
<i>let-363</i>	Target of rapamycin homolog	B0261.2	protein serine/threonine kinase activity	F: 5'-GCCACTCTCTGATTACCCTGT-3' R: 5'-GTGAGCCGCGTGTTCAAAT-3'	[19]
<i>sgk-1</i>	Serine/threonine-protein kinase sgk-1	W10G6.2	Phosphatidylinositol-3,4,5-trisphosphate binding activity and protein serine/threonine kinase activity	F: 5'-AAGACTGTTGACTGGTGGTG-3' R: 5'-AGACGAAGTGCTGGTTG-3'	[20]
<i>age-1</i>	Phosphatidylinositol 3-kinase age-1	B0334.8	1-phosphatidylinositol-3-kinase activity and 1-phosphatidylinositol-4-phosphate 3-kinase activity	F: 5'-GCTGCTCCGTGCAGAGATTG-3' R: 5'-CACGGAGGTAAGCTCCATC-3'	[21]

The relative expression of genes was calculated using the comparative threshold method, $2^{-\Delta\text{Ct}}$. Primers were purchased from BMLabosis (Ankara, Turkey). Ct values >35 did not yield consistent results and were considered below the detection limit of the assay.

Statistical Analysis

All experiments were repeated at least twice. The outcomes of the repeated experiments were comparable. The statistical software GraphPad Prism 6.0 (GraphPad software, San Diego, CA) was utilized for the analysis. For survival, log-rank tests were used. A one-way ANOVA test was used to compare statistical results between groups. When significant differences were discovered, the Newman-Keuls test was used to compare groups. $p < 0.05$ was considered statistically significant in all analyses. The data is shown as mean SEM.

Results

Effects of *A. vera* Gel Extract on *C. elegans* Fertilization

Our results showed that *A. vera* gel extract at concentrations of 0.312 - 5 mg/mL had a significant stimulatory effect on the number of eggs laid by *C. elegans* N2 worms (Figure 1). While it was observed that the number of eggs laid increased significantly compared to the control group at all *A. vera* concentrations applied to wild-type N2 worms, we observed the highest increase at 0.625 and 2.5 mg/ml.

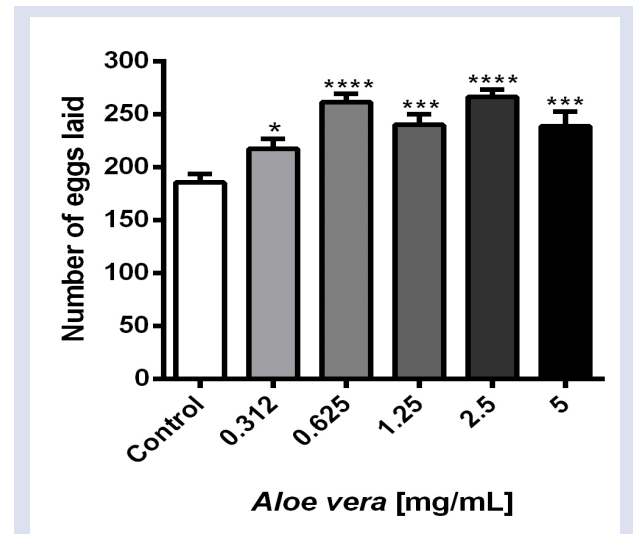


Figure 1. The effect of *A. vera* gel extract on egg-laying in N2 worms. The experiments were carried out on synchronized populations. Worms were assessed to be exposed to *A. vera* gel extract throughout their development from egg to young adulthood for the experiment, in which exposure to *A. vera* gel extract was shown at 7 days (the method by which L4 individuals attain fertile adulthood) according to the worm's developmental stage. During the egg stage, synchronized populations of wild-type and mutant *C. elegans* were transplanted to 24-well plates containing liquid media with *A. vera* gel extract (0.312 - 5 mg/mL). Significance relates to a comparison of egg-laying behaviour in *C. elegans* exposed to *A. vera* and control results. The number of eggs laid by each worm was counted every day for 7 days. Values represent the mean \pm SEM of two independent experiments in quadruplicate. * $p < 0.05$, *** $p < 0.001$, **** $p < 0.0001$; $n = 3$.

Effects of *A. vera* Gel Extract on Lifespan of *C. elegans*

We confirmed the effects of *A. vera* on *C. elegans* lifespan by survival analysis. Figure 2A shows the survival curve analysis results of N2 worms (Figure 2A). *A. vera* gel extract at concentrations of 0.312 mg/mL, 0.625 mg/mL, 1.250 mg/mL, 2.5 mg/mL and 5 mg/mL increased the average lifespan of N2 worms by 3.39%, 10.17%, 14.41%, 18.64% and 5.08%, respectively (Figure 2B). We determined 2.5 mg/mL *A. vera* gel extract as the concentration that most prolongs the lifespan of N2 worms.

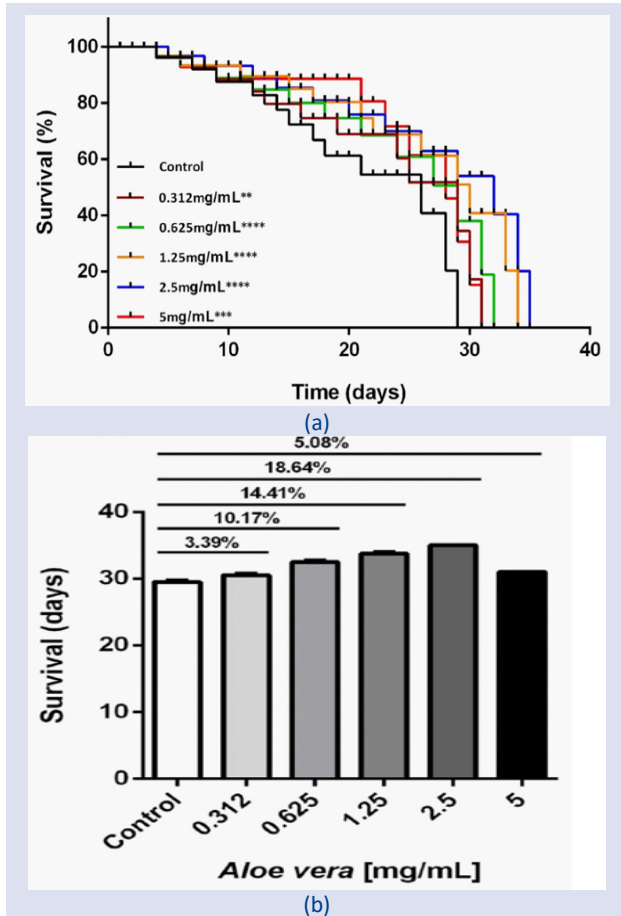


Figure 2. (A) Lifespan survival curves of N2 worms. (B) Graph showing the % increase in lifespan in the presence of *A. vera* gel extract compared to control. The experiments were carried out on synchronized populations. The synchronized populations of wild-type *C. elegans* were transplanted to 24-well plates containing liquid media with *A. vera* gel extract (0,312 - 5 mg/mL). Significance relates to a comparison of lifespan in *C. elegans* exposed to *A. vera* and control results. Values represent the mean \pm SEM of two measurements from two independent experiments. * $p < 0.05$, ** $p < 0.01$, *** $p < 0.001$, **** $p < 0.000$.

Body Size Measurement

In order to reveal the changes in the body size of *C. elegans* after 14 days of *A. vera* gel extract at concentrations of 0.312 - 5 mg/mL, we measured body size of N2 worms (Figure 3). We observed that the body length of wild-type N2 animals increased significantly

compared to the control as a result of *A. vera* treatment at concentrations of 1.250 mg/mL, 2.5 mg/mL (Figure 3A), while body width increased significantly at all applied concentrations (Figure 3B).

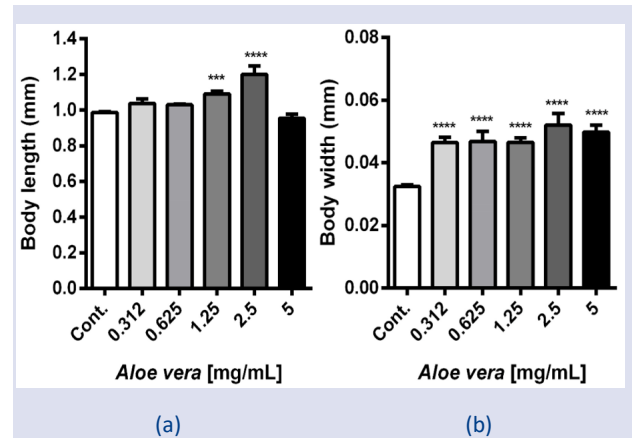


Figure 3. Body size of wild-type N2 strains grown in S-medium including different concentrations of *A. vera* gel extract (0.312 - 5mg/mL). Body length (A) and body width (B) of N2 grown in S-medium including *A. vera* gel extract compared with control. Body length and width size derived N2 worms after 14 days is in mm using ImageJ software. Values represent the mean \pm SEM of two independent experiments in duplicate. **** $p < 0.0001$, *** $p < 0.001$.

mRNA Expression Analysis in *C. elegans*

The mRNA expression of *sgk-1*, *age-1/PI3K*, *let-363/TOR*, and *rsk-1/S6K* mRNA expression of N2 worms cultured in S medium containing 2.5 mg/mL *A. vera* gel extract were determined by quantitative RT-PCR (Figure 4).

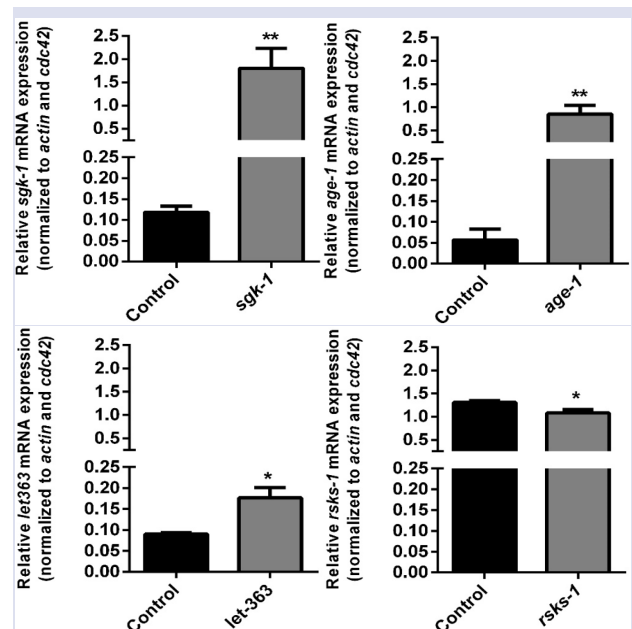


Figure 4. *Sgk-1*, *age-1*, *let-363* and *rsk-1* mRNA expression in N2 worms. *sgk-1*, *age-1*, *let-363* and *rsk-1* mRNA expression was measured relative to the levels of the house-keeping genes *cdc-42* and *act-1*. Values represent the mean \pm SEM of two measurements from two independent experiments. * $p < 0.05$, ** $p < 0.01$.

Since we obtained the highest egg production and longevity at 2.5 mg/mL *A. vera* concentration, we performed mRNA analyses in the presence of this concentration. Compared with the control, *sgk-1*, *age-1* and *let-363* mRNA expression increased significantly in N2 worms cultured with *A. vera* gel extract, while *rsk-1* mRNA expression significantly decreased (Figure 4).

Discussion

To our knowledge, there has been no previous study how adding *A. vera* gel extract to *C. elegans* growth medium affects fertilization and longevity. In this study we investigated the effects of *A. vera* gel extract on *in vivo* fertilization, lifespan and body size in N2 worms. We also evaluated differential mRNA expression of components of the insulin/IGF signalling (IIS) and target of rapamycin (TOR) pathways, which have been associated with two major nutrient sensing pathways of the best validated antiaging interventions.

In the literature, *C. elegans* drug applications have largely been carried out on NGM agar growth medium. Therefore, the high bioavailability of the drug applied to the worms in the agar medium has always been questionable. Therefore, when drug applications are carried out on NGM agar medium, it is recommended to apply the drug at high concentrations for bioavailability in *C. elegans*. Liquid culture conditions are preferred because the bioavailability efficiency of the drug is high [22]. Our study team cultured worms in liquid culture medium to increase the bioavailability of *A. vera* gel extract by worms. Therefore, while it increased the bioavailability of drugs/extracts applied to worms in liquid culture medium, it also allowed the culture medium and drugs/extracts to be refreshed more easily at regular intervals.

We found that the egg-laying capacity of all concentrations of *A. vera* gel extract applied to wild-type N2 worms was significantly increased compared to the control group. We observed the highest egg yield at 2.5 mg/ml *A. vera* concentration. According to the longevity analysis results, wild-type N2 worms extended their lifespan in the presence of all concentrations of *A. vera* gel extract. We determined that 2.5 mg/ml *A. vera* was the concentration that most increased the longevity of N2 worms. As expected, it was found that the lifespan of the worms was extended independently of concentration. Stated differently, survival did not increase further with increasing inhibitor concentration. There are no studies in the literature investigating the effects of *A. vera* extract on *C. elegans* fertility and longevity, but the effects of *A. vera* have been investigated in *Drosophila melanogaster*, another important model organism [23]. According to the findings of the study, adding *A. vera* extract (5ml/L) to the diet prolonged adult lifespan in both male and female flies without reducing fertility. The findings of this study are consistent with our findings, and *C. elegans* dietary supplementation containing *A. vera* extract prolonged both fertility and adult lifespan.

Another study examining the effects of long-term *A. vera* intake on the growth of Fischer 344 male rats showed that ingestion of *A. vera* by rats led to an increase in body weight [24]. They also suggested that *A. vera* intake did not cause any significant adverse effects in rats. According to the body size analysis results of our current study, when N2 worms were exposed to *A. vera* gel extract, significant increases in body length and width occurred in wild-type N2 worms, according to the results of its effect on body size. The fact that we observed a significant increase, especially in the body width of the worms, at all *A. vera* concentrations applied to the worms confirms the results of the study conducted with rats.

The insulin/IGF signaling (IIS) and rapamycin target (TOR) pathways are the two main nutrient sensing pathways associated with the most effective antiaging therapies that have been validated. When these pathways are activated, autophagy, mitochondrial biogenesis, and the expression of detoxifying and antioxidant enzymes are all induced. These processes taken together can enhance cellular function [25]. Diet composition influences the aging process in terms of lifestyle, a longer lifespan is linked to a high intake of phytochemicals and a low protein diet [25]. Notably, a recent analysis indicates that human longevity has a heritability of less than 10%, suggesting that lifestyle decisions have a significant impact on both longevity and aging [26].

Many natural substances can act by prolonging the lifespan of nematodes by regulating some important cellular signaling pathways [25]. The insulin pathway, which is triggered by food intake, is one of these cellular pathways that regulates the lifespan of *C. elegans* [5]. This pathway includes *daf-16*, the sole homolog of the FOXO family of transcription factors, multiple conserved protein kinases, and *daf-2*, the homolog of the human insulin receptor. In nematodes, insulin-like peptides bind to *daf-2* and activate intracellular signaling. *Daf-2* signaling results in phosphorylation of *age-1*, *pdh-1*, and *akt-1/2* inactivates DAF-16/FOXOs by retaining the protein in the cytosol. In the absence of *daf-2*, *age-1*, and *akt-1/2*, as when there is a lack of food, *daf-16* migrates to the nucleus and induces the expression of genes associated with longevity [5].

Nutrients and amino acids trigger the target of rapamycin (TOR), which is another pathway triggered by food consumption. In response to the presence of amino acids and growth factors, the TOR (target of rapamycin) pathway regulates growth and reproduction. TOR, as a nutrient sensor, mediates the metabolic response to dietary restriction; it is a conserved lifespan-extension paradigm with numerous connections to many other signaling pathways. In line with this, inhibiting TOR activity increased lifespan in several species [27]. The TOR ortholog in *C. elegans*, *let-363*, is a serine/threonine kinase, but no protein has been identified as a direct phosphorylation target of TORC1 or TORC2 for nearly all of the TOR-regulated processes in *C. elegans* [28]. p70 ribosomal S6 kinase (S6K), is a downstream target of mTOR and rapamycin, and *in vitro* studies in mammalian

cell culture and other model organisms have revealed that S6K is a direct phosphorylation target of mTORC1 [29]. Reduced translation of the S6K protein is the outcome of mTOR signaling inhibition [30]. Since reducing the expression of the S6K homolog in *C. elegans* (*rsk-1*) alone is sufficient to extend lifespan, this mechanism most likely contributes to lifespan extension via mTOR inhibition. Reduced *S6K/rsk-1* transcription and deletion mutations have been shown to increase *C. elegans* lifespan [31].

In mammalian cell culture, *sgk* inhibits FoxO3 activity [32], and *sgk-1* is thought to reduce lifespan in *C. elegans* through inhibiting DAF-16/FoxO activity [33]. However, some studies have shown that *sgk-1* mutations reduce the longevity of *C. elegans* [34-36], controversy the lifespan extension phenotype of *sgk-1* following RNAi knockdown. [33]. Additionally, they proposed that the mechanisms by which *Akt/PKB* and *sgk-1* influence lifespan, stress resistance, and FoxO transcription factor activity in *C. elegans* are distinct. In summary, while *sgk-1* and *age-1* limit lifespan by inhibiting DAF-16/FoxO activity, reduced transcription and deletion mutation of *let-363/TOR* and *S6K/rsk-1* are known to contribute to lifespan extension through mTOR inhibition. However, as mentioned above, processes that occur contrary to this observed lifespan extension phenotype are also included in the literature. Based on all these findings, studies on *C. elegans* aging and longevity remain complex, especially in associating these two processes with signaling pathways. In our current study, after adding *A. vera* extract to the diet of N2 worms, an increase in *sgk-1*, *age-1* and *let-363* mRNA expression was observed, while a decrease in *rsk-1* mRNA expression was observed. This suggested that the decrease in *rsk-1* expression in the presence of *A. vera* may extend the lifespan of N2 worms, especially through the inhibition of the TORC1 pathway.

According to some research, ROS may cause oxidative stress, which would shorten *C. elegans* life span above a certain concentration range. Furthermore, antioxidants with the capacity to scavenge excess radicals may increase longevity and postpone the negative effects of aging [37]. Many studies have shown that some plant extracts or phytochemicals extracted from plants can support stress tolerance and longevity in *C. elegans* through various signaling pathways [38]. The Aloe contains a large amount of bioactive compounds such as fatty acids, anthraquinones, flavonoids, lectins, terpenoids, mono- and polysaccharides, sterols (campesterol, β -sitosterol), enzymes, tannins, salicylic acid, vitamins and minerals [39]. This highly bioactive component of *A. vera* also causes it to have high antioxidant activity. A study by Ray et al. showed that *A. vera* gel extracts have high antioxidant capacity [40]. In our study, the phytochemicals contained in *A. vera* may have had a stimulating effect on longevity in N2 worms by acting as antioxidants that mainly scavenge ROS.

In conclusion, we showed that *A. vera* gel extracts applied to N2 worms at all concentrations increased fertilization capacity and longevity. Additionally, increases in body length and width of N2 worms were observed in

presence of *A. vera*. We observed that *sgk-1*, *age-1* and *let-363* mRNA expression significantly increased, while *rsk-1* mRNA expression significantly decreased in N2 worms cultured with 2.5mg/ml *A. vera* gel extract. We therefore conclude that it may extend lifespan through a mechanism specifically dependent on mTOR signaling. However, we measured only mRNA and not actual protein levels of IIS and mTOR signaling pathway components. More research is needed on this topic as mRNA levels do not necessarily reflect protein levels. It would also be useful to examine the protein expression levels of IIS and mTOR components, which play an active role in longevity and fertility processes. Our other conclusion is that the phytochemicals found in *A. vera* may extend the lifespan of N2 worms, primarily by acting as antioxidants. Therefore, it would be useful to elucidate these mechanisms with molecular and biochemical experiments in the future. All these observations will provide a new perspective on mammalian life extension through the model organism *C. elegans*.

Acknowledgements

The authors are thankful for the ongoing support of the Advanced Technology and Research Center (CUTAM), Sivas Cumhuriyet University. Further, we would like to thank Özgür Ülkü Özdemir, master student of the Department of Molecular Biology and Genetics at Sivas Cumhuriyet University, for providing the necessary convenience and encouragement for the maintain of the *C. elegans* culture.

Conflict of Interest

The author state that did not have conflict of interests

References

- [1] Kenyon C.J., The genetics of ageing, *Nature*, 464 (7288) (2010) 504-512.
- [2] Denzel M.S., Lapierre L.R., Mack H.I., Emerging topics in *C. elegans* aging research: Transcriptional regulation, stress response and epigenetics, *Mechanisms of ageing and development*, 177 (2019) 4-21.
- [3] Arya U., Das C.K., Subramaniam J.R., *Caenorhabditis elegans* for preclinical drug discovery, *Current Science*, (2010) 1669-1680.
- [4] Stein G.M., Murphy C.T., The intersection of aging, longevity pathways, and learning and memory in *C. elegans*, *Frontiers in Genetics*, 3 (2012) 259.
- [5] Uno M., Nishida E. Lifespan-regulating genes in *C. elegans*, *NPI Aging Mech Dis.*, 2 (2016) 16010.
- [6] Zhang S., Li F., Zhou T., Wang G., Li Z., *Caenorhabditis elegans* as a useful model for studying aging mutations, *Frontiers in endocrinology*, 11 (2020) 554994.
- [7] Beckman K.B., Ames B.N., The free radical theory of aging matures, *Physiol Rev.*, 78 (2) (1998) 547-81.
- [8] Yu B.P., Cellular defenses against damage from reactive oxygen species, *Physiological reviews.*, 74 (1) (1994) 139-162.
- [9] Liguori I., Russo G., Curcio F., et al, Oxidative stress, aging, and diseases, *Clinical interventions in aging*, (2018) 757-772.

- [10] de Castro E., de Castro S.H., Johnson T.E., Isolation of long-lived mutants in *Caenorhabditis elegans* using selection for resistance to juglone, *Free Radical Biology and Medicine*, 37 (2) (2004) 139-145.
- [11] Guo X., Mei N., Aloe vera: A review of toxicity and adverse clinical effects, *J. Environ. Sci. Health C. Environ. Carcinog. Ecotoxicol Rev.*, 34 (2) (2016) 77-96.
- [12] Panel C.I.R.E., Final report on the safety assessment of aloelandongensis extract, aloe andongensis leaf juice, aloe arborescens leaf extract, aloe arborescens leaf juice, aloe arborescens leaf protoplasts, aloe barbadensis flower extract, aloe barbadensis leaf, aloe barbadensis leaf extract, aloe barbadensis leaf juice, aloe barbadensis leaf polysaccharides, aloe barbadensis leaf water, aloe ferox leaf extract, aloe ferox leaf juice, and aloe ferox leaf juice extract, *International journal of toxicology*, 26 (2007) 1-50.
- [13] Kenawy E.-R.S., Kamoun E.A., Ghaly Z.S., Shokr A.-b.M., El-Meligy M.A., Mahmoud Y.A.G., Novel Physically Cross-Linked Curcumin-Loaded PVA/Aloe vera Hydrogel Membranes for Acceleration of Topical Wound Healing: In Vitro and In Vivo Experiments, *Arabian Journal for Science and Engineering*, 48 (1) (2023) 497-514.
- [14] Brenner S., The genetics of *Caenorhabditis elegans*, *Genetics*, 77 (1) (1974) 71-94.
- [15] Özdemir Ö., Yurt K., Pektaş A.N., Berk Ş., Evaluation and normalization of a set of reliable reference genes for quantitative *sgk-1* gene expression analysis in *Caenorhabditis elegans*-focused cancer research, *Nucleosides Nucleotides Nucleic Acids*, (2024) 1-20.
- [16] Vandesompele J., De Preter K., Pattyn F., et al, Accurate normalization of real-time quantitative RT-PCR data by geometric averaging of multiple internal control genes, *Genome Biology*, 3 (7) 2002/06/18 (2002) research0034.1.
- [17] Hoogewijs D., Houthoofd K., Matthijssens F., Vandesompele J., Vanfleteren J.R., Selection and validation of a set of reliable reference genes for quantitative *sod* gene expression analysis in *C. elegans*, *BMC Mol Biol.*, 9 (2008) 9.
- [18] Zhuang Z., Li M., Liu H., et al, Function of RSKS-1-AAK-2-DAF-16 signaling cascade in enhancing toxicity of multi-walled carbon nanotubes can be suppressed by mir-259 activation in *Caenorhabditis elegans*, *Scientific Reports.*, 6 (1) (2016) 32409.
- [19] Chalorak P., Dharmasaroja P., Meemon K., Downregulation of eEF1A/EFT3-4 Enhances Dopaminergic Neurodegeneration After 6-OHDA Exposure in *C. elegans* Model, *Front Neurosci.*, 14 (2020) 303.
- [20] Zhao Y., Yang R., Rui Q., Wang D., Intestinal Insulin Signaling Encodes Two Different Molecular Mechanisms for the Shortened Longevity Induced by Graphene Oxide in *Caenorhabditis elegans*, *Sci Rep.*, 6 (2016) 24024.
- [21] Xiao X., Zhang X., Bai J., et al, Bisphenol S increases the obesogenic effects of a high-glucose diet through regulating lipid metabolism in *Caenorhabditis elegans*, *Food Chem.*, 339 Mar 1 (2021) 127813.
- [22] Kokel D., Li Y., Qin J., Xue D., The nongenotoxic carcinogens naphthalene and para-dichlorobenzene suppress apoptosis in *Caenorhabditis elegans*, *Nat. Chem. Biol.*, 2 (6) (2006) 338-45.
- [23] Chandrashekara K.T., Shakarad M.N., Aloe vera or Resveratrol Supplementation in Larval Diet Delays Adult Aging in the Fruit Fly, *Drosophila melanogaster*, *The Journals of Gerontology: Series A*, 66A (9) (2011) 965-971. doi:10.1093/geron/glr103
- [24] Herlihy J., Bertrand H., Kim J., Ikeno Y., Yu B., Effects of Aloe vera ingestion in the rat. I. Growth, food and fluid intake and serum chemistry, *Phytotherapy Research: An International Journal Devoted to Pharmacological and Toxicological Evaluation of Natural Product Derivatives.*, 12 (3) (1998) 183-188.
- [25] Martel J., Wu C.Y., Peng H.H., et al, Plant and fungal products that extend lifespan in *Caenorhabditis elegans*, *Microb Cell.*, 7 (10) (2020) 255-269.
- [26] Ruby J.G., Wright K.M., Rand K.A., et al, Estimates of the heritability of human longevity are substantially inflated due to assortative mating, *Genetics.*, 210 (3) (2018) 1109-1124.
- [27] Kapahi P., Chen D., Rogers A.N., et al, With TOR, less is more: a key role for the conserved nutrient-sensing TOR pathway in aging, *Cell metabolism.*, 11 (6) (2010) 453-465.
- [28] Blackwell T.K., Sewell A.K., Wu Z., Han M., TOR Signaling in *Caenorhabditis elegans* Development, Metabolism, and Aging, *Genetics.*, 213 (2) (2019) 329-360.
- [29] Magnuson B., Ekim B., Fingar D.C., Regulation and function of ribosomal protein S6 kinase (S6K) within mTOR signalling networks, *Biochemical Journal.*, 441 (1) (2012) 1-21.
- [30] Abe Y., Yoon S.O., Kubota K., Mendoza M.C., Gygi S.P., Blenis J., p90 ribosomal S6 kinase and p70 ribosomal S6 kinase link phosphorylation of the eukaryotic chaperonin containing TCP-1 to growth factor, insulin, and nutrient signaling, *J Biol Chem.*, 284 (22) 29 (2009) 14939-48.
- [31] Pan K.Z., Palter J.E., Rogers A.N., et al, Inhibition of mRNA translation extends lifespan in *Caenorhabditis elegans*, *Aging Cell.*, 6 (1) (2007) 111-9. doi:10.1111/j.1474-9726.2006.00266.x
- [32] Brunet A., Park J., Tran H., Hu L.S., Hemmings B.A., Greenberg M.E., Protein kinase SGK mediates survival signals by phosphorylating the forkhead transcription factor FKHL1 (FOXO3a), *Molecular and cellular biology.*, 21 (3) (2001) 952-965.
- [33] Hertweck M., Göbel C., Baumeister R., *C. elegans* SGK-1 is the critical component in the Akt/PKB kinase complex to control stress response and life span, *Developmental cell.*, 6 (4) (2004) 577-588.
- [34] Alam H., Williams T.W., Dumas K.J., et al, EAK-7 controls development and life span by regulating nuclear DAF-16/FoxO activity, *Cell metabolism.*, 12 (1) (2010) 30-41.
- [35] Kwon E.-S., Narasimhan S.D., Yen K., Tissenbaum H.A., A new DAF-16 isoform regulates longevity, *Nature*, 466 (7305) (2010) 498-502.
- [36] Chen A.T., Guo C., Dumas K.J., Ashrafi K., Hu P.J., Effects of *Caenorhabditis elegans* *sgk-1* mutations on lifespan, stress resistance, and DAF-16/FoxO regulation, *Aging Cell*, 12 (5) (2013) 932-40.
- [37] Ristow M., Schmeisser S., Extending life span by increasing oxidative stress, *Free radical biology and medicine*, 51 (2) (2011) 327-336.
- [38] Duangjan C., Rangsinth P., Gu X., Wink M., Tencomnao T., Lifespan extending and oxidative stress resistance properties of a leaf extracts from *Anacardium occidentale* L. in *Caenorhabditis elegans*, *Oxidative medicine and cellular longevity*, 2019 (2019).
- [39] Hęś M., Dziejczak K., Górecka D., Jędrusek-Golińska A., Gujska E., Aloe vera (L.) Webb.: Natural Sources of Antioxidants - A Review, *Plant Foods Hum Nutr.*, 74 (3) (2019) 255-265.
- [40] Ray A., Gupta S.D., Ghosh S., Evaluation of anti-oxidative activity and UV absorption potential of the extracts of Aloe vera L. gel from different growth periods of plants, *Industrial Crops and Products*, 49 (2013) 712-719.

Chemometric Determination of Parkinson's Drugs Containing Multiple Active Substances

Ayşe Merve Arslan^{1,a}, Güzide Pekcan^{1,b*}

¹ Department of Chemistry, Faculty of Engineering and Natural Sciences, Süleyman Demirel University, 32260, Isparta, Türkiye.

*Corresponding author

Research Article

History

Received: 29/08/2023

Accepted: 02/01/2024



This article is licensed under a Creative Commons Attribution-NonCommercial 4.0 International License (CC BY-NC 4.0)

ABSTRACT

In this work, the active ingredients of Entacapone, Levodopa and Carbidopa in drug samples used in the treatment of Parkinson's disease were quantitatively determined by Ultraviolet Visible (UV-VIS) Spectroscopy and chemometrics. Firstly, the spectra of each drug active ingredient were taken individually and then synthetic mixtures identical to the drug sample were analyzed. In our method, validation parameters were calculated for each method. Percent (%) recoveries were found on average for both the synthetic mixture and the commercial sample. The recoveries were quantitative for each method. The accuracy of the methods was tested by applying ANOVA test to the results obtained from the PLS and PCR calibration methods. The developed methods are reproducible, sensitive, and accurate, and can be recommended for the analysis of drug samples containing Entacapone, Levodopa, and Carbidopa

Keywords: Entacapone, Levodopa, Carbidopa, Chemometry.

^a aysemerveakkaya@gmail.com

^{id} <https://orcid.org/0000-0001-6044-8403>

^b erdemcamurlu@gmail.com

^{id} <https://orcid.org/0000-0003-3170-4492>

Introduction

Parkinson's disease was defined by James Parkinson in 1817 [1]. Parkinson's disease is a type of disease known as trembling paralysis, which occurs with serious losses in brain cells and is more common in men than women. It progresses more slowly than other disease types. With the decrease in dopamine cells in the brain, the communication between brain cells decreases, which negatively affects movement control [2]. Parkinson's disease is treated with medication to compensate for the loss of dopamine-producing cells and improve quality of life. In the treatment of this disease, levodopa, a dopamine precursor, is given orally to the patient to replenish the diminished dopamine in the body. When levodopa is taken alone, a large amount of levodopa will be destroyed before reaching the brain, causing factors such as dizziness and nausea in the patient, and treatment will not be provided. For this reason, auxiliary active ingredients are used to ensure that levodopa reaches the brain more easily without being broken down in the blood. These are mainly active ingredients such as carbidopa and entacapone. Today, drugs used in the treatment of this disease contain one or more of these excipients [3,4].

It would be more specific to state that the active ingredients (levodopa, carbidopa, and entacapone) were quantitatively determined in drug samples used in the treatment of Parkinson's disease. Advances in chemometrics have made it possible to work with a wide variety of calibration methods to analyze complex chemical mixtures. Levodopa (L-DOPA) is an amino acid in

the structure of 3,4-dihydroxy-L-phenylalanine. It has a molecular weight of 197.19 g/mol and the chemical formula $C_9H_{11}N_1O_4$ [5] (Figure 1.).

Carbidopa is a $C_{10}H_{14}N_2O_4$ white crystalline substance with a molecular weight of 244.3 g/mol that allows levodopa to cross the blood-brain barrier faster [6].

Entacapone is a nitrocatechol compound with a chemical structure of $C_{14}H_{15}N_3O_5$ and molecular weight of 305.29 g/mol. It is used in the treatment of Parkinson's disease in addition to levodopa and carbidopa to increase the effectiveness of treatment [7].

Developments in the fields of computers, software, statistics, and applied mathematics have led to a new discipline in chemistry called chemometrics for the solution of complex systems. This new discipline provides ease of operation not only in chemistry but also in many other disciplines such as biology, medicine, engineering, and economics [8].

Advances in chemometrics have made it possible to work with a wide variety of calibration methods for the analysis of complex chemical mixtures. Some of the most widely used multivariate calibration methods are called Partial Least Squares (PLS) and Principal Component Regression (PCR). The advantages of chemometrics are as follows:

i) To apply chemometrics, which is the application of software, mathematics, and statistics to chemistry, to the simultaneous determination of the active substances to be analyzed.

ii) With the chemometrics program, to develop a new method that is alternative, faster, and more cost-effective than previous classical methods.
 iii) To facilitate spectrophotometric analysis of intricate systems without prior separation thus.

iv) With the chemometrics method, it is aimed to prevent the loss of time and work caused by the trial and error method by going through a correct experimental design [9].

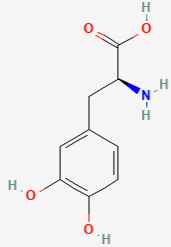
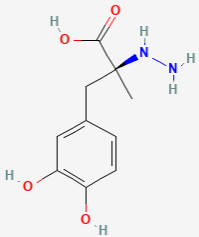
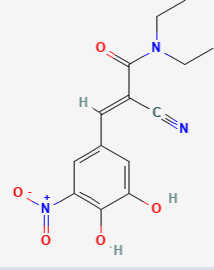
Active Substance	Formula	Molecular Weights	Structures
Levodopa	$C_9H_{11}N_1O_4$	197.19 g/mol	
Carbidopa	$C_{10}H_{14}N_2O_4$	244.3 g/mol	
Entacapone	$C_{14}H_{15}N_3O_5$	305.29 g/mol	

Figure 1. Chemical Structure of the Active Substance Levodopa, Carbidopa and Entacapone

Studies in the literature for the analysis of levodopa, carbidopa and entacapone are [10,11], [12,13] and [14,15], respectively. After the spectrophotometric method was applied to the drug tablet sample containing the active ingredients levodopa, carbidopa, and entacapone, the data obtained were evaluated by two different chemometric methods. Chemometric methods enabled the simultaneous evaluation of all data without any prior sorting of the drug samples. Furthermore, it was noted that the approach employed was precise, accurate, valid, consistent, and dependable when it came to the validation process—that is, it included the steps necessary to demonstrate that the approach is accurate, precise, and consistently delivers the desired results.

Materials and Methods

Levodopa, carbidopa, and entacapone, the active components of medications used to treat Parkinson's disease, were quantified in this work using UV/VIS spectrophotometry and chemometrics approaches.

Analytical-grade chemicals were obtained from (Sigma-Aldrich) and used in the experiment. Levodopa, carbidopa, and entacapone, the active components of medications used to treat Parkinson's disease, were determined using UV-VIS spectra using a UV 1700 PHARMASPEC SHIMADZU spectrophotometer equipped with a 1 cm long cell and controlled by a computer. The Minitab 17 [16] application was used to calculate the data. Chemometric techniques were used to evaluate the results. The spectra of artificial mixtures were recorded with the ratios of levodopa, carbidopa, and entacapone ranging from table 1. Finally, measurements were made on a sample of medicinal tablets that are sold commercially.

For the spectrophotometric measurements in the study, stock solutions of levodopa, carbidopa and entacapone were prepared as 25 mg / 250 mL in 0.1 M HCl. In this study, the spectra of levodopa, carbidopa and entacapone, first individually and then of synthetic mixtures prepared in different ratios, were obtained by spectrophotometric measurements. Finally, measurements were performed on a commercially available tablet sample. The data obtained were

evaluated by different chemometric methods. In the first step, calibration (zeroing) of the UV spectrophotometer device was performed. The calibration was first performed against air, leaving both cells empty. Then, the same procedure was performed by placing a blank sample prepared with our solvent in both light paths. The blank was always prepared in this way for all readings. When choosing the blank, solvent was preferred as the blank to eliminate interference effects. In the last step, the commercial tablet (Stalevo) is analyzed. In the preparation of the drug sample, all tablets in the package were crushed in an agate mortar, diluted and mixed. One tablet is weighed, dissolved in solvent, homogenized by stirring in a magnetic stirrer and absorbance readings are taken.

Results

Solutions of 100 ppm of the active substances levodopa, carbidopa and entacapone were prepared by using 0.1 M HCl as solvent at 25 mg/250 mL. In the next step, solutions were prepared to analyze the spectroscopic properties of each individual substance in the range of 1-40 µg/mL for each substance. The wavelengths at which levodopa, carbidopa and entacapone gave maximum absorbance (levodopa and carbidopa: 280 nm; entacapone: 306 nm) were determined.

Twenty synthetic mixture solutions of levodopa, carbidopa and entacapone in the range of 1-40 µg/mL were prepared (Table1.).

Table 1. Calibration set containing Levodopa, Carbidopa and Entacapone (µg/mL).

	Levodopa	Carbidopa	Entacapone
1	4	1	8
2	8	2	8
3	12	3	8
4	16	4	8
5	20	5	8
6	4	1	16
7	8	2	16
8	12	3	16
9	16	4	16
10	20	5	16
11	4	1	24
12	8	2	24
13	12	3	24
14	16	4	24
15	4	5	24
16	8	1	32
17	12	2	32
18	4	3	32
19	8	4	32
20	12	5	40

The absorbance values of the mixture solutions were obtained using UV spectroscopy (see Figure 2). Subsequently, chemometric methods were applied to these results. Chemometric calculations are currently the most popular, fast, and reliable methods used to quantify each component in multicomponent mixtures.

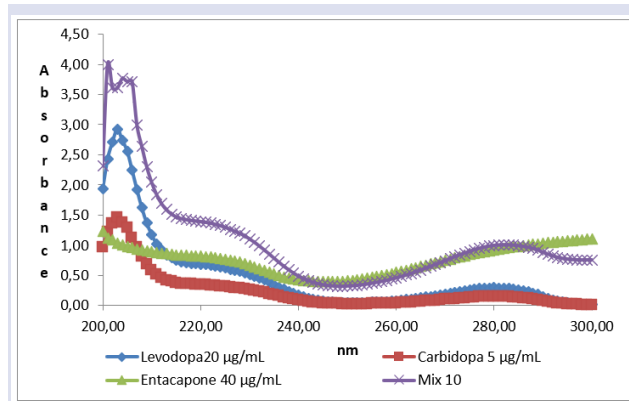


Figure 2. Absorption-Wavelength of Calibration Set containing Levodopa, Carbidopa and Entacapone

The relationship between absorbance and concentration is based on the principle of obtaining orthogonal lines by decomposing the absorbance values measured for the concentration set when examined using the principal component regression method. These lines are the coordinate order of the calibration to be established and calculations are based on this accuracy [17]. Principal component analysis (PCA) was performed as the first step before proceeding to chemometric calculations. Therefore, principal component analysis (PCA) was performed to reduce the dimensionality of the data and make it more manageable for chemometric calculations [18].

Values Calculated by Principal Component Regression (PCR)

Table 2. The results for each substance in the mixture containing Levodopa, Carbidopa, and Entacapone were calculated using principal component regression.

No	Levodopa			Carbidopa		
	Added (µg/mL)	Found (µg/mL)	Recovery %	Added (µg/mL)	Found (µg/mL)	Recovery %
1	4	3.95	98.75	1	1.01	101
2	8	7.94	99.25	2	1.99	99.5
3	12	11.95	99.58	3	2.97	99.00
4	16	15.99	99.94	4	3.98	99.50
5	20	19.96	99.80	5	4.96	99.20
6	4	3.98	99.50	1	0.96	96.00
7	8	7.94	99.25	2	1.97	98.50
8	12	11.95	99.58	3	2.98	99.33
9	16	15.98	99.88	4	3.98	99.50
10	20	19.96	99.80	5	4.98	99.60
11	4	3.86	96.50	1	0.94	94.00
12	8	7.98	99.75	2	1.89	94.50
13	12	11.97	99.75	3	3.00	100
14	16	15.94	99.63	4	3.98	99.50
15	4	3.86	96.50	5	4.96	99.20
16	8	7.98	99.75	1	0.98	98.00
17	12	11.89	99.08	2	1.97	98.50
18	4	3.65	91.25	3	2.95	98.33
19	8	7.84	98.00	4	3.89	97.25
20	12	11.79	98.25	5	4.72	94.40
		Mean	98.689		Mean	98.240
		Relative Standard Deviation	2.030		Relative Standard Deviation	1.992

Table 3. The results for each substance in the mixture containing Levodopa, Carbidopa, and Entacapone were calculated using principal component regression. (more).

No	Entacapone		
	Added (µg/mL)	Found (µg/mL)	Recovery %
1	8	7.98	99.75
2	8	7.95	99.38
3	8	7.89	98.63
4	8	7.94	99.25
5	8	7.96	99.50
6	16	15.96	99.75
7	16	15.87	99.19
8	16	15.97	99.81
9	16	15.96	99.75
10	16	15.99	99.94
11	24	23.96	99.83
12	24	23.97	99.88
13	24	23.89	99.54
14	24	23.56	98.17
15	24	23.88	99.50
16	32	31.97	99.91
17	32	31.88	99.63
18	32	31.97	99.91
19	32	31.94	99.81
20	40	39.45	98.63
		Mean	99.486
		Relative Standard Deviation	0.494

The recovery and relative standard deviation (RSD) data are shown in Table 3. Precision and accuracy data were checked.

ANOVA test [19] was applied to the calculated results to ensure the appropriateness of principal component regression. The F-test was used to determine whether the principal component regression model was statistically significant. For levodopa, carbidopa and entacapone, respectively, the calculated F-value (0.0024; 0.01; 0.01) was less than the critical F-value (4.09), indicating that the model is statistically significant. Since the calculated F value is less than the critical value, it was decided that the method is applicable. The Pearson correlation coefficient is defined in statistics as the measurement of the strength of the relationship between two variables and their relationship to each other. In simple terms, the Pearson correlation coefficient calculates the effect of the change in one variable when the other variable changes. The calculated p values were 0.96, 0.92 and 0.97 for levodopa, carbidopa and entacapone, respectively. The Pearson correlation coefficient with a p value should be greater than 0.05. The calculated ANOVA data were evaluated according to these steps. The significant F-value and p-value greater than 0.05 for all three active ingredients indicate that the principal component regression model is suitable for the simultaneous determination of levodopa, carbidopa, and entacapone.

Validation of the Principal Component Regression Method

Minimal data of the sum of squares of predicted errors (Predicted Residual Error Some of Squares → PRESS) were obtained in the cross-validation process for the calibration of PLS and PCR calibrations for the quantification of

substances in mixtures containing the active substances levodopa, carbidopa and entacapone. PRESS (Equation 1.) value close to zero increases the degree of accuracy [20]. The obtained PRESS values are small enough. Other parameters in the validation are the standard error of the calibration: SEC (Equation 2.) and the square root of the mean square error of the estimate: RMSEC (Equation 3.) [21].

$$PRESS = \sum_{i=1}^n (C_i^{added} - C_i^{found})^2 \tag{1}$$

where C_i^{added} is actual concentration, the added concentration of drug; and C_i^{found} is predicted concentration, the calculated concentration of drug.

$$SEC = \sqrt{\frac{\sum_{i=1}^n (C_i^{added} - C_i^{found})^2}{n-1}} \tag{2}$$

$$RMSEC = \sqrt{PRESS/n} \tag{3}$$

The limit of observability (LOD) and limit of detection (LOQ) parameters are related but have different definitions (Equations 4., 5.) [22].

$$LOD = 3,3Sa/m \tag{4}$$

$$LOQ = 10Sa/m \tag{5}$$

Sa: Standard deviation, m: Mean.

LOQ values were considered to be valid only if $LOQ > LOD$ [23].

Table 3. Validation Parameters for Principal Component Regression

Parameter	Levodopa	Carbidopa	Entacapone
SEC	0.027	0.016	0.034
PRESS	0.014	0.0059	0.029
RMSEC	0.026	0.017	0.038
LOD	0.131	0.107	0.225
LOQ	0.397	0.324	0.681

Application of Principal Component Regression and Partial Least Squares Method to Commercial Pharmaceutical Tablets

In a final step, the chemometric techniques used in this study were applied to commercial drug tablets after assessing the suitability of the methods and the analytical quality of the calculated data.

Table 4. Drug Sample Results

NO	Levodopa	Carbidopa	Entacapone
	(gram) PCR	(gram) PCR	(gram) PCR
1	0.097	0.0248	0.0198
2	0.098	0.0245	0.0195
3	0.089	0.0239	0.0197
4	0.101	0.0247	0.201
5	0.095	0.0246	0.0198
Mean	0.096	0.025	0.056
Relative Standard Deviation	0.047	0.014	1.449

It was studied with the drug Stalevo. It contains 100 mg levodopa, 25 mg carbidopa and 200 mg entacapone.

Values Calculated with Partial Least Squares Method (PLS)

The chemometric methods used in this study are partial least squares method (PLS) and principal component regression (PCR) [24,25]. The chemometric

model is created with the help of the matrix formed from the relationship between absorbance and concentration and chemometric calculations are created [26]. The most well-known chemometric calibration is the partial least squares method (PLS). According to the PLS algorithms used to create the calibration in the PLS method, orthogonalized PLS algorithm and non-orthogonalized PLS algorithm are used. The data obtained is more reliable than the classical methods.

Table 5. The results for each substance in the mixture containing Levodopa, Carbidopa, and Entacapon were calculated using the partial least squares method.

No	Levodopa			Karbidoopa		
	Added (µg/mL)	Found (µg/mL)	Recovery %	Added (µg/mL)	Found (µg/mL)	Recovery %
1	4	3.86	96.5	1	0.95	95.00
2	8	7.78	97.25	2	1.96	98.00
3	12	11.65	97.08	3	2.98	99.33
4	16	15.94	99.63	4	3.94	98.50
5	20	19.86	99.30	5	4.95	99.00
6	4	3.51	87.75	1	0.92	92.00
7	8	7.69	96.13	2	1.96	98.00
8	12	11.75	97.92	3	2.95	98.33
9	16	15.63	97.69	4	3.99	99.75
10	20	19.95	99.75	5	4.95	99.00
11	4	3.78	94.50	1	1.01	101.0
12	8	7.96	99.50	2	1.96	98.00
13	12	11.92	99.33	3	2.97	99.00
14	16	15.83	98.94	4	3.96	99.00
15	4	3.82	95.50	5	4.95	99.00
16	8	7.95	99.38	1	0.86	86.00
17	12	11.96	99.67	2	1.94	97.00
18	4	3.86	96.50	3	2.86	95.33
19	8	7.95	99.38	4	3.95	98.75
20	12	11.98	99.83	5	4.98	99.60
		Mean	97.575		Mean	97.48
		Relative Standard Deviation	2.826		Relative Standard Deviation	3.356

Table 5. The results for each substance in the mixture containing Levodopa, Carbidopa, and Entacapon were calculated using the partial least squares method. (more).

No	Entakapon		
	Added (µg/mL)	Found (µg/mL)	Recovery %
1	8	7.89	98.63
2	8	7.95	99.38
3	8	7.91	98.88
4	8	7.99	99.88
5	8	7.89	98.63
6	16	15.95	99.69
7	16	15.86	99.13
8	16	15.92	99.50
9	16	15.94	99.63
10	16	15.98	99.88
11	24	23.89	99.54
12	24	23.96	99.83
13	24	23.94	99.75
14	24	23.94	99.75
15	24	23.99	99.96
16	32	31.94	99.81
17	32	31.95	99.84
18	32	31.96	99.88
19	32	31.97	99.91
20	40	38.99	97.48
		Mean	99.447
		Relative Standard Deviation	0.625

When calculating the concentrations found against the added concentration, cross-validation was applied to avoid errors in the drug sample [27,28].

The method was deemed applicable for levodopa, carbidopa, and entacapone as the calculated F-values (0.01) were less than the critical value (4.09). The p-values were calculated as 0.92, 0.91, and 0.97 for levodopa, carbidopa, and entacapone, respectively. The Pearson correlation coefficient should have a p-value greater than 0.05.

Validation of Partial Least Squares Method (PLS)

Parameters were calculated for the quantification of substances in mixtures containing active pharmaceutical ingredients.

Table 6. Validation Parameters for the Partial Least Squares Method

Parameter	Levodopa	Carbidopa	Entacapone
SEC	0.056	0.017	0.037
PRESS	0.044	0.004	0.056
RMSEC	0.047	0.014	0.053
LOD	0.141	0.063	0.350
LOQ	0.427	0.191	1.061

Application of Partial Least Squares Method to Commercial Pharmaceutical Tablets

After assessing the suitability of the methods and the analytical quality of the calculated data, the chemometric techniques employed in this study were applied to commercial drug tablets in the final stage.

Table 7. Drug Sample Results.

NO	Levodopa (gram)	Carbidopa (gram)	Entacapone (gram)
	PCR	PCR	PCR
1	0.095	0.25	0.0193
2	0.089	0.0249	0.0198
3	0.094	0.0242	0.0196
4	0.094	0.0248	0.0194
5	0.097	0.0251	0.0195
Mean	0.094	0.07	0.02
Relative Standard Deviation	0.031	1.44	0.0099

It was studied with the drug Stalevo. It contains 100 mg levodopa, 25 mg carbidopa and 200 mg entacapone.

Discussion

The active substances levodopa, carbidopa, and entacapone were quantified in mixtures using UV Spectroscopy data supported by chemometric programs. For the active substances levodopa, carbidopa and entacapone, the method was statistically supported by developing UV. The values found were first quantified by principal component analysis (PCA). Then partial least squares (PLS) and principal component regression (PCR) chemometric methods were applied. In order to test the accuracy of the PLS and PCR methods, the ANOVA test was applied to both methods.

Both principal component regression (PCR) and partial least squares (PLS) methods yielded very high recovery values and sufficiently small relative standard deviation values. The correlation coefficients between the actual and estimated values were close to one, indicating a good fit of the chemometric models. Upon examination of the validation results for the method, it is evident that the LOD values are smaller than the LOQ values. Additionally, all other calculated parameters should be close to zero. Our own calculated data also showed values close to zero.

The suitability of the methods used was verified before proceeding to the commercial drug tablets. An ANOVA test was conducted to perform this procedure. The calculated F-values should be lower than the F-measure or F-theoretical values. Pearson's correlation coefficient with a P-value greater than 0.05 should be used. Based on the calculated values, it was determined that the methods used were appropriate. The chemometric methods applied in this study can be used to quantify multiple active ingredients in complex drug mixtures.

Conclusion

Statistical analysis of UV spectroscopy data using chemometric programmes was used to quantify the active substances levodopa, carbidopa, and entacapone in mixtures. Mixtures containing both substances were prepared. Before proceeding to commercial drug tablets containing these mixtures, both methods were tested, and the reliability of the data was examined. It was concluded that the applied methods could be recommended for the quantitative analysis of complex two-component drug mixtures.

Conflicts of interest

There are no conflicts of interest in this work.

References

- [1] Yaliman A., Şen E.İ., Parkinson Hastalığı ve Rehabilitasyonu, *Türk Fiz Tıp Rehab. Derg.*, 57 (2011) 38-44.
- [2] Şahin A.R., Arık A.C., Depresyon ve Parkinson hastalığı, *O.M.Ü. Tıp Dergisi*, 11(3) (1994) 239-246.
- [3] Yiğit G., Arıcıoğlu F., Günümüz ve Gelecekte Parkinson Hastalığı için Farmakolojik Tedavi Yaklaşımları, *MÜSBED*, 5(4) (2015) 265-273.
- [4] Pekcan Ertokuş G., Özer T., Parkinson Hastalığının Tedavisinde Kullanılan Levodopa ve Benserazid Etkin Maddelerinin Kemometrik Tayini, *Erzincan Üniversitesi Fen Bilimleri Enstitüsü Dergisi*, 13(2), (2020) 669-676.
- [5] Tashkhourian J., Hormozi-Nezhad M.R., Khodaveisi J., Application of silver nanoparticles and principal component-artificial neural network models for simultaneous determination of levodopa and benserazide hydrochloride by a kinetic spectrophotometric method, *Spectrochimica acta. Part A, Molecular and Biomolecular Spectroscopy*, 82(1) (2011) 25-30.
- [6] Damiani P.C., Moschetti A.C., Rovetto A.J., Benavente F., Olivieri A.C., Design and optimization of a chemometrics-assisted spectrophotometric method for the simultaneous determination of levodopa and carbidopa in pharmaceutical products, *Analytica Chimica Acta*, 543 (2005) 192-198.
- [7] Bugamelli F., Marcheselli C., Barba E., Raggi M.A., Determination of L-dopa, carbidopa, 3-O-methyldopa and entacapone in human plasma by HPLC-ED, *Journal of Pharmaceutical and Biomedical Analysis*, 54 (2011) 562-567.
- [8] Dinç E., Kemometri Çok Değişkenli Kalibrasyon Yöntemleri, *Hacettepe Üniversitesi Eczacılık Fakültesi Dergisi*, 27(1) (2007) 61-92.
- [9] Arslan A.M., Çoklu Etkin Madde İçeren Parkinson İlaçlarının Kemometrik Tayini, Süleyman Demirel Üniversitesi, Fen Bilimleri Enstitüsü, 2023.
- [10] Hosseini M.G., Faraji M., Momeni M.M., Ershad S., An innovative electrochemical approach for voltammetric determination of levodopa using gold nanoparticles doped on titanium dioxide nanotubes. *Microchim Acta*, 172 (2011) 103-108.
- [11] Benvidi A., Dehghani-Firouzabadi A., Mazloum-Ardakani M., Mirjalili B.F., Zare R., Electrochemical deposition of gold nanoparticles on reduced graphene oxide modified glassy carbon electrode for simultaneous determination of levodopa, uric acid and folic acid: Application of silver nanoparticles and principal component-artificial neural network models for simultaneous determination of

- levodopa and benserazide hydrochloride by a kinetic spectrophotometric. *Journal of Electroanalytical Chemistry*, 736 (2015) 22-29.
- [12] Gholivanda M.B., Jalalvanda A.R., Goicoechea H.C., Multivariate analysis for resolving interactions of carbidopa with DNA at a fullerene-C60, *International Journal of Biological Macromolecules*, 69 (2014) 369-381.
- [13] Tajika, S., Taher, M.A., Beitollahi, H., 2013, Simultaneous determination of droxidopa and carbidopa using a carbon nanotubes paste electrode, *Sensors and Actuators B: Chemical*, 188 (2013) 923-930.
- [14] Abdel-Ghany, M.F., Hussein, L.A., Ayad, M.F., Youssef, M.M., Investigation of different spectrophotometric and chemometric methods for determination of entacapone, levodopa and carbidopa in ternary mixture, *Spectrochimica Acta Part A: Molecular and Biomolecular Spectroscopy*, 171 (2017) 236-245.
- [15] Mantena, B.P.V., Rao, S.V., Rao, K.M.C.A., Ramakrishna, K., Reddy, R.S., Rapid Separation Technique for the Determination of Potential Impurities Present in Levodopa, Carbidopa, and Entacapone in Fixed Dose Combination Drug Product Using Trifunctionally Bonded Phase Ethylene Bridged Sorbent Column with Smaller Ion-Pair Reagent, *Journal of Liquid Chromatography & Related Technologies*, 38 (2015) 1073-1087.
- [16] Minitab, Available at: <https://www.inovadanismanlik.com.tr/>, Retrieved: 21.08.2023.
- [17] Dinç E., Kemometrik İşlem ve Yöntemlerin Analitik Kimyadaki Tipik Uygulamaları, *Uygulamalı Kemometri Yaz Okulu Notları*. (2009) 13-17.
- [18] Saganowska P., Wesolowski M., Principal Component and Cluster Analyses as Supporting Tools for Co-Crystals Detection, *J. Therm. Anal. Calorim.*, (2017) 45-55.
- [19] Bajpai V., Kumar S., Singh A., Singh J., Negi M.P.S., Bag S.K., Kumar N., Konwar R., Kumar B., Chemometric based identification and validation of specific chemical markers for geographical, seasonal and gender variations in *inospora cordifolia* stem using HPLC-ESI-QTOF-MS Analysis, *Photochemical Analysis*, 28(4), (2017) 277-288.
- [20] Uyanık A., Analitik Kimya İçin İstatistik ve Kemometri", Pegem Akademi Yayıncılık, 6. Baskı (2012) 254-259.
- [21] Bilgili A.V., Çullu M.A., Aydemir S., 2014, Tuzdan etkilenmiş toprakların yakın kızılötesi yansıma spektrometre ve elektromanyetik indüksiyon tekniği yardımıyla karakterize edilebilme potansiyelinin araştırılması , *Harran Tarım ve Gıda Bilimleri Dergisi*, 18(1) (2014) 32-45.
- [22] A. Shrivastava, V.B. Gupta, Methods for the determination of limit of detection and limit of quantitation of the analytical methods, *Chronicles of Young Scientist*, 2 (1), (2011) 21-25.
- [23] Armbruster D.A., Pty T., Limit of blank, limit of detection and limit of quantitation, *Clin Biochem Rev*, 29 (2008) 49-52.
- [24] Dinç E., Baleanu D., Spectrophotometric quantitative determination of cilazapril and hydrochlorothiazide in tablets by chemometric methods, *Journal of Pharmaceutical and Biomedical Analysis*, 30 (2002) 715-723.
- [25] Dinç E., Özdemir A., Baleanu D., Comparative study of the continuous wavelent transform, derivative and partial least squares methods applied to the overlapping spectra for the simultaneous quantitative resolution of ascorbic acid and asetilsalicylic acid in effervescent tablets, , *Journal of Pharmaceutical and Biomedical Analysis*, 37 (2005) 715-723.
- [26] Aktaş A.H., Sarıdağ A.M., Liquid chromatographic-chemometric techniques for the simultaneous HPLC determination of lansoprazole, amoksisilin and clarithromisin in commercial preparation, *Journal of Chromatographic Science*, (2017) 1-7.
- [27] Porfire A., Muntean D., Achim M., Vlase L., Tomuta I., Simultaneous Quantification of Simvastatin and Excipients in Liposomes Using Near Spectroscopy and Chemometry, *Journal of Pharmaceutical and Biomedical Analysis*, 107 (2015) 40-49.
- [28] Tarhan I., Kara A.A.I.H, Quantitative Determination of Free Fatty Acids in Extra Virgin Olive Oils by Multivariate Methods and Fourier Transform Infrared Spectroscopy Considering Different Absorption Modes, *International Journal of Food Properties*, (2017) 1-8.

Synthesis of Gum Arabic-Based Biopolymer Network and Determination of Its Toxicity Properties in In Vitro - In Vivo Model Systems

İdil Karaca Açarı ^{1,a,*}, Duygu Özhan Turhan ^{2,b}, Ali Kuruçay ^{3,c}, Süleyman Köytepe ^{3,d}, Burhan Ateş ^{3,e}

¹ Department of Basic Engineering Sciences, Faculty of Engineering and Natural Sciences, Malatya Turgut Özal University, Malatya, Türkiye.

² Department of Biology, Faculty of Science, İnönü University, Malatya, Türkiye.

³ Department of Chemistry, Faculty of Science, İnönü University, Malatya, Türkiye.

*Corresponding author

Research Article

History

Received: 03/11/2023

Accepted: 11/03/2024





This article is licensed under a Creative Commons Attribution-NonCommercial 4.0 International License (CC BY-NC 4.0)


ABSTRACT


In this study, gum arabic based network polymers were prepared using epoxy functional PEG structures. The basic physicochemical properties of these structures, their structural characterization, thermal properties and morphological properties were investigated. Toxicity properties of constructs synthesized on zebrafish (*Danio rerio* (Hamilton)) offspring were determined in vivo. In addition, in vitro toxicity tests were performed on L929 fibroblast cells. When the general properties of these structures were examined. Structural and thermal properties were better with increasing cross-linker rates ratios (1%, 3%, 5%). According to the toxicity test performed on zebrafish juveniles; GA-PEG-Epoxy (1%) constructs are non-toxic to zebrafish juveniles. The mortality rate of GA-PEG-Epoxy (3%) and GA-PEG-Epoxy (5%) structures was observed as 12.5% and 20.8%, respectively. It was observed that the structures were not toxic to zebrafish juveniles. MTT test performed on L929 fibroblast cells, high cell viability (>90%) was observed in all synthesized structures. These results are evaluated as Grade 1 according to ISO standards.


Keywords: Biopolymer network, Gum arabic, Toxicity, Zebrafish juveniles, MTT.


 idal.karaca@ozal.edu.tr

 alidikurucay95@gmail.com


 burhan.ates@inonu.edu.tr

 <https://orcid.org/0000-0001-6783-7030>


 <https://orcid.org/0000-0002-8816-0425>

 <https://orcid.org/0000-0001-6080-229X>

 duygu.turhan@inonu.edu.tr

 suleyman.koytepe@inonu.edu.tr

 <https://orcid.org/0000-0002-7111-4289>

 <https://orcid.org/0000-0002-4788-278X>

Introduction

Biopolymers can be naturally occurring materials. Many materials formed during the life cycles of animals, fungi, bacteria and green plants are polymers or polymer matrix composites. Starch, cellulose are carbohydrate polymers produced by bacteria and fungi. Collagen, gelatin and silk are widely known animal biopolymers. [1]. Biopolymers are used in many areas such as pharmaceuticals, medicine, food and nutraceuticals due to their low relative density, high strength, renewable, biodegradable and inexpensive [2-4]. Biopolymers are materials of interest in many areas, such as drug release, because their thermal, electrical, and mechanical properties change when reinforced with natural substances [5]. Biopolymers such as gum arabic, chitosan, and wheat starch are commercially available, economical, and widely used examples in a variety of applications [6]. Gum Arabic (GA) is obtained from acacia wood, a type of natural polysaccharide. The structure of GA consists of galactose, arabinose, rhamnose, and glucuronic acid. Its main skeleton consists of 1,3-linked β -d-galactopyranosyl units. The presence of these units gives GA a densely branched structure [7,8]. Due to its high branching network, the hydrodynamic volume of GA is small. Thus,

intermolecular interaction decreases. With its low viscosity, GA mixes easily with other ingredients without forming bubbles [9]. Determining the toxicity levels of biopolymer and polymer structures is very essential. Recently, zebrafish has rapidly gained popularity as an in vivo model for screening new materials [10,11]. Zebrafish is one of the widely used model organisms in aquatic toxicology and in vivo studies. The advantage is that these organisms are small and easy to maintain at low cost [12]. Zebrafish is widely used in determining the toxicity of water contaminants [13]. The molecular and cellular mechanisms in the nervous system development of zebrafish and its response to toxins are similar to mammalian organisms [12]. In addition to its utility advantages, we can add its high fecundity and the fact that its genome shares more than 70% of its genes with humans when compared to more complex organisms [14-16]. 3-(4,5-dimethyliazol-2-yl)-2,5-difeniltetrazolio (MTT) test which is a widely used method, was used to determine in vitro cytotoxicity. The MTT assay is a colorimetric assay of living cells [17]. *Mus musculus* mouse fibroblast cells (L-929) were used in the MTT test. There are studies on GA based biopolymer structures in the

literature. Ibrahim et al. synthesized a combination of GA and polyethylene glycol dimethacrylate (PEGDMA), a synthetic polymer [18]. Amalraj et al. produced BPEO and GEO based biocomposite films containing chitosan, gum arabic and PEG [19]. Namasivayam et al. synthesized gum arabic, polyethylene glycol grafted iron oxide nanocomposite (GA-PEG-IONC) [20]. In this study, unlike the literature, gum arabic-based network polymers were prepared for the first time using epoxy functional PEG structures. It is known that there is a strong interaction between the epoxy and PEG phases in the interfacial region [21]. In this way, PEG-Epoxy structures were obtained. PEG-Epoxy structures were cross-linked with GA to obtain the GA-PEG-Epoxy structure. Finally, the toxicity of the prepared constructs was investigated both in vivo (zebrafish juveniles) and in vitro (L929 fibroblast cells).

Materials and Methods

Within the scope of the study, gum arabic (GA) and polyethylene glycol (PEG 1000) used in the synthesis of cross-linked polymeric structures were obtained from Sigma Aldrich. Epichlorhydrin was obtained from Alfa Aesar company. K_2CO_3 , NaOH and other solvents used were purchased from Merc. High glucose Dulbecco's Modified Eagle Medium (DMEM), Fetal Bovine Serum (FBS), Penicillin-Streptomycin (Pen-Strep) and Phosphate Buffer (PBS) were obtained from Capricorn Scientific. Dimethyl sulfoxide (DMSO) and 3-(4,5-dimethylthiazol-2-yl)-2,5-diphenyltetrazolium bromide (MTT) were purchased from Sigma Aldrich. The chemicals used in the study were purchased directly and used pure. Pre-purification was not carried out. The drying process of the synthesized gum arabic-PEG-Epoxy polymeric structure was carried out with Biobase brand BK-FD12S(-80°C) model lyophilizer. Chemical characterization of the synthesized structures was investigated using Perkin Elmer Spectrum Two model fourier-transform infrared spectroscopy (FTIR). FTIR spectra were taken in the 400-4000 cm^{-1} working range and the data were provided by the ATR technique. 4 cm^{-1} wavenumber measurement sensitivity was used in FTIR analysis. Characterization was also supported by nuclear magnetic resonance (NMR) spectra. NMR spectra were taken on Bruker Ultra Shield 300 MHz NMR spectroscopy. DMSO- d_6 was used as the solvent. The thermal properties of the obtained structures were realized by using differential thermal analysis (DTA), thermogravimetric analysis (TGA), differential scanning calorimetry (DSC) techniques. TGA analyzes were used to determine the

thermal stability of the structures and the results were determined with the Shimadzu TGA-50 model device. Analyzes were carried out at 500 °C in air atmosphere by taking 10 mg sample. The thermal stability and structural stability properties of the obtained networked polymeric structures were determined using the Shimadzu DTA-50 model device. DTA analyzes were performed in the range of 20-400 °C. Shimadzu DSC-60 model device was used in the range of 20-500 °C to examine the softening temperatures and general structural properties of the polymers. In DSC analyses, 5 mg of sample was analyzed in aluminum cuvettes and these analyzes were carried out in a constant air atmosphere. In all thermal analyzes, the measurements were taken at a heating rate of 10°C/min. The surface and morphological properties of the obtained network polymers were determined using the Leo-Evo-40 XVP model scanning electron microscope (SEM). During SEM analysis, 10 nm Au-Pd coating was carried out using Bal-Tec SCD 050 brand sputter to ensure conductivity on the samples. ESCO brand carbon dioxide incubator was used in cell culture studies. The surface, morphology and cavities of all samples were examined in detail at three different magnifications. Zebrafish juveniles and L929 cell lines were used to determine the toxicity properties of gum arabic-based networks both in vivo and in vitro, respectively.

Synthesis of Polymeric Structures

GA is a polysaccharide of plant origin and has a high molecular weight [17]. It is in the polysaccharide class due to its general structure and is used directly in many biomaterial designs. However, structurally, gum arabic type polymers are polymeric structures with very poor biopermanence. These properties limit the usage options of these polymers [22]. In the scope of the study, in order to eliminate this disadvantage, cross-linking of polymers with biocompatible PEG structures was carried out. This crosslinking process was carried out by a two-step procedure. First of all, diglycidyl ether structures were prepared using PEG 1000 and epichlorhydrin [23]. In this process, firstly, PEG 1000/epichlorhydrin at a ratio of 1:2 (mole) was taken into a two-necked balloon. K_2CO_3 [~0.1% (w/w)] was added to the existing medium. THF was preferred as the solvent. The reaction was carried out at 90°C for 3 hours. After addition of calculated PEG 1000 and epichlorhydrin to a two-necked flask, the reaction was continued at 90°C for 3 hours. THF with the addition of ~0.1% (w/w) K_2CO_3 to the medium. After the reaction, it was first checked whether the PEG-Epoxy structure was obtained with the FTIR technique.

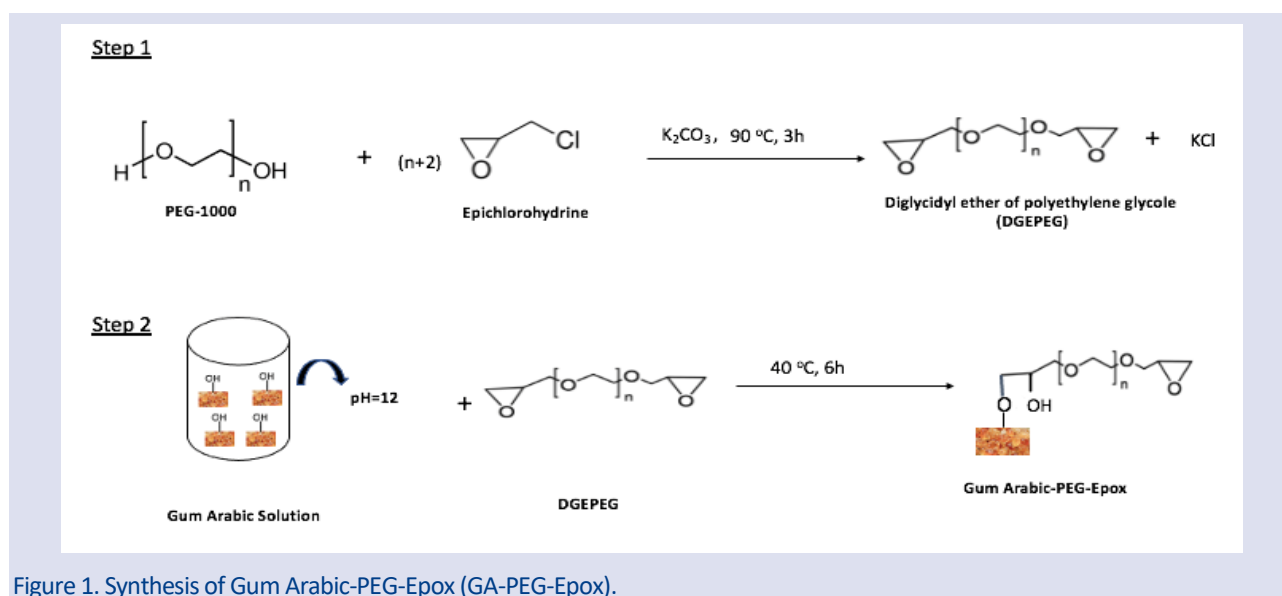


Figure 1. Synthesis of Gum Arabic-PEG-Epoxy (GA-PEG-Epoxy).

After obtaining the PEG-Epoxy structure, the second step was started. In the second step; The pH of the gum arabic (~ 2 mM) structure prepared in water was adjusted to pH 12 using 0.25 M NaOH solution. Gum arabic, whose pH was adjusted, was reacted with PEG-Epoxy at different rates (1, 3 and 5%) at 40 °C for 6 h under reflux. Briefly, in this second stage of the study, cross-linking of gum arabic structures was carried out using diglycidyl ether PEG 1000 structures at different rates. GA-PEG-Epoxy structures obtained after processing were dried using a lyophilizer. The reaction steps are given in Figure 1. The structures obtained after the reaction were confirmed by FTIR and NMR techniques.

Determination of In Vivo Toxicity Properties of Synthesized Structures on Zebrafish Juveniles

Adult AB zebrafish were grown in the Environmental Toxicology Laboratory of the Department of Biology, Faculty of Arts and Sciences, İnönü University. These fish were reared in the zebrafish aquatic system (28°C, 14:10 hours light:dark photoperiod). The system under study has automatic controls for water circulation at pH (7.30), temperature (28.5 °C), conductivity (720 µS/cm), and light-dark photoperiod (14:10 hours). Zebrafish fry is produced in the system connected to the filtered zebrafish water system (iSpawn, Tecniplast, Italy). The grown embryos were collected within 3 hours and washed with E2 medium. Then, they were placed in petri dishes, according to Westerfield [24]. The developmental stages of embryos were identified according to Kimmel et al. [25]. Solutions containing gum arabic, gum arabic-PEG-Epoxy (1%), gum arabic-PEG-Epoxy (3%) and gum arabic-PEG-Epoxy (5%) in E2 medium water at 100 mg/L⁻¹ was prepared. Embryos were exposed to 250 µL (pH 7.3) solutions in 96 well microplates. One embryo was added to each well of microplates. Embryos were monitored using a stereo microscope for 96 hours with 24-hour intervals. After 96 hours, body length of the surviving embryos was determined. The dimensions of the embryos

were determined with Euromex Image Focus 4.0 software.

Determination of In Vitro Toxicity Properties of Synthesized Structures on L929 Fibroblast Cells

L929 cells were grown in high-glucose DMEM with 1% Pen-Strep-10% FBS in a 5% CO₂ incubator at 37 degrees. 10,000 cells from L929 were seeded in a 96-well plate. The well plate remained in the CO₂ incubator for 24 hours. 2 grams of each material was weighed in a sterile centrifuge tube and dissolved with 2000 µL of DMEM, prepared as 1 mg/ml. Then, the samples were prepared at different concentrations between 12.5-1000 µg/mL by serial dilution method using DMEM. The waiting medium in the well plate was removed and replaced with 100 µL of the medium containing different materials and different concentrations. It was then incubated for 24 hours at 37 degrees in an incubator with 5% CO₂. MTT dye at 5 mg/mL was dissolved in PBS (pH: 7.4 in Phosphate Buffer). After 24 hours, the old medium was removed from all well plates and replaced with 90 µL of DMEM in each well and 10 µL of 5mg/ml prepared MTT in each well, 100 µL of the mixture was added and incubated in a CO₂ incubator for 4 hours. After incubation, the medium with MTT in the well plates was withdrawn and escaped. 100 µL of DMSO was added to each well in the well plates. The well plates were read with the help of spectrophotometer at wavelengths of 540 nm [26] directly after treating with DMSO.

Results and Discussion

Characterization by FTIR and NMR Techniques

Within the scope of the study, GA-PEG-Epoxy structures were synthesized from GA and diglycidyl PEG structures, including epoxidized PEG-1000 structures at different rates. FTIR spectra of the structures obtained are given in Figure 2 by comparing them with pure gum arabic and PEG-Epoxy structures. Pure gum arabic structure is a polysaccharide structure and we prove the existence of monosaccharides in GA with the presence of free -OH groups [26]. In the FTIR spectrum of the pure GA structure,

stretching vibrations of free -OH groups and hydrogen bonding are seen in the range of 3000-3600 cm^{-1} [27]. The -OH stretching is due to the property of the glucosidic ring [28]. In addition, the aliphatic C-H stretching vibration is clearly evident in the range of 2850-2950 cm^{-1} . Gum arabic structures contain free carboxyl groups. At 1430 cm^{-1} , the characteristic O-H in-plane bending band is observed for carboxylic acid [29]. When we look at the FTIR spectrum, we see the symmetric and asymmetric vibrations of the carboxyl groups, respectively, in the range of 1409-1595 cm^{-1} . It is known that the peak at 1409 cm^{-1} is caused by symmetric stretching of the carboxylic groups of uronic acid residues in the gum polysaccharide [27]. In the GA structure, we see a very wide and broad peak in the range of 900-1200 cm^{-1} , which is known as the fingerprint of carbohydrates in the literature [30]. These rather broad observed peaks represent the C-C, C-O and C-O-C stretching of the polymer backbone and the C-H, C-O-H bending modes [31]. Unlike other carbohydrate structures, since the C-OH structures in gum arabic show

strong hydrogen bond interactions, the peak in the range of 3200-2600 cm^{-1} is quite wide and flat. However, since the PEG-Epoxy groups generally tend to bind through these -OH groups, the intensity of this peak both decreases and the peak range narrows in gum arabic-PEG-Epoxy structures as the cross-linking rate increases. In Gum Arabic-PEG-Epoxy structures, C-OH stretching vibration in the range of 1780 cm^{-1} , etheric stretching vibration around 1080 cm^{-1} , C-C aliphatic C-H stretching vibration around 1380 cm^{-1} , which comes from the gum arabic structure visible. In addition, the tension vibration of the epoxy ring at 897 cm^{-1} within the epoxy unit coming from the PEG-Epoxy structure is clearly seen. When the epoxy ring and PEG unit are included in the structure, the aliphatic C-H stress vibration intensifies and the C-C stress vibration intensity on the structure also increases. All these findings show that the desired Gum Arabic-PEG-Epoxy structures are intensified with an increasing amount of crosslinking.

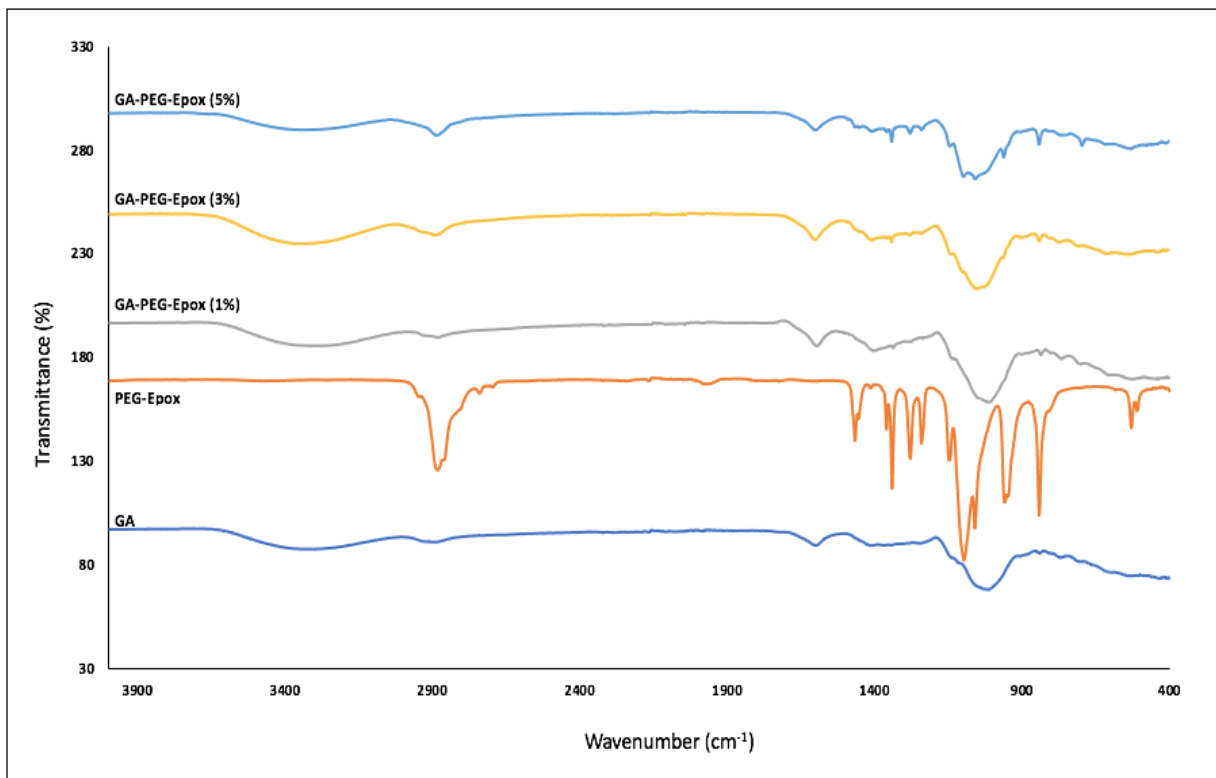


Figure 2. FTIR spectra of GA structures containing pure GA, PEG-Epoxy, and GA-PEG-Epoxy in different rates (1, 3, 5 %).

The ^1H NMR and ^{13}C NMR spectra of the obtained epoxy functional structures were given (Figure 3). According to the ^1H NMR spectra, groups such as methylene and methine in the poly(ethylene glycol) diglycidyl ether structure show similar chemical shifts. The characteristic peaks at 3.70-3.75 (m, 2H) and 3.33-3.39 (m, 2H) ppm are thought to belong to methylene hydrogen (c_1 and c_2). The peaks at 3.06-3.12 (m, 2H) ppm indicate the text hydrogen signal (b). The peaks at 2.71-2.75 (t, 2H) and 2.53-2.57 (m, 2H) ppm are due to methylene

hydrogen (a_1 and a_2) (Figure 3). According to these results, epichlorohydrin is chemically bonded to both ends of the PEG chain.

In the ^{13}C NMR spectra, characteristic peaks in the poly(ethylene glycol) diglycidyl ether structure are observed. For example, after the epichlorohydrin binding of PEG, the presence of new characteristic peaks belonging to Cs in the epoxy ring is observed at 44.15 ppm (a) and 50.73 ppm (b) in the ^{13}C NMR spectrum (Figure 3).

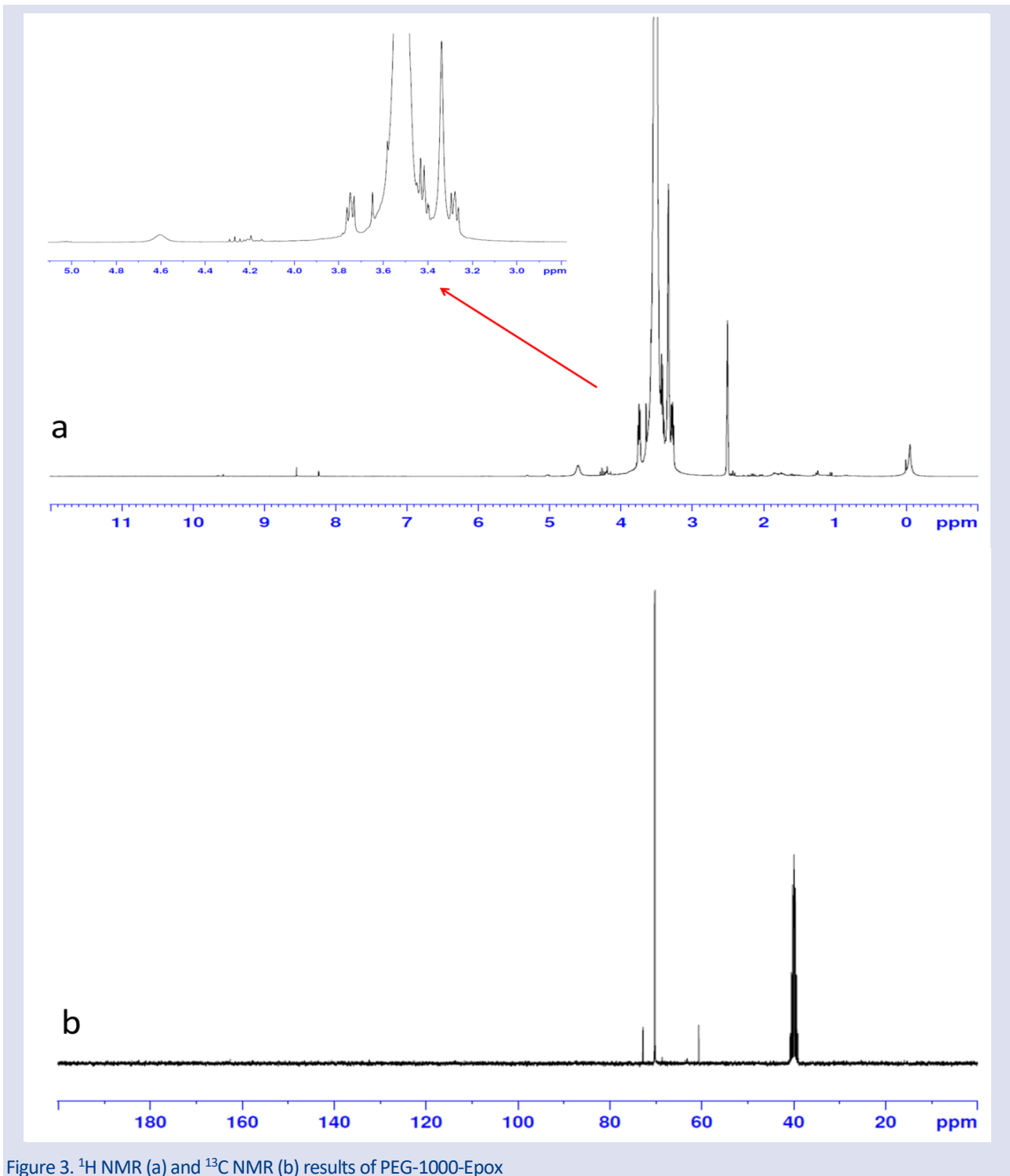


Figure 3. ^1H NMR (a) and ^{13}C NMR (b) results of PEG-1000-Epox

Investigation of Thermal Properties

The DTA thermograms of the obtained structures are shown in Figure 4. Gum Arabic-PEG-Epox structures were prepared with three different crosslinking rates and biopolymers with different structural stability were obtained. The thermal properties of these structures were first investigated with DTA thermograms. The thermal structures of 3 different crosslinkers are given in Figure 4 comparatively. There are 4 basic exotherms in the structure of Gum arabic-PEG-Epox 1%. 1. exotherm;

between 180-200 °C, 2. exotherm; between 220-290 °C, 3rd exotherm; it appears prominently between 300-340 °C and the final exotherm between 340-380 °C.

It is due to the PEG-Epox cross-linking units bound to the first exotherm structure, and this peak intensifies as the amount of PEG-Epox in these structures increases. The second exotherm is caused by the thermal degradation of the side group units in the gum arabic structure. The third exotherm is due to thermal degradation of the main chain gum arabic structure. The final exotherm is due to the carbonization of the decay products.

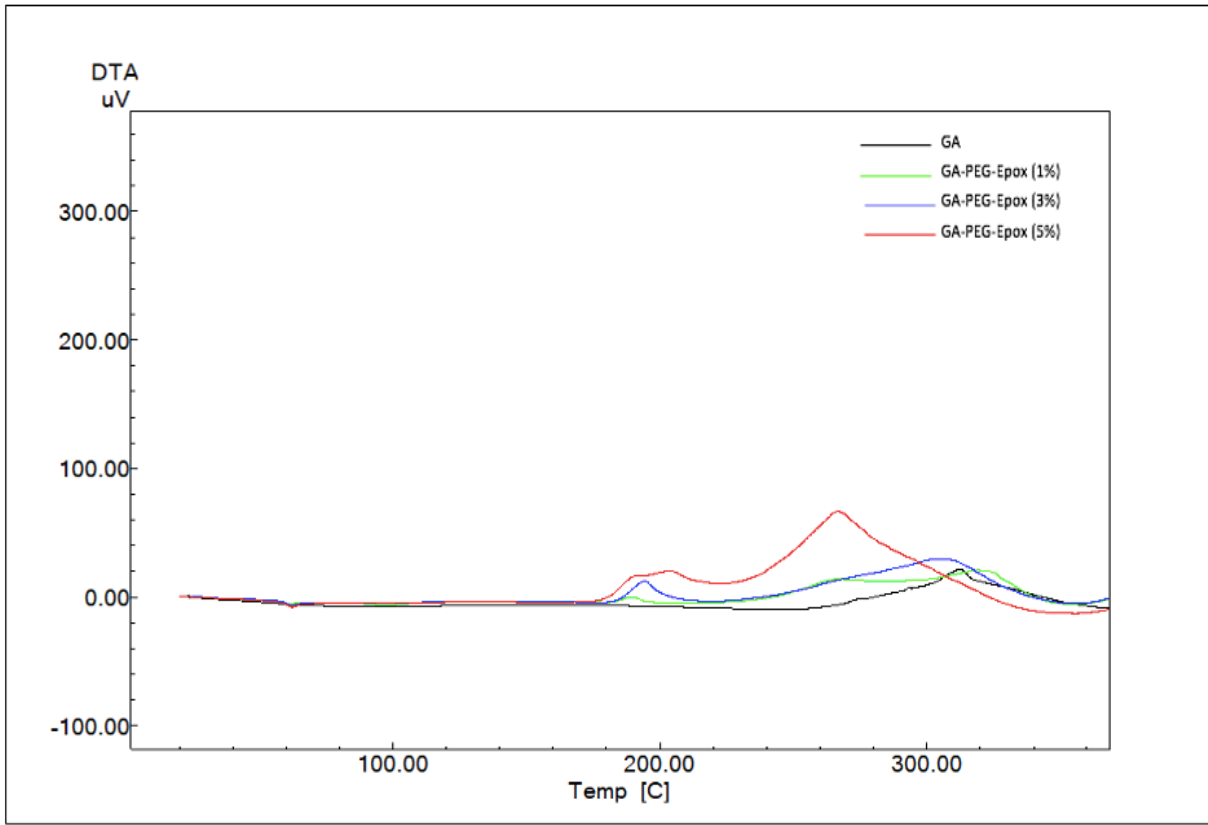


Figure 4. DTA thermograms of GA, GA-PEG-Epoxy (1%), GA-PEG-Epoxy (3%) and GA-PEG-Epoxy (5%) structures.

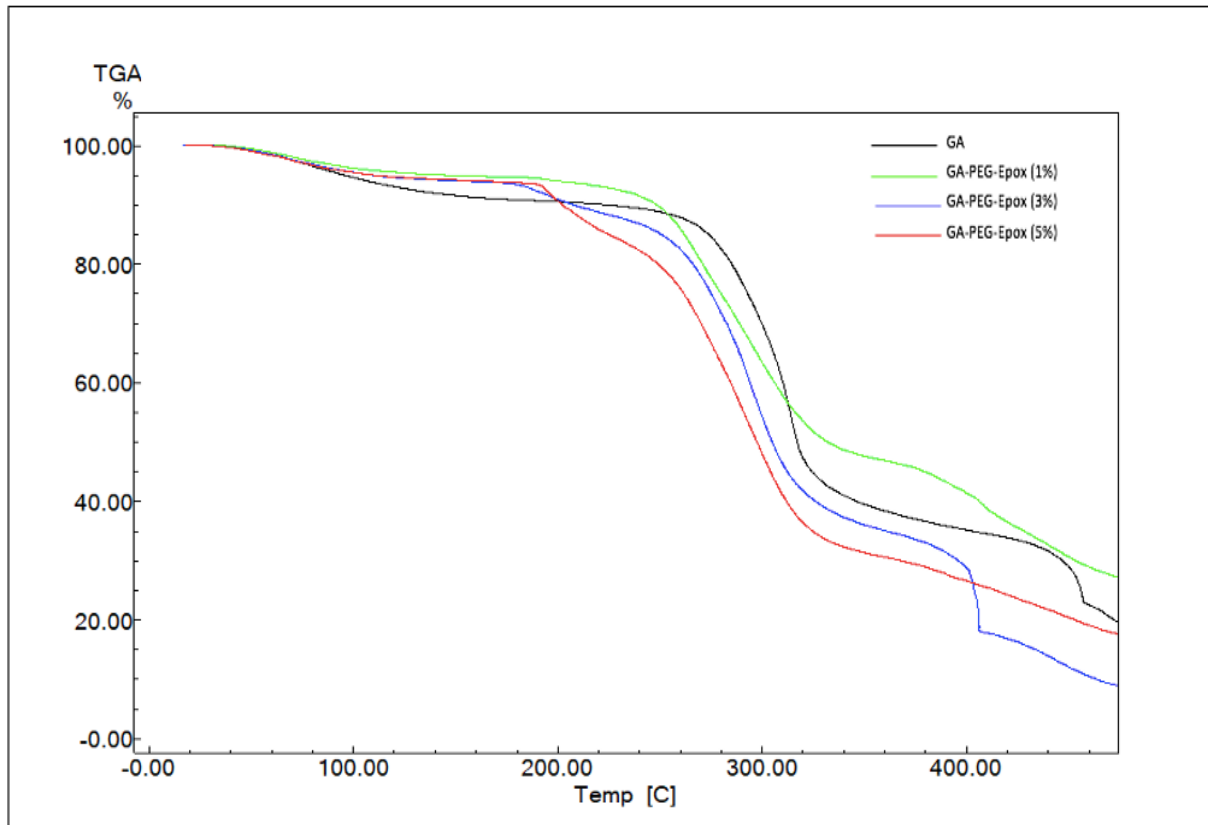


Figure 5. TGA thermograms of GA, GA-PEG-Epoxy (1%), GA-PEG-Epoxy (3%) and GA-PEG-Epoxy (5%) structures.

According to these DTA thermograms, the structural stability of PEG-Epoxy structures appears to be around 190°C. TGA analyzes were carried out between 20 and 500°C temperatures to see the related structural stability in more detail. TGA analyzes of the related structures are given in Figure 5.

In the TGA analysis of pure Gum Arabic and Gum Arabic-PEG-Epoxy containing different rates of PEG-Epoxy, basically 3 different mass losses are observed. 1. mass loss; it is the loss of mass due to the removal of structural moisture, which appears around 20 and about 200 °C. Nep and Conway emphasized in their study that this mass loss is due to the loss of structural water adsorbed in the gums. In addition, the loss of mass is attributed to the desorption of moisture as hydrogen bonded water to the polysaccharide structure [32]. 2. the loss of mass is defined as Zohuriaan and Shokrolahi polysaccharide decomposition [33]. 2. mass loss; these are the mass losses that appear to be around 80%, resulting from the degradation of the side groups and epoxy units in the gum arabic structure. The final mass loss is the mass loss from the carbonization of the decomposition products, seen between 350-450°C and consistent with the DTA thermograms. When TGA thermograms are examined, we see that as the crosslinking rate in the structure increases, the thermal stability increases partially because a more

rigid and more complex structure is formed. The most important reason for this increase is the cage effect. The increased thermal stability is the proof that the desired structures are obtained at the desired rate. DSC thermograms of the structures obtained are shown in Figure 6.

Endotherm and three main exotherm peaks are seen around ~80°C in these thermograms. Daoub et al. stated in their study that endothermic peaks are caused by the loss of water content in the gums, and the exothermic peaks correspond to the decomposition of the gums [34]. First exotherm; it is the decay peak of the groups originating from PEG-Epoxy structures, which is also compatible with DTA thermograms and increases as the crosslinking rate increases. Second exotherm; it originates from gum arabic thermal degradation and is a fairly large peak. The last exotherm is the exotherm caused by carbonization between 360-450°C. The endotherm, around 65°C, corresponds to the softening temperature of these structures and was observed in the same temperature range in all structures.

SEM analyzes were performed to determine the surface properties and morphological structures of the GA-PEG-Epoxy structures obtained within the scope of the study. In these analyzes, the pore structures of the obtained structures were investigated.

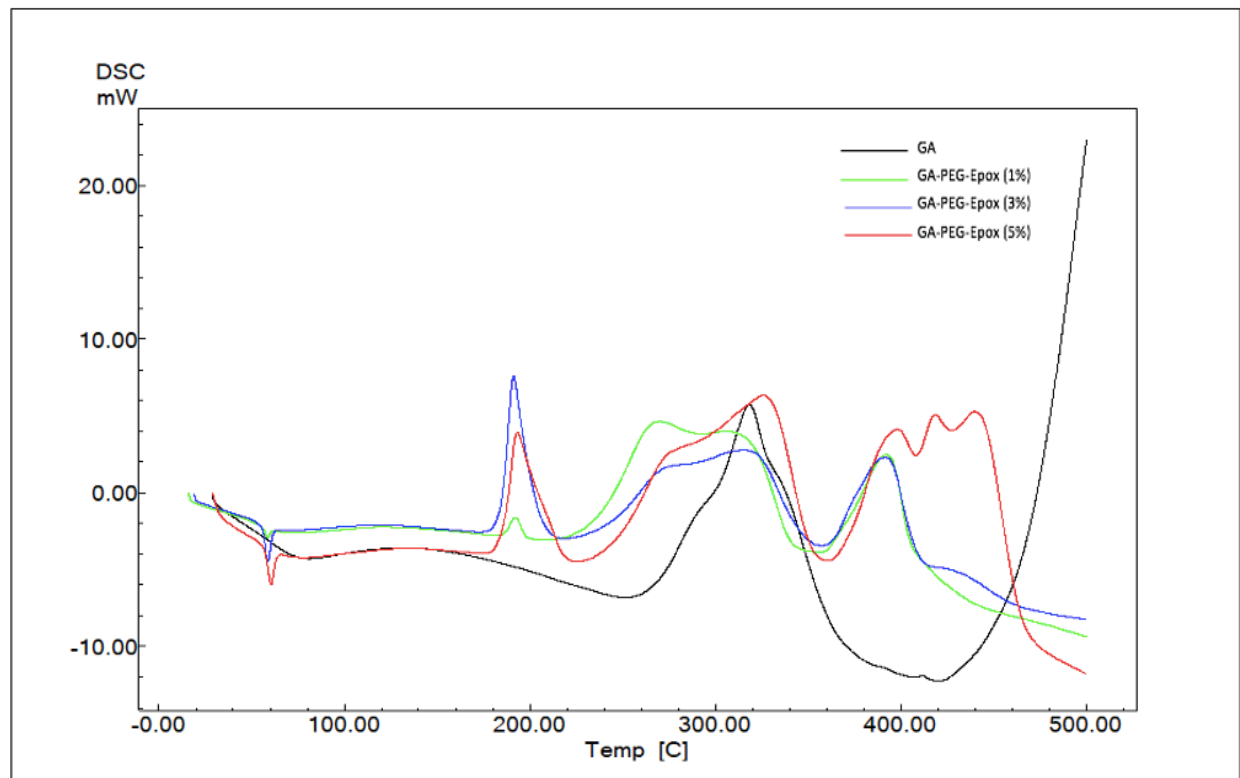


Figure 6. DSC thermograms of GA, GA-PEG-Epoxy (1%), GA-PEG-Epoxy (3%) and GA-PEG-Epoxy (5%) structures.

Investigation of Surface Morphological Properties

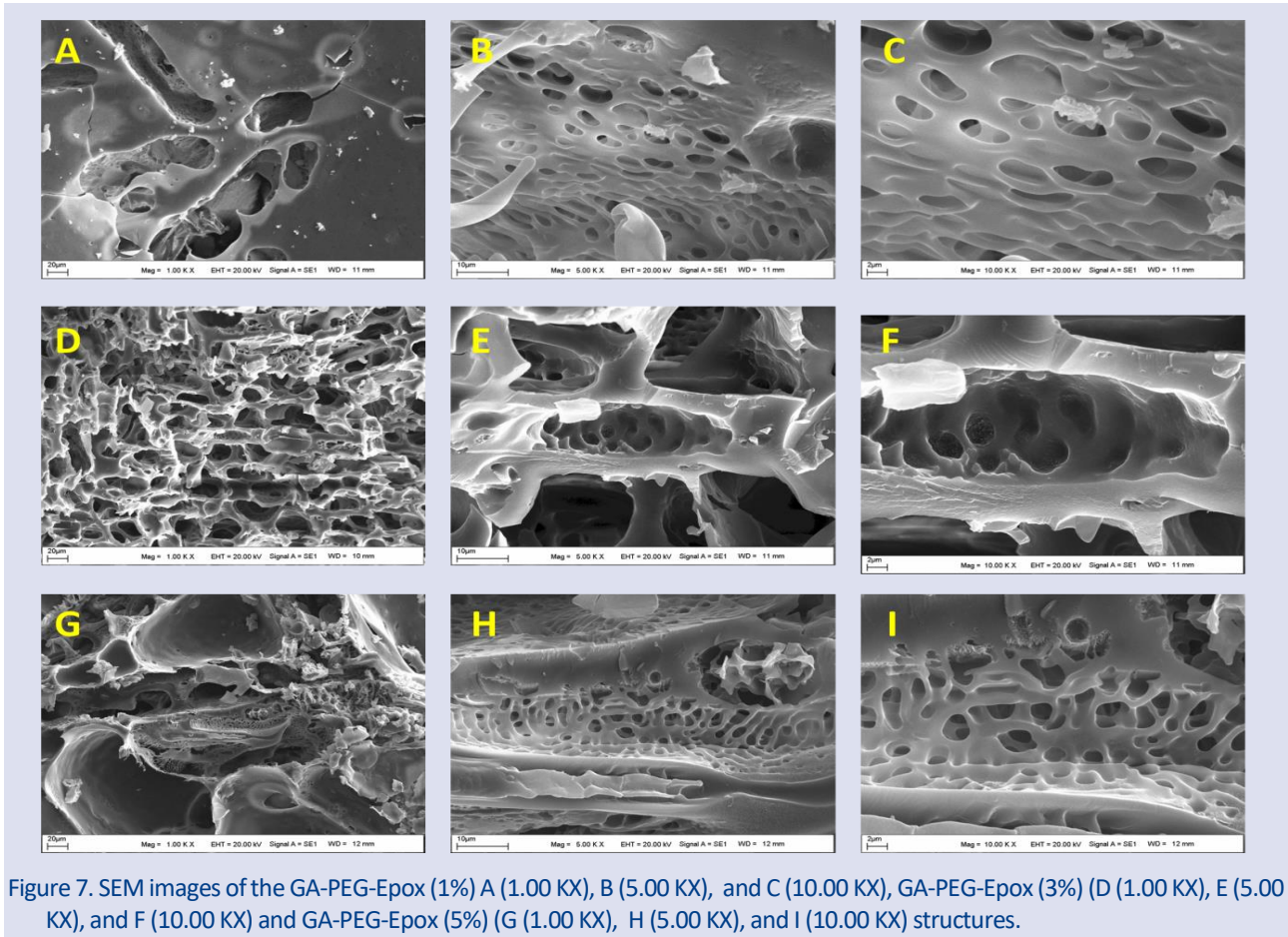


Figure 7. SEM images of the GA-PEG-Epoxy (1%) A (1.00 KX), B (5.00 KX), and C (10.00 KX), GA-PEG-Epoxy (3%) (D (1.00 KX), E (5.00 KX), and F (10.00 KX) and GA-PEG-Epoxy (5%) (G (1.00 KX), H (5.00 KX), and I (10.00 KX) structures.

The SEM images obtained at different magnifications are given in Figure 7. When the SEM images of GA-PEG-Epoxy (1%), GA-PEG-Epoxy (3%) and GA-PEG-Epoxy (5%) structures are evaluated, there are pores of different sizes and distributions in all three structures. However, it is clearly seen in Figure 7D that the GA-PEG-Epoxy (3%) structure has a more regular pore structure than the other structures. The pores in this structure are dense, similar in size, and distributed throughout the structure. Therefore, it shows a more ideal absorbent appearance. It is known that pore size and homogeneous distribution are very effective on absorption. Wang et al. observed that heavy metal absorption was higher in the structure with a more distinct and homogeneous pore structure [35].

Evaluation of Toxicity Properties of Synthesized Structures on Zebrafish Juveniles

The results showed that GA and GA-PEG-Epoxy (1%) solutions at the concentration used did not cause mortality in zebrafish. 0.1 mg/L⁻¹ GA and GA-PEG-Epoxy (1%) are non-toxic to zebrafish juveniles. However, mortality was observed in solutions GA-PEG-Epoxy (3%) and GA-PEG-Epoxy (5%) at a rate of 12.5% and 20.8%, respectively. No significant differences were observed in the lengths of zebrafish juveniles exposed to all solutions when compared with the control groups (Table1).

Table 1. Lengths and mortality in Zebrafish juveniles exposed to the synthesized structures for 96 hours.

	n	Σ (Mortality)				Lengths (mm)
		24h	48h	72h	96h	
Control	24	0	0	0	0	3.24 ± 0.08
GA	24	0	0	0	0	3.18 ± 0.06
GA-PEG-Epoxy (1%)	24	0	0	0	0	3.29 ± 0.12
GA-PEG-Epoxy (3%)	24	1	0	2	3	3.14 ± 0.05
GA-PEG-Epoxy (5%)	24	0	0	2	5	3.08 ± 0.09

Evaluation of in Vitro Toxicity Properties of Synthesized Structures on L929 Mouse Fibroblast Cells

Mus musculus mouse fibroblast cells (L929) were used in the toxicity test of materials that are well soluble in water and performed by the direct method. Cell viability result is given in Figure 8. Cell images are shown in Figure 9. According to ISO-10993-5, more than 30% inhibition of cell viability is considered a cytotoxic effect [36]. The GA-PEG-Epoxy series (1%, 3%, and 5%) exhibited high cell viability (>90%) in the range of 12.5 to 1000 µg/mL. These results were also evaluated as Grade 1 according to ISO standards [36]. The GA-PEG-Epoxy series (1%, 3%, and 5%) have been observed that the materials are non-toxic and biocompatible.

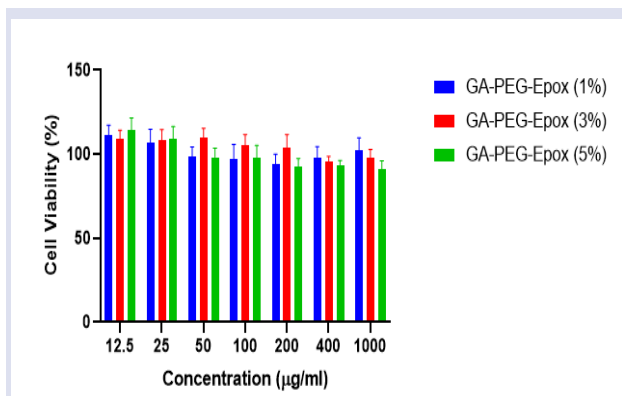


Figure 8. Cell viability results of GA-PEG-Epoxy (1%), GA-PEG-Epoxy (3%) and GA-PEG-Epoxy (5%) structures.

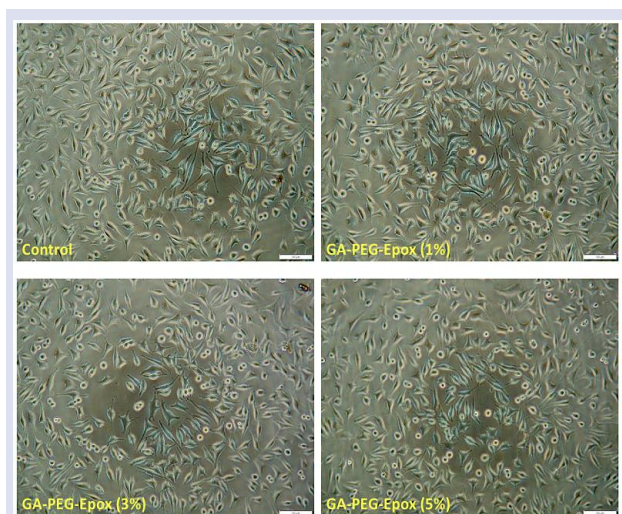


Figure 9. Cell images of GA, GA-PEG-Epoxy (1%), GA-PEG-Epoxy (3%) and GA-PEG-Epoxy (5%) structures.

GA, a natural polysaccharide, has a very complex molecular structure. GA contains 24%–27% arabinose, 12%–16% rhamnose, 39%–42% galactose, 15%–16% glucuronic acid, 0.22%–0.39% nitrogen, 1.5%–2.6% protein, and 12.5%–16% moisture. GA is widely used in the pharmaceutical, medical, cosmetic, and food industries. Especially in recent years, GA has been used as an effective auxiliary material in biomedical applications, drug delivery, and the realization of nanostructure scaffolds [37]. In addition, it is widely used in heavy metal removal. Abreu et al. used gum arabic to increase the adsorbent potential of chitosan-based nanoparticle structures for heavy metal removal [38]. Errich et al. performed toxic heavy metal removal using gum arabic-modified hydroxyethyl cellulose and hydroxyapatite [39]. Saeedi-Jurkuyeh et al. used PEG in the modification step to remove heavy metals from aqueous solutions [40]. It is thought that the non-toxic, biocompatible GA-PEG-Epoxy series we synthesized in this study can be used as an alternative design to other designs, especially for the removal of heavy metal ions from water sources.

Conclusions

In this study, network polymers were prepared by using gum arabic based epoxy functional PEG structures,

which is an important natural polysaccharide. Preparation took place in two steps. In the first step, diglycidyl ether structures were prepared using PEG 1000 and epichlorohydrin. The process was followed by the FTIR technique. After obtaining PEG-Epoxy, gum arabic was reacted with PEG-Epoxy under a reflux system. After reaction, GA-PEG-Epoxy series (1%, 3% and 5%) were obtained. Structural characterization was elucidated by FTIR and NMR techniques. Thermal properties were determined by TGA, DTA and DSC techniques. Surface morphology was elucidated by SEM technique. In vivo and in vitro toxicity tests were performed on zebrafish juveniles and L929 fibroblast cells, respectively. All findings proved that GA-PEG-Epoxy (1%, 3%, 5%) serial network polymeric structure was synthesized and non-toxic. In future studies, whether non-toxic GA-PEG-Epoxy (1%, 3%, 5%) network polymeric structures can be an alternative adsorbent for removing heavy metals, an essential problem in water resources, will be studied in detail.

Conflicts of interest

There are no conflicts of interest in this work.

References

- [1] Singh A.V., Biopolymers in Drug Delivery: A Review, *Pharmacologyonline*, 1 (2011) 666-674.
- [2] Gopi S., Amalraj A., Kalarikkal N., Zhang J., Thomas S., Guo Q., Preparation and Characterization of Nanocomposite Films Based on Gum Arabic, Maltodextrin and Polyethylene Glycol Reinforced with Turmeric Nanofiber Isolated from Turmeric Spent. *Mater. Sci. Eng. C.*, 97 (2019) 723-729.
- [3] Andrade-Mahecha M.M., Pelissari F.M., Tapia-Blácido D.R., Menegalli F.C., Achira as A Source of Biodegradable Materials: Isolation and Characterization of Nanofibers. *Carbohydr. Polym.*, 123 (2015) 406-415.
- [4] Wang W., Cai Z., Yu J., Xua Z., Changes in Composition, Structure and Properties of Jute Fibers After Chemical Treatments, *Fibers Polym.*, 10 (2009) 776-780.
- [5] Gopi S., Amalraj A., Sukumaran N.P., Haponiuk J.T., Thomas S, Biopolymers and Their Composites for Drug Delivery: A Brief Review, *Macromol. Symp.*, 380 (2018) 1800114.
- [6] Rani S., Kadam V., Rose N.M., Jose S., Yadav S., Shakyawar D.B., Wheat Starch, Gum Arabic and Chitosan Biopolymer Treatment of Wool Fabric for Improved Shrink Resistance Finishing, *Int. J. Biol. Macromol.*, 163 (2020) 1044-1052.
- [7] Khan M., Shah L.A., Rehman T., Khan A., Iqbal A., Ullah M., Alam S, Synthesis of Physically Cross-Linked Gum Arabic-Based Polymer Hydrogels with Enhanced Mechanical, Load Bearing and Shape Memory Behavior, *Iran. Polym. J.*, 29 (2020) 351-360.
- [8] Sarika P., Cinthya K., Jayakrishnan A., Anilkumar P., James N.R., Modified Gum Arabic Cross-Linked Gelatin Scaffold for Bio-Medical Applications, *Mater. Sci. Eng. C.*, 43 (2014) 272-279.
- [9] Tsai R.Y., Kuo T.Y., Hung S.C., Lin C.M., Hsien T.Y., Wang D.M., Hsieh H.J., Use of Gum Arabic to Improve the Fabrication of Chitosan-Gelatin-Based Nanofibers for Tissue Engineering, *Carbohydr Polym.*, 115 (2015) 525-532.

- [10] Teijeiro-Valiño C., Yebra-Pimentel E., Guerra-Varela J., Csaba N., Alonso M.J., Sánchez L., Assessment of the Permeability and Toxicity of Polymeric Nanocapsules Using the Zebrafish Model, *Nanomedicine (Lond)*, 12 (2017) 2069-2082.
- [11] Macrae C.A., Peterson R.T., Zebrafish as Tools for Drug Discovery, *Nat Rev Drug Discov.*, 14 (2015) 721-731.
- [12] Magyary I., Recent Advances and Future Trends in Zebrafish Bioassays for Aquatic Ecotoxicology, *Ecocycles*, 4 (2018) 12-18.
- [13] Moşneang C.L., Dumitrescu E., Muselin F., Ciulan V., Grozea A., Cristina R.T., Use of Zebra Fish Eggs as Early Indicators of Aquatic Environmental Pollution, *Pol. J. Environ. Stud.*, 24 (2015) 2079-2085.
- [14] Zon L.I., Peterson R.T., In Vivo Drug Discovery in The Zebrafish, *Nat Rev Drug Discov.*, 4 (2005) 35-44.
- [15] Howe K, Clark MD, Torroja CF et al., The Zebrafish Reference Genome Sequence and Its Relationship to The Human Genome, *Nature*, 496 (2013) 498-503.
- [16] Mcgrath P., Li C.Q., Zebrafish: A Predictive Model for Assessing Drug-Induced Toxicity, *Drug Discovery Today*, 13 (2008) 394-401.
- [17] Truzzi F., Mandrioli D., Gnudi F., Scheepers P.T.J., Silbergeld E.K., Belpoggi F., Dinelli G., Comparative Evaluation of the Cytotoxicity of Glyphosate-Based Herbicides and Glycine in L929 and Caco2 Cells, *Front. Public Health.*, 9 (2021) 643898.
- [18] Ibrahim S.M., Yin T.Y., Misran M., Arabic Gum Grafted PEGDMA Hydrogels: Synthesis, Physico-Chemical Characterization and In-vitro Release of Hydrophobic Drug, *Macromol. Res.*, 28 (2020) 1220-1231.
- [19] Amalraj A., Raj K.K.J, Haponiuk J.T., Thomas S., Gopi S., Preparation, Characterization, and Antimicrobial Activity of Chitosan/Gum Arabic/Polyethylene Glycol Composite Films Incorporated with Black Pepper Essential Oil and Ginger Essential Oil as Potential Packaging and Wound Dressing Materials, *Adv. Compos. Hybrid Mater.*, 3 (2020) 485-497.
- [20] Namasivayam S.K.R., Rabel A.M., Prasana R., Bharani R.S.A., Nachiyar C.V., Gum Acacia PEG Iron Oxide Nanocomposite (GA-PEG-IONC) Induced Pharmacotherapeutic Activity on The Las R Gene Expression of Pseudomonas Aeruginosa and HOXB13 Expression of Prostat Cancer (Pc 3) Cell Line. A Green Therapeutic Approach of Molecular Mechanism Inhibition, *Int. J. Biol. Macromol.*, 190 (2021) 940-959.
- [21] Zavareh S., Samandari G., Polyethylene Glycol as an Epoxy Modifier with Extremely High Toughening Effect: Formation of Nanoblend Morphology, *Polym. Eng. Sci.*, 54 (2013) 1833-1838.
- [22] Masuelli M.A., Hydrodynamic Properties of Whole Arabic Gum, *Am. J. Food Technol.*, 1 (2013) 60-66.
- [23] Motawie A.M., Sherif M.H., Badr M.M., Amer A.A., Shehat A.S., Synthesis and Characterization of Waterborne Epoxy Resins for Coating Application, *Aust. J. Basic & Appl. Sci.*, 4 (2010) 1376-1382.
- [24] Westerfield M., The zebrafish book, 5th Edition; A guide for the laboratory use of zebrafish (Danio rerio). University of Oregon Press; Eugene, Oregon (2007).
- [25] Kimmel C.B., Ballard W.W., Kimmel S.R., Ullmann B., Schilling T.F., Stages of Embryonic-Development of the Zebrafish, *Dev Dynam.*, 203 (1995) 253-310.
- [26] Resmi R., Yoonus J., Beena B, A Novel Greener Synthesis of ZnO Nanoparticles from Nilgiri antuscilantus Leaf Extract and Evaluation of Its Biomedical Applications, *Mater. Today: Proc.*, 46 (2021) 3062-3068.
- [27] Bashir M., Haripriya S., Assessment of Physical and Structural Characteristics of Almond Gum, *Int. J. Biol. Macromol.*, 93 (2016) 476-482.
- [28] Ibekwe C.A., Oyatogun G.M., Esan T.A., Oluwasegun K.M., Synthesis and Characterization of Chitosan/Gum Arabic Nanoparticles for Bone Regeneration, *American Journal of Materials Science and Engineering*, 5 (2017) 28-36.
- [29] Stuart B.H., Infrared Spectroscopy: Fundamentals and Applications, first ed., John Wiley & Sons Ltd, West Sussex, 2004.
- [30] Vodnar D.C., Pop O.L., Socaciu C., Monitoring Lactic Acid Fermentation in Media Containing Dandelion (*Taraxacum officinale*) by FTIR Spectroscopy, *Notulae Botanicae Horti Agrobotanici Cluj-Napoca*, 40 (2012) 65-68.
- [31] Mudgil D., Barak S., Khatkar B.S., X-ray diffraction, IR spectroscopy and thermal characterization of partially hydrolyzed guar gum., *Int. J. Biol. Macromol.*, 50 (2012) 1035-1039.
- [32] Nepa E.I., Conway B.R., Characterization of Grewia Gum, a Potential Pharmaceutical Excipient, *J. Excipients and Food Chem.*, 1 (2010) 30-40.
- [33] Zohuriaan M.J., Shokrolahi F., Thermal Studies on Natural and Modified Gums, *Polym. Test.*, 23 (2004) 575-579.
- [34] Daoub R.M.A., Elmubarak A.H., Misran M., Hassan E.A., Osman M.E., Characterization and Functional Properties of Some Natural Acacia Gums, *J. Saudi Soc. Agric. Sci.*, 17 (2018) 241-249.
- [35] Wang C., Yang Z., Song W., Zhong Y., Sun M., Gan T., Bao B., Quantifying Gel Properties of Industrial Waste-Based Geopolymers and Their Application in Pb²⁺ and Cu²⁺ Removal, *J. Clean. Prod.*, 315 (2021) 128203.
- [36] Karaca Acari I., Yilmaz I., Koytepe S., Ates B., Balcioglu S., Seckin T., Synthesis, Characterization of Polyhedral Oligomeric Silsesquioxane-Metronidazole Conjugate and Determination of Antibacterial, Biocompatible Properties, *Acta Chim Pharm Indica.*, 8 (2018) 134-148.
- [37] De A., Nayak A.K., Kundu A., Das B., Samanta A., Chapter 7 - Gum arabic-based nanomaterials in drug delivery and biomedical applications. Biopolymer-Based Nanomaterials in Drug Delivery and Biomedical Applications, (2021) 165-182.
- [38] Abreu F.O.M. da S., Silva N.A. da., Sipaubá M. de S., Pires T.F.M., Bomfim T.A., Monteiro Junior O.A. de C., Forte M.M. de C., Chitosan and Gum Arabic Nanoparticles for Heavy Metal Adsorption, *Polímeros*, 28 (2018) 231-238.
- [39] Errich A., Azzaoui K., Mejdoubi E., Hammouti B., Abidi N., Akartasse N., Benidire L., Hajjaji S.E.L., Sabbahi R., Lamhamdi A., Toxic Heavy Metals Removal Using a Hydroxyapatite and Hydroxyethyl Cellulose Modified with A New Gum Arabic, *Indones. J. Sci. Technol.*, 6 (2021) 41-64.
- [40] Saeedi-Jurkuyeha A., Jafarib A.J., Kalantarya R.R., Esrafilia A.A., Novel Synthetic Thin-Film Nanocomposite Forward Osmosis Membrane Modified by Graphene Oxide and Polyethylene Glycol for Heavy Metals Removal from Aqueous Solutions, *React. Funct. Polym.*, 146 (2019) 104397

Removal of Bromophenol Blue from Aqueous Solution Using Bentonite, Zeolite and Graphene Oxide

Nuket Kartal Temel ^{1,a,*}, İbrahim Gökçe Erdem ^{1,b}

¹ Department of Chemistry, Faculty of Science, Sivas Cumhuriyet University, Sivas, Türkiye.

*Corresponding author

Research Article

History

Received: 23/01/2024

Accepted: 23/03/2024



This article is licensed under a Creative Commons Attribution-NonCommercial 4.0 International License (CC BY-NC 4.0)

ABSTRACT

In this study, an anionic dyestuff bromophenol blue (BrPB) from the aqueous solution was removed by adsorption in the presence of bentonite (B), zeolite (Z) and graphene oxide (GO). The effects of pH, adsorbent amount, initial concentration of BrPB, temperature and time on adsorption were investigated. After the adsorption process, ultraviolet-visible region spectrophotometer (UV-VIS) was used to measure the amount of dyestuff remaining in the solution which is not adsorbed. It's found that; the optimum values obtained for the adsorption process; the optimum pH value 5 for B and Z, 4 for GO; 0.03 g amount of adsorbent and 60 minutes for the equilibrium time. The compatibility of Langmuir and Freundlich isotherm models was found as Z> GO> B and GO> B> Z respectively. In terms of kinetics aspect, it was observed that all adsorbents were comply with pseudo-second order reaction kinetics. To be positive of ΔG° value for B and Z is of physical nature of adsorption, to be negative of ΔG° value for GO requires to be chemical nature of adsorption. When the obtained ΔH° values were examined, it was observed that the reaction was endothermic for B and Z and exothermic for GO. The negative value of ΔS° for B and Z adsorbent species indicates that the randomness between solid and liquid decreases, whereas the positive ΔS° value for GO indicates that the randomness between solid and liquid increases. The highest adsorption capacity value obtained after the measurements made under optimum conditions is 589 mg g⁻¹ for GO and 15.7 and 19.8 mg g⁻¹ for B and Z, respectively.

Keywords: Adsorption, Bentonite, Bromophenol blue, Graphene oxide, Zeolite.

^a nkartal@cumhuriyet.edu.tr

^{id} <https://orcid.org/0000-0002-3539-4930>

^b ibogokcerdem@gmail.com

^{id} <https://orcid.org/0000-0002-3765-2307>

Introduction

Today, water pollution is one of the main factors that adversely affect human health. The rapid increase in industrialization and urbanization have been effective in the rapid deterioration of water quality. Scientific studies suggest that different industrial wastes such as textile, leather, food, paint, etc. are composed of toxic compounds, some of which are carcinogenic [1]. Uncontrolled and untreated wastes containing dyestuffs can cause major environmental disasters even at low concentrations in receiving environments. Whether or not these dye-containing wastewaters are toxic and carcinogenic, they are characterized by a high chemical oxygen demand (COD) / biological oxygen demand (BOD) ratio, suspended solids and intense colour. In addition, these wastewaters prevent the self-treatment capacity of the receiving environment, cause colouration of the receiving water, decrease the light transmittance of the water, slow down the photosynthesis rate of aquatic flora [2].

Water is an indispensable need and source of life for all living things. Therefore, it is of great importance to protect our existing water resources and to make wastewater reusable. Among the impurities contained in wastewater, there are also dyestuffs that have toxic effects. Industrial wastewater contains large amounts of dyestuffs that are resistant to biodegradation and whose contents can vary greatly. These wastewaters containing

dyestuffs, which also have toxic effects, have a high risk potential for receiving waters. Therefore, removal of industrial wastewater by simple, economical and effective methods is of great importance in terms of usable water resources.

Especially the discharge of wastewater containing dyestuffs from the textile industry to the aquatic environment without any treatment process is one of the main reasons for the formation of carcinogenic and toxic aromatic amines. The discharge of wastewater containing dyestuffs even at low concentrations into streams and river beds causes pollution in the waters [3]. Dyes discharged into receiving environments may cause irreversible problems in receiving environments by preventing sunlight from passing into water due to their structural properties. Dyes are resistant to biodegradation due to their chemical composition [4]. The release of aromatic amines during the anaerobic degradation of some azo dyes is another cause of pollution [4-5].

Significant researches are being carried out for the treatment of wastewater from dyestuffs. Among the methods used in the treatment of dyestuffs are chemical, biological, and physical methods. The methods used in treatment vary depending on the nature of the receiving environment [6].

It is known that adsorption method is an easy and very effective physical separation method in wastewater

treatment. The most commonly used adsorbents in the adsorption method include zeolite, bentonite and carbon-based nano materials [7].

Adsorbents are porous solids that bind molecules on their surfaces that are liquid, gaseous or dissolved in water. In adsorption, they are generally used to remove heavy metals and dyestuffs from wastewater by binding them to adsorbents such as bentonite, zeolite, activated carbon or silica gel.

The majority of zeolites consist of natural aluminum silicates. Zeolites are alumina silicates formed by forming a network structure of tetrahedral AlO_4 and SiO_4 , bonded to each other by oxygen atoms. Zeolites are widely used as ion exchange agents, catalysts and molecular filters in a number of industrial processes [8].

Bentonite is a widely available abundant natural clay mineral, known as a low-cost adsorbent for water and wastewater treatment. The chemical structure and pore structure of bentonite usually determine its adsorption capacities [9]. Bentonites exhibit high capacity adsorbent properties due to their colloidal structure, electrically charged particles, high liquid absorbency, high water retention capacity and large surface areas despite their small size. Bentonite has many advantages over other clay minerals due to its unique properties such as high cation exchange capacity, high specific surface area, excellent physical and chemical stability and surface properties.

Allotropes of carbon, which has a two-dimensional planar structure formed by the arrangement of carbon atoms in hexagons in a honeycomb structure, are called graphene. The modified Hummers method, one of the chemical methods, was used to obtain graphene oxide from graphite. When graphite layers are oxidized, the layers are opened thanks to oxide derivatives, and these opened layers are separated from each other by sonication. In this way, graphene oxide layers are obtained [10]. GO, which has many oxygen-containing groups such as hydroxyl, epoxide, carboxyl and carbonyl functional groups, is hydrophilic, negatively charged and can be easily dispersed in water to form a stable colloidal suspension [11].

GO and graphene, the newly discovered carbon nanoscale materials, interact strongly with organic molecules thanks to their characteristic structures and electronic properties and non-covalent forces such as Van der Waals interactions. They have many advantages for use as adsorbents, such as their nano-sized structure, rapid equilibration, high adsorption capacity and operation in a wide pH range [12].

A literature search revealed that bromophenol blue adsorption, despite its importance in water quality management, has not been reviewed. The purpose of this paper is to review the use of different adsorbents for the removal of bromophenol blue from contaminated water. The adsorption capacities of the adsorbents were compared under different experimental conditions. Due to their high specific surface area and various morphologies, carbon nanomaterials such as GO are a type of adsorbent with high efficiency in water treatment.

Materials and Methods

Instrumentation

Analytical signals at 610 nm were obtained using a UV-Vis spectrophotometer (Shimadzu UV-1800 PC, Kyoto, Japan). Phases separation was facilitated with the aid of a Universal Hettich centrifuge model (London, England). The pH was measured using a pH meter (pH-2005 model, JP Selecta, Spain).

Reagents and Standard Solutions

Analytical pure materials and double-distilled water were used throughout the analysis. A 50 mg L^{-1} solution of Bromophenol Blue (BrPB) dye (Merck, Germany) was prepared from 1000 mg L^{-1} BrPB stock solution. The clear molecular structure of BrPB is given in Figure 1.

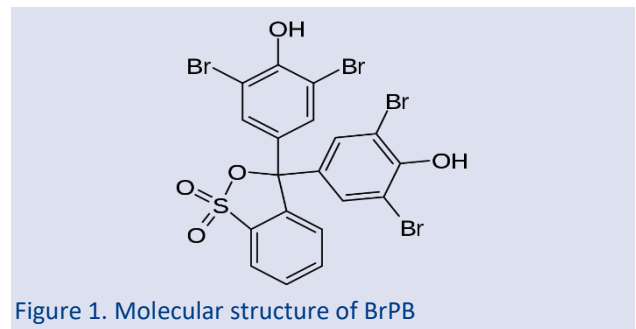


Figure 1. Molecular structure of BrPB

Dilute solutions of 1.0 mol L^{-1} HCl and NaOH (Merck, Germany) were used to adjust the solution pH. Bentonite (B) and Zeolite (Z) used as adsorbents were purchased. Graphene oxide (GO) was synthesised by oxidation of graphite using a modified Hummers method. Acid mixtures were added to the powdered graphite pieces and mixed in a sonification device at room temperature. The sonification process was continued by adding a certain amount of weighed KMnO_4 . After being kept at 55 $^\circ\text{C}$ for 30 minutes, it was taken from the sonification device and allowed to cool at room temperature. Ice water containing 30% H_2O_2 was added to the cooled mixture and sonification was continued. The solid obtained after this process was washed with distilled water until it reached pH 7 and dried in an oven at 60 $^\circ\text{C}$. GO was synthesised in the laboratory of Sivas Cumhuriyet University, Faculty of Engineering [13,14].

Adsorption Experiment

Certain volumes of BrPB solution, prepared daily at certain concentrations, were put into the test tube. By keeping the solutions in the natural pH environment, 0.1g B, 0.1g Z and 0.05g GO were added to the tubes containing BrPB solutions at different concentrations, and they were kept at room temperature for 24 hours to equilibrate. After 24 hours, each tube was centrifuged in a centrifuge device at 4000 rpm for 15 minutes to separate the adsorbent from the solution. After centrifugation, the phases were separated from each other and the absorbance value of the taken solutions was measured at 592 nm on a UV-VIS spectrophotometer in order to

determine the concentration of dye remaining without adsorption on the adsorbent. After determining the equilibration time of the solution for each adsorbent, other experimental conditions were optimised. Adsorption capacity was calculated using Equation 1.

$$q_e = \frac{(C_0 - C)}{m} \times V(1) \quad (1)$$

q_e = Amount of species adsorbed by adsorbent (mg g^{-1})
 C_0 = Initial concentration of the species to be adsorbed (mg L^{-1})
 C = Adsorbed concentration remaining in aqueous solution after adsorption (mg L^{-1})
 m = Adsorbent amount (g)
 V = Solution volume (L)

pH effect

Based on the adsorption processes mentioned above, 0.1g B, 0.1g Z and 0.05 g GO were added to 10 mL of 50 mg L^{-1} BrPB solution taken into separate tubes. The pH of the solution was adjusted to the desired pH value with dilute HCl and NaOH and kept at room temperature for 24 hours. After centrifugation for phase separation, absorbance values were measured at 592 nm. To determine the optimum pH value, simultaneous experiments were carried out in the pH range of 3-9.

Effect of Adsorbent amount

After the initial concentration and pH value were determined, the effect of the amount of adsorbent was investigated. The effect of the amount of adsorbent in the range of 0.01-0.7 g for B and Z in a 50 mg L^{-1} BrPB solution at pH 5 was investigated. For GO, since it is a more effective adsorbent by nature, the amount of adsorbent was reduced considerably and was kept in the range of 0.001-0.1 g.

Effect of initial concentration of BrPB

The effect of the initial concentration of BrPB in the BrPB solution of 5-100 mg L^{-1} was determined at the pH value determined in the previous step for each adsorbent type, by keeping the system pH constant, with 0.1 g B and Z, 0.05 g GO at 25 °C was investigated.

Temperature effect

In order to investigate the effect of temperature on the system under the optimum conditions determined in the previous experimental stages, a series of experiments were carried out in the range of 5-40 °C.

Examination of adsorption kinetics

Once the optimum experimental conditions were determined, the reaction kinetics were determined for each adsorbent species.

Investigation of adsorption thermodynamics

Examination of adsorption thermodynamics was also evaluated under determined optimum conditions;

Thermodynamic parameters such as K_c , ΔG° , ΔH° and ΔS° were calculated.

Results

pH Effect

pH value is one of the most important parameters in changing the adsorption capacity since it affects the surface charge and ionization degree of the adsorbent. The effect of pH on adsorption capacity was investigated in the pH range of 3-9, 0.1 g B and Z, 0.05 g GO, 50 mg L^{-1} BrPB, 25 \pm 1 °C, and the results are given in Figure 2.

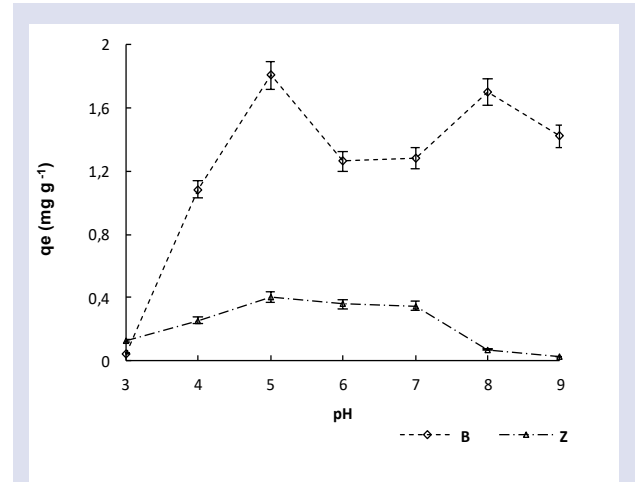


Figure 2. pH effect on the BrPB adsorption capacity of B and Z

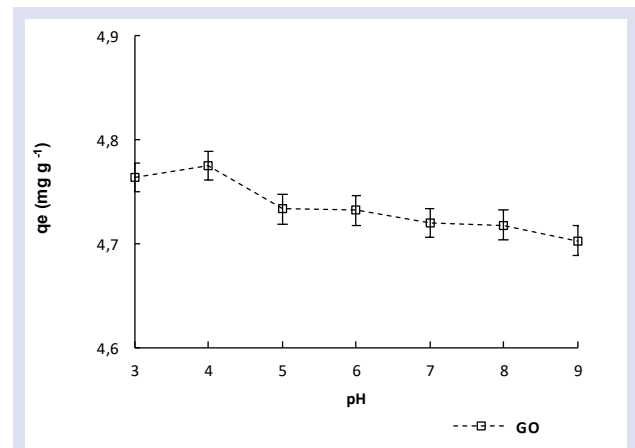


Figure 3. Effect of pH on the adsorption capacity of GO on BrPB

As can be seen in Figure 2 and Figure 3, the adsorption capacity of BrPB increased with increasing pH for all adsorbents up to a certain value and then remained at almost constant values. The best adsorption capacity for B and Z was observed at pH 5, while for GO at pH 4. BrPB is a weakly acidic anionic compound, so it exists in a neutral form at $\text{pH} < 7$ and in an ionic form at $\text{pH} > 7$ [15]. When the pH is above 7, the surface charge of the adsorbent becomes more negative and the electrostatic repulsion between the negative groups becomes effective due to the anionic state of BrPB [16].

Effect of Initial Concentration of Dyestuff

The effect of the initial concentration of 5-100 mg L⁻¹ BrPB solution was investigated at pH 5 for adsorbent types B and Z, pH 4 for GO, at 0.1 g B and Z, 0.05 g GO adsorbent amount, at 25 ± 1 °C. The results obtained are given in Figure 4- Figure 5. As can be seen from Figure 4- Figure 5, for all adsorbent types, the adsorption capacity increased up to a certain value with the increase in the initial concentration of BrPB and then this value became almost constant when the system reached equilibrium. Increasing the initial concentration of BrPB means that the species to be adsorbed in the solution increases, but since the amount of adsorbent in the system is fixed, the maximum value that the adsorbent can adsorb does not change. After the equilibrium and saturation point, the remaining unadsorbed BrPB remains in solution and the adsorption percentage decreases or remains constant [17, 18].

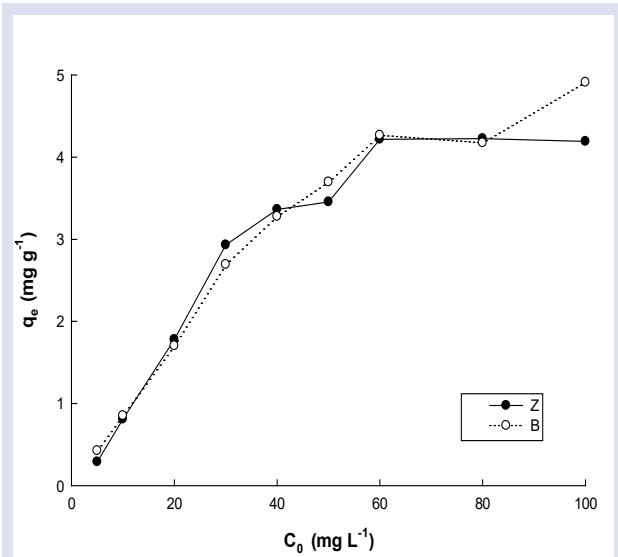


Figure 4. Effect of initial concentration of BrPB on B and Z adsorption capacities

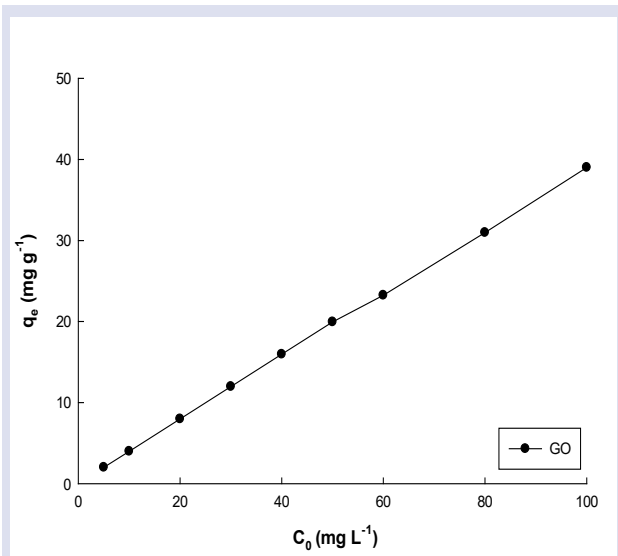


Figure 5. Effect of initial concentration of BrPB on GO adsorption capacity

Effect of Adsorbent Amount

The experiments were carried out at pH 5 for B and Z, pH 4 for GO, 50 mg L⁻¹ BrPB, 25 °C, to investigate the effect of the amount of adsorbent taken in the range of 0.01-0.7 g for B and Z and 0.001-0.1 g for GO on the adsorption capacity. The results obtained are given in Figure 6.

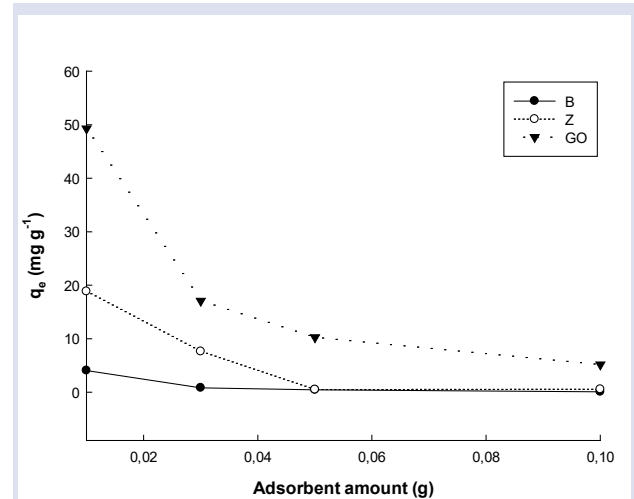


Figure 6. Effect of adsorbent amount on the BrPB adsorption capacity of different adsorbents

It can be seen in Figure 6 that, as the amount of adsorbent increases, the adsorption capacity for all adsorbent types initially increases and after a certain value it decreases. While the adsorption capacity was expected to increase with the increase in the amount of adsorbent, on the contrary, a decrease in adsorption was observed. On the one hand, while the amount of adsorbent increased, on the other hand, the amount of BrPB, the species to be adsorbed, was constant and the adsorption capacity decreased because the adsorbent surface became saturated [19-22]. Considering the values in Equation 2.3.1, it is expected that the adsorption capacity will decrease as the amount of adsorbent increases.

Temperature Effect

The pH of the solution was adjusted to 5 for B and Z and 4 for GO, the amount of adsorbent was taken as 0.1g for B and Z and 0.01g for GO and the effect of temperature on adsorption at an initial concentration of 50 mg L⁻¹ for B and Z and 600 mg L⁻¹ for GO BrPB was investigated at 5, 25 and 40 °C and the results are given in Figure 7- 8. It was observed that the adsorption capacities increased with the increase in temperature for B and Z adsorbents. The increase in adsorption capacity with increasing temperature shows that the system is an endothermic system.

For GO, on the contrary to B and Z adsorbents, the adsorption capacity started to decrease with the increase in temperature. Increasing the temperature may have a decreasing effect on the adsorption capacity, as it may cause the functional groups on GO to break off.

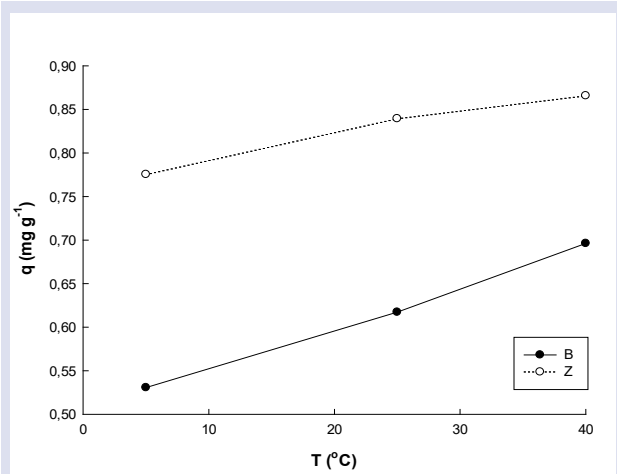


Figure 7. Effect of temperature on the adsorption of BrPB by B and Z

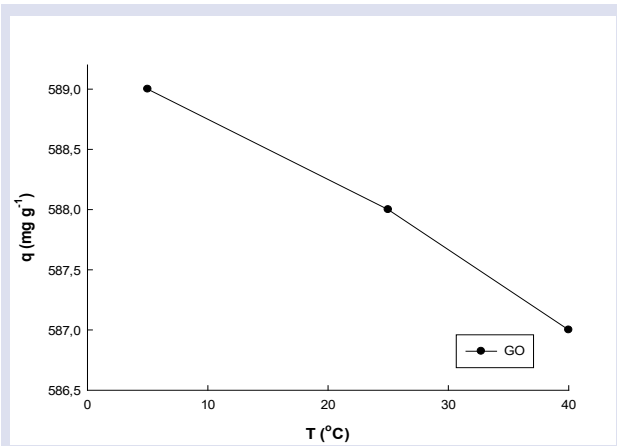


Figure 8. Effect of temperature on GO adsorption of BrPB

Evaluation of Isotherms

The Langmuir and Freundlich isotherm models are described in Equation 2- 3 respectively.

$$q_e = \frac{q_m K_L C_e}{1 + K_L C_e} \tag{2}$$

C_e : Concentration of the substance remaining in the solution after adsorption (mg L^{-1})

q_e : Amount of material collected per unit adsorbent (mg g^{-1})

K_L : Constant that depends on the adsorptivity of the adsorbate (g^{-1})

q_m : Maximum adsorption capacity of the adsorbent (mg g^{-1})

$$q_e = K_F C_e^{\frac{1}{n}} \tag{3}$$

C_e : Concentration of the substance remaining in the solution after adsorption (mg L^{-1})

q_e : Amount of material collected per unit adsorbent (mg g^{-1})

K_F : (Adsorption capacity (g^{-1}))

n : Adsorption intensity

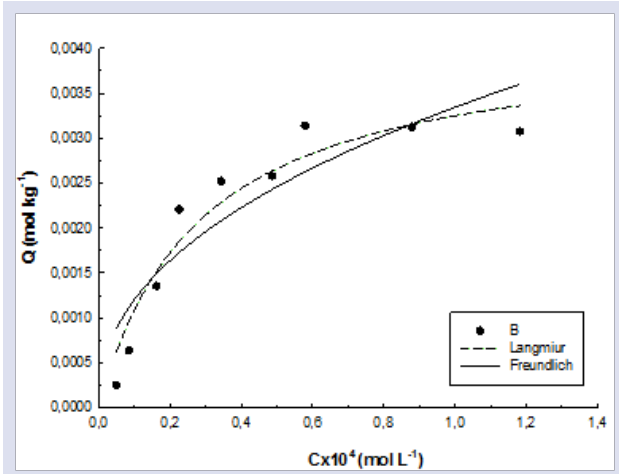


Figure 9. Langmuir and Freundlich isotherms of B

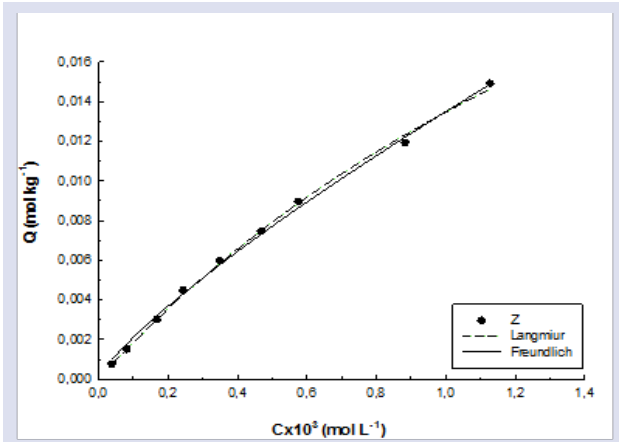


Figure 10. Langmuir and Freundlich isotherms of Z

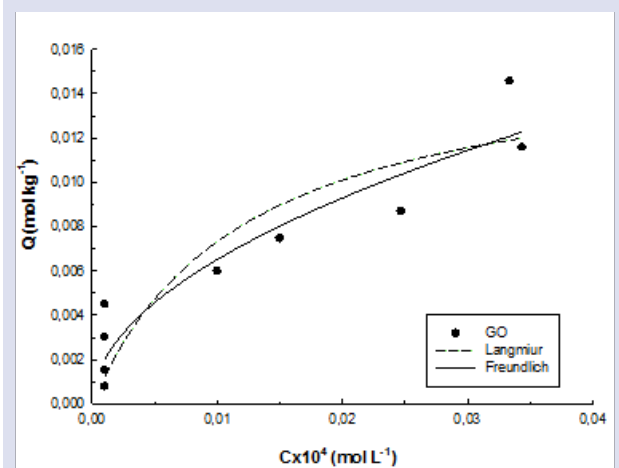


Figure 11. Langmuir and Freundlich isotherms of GO

Table 1. Langmuir and Freundlich parameters derived from BrPB adsorption isotherms to B, Z and GO

Material	Langmuir			Freundlich		
	$X_L/\text{mol kg}^{-1}$	$K_L/\text{L mol}^{-1}$	R^2	X_F	B	R^2
B	0.0042	35340	0.931	0.198	0.443	0.829
Z	0.045	4252	0.998	22.9	0.807	0.998
GO	0.02	464100	0.831	7.75	0.513	0.889

When the 'monolayer adsorption capacities, X_i ' found from the Langmuir model are compared, it is seen that the order is $Z > GO > B$. The XF values found in the Freundlich and D-R models also confirm the result. The comparison of the KL values, which is a measure of the tendency of adsorption, was found to be in the order of $GO > B > Z$. The order of the heterogeneity measure β (decreasing value, increasing interest) in the Freundlich model is $Z > GO > B$. As a result, when the adsorption capacities were evaluated, it was found that the adsorption capacity of Z for BrPB adsorbent had the highest value compared to B and GO , and in the comparison of adsorption tendency values, GO had the highest value compared to B and Z .

Evaluation of Kinetics

Pseudo-first order equation and pseudo-second order equation were used to evaluate the adsorption kinetics. The pseudo-first order kinetics equation and the pseudo-second-order kinetics are given by Equation 4-5 respectively.

$$\ln \left(1 - \frac{q_t}{q_e} \right) = -k_1 t \tag{4}$$

$$\frac{t}{q_t} = \frac{1}{k_2 q_e^2} + \frac{t}{q_e} \tag{5}$$

where q_t and q_e are the averaged current and equilibrium concentrations, respectively, in a sorbent; and k with different subscripts are rate constants.

Kinetic values were calculated for each adsorbent type, and the results are given in Figure 12-17 and Table 2. Pseudo-first-order and pseudo-second-order constants were calculated by plotting the $\ln(q_e - q_t)$ and t/q_t values separately against the t value, respectively. As a result of the examination of both kinetic values, the R^2 (correlation coefficient) values of B , Z and GO show that they conform to pseudo-quadratic rate kinetics. The rate constants for B , Z and GO were found in the order $Z > B > GO$. The results showed that adsorption was completed in about 30-60 minutes for all three materials.

Table 2. Pseudo-first order and pseudo-second order reaction kinetics constants of BrPB on adsorbents

Pseudo-first-order kinetic values			
Adsorbents	$k_1(\text{min}^{-1})$	$q_e(\text{mg g}^{-1})$	R^2
B	0,0207	6,638	0,9671
Z	0,0021	3,454	0,5621
GO	0,0256	15,706	0,8074
Pseudo-second-order kinetic values			
Adsorbents	$k_2(\text{g mg}^{-1}\text{min}^{-1})$	$q_e(\text{mg g}^{-1})$	R^2
B	0,0171	15,31	0,998
Z	0,253	17,0357	1
GO	0,00974	583,235	1

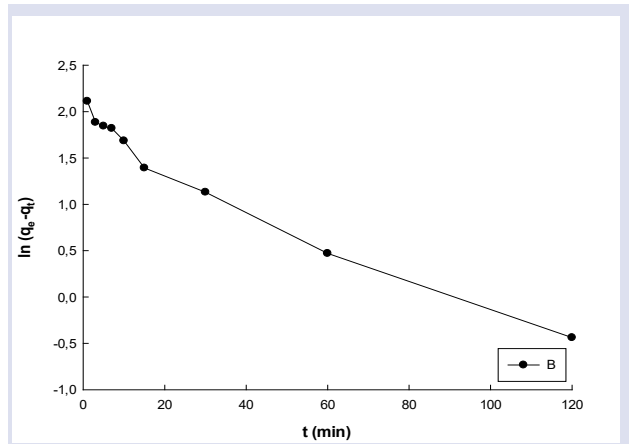


Figure 12. Pseudo-first-order kinetics of BrPB on B

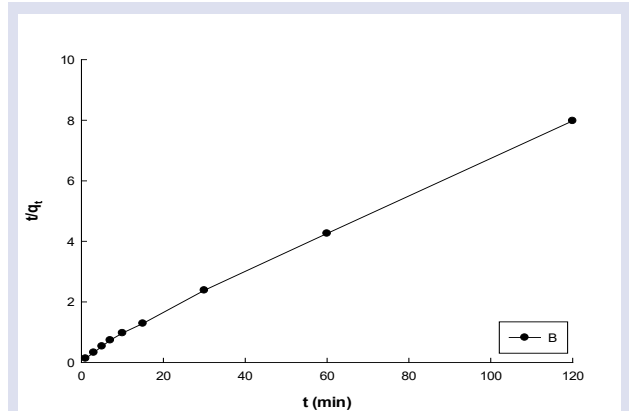


Figure 13. Pseudo second-order kinetics of BrPB on B

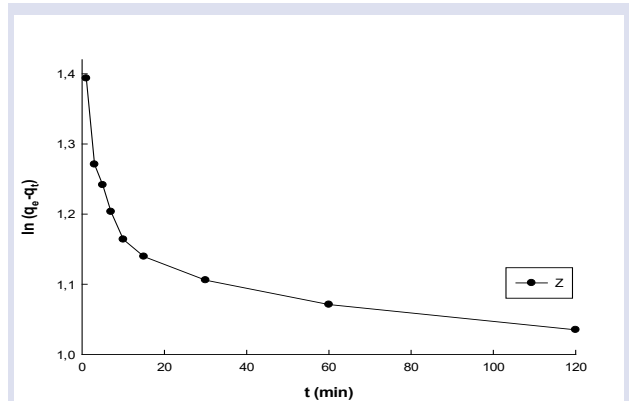


Figure 14. Pseudo-first-order kinetics of BrPB on Z

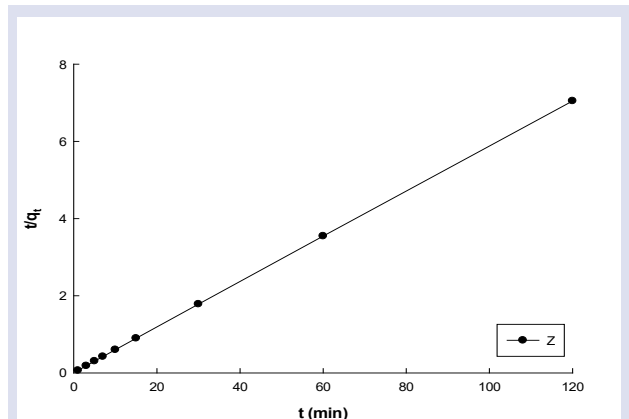


Figure 15. Pseudo-second-order kinetics of BrPB on Z

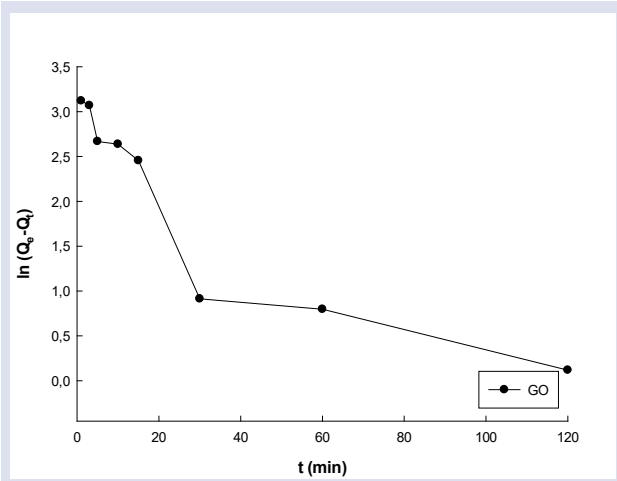


Figure 16. Pseudo-first-order kinetics of BrPB on GO

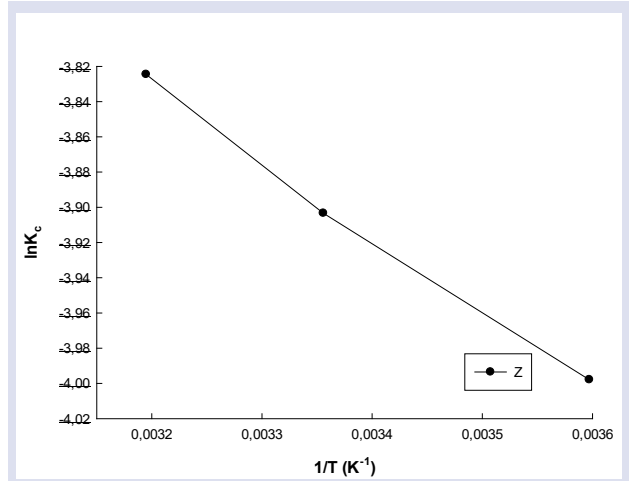


Figure 19. Thermodynamic parameters in Z adsorption

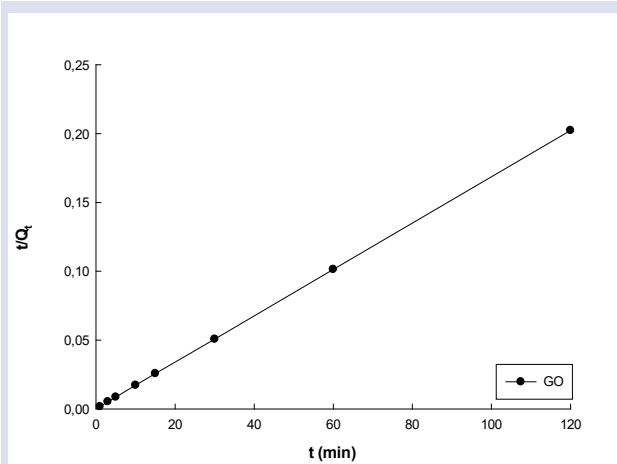


Figure 17. Pseudo-second-order kinetics of BrPB on GO

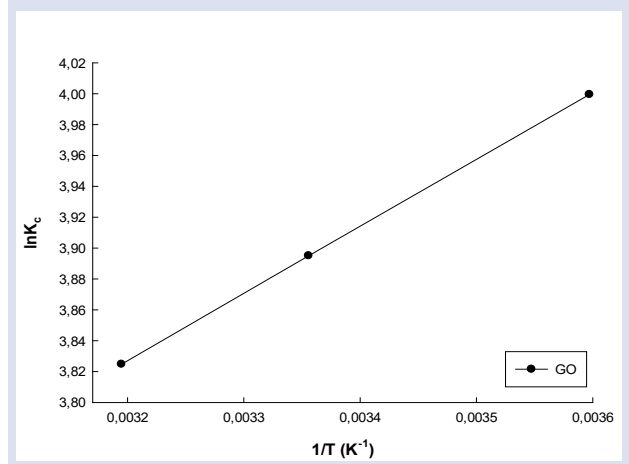


Figure 20. Thermodynamic parameters in GO adsorption

Evaluation of Thermodynamics

For each temperature value, K_c was calculated from Equation 6 and ΔG° from Equation 7. ΔH° and ΔS° values were calculated from the slope and intercept of the line formed by plotting the $\ln K_c$ value against $1/T$ (Van't Hoff). The thermodynamic values obtained are given in Table 3.

$$K_c = \frac{c_a}{c_e} \tag{6}$$

$$\ln K_c^0 = - \frac{\Delta S^\circ - \Delta H^\circ}{R} \times \frac{1}{T} \tag{7}$$

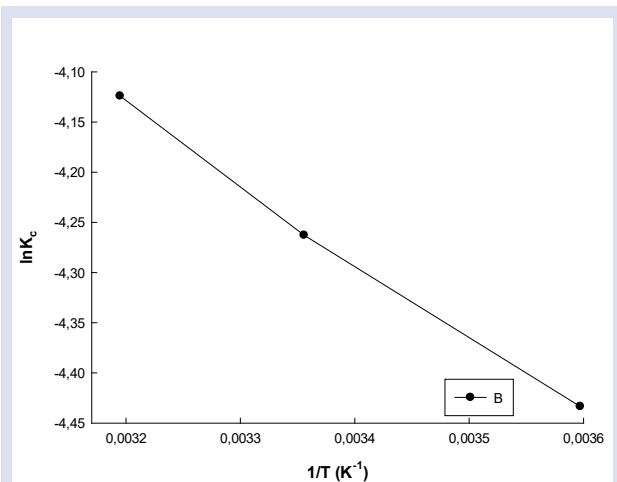


Figure 18. Thermodynamic parameters in B adsorption

Table 3. Thermodynamic constants of adsorption of BrPB on B, Z and GO

	T(K)	ΔG° (kJ mol ⁻¹)	ΔH° (kJ mol ⁻¹)	ΔS° (J mol ⁻¹ K ⁻¹)
B	278	10,25		
	298	10,56	6,36	-14,03
	313	10,73		
Z	278	9,24		
	298	9,67	3,56	-20,46
	313	9,95		
GO	278	-9,24		
	298	-9,65	-3,61	20,27
	313	-9,95		
B	278	10,25		
	298	10,56	6,36	14,03
	313	10,73		
Z	278	9,24		
	298	9,67	3,56	-20,46
	313	9,95		
GO	278	-9,24		
	298	-9,65	-3,61	20,27
	313	-9,95		

Table 3. shows that a positive ΔG° value for B and Z indicates that the adsorption process is not spontaneous, while a negative ΔG° value for GO indicates that the reaction, i.e. adsorption, is spontaneous in the direction in which it proceeds. A positive ΔH° value for B and Z

indicates that the reaction is endothermic, while a negative ΔH° value for GO indicates that the reaction is exothermic. A negative ΔS° value for B and Z adsorbent species indicates a decrease in the randomness between solid and liquid, while a positive ΔS° value for GO indicates an increase in the randomness between solid and liquid.

Discussion and Conclusions

In this study, it was aimed to remove BrB, a dyestuff, as a pollutant species from existing environments by traditional adsorption method. In addition to being simple, fast and economical, the use of carbon-based nanomaterials as adsorbent species makes this study superior to traditional methods. Carbon-based nanomaterials are known as the material of the century, which has attracted great interest not only in pollution removal but also in many other application areas. For this purpose, GO, a carbon-based nanomaterial, was used as adsorbent species in addition to traditional adsorbent species such as B and Z in the removal of BrB by adsorption method. Parameters affecting adsorption such as pH, adsorbent amount, initial concentration of BrB, temperature, time were studied in various ranges. On the other hand, isotherm, kinetic and thermodynamic parameters were investigated. Considering the results obtained, it was observed that Langmuir isotherm was more favorable for all adsorbent types in terms of isotherm and pseudo-second order kinetic equation was observed in terms of kinetics. From the thermodynamic point of view, it was concluded that the reaction for GO was more tendency to be spontaneous. The reason why GO is more effective than other adsorbent species is that the functional groups on the surface of the adsorbent increase the surface area of the adsorbent. A significant increase in adsorption capacity was also observed due to the active functional groups on the adsorbent surface. Some of the literature studies on the removal of BrB by adsorption and the results of the current study are presented in Table 4. When the studies in this table are compared both among themselves and with our current study, it can be seen that the adsorption efficiency obtained for GO in this study (589 mg g^{-1}) is quite high. In addition, it is seen that the adsorption capacity value of carbon-based nanomaterials used as adsorbents in the studies referenced in Table 4.1 is higher than other adsorbents.

The results of this study on the removal of synthetically prepared BrB by adsorption method show that the method can be applied to real wastewater samples. Thus, wastewater containing organic and inorganic species that greatly threaten human and environmental health can be removed before being discharged directly into nature. Wastewater reuse has become an important necessity due to the insufficiency of existing water resources depending on the population growth. Nanomaterials are promising materials for wastewater recovery as in many other fields.

Table 4. Comparison of adsorption removal of BrPB with different adsorbents

Adsorbents	$q_m(\text{mg g}^{-1})$	
CNP	22,72	[18]
Magnetite Nanoparticles	400,50	[23]
CuS-NP-AC	106,38	[24]
Activated carbon obtained from Astragalus bisulcatus tree	51,21	[25]
Sorel's cement nanoparticles	4,88	[26]
$\text{Fe}_2\text{O}_3\text{-ZnO-ZnFe}_2\text{O}_4/\text{carbon}$ nanocomposite	90,91	[27]
Polymer-clay composite	10,78	[28]
Thermally modified granular charcoal	101,62	[29]
Mesoporous hybrid gel derived from tetraethoxysilane and bis(trimethoxysilyl)hexane	27,60	[30]
Bentonit	15,7	Thisstudy
Zeolit	19,8	Thisstudy
Grafen oksit	589	Thisstudy

Acknowledgements

The present work was realized as a part of F-497 projects supported by Cumhuriyet University Scientific Research Council.

Conflicts of Interest

The authors declare no conflict of interest.

References

- [1] Rai H. S., Bhattacharyya M. S., Singh J., Bansal T. K., Vats P., Banerjee U. C., Removal of dyes from the effluent of textile and dyestuff manufacturing industry: a review of emerging techniques with reference to biological treatment. *Critical Reviews in Environmental Science And Technology*, 35(3) (2005) 219-238.
- [2] Ada K., Ergene A., Tan S., Yalçın E., Adsorption of Remazol Brilliant Blue R using ZnO fine powder: Equilibrium, kinetic and thermodynamic modeling studies. *Journal of Hazardous Materials*, 165(1-3) (2009) 637-644.
- [3] Nigam P., Armour G., Banat I. M., Singh D., Marchant R., Physical removal of textile dyes from effluents and solid-state fermentation of dye-adsorbed agricultural residues. *Bioresource Technology*, 72(3) (2000) 219-226.
- [4] Banat I. M., Nigam P., Singh D., Marchant R., Microbial decolorization of textile-dye-containing effluents: A review (vol 58, pg 217, 1996). *Bioresource Technology*, 61(1) (1997) 103-103.
- [5] Brown M. A., De Vito S. C., Predicting azo dye toxicity. *Critical Reviews in Environmental Science And Technology*, 23(3) (1993) 249-324.

- [6] Wang S., Boyjoo Y., Choueib A., Zhu Z. H., Removal of dyes from aqueous solution using fly ash and red mud. *Water Research*, 39(1) (2005) 129-138.
- [7] Annadurai G. Adsorption of basic dye on strongly chelating polymer: batch kinetics studies. *Iranian Polynter Journal* 11(4) (2002) 1026-1265.
- [8] Soylu M., Gökkuş Ö., Türkiye'deki Doğal Zeolitler Ve İyon Değişimi Uygulamaları. *Ömer Halisdemir Üniversitesi Mühendislik Bilimleri Dergisi*, 6(1) (2017) 11-20.
- [9] İşçi S. Bentonit dispersiyonlarına organik ve inorganik katkıların adsorbsiyonunun reolojik özellikleri üzerine etkisi, *İstanbul Teknik Üniversitesi, Fen Bilimleri Enstitüsü*, (2002).
- [10] Tiyek İ., Dönmez U., Yıldırım B., Alma M. H., Ersoy M. S., Karataş Ş., Kimyasal yöntem ile indirgenmiş grafen oksit sentezi ve karakterizasyonu. *Sakarya University Journal of Science*, 20(2) (2016) 349-357.
- [11] Zhang W., Zhou C., Zhou W., Lei A., Zhang Q., Wan Q., Zou B., Fast and considerable adsorption of methylene blue dye onto graphene oxide. *Bulletin of Environmental Contamination and Toxicology*, 87(1) (2011) 86.
- [12] Li Y, Du Q, Liu T, Peng X, Wang J, Sun J, Wang Y, Wu S, Wang Z, Xia Y, Xia L. Comparative study of methylene blue dye adsorption onto activated carbon, graphene oxide, and carbon nanotubes. *Chemical Engineering Research and Design*, 91(2) (2013) 361-368.
- [13] Kartal Temel N. Sertakan K., Temel Ü.N. Grafen Oksit Hummers Metodu ile Sentezlenmesine Etki Eden Parametrelerin İyileştirilmesi. *Cumhuriyet Science Journal*, 38(4) (2017) 674-680.
- [14] Hummers Jr. W.S., Offeman R. E. Preparation of graphitic oxide. *Journal of The American Chemical Society*, 80(6) (1958) 1339-1339.
- [15] Liu J., Yao S., Wang L., Zhu W., Xu J., Song H. Adsorption of bromophenol blue from aqueous samples by novel supported ionic liquids. *Journal of Chemical Technology & Biotechnology*, 89(2) (2014) 230-238.
- [16] Okoye C.C. Adsorptive Removal of Bromophenol Blue Dye from Aqueous Solution using Acid Activated Clay. *International Journal of Scientific Research and Management*, 6(03) (2018).
- [17] El-Sayed G.O. Removal of methylene blue and crystal violet from aqueous solutions by palm kernel fiber. *Desalination*, 272(1-3) (2011) 225-232.
- [18] Dhananasekaran S., Palanivel R., Pappu S., Adsorption of methylene blue, bromophenol blue, and coomassie brilliant blue by α -chitin nanoparticles. *Journal of Advanced Research*, 7(1) (2016) 113-124.
- [19] El-Dars F.M., Ibrahim H.M., Farag H.A., Abdelwahhab M.Z., Shalabi, M.E.H. Adsorption kinetics of bromophenol blue and eriochrome black t using bentonite carbon composite material. *International Journal Of Scientific & Engineering Research*, 6(5) (2015) 679-688.
- [20] Akpomie K. G., Adegoke K. A., Oyedotun K. O., Ighalo J. O., Amaku J. F., Olisah C., Conradie J. Removal of bromophenol blue dye from water onto biomass, activated carbon, biochar, polymer, nanoparticle, and composite adsorbents. *Biomass Conversion and Biorefinery*, (2022) 1-29.
- [21] Khan H., Khalil A. K., Khan A., Saeed K., Ali N. Photocatalytic degradation of bromophenol blue in aqueous medium using chitosan conjugated magnetic nanoparticles. *Korean Journal of Chemical Engineering*, 33 (2016) 2802-2807.
- [22] Shah T., Gul T., Saeed K. Photodegradation of bromophenol blue in aqueous medium using graphene nanoplates-supported TiO₂. *Applied Water Science*, 9(4) (2019) 1-7.
- [23] Saha B., Das S., Saikia J., Das G., Preferential and enhanced adsorption of different dyes on iron oxide nanoparticles: a comparative study. *The Journal of Physical Chemistry C*, 115(16) (2011) 8024-8033.
- [24] Mazaheri H., Ghaedi M., Asfaram A., Hajati S., Performance of CuS nanoparticle loaded on activated carbon in the adsorption of methylene blue and bromophenol blue dyes in binary aqueous solutions: using ultrasound power and optimization by central composite design. *Journal of Molecular Liquids*, 219 (2016) 667-676.
- [25] Ghaedi M., Ghaedi A.M., Negintaji E., Ansari A., Vafaei A., Rajabi M., Random forest model for removal of bromophenol blue using activated carbon obtained from *Astragalus bisulcatus* tree. *Journal of Industrial and Engineering Chemistry*, 20(4) (2014) 1793-1803.
- [26] El-Gamal S.M A., Amin M.S., Ahmed M.A., Removal of methyl orange and bromophenol blue dyes from aqueous solution using Sorel's cement nanoparticles. *Journal of Environmental Chemical Engineering*, 3(3) (2015) 1702-1712.
- [27] Mohammadzadeh A., Ramezani M., Ghaedi A.M., Synthesis and characterization of Fe₂O₃-ZnO-ZnFe₂O₄/carbon nanocomposite and its application to removal of bromophenol blue dye using ultrasonic assisted method: optimization by response surface methodology and genetic algorithm. *Journal of the Taiwan Institute of Chemical Engineers*, 59 (2016) 275-284.
- [28] El-Zahhar Adel A., Awwad Nasser S., El-Katori Emad E., Removal of bromophenol blue dye from industrial waste water by synthesizing polymer-clay composite. *Journal of Molecular Liquids*, 199 (2014) 454-461.
- [29] Haider S., Bukhari N., Park S.Y., Iqbal Y., Al-Masry W.A. Adsorption of bromo-phenol blue from an aqueous solution onto thermally modified granular charcoal. *Chemical Engineering Research and Design*, 89 (1) (2011) 23-28.
- [30] You L., Wu Z., Kim T., Lee K. Kinetics and thermodynamics of bromophenol blue adsorption by a mesoporous hybrid gel derived from tetraethoxysilane and bis(trimethoxysilyl) hexane. *Journal of colloid and interface science*, 300 (2) (2006) 526-53

Fluorescence Cell Imaging by Carbon Quantum Dots Derived from the Medicinal Plant *Malva Sylvestris*

Layth Shakir Mahmood ^{1,a}, Gulsin Arslan ^{1,b}, Idris Sargin ^{1,c,*}, Serdar Karakurt ^{2,d}

¹ Department of Biochemistry, Faculty of Science, Selcuk University, Konya, Türkiye.

*Corresponding author

Research Article

History

Received: 27/07/2023

Accepted: 31/01/2024



This article is licensed under a Creative Commons Attribution-NonCommercial 4.0 International License (CC BY-NC 4.0)

ABSTRACT

Carbon quantum dots (CQDs) derived from biological samples exhibit low cytotoxicity and are often used as fluorescent agents for bioimaging cells or bacteria. In this study, fluorescent CQDs derived from *Malva sylvestris*, a wild edible medicinal plant (common mallow), were used to visualize the human epithelial cells (PNT1A). CQDs with strong blue photoluminescence were synthesized by microwave irradiation of dried *M. sylvestris* in water. CQDs' structural, morphological, surface features and photoluminescence properties were evaluated. *In vitro*, cytotoxicity assays revealed that carbon quantum dots from *M. sylvestris* have no cytotoxic effects on human epithelial cells. Non-cytotoxic and high photoluminescent CQDs from *M. sylvestris* can be exploited in bioimaging applications as a fluorophore agent.

Keywords: Carbon dots, *Malva sylvestris*, Cell viability, PNT1A

^a layth.sh2016@gmail.com
^c idris.sargin@selcuk.edu.tr

^b <https://orcid.org/0000-0002-2551-4329>
^d <https://orcid.org/0000-0003-3785-9575>

^b 71arslan@gmail.com
^d kserdar1@yahoo.com

^b <https://orcid.org/0000-0002-4836-8651>
^d <https://orcid.org/0000-0002-4449-6103>

Introduction

There is a growing interest in *in vitro* cellular imaging with fluorescent nanomaterials. Fluorescent CQDs are attracting attention as an alternative to organic or inorganic fluorophore agents due to their multicolor luminescence and biocompatibility [1]. Recent studies have demonstrated their high potential to be used in bioimaging and bio-sensing applications as an alternative fluorophore agent [2, 3].

Fluorescence emission of CQDs is ascribed to their surface defects and sp^2/sp^3 hybridized surface functionalities. CQDs exhibit multicolor luminescence depending on the excitation wavelength [4]. Their surface functionalities are also responsible for the solubility of CQDs in aqueous solutions. The water solubility of carbon quantum dots is particularly important for biological studies requiring bodily fluids or simulated bodily fluids [5]. Hydroxyl, amino or carboxylic moieties on the CQDs surface are key in interacting with cells, tissues, or biological molecules [6]. Biocompatibility low/non-cytotoxicity of carbon quantum dots is often related to the surface moieties [7].

CQDs derived, particularly biological samples, exhibit low cytotoxicity and are often called green and biocompatible nanoparticles. Their size, biocompatibility, and water-dispersible properties make it possible to use these fluorescent nanoparticles as fluorophore probes for bioimaging cells or bacteria [8]. Numerous literature reports have demonstrated the potential and suitability of CQDs derived from natural sources for fluorescence imaging of live cells. Cabbage-derived CQDs, for example, were used to visualize human keratinocyte cancer cells

[9]. Green fluorescent carbon dots from coriander leaves were evaluated for *in vitro* cell imaging of normal and cancerous cells [10]. In another study, blue/green/red emissive CQDs from onion wastes were used as fluorophore probes for multicolored imaging of HeLa cells [11]. In a report by Jeong et al. (2014), CQDs from mango fruit exhibited blue, green, and yellow emission colors. They were administered intravenously to a mouse to evaluate their suitability for bioimaging applications [12]. The distribution of the carbon dots in a nude mouse was assessed with reference to their multicolor luminescence.

CQDs have tunable/modifiable surfaces. For instance, the intensity of their photoluminescence emission can be increased by surface passivation, a form of surface modification. Surface functionalities are effective in the chemical modification of the surface [13]. Numerous recent literature reports revealed that CQDs could be evaluated in drug delivery studies as vehicles [14-16].

Furthermore, CQDs can be synthesized by carbonization of plants, mushrooms, or biopolymers using laser energy, electrochemical oxidation, and thermal and microwave irradiation [17, 18]. Compared to other techniques, microwave-assisted methods do not require longer operational time, the use of organic solvents, and higher temperatures [19].

Malva sylvestris is an edible wild plant commonly used in pharmaceutical ethnobotany. It grows wild in North Africa, Europe, and Asia. It contains phenolic compounds, flavonoids, carotenoids, tocopherols, and unsaturated fatty acids [20]. This medicinal plant is being extensively studied due to its therapeutic properties and nutrient

contents [21-23]. In recent studies, *M. sylvestris* extracts were used to synthesize nanoparticles such as CuO [24], Fe₃O₄ [25], and Ag/AgCl [26].

In this study, the plant was used to synthesize carbon-based nanoparticles for the first time. Fluorescent CQDs were obtained by microwave-assisted carbonization of dried aerial parts of *M. sylvestris* without using any chemicals. In this study, the synthesis of carbon quantum dots from *M. sylvestris* was explored for the first time. The synthesis process was refined to produce CQDs with heightened photoluminescence emission. Various analytical tools, including TEM, XRD analysis, FT-IR spectroscopy, XPS, UV-visible absorption spectrophotometry, and fluorescence spectroscopy, were used to examine the structural and photophysical features of the CQDs. The fluorescence quantum yield of the CQDs was also calculated. In addition, the paper reports on the cytotoxic effects of the CQDs on the PNT1A human prostate epithelial cell line.

Experimental

Materials

M. sylvestris specimens were collected in Sizma (Selcuklu, Konya, Turkey) and identified by the Faculty of Pharmacy, Department of Pharmaceutical Botany (Selcuk University, Konya, Turkey). The roots of the plants were removed, and the remaining parts, including the leaves, stems, flowers, and leafy flowered stems were rinsed with water and dried. *M. Sylvestris* specimens were ground using a metal blade grinder and stored in powder form in sealed glass bottles at +4°C. Quinine hemisulphate salt monohydrate was purchased from Sigma.

Optimization of Experimental Parameters

CQDs were synthesized by microwave irradiating dried *M. sylvestris* powder in water. The experimental parameters, i.e., the microwave power levels, the microwave irradiation time, and the mass of *M. sylvestris* powder were studied as follows.

The microwave power level: 0.25 g of *M. sylvestris* in 10 mL of distilled water was exposed to microwave irradiation (CEM Mars 5) for 20 min (at 400 W). The crude solution was centrifuged (at 3260 x *g*), and the supernatant was recovered and filtrated using a microfilter (0.22 μm). The filtrate was dialyzed against distilled water. The dialysis medium was refreshed three times overnight. The fluorescence emission of the CQDs in water was recorded ($\lambda_{ex} = 365$ nm) on Perkin Elmer LS 55 instrument. The same procedure was followed for 800 and 1600 W power levels. The CQDs solution with the highest fluorescence emission was recorded as the optimum power level (Figure 1, top). The carbon quantum dots in the solution were recovered by lyophilization.

The exposure time: The microwave exposure time was optimized at the specified power level. The same procedure was followed at varying exposure times (Figure 1, middle).

The mass of the plant: Finally, the mass of *M. sylvestris* was optimized at the specified power level and the exposure time. The same procedure was followed at varying plant masses (Figure 1, bottom).

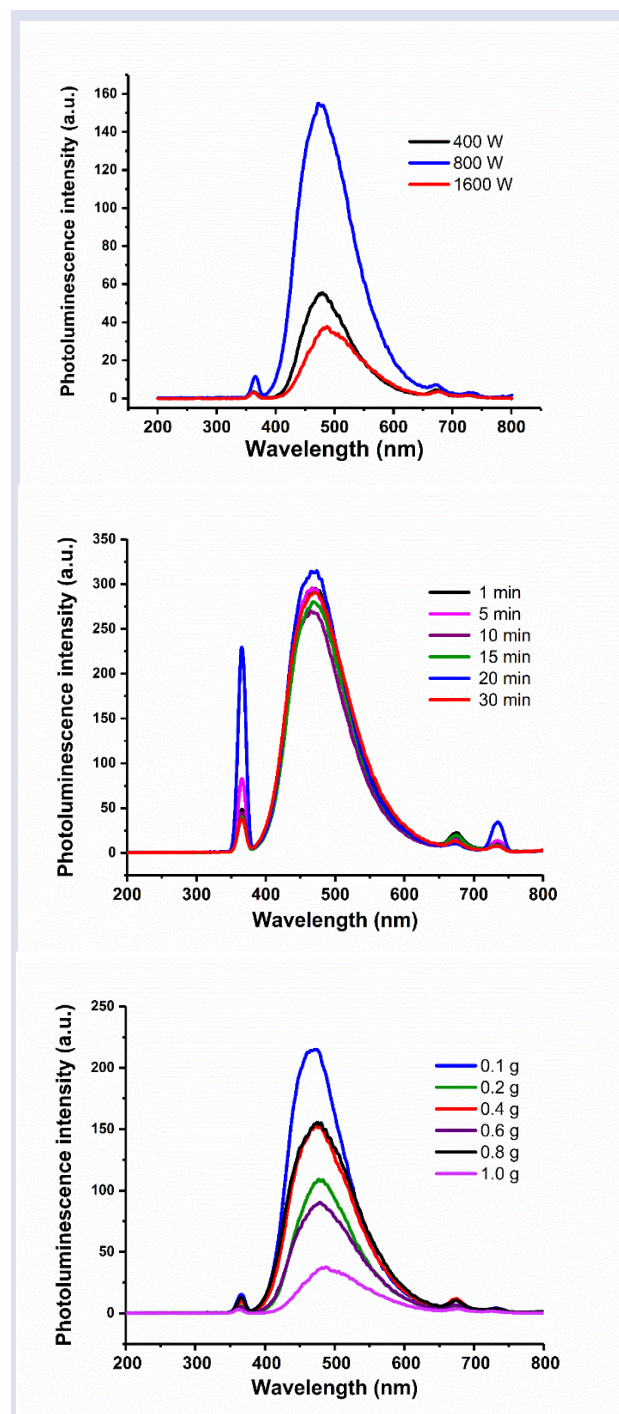


Figure 1. Optimization of operational parameters for synthesizing CQDs from *M. sylvestris* through microwave irradiation (Microwave power level: 800 W, exposure time: 20 min, the mass of *M. sylvestris* plant powder: 0.1 g and the volume of distilled water: 10 mL).

Preparation of CQDs from *M. sylvestris*

The optimized method mentioned above was used to obtain CQDs from *M. sylvestris*. In short, 0.1 g of *M. sylvestris* was mixed with 10 mL of distilled water and exposed to microwave irradiation at 800 W for 20 minutes. The mixture was then centrifuged, filtered with a syringe filter, and dialyzed against distilled water. Finally, the solution was recovered through lyophilization, as shown in Figure 2.

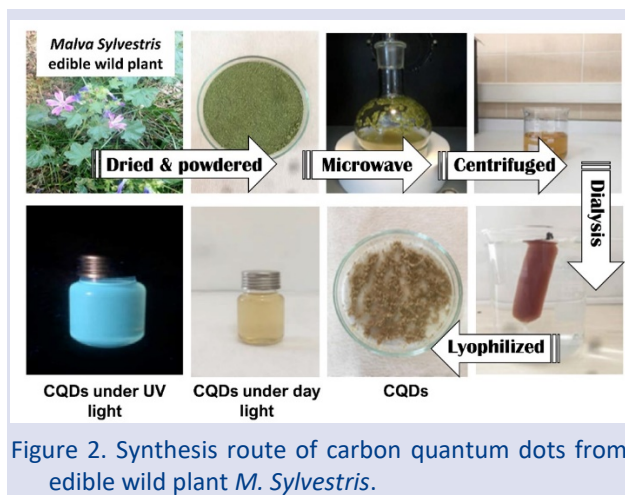


Figure 2. Synthesis route of carbon quantum dots from edible wild plant *M. Sylvestris*.

Characterization of CQDs

Structural properties of CQDs: The visualization of CQDs was accomplished through TEM (JEOL JEM-2100, UHR- Ultra High-Resolution instrument). The transmission electron microscopy (TEM) images gave insights into the surface and structural properties of CQDs. The X-ray diffraction pattern for CQDs was obtained using a Bruker D8 Advance instrument (2θ angle, 0° - 90° , scan rate 3° min^{-1}) to reveal the core structure and the crystallinity of CQDs.

Surface characterization of CQDs: FT-IR spectroscopy (Bruker Vertex 70 FT-IR spectrometer, in the range of 4000 - 500 cm^{-1}) and XPS (PHI 5000 VersaProbe Thermo Scientific K-alpha X-ray Photoelectron Spectrometer) were used to examine surface atomic groups of CQDs.

Photophysical features of CQDs: CQDs' luminescence was analyzed using (UV-vis Shimadzu UV1800) absorption spectrophotometer and fluorescence emission spectra.

Fluorescence quantum yield of CQDs: To determine the fluorescence quantum yield of CQDs, the method described in a previous report [27] was followed.

Cytotoxicity and cell imaging

PNT1A cells (Epithelial cells, ATCC) were cultured in RPMI 1640 medium with 2 mM L-glutamine and 1% penicillin. Then, the cells were incubated for 24 hours at 37°C with 5% CO_2 . Next, the cells were exposed to a solution of CQDs ranging from 0 to $1000 \mu\text{g mL}^{-1}$, maintained at a temperature of 37°C . Following the 48 h-incubation, the cell proliferation assays were performed using the Alamar Blue Method, and IC_{50} of the carbon quantum dots solution was calculated from a sigmoidal plot of cell viability [28]. PNT1A cells were grown in RPMI-1640 growth medium containing 10% FBS (Foetal Bovine

Serum) and 2 mM L-Glutamine. This medium was also used to dilute the carbon quantum dots solutions. Once the cells reached the confluency, they were washed with phosphate buffer (10 mM), detached with the trypsin-EDTA solution, and transferred to 96-well plates. The wells' cells were subjected to CQDs solutions ranging from 0 - $1000 \mu\text{g mL}^{-1}$ before being incubated at 37°C and 5% CO_2 for 24 hours. In the assay, the absorbance values depend on the amount of the strongly fluorescent product, resorufin, formed by cellular reduction of resazurin, a blue-colored weak fluorescent dye. A microplate reader spectrophotometer was used to analyze the fluorescence of Resorufin. Then, the cell viability percentage was calculated.

The cytotoxic effect of CQDs was determined from the sigmoidal graph of the viability ratio, and IC_{50} values were calculated.

Bio-imaging studies were performed using a fluorescent microscope (ZOE, Bio-rad, USA). The cells (1×10^5) were placed on a 3-well chamber microscopy glass slide (ibidi, USA) and then incubated at 37°C for 24 hours. Next, the old growth medium was substituted with a new growth medium containing $50 \mu\text{g/mL}$ of CQDs and left to incubate at a temperature of 37°C for a duration of 45 minutes. Finally, the slides were rinsed with 10 mM PBS to remove excess carbon quantum dots solution and examined under a fluorescence microscope.

Results and Discussion

Optimization studies

The effects of experimental design manipulation on photoluminescence emission of the CQDs were studied at varying microwave power levels, microwave exposure time, and mass of dried *M. sylvestris*. The synthesis of CQDs from *M. sylvestris* was optimized by measuring the photoluminescence intensity of the resulting aqueous solutions of the CQDs (Figure 3). The optimum synthesis conditions were recorded as follows: Microwave power level: 800 W, exposure time: 20 min, the mass of *M. sylvestris* plant powder: 0.1 g, and the volume of distilled water: 10 mL.

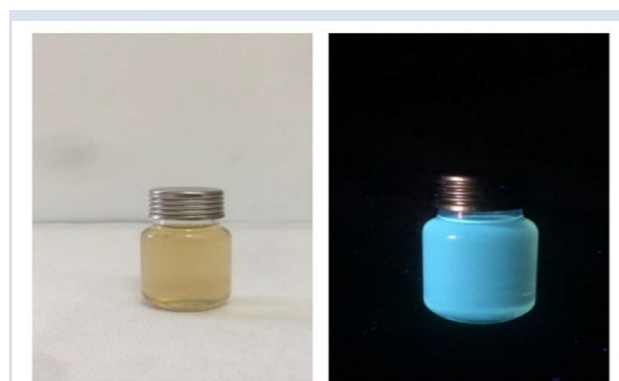


Figure 3. The image of carbon quantum dots from *M. sylvestris* dissolved in water (left) and blue fluorescence emission of the CQDs under UV light (at 365 nm) (right).

Structural and Physical Properties of CQDs

CQDs from *M. sylvestris* were visualized using TEM. The TEM and HR-TEM images provided information on CQDs' morphology, size, and crystalline structure (Figure 4 a-d). The CQDs had a crystalline core, and their size varied in the ~10–50 nm (Figure 4 b, c). Figure 4d displays the crystal lattice of the graphitic core. The lattice spacing of CQDs was found to be similar to that of graphite, around 0.35 nm. This suggests that the CQDs derived from *M. sylvestris* have a crystalline structure. In TEM images, some long rod-like structures were also observed (Figure 4 a).

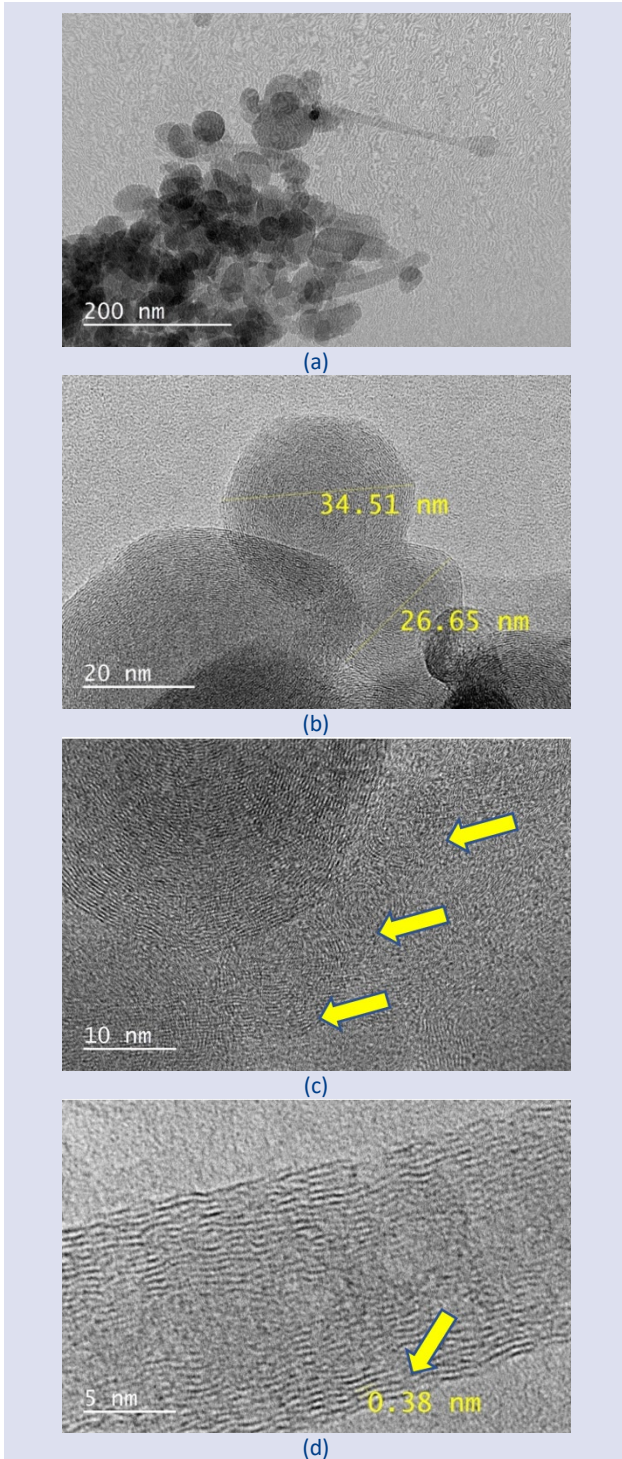


Figure 4. TEM (a) and HR-TEM (b, c, and c) images of CQDs synthesized from *M. sylvestris*.

Figure 5 displays the crystallinity of CQDs as demonstrated by the X-ray diffraction (XRD) pattern. Based on the diffraction peaks observed at around 22 and 26°, it can be concluded that the CQDs derived from *M. sylvestris* possess graphitic crystallinity. The presence of a weak diffraction peak around 15° may be due to the CQDs' amorphous characteristics [29, 30].

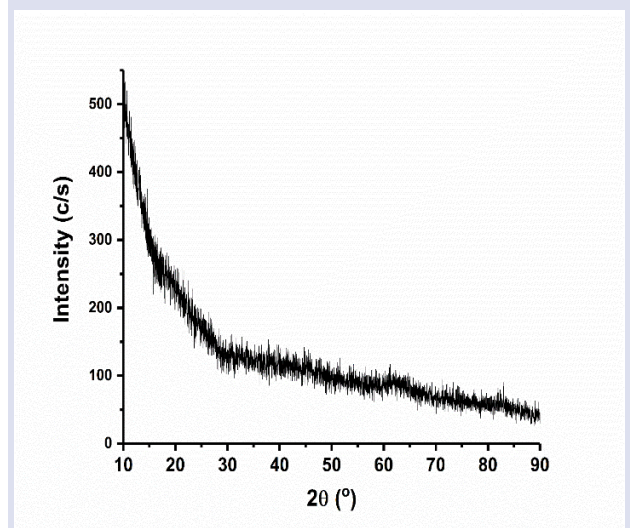


Figure 5. X-ray diffractogram of carbon quantum dots synthesized from *M. sylvestris*.

The analysis of the CQDs' surface functional groups was conducted using FT-IR spectroscopy (as shown in Figure 6). The spectrum analysis identified two vibrational bands: one at 3281 cm^{-1} for $-\text{NH}$ and $-\text{OH}$ stretching, and another at 2927 cm^{-1} for $-\text{C-H}$ stretching. The bands at 1597 cm^{-1} corresponded to the C=C stretching of polycyclic aromatic hydrocarbons [31]. The CQDs were found to contain sp^2 hybridized C-H and C-O bonds, which were confirmed through vibrational bands at 1412 cm^{-1} and 1040 cm^{-1} , respectively. The existence of hydrophilic functional groups such as $-\text{COOH}$ and $-\text{NH}_2$ implies that CQDs could be useful for biological purposes [32].

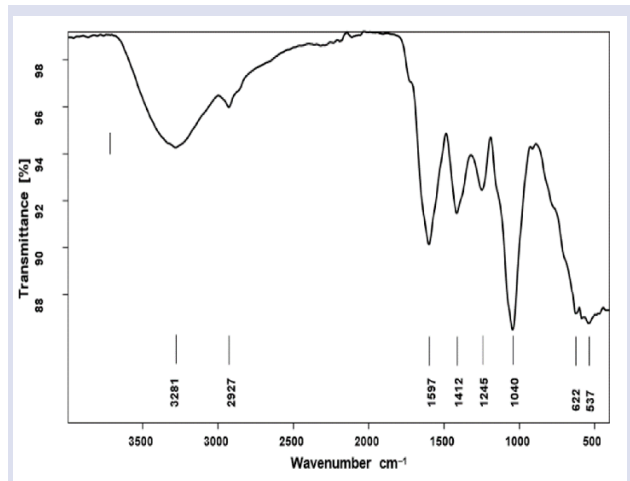


Figure 6. FT-IR spectrum of carbon quantum dots synthesized from *M. sylvestris*.

The surface atomic groups of the CQDs were analyzed using X-ray photoelectron spectroscopy. XPS spectrum showed two major signals corresponding to C1s and O 1s and minor signals for N 1s and Ca 2p (Figure 7).

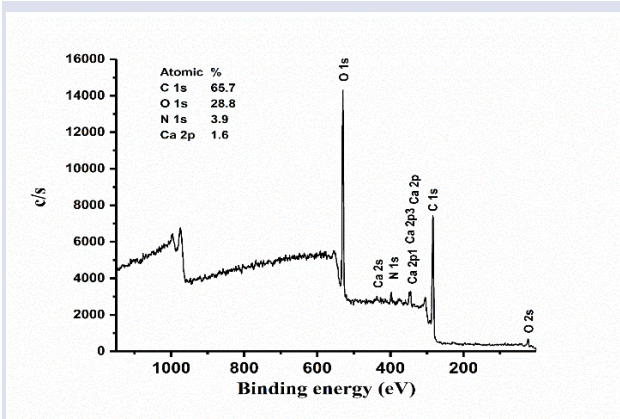


Figure 7. XPS survey spectra of CQDs from *M. sylvestris*.

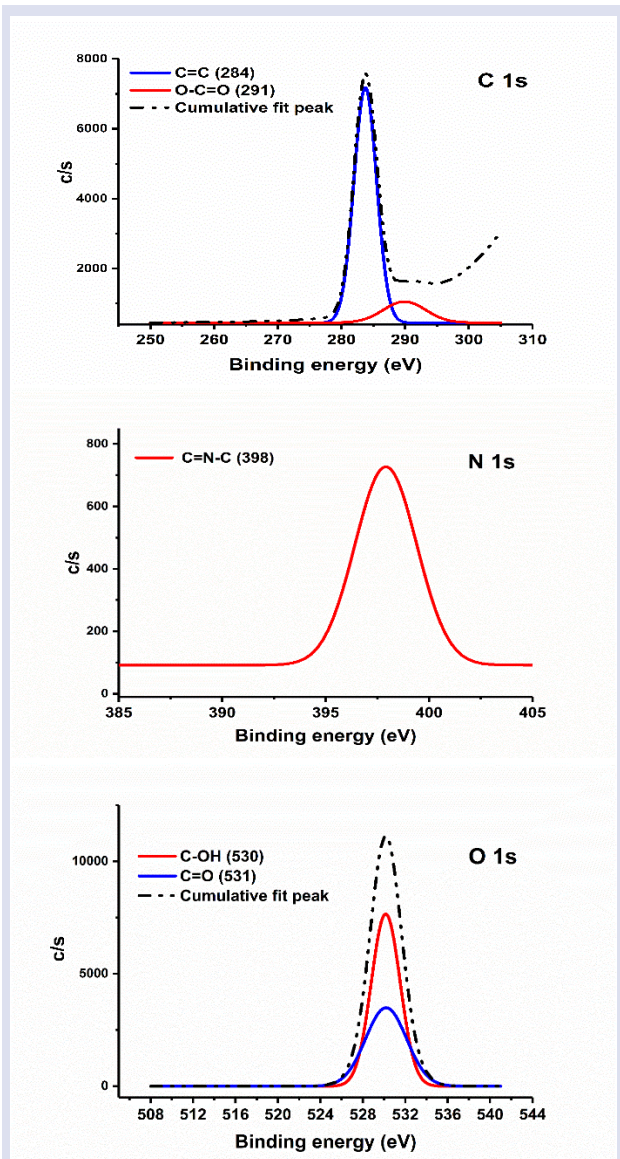


Figure 8. CQDs from *M. sylvestris* showed distinct C, N, and O bands in their XPS spectrum. The spectrum shows which functional groups correspond to different atoms on the surface of CQDs.

The atomic percentages were as follows; C 1s: 65.7; O 1s: 28.8; N 1s: 3.9, and Ca 2p: 1.6%. CQDs from *M. sylvestris* mainly comprised C, O, and N atoms.

In Figure 8, the high-resolution C 1s spectrum was deconvoluted and showed two peaks that corresponded to C=C and -O-C=O. In the deconvoluted high-resolution N 1s spectrum, C=N-C at 398 eV dominated the N 1s spectrum. The signal at O 1s was separated into two peaks at 530 eV and 531 eV. These peaks represent groups containing C-OH and C=O [30, 33].

The UV-visible absorbance spectrum of the CQDs displays a wide absorbance peak, reaching up to 600 nm. This peak can be attributed to the energy-absorbing groups found on the surface of the CQDs (Figure 9, top) [17]. In the UV-vis absorbance spectrum, two peaks could be corresponded to the π - π^* and n- π^* transitions. CQDs from *M. sylvestris* exhibited excitation-dependent photoluminescence, which is typical of CQDs (Figure 9, bottom). When the aqueous solution of CQDs was excited at 400 nm, it produced the strongest fluorescence emission. The fluorescence quantum yields (Φ) of CQDs were determined by comparing them to the quinine sulfate solution ($\Phi = 0.54$). The quantum yield of CQDs was calculated to be $\Phi = 0.07$.

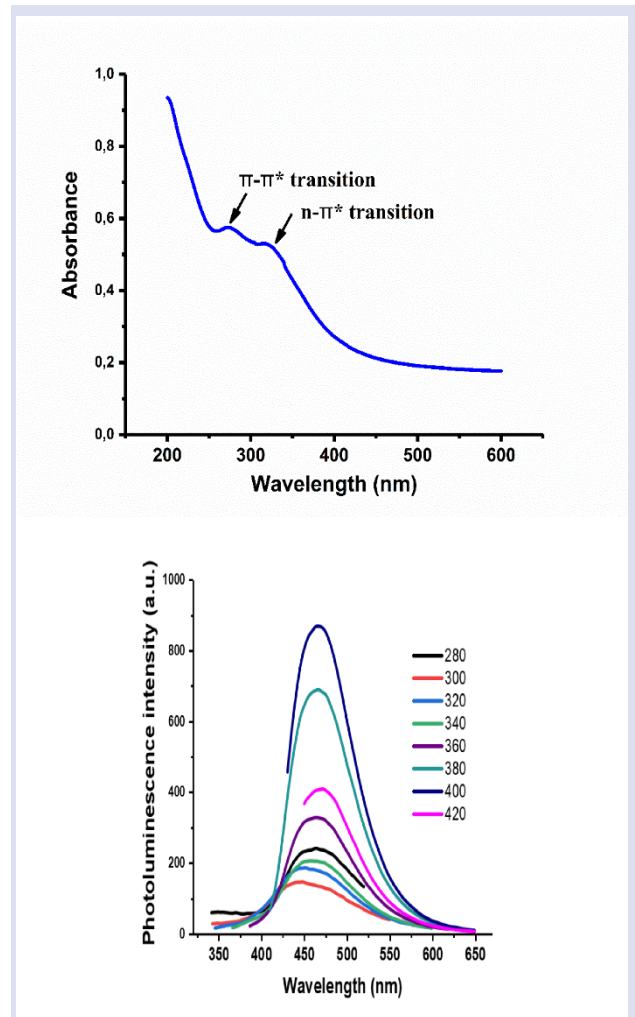


Fig. 9. UV-vis absorbance (top) and photoluminescence emission spectra (bottom) of CQDs from *M. sylvestris* (in distilled water).

Cell viability rate and cytotoxic effects of CQDs

The cytotoxic effects of CQDs on human epithelial cells were studied using the Alamar Blue assay, and the IC_{50} values were determined. In the cell proliferation experiments, the cells were exposed to the CQDs solutions at varying concentrations of 0-1000 $\mu\text{g mL}^{-1}$. Following the 48-hour incubation, the IC_{50} of CQDs was calculated as 600 $\mu\text{g mL}^{-1}$. The assay revealed that green synthesized carbon quantum dots from the medicinal plant *M. sylvestris* did not show cytotoxicity against human prostate epithelial cells (Figure 10-d). When CQDs from *M. sylvestris* were applied to the cells, the cell membrane and cytoplasm showed a blue-color emission (Figure 10 a-c). The CQDs were localized in the cytoplasm of PNT1A cells. This indicated that the high fluorescence properties of carbon quantum dots from *M. sylvestris* could be used for *in vitro* imaging of other mammalian cells.

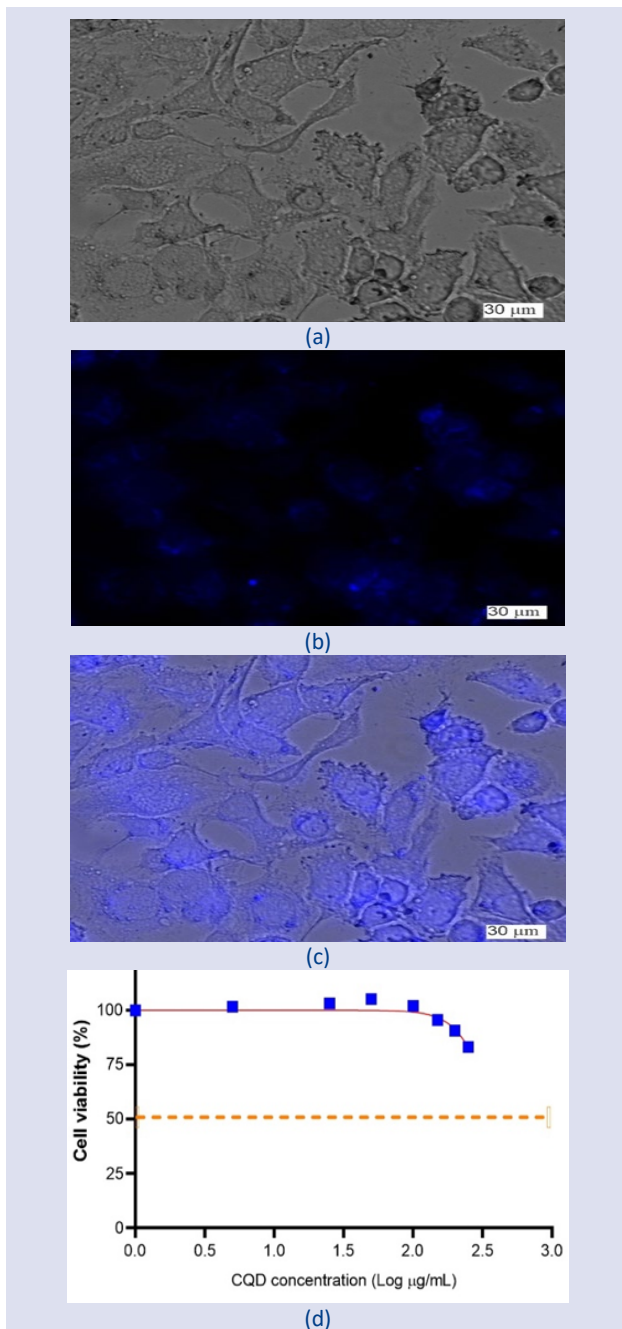


Fig. 10. Cytotoxicity and bio-imaging of CQDs from *M. sylvestris* in human epithelial cells. a) Bright field imaging of PNT1A cells, b) Fluorescence imaging of PNT1A cells, c) Fluorescence imaging of PNT1A cells (merged), and d) Cytotoxicity of CQDs.

Conclusions

The findings of this research highlight the ease of synthesizing biocompatible fluorescent CQDs from the medicinal wild plant *M. sylvestris*, without the need for organic solvents or chemicals. The CQDs exhibited no cytotoxicity against human prostate epithelial cells. The fluorescent CQDs demonstrated excellent cell permeability and are therefore ideal for utilizing in fluorescence imaging of mammalian cells, specifically PNT1A. Carbon quantum dots from *M. sylvestris* localized in the membrane and cytoplasm of PNT1A cells. CQDs from *M. sylvestris* in further studies should be tested in imaging bacterial, fungal, and plant cells. Carbon quantum dots derived from *M. sylvestris* also can be evaluated *in vivo* imaging and bio-sensing applications.

Acknowledgments

The authors thank Selcuk University Research Foundation for funding the study (BAP-19201057).

Conflicts of interest

The authors report no conflicts of interest in this work.

References

- [1] Song, Y., Zhu, S., Yang, B., Bioimaging based on fluorescent carbon dots, *RSC Adv.*, 4 (52) (2014) 27184-27200.
- [2] Devi, P., Saini, S., Kim, K.-H., The advanced role of carbon quantum dots in nanomedical applications, *Biosens. Bioelectron.*, 141, (2019) 111158.
- [3] Janus, Ł., Radwan-Pragłowska, J., Piątkowski, M., Bogdał, D., Facile Synthesis of Surface-Modified Carbon Quantum Dots (CQDs) for Biosensing and Bioimaging, *Materials*, 13 (15) (2020) 3313.
- [4] Kou, X., Jiang, S., Park, S.-J., Meng, L.-Y., A review: recent advances in preparations and applications of heteroatom-doped carbon quantum dots, *Dalton T.*, 49 (21) (2020) 6915-6938.
- [5] Molaei, M.J., The optical properties and solar energy conversion applications of carbon quantum dots: A review, *Sol. Energy*, 196, (2020) 549-566.
- [6] Travlou, N.A., Giannakoudakis, D.A., Algarra, M., Labella, A.M., Rodríguez-Castellón, E., Bandoz, T.J., S- and N-doped carbon quantum dots: Surface chemistry dependent antibacterial activity, *Carbon*, 135, (2018) 104-111.
- [7] Ko, N.R., Nafiujjaman, M., Cherukula, K., Lee, S.J., Hong, S. J., Lim, H.N., Park, C. H., Park, I.K., Lee, Y.K., Kwon, I.K., Microwave-assisted synthesis of biocompatible silk fibroin-based carbon quantum dots, *Part. Part. Syst. Char.*, 35 (3) (2018) 1700300.

- [8] Tejwan, N., Saha, S.K., Das, J., Multifaceted applications of green carbon dots synthesized from renewable sources, *Adv. Colloid and Interface Science*, 275 (2020) 102046.
- [9] Alam, A.-M., Park, B.-Y., Ghouri, Z.K., Park, M., Kim, H.-Y., Synthesis of carbon quantum dots from cabbage with down-and up-conversion photoluminescence properties: excellent imaging agent for biomedical applications, *Green Chem.*, 17 (7) (2015) 3791-3797.
- [10] Sachdev, A., Gopinath, P., Green synthesis of multifunctional carbon dots from coriander leaves and their potential application as antioxidants, sensors and bioimaging agents, *Analyst*, 140 (12) (2015) 4260-4269.
- [11] Bandi, R., Gangapuram, B.R., Dadigala, R., Eslavath, R., Singh, S.S., Guttena, V., Facile and green synthesis of fluorescent carbon dots from onion waste and their potential applications as sensor and multicolour imaging agents, *RSC Adv.*, 6 (34) (2016) 28633-28639.
- [12] Jeong, C.J., Roy, A.K., Kim, S.H., Lee, J.-E., Jeong, J.H., In, I., Park, S.Y., Fluorescent carbon nanoparticles derived from natural materials of mango fruit for bio-imaging probes, *Nanoscale*, 6 (24) (2014) 15196-15202.
- [13] Pan, J., Zheng, Z., Yang, J., Wu, Y., Lu, F., Chen, Y., Gao, W., A novel and sensitive fluorescence sensor for glutathione detection by controlling the surface passivation degree of carbon quantum dots, *Talanta*, 166 (2017) 1-7.
- [14] Hua, X.-W., Bao, Y.-W., Wu, F.-G., Fluorescent carbon quantum dots with intrinsic nucleolus-targeting capability for nucleolus imaging and enhanced cytosolic and nuclear drug delivery, *ACS Appl Mater. Inter.*, 10 (13) (2018) 10664-10677.
- [15] Su, W., Guo, R., Yuan, F., Li, Y., Li, X., Zhang, Y., Zhou, S., Fan, L., Red-emissive carbon quantum dots for nuclear drug delivery in cancer stem cells, *J. Phys. Chem. Lett.*, 11 (4) (2020) 1357-1363.
- [16] Matea, C.T., Mocan, T., Tabaran, F., Pop, T., Mosteanu, O., Puia, C., Iancu, C., Mocan, L., Quantum dots in imaging, drug delivery and sensor applications, *Int. J. Nanomed.*, 12 (2017) 5421.
- [17] Wang, Y., Hu, A., Carbon quantum dots: synthesis, properties and applications, *J. Mater. Chem. C*, 2 (34) (2014) 6921-6939.
- [18] Das, R., Bandyopadhyay, R., Pramanik, P., Carbon quantum dots from natural resource: A review, *Mater. Today Chem.*, 8 (2018) 96-109.
- [19] Singh, R., Kumar, R., Singh, D., Savu, R., Moshkalev, S., Progress in microwave-assisted synthesis of quantum dots (graphene/carbon/semiconducting) for bioapplications: a review, *Mater. Today Chem.*, 12 (2019) 282-314.
- [20] Barros, L., Carvalho, A.M., Ferreira, I.C.F.R., Leaves, flowers, immature fruits and leafy flowered stems of *Malva sylvestris*: A comparative study of the nutraceutical potential and composition, *Food Chem. Toxicol.*, 48 (6) (2010) 1466-1472.
- [21] Almasian, A., Najafi, F., Eftekhari, M., Ardekani, M.R.S., Sharifzadeh, M., Khanavi, M., Polyurethane/carboxymethylcellulose nanofibers containing *Malva sylvestris* extract for healing diabetic wounds: Preparation, characterization, in vitro and in vivo studies, *Mater. Sci. Eng.: C*, 114 (2020) 111039.
- [22] Benso, B., Franchin, M., Massarioli, A.P., Paschoal, J.A.R., Alencar, S.M., Franco, G.C.N., Rosalen, P.L., Anti-Inflammatory, Anti-osteoclastogenic and antioxidant effects of *Malva sylvestris* extract and fractions: In vitro and in vivo studies, *PLoS One*, 11 (9) (2016) e0162728.
- [23] Gasparetto, J.C., Martins, C.A.F., Hayashi, S.S., Otuky, M.F., Pontarolo, R., Ethnobotanical and scientific aspects of *Malva sylvestris* L.: a millennial herbal medicine, *J. Pharm. Pharmacol.*, 64 (2) (2012) 172-189.
- [24] Benhammada, A., Trache, D., Green synthesis of CuO nanoparticles using *Malva sylvestris* leaf extract with different copper precursors and their effect on nitrocellulose thermal behavior, *J. Therm. Anal. Calorim.*, (2021) 1-16.
- [25] Mousavi, S.M., Hashemi, S.A., Zarei, M., Bahrani, S., Savardashtaki, A., Esmaili, H., Lai, C. W., Mazraedoost, S., Abassi, M., Ramavandi, B., Data on cytotoxic and antibacterial activity of synthesized Fe₃O₄ nanoparticles using *Malva sylvestris*, *Data in Brief*, 28 (2020) 104929.
- [26] Feizi, S., Taghipour, E., Ghadam, P., Mohammadi, P., Antifungal, antibacterial, antibiofilm and colorimetric sensing of toxic metals activities of eco friendly, economical synthesized Ag/AgCl nanoparticles using *Malva Sylvestris* leaf extracts, *Microb. Pathogenesis*, 125 (2018) 33-42.
- [27] Mao, X.-J., Zheng, H.-Z., Long, Y.-J., Du, J., Hao, J.-Y., Wang, L.-L., Zhou, D.-B., Study on the fluorescence characteristics of carbon dots, *Spectrochim. Acta A*, 75 (2) (2010) 553-557.
- [28] Karakurt, S., Adali, O., Tannic acid inhibits proliferation, migration, invasion of prostate cancer and modulates drug metabolizing and antioxidant enzymes, *Anti-Cancer Agents Me. (Formerly Current Medicinal Chemistry-Anti-Cancer Agents)*, 16 (6) (2016) 781-789.
- [29] Venkateswarlu, S., Viswanath, B., Reddy, A.S., Yoon, M., Fungus-derived photoluminescent carbon nanodots for ultrasensitive detection of Hg²⁺ ions and photoinduced bactericidal activity, *Sensor. Actuator. B-Chemical*, 258 (2018) 172-183.
- [30] Kumari, B., Kumari, R., Das, P., Visual detection of G-quadruplex with mushroom derived highly fluorescent carbon quantum dots, *J. Pharmaceut. Biomed.*, 157 (2018) 137-144.
- [31] Fan, R.-J., Sun, Q., Zhang, L., Zhang, Y., Lu, A.-H., Photoluminescent carbon dots directly derived from polyethylene glycol and their application for cellular imaging, *Carbon*, 71 (2014) 87-93.
- [32] Sarkar, N., Sahoo, G., Das, R., Prusty, G., Swain, S.K., Carbon quantum dot tailored calcium alginate hydrogel for pH responsive controlled delivery of vancomycin, *Eur. J. Pharm. Sci.*, 109 (2017) 359-371.
- [33] Xu, O., Wan, S., Zhang, Y., Li, J., Zhu, X., A unique dual-excitation carbon quantum dots: Facile synthesis and application as a dual-"on-off-on" fluorescent probe, *Sensor. Actuator. B-Chemical*, 340 (2021) 129904.

Synthesis, Cytotoxic Activity Evaluation and Molecular Docking Studies of Some Benzimidazole Derivatives

Aybüke Züleyha Kaya ^{1,a,*}, Derya Osmaniye ^{1,b}, Asaf Evrim Evren ^{1,2,c}, Leyla Yurttas ^{1,d}, Şeref Demirayak ^{3,e}

¹ Department of Pharmaceutical Chemistry, Faculty of Pharmacy, Anadolu University, Eskişehir, Türkiye.

² Department of Pharmacy Services, Vocational School of Health Services, Bilecik Seyh Edebali University, Bilecik, Türkiye.

³ Department of Pharmaceutical Chemistry, Faculty of Pharmacy, Istanbul Health & Technology University, Istanbul, Türkiye.

*Corresponding author

Research Article

History

Received: 16/11/2023

Accepted: 12/03/2024



This article is licensed under a Creative Commons Attribution-NonCommercial 4.0 International License (CC BY-NC 4.0)

ABSTRACT

In this study, the synthesis of 2-(2-acetyl-1H-benzimidazol-1-yl)-1-arylethanone (3a-3d) and 1-methyl-3-phenylbenzo[4,5]imidazo[1,2-a]pyrazine derivatives (4a-4d) and to investigate their cytotoxic activity were aimed. APCI, IR, ¹HNMR, and ¹³CNMR spectra were utilized to determine the structure of the synthesized compounds. The cytotoxic activity of selected compounds were detected in A549 (human lung carcinoma) and NIH3T3 (mouse embryonic fibroblasts) cell lines. Compounds 4c and 4d were found to be selectively cytotoxic against A549 and NIH3T3 cell lines. Molecular docking studies were performed using the data retrieved from the Protein Data Bank server (PDBID: 4QTX).

Keywords: Benzimidazole, Pyrazinobenzimidazole, Anticancer, Molecular docking.

^a aybukezuleyhakaya@anadolu.edu.tr  <https://orcid.org/0009-0002-1614-2380>

^c asafevrimevren@anadolu.edu.tr  <https://orcid.org/0000-0002-8651-826X>

^e seref.demirayak@istun.edu.tr  <https://orcid.org/0000-0002-0841-1299>

^b dosmaniye@anadolu.edu.tr  <https://orcid.org/0000-0002-0499-436X>

^d lyurttas@anadolu.edu.tr  <https://orcid.org/0000-0002-0957-6044>

Introduction

Cancer is one of the diseases with the highest mortality and morbidity rates throughout history. According to the research statistics from the American Cancer Society, although the incidence of cancer has decreased since the beginning of the 21st century, the incidence of breast cancer, lung cancer, and liver cancer has increased [1]. Cancer is the second leading cause of death worldwide after cardiovascular disease [2].

The disease, which is observed as a result of uncontrolled division and development of abnormal cells, can develop under the influence of environmental factors as well as hereditary. Although there is no radical treatment for cancer, the progression of the disease is

tried to be prevented with chemotherapy, radiotherapy, and surgical interventions. Due to the development of drug resistance to existing anticancer drugs and the side effects of these drugs, which negatively affect patient compliance, there is a need for researchers to synthesise new anticancer compounds. Benzimidazole and pyrazine ring structures are frequently encountered in anticancer compound syntheses [3–5].

The benzimidazole ring (1H-benzimidazole, 1,3-benzodiazole), which is a heterocyclic compound, is found both in the structure of compounds that occur naturally in the human body and in the structure of many compounds that have therapeutic effects today [6].

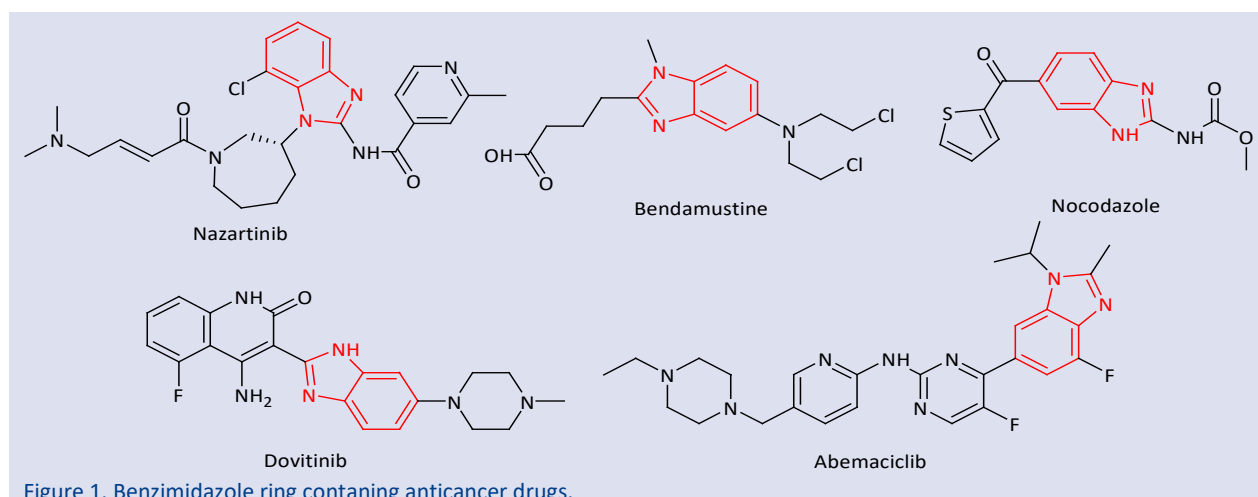


Figure 1. Benzimidazole ring containing anticancer drugs.

Compounds containing the benzimidazole ring structure show a wide range of activities such as antiulcer, antiviral, antibacterial, anti-inflammatory, and anticancer [7]. Compounds containing benzimidazole ring have been reported in many studies to have anticancer effects [8,9]. EGRF inhibitor nazartinib, bendamustine used in the treatment of chronic myeloid leukaemia [10], dovitinib, tyrosine kinase inhibitor [11], nocodazole effective in microtubule polymerization [12], abemaciclib used in the treatment of advanced and metastatic breast cancer [13]

can be given as examples of anticancer drugs containing benzimidazole ring (Figure 1).

The pyrazine ring (1,4-diazine, p-diazine) is also found in the structure of drugs with different therapeutic effects such as anti-viral, antibacterial, antituberculosis, and anticancer. A variety of anticancer drugs contain the pyrazine ring, i.e. bortezomib (used to treat multiple myeloma), barrenazine A/B, botryllazine A, cephalostatin (anti-cancer drug) (Figure 2) [14].

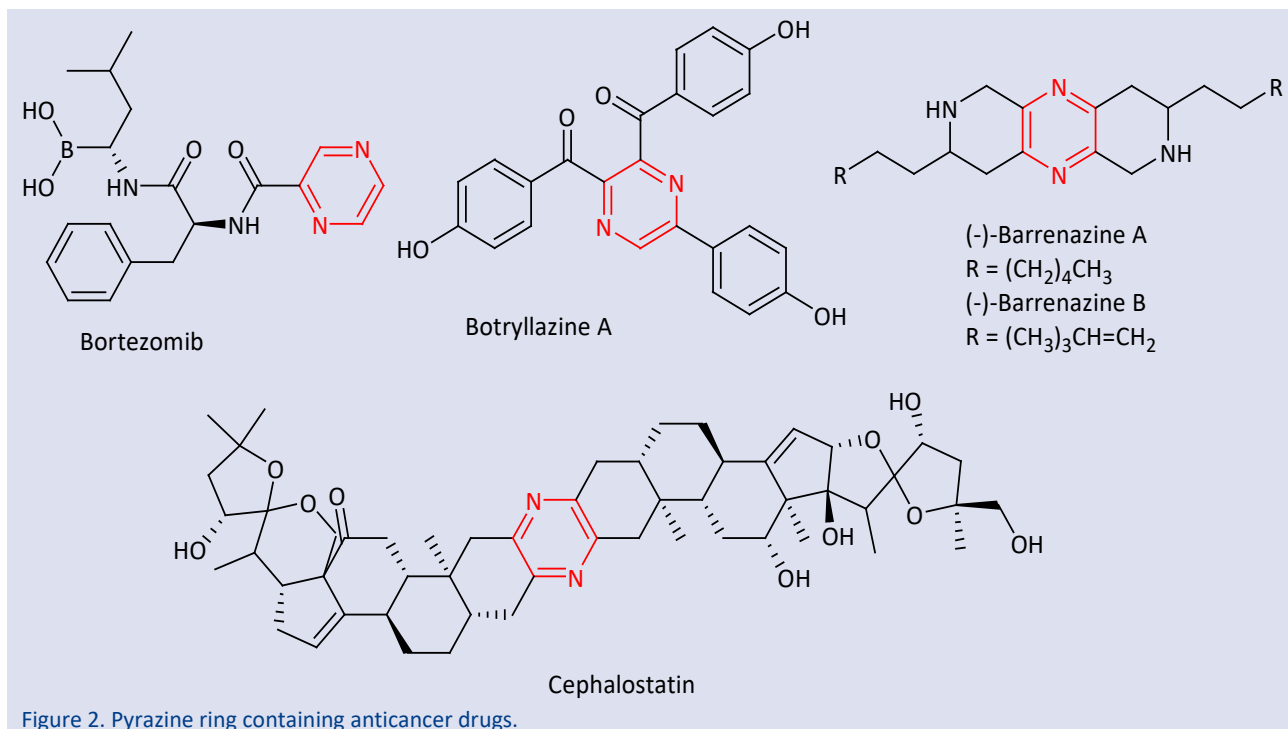


Figure 2. Pyrazine ring containing anticancer drugs.

The aim of this study is to extend the findings of our previous study [15] and to synthesize new compounds in the light of these findings and to examine the cytotoxic activities of these compounds using the A549 and NIH3T3 cell lines.

Experimental Section

Chemistry

All chemicals were purchased from Merck Chemicals (Merck KGaA, Germany) or Sigma-Aldrich Chemical (Poole, UK). The progress of the reactions was monitored by thin layer chromatography (TLC) on pre-coated silica gel 60 F₂₅₄ sheets (acquired from Merck, Germany). The melting points of the compounds were determined by MP90 digital melting point device (Mettler Toledo, USA). Structural analyze of all compounds were obtained with ¹H-NMR (300 MHz and 400 MHz) and ¹³C-NMR (75 MHz and 100 MHz) spectra. Bruker 300 MHz and 400 MHz digital FT-NMR spectrometer (Bruker Bioscience, USA) in DMSO-*d*₆ was used for NMR, and LC/MS-IT-TOF system (Shimadzu, Japan) and compact mass spectrometer APCI (Advion, ABD) were used for HRMS.

2-(1-Hydroxyethyl)benzimidazole (1)

A mixture of the *o*-phenylenediamine (100 mmol) and lactic acid (100 mmol) was stirred and refluxed in 4 N HCl solution (100 mL) for 8 hours. The excess water in the Dean-stark apparatus was drained off from time to time. At the end of the reaction, the cooled mixture poured into crushed ice-water and neutralized with ammonia solution. The precipitate was filtered and crystallised from ethanol-water. Yield: 71% m.p. 178–180°C (ref. 178.5–179.5°C) [16].

2-Acetylbenzimidazole (2)

2-(1-Hydroxyethyl)benzimidazole (10 mmol) was resolved in 100 mL acetic acid and the mixture was heated to 90°C. The solution of chromium trioxide (7.5 mmol) in 15 mL water was slowly added drop by drop to this mixture and the temperature was fixed at 90°C. After addition, the cooled mixture was poured into its volume of water, waited for one hour and the precipitate formed was filtered off. The substance extracted with chloroform was recrystallised from toluene after the solvent was evaporated to dryness at reduced pressure.

Yield: 76% m.p. 188–190°C (ref. 188–189°C)²⁶. IR(KBr) ν_{\max} (cm⁻¹): 3288–2400 (–N–H), 1674 (–C = O), 1600–1420 (–C = C, –C = N). ¹H-NMR (DMSO-*d*₆): (ppm) 2.71 (3H, s,–

COCH₃), 7.36–7.48 (2H, m, Ar-H), 7.86–8.14 (2H, m, Ar-H), 12.4 (1H, brs, N-H).

2-(2-Acetyl-1H-benzimidazol-1-yl)-1-arylethanone derivatives (3a–3d)

The appropriate 2-bromoacetophenone (5 mmol), 2-acetylbenzimidazole (5 mmol), and potassium carbonate (5 mmol) were stirred in acetone (50 mL) at room temperature. Thin-layer chromatography was used to determine the completion of the reaction (4–6 h). The solvent was vaporized at low pressure, and the precipitate was washed with water and ethanol. The product was recrystallized from ethanol.

2-(2-Acetyl-1H-benzimidazol-1-yl)-1-phenylethanone (3a)

Yield 75%. m.p. 167°C (ref. 166–168°C) [18]. IR (KBr) ν_{\max} (cm⁻¹): 3132–3061 (aromatic –C–H), 2937–2850 (aliphatic –C–H), 1686 and 1676 (–C = O), 1593–1446 (–C = C, –C = N). ¹H-NMR (DMSO-d₆): (ppm) 2.71 (3H, s, –COCH₃), 6.23 (2H, s, –CH₂CO), 7.36–7.48 (2H, m, Ar-H), 7.60 (1H, m, Ar-H), 7.72–7.82 (2H, m, Ar-H), 7.92 (2H, d, *J*: 7.95 Hz Ar-H), 8.13 (2H, d, *J*: 8.09 Hz, Ar-H). ¹³C NMR (125 MHz, DMSO-d₆): 27.56, 52.13, 112.39, 123.03, 124.57, 126.42, 129.43, 130.36, 134.04, 135.21, 140.12, 143.36, 147.02, 193.82 and 194.10. MS: *m/z* 279 (M + 1). APCI-MS (–*m/z*): [M+H]⁺: 279.6.

2-(2-Acetyl-1H-benzimidazol-1-yl)-1-(4-methoxyphenyl)ethanone (3b)

Yield 65%. m.p. 141–142°C (ref. 141–142°C) [17]. IR (KBr) ν_{\max} (cm⁻¹): 3052–3016 (Aromatic –C–H), 2983–2851 (Aliphatic –C–H), 1689 and 1674 (–C = O), 1641–1463 (–C = C, –C = N). ¹H-NMR (DMSO-d₆): (ppm) 2.71 (3H, s, –COCH₃), 3.72 (3H, s, –COCH₃), 6.24 (2H, s, –CH₂CO), 7.15–7.24 (4H, m, Ar-H), 7.58 (2H, d, *J*: 8.15 Hz, Ar-H), 7.92 (2H, d, *J*: 8.14 Hz, Ar-H). ¹³C NMR (125 MHz, DMSO-d₆): 27.68, 52.94, 56.06, 113.08, 123.44, 124.52, 127.29, 130.07, 132.14, 139.52, 140.63, 142.45, 147.53, 150.12, 193.69 and 194.55. MS: *m/z* 309 (M + 1). APCI-MS (–*m/z*): [M+H]⁺: 309.7.

2-(2-Acetyl-1H-benzimidazol-1-yl)-1-(3-chlorophenyl)ethanone (3c)

Yield 72%. m.p. 151–153°C. IR (KBr) ν_{\max} (cm⁻¹): 3068–3020 (Aromatic –C–H), 2993–2931 (Aliphatic –C–H), 1695 and 1675 (–C = O), 1620–1452 (–C = C, –C = N). ¹H-NMR (DMSO-d₆): (ppm) 2.71 (3H, s, –COCH₃), 6.24 (2H, s, –CH₂CO), 7.39–7.42 (1H, m, Ar-H), 7.45–7.49 (1H, m, Ar-H), 7.69 (1H, t, *J*: 7.88 Hz, Ar-H), 7.82 (1H, d, *J*: 8.24 Hz, Ar-H), 7.84–7.87 (1H, m, Ar-H), 7.91 (1H, d, *J*: 8.13 Hz, Ar-H), 8.06–8.09 (1H, m, Ar-H), 8.17 (1H, t, *J*: 1.82 Hz, *J*: 1.77 Hz, *J*: 1.81 Hz, Ar-H). ¹³C NMR (125 MHz, DMSO-d₆): 27.98, 52.78, 112.66, 122.53, 124.90, 127.44, 128.02, 129.15, 132.28, 135.03, 135.17, 137.68, 138.19, 142.35, 147.21, 194.02 and 194.30. MS: *m/z* 312.9 (M + 1). APCI-MS (–*m/z*): [M+H]⁺: 313.7.

2-(2-Acetyl-1H-benzimidazol-1-yl)-1-(4-chlorophenyl)ethanone (3d)

Yield 71%. m.p. 161–162°C (ref. 161–162°C) [18]. IR (KBr) ν_{\max} (cm⁻¹): 3045–3025 (Aromatic –C–H), 2933–2833 (Aliphatic –C–H), 1695 and 1674 (–C = O), 1587–1452 (–C = C, –C = N). ¹H-NMR (DMSO-d₆): (ppm) 2.73 (3H, s, –COCH₃), 6.24 (2H, s, –CH₂CO), 7.39–7.44 (2H, m, Ar-H), 7.70 (2H, d, *J*: 6.12 Hz, Ar-H), 7.96–7.97 (1H, m, Ar-H), 8.10 (2H, d, *J*: 8.15 Hz, Ar-H), 8.22 (1H, d, *J*: 7.75 Hz, Ar-H). ¹³C NMR (125 MHz, DMSO-d₆): 27.99, 52.62, 112.68, 122.52, 124.87, 127.10, 130.37, 131.35, 134.54, 138.22, 140.29, 142.36, 147.24, 193.97 and 194.31. MS: *m/z* 313.1 (M + 1). APCI-MS (–*m/z*): [M+H]⁺: 313.7.

1-Methyl-3-phenyl-benzo[4,5]imidazo[1,2-a]pyrazine derivatives (4a-4d)

A mixture of the appropriate 2-(2-acetyl-1H-benzimidazol-1-yl)-1-arylethanone (3a-3d) (1 mmol) and ammonium acetate (10 mmol) was refluxed in acetic acid (50 ml). The solution was cooled and poured into distilled water. The precipitate was filtered and crystallised from ethanol.

1-Methyl-3-phenyl-benzo[4,5]imidazo[1,2-a]pyrazine (4a)

Yield 85%. m.p. 157°C. IR (KBr) ν_{\max} (cm⁻¹): 688 (Aromatic –C–H), 739-764 (Aromatic –C–H), 1206-1296 (Aromatic –C–N), 1458-1506 (Aromatic –C=C). ¹H-NMR (DMSO-d₆): (ppm) 2.95 (3H, s, CH₃), 7.42 (1H, t, *J*: 6.75 Hz, *J*: 7.42 Hz, Ar-H), 7.54 (3H, t, *J*: 7.37 Hz, *J*: 7.26 Hz, Ar-H), 7.63 (1H, t, *J*: 7.90 Hz, *J*: 7.26 Hz, Ar-H), 7.99 (1H, d, *J*: 8.21 Hz, Ar-H), 8.18 (2H, d, *J*: 7.79 Hz, Ar-H), 8.51 (1H, d, *J*: 8.21 Hz, Ar-H), 9.56 (1H, s, Aromatic –C–H). ¹³C NMR (125 MHz, DMSO-d₆): 21.55, 113.78, 114.69, 121.02, 123.13, 126.15, 127.06, 128.64, 129.23, 129.50, 136.78 and 152.75. APCI-MS (–*m/z*): [M+H]⁺: 260.5.

3-(4-Methoxy-phenyl)-1-methyl-benzo[4,5]imidazo[1,2-a]pyrazine (4b)

Yield 80%. m.p. 160°C. IR (KBr) ν_{\max} (cm⁻¹): 736 (Aromatic –C–H), 829 (Aromatic –C–H), 1026-1246 (Aromatic –C–N), 1458-1514 (Aromatic –C=C), 1606-1724 (Aromatic –C=N), 2839-2914 (Aliphatic –C–H). ¹H-NMR (DMSO-d₆): (ppm) 2.92 (3H, s, CH₃), 3.83 (3H, s, OCH₃), 7.08 (2H, d, *J*: 8.88 Hz, Ar-H), 7.48-7.63 (2H, m, Ar-H), 7.96 (1H, d, *J*: 8.13 Hz, Ar-H), 8.07-8.11 (2H, m, Ar-H), 8.48 (1H, d, *J*: 8.13 Hz, Ar-H), 9.46 (1H, s, Aromatic –C–H). ¹³C NMR (125 MHz, DMSO-d₆): 21.55, 55.68, 55.71, 113.38, 113.74, 114.64, 120.96, 122.96, 126.95, 127.45, 129.19, 129.42, 135.47, 141.23, 144.16, 152.56 and 159.90. APCI-MS (–*m/z*): [M+H]⁺: 290.7.

3-(3-Chloro-phenyl)-1-methyl-benzo[4,5]imidazo[1,2-a]pyrazine (4c)

Yield 82%. m.p. 168°C. IR (KBr) ν_{\max} (cm⁻¹): 684 (Aromatic –C–H), 740-758 (Aromatic –C–H), 1080-1203 (Aromatic –C–N), 1456-1568 (Aromatic –C=C), 1595-1681 (Aromatic –C=N). ¹H-NMR (DMSO-d₆): (ppm) 2.93 (3H, s,

CH₃), 7.44-7.52 (1H, m, Ar-H), 7.53-7.58 (2H, m, Ar-H), 7.60-7.65 (1H, m, Ar-H), 7.98 (1H, d, *J*: 8.14 Hz, Ar-H), 8.15 (1H, d, *J*: 7.62 Hz, Ar-H), 8.23 (1H, s, Ar-H), 8.49 (1H, d, *J*: 8.16 Hz, Ar-H), 9.67 (1H, s, Aromatic C-H). ¹³C NMR (125 MHz, DMSO-d₆): 21.53, 113.79, 115.61, 121.07, 123.31, 124.59, 125.58, 127.18, 128.33, 129.53, 131.13, 133.70, 134.25, 138.97, 141.41, 144.22 and 152.91. APCI-MS (-m/z): [M+H]⁺: 294.7.

3-(4-Chloro-phenyl)-1-methyl-benzo[4,5]imidazo[1,2-a]pyrazine (4d)

Yield 90%. m.p. 217°C. IR (KBr) ν_{\max} (cm⁻¹): 735-756 (Aromatic -C-H), 812 (Aromatic -C-H), 1009-1204 (Aromatic -C-N), 1458-1477 (Aromatic -C=N), 1682 (Aromatic -C=N), 3022-3084 (Aliphatic -C-H). ¹H NMR (DMSO-d₆): (ppm) 2.51 (3H, s, CH₃), 7.52-7.61 (4H, m, Ar-H), 7.98 (1H, d, *J*: 8.05 Hz, Ar-H), 8.20 (2H, d, *J*: 7.86 Hz, Ar-H), 8.49 (1H, d, *J*: 8.05 Hz, Ar-H), 9.62 (1H, s, Aromatic -C-H). ¹³C NMR (125 MHz, DMSO-d₆): 21.52, 113.73, 115.03, 121.03, 123.23, 127.12, 127.72, 129.23, 129.48, 133.26, 134.12, 135.64, 141.31, 144.20, 152.83 and 172.48. APCI-MS (-m/z): [M+H]⁺: 294.6.

Cytotoxicity

The MTT assay based on the reduction of 3-(4,5-dimethylthiazol-2-yl)-2,5-diphenyltetrazolium salt to the formazan product is used to determine the metabolic activity of living cells. Cell viability can be determined spectrometrically using the formazan salt, which turns purple at the end of the incubation period [19]. The anti-cancer activities of the compounds were determined using the 24-hour MTT assay. MTT assays were performed on NIH3T3 and A549 cells. NIH3T3 cells were grown in DMEM medium (Sigma-Aldrich, St. Louis, MO, USA) supplemented with fetal calf serum, penicillin (100 IU/ml), streptomycin (100 mg/ml) and 7.5% NaHCO₃ at 37°C in a humidified atmosphere of 95% air and 5% CO₂. A549 cells were grown in RPMI medium (Hyclone, Thermo Scientific, USA) supplemented with fetal calf serum, penicillin (100 IU/ml), streptomycin (100 mg/ml) and 7.5% NaHCO₃ at 37°C in a humidified atmosphere of 95% air and 5% CO₂. NIH3T3 and A549 cell lines were seeded in 96-well plates at 1 × 10⁴ cell density. The culture media were removed, and the test compounds were added at concentrations of 0.000316 - 1 mM after 24 h of incubation. After 24 h incubation, colorimetric measurements were performed using a microplate reader (Biotek, USA) at 540 nm. The percentage of inhibition at all concentrations was determined using the formula below, and the IC₅₀ values were calculated from a dose-response curve obtained by plotting the percentage of inhibition versus the log concentration with the use of Microsoft Excel 2013. The results were expressed as the mean value ± standard deviation (SD). As positive control, doxorubicin was used. The inhibition of cell proliferation for the cell lines A549 (human lung carcinoma) and NIH3T3 (mouse embryonic fibroblasts) is presented in Table 1. The cytotoxicity test of compounds 3a-3d and 4a-4d was screened according to MTT experiments. Doxorubicin is used as a reference drug. MTT assays were performed as previously described [20-22].

% inhibition = 100 - (mean sample x 100/mean solvent)

Molecular Docking Studies

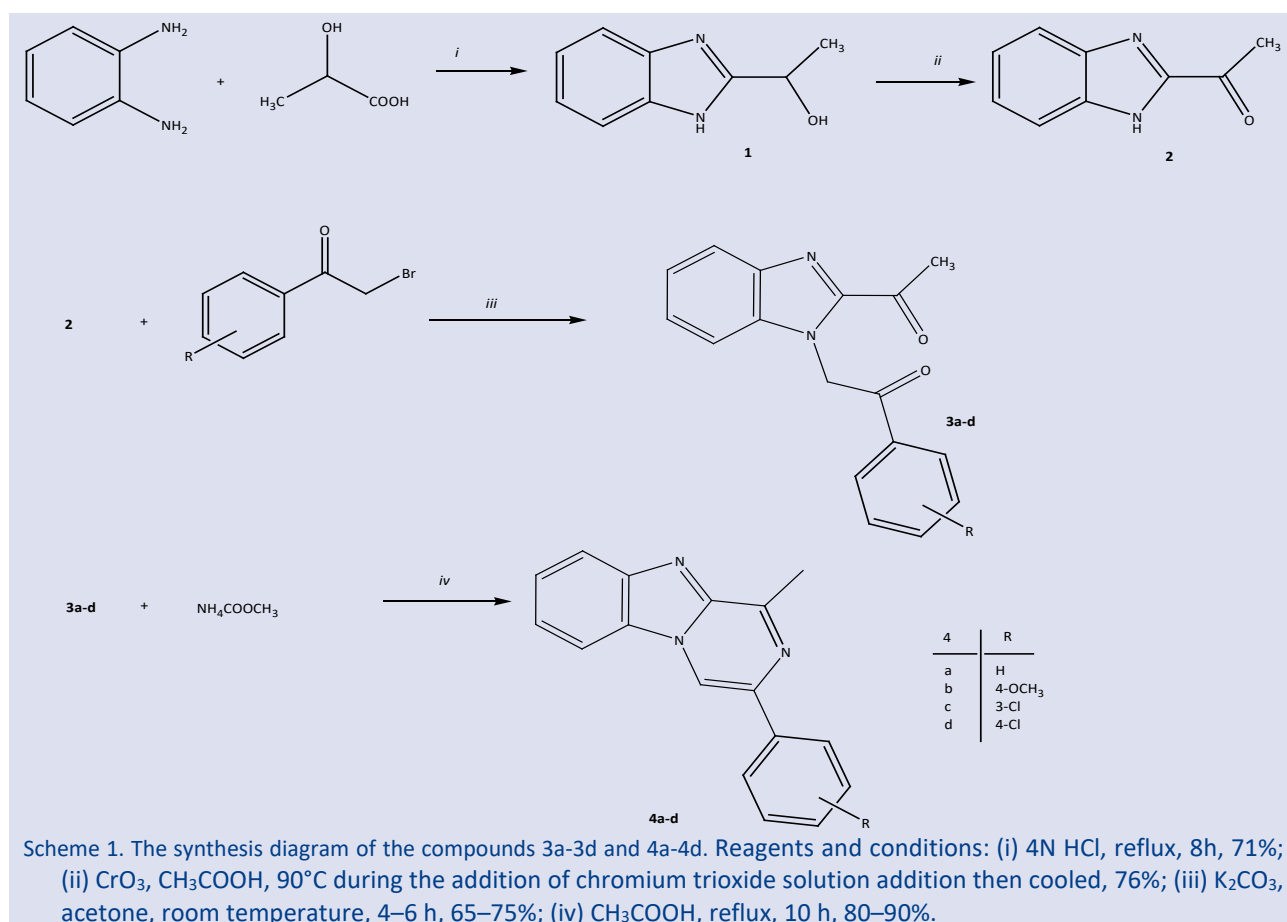
Molecular docking studies were performed using an *in-silico* procedure as previously described [3,23]. The crystal data were retrieved from the Protein Data Bank server (PDBID: 4QTX) [24]. The Schrödinger Maestro [25] interface was used for the molecular docking study, and the enzyme crystal was processed using the Protein Preparation Wizard protocol of the Schrödinger Suite 2020. Active molecules (4c and 4d) were prepared using LigPrep module [26].

The molecular docking study for compounds 4c and 4d were run according to the previously published procedures [27]. For that, ligands atoms correctly assigned the protonation states (pH=7.4±1.0) as well using LigPrep module. Bond orders were assigned, and hydrogen atoms were added to the structures. The grid generation was formed using the Glide module [28]. These grids were built up using the native ligand and its binding regions around 20 Å. After the generation of the grid maps, all of them were used in the docking runs. The docking runs were performed in extra precision docking mode (XP), and the best docking poses were determined among all outputs.

Results and Discussions

Chemistry

In this study, 2-(2-acetyl-1H-benzimidazol-1-yl)-1-arylethanone (3a-3d) and 1-methyl-3-phenylbenzo[4,5]imidazo[1,2-a]pyrazine derivatives (4a-4d) were synthesized as shown in Scheme 1. Primarily *o*-phenylenediamine was reacted with lactic acid as a result compound 1 formed via Phillips reaction. Then the solution of chromium trioxide and compound 1 were heated in acetic acid for oxidation reaction. The resulting compound (2) was stirred with 2-bromoacetophenone derivatives at room temperature. Ultimately 2-(2-acetyl-1H-benzimidazol-1-yl)-1-arylethanone derivatives (3a-3d) formed. APCI, IR, ¹H NMR, and ¹³C NMR spectra were utilized to determine the structure of the synthesized compounds. In the IR spectrum of the compounds 3a-3d, carbonyl bands were spotted at 1695-1674 cm⁻¹ and methylene protons were spotted at 6.23-6.24 ppm. At the last step, 2-(2-acetyl-1H-benzimidazol-1-yl)-1-(substituted phenyl)ethanone derivatives (3a-3d) and sufficient amount of ammonium acetate were refluxed in acetic acid. Thus the resulting products, 1-methyl-3-phenylbenzo[4,5]imidazo[1,2-a]pyrazine derivatives (4a-4d), were synthesized. In the IR spectrum of the final products, all bands, except aliphatic -C-H bands, were observed at the fingerprint area as expected. ¹H NMR spectra have shown aliphatic -C-H protons' peaks at 2.51-2.95 ppm. The singlet peaks were spotted at 9.56-9.67 ppm belonging to pyrazine proton. The other aromatic protons were pursued at the expected area, approximately 7.08-8.51 ppm. M+1 values were measured with the APCI instrument and the values were similar to the calculated molecular weights of the final compounds.

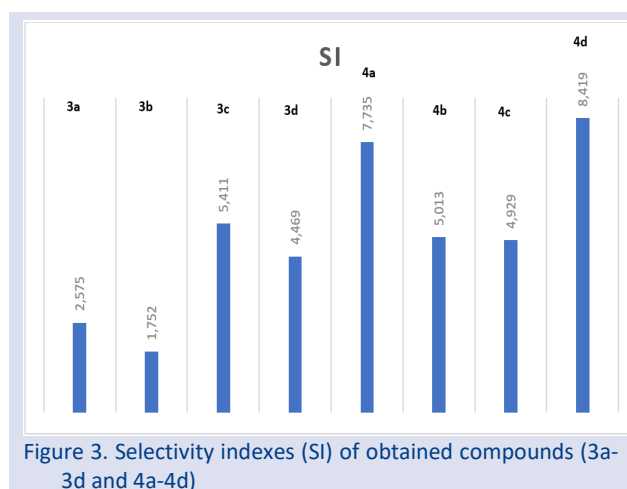


Cytotoxic Activity Evaluation

Table 1. IC₅₀ (μM) values of synthesized compounds (3a-d and 4a-d)

Compounds	A549	NIH3T3	Compounds	A549	NIH3T3
3a	40.667±0.343	104.731±2.492	4a	32.965±0.866	254.997±1.416
3b	111.118±4.619	194.657±1.634	4b	41.267±1.439	206.877±2.036
3c	48.191±1.576	260.762±1.369	4c	26.469±0.313	130.455±0.964
3d	33.883±0.499	151.411±2.748	4d	20.137±0.311	169.542±1.069
Doxorubicin	3.001±0.071	>1000			

The test results were expressed as means of quartet assays



Final compounds 4a-4d and compounds 3a-3d were subjected to MTT assay to investigate their cytotoxic activity. Doxorubicin was chosen as the standard drug to perform the MTT test. IC₅₀ value of doxorubicin against A549 cancer cell line is 3.001 μM and against NIH3T3 is

over 1000 μM. IC₅₀ value of compound 4c and 4d detected as 26.469 μM and 20.137 μM, respectively. Although compounds 4c and 4d were not found as effective as the standard drug doxorubicin, they have a selective toxic effect against cancer cells. Compounds that are selective for cancer cells are toxic to the cancer cells but have no effect on healthy cells. This makes it possible to treat the cancer without harming the healthy cells inside.

In our previous study [11], compounds containing benzimidazole ring and diketone structure (3a-3d) were found to be more active than compounds containing methylene-carrying pyrazino[1,2-a]benzimidazole. In this study 3-chloro and 4-chloro substituted pyrazinobenzimidazole ring containing compounds (4c and 4d) found more effective than compounds 3a-3d.

Molecular Docking Study

To estimate the binding modes of the two active (4c and 4d) compounds, they docked to the active site of the caspase enzyme. The 4QTX crystal form of the enzyme was chosen to dock the compounds. According to the given data, compound 4c interacted with Arg64, Gln161, and Arg207 via halogen bonds, with Hie121 via π-π

stacking, aromatic H-bond and water-mediated H-bond, with Ser120 via aromatic H-bond. On the other hand, 4d interacted with Arg64 and Gln161 via halogen bonds, with

Thr62 via water-mediated H-bond, with Hie121 via aromatic H-bond.

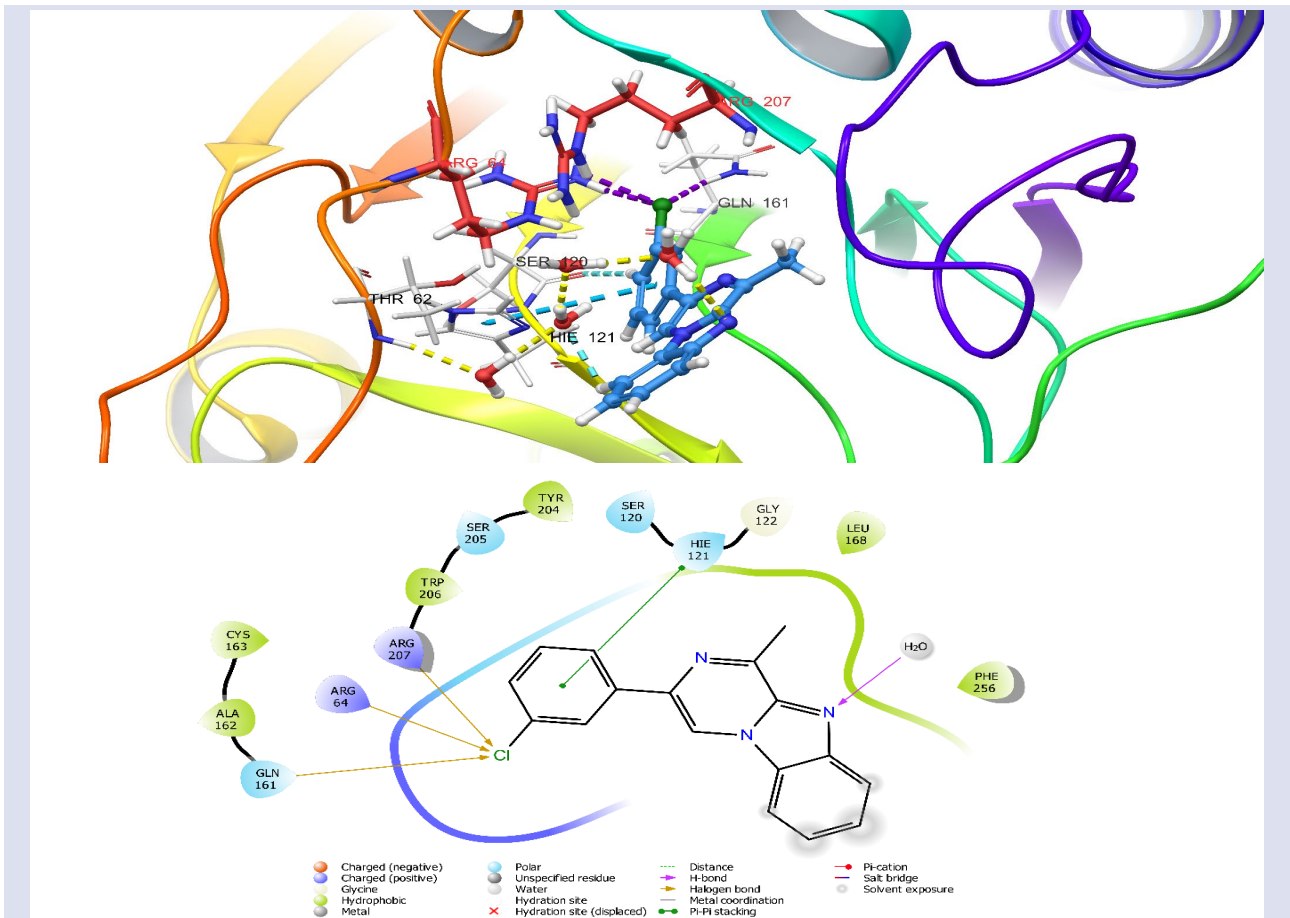
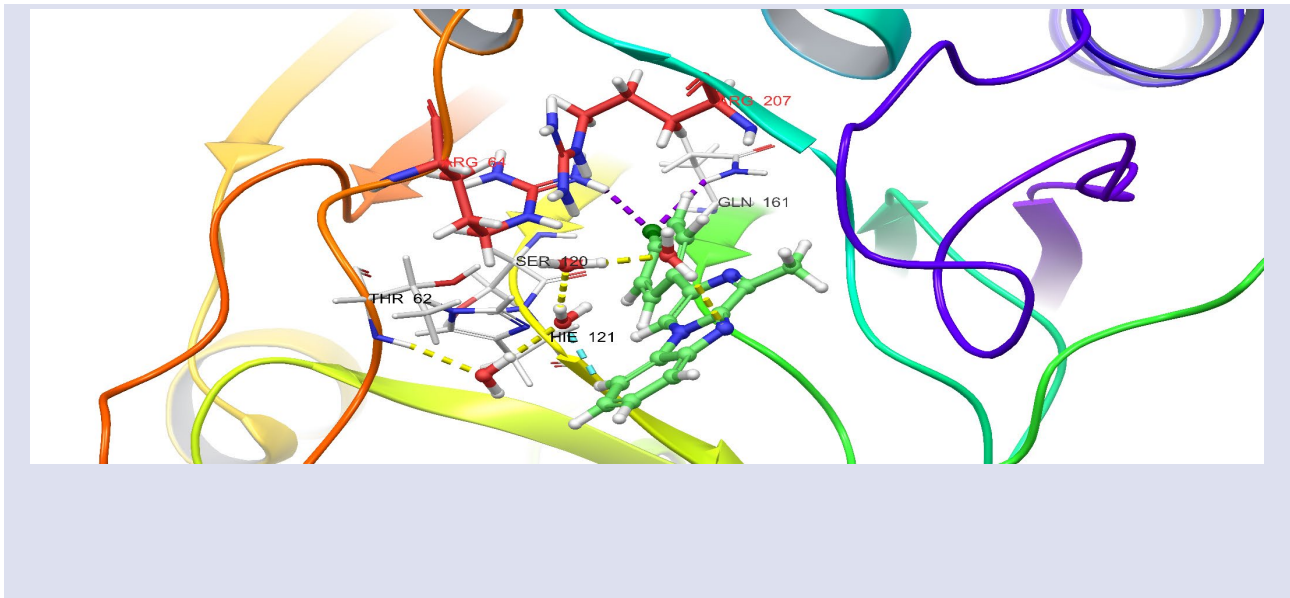


Figure 4. 3D (top) and 2D (bottom) docking poses of compound caspase-3-4c enzyme complex (PDBID: 4QTX).



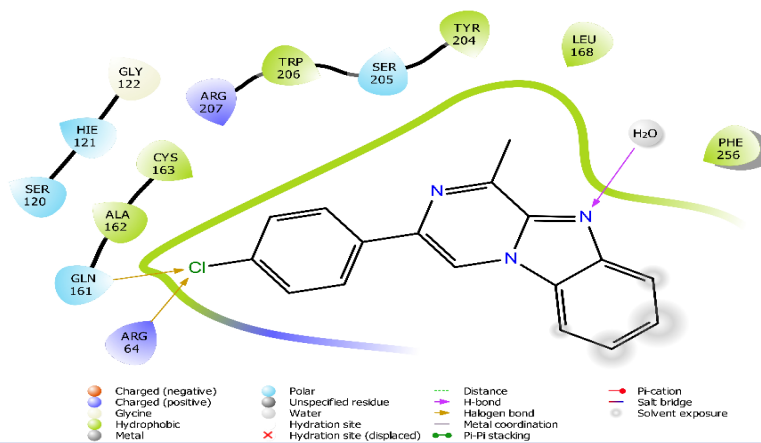


Figure 5. 3D (top) and 2D (bottom) docking poses of compound caspase-3-4d enzyme complex (PDBID: 4QTX).

Briefly, interactions with arginine residues (Arg64 and Arg207) were identified as key points in the allosteric activation of caspase-3 enzyme, and both compounds formed halogen bonds. In addition to that, both compounds showed affinity to Hie121 residue, which is this residue is a member of the loop region, thus, it has an important role in allosteric activation of the enzyme. In a result, the *in-silico* study suggests that both active compounds may be anticancer agents because they prompt the induction of the apoptotic pathway.

Conclusions

In this study, we designed and synthesized 2-(2-acetyl-1*H*-benzimidazol-1-yl)-1-arylethanone (3a-3d) and 1-methyl-3-phenyl-benzo[4,5]imidazo[1,2-*a*]pyrazine derivatives (4a-4d). Spectroscopic methods were used to determine the structure of the final compounds. Compounds 4c and 4d showed selective cytotoxic activity against the A549 cell lines. In the molecular docking study, compounds 4c and 4d were observed interact with arginine and histamine residues, which are key amino acids of the caspase enzyme. As a result of our study, the compounds we synthesized contain benzimidazole ring structure, which is known to have anticancer activity, and it was determined that they did not show toxic activity. Our study has been submitted to the literature for further studies for the design of anticancer drugs containing benzimidazole ring.

Acknowledgements

Our authors express their gratitude to the Herbal, Pharmaceutical, and Scientific Research Application and Research Center (AUBİBAM).

Conflicts of interest

The authors declare no conflicts of interest.

References

- [1] [M. Hou, H.C. Li, N. An, S.Y. Pang, W.G. Li, J. Tong, Synthesis, crystal structures and anticancer studies of Ni (II), Co (III) and Zn (II) complexes based on 5-bromosalicylaldehyde- 2-(2-aminophenyl)benzimidazole Schiff base, *J. Mol. Struct.*, 1294 (2023) 136500.
- [2] The top 10 causes of death, (n.d.). <https://www.who.int/news-room/fact-sheets/detail/the-top-10-causes-of-death> (accessed November 15, 2023).
- [3] D. Nuha, A.E. Evren, Z.Ş. Çiyancı, H.E. Temel, G. Akalin Çiftçi, L. Yurttas, Synthesis, density functional theory calculation, molecular docking studies, and evaluation of novel 5-nitrothiophene derivatives for anticancer activity, *Arch Pharm (Weinheim)*, 355 (2022).
- [4] İ. Celik, G. Ayhan-Kılıçgil, B. Guven, Z. Kara, A.S. Gurkan-Alp, A. Karayel, A. Onay-Besikci, Design, synthesis and docking studies of benzimidazole derivatives as potential EGFR inhibitors, *Eur. J. Med. Chem.*, 173 (2019) 240–249.
- [5] A.E. Evren, L. Yurttas, B. Ekselli, G. Akalin-Ciftci, Novel Tri-substituted Thiazoles Bearing Piperazine Ring: Synthesis and Evaluation of their Anticancer Activity, *Lett Drug Des Discov* 16 (2019) 547–555. <https://doi.org/10.2174/1570180815666180731122118>.
- [6] A. Sharma, V. Luxami, K. Paul, Purine-benzimidazole hybrids: Synthesis, single crystal determination and in vitro evaluation of antitumor activities, *Eur. J. Med. Chem.*, 93 (2015) 414–422.
- [7] G. Satija, B. Sharma, A. Madan, A. Iqbal, M. Shaquiquzzaman, M. Akhter, S. Parvez, M.A. Khan, M.M. Alam, Benzimidazole based derivatives as anticancer agents: Structure activity relationship analysis for various targets, *J. Heterocycl Chem.*, 59 (2022) 22–66.
- [8] R. Singla, K.B. Gupta, S. Upadhyay, M. Dhiman, V. Jaitak, Design, synthesis and biological evaluation of novel indole-benzimidazole hybrids targeting estrogen receptor alpha (ER- α), *Eur. J. Med. Chem.*, 146 (2018) 206–219.
- [9] T.S. Reddy, H. Kulhari, V.G. Reddy, V. Bansal, A. Kamal, R. Shukla, Design, synthesis and biological evaluation of 1,3-diphenyl-1*H*-pyrazole derivatives containing benzimidazole skeleton as potential anticancer and apoptosis inducing agents, *Eur. J. Med. Chem.*, 101 (2015) 790–805.

- [9] M.L. Di Gioia, R. Cassano, P. Costanzo, N. Herrera Cano, L. Maiuolo, M. Nardi, F.P. Nicoletta, M. Oliverio, A. Procopio, Green Synthesis of Privileged Benzimidazole Scaffolds Using Active Deep Eutectic Solvent, *Molecules*, 24 (2019) 2885.
- [10] K. Laxmikeshav, A. Himaja, N. Shankaraiah, Exploration of benzimidazoles as potential microtubule modulators: An insight in the synthetic and therapeutic evolution, *J. Mol. Struct.*, 1253 (2022) 132251.
- [11] N. Shrivastava, Mohd.J. Naim, Md.J. Alam, F. Nawaz, S. Ahmed, O. Alam, Benzimidazole Scaffold as Anticancer Agent: Synthetic Approaches and Structure–Activity Relationship, *Arch Pharm (Weinheim)*, 350 (2017).
- [12] Y.T. Lee, Y.J. Tan, C.E. Oon, Benzimidazole and its derivatives as cancer therapeutics: The potential role from traditional to precision medicine, *Acta. Pharm. Sin. B*, 13 (2023) 478–497.
- [13] W. Hou, W. Dai, H. Huang, S.-L. Liu, J. Liu, L.-J. Huang, X.-H. Huang, J.-L. Zeng, Z.-W. Gan, Z.-Y. Zhang, J.-X. Lan, Pharmacological activity and mechanism of pyrazines, *Eur. J. Med. Chem.*, 258 (2023) 115544.
- [14] Ş. Demirayak, L. Yurttaş, Synthesis and anticancer activity of some 1,2,3-trisubstituted pyrazinobenzimidazole derivatives, *J. Enzyme Inhib. Med. Chem.*, 29 (2014) 811–822.
- [15] W.R. Siegart, A.R. Day, Metabolite Analogs. VII. Preparation of Some Benzimidazolyl Analogs of Ethyl Pteroylglutamate, *J. Am. Chem. Soc.*, 79 (1957) 4391–4394..
- [16] G. Cheeseman, 2-ACETYLBENZIMIDAZOLE, *J. Chem. Soc.*, (1964).
- [17] S. Demirayak, K. Güven, Synthesis of some pyrido- and pyrazino-benzimidazole derivatives and their antifungal activity., *Pharmazie*, 50 (1995) 527–9.
- [18] Demirayak S, Abu Mohsen U., Anticancer and anti-HIV activities of some pyrido/pyrazino-benzimidazole derivatives, *Acta Pharm. Turc.*, 40 (1998) 9–12.
- [19] M. V. Berridge, P.M. Herst, A.S. Tan, Tetrazolium dyes as tools in cell biology: New insights into their cellular reduction, (2005) 127–152.
- [20] D. Osmaniye, S. Levent, C.M. Ardiç, Ö. Atlı, Y. Özkay, Z.A. Kaplancıklı, Synthesis and anticancer activity of some novel benzothiazole-thiazolidine derivatives, *Phosphorus Sulfur Silicon Relat. Elem.*, 193 (2018) 249–256.
- [21] D. Osmaniye, B. Korkut Çelikateş, B.N. Sağlık, S. Levent, U. Acar Çevik, B. Kaya Çavuşoğlu, S. İlgin, Y. Özkay, Z.A. Kaplancıklı, Synthesis of some new benzoxazole derivatives and investigation of their anticancer activities, *Eur. J. Med. Chem.*, 210 (2021) 112979.
- [22] D. Osmaniye, S. Levent, A. Karaduman, S. İlgin, Y. Özkay, Z. Kaplancıklı, Synthesis of New Benzothiazole Acylhydrazones as Anticancer Agents, *Molecules*, 23 (2018) 1054.
- [23] A.E. Evren, D. Nuha, L. Yurttaş, Focusing on the moderately active compound (MAC) in the design and development of strategies to optimize the apoptotic effect by molecular mechanics techniques, *European Journal of Life Sciences*, 1 (2023) 118–126.
- [24] Protein Data Bank, (n.d.).
- [25] Schrödinger Release. 2020-3, Maestro. Schrödinger, LLC, New York, NY, USA; 2020., (n.d.).
- [26] LigPrep module, Schrödinger Release. 2020-3, Maestro. Schrödinger, LLC, New York, NY, USA; 2020., (n.d.).
- [27] A.E. EVREN, S. DAWBAA, D. NUHA, Ş.A. YAVUZ, Ü.D. GÜL, L. YURTTAŞ, Design and synthesis of new 4-methylthiazole derivatives: In vitro and in silico studies of antimicrobial activity, *J. Mol. Struct.*, 1241 (2021) 130692.
- [28] Glide module, Schrödinger Release 2020-3, Glide, Schrödinger, LLC, New York, NY, USA (2020), (n.d.).

Electrospun Poly(ϵ -caprolactone) Nanofibers Containing Pomegranate Peel Extract and Bioactive Glass as Potential Wound Dressings

Aysen Akturk ^{1,a,*}

¹ Chemical Engineering Department, Faculty of Chemical and Metallurgical Engineering, Istanbul Technical University, Istanbul, Türkiye.

*Corresponding author

Research Article

History

Received: 30/10/2023

Accepted: 12/03/2024



This article is licensed under a Creative Commons Attribution-NonCommercial 4.0 International License (CC BY-NC 4.0)

ABSTRACT

This study focuses on the effect of pomegranate peel extract (PPE) as a natural medicinal substance and 45S5 bioglass (BG) particles as a bioactive material on the microstructure, antioxidant properties, and fibroblast cell cytotoxicity of biocompatible poly(ϵ -caprolactone) (PCL) nanofiber scaffolds. The hybrid nanofibers were fabricated via the electrospinning technique. The microstructure of nanofiber scaffolds was characterized by using scanning electron microscopy (SEM). The results indicated that the incorporation of PPE and BG particles did not change the morphology of the fibrous structure of the PCL nanofiber scaffolds. The DPPH analysis was performed to determine the antioxidant properties of nanofiber scaffolds and demonstrated that the incorporation of PPE improves the antioxidant properties of scaffolds. Cell cytotoxicity studies using fibroblast L929 cells also showed that high cell viability values were observed for hybrid PPE and BG loaded PCL nanofiber scaffolds. The findings proved that the integration of PPE and BG particles into PCL nanofibers yielded favorable characteristics suitable for wound dressing purposes, involving improved antioxidant capacity.

Keywords: Electrospinning, Wound dressings, Polycaprolactone, Pomegranate peel extract, Bioactive glass.

^a akturkay@itu.edu.tr

^{ib} <https://orcid.org/0000-0003-2880-2999>

Introduction

Wound dressings have been suggested to be one of the most advanced treatment methods for various skin injuries caused by external damage or accident [1,2]. The increase in the prevalence of non-healing wounds has also led to the development of new wound dressing materials for tissue engineering applications [2]. Wound healing is a complex process involving blood coagulation, epithelialization, wound contraction, collagen synthesis, and blood vessel formation. The healing process involves an accurate pattern of synchronized steps involving migratory and resident cell populations, extracellular matrix components, and soluble mediators [3]. Therefore, biologically inspired wound dressing materials have been developed to mimic the extracellular matrix's (ECM) structural function as well as serve as a platform for cell migration and proliferation during wound healing [2]. Diverse forms of wound dressings, including hydrogels, films, membranes, sponges, and nanofibers, have been developed in order to accelerate the healing process [3]. Electrospun nanofibrous dressings have drawn the most interest among these types of wound dressings due to their structural resemblance to the ECM, high specific surface area, exceptional mechanical qualities, and high porosity [4].

Bioactive glasses (BGs) have shown promising results in soft tissue applications. The original 45S5 Bioglass[®] promoted angiogenesis [5]. The composition of 45S5 Bioglass[®] consists of 45 wt% SiO₂, 24.5 wt% CaO, 24.5 wt% Na₂O, and 6.0 wt% P₂O₅ [6,7]. Silica functions as a network

modifier, while calcium, potassium, and sodium ions are network formers. Si facilitates precipitation or surface reconstruction by non-bridging oxygen sites. It promotes bone bonding and mechanical stability by attaching other metal ions and functional groups. These features make BGs better for soft tissue engineering than hard tissue engineering or implants. The primary advantage that BGs provide to the field of soft tissue engineering is their high degree of bioactivity under physiological conditions as well as their high surface reactivity for the formation of hydroxyl carbonate apatite (HCA) layers on soft tissue [7]. Due to their osteogenicity, angiogenesis, proliferators, and biocompatibility, BGs were extensively used in soft tissue engineering for wound healing [3,4,7–10]. However, cell injury and inflammatory responses may result from the intrinsic brittleness and sharp morphology of BG particles and fibers. Moreover, if glass powder is placed directly on a wound without a secondary dressing, it could be quickly removed from the surrounding area. Thus, combining polymers (i.e., chitosan, poly(lactic acid), poly(ϵ -caprolactone), and polyvinyl alcohol) with inorganic materials like glass particles is an efficient way to make use of both the therapeutic properties of glasses and the adaptability of polymers [2,11].

Poly(ϵ -caprolactone) (PCL) is often employed as the matrix in many biomedical applications due to its semi-crystalline microstructure, high mechanical flexibility, intrinsic non-toxicity, low biodegradability, high biocompatibility, and high ability to imitate the ECM.

Furthermore, the low hydrophilic nature of PCL, which affects adhesion and cell proliferation, makes this biopolymer a unique choice [12]. But due to its low stiffness, hydrophobic nature, and lack of bioactivity, it has limits in biological applications [8]. The usage of BG particles as modifiers of PCL matrix has been extensively documented in the literature. This approach enables the fabrication of bioactive composites with enhanced mechanical behavior and osteostimulative characteristics [13].

Pomegranate has a wide variety of different types of bioactive compounds, is native to the nations of the Mediterranean region, and may be consumed in the form of the fruit itself as juice, flower extract, seed oil, roots, leaves, or peel [14]. It contains polyphenols, flavonoids, anthocyanin, ascorbic acid, ellagic acid, carotenoids, tannins, and other compounds [15]. As modern medicine explores phytochemicals with minimal side effects, pomegranate emerges as a valuable natural resource with antibacterial properties and high concentrations of flavonoids and tannins [16–18]. There has also been a long-standing interest in the use of pomegranate peel extract for therapeutic purposes due to its high phenolic content [18]. Several studies combined pomegranate peel extract with different materials to improve the properties of scaffold materials for various tissue engineering applications. Garcia et al. combined collagen, nanohydroxyapatite and pomegranate peel extract to design gels for bone tissue regeneration [19]. Azarfam et al. fabricated gelatin/agarose/zeolite hydrogel composites for tissue engineering applications [18]. Costa et al. prepared PVA/starch/polyacrylic acid films with pomegranate peel extract by using the solvent casting method [20]. Karabulut et al. fabricated 3D-printed scaffolds by combining pomegranate peel extract, pomegranate seed extract, starch, and polyvinyl alcohol [21].

The novelty of the present study is the fabrication of nanofibrous scaffolds for wound dressing applications made by a natural compound (pomegranate peel extract), which has advantages over common PCL-based scaffolds and improves the wound dressing properties such as microstructure, antioxidant, and cytotoxicity behaviors. This study aims to investigate the effect of pomegranate peel extract and bioactive glass as combined additives on the wound dressing application of PCL-based scaffolds. Hence, the bioactive glass particles were synthesized using the melt quenching method, and hybrid scaffolds were produced using the electrospinning method. The synergetic effect of pomegranate peel extract and bioactive glass was studied.

Materials and Methods

Materials

Poly(ϵ -caprolactone) (PCL, average Mn 80,000, Sigma Aldrich), N, N-dimethylformamide (DMF, for gas chromatography ECD and FID, Merck), and dichloromethane (DCM, extra pure, Merck) were used to

prepare electrospinning polymer solutions. Silicon dioxide (SiO₂, Sand, white quartz, purum p.a., powder, Sigma-Aldrich), di-sodium hydrogen phosphate (Na₂HPO₄, anhydrous for analysis, Merck), calcium carbonate (CaCO₃, precipitated for analysis, Merck), and sodium carbonate (Na₂CO₃, anhydrous, puriss, Riedel-de Haën) were used to prepare 45S5 bioactive glass. Pomegranates were purchased from the local market to prepare pomegranate peel extract. Ethanol (C₂H₅OH, absolute for analysis, Merck) and deionized water were used to prepare pomegranate peel extract (PPE).

Bioactive Glass Preparation

Traditional melt quenching was used for the production of bioactive glass particles with the following compositions: 45 w% SiO₂, 24.5 w% CaO, 24.5 w% Na₂O, and 6.0 w% P₂O₅. Precursor compounds were heated to 1250 °C in a platinum crucible. The melt was rapidly quenched into deionized water after two hours. The produced frits were then remelted for a second time for two hours at 1250 °C, and the melt was then quenched to produce a homogenous and amorphous structure. By grinding and sieving below 45 μ m, glass particles were produced. In our prior study, the characterization of these BGs was carried out [22].

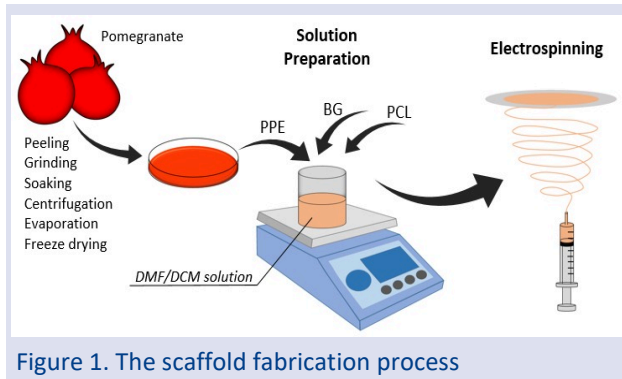
Pomegranate Peel Extract Preparation

Pomegranate peel extract (PPE) was prepared by the method described by Bodbodak et al. [23]. Briefly, fresh pomegranates were purchased from local markets in Istanbul, Türkiye. Pomegranates were peeled and dried in an oven at 40 °C for 48 hours. Then, the dried peels were powdered using a grinder. The PPE was then obtained by soaking 5g of powder in 250 mL of 80% (v/v) ethanol and stirring for 48 hours at room temperature. The obtained solution was centrifuged and filtered through Whatman No:1 filter paper. The supernatant was concentrated with a rotary evaporator at 50 °C. For further usage, the concentrated supernatant was freeze dried to obtain PPE.

Scaffold Preparation

The polymer solution (10% w/v) was provided by dissolving PCL in the DMF/DCM mixture (1:4 v/v) under continuous stirring for two hours. BG particles were added to this solution at a 15% w/w concentration with respect to the polymer. The quantities of BG and PCL utilized in this study were determined in accordance with the quantities specified in our previous study [10]. Then, PPE with different concentrations (5, 10, and 15 w% with respect to polymer) was introduced into the polymer solution and stirred overnight. PCL/BG/PPE solutions were placed in syringes. An electrospinning device (Nanospinner 24 Touch, Inovenso Co.) was used to prepare scaffolds. The applied voltage of 25 kV was applied to the tip of the needle. The distance between tip to collector was adjusted to 17 cm, and a polymer flow rate of 2 ml/h was used. An aluminium foil was wrapped around the collector, positioned perpendicular to the tip. The electrospinning process was performed under

ambient conditions. The samples with BG particles and PPE with contents of 5%, 10%, and 15% were named PCL/BG/5PPE, PCL/BG/10PPE, and PCL/BG/15PPE, respectively. The scaffold fabrication process was illustrated in Figure 1.



Characterization Studies

A scanning electron microscope (SEM, JSM-5410, Jeol) was used to examine the morphology of electrospun scaffolds. A Matlab-based image analysis program called SIMPoly was utilized to estimate the diameters of nanofibers and their standard deviations [24]. Functional molecular groups of PPE were analyzed in the 450–4000 cm^{-1} range using a Fourier transform infrared (FTIR) spectrometer (Perkin-Elmer, Spectrum Two).

Antioxidant Activity

The DPPH assay was employed to evaluate the free radical scavenging activity of each nanofiber mat. A DPPH assay solution was prepared by mixing 1 mg of nanofiber mat and 3 mL of DPPH methanol solution (0.3 mM). The mixture was shaken for a minute before being incubated for 30 minutes. Following this, the UV absorbance of the DPPH test solution was determined at 517 nm. The average values were taken from three specimen tests. The antioxidant activity was calculated by:

$$\text{Antioxidant activity} = \frac{A_{DPPH} - A_S}{A_{DPPH}} \times 100 \quad (1)$$

where A_{DPPH} is the absorbance of the DPPH methanol solution at 517 nm and A_S is the absorbance of the DPPH assay solution at 517 nm [25].

Cell Culture Study

Mouse L929 fibroblast cells were used for the MTT cytotoxicity assay. Nanofibers were placed on a 96-well plate and sterilized with UV light for 20 minutes before the test. After that, 10^5 cells per well were seeded on the scaffolds and incubated for 72 h at 37 °C with 85% humidity. MTT (3-(4,5)-dimethylthiazol-2yl)-2,5-diphenyltetrazolium bromide) was used to determine the in vitro cytotoxicity of scaffolds after 72 h. MTT solution was added in each well, and crystallized formazon substance dissolved in dimethyl sulfoxide were formed after incubation for 4 h at 37 °C and with 5% CO_2 . Optical

densities of the obtained solutions were measured at 570 nm.

Results and Discussion

Characterization of PPE

FTIR spectroscopy was employed to identify and analyse the characteristic peaks associated with PPE (Figure 2). As shown in the figure, the FTIR spectrum of PPE exhibited an apparent peak at 3293.70 cm^{-1} , indicating the presence of alcohol and carboxylic acid functional groups. This peak corresponds to the stretching vibrations of OH groups. The CH stretching vibration peak was detected at 2932.22 cm^{-1} . A distinct peak at 1717.22 cm^{-1} was observed, representing the existence of a carbonyl group (C=O). This confirms the presence of aldehydes, ketones, and carboxylic acid groups in the extract. The peak observed at 1611.05 cm^{-1} signifies the occurrence of H-O-H bending vibrations. The peak at 1441.00 cm^{-1} corresponds to the O-CH₃ deformation, while the peak at 1338.61 cm^{-1} represents CH bending. Additionally, the band identified at 1222.72 cm^{-1} indicates the presence of esters and ether functional groups, specifically CH₂CO stretching. The C-O-C vibration was displayed by the peak at 1029.09 cm^{-1} [26]. Based on the similarity between the identified peaks and the existing literature, it can be inferred that the preparation of PPE was accomplished effectively.

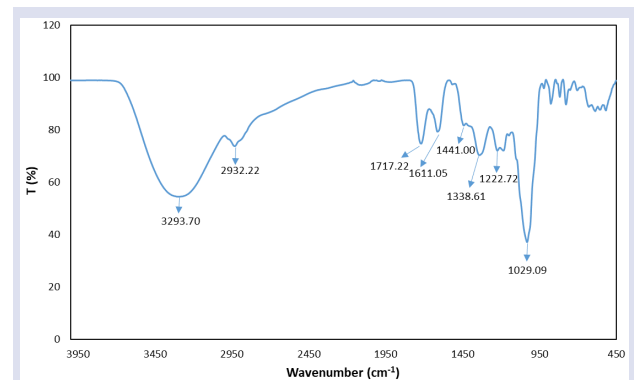


Figure 2. FTIR Spectrum of PPE

Surface Morphology of Scaffolds

In this study, a series of PCL/BG/PPE nanofibrous scaffolds with biocompatibility and antioxidant activity were prepared for wound healing applications. SEM analysis was utilized to investigate the surface morphology and size distribution of nanofibers. As illustrated in Figure 3, fibers with homogenous, bead-free, and randomly oriented architectures were formed by incorporating BG with varying concentrations of PPE into PCL nanofibers. The nanofiber diameters of composite nanofibers were 799 ± 128 nm (PCL/BG/5PPE), 709 ± 109 nm (PCL/BG/10PPE), and 741 ± 109 nm (PCL/BG/15PPE), respectively. The results showed that the incorporation of PPE and BG had no adverse impact on fiber formation. The incorporation of PPE was found to result in an increase in fiber diameter compared to the fiber diameter size

(389 ± 72 nm) of the PCL/BG nanofiber structure in our previous study [10]. This increase in fiber diameter is caused by the reduction of the electrical conductivity of

the polymer solutions with the incorporation of extracts. Similar results were observed in the studies using several extracts as additives for electrospun nanofibers [27,28].

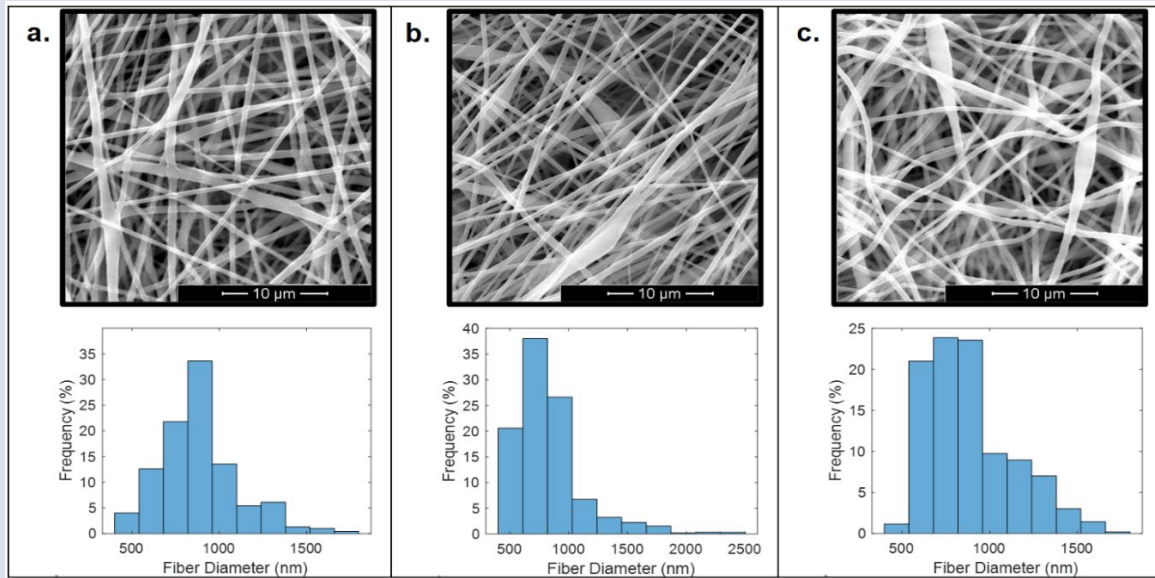


Figure 3. SEM images and fiber distributions of PCL/BG/5PPE (a), PCL/BG/10PPE (b), and PCL/BG/15PPE (c) scaffolds

Antioxidant Activity of Scaffolds

During wound injury, the excessive generation of free radical molecules known as reactive oxygen species (ROS) damages the extracellular matrix and cell membranes, hindering wound healing [29]. Plants' wound healing properties are linked to their antioxidant activities, mainly involving phenolic compounds like phenolic acids and flavonoids, which scavenge free radicals [30,31]. These antioxidants protect cells from ROS's harmful effects and regulate the wound healing process. Physical skin injuries trigger inflammation and immune cell responses to restore tissue. However, ROS's presence can impede healing by damaging cells and promoting infections. Plant-derived antioxidants, such as tannins, phenolic acids, flavones, flavonols, catechins, and others, act as natural free radical scavengers, helping deactivate and remove ROS, safeguarding cells, and supporting effective wound healing [31]. The hydrolysable tannins (ellagic acid, gallic acid, punicalin, pedunculagin, and punicalagin) are largely responsible for the biological activities of pomegranate peel extract [16,32,33]. The integration of these compounds into fibrous PCL based materials could serve to impart antioxidant properties to them. As a result, the antioxidant activity of PCL/BG/5PPE, PCL/BG/10PPE, and PCL/BG/15PPE scaffolds was assessed through the utilization of the DPPH radical scavenging assay. PCL/BG/5PPE, PCL/BG/10PPE, and PCL/BG/15PPE scaffolds exhibited antioxidant activities of 46.21%, 50.24%, and 62.61%, respectively (Figure 4). The results revealed an increase in correlation between the quantity of PPE incorporated into scaffolds and the observed improvement in antioxidant activity.

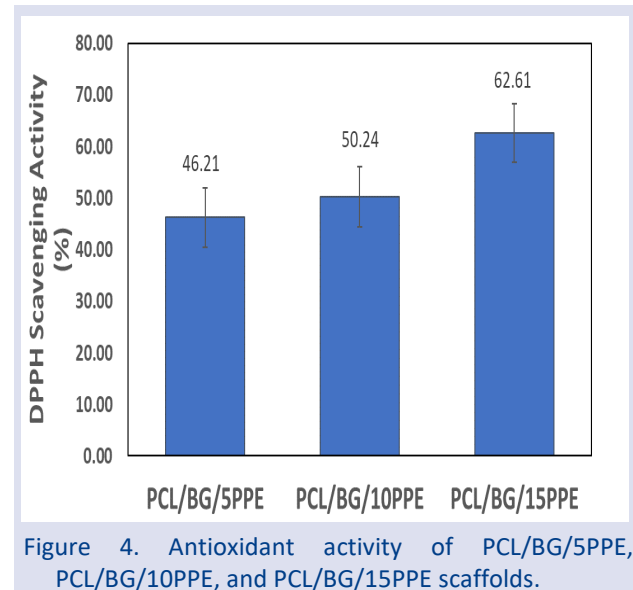


Figure 4. Antioxidant activity of PCL/BG/5PPE, PCL/BG/10PPE, and PCL/BG/15PPE scaffolds.

Cytotoxicity of Scaffolds

Fibroblasts are the primary cells of the dermis that play a vital role in tissue repair [34]. Hence, the L929 cell line is employed in a 72-hour direct MTT assay (Figure 5). The cell viability (expressed in%) observed with the varying extract concentrations was 103.35 ± 3.72 for PCL/BG/5PPE, 95.52 ± 3.16 for PCL/BG/10PPE, and 85.23 ± 5.66 for PCL/BG/15PPE. In accordance with EN ISO-10993-5/12, cell viability greater than 80% is classified as non-toxic [35,36]. The viability of the L929 cells incubated at all the extract concentrations was above 80%. Therefore, the biocompatibility of the scaffold made it acceptable for usage in wound dressing applications.

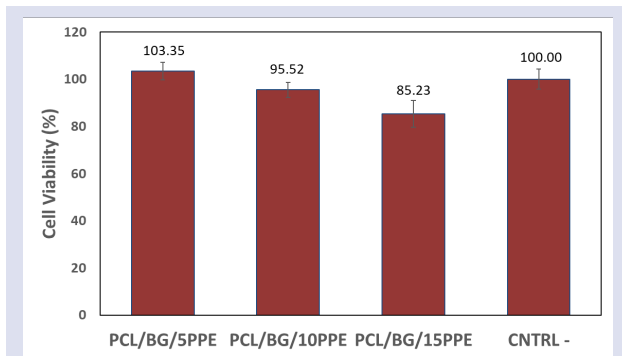


Figure 5. Viability percentage of L929 fibroblast cells treated with PCL/BG/5PPE, PCL/BG/10PPE, and PCL/BG/15PPE scaffolds for 72h incubation.

Conclusion

In summary, poly(ϵ -caprolactone) (PCL) fibers functionalized with pomegranate peel extract (PPE) and 45S5 bioglass particles (BG) were successfully obtained by electrospinning using PCL as polymer in N,N-dimethylformamide/dichloromethane (1:4 v/v) as organic solvents to prepare polymeric solutions. The electrospun fibers produced from PCL/BG/PPE were homogeneous, bead-free and randomly oriented structures and had no toxic effect on L929 cell cultures. This study demonstrated that electrospinning is a promising advance for the production of scaffolds composed of nanofibers containing recovered bioactive compounds of pomegranate peel extracted with deionized water/ethanol (1:4 v/v) solution. Antioxidant tests have revealed that PPE imparts antioxidant properties to the scaffolds. Moreover, cell toxicity studies showed that biocompatible structures can be obtained by using BG prepared by traditional melt quenching method and PPE in PCL nanofiber structures. This study is novel in its investigation of the utilization of nanofibers produced through the electrospinning technique, which involves the incorporation of biologically functional components derived from pomegranate peel and 45S5 bioactive glass into the PCL polymer for the purpose of developing wound dressings.

Conflicts of interest

There are no conflicts of interest in this work.

References

- [1] Dhivya S., Padma V.V., Santhini E., Wound dressings - A review, *Biomed.* 5 (4) (2015) 22.
- [2] Yang M., Yu S., Zhao P., Shi G., Guo Y., Xie L, Lyu G., Yu J., Fabrication of biologically inspired electrospun collagen/silk fibroin/bioactive glass composited nanofibrous to accelerate the treatment efficiency of wound repair, *Int. Wound J.* 20 (3) (2023) 687-698.
- [3] Sergi R., Bellucci D., Salvatori R., Cannillo V., Chitosan-based bioactive glass gauze: Microstructural properties, in vitro bioactivity, and biological tests, *Materials (Basel)*, 13 (12) (2020) 2819.
- [4] Zhou J., Wang H., Zhao S., Zhou N., Li L., Huang W., Huang W., Wang D., Zhang C., In vivo and in vitro studies of borate based glass micro-fibers for dermal repairing, *Mater. Sci. Eng. C.* 60 (2016) 437-445.
- [5] Baino F., Bioactive glasses – When glass science and technology meet regenerative medicine, *Ceram. Int.* 44 (13) (2018) 14953-14966.
- [6] Bakar S.A.A, Ali A.M., Noor S.N.F.M., Hamid S.B.S., Azhar N.A., Mohamad N.M., Ahmad N.H., Combination of Goniotalamin and Sol-Gel-Derived Bioactive Glass 45S5 Enhances Growth Inhibitory Activity via Apoptosis Induction and Cell Cycle Arrest in Breast Cancer Cells MCF-7, *Biomed Res. Int.* 2022 (2022).
- [7] Nandhakumar M., Thangaian D.T., Sundaram S., Roy A., Subramanian B., An enduring in vitro wound healing phase recipient by bioactive glass-graphene oxide nanocomposites, *Sci. Rep.* 12 (1) (2022) 16162.
- [8] Deliormanlı A.M, Konyalı R., Bioactive glass/hydroxyapatite-containing electrospun poly(ϵ -caprolactone) composite nanofibers for bone tissue engineering, *J. Aust. Ceram. Soc.* 55 (2) (2019) 247-256.
- [9] Sergi R., Cannillo V., Boccaccini A.R., Liverani L., Incorporation of bioactive glasses containing Mg, Sr, and Zn in electrospun PCL fibers by using benign solvents, *Appl. Sci.* 10 (16) (2020) 5530.
- [10] Akturk A., Erol-Taygun M., Goller G., Küçükbayrak S., Optimization and characterization of poly(ϵ -caprolactone) nanofiber mats doped with bioactive glass and copper metal nanoparticles, *Chem. Pap.* 75 (11) (2021) 5929-5943.
- [11] Mehrahi T., Mesgar A.S, Mohammadi Z., Bioactive Glasses: A Promising Therapeutic Ion Release Strategy for Enhancing Wound Healing, *ACS Biomater. Sci. Eng.* 6 (10) (2020) 5599-5430.
- [12] Ghiyasi Y., Salahi E., Esfahani H., Synergy effect of Urtica dioica and ZnO NPs on microstructure, antibacterial activity and cytotoxicity of electrospun PCL scaffold for wound dressing application, *Mater. Today Commun.* 26 (2021) 102163.
- [13] Dziadek M., Dziadek K., Checinska K., Zagrajczuk B., Golda-Cepa M., Brzychczy-Wloch M, Kopec E., Menaszek, E., Kopec, A., Cholewa-Kowalska, K., PCL and PCL/bioactive glass biomaterials as carriers for biologically active polyphenolic compounds: Comprehensive physicochemical and biological evaluation, *Bioact. Mater.* 6 (6) (2021) 1811-1826.
- [14] Atsü A.N., Tosuner Z., Bilgiç T., Evaluation of the Effect of Pomegranate Seed Oil on Healing in a Rat Wound Model With Antioxidant, Vascular, and Histopathological Parameters, *Int. J. Low. Extrem. Wounds* (2021) 15347346211040593.
- [15] Pamisetty A., Kumar K.A., Indrani D., Singh R.P., Rheological, physico-sensory and antioxidant properties of puniceic acid rich wheat bread, *J. Food Sci. Technol.* 57 (1) (2020) 253-262.
- [16] Bokhari N., Fatima T., Nosheen S., Iqbal F., Moeen F., Sharif F., Bioactive bacterial cellulose–chitosan composite scaffolds for prospective periodontal tissue regeneration, *J. Mater. Res.* 38 (7) (2023) 1952-1962.
- [17] Mutra J.K.R, Jujjavarapu S.E., Verma N., Emergence of Plant-Based Decellularized Scaffolds for Tissue Regeneration: A Review, *ACS Sustain. Chem. Eng.* 11(17) (2023) 6485–6497.
- [18] Azarfam M.Y., Nasirinezhad M., Naeim H., Zarrintaj P., Saeb M., A green composite based on gelatin/agarose/zeolite as a potential scaffold for tissue engineering applications, *J. Compos. Sci.* 5 (5) (2021) 125.
- [19] Garcia C.F., Marangon C.A., Massimino L.C., Klingbeil

- M.F.G., Martins V.C.A., de Guzzi Plepis A.M., Development of collagen/nanohydroxyapatite scaffolds containing plant extract intended for bone regeneration, *Mater. Sci. Eng. C* 123 (2021) 111955.
- [20] Costa N.N., de Faria Lopes L., Ferreira D.F., de Prado E.M.L., Severi J.A., Resende J.A., de Paula Careta F., Ferreira M.C.P., Carreira L.G., de Souza S.O.L., Cotrim M.A.P., Polymeric films containing pomegranate peel extract based on PVA/starch/PAA blends for use as wound dressing: In vitro analysis and physicochemical evaluation, *Mater. Sci. Eng. C* 109 (2020) 110643.
- [21] Karabulut H., Ulag S., Dalbayrak B., Arisan E.D., Taskin T., Guncu M.M., Aksu B., Valanezhad A., Gunduz, O., A Novel Approach for the Fabrication of 3D-Printed Dental Membrane Scaffolds including Antimicrobial Pomegranate Extract, *Pharmaceutics* 15 (3) (2023) 737.
- [22] Akturk A., Erol Taygun M., Goller G., Optimization of the electrospinning process variables for gelatin/silver nanoparticles/bioactive glass nanocomposites for bone tissue engineering, *Polym. Compos.* 41 (6) (2020) 2411-2425.
- [23] Bodbodak S., Shahabi N., Mohammadi M., Ghorbani M. Pezeshki A., Development of a Novel Antimicrobial Electrospun Nanofiber Based on Polylactic Acid/Hydroxypropyl Methylcellulose Containing Pomegranate Peel Extract for Active Food Packaging, *Food Bioprocess Technol.* 14(12) (2021) 2260-2272.
- [24] Murphy R., Turcott A., Banuelos L., Dowey E., Goodwin B., Cardinal, K. O. H., Simply: A Matlab-based image analysis tool to measure electrospun polymer scaffold fiber diameter, *Tissue Eng. Part C Methods*, 26(12), (2020) 628-636.
- [25] He L., Lan W., Ahmed S., Qin W., Liu Y., Electrospun polyvinyl alcohol film containing pomegranate peel extract and sodium dehydroacetate for use as food packaging, *Food Packag. Shelf Life* 22 (2019) 100390.
- [26] Ul-Islam M., Alhajaim W., Fatima A., Yasir S., Kamal T., Abbas Y., Khan S., Khan A.H., Manan S., Ullah M.W., Yang, G., Development of low-cost bacterial cellulose-pomegranate peel extract-based antibacterial composite for potential biomedical applications, *Int. J. Biol. Macromol.* 231 (2023) 123269.
- [27] Anaya-Mancipe J.M., Queiroz V.M., Dos Santos R.F., Castro R.N., Cardoso V.S., Vermelho A.B., Dias M.L., Thiré R.M., Electrospun Nanofibers Loaded with Plantago major L. Extract for Potential Use in Cutaneous Wound Healing, *Pharmaceutics* 24 15(4) (2023) 1047.
- [28] Estrella-Osuna D.E., Tapia-Hernández J.A., Ruíz-Cruz S., Márquez-Ríos E., Ornelas-Paz J.D., Del-Toro-Sánchez C.L., Ocaño-Higuera V.M., Rodríguez-Félix F., Estrada-Alvarado M.I., Cira-Chávez L.A., Nanoencapsulation of eggplant (solanum melongena L.) peel extract in electrospun gelatin nanofiber: Preparation, characterization, and in vitro release, *Nanomaterials* 12(13) (2022) 2303.
- [29] Maver T., Kurečić M., Pivec T., Maver U., Gradišnik L., Gašparič P., Kaker B., Bratuša A., Hribernik S., Stana Kleinschek K., Needleless electrospun carboxymethyl cellulose/polyethylene oxide mats with medicinal plant extracts for advanced wound care applications, *Cellulose* 27 (8) (2020) 4487-4508.
- [30] Spasova M., Stoyanova N., Manolova N., Rashkov I., Taneva S., Momchilova S., Georgieva, A., Facile preparation of novel antioxidant fibrous material based on natural plant extract from Portulaca oleracea and polylactide by electrospinning for biomedical applications, *Polym. Int.* 71 (6) (2022) 689-696.
- [31] Amer A.A., Mohammed RS, Hussein Y, Ali ASM, Khalil AA. Development of Lepidium sativum Extracts/PVA Electrospun Nanofibers as Wound Healing Dressing, *ACS Omega* 7 (24) (2022) 20683–20695.
- [32] Spilmont M., Léotoing L., Davicco M.J., Lebecque P., Miot-Noirault E., Pilet P., Rios L., Wittrant Y., Coxam V., Pomegranate peel extract prevents bone loss in a preclinical model of osteoporosis and stimulates osteoblastic differentiation in vitro, *Nutrients* 7 (11) (2015) 9265-9284.
- [33] Spilmont M., Léotoing L., Davicco M.J., Lebecque P., Mercier S., Miot-Noirault E., Pilet P., Rios L., Wittrant Y., Coxam V., Pomegranate and its derivatives can improve bone health through decreased inflammation and oxidative stress in an animal model of postmenopausal osteoporosis, *Eur. J. Nutr.* 53 (5) (2014) 1155-1164.
- [34] Wang Y., Wang X., Zhou D., Xia X., Zhou H., Wang Y., Ke, H., Preparation and Characterization of Polycaprolactone (PCL) Antimicrobial Wound Dressing Loaded with Pomegranate Peel Extract, *ACS Omega* 8 (23) (2023) 20323–20331.
- [35] Ullah A., Saito Y., Ullah S., Haider M.K., Nawaz H., Duy-Nam P., Kharaghani D., Kim I.S., Bioactive Sambong oil-loaded electrospun cellulose acetate nanofibers: Preparation, characterization, and in-vitro biocompatibility, *Int. J. Biol. Macromol.* 166 (2021) 1009-1021.
- [36] Akturk A., Enrichment of Cellulose Acetate Nanofibrous Scaffolds with Retinyl Palmitate and Clove Essential Oil for Wound Healing Applications, *ACS Omega* 8 (6) (2023) 5553–5560.

Production and Characterization of Ni_{0.50}Al_{0.50} and Ni_{0.55}Al_{0.45} Powders by Volume Combustion Synthesis

Gülizar Sarıyer ^{1,a}, Hasan Erdem Çamurlu ^{2,b,*}¹Department of Space Sciences and Technologies, Akdeniz University, Antalya, Türkiye.²Department of Mechanical Engineering, Akdeniz University, Antalya, Türkiye.

*Corresponding author

Research Article

History

Received: 10/04/2023

Accepted: 01/02/2024



This article is licensed under a Creative Commons Attribution-NonCommercial 4.0 International License (CC BY-NC 4.0)

ABSTRACT

Nickel aluminide (NiAl) is an essential intermetallic material with a high melting point and excellent high temperature corrosion resistance. It is a solid solution of Ni and Al in 40-61 mol.% Ni range. In this study, Ni_{0.50}Al_{0.50} and Ni_{0.55}Al_{0.45} powders were formed by using nickel and aluminum elemental powders through volume combustion synthesis (VCS). MgO powder was utilized as the thermal diluent. According to adiabatic temperature calculations, MgO was added to the reactant mixture in 10-40 vol.% range for preventing the melting and sintering of the formed Ni_{0.50}Al_{0.50} and Ni_{0.55}Al_{0.45} particles. After VCS, the products were ground into powder form and leached in 3M HCl solution in order to remove the MgO particles. After VCS, the samples which were obtained with 10 - 30 vol.% MgO addition were quite hard and difficult to grind. This indicated the partial sintering of the formed particles. It was relatively easier to grind into powder form the samples which contained 40 vol.% MgO. Therefore, it was determined that the most suitable MgO ratio for the formation of Ni_{0.50}Al_{0.50} and Ni_{0.55}Al_{0.45} powders was 40 vol.%. Formed powders were mostly in 5-100 µm particle size range. The formation of single phase pure powders was confirmed by the XRD analyses. A shift of about 0.1 degrees to higher 2-theta values was determined in the XRD peaks of the Ni_{0.55}Al_{0.45} powder as compared to the Ni_{0.50}Al_{0.50} phase, after annealing the powders. The results were in agreement with the crystallographic data.

Keywords: NiAl powder, Thermal diluent, Volume combustion synthesis.glzrysn@gmail.com<https://orcid.org/0000-0001-7754-4549>erdemcamurlu@gmail.com<https://orcid.org/0000-0003-3170-4492>

Introduction

NiAl has useful traits such as high melting temperature, low density, good environmental resistance and high thermal conductivity. NiAl is a solid solution of Ni and Al in 40-61 mol.% Ni range [1]. Due to its beneficial properties, it has long been studied as a potential material in various areas requiring especially high temperatures, such as the aerospace industry [2,3]. NiAl provides excellent high temperature properties and specific strength that is close to those of superalloys and ceramics at high temperatures. This is mainly due to the strong bond between aluminum and nickel [4].

NiAl powders can be produced by different methods with certain compositions by using elemental powder mixtures of nickel and aluminum such as reactive sintering and combustion synthesis [1,5,6]. In the study of Portnoy et al. [1], NiAl powders were produced through mechanical alloying of Ni and Al powders. A vibratory mill was utilized and NiAl formation was seen to be completed after 220 min of milling. It was reported that the NiAl (B2) phase was obtained by a fast exothermic reaction in solid form, and no intermediate solid solutions formed. Samples were annealed at 720 °C homogenization. It was reported that better crystallinity was obtained, with reduction in the width of the XRD peaks and approaching of the lattice parameter to equilibrium value.

Povarova et al. [5] studied on production of NiAl powders by various methods. They conducted mechanical alloying, carbonyl decomposition and also by spraying of NiAl melts. For mechanical alloying, they employed an attritor. After annealing of the obtained powders, a decrease in the XRD peak width was observed. It was suggested that the reaction in reactive sintering starts in the solid phase and continues with diffusion, during which pore formation takes place as a result of Kirkendall effect. The NiAl particles which were obtained by melt spraying were in 100-400 micrometer size range. Microheterogeneity was detected in this type of powder, in which Al deficiency was observed near the grain boundaries.

Combustion synthesis is a technique that utilizes the exothermic enthalpy of the reactions. In volume combustion synthesis, the reaction between the reactants takes place in the whole volume of the reactant mixture instantaneously during heating [7,8]. Therefore, this method bears the advantages of being easy to apply, low cost and simple.

In the Ni-Al system, combustion synthesis results in partial melting of the product NiAl phase. Since the temperature of the products reaches the melting point of NiAl, as a result of the exothermicity of the reaction. In order to reduce the combustion temperature, thermal

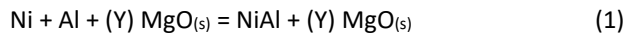
diluents are utilized. Generally, some of the product powder is added to the initial reactant mixture in order to absorb some of the released heat and to decrease the combustion temperature [9,10]. In our previous study, effect of addition of preformed NiAl powder as the thermal diluent, on the formation of porous NiAl was investigated [10].

In the present study, the thermal diluent MgO, which is used to prevent NiAl from melting during combustion synthesis is preferred because MgO does not react with the reactants or the products in the Ni-Al system. In addition, it does not melt during the reaction and can be selectively separated with the help of acid solution after the reaction. As to the knowledge of the authors, the utilization of MgO as a thermal diluent in the Ni-Al system has not been investigated in the literature, previously. The aim of this study is to base the starting powder generation method for the production of Ni_{0.50}Al_{0.50} and Ni_{0.55}Al_{0.45} powders by volume combustion synthesis and to examine the structure of the produced powders. It was reported that the changes in the stoichiometry of the NiAl solid solution provides tailoring of some of the properties. For example, the thermal conductivity of Ni_{0.55}Al_{0.45} is about 50 % less than that of Ni_{0.50}Al_{0.50} [11]. Thus in this study, formation of powders in the solid solution region of NiAl has been demonstrated.

Materials and Methods

Sample Preparation

Ni_{0.50}Al_{0.50} and Ni_{0.55}Al_{0.45} powders were produced via volume combustion synthesis (VCS) by using Ni, Al powders according to Reaction (1). Y denotes the amount of MgO, which was added to Ni and Al powder mixture.



MgO powder (Merck, purity 99.5%, particle size <1 μm) was added to the Ni and Al starting powders as a thermal diluent in order to reduce the combustion temperature and to prevent the melting and sintering of the formed Ni_{0.50}Al_{0.50} and Ni_{0.55}Al_{0.45} particles. With the experiments, it was understood that MgO did not react with Ni and Al. Adiabatic temperature calculation was made by using the HSC Chemistry software and database, to determine the diluent MgO ratio to be used. In this study, according to adiabatic temperature calculations, MgO was added to the Ni-Al reactant mixture in 10-40 vol.% range. Ni and Al powders containing 10-40 vol.% MgO were weighed and mixed. The prepared powder mixture was taken into a steel mold with a diameter of 10 mm, a pressure of 50 MPa was applied.

The compressed sample was placed in a ceramic crucible and it was heated in an induction furnace (Indutherm, Model: MC20V, 3.5kW (Fig. 1)). Inside the ceramic crucible there was a graphite liner, which enabled the heating of the sample by induction current. Inside of the graphite liner was covered with hexagonal boron nitride coating (Ekamold) in order to prevent

contamination and sticking of the pellet to the crucible. The induction furnace is equipped with an optical pyrometer. 2 consecutive vacuum-argon filling cycles were applied prior to heating the samples. Thus, VCS reaction was conducted in an argon atmosphere.

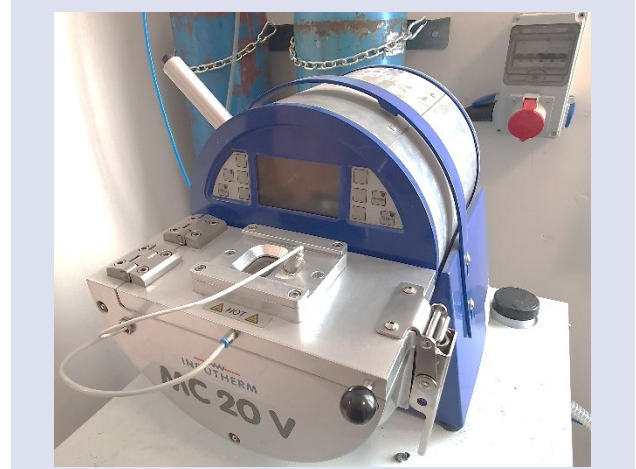


Figure 1. Induction furnace that was used in heating the samples for VCS under Ar atmosphere

It was determined that VCS reaction occurred with the hasty increase in temperature, which was measured by the optical pyrometer of the device.

Leaching and Characterization

The resulting product was crushed in a mortar and it was mixed in 3M HCl with a magnetic stirrer for about 2 hours to remove the MgO. In this process, a solid-liquid ratio of 1:100 was applied. Then, this mixture was separated by centrifugation (Eppendorf) at 5000 rpm for 5 minutes and the obtained powder was dried in an oven at 65 °C for 1 day. By applying the same processes, nickel aluminide powder with the stoichiometry of Ni_{0.55}Al_{0.45} was also produced. Obtained powders were examined by a stereo microscope and scanning electron microscope (SEM, FEI at Süleyman Demirel University). XRD analyses were performed by using Cu-Kα radiation, at a scan rate of 2 degrees per minute, with 0.02 degrees steps (Rigaku, Multiflex at Hatay Mustafa Kemal University). Phase analyses were performed and the 2-theta values of the XRD peaks of the produced samples were acquired by the Quantitative Analysis Software.

Results and Discussion

Adiabatic Temperature

The adiabatic temperature is defined as the theoretical maximum temperature that the products can achieve, as a result of an exothermic reaction. The results of the adiabatic temperature calculations of the Ni-Al systems containing 0-60 vol.% MgO, made by the HSC Chemistry software and database according to Reaction (1) are presented in Fig.2. It can be seen that the adiabatic temperature keeps unchanged up to 25 vol.% MgO addition. 1638.9 °C is the melting temperature of NiAl.

When there is no diluent in the system, a certain fraction of NiAl in the products melts. When the diluent MgO is not sufficient, the high amount of liquid phase formed in the system causes the product pellet to lose its form. The ratio of the liquid phase is expected to decrease with increasing addition of the thermal diluent MgO to the initial mixture. Because, both the amount of Ni+Al that generates heat is reduced, and MgO takes some of the evolved heat.

The adiabatic temperature starts to decrease after 25% addition of MgO. Theoretically, the heat generated after this point is not sufficient to cause the formation of any molten phase, when the ignition temperature is 25 °C. Therefore, there will be no liquid phase formation in the products. As a result of 40% MgO is addition to the Ni+Al mixture, the adiabatic temperature is calculated as 1460.8 °C. Considering the preheating of the pellet and the fact that ignition takes place at about 500°C, the attained combustion temperature may be higher than the calculated adiabatic temperature. However, when the heat losses from the pellet to the substrate and the crucible is taken into account, it is possible to consider the calculated adiabatic temperatures as close to the attained combustion temperatures. Thus, in the present study, according to adiabatic temperature calculations, MgO was added to the reactant mixture in 10, 20, 30 and 40 vol.% range.

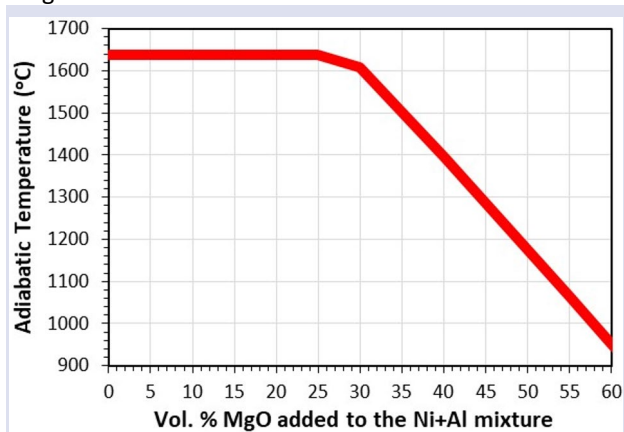


Figure 2. Change in the adiabatic temperature of Ni-Al system as a function of MgO thermal diluent addition.

Form of the Products After VCS

During heating in the induction furnace, the samples were found to ignite at about 660 °C. An increase in the temperature was observed at that point. In some experiments during heating, the pellets that contained 10-30 vol.% MgO exhibited cracking and fragmentation. This was attributed to the fast temperature increase. In the sample which contained 10 vol.% MgO, formation of droplets of NiAl was observed on the surface of the product pellet (Fig. 3(a)). The form of the pellet was seen to be observed much better when 30 vol.% MgO was utilized (Fig. 3(b)).

After VCS, the samples which were obtained with 10-30 vol.% MgO addition were quite hard and difficult to grind. This indicated the partial sintering of the formed particles. It was relatively easier to grind into powder form the samples which contained 40 vol.% MgO.

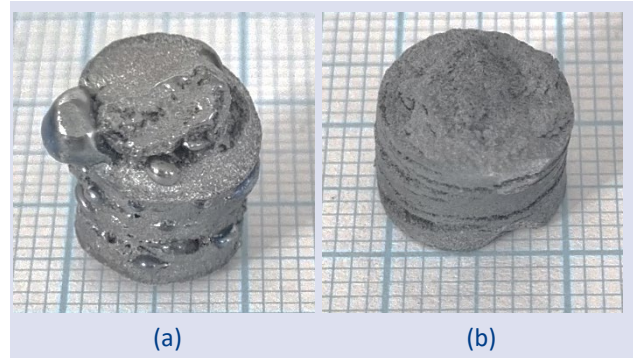


Figure 3. Macro images of the product pellets after VCS having (a) 10 vol.% MgO, (b) 30 vol.% MgO (small squares are 1 x 1 mm²)

Therefore, it was determined that the most suitable MgO ratio for the formation of Ni_{0.50}Al_{0.50} and Ni_{0.55}Al_{0.45} powders was 40 vol.%. This result shows that MgO acted as an effective thermal diluent and melting and sintering of the formed NiAl particles could be prevented.

XRD Analyses After VCS

The production of Ni_{0.50}Al_{0.50} and Ni_{0.55}Al_{0.45} powders was carried out by the same methods. Ni_{0.55}Al_{0.45} composition is in the NiAl solid solution region according to the Ni-Al phase diagram [12]. The XRD patterns of Ni₅₀Al₅₀ and Ni₅₅Al₄₅ powders obtained from VCS reaction of 40 vol.% MgO added reactants, after acid dissolution, centrifugation separation and drying are presented in Fig. 4. The indices of the pertaining planes are indicated on the XRD peaks.

The XRD peaks of Ni₅₅Al₄₅ is expected to be at about 0.1 degrees to higher 2-theta values as compared to those of Ni₅₀Al₅₀ according to the provided international center for diffraction data (ICDD) card values given in Table 1. The obtained results are in favor of this expectation. The 2-theta values of the XRD peaks of the produced samples were acquired by the Quantitative Analysis Software. According to the XRD analysis, it was understood that single phase, pure Ni₅₀Al₅₀ and Ni₅₅Al₄₅ powders were obtained by the applied method. All of the peaks in the XRD patterns in Fig. 4 pertain to the expected phases. From XRD analysis, it was inferred that Reaction (1) was completed and no by-products were formed. In addition, there were no MgO peaks in the XRD patterns. This shows that the MgO used as the thermal diluent was completely removed from the products.

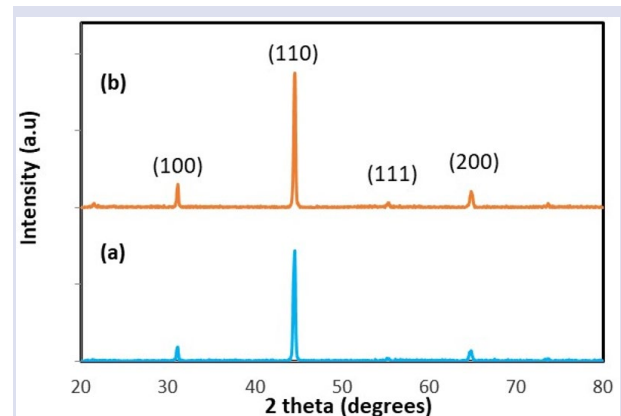


Figure 4. XRD patterns of VCS produced a) Ni_{0.50}Al_{0.50} and b) Ni_{0.55}Al_{0.45} powders.

Table 1. Two-theta and interplanar spacing (d) values of the produced Ni_{0.50}Al_{0.50} and Ni_{0.55}Al_{0.45} powders after VCS, as acquired by the Quantitative Analyses Software. (Crystallographic database values are also presented).

hkl	Ni _{0.50} Al _{0.50} #20-0019		Ni _{0.50} Al _{0.50} After VCS		Ni _{0.55} Al _{0.45} #44-1185		Ni _{0.55} Al _{0.45} After VCS	
	2 theta (deg.)	d (Å°)	2 theta (deg.)	d (Å°)	2 theta (deg.)	d (Å°)	2 theta (deg.)	d (Å°)
100	30.92	2.89	31.05	2.8779	31.08	2.876	31.10	2.8734
110	44.37	2.04	44.50	2.0343	44.51	2.034	44.55	2.0322
111	55.04	1.667	55.10	1.6654	55.26	1.661	55.30	1.6599
200	64.48	1.444	64.80	1.4376	64.77	1.438	64.85	1.3626

The expanded 44-45 degrees region of the XRD patterns of the Ni_{0.50}Al_{0.50} and Ni_{0.55}Al_{0.45} powders are presented in Fig. 5. The peaks pertaining to the (110) planes of the obtained powders can be seen. The Ni_{0.50}Al_{0.50} powder exhibited a double peak at 44.35° and one is at 44.55° 2-theta values. This can be attributed to insufficient diffusion, which may have resulted from quick heating and cooling that took place during VCS. In addition, it is probable that some Al may have been lost, due to probable oxidation during synthesis. Thus, the stoichiometry of the Ni_{0.50}Al_{0.50} powder seems to have slightly shifted to Ni rich values. Nevertheless, the difference in the lattice parameters of the NiAl powders having 2 different compositions can be seen in the XRD analyses. The (110) peak of the Ni_{0.55}Al_{0.45} is at 44.55°.

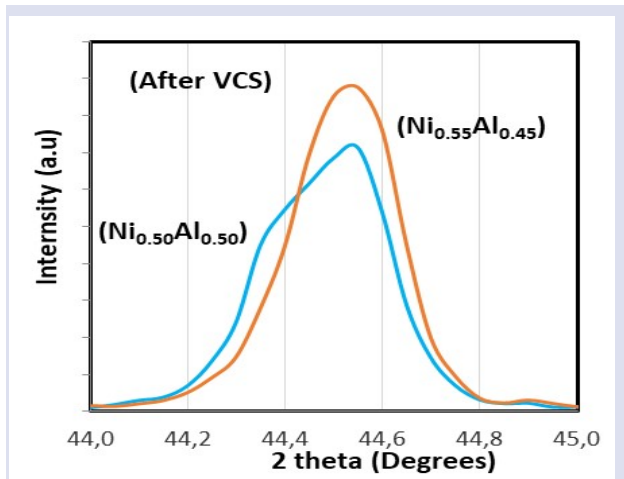


Figure 5. Expanded 44-45 degrees portion of the XRD patterns of VCS produced samples exhibiting the peak pertaining to the (110) plane. Ni_{0.50}Al_{0.50} and Ni_{0.55}Al_{0.45} powders.

XRD Analyses After Annealing

XRD patterns of VCS produced a) Ni₅₀Al₅₀ and b) Ni₅₅Al₄₅ powders after annealing at 1200 °C for 2 h are presented in Fig. 6. It was observed that the width of the XRD peaks decreased after annealing of the produced powders. Similar findings were also reported by Portnoy (2002)[1] after annealing the NiAl powders which were produced by mechanical alloying. The decrease in the width of the XRD peaks may be attributed to the increase in the crystallite size [13].

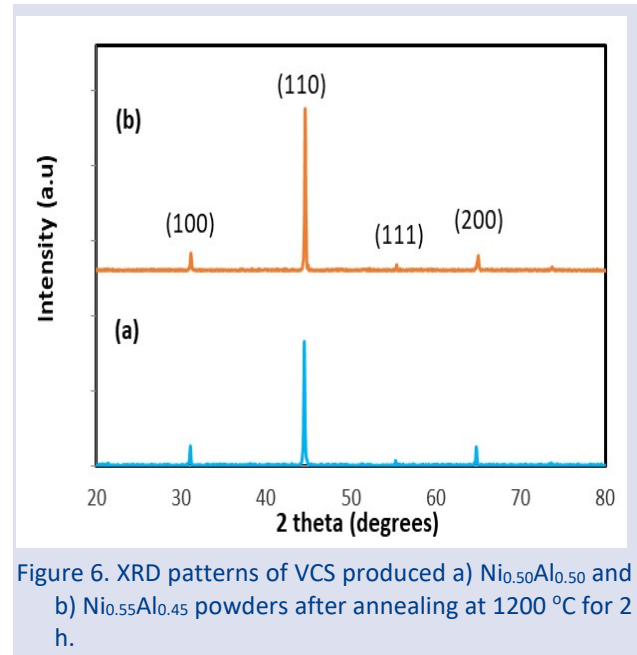


Figure 6. XRD patterns of VCS produced a) Ni_{0.50}Al_{0.50} and b) Ni_{0.55}Al_{0.45} powders after annealing at 1200 °C for 2 h.

In addition, the XRD peaks of Ni₅₅Al₄₅ was seen to which to slightly higher 2-theta values as compared to the non-annealed condition (Table 2).

Table 2 Two-theta and interplanar spacing (d) values of the produced Ni_{0.50}Al_{0.50} and Ni_{0.55}Al_{0.45} powders after annealing at 1200 °C for 2h. (Crystallographic database values are also presented).

hkl	Ni _{0.50} Al _{0.50} #20-0019		Ni _{0.50} Al _{0.50} After VCS and annealing at 1200 oC		Ni _{0.55} Al _{0.45} #44-1185		Ni _{0.55} Al _{0.45} After VCS and annealing at 1200 oC	
	2 theta (deg.)	d (Å°)	2 theta (deg.)	d (Å°)	2 theta (deg.)	d (Å°)	2 theta (deg.)	d (Å°)
100	30.92	2.89	31.10	2.8734	31.08	2.876	31.15	2.8689
110	44.37	2.04	44.50	2.0343	44.51	2.034	44.60	2.030
111	55.04	1.667	55.30	1.6599	55.26	1.661	55.35	1.6585
200	64.48	1.444	64.75	1.4386	64.77	1.438	65.00	1.4336

The expanded 44-45 degrees region of the XRD patterns of the $\text{Ni}_{0.50}\text{Al}_{0.50}$ and $\text{Ni}_{0.55}\text{Al}_{0.45}$ powders after annealing are presented in Fig. 7. The double peak which was present in the XRD pattern of $\text{Ni}_{0.50}\text{Al}_{0.50}$ powder before annealing was seen to convert into a single peak at 44.50 degrees. This is believed to take place due to diffusion during annealing at 1200 °C. The (110) peak of the $\text{Ni}_{0.55}\text{Al}_{0.45}$ is at 44.60°. The 2-theta values of the $\text{Ni}_{0.55}\text{Al}_{0.45}$ sample is at about 0.1 degrees higher 2-theta values, as compared to $\text{Ni}_{0.50}\text{Al}_{0.50}$ sample. This result is in accordance with the ICDD data. The width of the peaks can be seen to decrease by annealing, as compared to the peaks of the non-annealed samples given in Fig.5. These results are in agreement with the literature. In the study of Portnoy (2002), similar results were obtained.

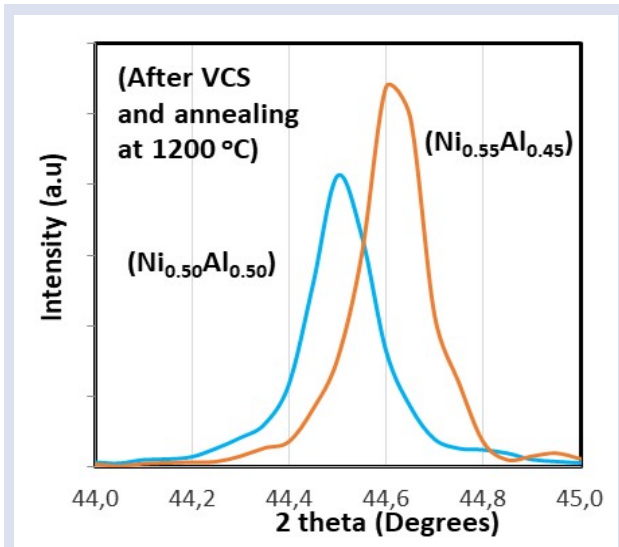


Figure 7. Expanded 44-45 degrees portion of the XRD patterns of VCS produced samples after annealing at 1200 °C for 2 h, exhibiting the peak pertaining to the (110) plane. $\text{Ni}_{0.50}\text{Al}_{0.50}$ and $\text{Ni}_{0.55}\text{Al}_{0.45}$ powders.

Microscopic Examination of the Produced Powders

Macro image of the produced $\text{Ni}_{0.50}\text{Al}_{0.50}$ powder, which was obtained by a stereo microscope, is presented in Fig. 8. The NiAl powder can be seen as the black particles on the graded paper (small squares are 1 x 1 mm²). The product pellet could be finely ground. Particles having sizes below 100 µm were obtained. No difference in the size and morphology of the produced NiAl powders having different compositions was observed by the microscopic examinations.

SEM images of the prepared powders are presented in Figure 4. In SEM examinations, it was observed that the produced NiAl particles had irregular shape. They generally consisted of 5-10 µm sized parts (Figure 4 (a)) and partially incompletely fragmented porous chunks of about 100 µm (Figure 9). Formed powders were in 5-100 µm particle size range.

It can be proposed that the particles size of the formed powder can be modified by altering the duration of grinding operation.

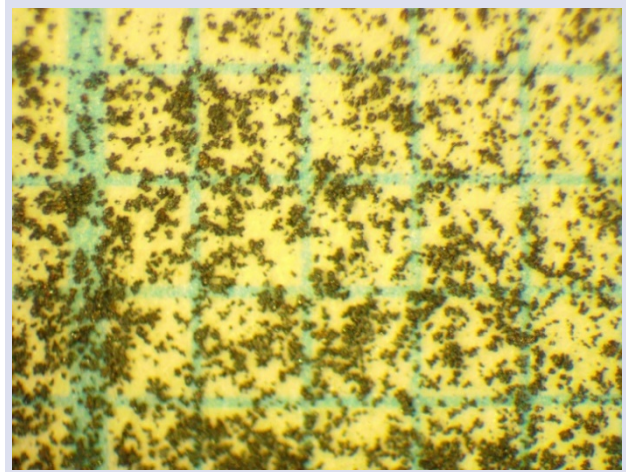


Figure 8. Macro image of the produced $\text{Ni}_{0.50}\text{Al}_{0.50}$ powder (small squares: 1 x 1 mm²)

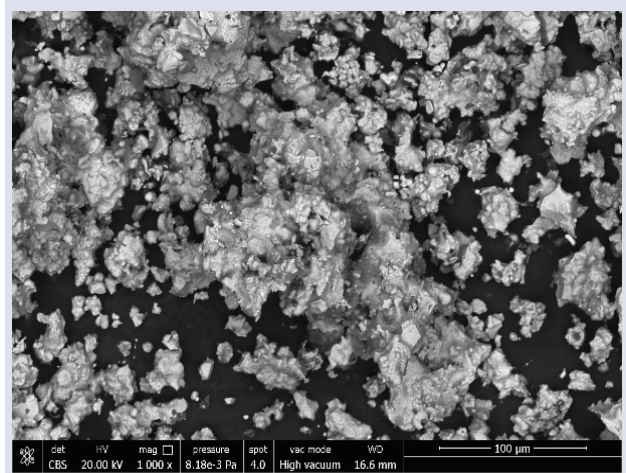


Figure 9. SEM image of the produced NiAl powder (1000X)

The chunks are seen to have a porous character (Fig. 10). This may be due to the removed MgO particles from the structure. In addition, during the reaction between Ni and Al, micro porosity was suggested to form due to Kirkendall effect, and also due to the density difference between the reactants and the products.

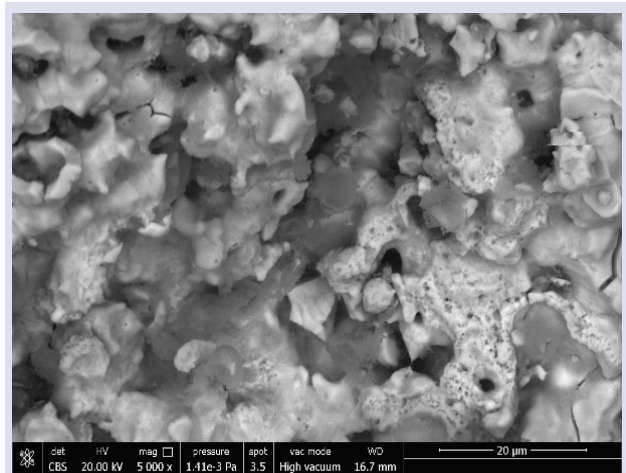


Figure 10. SEM images of the produced NiAl powder showing the structure of a large particle (5000 X)

Conclusion

Formation of $\text{Ni}_{0.50}\text{Al}_{0.50}$ and $\text{Ni}_{0.45}\text{Al}_{0.55}$ powders was achieved by volume combustion synthesis through heating the Ni, Al and 40 vol.% MgO powder mixtures in an induction furnace. When the samples were produced by adding 10-20 vol. % MgO, they exhibited partial melting. The samples which contained 10-30 vol. % MgO were hard and difficult to grind. As the MgO ratio by volume increased (40% MgO), it was easier to grind the produced samples. For this reason, the 40% vol. MgO was chosen as the most suitable ratio for the production of NiAl powders. The particle sizes of the produced powders were in the range of 5-100 μm . Formation of single-phase pure powders of $\text{Ni}_{0.50}\text{Al}_{0.50}$ and $\text{Ni}_{0.45}\text{Al}_{0.55}$ were verified by XRD analyses. After annealing the powders, the XRD peaks of the $\text{Ni}_{0.55}\text{Al}_{0.45}$ powder were at about 0.1 degrees higher 2-theta values as compared to the $\text{Ni}_{0.50}\text{Al}_{0.50}$ phase. The results were in agreement with the crystallographic data.

Acknowledgements

Authors thank to Akdeniz University Scientific Research Projects Coordination Unit for supporting this study with Project No: FDK-2021-5653.

Conflict of Interest

Authors declare no conflict of interest.

References

- [1] Portnoy V. K., Blinov A.M., Tomilin I. A., Kuznetsov V. N., Kulik T, Formation of nickel aluminides by mechanical alloying and thermodynamics of interaction, *J. Alloys Compd.*, 336(1-2) (2002) 196-201.
- [2] Pasturel A., Colinet C., Paxton A.T., Van Schilfgaarde M., First-principles determination of the Ni-Al phase diagram, *J. Phys. Condens.*, 4(4) (1992) 945.
- [3] Bochenek K., Basista M., Advances in processing of NiAl intermetallic alloys and composites for high temperature aerospace applications, *Prog. Aerosp. Sci.*, 79 (2015) 136-146.
- [4] Scheppe F., Sahm P.R., Hermann W., Paul U., Preuhs J., Nickel aluminides: a step toward industrial application, *Mater. Sci. Eng. A* , 329 (2002) 596-601.
- [5] Povarova K.B., Skachkov O.A., Kazanskaya N.K., Drozdov A.A., Morozov A. E., Makarevich O. N., NiAl powder alloys: I. Production of NiAl powders, *Russ. Metall.*, 2011 (2011) 844-852.
- [6] Kaplanskii Y.Y., Zaitsev A.A., Sentyurina Z.A., Levashov E.A., Pogozhev Y.S., Loginov P.A., Logachev I.A., The structure and properties of pre-alloyed NiAl-Cr (Co, Hf) spherical powders produced by plasma rotating electrode processing for additive manufacturing, *J. Mater. Res. Technol.*, 7(4) (2018) 461-468.
- [7] Varma A., Rogachev A.S., Mukasyan A.S., Hwang S., Combustion synthesis of advanced materials: principles and applications, *Adv. Chem. Eng.*, 24 (1998) 79-226.
- [8] Liu Y., Cai X., Sun Z., Zhang H., Akhtar F., Czujko T., Feng P., Fabrication and Characterization of Highly Porous FeAl-Based Intermetallics by Thermal Explosion Reaction, *Adv. Eng. Mater.*, 21(4) (2019) 1801110.
- [9] Yeh C.L., Su S.H., Chang H.Y., Effects of TiC addition on combustion synthesis of NiAl in SHS mode, *J. Alloys Compd.*, 398(1-2) (2005) 85-93.
- [10] Sariyer G., Çamurlu, H.E., Effect of Diluent Amount on Properties of Porous NiAl, *Gazi Univ. J. Sci. Part A : Eng. Innov.*, 9(4) (2022) 429-438.
- [11] Terada Y., Ohkubo K., Mohri T., Suzuki T., Thermal conductivity of intermetallic compounds with metallic bonding, *Mater. Trans.*, 43 (12) (2002) 3167-3176.
- [12] López G.A., Sommadossi S., Gust W., Zieba P., Phase Characterization of Diffusion Soldered Ni/Al/Ni Interconnections, *Interface Science* 10(1) (2002) 13-19.
- [13] Cullity B.D., Elements of X-ray Diffraction, Addison-Wesley Publishing, (1956).

Treatment of Sugar Industry Wastewater via Fenton Oxidation with Zero-Valent Iron

Ceren Orak ^{1,a,*}

¹ Department of Chemical Engineering, Faculty of Engineering and Natural Sciences, Sivas University of Science and Technology, Sivas, Türkiye.

*Corresponding author

Research Article

History

Received: 17/07/2023

Accepted: 02/01/2024




This article is licensed under a Creative Commons Attribution-NonCommercial 4.0 International License (CC BY-NC 4.0)

ABSTRACT

The sugar industry is a significant contributor to wastewater production, primarily due to its substantial water usage. The treatment and reuse of this wastewater have become pressing concerns. In the present study, sugar industry wastewater was treated via Fenton oxidation using zero-valent iron (ZVI). The study focused on assessing the impact of key reaction parameters, namely pH, ZVI amount, $[H_2O_2]_0$ on the removal of TOC. Optimal reaction conditions for the Fenton oxidation process were identified, with a pH of 3.5, 2 g/L of ZVI, and 4 mM of H_2O_2 , resulting in nearly 65% of TOC removal. The kinetic study revealed that the observed reaction adhered to a second-order kinetic reaction model. Furthermore, the activation energy for this observed reaction was determined as 49.14 kJ/mol. These findings suggest that Fenton oxidation, utilizing ZVI, holds promise as an effective method for treating wastewater originating from the sugar industry.

Keywords: Wastewater treatment, Fenton oxidation, Sugar industry, Zero-valent iron.

 crn.orak@gmail.com

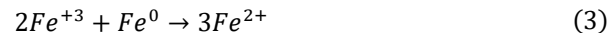
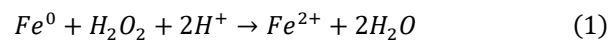
 <https://orcid.org/0000-0001-8864-5943>

Introduction

Various industries (i.e., textile, paper, sugar, petrochemistry, etc.) generate a large amount of wastewater and industrial wastewater streams are one of the important contamination sources in the water environment. Therefore, it could lead to serious problems in the water environment and it might cause negative impacts on the ecosystem and human life. [1-4]. Before discharge, they must be treated and several wastewater treatment methods were applied to reduce TOC, COD, and BOD in various wastewater streams. In this context, the Fenton process is an effective, feasible control, and inexpensive wastewater treatment method in Advanced Oxidation Processes (AOPs) that have some advantages over biological treatment methods. Additionally, it could be used for the remediation of recalcitrant and biologically non-degradable compounds in industrial wastewater streams and it is applicable to various industrial wastewater streams [5, 6]. For instance, in the literature, it was used for the treatment of olive mills, textiles, antibiotics wastewater, etc. [7-10]. In addition to them, it could be used for sugar industry wastewater which produces large amounts of wastewater due to the high amount of water usage in sugar production steps. Turkey is the fifth country among the sugar beet producer countries in the world and a high amount of sugar is produced in our country [11]. Due to the production process of sugar, a high amount of wastewater is generated in the sugar factories in Turkey so they should be treated since they contain organic and inorganic

compounds that are hazardous to the water and soil environment if they accumulate in these environments [12, 13]. Therefore, the remediation of sugar industry wastewater has become a significant concern for environmental health.

Zero-valent iron (ZVI) could be a good alternative to remediate the sugar industry wastewater via Fenton oxidation since it is non-toxic and inexpensive. In addition, it has high reactivity and fast kinetics and thus, it has some advantages in Fenton-like processes [5, 7-9]. In the presence of H_2O_2 , iron ions easily release in acidic reaction media to initiate the Fenton reaction and these reactions are given in equation (1) and equation (2). Thereafter, the generated ferric ions react with ZVI as given in equation (3) and hence, a continuous Fenton-like reaction could be achieved [5].



To our knowledge, various wastewater treatment methods based on biological and chemical treatment were used to treat sugar industry wastewater, however, it has not been treated via Fenton-like oxidation using ZVI. Therefore, in this study, ZVI was used to treat sugar industry wastewater, and the impact of reaction parameters (pH, initial H_2O_2 concentration, ZVI amount) over TOC removal % from sugar industry wastewater was investigated.

Material and Method

Sugar industry wastewater was supplied from Eskişehir Sugar Factory (Eskişehir, Turkey) and its characterization study was published elsewhere [14]. The other chemicals (ZVI (≥ 99.9), H_2O_2 (35%), HCl (37%), and NaOH (≥ 97 , pellet)) were supplied from Sigma-Aldrich.

The experimental study was carried out using 100 mL of sugar industry wastewater at room temperature and the pH of wastewater was adjusted to the desired pH using 0.1 M of HCl and NaOH solutions. After pH adjustment, desired amounts of ZVI (1-4 g/L) and H_2O_2 (2-10 mM) were added into the wastewater. The experiments were carried out for 1 h and hence, the impacts of catalyst amount and initial H_2O_2 concentration over TOC removal % from sugar industry wastewater were investigated. The experimental set-up and conditions are given in Figure 1(a) and Figure 1(b), respectively. All experiments were performed three times and at the end of the experiments, liquid products were analyzed via TOC (Shimadzu TOC-Vcph TNM-1/SSM-5000A) to determine TOC removal % from sugar industry wastewater.

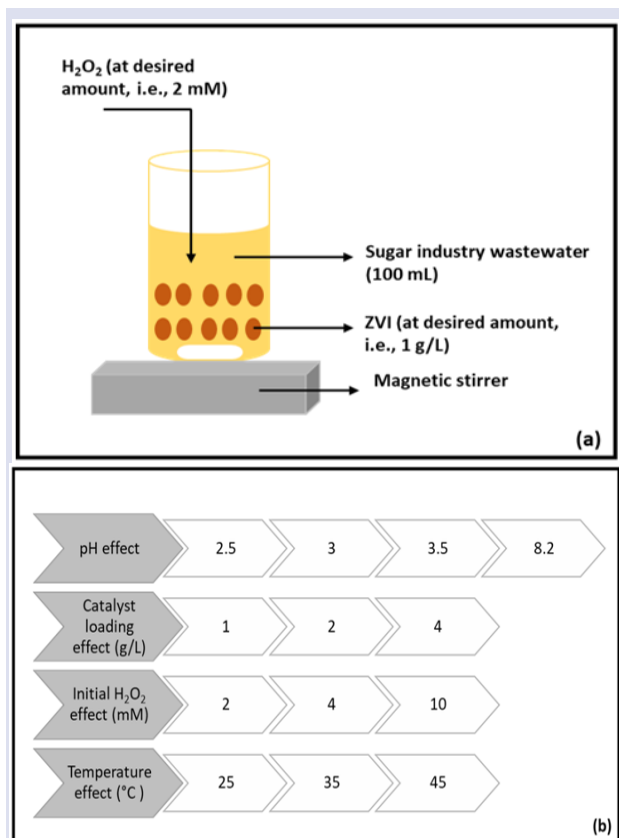


Figure 1. Experimental set-up (a) and reaction conditions (b)

Results and Discussion

The treatment of the sugar industry has significant importance because it consumes a high volume of water during sugar production. In the sugar production process, water is used to remove impurities by washing and flotation. Due to the high consumption of water, a high volume of wastewater is generated by the sugar industry

[13,15]. In this study, sugar industry wastewater was treated via Fenton oxidation using ZVI, and impacts of reaction parameters (pH, ZVI loading, and, initial H_2O_2 concentration) and reaction temperature were investigated. The effect of pH of sugar industry wastewater was investigated within 2.5 and 8.2 (natural pH of sugar industry wastewater) of pH and the results are given in Figure 2. The highest TOC removal efficiency ($\sim 20\%$) was achieved at a pH of 3.5 whereas the lowest TOC removal was observed at the natural pH of sugar industry wastewater. Almost the same degradation efficiency was observed for pH 2.5 and 3. In acidic media, the formation of $\bullet\text{OH}$ radicals that are highly reactive to degrade organic compounds could enhance and it is expected that higher TOC removal efficiency might be observed with a decrease in pH [16, 17]. In this study, higher TOC removal efficiencies were observed in acidic reaction media and it is consistency with the literature. Therefore, the optimum pH value was selected as 3.5 for the sugar industry wastewater treatment using ZVI since usage of less amount of HCl acid to arrange the pH value of sugar industry wastewater offers an economical benefit. In addition, the set-up might prevent from its corrosive effects for a long term.

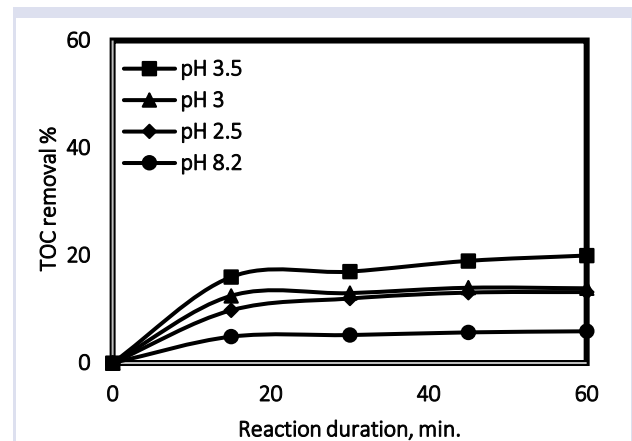


Figure 2. pH effect (Reaction conditions: 100 mL sugar industry wastewater, pH: 2.5-8.2, ZVI: 1 g/L, $[\text{H}_2\text{O}_2]_0$: 2 mM, T: 25 $^{\circ}\text{C}$ t: 60 min)

After that, the effect of ZVI amount was investigated, and the results are given in Figure 3. The highest removal efficiency was observed using 4 g/L of ZVI. However, there is no significant difference between the TOC removal % when 2 g/L or 4 g/L of ZVI was used for the treatment of sugar industry wastewater. ZVI amount doubling did not result in a twofold increase in TOC removal efficiency. It only caused almost a %5 increase in TOC removal efficiency and thus, it is not considerable to use 4 g/L of ZVI. In addition, the usage of iron species might cause iron leaching in treated wastewater streams, and the allowable iron limit in drinking waters based on EU regulation is 0.2 ppm [18, 19]. To determine the optimum ZVI amount, the increase in TOC removal % should be considered alongside with the iron concentration that will leach into the treated wastewater. Therefore, to avoid the

excess usage of ZVI and higher leaching amounts of ZVI in treated sugar industry wastewater, the optimum ZVI loading was selected as 2 g/L.

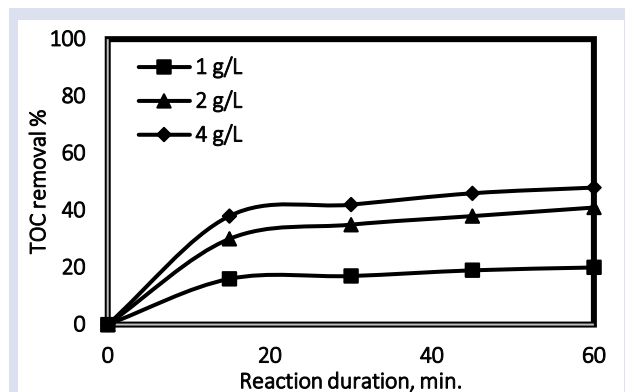


Figure 3. ZVI loading effect (Reaction conditions: 100 mL sugar industry wastewater, pH: 3.5, ZVI: 1-4 g/L, $[H_2O_2]_0$: 2 mM, T: 25 °C t: 60 min)

Another significant reaction parameter is the initial H_2O_2 concentration for Fenton processes because excessive usage of hydrogen peroxide might cause a scavenging effect so it should be optimized [20-22]. For this purpose, the experiments were carried out using 2, 4, and 10 mM of hydrogen peroxide, and the results are given in Figure 4. The utilization of 4 mM H_2O_2 demonstrated nearly double TOC removal efficiency compared to the usage of 2 mM. Therefore, it can be inferred that doubling the initial H_2O_2 concentration leads to a doubling of TOC removal.

The highest TOC removal % was observed using 10 mM of H_2O_2 ; however, it is not a considerable increase. In addition, H_2O_2 is generally considered to be a relatively environmentally friendly compound when used in appropriate concentrations and applications. However, like any chemical substance, hydrogen peroxide can have hazardous effects on environmental health under certain conditions. For instance, high concentrations of H_2O_2 may be toxic to aquatic organisms, including fish and other aquatic life. Discharge of untreated or high-strength H_2O_2 into water bodies may result in adverse effects on the local aquatic ecosystem [23-24]. Thus, considering the economic and environmental reasons, it could be decided that the usage of a lower concentration of H_2O_2 is more appropriate since in this study, a real wastewater stream was treated and hence, to avoid high H_2O_2 concentration in the treated wastewater, 4 mM of H_2O_2 was selected as the optimum initial H_2O_2 concentration. Consequently, optimum reaction conditions for the treatment of real sugar industry wastewater using ZVI were determined as pH of 3.5, 2 g/L of ZVI, and 4 mM of H_2O_2 , and almost 65% of TOC removal was achieved at these reaction conditions.

In literature, Kallel et al. studied the treatment of olive-mill wastewater via Fenton oxidation using ZVI and H_2O_2 . They found that higher COD removal was achieved at acidic reaction media (pH 2-4). Also, 20 g/L and 9.5 M were selected as the optimum ZVI amount and H_2O_2 concentration, respectively [8]. In addition to this study,

Kallel et al. carried out another study to remove phenolic compounds from olive mill wastewater in the presence of ZVI and they found similar results [9]. In the present study, to treat sugar industry wastewater, relatively lower amounts of ZVI and H_2O_2 were used. Consequently, the results are in line with the literature.

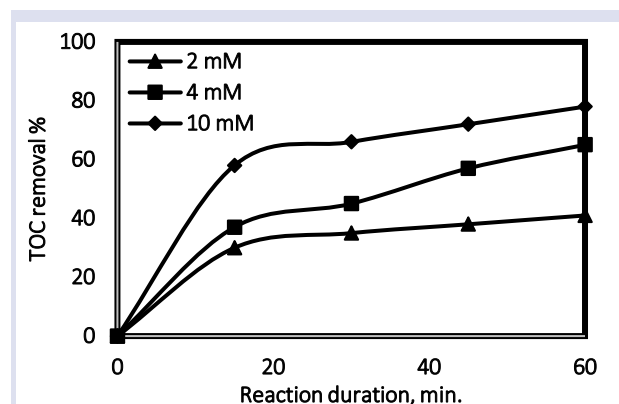


Figure 4. Initial H_2O_2 effect (Reaction conditions: 100 mL sugar industry wastewater, pH: 3.5, ZVI: 2 g/L, $[H_2O_2]_0$: 2-10 mM, T: 25 °C t: 60 min)

After that, a kinetic study was carried out to comprehend the characteristics of the reaction that occurred during the treatment of the sugar industry wastewater via Fenton using ZVI. In this context, the experiments were carried out at the optimum reaction conditions, and the effect of reaction temperature was investigated at 25, 35, and 45 °C. The results were given in Figure 5 and the obtained experimental data was analyzed to determine the reaction kinetic model and rate constants. The experimental data were fitted to the second-order reaction model and the linearized second-order kinetic model was given in Figure 6. The reaction rate constants were found as 0.00002, 0.00003, 0.00007 for 25, 35, and 45 °C and the activation energy for this reaction was determined from Figure 6 as 49.14 kJ/mol. In the literature, cork, and olive mill wastewater were treated using $Fe^{+2}:H_2O_2$, and the activation energies were found as 70.7 and 28.2 kJ/mol, respectively [25, 26]. Consequently, the determined activation energy in this study is in line with the previously reported values.

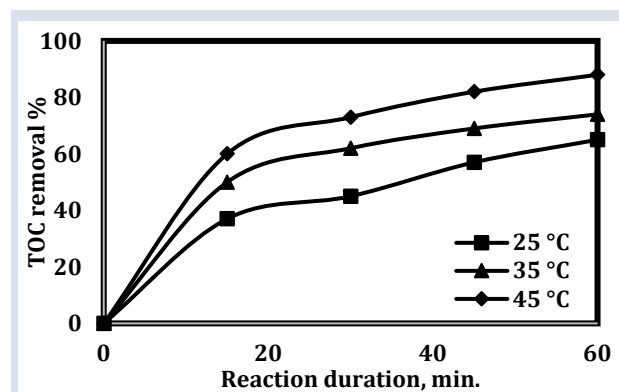


Figure 5. Temperature effect (Reaction conditions: 100 mL sugar industry wastewater, pH: 3.5, ZVI: 2 g/L, $[H_2O_2]_0$: 4 mM, T: 25-45 °C t: 60 min)

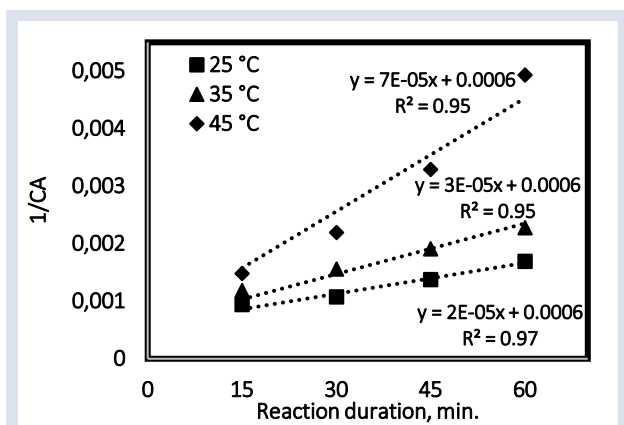


Figure 6. Linearized second-order kinetic plot (Reaction conditions: 100 mL sugar industry wastewater, pH: 3.5, ZVI: 2 g/L, [H₂O₂]₀: 4 mM, T: 25-45 °C t: 60 min)

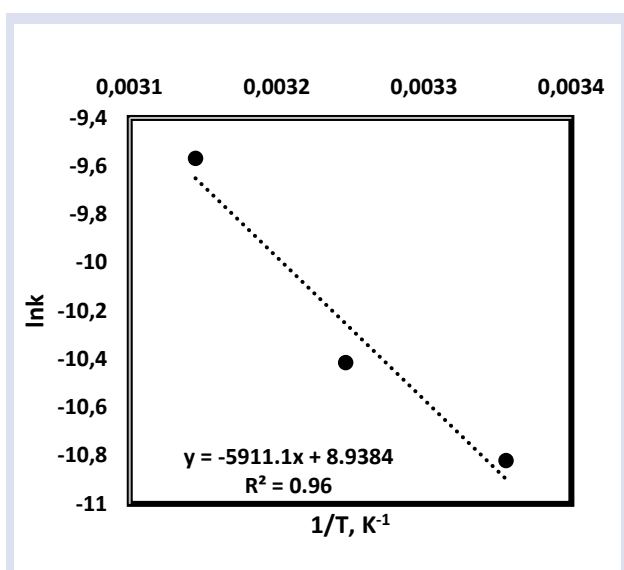


Figure 7. lnk vs 1/T

Conclusion

The sugar industry stands out as one of the major contributors to wastewater generation, underscoring the critical need for effective reuse and treatment methods within this sector. This study focused on employing Fenton oxidation in the presence of ZVI to treat wastewater from the sugar industry. Various wastewater treatment processes were explored previously, and the impact of different reaction parameters on the removal of total organic carbon (TOC) was assessed. Optimal conditions were identified as a pH of 3.5, 2 g/L of ZVI, and 4 mM of H₂O₂ in this study. Furthermore, the influence of reaction temperature was examined, and the results of kinetic study indicated that the observed reaction adhered to a second-order kinetic reaction model, with the activation energy calculated at 49.14 kJ/mol. These findings contribute to our understanding of effective wastewater treatment methods for the sugar industry, emphasizing the importance of specific reaction conditions in achieving optimal results.

Acknowledgment

I would like to thank Assoc. Prof. Dr. Aslı Yüksel Özşen and Assoc. Prof. Dr. Gülin Ersöz for their help and support to carry out this study.

Conflicts of interest

There are no conflicts of interest in this work.

References

- [1] Ashrafi O., Yerushalmi L., Haghighat F. Wastewater treatment in the pulp-and-paper industry: A review of treatment processes and the associated greenhouse gas emission, *J. Environ. Manage.*, 158 (2015) 146-157.
- [2] Kishor R., Purchase D., Saratale G. D., Saratale R. G., Ferreira L. F. R., Bilal M., Chandra R., Bharagava R. N. Ecotoxicological and health concerns of persistent coloring pollutants of textile industry wastewater and treatment approaches for environmental safety, *J. Environ. Che. Eng.*, 9 (2021) 105012-105029.
- [3] Verma S., Kumar P., Srivastava V. C., Ştanger U. L., Application of Advanced Oxidation Processes (AOPs) for the Treatment of Petrochemical Industry Wastewater In: Roy, S., Garg, A., Garg, S., Tran, T.A. (eds) *Advanced Industrial Wastewater Treatment and Reclamation of Water, Environ. Sci. Eng.*, (2021) 103-128.
- [4] Rakhmania; Kamyab H., Yuzir M. A., Abdullah N., Quan L. M., Riyadi F. A., Marzouki R., Recent Applications of the Electrocoagulation Process on Agro-Based Industrial Wastewater: A Review, *Sustainability*, 14 (2022) 1985-1204.
- [5] Raji M., Mirbagheri S. A., Ye F., Dutta J., Nano zero-valent iron on activated carbon cloth support as Fenton-like catalyst for efficient color and COD removal from melanoidin wastewater, *Chemosphere*, 263 (2021) 127945-127954.
- [6] Xie S., Su J., Zhao J., Yang H., Qian H., An amorphous zero-valent iron decorated by Fe₃O₄ significantly improves the Fenton-like reaction, *J. Alloys Compd.*, 929 (2022) 167306-167315.
- [7] Kallel M., Belaid C., Mechichi T., Ksibi M., Elleuch B., Removal of organic load and phenolic compounds from olive mill wastewater by Fenton oxidation with zero-valent iron, *Che. Eng. J.*, 150 (2009) 391-395.
- [8] Kallel M., Belaid C., Boussahel R., Ksibi M., Montiel A., Elleuch B., Olive mill wastewater degradation by Fenton oxidation with zero-valent iron and hydrogen peroxide. *J. Hazard. Mater.*, 163 (2009) 550-554.
- [9] Furia F., Minella M., Gosetti F., Turci F., Sabatino R., Di Cesare A., Corno G., Vione D., Elimination from wastewater of antibiotics reserved for hospital settings, with a Fenton process based on zero-valent iron, *Chemosphere*, 283 (2021) 131170-131169.
- [10] Çalık Ç., Çiftçi D. İ., Comparison of kinetics and costs of Fenton and photo-Fenton processes used for the treatment of a textile industry wastewater, *J. Environ. Manage.*, 304 (2022) 114234-114239.
- [11] www.sekerkurumu.gov.tr (access date: 12.12.2022)
- [12] Kaya Ş., Asçı Y., Application of Combined Ultrasound and Fenton Reagent in Sugar Industry Wastewater Treatment, pp. 273-283. Atik, A. ed. 2019. *Research & Reviews in Engineering*. Gece Kitaplığı, Turkey, 361s.

- [13] Kushwaha J. P., A review on sugar industry wastewater: sources, treatment technologies, and reuse, *Desalin. Water Treat.*, 53(2) (2013) 309-318.
- [14] Orak C., Yüksel A., Photocatalytic hydrogen energy evolution from sugar beet wastewater, *ChemistrySelect*, 6(43) (2021) 12266-12275.
- [15] Orak C., Öcal B., Yüksel A., Treatment of Sugar Industry Wastewater by Using Subcritical Water as a Reaction Media, *ChemistrySelect*, 8(1) (2023), e202203300.
- [16] Rezaei F., Vione D., Effect of pH on Zero Valent Iron Performance in Heterogeneous Fenton and Fenton-Like Processes: A Review, *Molecules*, 23 (2018) 3127-3154.
- [17] Donadelli J. A., Carlos L., Arques A., Einschlag F. S. G., Kinetic and mechanistic analysis of azo dyes decolorization by ZVI-assisted Fenton systems: pH-dependent shift in the contributions of reductive and oxidative transformation pathways, *App. Catal. B-Environ.*, 231 (2018) 51-61.
- [18] Ramirez J. H., Maldonado-Hódar F. J., Pérez-Cadenas A. F., Moreno-Castilla C., Costa C. A., Maderina L. M., Azo-dye Orange II degradation by heterogeneous Fenton-like reaction using carbon-Fe catalysts, *App. Catal. B-Environ.*, 75 (2007) 312-323.
- [19] Orak C., Atalay S., Ersöz G., Photocatalytic and photo-Fenton-like degradation of methylparaben on monolith-supported perovskite-type catalysts, *Sep. Sci. Technol.*, 52(7) (2017) 1310-1320.
- [20] Li W., Wang Y., Irini A., Effect of pH and H₂O₂ dosage on catechol oxidation in nano-Fe₃O₄ catalyzing UV-Fenton and identification of reactive oxygen species, *Che. Eng. J.*, 244 (2014) 1-8.
- [21] Hwang S., Huling S. G., Ko S., Fenton-like degradation of MTBE: Effects of iron counter anion and radical scavengers, *Chemosphere*, 78 (2010) 563-568.
- [22] Jiang C., Pang S., Ouyang F., Ma J., Jiang J., A new insight into Fenton and Fenton-like processes for water treatment, *J. Hazard. Mater.*, 174 (2010) 813-817.
- [23] Razas O., Vidal C., Baeza C., Jardim W. F., Rossner A., Mansilla H. D., Organic micropollutants (OMPs) in natural waters: Oxidation by UV/H₂O₂ treatment and toxicity assessment, *Water Res.*, 98 (2016) 109-118.
- [24] de Oliveira T. D., Martini W. S., Santos M. D. R., Matos M. A. C., da Rocha L. L., Caffeine Oxidation in Water by Fenton and Fenton-Like Processes: Effects of Inorganic Anions and Ecotoxicological Evaluation on Aquatic Organisms, *J. Brazil Chem. Soc.*, 26(1) (2015) 178-184.
- [25] Guedes A. M. F. M., Madeira L. M. P., Boaventura R. A. R., Costa C. A. V., Fenton oxidation of cork cooking wastewater—overall kinetic analysis, *Water Res.*, 37 (2003) 3061-3069.
- [26] Lucas M. S., Peres J. A., Removal of COD from olive mill wastewater by Fenton's reagent: Kinetic study, *J. Hazard. Mater.*, 168 (2009) 1253-1259.

Cytotoxicity Analysis of the Effects of *Heterobasidion Annosum* Mycelia and Cisplatin on Colon Adenocarcinoma (CACO-2) Cell Line

Çiğdem Sevim ^{1,a,*}, Sabri Ünal ^{2,b}, Temel Kan Bakır ^{3,c}, Mertcan Karadeniz ^{2,d}, Ali Taghizadeh ^{4,e}

¹ Department of Medical Pharmacology, Faculty of Medicine, Kastamonu University, Kastamonu, Türkiye.

² Department of Forest Engineering, Faculty of Forestry, Kastamonu University, Kastamonu, Türkiye.

³ Department of Chemistry, Faculty of Science, Kastamonu University, Kastamonu, Türkiye.

⁴ Department of Medical Pharmacology, Faculty of Medicine, University of Bilecik Şeyh Edebali, Bilecik, Türkiye.

*Corresponding author

Research Article

History

Received: 08/09/2023

Accepted: 27/02/2024



This article is licensed under a Creative Commons Attribution-NonCommercial 4.0 International License (CC BY-NC 4.0)

ABSTRACT

Colorectal cancer ranks as the third most prevalent form of cancer and stands as the second leading cause of mortality. Both environmental and genetic risk factors contribute to its manifestation. Presently, 5-fluoruracil/leucovorin (5-FU/LV) remains the recommended course for adjuvant therapy in addressing this condition. Conversely, mushrooms, celebrated for their biologically active constituents, including valuable enzymes, have emerged as a captivating subject in diverse medical disciplines, particularly within the realm of cancer therapy, due to their promising therapeutic properties. This specific investigation aimed to conduct in vitro cytotoxic experiments using extracts obtained from *Heterobasidion annosum* micelles cultivated in a liquid malt extract medium. The pulverized extracts were dissolved in Dulbecco's Modified Eagle Medium (DMEM) at varied concentrations ranging from 25ng/mL to 200ng/mL and subsequently administered to colon adenocarcinoma (Caco-2) cells. The cytotoxic effects of both the fungus and cisplatin, a well-known anticarcinogenic agent, were examined at intervals of 24, 48, and 72 hours. The findings indicated a significant inhibition of cancer cell development within this timeframe. Moreover, a noteworthy discovery emerged, revealing that cisplatin, known for its efficacy in various cancer studies, substantially diminished the viability of cancer cells after 72 hours in comparison to the control group.

Keywords: Cisplatin, Colon adenocarcinoma, *Heterobasidion annosum*.

^a cigdemsevim@kastamonu.edu.tr ^{id} <https://orcid.org/0000-0002-0575-3090>

^c temelkan@kastamonu.edu.tr ^{id} <https://orcid.org/0000-0002-7447-1468>

^e ali.tgzd@bilecik.edu.tr ^{id} <https://orcid.org/0000-0002-3506-0324>

^b sabriunal@kastamonu.edu.tr ^{id} <https://orcid.org/0000-0002-3026-0597>

^d mkaradeniz@kastamonu.edu.tr ^{id} <https://orcid.org/0000-0002-3627-9424>

Introduction

Colorectal cancer is the third most commonly diagnosed and second most lethal type of malignancy in which environmental and genetic risk factors play a role [1]. Adenocarcinomas account for more than 90% of this cancer type. Currently, the main treatment principle for non-metastatic stage colon cancer is surgical resection. Although neoadjuvant treatment is not standard, if surgery is planned in advanced disease, adjuvant treatment in stage 3 (node-positive) patients and surgery in combination with chemotherapy in oligo-metastatic lung and liver disease provide curative benefit [1–3]. Adjuvant fluoruracil (5-FU)-based chemotherapy has become the standard for stage 3 colon cancer. 6 months of adjuvant therapy with the combination of leucovorin (LV), 5-FU has been shown to improve 5-year disease-free survival. In a study conducted in 2004 by adding drugs such as oxaliplatin, capecitabine, and irinotecan, the effect of adjuvant 5-FU/LV on survival times was investigated [1]. Dichlorodiammineplatinum II (also known as cisplatin) is the initial platinum compound that has been approved by the Food and Drug Administration (FDA) for treating cancer. It has demonstrated anti-cancer properties in a range of tumors, including ovarian,

testicular, as well as head and neck tumors [4]. Studies have shown that cisplatin, a heavy metal complex, shows significant activity in human colorectal carcinoma cell lines. The primary organs typically impacted by cisplatin toxicity include the liver, heart, kidney, and auditory system. However, given the nature of cell damage induced by cisplatin, it is plausible that all organs could be potentially affected. As an illustration, to mitigate cisplatin-induced kidney damage, outpatient treatment often includes strategies such as maintaining hydration in all patients and administering magnesium supplements along with forced diuresis using mannitol [5,6]. At this juncture, the inclusion of various natural agents with anticarcinogenic properties and minimal adverse effects alongside chemotherapy hints at the potential for mitigating these side effects. Otherwise, there is a strong relationship between colorectal cancer patients and fungal microbiota profiles. Therefore, therapeutic methods used to alter the composition and activity of the gut microbiota have been investigated and, although controversial, effective results have been found [7]. At this point, the question of to what extent we can

benefit from fungi with high environmental contributions that are not present in the microbiota comes to the fore.

Recently, there has been an increase in the desire for safer and more effective therapeutic agents for the chemoprevention of cancer. As a result, natural ingredients including fruits, vegetables, plant extracts, and herbs are essential to the chemotherapeutic treatment of cancer [8,9]. This demonstrates how natural products will significantly impact cancer chemotherapy in the future.

Therapeutic effects with their biological contents such as high amount of protein, vitamins, minerals, essential unsaturated fatty acids, aromatic phenols, terpenoids and steroids [10]. It can be used in the treatment of fungi, many mutagenic and oxidant diseases with the benzoic acid, riboflavin and other B group vitamins, phenolic substances such as quercetin, catechin and crissula (Papaspiride) and flavonoids they contain [11,12]. Most mushroom extracts contain proteins, phenolics, tocopherols, carotenoids, and flavonoids that inhibit the growth of blood vessels, as well as bioactive compounds that can restrict the growth of abnormal cells [13]. Therefore, mushrooms have been utilized in traditional medicine for an extended period to treat various illnesses, including several forms of cancer.

Heterobasidion species are fungi that cause white rot with the enzymes they secrete on the trunk and roots of living and dead trees, infecting the newly cut stumps of coniferous and broad-leaved trees, wounds and even through root fusion [14–16]. Of these species, *H. annosum* is known as one of the most serious pathogens that cause root and bottom rot in forest trees in the northern hemisphere of the world and has made it the subject of many studies in recent years [17–19].

This fungus, which is known to cause damage to many tree species in the world, has also been the focus of interest in anti-cancer studies today. Sadowska et al. (2020) showed that it has beneficial potential against colon cancer as a cytotoxic agent or adjuvant anticancer therapy in their study with *H. annosum* sporocarps [20]. Extracts from the fungus, which was previously investigated as a remedy against various ailments, including cancer, are usually obtained from sporocarps [21,22]. Unlike other studies, this study was carried out with extracts obtained from mushroom micelles instead of sporocarps. For this purpose, in this study, the effect of methanolic extracts isolated from *H. annosum* micelles. This research assessed the efficacy of cisplatin and *Heterobasidion* micelles, both individually and in combination, on human colon adenocarcinoma cells. Additionally, we explored how the impact of cisplatin on cancer cell proliferation would be altered when combined with *Heterobasidion* micelles.

Materials and Methods

Research Design

This is an in vitro analysis (cell culture) study.

Research Location and Time

This study was conducted in the laboratories of Kastamonu University and Erzurum Atatürk University.

Study Design

Preparation of mushroom mycelial extracts

H. annosum micelles with the code Tr501 used in the study were obtained from Isparta University of Applied Sciences, Faculty of Forestry, Dendrochronology Laboratory. These micelles were allowed to grow in liquid malt extract medium at 23°C for one week. For the preparation of micelial extracts, Sadowska et al. (2020)'s method was used with minor modifications [14]. Developed micelles were taken from Erlenmeyer flask and washed with distilled water for extraction. Then it was filtered with filter paper and weighed (Wet weight: 0.2893 gr). The micelles were then dried in a room dryer (NUVE KD 400, Turkey) at 45°C for 1 hour. The micelle sample dried on the filter paper was weighed again (Dry weight: 0.0837 g). Dry micelle samples were extracted with 8.37 mL of 99.8% methanol, anhydrous. It was mixed in the homogenizer. It was kept in the mixer for 24 hours. It's been filtered. The filtrate was evaporated in the evaporator. The obtained isolate was homogeneously powdered for use in cytotoxic analyses. In this study, all chemicals supplied from Merck KGaA, Darmstadt, Germany were of analytical purity and deionized water was used in each step.

In vitro Analyses

Cytotoxicity Analysis of *Heterobasidion Annosum*

Caco-2 Cell Culture

Caco-2 cells (HTB-37™) were obtained from the Department of Medical Pharmacology at Ataturk University in Erzurum, Turkey. Upon thawing, the cells underwent a brief centrifugation process to generate a pellet. Cells were cultured in DMEM (1% antibiotics—amphotericin B, penicillin, and streptomycin—and 10% FBS) and maintained under optimal conditions (37 °C; 5% CO₂). Once they achieved 85% confluency, the cells were harvested and seeded into 48-well plates (Corning, Corning, NY, USA) at a concentration of 1×10⁵ cells/mL per well.

Cell Treatments

Subjected to various concentrations of *H. annosum* (25–200 ng/ml) and 15 µg/ml cisplatin, the cells were incubated for 24 hours under conditions of 5% CO₂ and 37 °C. The cells underwent exposure to different treatments for durations of 24, 48, or 72 hours. 3-(4,5-

Dimethylthiazol-2-yl)-2,5-Diphenyltetrazolium Bromide (MTT) Cell Viability Assay

For the assessment of cell viability, 5,000 cells per well were seeded in a 96-well plate. Following a growth period of 24, 48, and 72 hours, the cells were exposed to varying concentrations of *Heterobasidion annosum* (25–200 ng/ml) and 15 µg/ml cisplatin, excluding the control cells.

The MTT kit, in accordance with the manufacturer's guidelines (Cayman Chemical, MI, USA), was employed to determine cell viability after 24, 48, and 72-hour intervals. The stock MTT solution, prepared in sterile PBS, was added to the 96-well plates at a concentration of 10%, depending on the desired time point. Subsequent to a 4-hour incubation at 37 °C in an environment with 5% CO₂, 100 µL of DMSO was introduced to dissolve the formazan crystals. Formazan absorbance was evaluated using an ELISA reader (Thermo Scientific, Canada) at a wavelength of 570 nm [23].

Statistical Analysis

For the comparison of MTT data among various groups, we employed one-way analysis of variance (ANOVA) with the statistical software IBM SPSS 20.0. To examine the uniformity of variances within the groups, Levene's test was utilized, and the normal distribution within each group was assessed using the Shapiro–Wilk test. Distinctions between groups were determined through the application of one-way ANOVA, followed by a Duncan multiple range test (DMRT) ($p < 0.05$). The outcomes for each group are presented as the mean ± SD.

Results

There was no statistical significance between the 24-hour cisplatin-treated control group and the untreated group, a decrease in cancer cell viability was observed. A significant difference was found between Cisplatin-control (Cis-control) and Cisplatin + *Heterobasidion* (Cis+H) 100 ng/mL dose group ($p < 0.010$) and Cisplatin + *Heterobasidion* 200 ng/mL dose group ($p < 0.004$) (Figure 1).

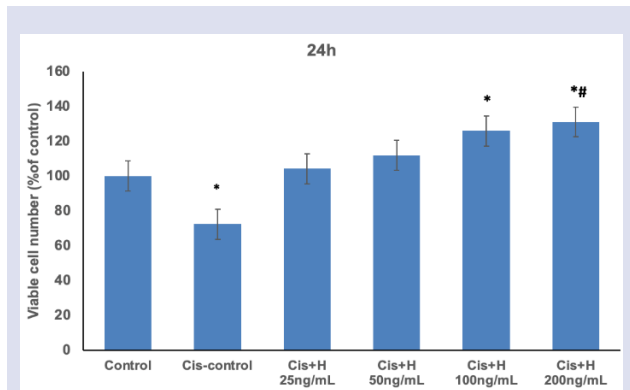


Figure 1. MTT assay in a human colon adenocarcinoma cell line called Caco-2. The cells were treated with cisplatin and *Heterobasidion* annosum for a duration of 24 hours. The viability of the cells was determined using the MTT assay. The results were expressed as the mean and standard deviation. Values with * shows significantly different to the control group; # shows $p < 0.005$ shows significantly different to the cisplatin control group. (Cis: Cisplatin; H: *Heterobasidion* annosum; each group was studied in triplicate.)

Although there was no statistical significance between the 48-hour cisplatin-treated control group and the untreated group, a decrease in cancer cell viability was observed. A significant difference was found between Cis-control and Cis+H 25 ng/mL dose group ($p < 0.041$) and Cis+H 200 ng/mL dose group ($p < 0.001$) (Figure 2).

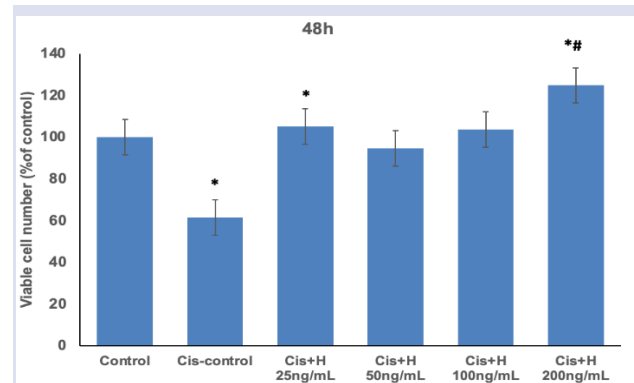


Figure 2. MTT assay in a human colon adenocarcinoma cell line called Caco-2. The cells were treated with cisplatin and *Heterobasidion* annosum for a duration of 48 hours. The viability of the cells was determined using the MTT assay. The results were expressed as the mean and standard deviation. Values with * shows significantly different to the control group; # shows $p < 0.005$ shows significantly different to the cisplatin control group. (Cis: Cisplatin; H: *Heterobasidion* annosum; each group was studied in triplicate.)

A notable reduction in the survival of cancer cells was observed when comparing the 72-hour cisplatin-treated control group with the group that received no treatment ($p < 0.000$). There was also a significant difference between the Cis-control group and the Cis+H group at doses of 25 ng/mL ($p < 0.000$), 50 ng/mL ($p < 0.000$), 100 ng/mL ($p < 0.000$), and 200 ng/mL ($p < 0.000$) (see Figure 3).

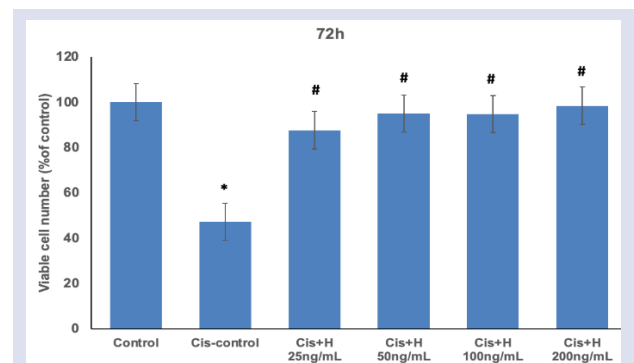


Figure 3. MTT assay in a human colon adenocarcinoma cell line called Caco-2. The cells were treated with cisplatin and *Heterobasidion* annosum for a duration of 72 hours. The viability of the cells was determined using the MTT assay. The results were expressed as the mean and standard deviation. Values with * shows significantly different to the control group; # shows $p < 0.005$ shows significantly different to the cisplatin control group. (Cis: Cisplatin; H: *Heterobasidion* annosum; each group was studied in triplicate.)

Discussion

Colorectal cancer is one of the most common malignancies, however its morbidity and mortality rates vary [24]. Even though chemotherapy holds a crucial role in cancer therapies, there has been a growing emphasis on the efficacy and synergistic potential of natural product molecules in cancer treatment in recent years. The principal objective of chemotherapy is to provoke the demise of cancer cells while causing minimal or no damage to non-cancerous cells or tissues. Cisplatin stands as a chemotherapy agent employed in treating various tumors, such as colon cancer and multiple other cancer types. The prevalence of side effects such as mucositis, cardiotoxicity, and myelosuppression constrains the range of treatment indications. Consequently, researchers aim to harness the positive impact of the drug while mitigating its adverse side effects [25–27]. Upon examining the literature, indications propose that certain mushroom extracts may possess anticancer attributes and offer therapeutic benefits against diverse types of cancers. The presence of bioactive compounds, including lectins, terpenoids, and secondary metabolites, contributes to these therapeutic effects. Typically, their mechanisms involve the initiation of apoptotic pathways and the induction of DNA damage in cancer cells [25–28].

In a 2020 investigation, Sadowska and her team explored the efficacy of HA extract in treating colorectal cancer in mice. The reference drug for the treatment was 5-fluorouracil (5FU), and the study delved into the effectiveness of combining HA extract with 5FU. The findings indicated that the control group with cancer exhibited the largest tumor volume, while the group treated with 5FU and/or HA extract demonstrated the smallest tumor volume. In the combination treatment, there was an increase in caspase 8 and p53 protein concentrations compared to the patient control group, accompanied by a decrease in survivin and Bcl-2 levels. This research furnished insights into the antitumor activity of HA extract and its interaction with anticancer chemotherapeutic agents [20].

Fungal species complex of *Heterobasidion annosum* s.l. There are five phylogenetically distinct species. Two of these five members are *H. annosum* s.s., which causes infection in pine. and *H. irregulare*, and the other three are *H. parviporum*, *H. abietinum* and *H. occidentale*, which cause infection in non-pine species [29,30]. *H. annosum* s.l. It produces toxins that inhibit plant growth and these substances cause physiological disorders in the plant [31]. Fomannosine, which causes stem wounds in *Pinus taeda* seedlings, and fomannoxin, which has a much more toxic effect on plant cells, are some of these substances [32].

Unlike other studies, in this study, the mycelium of *H. annosum* was used instead of its fruit bodies. The mycelium of the mushroom has been cultivated and isolated in liquid Malt Extract medium. Upon reviewing the literature, no applications utilizing the mycelia of this mushroom have been identified. Therefore, the results of this study are considered to possess originality, as no prior

applications utilizing the mycelia of this mushroom have been found in the literature. It is believed that these findings will contribute to the existing body of knowledge. Since the anticancer effects of mushrooms are known, whether the mycelium also possesses this effect and its synergistic effect with cisplatin were investigated on cancer cell lines at three different time intervals. The similarity between the Cis + H dose group and the control group indicates that they did not contribute to the development of tumor cells. Previously, in a study conducted by Sadowska et al., the methanolic extract of *H. annosum* was analyzed for its active components, and their effects on colorectal cancer were investigated both in vitro and in vivo. It has been found that the extract of *H. annosum* significantly reduces the viability and proliferation of DLD-1 cells in a concentration-dependent manner. Additionally, in the group of mice receiving the extract, tumor growth was reduced. However, it exhibited mild to moderate toxicity [20].

David Hansson et al.'s (2014) study on pine-infecting and non-pine-infecting *Heterobasidion annosum* s.l. In their study, which included secondary metabolite comparison of the species within the and *H. irregulare* samples were found to form more clumps. Additionally, in the same study, in the *H. annosum* s.s species, (S)-2-(2-hydroxypropan-2-yl)-2,3-dihydrobenzofuran-5-carbaldehyde, 2-(2-hydroxypropan-2-yl)-benzofuran-5-carbaldehyde; 2-(1,2-dihydroxy-2-propanyl)-2,3-dihydrobenzofuran-5-carbaldehyde; 3-hydroxy-2-(prop-1-en-2-yl)-2,3-dihydrobenzofuran-5-carbaldehyde; 5-formyl-2-hydroxybenzoic acid; Fomajorin D; Amino acids such as Epoxydrimenol and Tryptophan were detected [33].

The lack of an increase in the viability of tumor cells obtained in our study raises the question of whether the tumor cells can continue their development at this point. The answer to this question is difficult to assess in detail solely through cytotoxicity analyses. This significant finding reveals that cisplatin, which has been shown to be effective in many cancer studies, significantly reduces the viability of cancer cells compared to the control group after 72 hours when administered alone. The effect of the combination therapy group has shown that it is not as effective as the group receiving cisplatin alone. However, it raises the possibility that further studies on cancer cell lines using *H. annosum* mycelia could shed light on potential applications.

Conclusion and Suggestions

With this analysis in terms of cytotoxicity, it is not possible to say that the combination of cisplatin and mushrooms is effective in this dose range. Different doses of mushrooms may have an effect in different areas by evaluating their efficacy alone, as well as by looking at their oxidant capacity. Apart from these missing points, it should not be overlooked that they do not stimulate the growth of cancer cells. We have focused our attention on the fact that the combination groups showed similar

characteristics to the control group and that cisplatin reduced cancer cell stimulation compared to the control group at 72 hours. The literature information which were reviewed did not provide any information on both dosing and combination therapy and from this point of view, it was conducted to provide data for the in vivo study. It is essential to determine effective dose ranges before proceeding with animal experiments. When looking at the literature, the dose ranges of mushroom extracts can be found, but it could not come across studies with the mycelia of this mushroom. With this study, on which will be added many more studies, it can touch the missing parts in the literature to some extent.

Aknowledgement

We would like to thank Isparta University of Applied Sciences Faculty of Forestry faculty member Dr. Lecturer Ayşe Gülden ADAY KAYA for providing the *Heterobasidion annosum* isolate TR501 used in the study and contributing to our study.

Conflict of Interest

Authors declare no conflict of interest.

References

- [1] Lotfollahzadeh S., Recio-Boiles A., Cagir B., Colon cancer, *Florida: StatPearls Treasure*, (2021).
- [2] Alvarez-Gonzalez MA., Pantaleon MA., Flores-Le Roux JA., Zaffalon D., Amorós J., Bessa X., Seoane A., Pedro-Botet J., Randomized Clinical Trial: A Normocaloric Low-Fiber Diet the Day Before Colonoscopy Is the Most Effective Approach to Bowel Preparation in Colorectal Cancer Screening Colonoscopy, *Dis Colon Rectum.*, 62(4) (2019) 491-497.
- [3] Peters WR., What Every Colorectal Surgeon Should Know About the New American Cancer Society's Colorectal Cancer Screening Guidelines, *Dis Colon Rectum.*, 62(4) (2019) 397-398.
- [4] Dasari S., Tchounwou PB., Cisplatin in cancer therapy: molecular mechanisms of action, *Eur J Pharmacol.*, 740 (2014) 364-78.
- [5] Galligioni E., Canobbio L., Figoli F., Fassio T., Frustaci S., Crivellari D., Vaccher E., Lo Re G., Gasparini G., Veronesi A., Cisplatin and 5-fluorouracil combination chemotherapy in advanced and/or metastatic colorectal carcinoma: a phase II study, *Eur J Cancer Clin Oncol.*, 23(6) (1987) 657-61.
- [6] Gürbüz V., Yilmaz A., Gökçe Ö., Konaç E., İnsan kolon kanser hücre hattında (HT29) sislplatin'in apoptotik etkisi, *MarmaraMedJ* 24 (2) (2011) 100-105.
- [7] Kaźmierczak-Siedlecka K., Dvořák A., Folwarski M., Daca A., Przewłócka K., Makarewicz W., Fungal Gut Microbiota Dysbiosis and Its Role in Colorectal, Oral, and Pancreatic Carcinogenesis, *Cancers (Basel)*, 12(5) (2020)1326.
- [8] Mann, J., Natural products in cancer chemotherapy: past, present and future, *Nat Rev Cancer.*, 2(2) (2002)143-148.
- [9] Reddy L., Odhav B., Bhoola KD., Natural products for cancer prevention: a global perspective, *Pharmacol Ther.*, 99(1) (2003) 1-13.
- [10] Sande D, Oliveira GP, Moura MAFE, Martins BA, Lima MTNS, Takahashi JA., Edible mushrooms as a ubiquitous source of essential fatty acids, *Food Res Int.*, 125 (2019)108524.
- [11] Yilmaz, N., Solmaz, M., Türkekul, I., Elmastaş, M., Fatty acid composition in some wild edible mushrooms growing in the middle Black Sea region of Turkey, *Food Chem.*, 99(1) (2006) 168-174.
- [12] Feeney MJ, Dwyer J, Hasler-Lewis CM, Milner JA, Noakes M, Rowe S, Wach M, Beelman RB, Caldwell J, Cantorna MT, Castlebury LA, Chang ST, Cheskin LJ, Clemens R, Drescher G, Fulgoni VL 3rd, Haytowitz DB, Hubbard VS, Law D, Myrdal Miller A, Minor B, Percival SS, Riscuta G, Schneeman B, Thornsbury S, Toner CD, Woteki CE, Wu D. Mushrooms and Health Summit proceedings. *J Nutr.*, 144(7) (2014) 1128S-1136S.
- [13] Simmons EG., The International Mycological Association: its history in brief with summaries of its International Mycological Congresses and diverse international relationships, *IMA Fungus.*, 1(1) (2010) 18-100.
- [14] Asiegbu FO., Abu S., Stenlid J., Johansson M., Sequence polymorphism and molecular characterization of laccase genes of the conifer pathogen *Heterobasidion annosum*, *Mycol Res.*, 108(Pt 2) (2004) 136-48.
- [15] Haars A., Chet, I., Hüttermann A., Effect of phenolic compounds and tannin on growth and laccase activity of *Fomes annosus*, *For. Pathol.*, 11(1-2) (1981) 67-76.
- [16] Daniel G., Asiegbu F., Johansson M., The saprotrophic wood-degrading abilities of *Heterobasidion annosum* intersterility groups P and S, *Mycol. Res.*, 102(8) (1998) 991-997.
- [17] Doğmuş Lehtijarvi H., Lehtijarvi A., Oskay F., Aday A., Karadeniz M., Incidence of Annosum Root and but Rot on *Abies bornmulleriana* and *Abies cilicica*, *ACUJFF.*, 9 (2008) 111-120.
- [18] Korhonen K., Capretti P., Karjalainen R., Stenlid J., Distribution of *Heterobasidion annosum* intersterility groups in Europe. In: *Heterobasidion annosum: Biology, Ecology, Impact and Control* (Woodward S., Stenlid J., Karjalainen R., Hüttermann A., eds), *CAB International.*, (1998) 93-105.
- [19] Garbelotto M., Gonthier P., Biology, epidemiology, and control of *Heterobasidion* species worldwide, *Annu. Rev. Phytopathol.*, 51(1) (2013) 39-59.
- [20] Sadowska A., Zapora E., Sawicka D., Niemirowicz-Laskowska K., Surazyński A., Sułkowska-Ziaja K., Kała K., Stocki M., Wołkowycki M., Bakier S., Pawlik A., Jaszek M., Muszyńska B., Car H., *Heterobasidion annosum* Induces Apoptosis in DLD-1 Cells and Decreases Colon Cancer Growth in In Vivo Model, *Int J Mol Sci.*, 21(10) (2020) 3447.
- [21] Kladar NV., Gavarić NS., Božin BN., Ganoderma: insights into anticancer effects, *Eur J Cancer Prev.*, 25(5) (2016) 462-71.
- [22] Glamočlija J., Ćirić A., Nikolić M., Fernandes Â., Barros L., Calhella RC., Ferreira IC., Soković M., van Griensven LJ., Chemical characterization and biological activity of Chaga (*Inonotus obliquus*), a medicinal "mushroom", *J Ethnopharmacol.*, 162 (2015) 323-32.
- [23] Varmazyari A., Taghizadehghalehjouhi A., Sevim C., Baris O., Eser G., Yildirim S., Hacimuftuoglu A., Buha A., Wallace DR., Tsatsakis A., Aschner M., Mezhev Y., Cadmium sulfide-induced toxicity in the cortex and cerebellum: In vitro and in vivo studies, *Toxicol Rep.*, 7 (2020) 637-648.
- [24] Bray F., Ferlay J., Soerjomataram I., Siegel RL., Torre LA., Jemal A., Global cancer statistics 2018: GLOBOCAN estimates of incidence and mortality worldwide for 36

- cancers in 185 countries, *CA Cancer J Clin.*, 68(6) (2018) 394-424.
- [25] Sadowska A., Sawicka D., Godlewska K., Guzińska-Ustymowicz K., Zapora E., Sokołowska E., Car H., Beneficial Proapoptotic Effect of Heterobasidion Annosum Extract in Colorectal Cancer Xenograft Mouse Model, *Molecules.*, 28(3) (2023) 1352.
- [26] Torres DM., Tooley KL., Butler RN., Smith CL., Geier MS., Howarth GS., Lyprinol only partially improves indicators of small intestinal integrity in a rat model of 5-fluorouracil-induced mucositis, *Cancer Biol Ther.*, 7(2) (2008) 295-302.
- [27] Bunz F., Hwang PM., Torrance C., Waldman T., Zhang Y., Dillehay L., Williams J., Lengauer C., Kinzler KW., Vogelstein B., Disruption of p53 in human cancer cells alters the responses to therapeutic agents, *J Clin Invest.*, 104(3) (1999) 263-9.
- [28] Jakopovic, Boris, Nada Oršolić, and Sandra Kraljević Pavelić. "Antitumor, immunomodulatory and antiangiogenic efficacy of medicinal mushroom extract mixtures in advanced colorectal cancer animal model." *Molecules* 25.21 (2020): 5005.
- [29] Dalman, K., Olson, A., Stenlid, J., 2010. Evolutionary history of the conifer root rot fungus *Heterobasidion annosum* sensu lato. *Mol. Ecol.* 19 (2010): 4979–4993.
- [30] Linzer, R.E., Otrosina, W.J., Gonthier, P., Bruhn, J., Laflamme, G., Bussieres, G., Garbelotto, M.,. Inferences on the phylogeography of the fungal pathogen *Heterobasidion annosum*, including evidence of the interspecific horizontal genetic transfer and of human-mediated, long-range dispersal. *Mol. Phylogenet. Evol.* 46 (2008): 844–862.
- [31] Hoque, E., Growth inhibitors produced by the in vitro culture of *Heterobasidion annosum*. *Forest Pathol.* 14 (1984): 43–51.
- [32] Hirotsani, M., O' Reilly, J., Donnelly, D.M.X., Fomannoxin – toxic metabolites of *Fomes annosus*. *Tetrahedron Lett.* 18 (1977): 651–652.
- [33] David Hansson, Sileshi Wubshet, Åke Olson, Magnus Karlsson, Dan Staerk, Anders Broberg, Secondary metabolite comparison of the species within the *Heterobasidion annosum* s.l. complex, *Phytochemistry*, 108 (2014): 243-251.

Some Sums Involving Generalized Harmonic and r – Derangement Numbers

Sibel Koparal ^{1,a,*}

¹ Department of Mathematics, Faculty of Sciences and Arts, Bursa Uludağ University, Bursa, Türkiye.

*Corresponding author

Research Article

History

Received: 23/09/2023

Accepted: 28/11/2023




This article is licensed under a Creative Commons Attribution-NonCommercial 4.0 International License (CC BY-NC 4.0)

ABSTRACT

In this paper, we derive some sums involving generalized harmonic and r – derangement numbers by using generating functions of these numbers and some combinatorial identities. The relationship between Daehee numbers and generalized harmonic numbers of rank r , $H(n, r, \alpha)$ is given. In addition, sums including Daehee numbers of order r , D_n^r , generalized hyperharmonic numbers of order r , $H_n^r(\alpha)$, Cauchy numbers of order r , C_n^r and the stirling numbers of the first kind, $s(n, i)$ are also calculated.

Keywords: Generalized harmonic numbers, r – Derangement numbers, Generating functions, Special numbers.

 sibelkoparal@uludag.edu.tr

 <https://orcid.org/0000-0003-2889-2832>

Introduction

Harmonic numbers are important in various branches of combinatorics and number theory. The harmonic numbers are defined by

$$H_0 = 0 \text{ and } H_n = \sum_{i=1}^n \frac{1}{i} \text{ for } n = 1, 2, \dots$$

Some harmonic numbers are $1, \frac{3}{2}, \frac{11}{6}, \frac{25}{12}, \dots$. Recently, some authors have generalized them [1, 2, 4, 8, 13, 19].

In [8], for any $\alpha \in \mathbb{R}^+$, the generalized harmonic numbers $H_n(\alpha)$ are defined by

$$H_0(\alpha) = 0 \text{ and } H_n(\alpha) = \sum_{i=1}^n \frac{1}{i\alpha^i} \text{ for } n = 1, 2, \dots$$

When $\alpha = 1$, $H_n(1) = H_n$ and the generating function of these numbers is

$$\sum_{n=1}^{\infty} H_n(\alpha)x^n = -\frac{\ln\left(1 - \frac{x}{\alpha}\right)}{1 - x}.$$

In [12], for the generalized harmonic numbers $H_n(\alpha)$, Ömür and Bilgin defined the generalized hyperharmonic numbers of order r , $H_n^r(\alpha)$ by: For $r < 0$ or $n \leq 0$, $H_n^r(\alpha) = 0$ and for $n \geq 1$,

$$H_n^r(\alpha) = \sum_{i=1}^n H_i^{r-1}(\alpha), \quad r \geq 1,$$

where $H_n^0(\alpha) = \frac{1}{n\alpha^n}$.

When $\alpha = 1$, $H_n^r(1) = H_n^r$ are the hyperharmonic numbers of order r . The generating function of $H_n^r(\alpha)$ is

$$\sum_{n=1}^{\infty} H_n^r(\alpha)x^n = -\frac{\ln\left(1 - \frac{x}{\alpha}\right)}{(1 - x)^r}. \quad (1)$$

In [4, 19], the generalized harmonic numbers $H(n, r)$ of rank r are defined as for $n \geq 1, r \geq 0$,

$$H(n, r) = \sum_{1 \leq n_0 + n_1 + \dots + n_r \leq n} \frac{1}{n_0 n_1 \dots n_r}.$$

When $r = 0$, $H(n, 0) = H_n$. The generating function of the generalized harmonic numbers $H(n, r)$ of rank r is

$$\sum_{n=1}^{\infty} H(n, r)x^n = \frac{(-\ln(1 - x))^{r+1}}{1 - x}.$$

In [7], inspiring from these definitions, $H(n, r, \alpha)$ are defined as for $n \geq 1, r \geq 0$,

$$H(n, r, \alpha) = \sum_{1 \leq n_0 + n_1 + \dots + n_r \leq n} \frac{1}{n_0 n_1 \dots n_r \alpha^{n_0 + n_1 + \dots + n_r}}.$$

For $\alpha = 1$, $H(n, r, 1) = H(n, r)$. The generating function of the generalized harmonic numbers of rank r , $H(n, r, \alpha)$ is given by

$$\sum_{n=0}^{\infty} H(n, r, \alpha)x^n = \frac{\left(-\ln\left(1 - \frac{x}{\alpha}\right)\right)^{r+1}}{1 - x}. \quad (2)$$

The Cauchy numbers of order r , C_n^r have an exponential generating function

$$\left(\frac{x}{\ln(1+x)}\right)^r = \sum_{n=0}^{\infty} C_n^r \frac{x^n}{n!}. \tag{3}$$

The Daehee numbers of order r , D_n^r have an exponential generating function

$$\left(\frac{\ln(1+x)}{x}\right)^r = \sum_{n=0}^{\infty} D_n^r \frac{x^n}{n!}. \tag{4}$$

When $r = 1$, $D_n^1 = D_n$ are called Daehee numbers.

In [22], the r -derangement numbers, $D_r(n)$ have an exponential generating function

$$\frac{x^r e^{-x}}{(1-x)^{r+1}} = \sum_{n=0}^{\infty} D_r(n) \frac{x^n}{n!}. \tag{5}$$

For $r = 0$, $D_0(n) = d_n$ are called derangement numbers.

The generalized geometric series are given by for positive integers a, b ,

$$\frac{x^b}{(1-x)^{a+1}} = \sum_{n=b}^{\infty} \binom{n+a-b}{a} x^n. \tag{6}$$

The exponential generating function is

$$e^x = \sum_{n=0}^{\infty} \frac{x^n}{n!}. \tag{7}$$

The Stirling numbers of the first kind $s(n, i)$ are defined by

$$x^n = \sum_{i=0}^n s(n, i) x^i,$$

$$\text{where } x^n = \begin{cases} x(x-1)\cdots(x-n+1) & \text{if } n \geq 1, \\ 0 & \text{if } n = 0. \end{cases}$$

The Stirling numbers of the first kind $s(n, k)$ satisfy the recurrence relation

$$s(n+1, k) = s(n, k-1) - ns(n, k),$$

and the generating functions of these numbers are given by

$$\sum_{n=0}^{\infty} s(n, k) \frac{x^n}{n!} = \frac{(\ln(1+x))^k}{k!}, k \geq 0. \tag{8}$$

Recently, using generating functions, there are some works including generalized harmonic, r -derangement and special numbers by authors [5, 6, 7, 9, 10, 11, 14, 15,

16, 17, 18, 20, 23, 24, 25, 26, 27, 31]. At the same time, many studies have been carried out on the degenerate states of these numbers [28, 29, 30, 32, 33].

In [22], the authors gave many formulas for the r -derangement numbers. For example, for a positive integer r and $r \leq n$,

$$(r+1)!L(n, r+1) = \sum_{i=1}^n \binom{n}{i} i D_r(n-i),$$

where $L(n, k)$ are the Lah numbers.

In [18], Rim, et al. examined some identities relating the hyperharmonic and the Daehee numbers. For example, for any positive integer n ,

$$n! H_n^r = (-1)^{n-1} \sum_{i=0}^{n-1} \binom{n}{i} (n-i)(-r)^{i-1} D_i.$$

In [7], some sums including generalized harmonic numbers have been obtained by Duran et al. For example, for any positive integers n and r ,

$$H(n, r, \alpha) = (-1)^{n-r} \sum_{i=0}^n \frac{(-1)^i s(n-i, r) r!}{\alpha^{n-i} (n-i)!} H_i(\alpha).$$

Let $F(x) = \sum_{n=0}^{\infty} a_n x^n$ and $G(x) = \sum_{n=0}^{\infty} b_n x^n$ be two infinite series. The Cauchy product of these series is given as follows:

$$F(x)G(x) = \left(\sum_{n=0}^{\infty} a_n x^n\right) \left(\sum_{n=0}^{\infty} b_n x^n\right) = \sum_{n=0}^{\infty} c_n x^n,$$

where $c_n = \sum_{k=0}^n a_k b_{n-k}$ for all positive integer n .

In this paper, we derive some sums involving generalized harmonic and r -derangement numbers by using generating functions of these numbers and some combinatorial identities. The relationship between Daehee numbers and generalized harmonic numbers of rank r , $H(n, r, \alpha)$ is given. In addition, sums including Daehee numbers of order r , D_n^r , generalized hyperharmonic numbers of order r , $H_n^r(\alpha)$, Cauchy numbers of order r , C_n^r and the stirling numbers of the first kind, $s(n, i)$ are also calculated.

Some Sums Involving Generalized Harmonic and r -Derangement Numbers

This section, we will give some sums including generalized harmonic and r -derangement numbers by using generating functions of these numbers and some combinatorial identities.

Theorem 1. Let n, r and m be positive integers. For $n \geq m(r+1)$, then

$$\sum_{j=0}^n \sum_{i=0}^j (-1)^{j-i} r^{j-i} \binom{n-j+r-1}{n-j} \binom{j}{i} \frac{D_{m(r+1)}(i)}{j!}$$

$$= \sum_{l_1+l_2+\dots+l_{r+1}=n} \frac{D_m(l_1)D_m(l_2)\dots D_m(l_{r+1})}{l_1!l_2!\dots l_{r+1}!}.$$

Proof. By (5), (6) and (7), we consider

$$\frac{x^{m(r+1)}e^{-x}}{(1-x)^{m(r+1)+1}} e^{-rx} \frac{1}{(1-x)^r}$$

$$= \sum_{n=0}^{\infty} \frac{D_{m(r+1)}(n)}{n!} x^n \sum_{n=0}^{\infty} (-1)^n \frac{r^n}{n!} x^n \sum_{n=0}^{\infty} \binom{n+r-1}{n} x^n$$

$$= \sum_{n=0}^{\infty} \sum_{i=0}^n (-r)^{n-i} \frac{D_{m(r+1)}(i)}{i!(n-i)!} x^n \sum_{n=0}^{\infty} \binom{n+r-1}{n} x^n,$$

and from product of generating functions, equals

$$\sum_{n=0}^{\infty} \sum_{j=0}^n \sum_{i=0}^j (-r)^{j-i} \binom{n-j+r-1}{n-j} \binom{j}{i} \frac{D_{m(r+1)}(i)}{j!} x^n,$$

and

$$\frac{x^{m(r+1)}e^{-x}}{(1-x)^{m(r+1)+1}} e^{-rx} \frac{1}{(1-x)^r}$$

$$= \left(\frac{x^m e^{-x}}{(1-x)^{m+1}} \right) \left(\frac{x^m e^{-x}}{(1-x)^{m+1}} \right) \dots \left(\frac{x^m e^{-x}}{(1-x)^{m+1}} \right)$$

$$= \sum_{l_1=0}^{\infty} \frac{D_m(l_1)}{l_1!} x^{l_1} \sum_{l_2=0}^{\infty} \frac{D_m(l_2)}{l_2!} x^{l_2} \dots \sum_{l_{r+1}=0}^{\infty} \frac{D_m(l_{r+1})}{l_{r+1}!} x^{l_{r+1}}$$

$$= \sum_{n=0}^{\infty} \sum_{l_1+l_2+\dots+l_{r+1}=n} \frac{D_m(l_1)D_m(l_2)\dots D_m(l_{r+1})}{l_1!l_2!\dots l_{r+1}!} x^n.$$

Hence, comparing the coefficients on both sides, we have the proof.

Theorem 2. For $n \geq r$, then

$$(-1)^{n-r} \frac{D_{n-r}^r}{\alpha^n (n-r)!}$$

$$= H(n, r-1, \alpha) - H(n-1, r-1, \alpha),$$

and for $n > 2r$,

$$\sum_{i=0}^n \binom{i-1}{r-1} H(n-i, r, \alpha)$$

$$= \sum_{j=0}^n \sum_{i=0}^j \binom{n}{j} \binom{j}{i} \frac{(-1)^{i-r-1} s(i, r+1) (r+1)!}{\alpha^i n!} D_r(j-i).$$

Proof. From (4), we have

$$\sum_{n=r}^{\infty} (-1)^{n-r} \frac{D_{n-r}^r}{\alpha^n (n-r)!} x^n$$

$$= \frac{x^r}{\alpha^r} \sum_{n=0}^{\infty} (-1)^n \frac{D_n^r x^n}{\alpha^n n!} = \left(-\ln \left(1 - \frac{x}{\alpha} \right) \right)^r.$$

By (2), we get

$$\sum_{n=r}^{\infty} (-1)^{n-r} \frac{D_{n-r}^r}{\alpha^n (n-r)!} x^n = \frac{\left(-\ln \left(1 - \frac{x}{\alpha} \right) \right)^r}{1-x} (1-x)$$

$$= \frac{\left(-\ln \left(1 - \frac{x}{\alpha} \right) \right)^r}{1-x} - x \frac{\left(-\ln \left(1 - \frac{x}{\alpha} \right) \right)^r}{1-x}$$

$$= \sum_{n=0}^{\infty} H(n, r-1, \alpha) x^n - \sum_{n=0}^{\infty} H(n, r-1, \alpha) x^{n+1}$$

$$= \sum_{n=1}^{\infty} (H(n, r-1, \alpha) - H(n-1, r-1, \alpha)) x^n.$$

Secondly, by product of exponential generating functions, we write

$$\left(-\ln \left(1 - \frac{x}{\alpha} \right) \right)^{r+1} \frac{x^r e^{-x}}{(1-x)^{r+1}} e^x$$

$$= \sum_{n=0}^{\infty} \frac{(-1)^{n-r-1} s(n, r+1) (r+1)! x^n}{\alpha^n n!}$$

$$\times \sum_{n=0}^{\infty} D_r(n) \frac{x^n}{n!} \sum_{n=0}^{\infty} \frac{x^n}{n!}$$

$$= \sum_{n=0}^{\infty} \sum_{i=0}^n \binom{n}{i} \frac{(-1)^{i-r-1} s(i, r+1) D_r(n-i) (r+1)! x^n}{\alpha^i n!}$$

$$\times \sum_{n=0}^{\infty} \frac{x^n}{n!}$$

$$= \sum_{n=0}^{\infty} \sum_{j=0}^n \sum_{i=0}^j \binom{n}{j} \binom{j}{i} \frac{(-1)^{i-r-1} s(i, r+1) D_r(j-i) (r+1)! x^n}{\alpha^i n!} x^n,$$

and by (2) and (6), we have

$$\left(-\ln \left(1 - \frac{x}{\alpha} \right) \right)^{r+1} \frac{x^r}{(1-x)^{r+1}}$$

$$= \frac{\left(-\ln \left(1 - \frac{x}{\alpha} \right) \right)^{r+1} x^r}{1-x (1-x)^r}$$

$$= \sum_{n=0}^{\infty} H(n, r, \alpha) x^n \sum_{n=r}^{\infty} \binom{n-1}{r-1} x^n$$

$$= \sum_{n=0}^{\infty} \sum_{i=0}^n \binom{i-1}{r-1} H(n-i, r, \alpha) x^n.$$

Comparing the coefficients of x^n in the first and last series. So, we have the proof.

Theorem 3. Let m be positive integer. For $n > r$, then

$$\sum_{i=0}^n \frac{(-1)^i}{i! \alpha^{i-m}} C_i^m H(n+m-i, r+m, \alpha) = H(n, r, \alpha),$$

and

$$\sum_{j=0}^n \sum_{i=0}^j \binom{j}{i} \frac{(-1)^i}{j! \alpha^{i-r}} C_i^r d_{j-i} H(n-j, r-1, \alpha) = \sum_{i=0}^n (-1)^i \binom{r-1}{i} \frac{D_r(n-i)}{(n-i)!}.$$

Proof. From (2) and (3), we write

$$\begin{aligned} \sum_{n=0}^{\infty} H(n, r, \alpha) x^n &= \frac{(-\ln(1-\frac{x}{\alpha}))^{r+1}}{1-x} \\ &= \frac{(-\ln(1-\frac{x}{\alpha}))^{r+m+1}}{1-x} \frac{(-x/\alpha)^m \alpha^m}{(\ln(1-\frac{x}{\alpha}))^m x^m} \\ &= \sum_{n=0}^{\infty} H(n, r+m, \alpha) x^{n-m} \sum_{n=0}^{\infty} (-1)^n \alpha^{m-n} C_n^m \frac{x^n}{n!} \\ &= \sum_{n=0}^{\infty} H(n+m, r+m, \alpha) x^n \sum_{n=0}^{\infty} (-1)^n \alpha^{m-n} C_n^m \frac{x^n}{n!}, \end{aligned}$$

and by product of exponential generating functions,

$$\begin{aligned} \sum_{n=0}^{\infty} H(n, r, \alpha) x^n &= \sum_{n=0}^{\infty} \sum_{i=0}^n \frac{(-1)^i}{i! \alpha^{i-m}} C_i^m H(n+m-i, r+m, \alpha) x^n, \\ &\text{as claimed.} \end{aligned}$$

Secondly, we will give the proof of the other sum. From Binomial theorem and (5), we have

$$\begin{aligned} (1-x)^{r-1} \frac{x^r e^{-x}}{(1-x)^{r+1}} &= \sum_{n=0}^{r-1} (-1)^n \binom{r-1}{n} x^n \sum_{n=0}^{\infty} D_r(n) \frac{x^n}{n!} \\ &= \sum_{n=0}^{\infty} \sum_{i=0}^n (-1)^i \binom{r-1}{i} \frac{D_r(n-i)}{(n-i)!} x^n, \quad (9) \end{aligned}$$

and by product of generating functions,

$$\begin{aligned} (1-x)^{r-1} \frac{x^r e^{-x}}{(1-x)^{r+1}} &= \frac{e^{-x}}{1-x} \left(\frac{-x}{\alpha} \right)^r \alpha^r \frac{(-\ln(1-\frac{x}{\alpha}))^r}{1-x} \\ &= \sum_{n=0}^{\infty} d_n \frac{x^n}{n!} \sum_{n=0}^{\infty} \frac{(-1)^n C_n^r x^n}{\alpha^{n-r} n!} \sum_{n=0}^{\infty} H(n, r-1, \alpha) x^n \\ &= \sum_{n=0}^{\infty} \sum_{i=0}^n (-1)^i \binom{n}{i} \frac{C_i^r d_{n-i} x^n}{\alpha^{i-r} n!} \sum_{n=0}^{\infty} H(n, r-1, \alpha) x^n \\ &= \sum_{n=0}^{\infty} \sum_{j=0}^n \sum_{i=0}^j (-1)^i \binom{j}{i} \frac{C_i^r d_{j-i} H(n-j, r-1, \alpha)}{\alpha^{i-r} j!} x^n. \quad (10) \end{aligned}$$

By (9) and (10), comparing the coefficients on both sides, we get the desired result. So, the proof is complete.

Theorem 4. For $n \geq m$ and $n > r \geq 1$, then

$$\sum_{j=0}^n \sum_{i=0}^j H(i, r-1, \alpha) H_{j-i}^m(\alpha) \frac{d_{n-j}}{(n-j)!} = \sum_{i=0}^n H(n-i+m, r, \alpha) \frac{D_m(i)}{i!},$$

and for $n \geq r \geq 1$,

$$\begin{aligned} D_r(n) &= n! \sum_{j=0}^{n-r} \sum_{i=0}^j \frac{(-1)^{i+j} D_{r-1}(i+r-1) C_{j-i}^r H(n-j, r-1, \alpha)}{(i+r-1)! (j-i)! \alpha^{j-i-r}}. \end{aligned}$$

Proof. From product of exponential generating functions, we write

$$\begin{aligned} \frac{(-\ln(1-\frac{x}{\alpha}))^{r+1}}{(1-x)^{m+2}} e^{-x} &= \frac{(-\ln(1-\frac{x}{\alpha}))^{r+1}}{1-x} \frac{x^m e^{-x}}{(1-x)^{m+1} x^{-m}} \\ &= \sum_{n=0}^{\infty} H(n, r, \alpha) x^{n-m} \sum_{n=0}^{\infty} \frac{D_m(n)}{n!} x^n \\ &= \sum_{n=-m}^{\infty} H(n+m, r, \alpha) x^n \sum_{n=0}^{\infty} \frac{D_m(n)}{n!} x^n \\ &= \sum_{n=0}^{\infty} \sum_{i=0}^n H(i+m, r, \alpha) \frac{D_m(n-i)}{(n-i)!} x^n, \quad (11) \end{aligned}$$

and

$$\begin{aligned} \frac{(-\ln(1-\frac{x}{\alpha}))^{r+1}}{(1-x)^{m+2}} e^{-x} &= \frac{(-\ln(1-\frac{x}{\alpha}))^r}{1-x} \frac{-\ln(1-\frac{x}{\alpha})}{(1-x)^m} \frac{e^{-x}}{1-x} \\ &= \sum_{n=0}^{\infty} H(n, r-1, \alpha) x^n \sum_{n=0}^{\infty} H_n^m(\alpha) x^n \sum_{n=0}^{\infty} \frac{d_n}{n!} x^n \\ &= \sum_{n=0}^{\infty} \sum_{i=0}^n H(i, r-1, \alpha) H_{n-i}^m(\alpha) x^n \sum_{n=0}^{\infty} \frac{d_n}{n!} x^n \\ &= \sum_{n=0}^{\infty} \sum_{j=0}^n \sum_{i=0}^j H(i, r-1, \alpha) H_{j-i}^m(\alpha) \frac{d_{n-j}}{(n-j)!} x^n. \quad (12) \end{aligned}$$

From here, (11) and (12) yield the desired result.

Now, we will give the other sum. With the help of generating functions of (2), (3) and (5), we get

$$\begin{aligned} \sum_{n=0}^{\infty} \frac{D_r(n)}{n!} x^n &= \frac{x^r e^{-x}}{(1-x)^{r+1}} \\ &= x^{-r+1} \frac{x^{r-1} e^{-x}}{(1-x)^r} \left(\frac{-x}{\alpha} \right)^r \alpha^r \frac{(-\ln(1-\frac{x}{\alpha}))^r}{1-x} \\ &= \sum_{n=r-1}^{\infty} \frac{D_{r-1}(n) x^{n-r+1}}{n!} \sum_{n=0}^{\infty} \frac{(-1)^n C_n^r x^n}{\alpha^{n-r} n!} \\ &\quad \times \sum_{n=0}^{\infty} H(n, r-1, \alpha) x^n \\ &= \sum_{n=0}^{\infty} \sum_{i=0}^n (-1)^{n-i} \frac{D_{r-1}(i+r-1) C_{n-i}^r}{(i+r-1)! (n-i)! \alpha^{n-i-r}} x^n \\ &\quad \times \sum_{n=0}^{\infty} H(n, r-1, \alpha) x^n \\ &= \sum_{n=0}^{\infty} \sum_{j=0}^n \sum_{i=0}^j (-1)^{j-i} \frac{D_{r-1}(i+r-1) C_{j-i}^r H(n-j, r-1, \alpha)}{(i+r-1)! (j-i)! \alpha^{j-i-r}} x^n. \end{aligned}$$

Thus, the desired result is given.

Theorem 5. For $n \geq 2r + 1$, then

$$\begin{aligned} \sum_{i=0}^n (-1)^{i+r+1} \binom{n}{i} \frac{s(i, r+1) D_r(n-i) (r+1)!}{\alpha^i n!} \\ = \sum_{i=0}^n H(i-1, r, \alpha) \frac{D_{r-1}(n-i)}{(n-i)!}, \end{aligned}$$

and for $n > r$,

$$\begin{aligned} H(n, r, \alpha) \\ = \frac{(r+1)!}{n!} \sum_{j=0}^n \sum_{i=0}^j (-1)^{i+r+1} \binom{n}{j} \binom{j}{i} \alpha^{-i} s(i, r+1) d_{j-i}. \end{aligned}$$

Proof. By product of exponential generating functions, we have

$$\begin{aligned} \left(-\ln\left(1 - \frac{x}{\alpha}\right) \right)^{r+1} \frac{x^r e^{-x}}{(1-x)^{r+1}} \\ = \sum_{n=0}^{\infty} (-1)^{n+r+1} \alpha^{-n} s(n, r+1) (r+1)! \frac{x^n}{n!} \sum_{n=0}^{\infty} D_r(n) \frac{x^n}{n!} \\ = (-1)^{r+1} (r+1)! \\ \times \sum_{n=0}^{\infty} \sum_{i=0}^n \binom{n}{i} (-1)^i s(i, r+1) D_r(n-i) \frac{x^n}{\alpha^i n!}, \end{aligned}$$

and from product of generating functions,

$$\begin{aligned} \left(-\ln\left(1 - \frac{x}{\alpha}\right) \right)^{r+1} \frac{x^r e^{-x}}{(1-x)^{r+1}} \\ = \frac{\left(-\ln\left(1 - \frac{x}{\alpha}\right) \right)^{r+1} x^{r-1} e^{-x}}{1-x} \frac{1}{(1-x)^r} x \end{aligned}$$

$$\begin{aligned} &= \sum_{n=0}^{\infty} H(n, r, \alpha) x^{n+1} \sum_{n=0}^{\infty} \frac{D_{r-1}(n)}{n!} x^n \\ &= \sum_{n=0}^{\infty} H(n-1, r, \alpha) x^n \sum_{n=0}^{\infty} \frac{D_{r-1}(n)}{n!} x^n \\ &= \sum_{n=0}^{\infty} \sum_{i=0}^n \frac{H(i-1, r, \alpha) D_{r-1}(n-i)}{(n-i)!} x^n. \end{aligned}$$

Thus, comparing the coefficients on both sides, we get the desired result.

Similarly, considering

$$\begin{aligned} \sum_{n=0}^{\infty} H(n, r, \alpha) x^n \\ = \frac{\left(-\ln\left(1 - \frac{x}{\alpha}\right) \right)^{r+1}}{1-x} = \left(-\ln\left(1 - \frac{x}{\alpha}\right) \right)^{r+1} \frac{e^{-x}}{1-x} e^x \\ = \sum_{n=0}^{\infty} (-1)^{n+r+1} \alpha^{-n} s(n, r+1) (r+1)! \frac{x^n}{n!} \\ \quad \times \sum_{n=0}^{\infty} d_n \frac{x^n}{n!} \sum_{n=0}^{\infty} \frac{x^n}{n!} \\ = (-1)^{r+1} (r+1) \\ \times \sum_{n=0}^{\infty} \sum_{j=0}^n \sum_{i=0}^j \frac{(-1)^i}{n!} \binom{n}{j} \binom{j}{i} \alpha^{-i} s(i, r+1) d_{j-i} x^n, \end{aligned}$$

the proof of the other sum is obtained.

Conclusion

With the help of product of generating functions and then comparing the coefficients of x^n in the first and last series, some sums are obtained involving generalized harmonic, r-derangement, Cauchy numbers and some special numbers. In the future, it is aimed to find new sums with the help of the derivative operator.

Acknowledgments

The author would like to thank the referees for their valuable comments and suggestions for the improvement of the present paper.

Conflicts of interest

There are no conflicts of interest in this work.

References

- [1] Benjamin A.T., Gaebler D., Gaebler R., A Combinatorial Approach to Hyperharmonic Numbers, *Integers*, 3 (2013) 1-9.
- [2] Benjamin A.T., Preston G.O., Quinn J.J., A Stirling Encounter with Harmonic Numbers, *Math. Mag.*, 75 (2002) 95-103.

- [3] Caralambides C.A., Enumerative combinatorics, Chapman&Hall/Crc, Press Company, 1st ed. New York, (2002), 1-632.
- [4] Cheon G.S., El-Mikkawy M., Generalized Harmonic Numbers with Riordan Arrays, *J. Number Theory*, 128(2) (2008) 413-425.
- [5] Dattoli G., Licciardi S., Sabia E., Srivastava H.M., Some Properties and Generating Functions of Generalized Harmonic Numbers, *Mathematics*, 7(7) (2019), Article ID 577.
- [6] Dattoli G., Srivastava H.M., A Note on Harmonic Numbers, Umbral Calculus and Generating Functions, *Appl. Math. Lett.*, 21 (7) (2008) 686-693.
- [7] Duran Ö., Ömür N., Koparal S., On Sums with Generalized Harmonic, Hyperharmonic and Special Numbers, *Miskolc Math. Notes*, 21(2) (2020) 791-160.
- [8] Geñcev M., Binomial Sums Involving Harmonic Numbers, *Math. Slovaca*, 61(2) (2011) 215-226.
- [9] Koparal S., Ömür N., Südemen K.N., Some Identities for Derangement Numbers, *Miskolc Math. Notes*, 23(2) (2022) 773-785.
- [10] Koparal S., Ömür N., Duran Ö., On Identities Involving Generalized Harmonic, Hyperharmonic and Special Numbers with Riordan Arrays, *Spec. Matrices*, 9 (2021) 22-30.
- [11] Kwon H.I., Jang G.W., Kim T., Some Identities of Derangements Numbers Arising from Differential Equations, *Adv. Stud. Contemp. Math.*, 28(1) (2018) 73-82.
- [12] Ömür N., Bilgin G., Some Applications of Generalized Hyperharmonic Numbers of Order r , $H_n^r(\alpha)$, *Adv. Appl. Math. Sci.*, 17(9) (2018) 617-627.
- [13] Ömür N., Koparal S., On the Matrices with the Generalized Hyperharmonic Numbers of Order r , *Asian-European J. Math.*, 11(3) (2018) Article ID 1850045.
- [14] Ömür N., Südemen K.N., Koparal S., Some Identities with Special Numbers, *Cumhuriyet Sci. J.*, 43(4) (2022) 696-702.
- [15] Ömür N., Koparal S., Sums Involving Generalized Harmonic and Daehee Numbers, *Notes on Number Theory and Discrete Math.*, 28(1) (2022) 92-99.
- [16] Qi F., Zhao J.L., Guo B.N., Closed Forms for Derangement Numbers in terms of the Hessenberg Determinants, *Rev. R. Acad. Cienc. Exactas Fís. Nat. Ser. A Mat. RACSAM*, 112 (2018) 933-944.
- [17] Qi F., Guo B.N., Explicit Formulas for Derangement Numbers and Their Generating Function, *J. Nonlinear Funct. Anal.*, 2016 (2016) Article ID 45.
- [18] Rim S.H., Kim T., Pyo S.S., Identities Between Harmonic, Hyperharmonic and Daehee Numbers, *J. Inequal. Appl.*, 2018 (2018) Article ID 168.
- [19] Santmyer J.M., A Stirling like Sequence of Rational Numbers, *Discrete Math.*, 171(1-3) (1997) 229-235.
- [20] Sofo A., Srivastava H.M., Identities for the Harmonic Numbers and Binomial Coefficients, *Ramanujan J.*, 25(1) (2011) 93-113.
- [21] Şimşek Y., Special Numbers on Analytic Functions, *Appl. Math.*, 5(7) (2014) 1091-1098.
- [22] Wang C., Miska P., Mezö I., The r -Derangement Numbers, *Discrete Math.*, 340(2017) 1681-1692.
- [23] Choi J., Srivastava H.M., Some summation formulas involving harmonic numbers and generalized harmonic numbers, *Math. Comput. Model.*, 54(9-10) (2011) 2220-2234.
- [24] Simsek Y., Some classes of finite sums related to the generalized Harmonic functions and special numbers and polynomials, *Montes Taurus J. Pure Appl. Math.*, 4(3) (2022) 61-79.
- [25] Simsek Y., New integral formulas and identities involving special numbers and functions derived from certain class of special combinatorial sums, *RACSAM*, 115(66) (2021) 1-14.
- [26] Simsek Y., Apostol type Daehee numbers and polynomials, *Adv. Stud. Contemp. Math.*, 26(3) (2016) 555-566.
- [27] Rassias T.M., Srivastava H.M., Some classes of infinite series associated with the Riemann Zeta and Polygamma functions and generalized harmonic numbers, *Appl. Math. Comput.*, 131(2002) 593-605.
- [28] Kim T., Kim D.S., Combinatorial identities involving degenerate harmonic and hyperharmonic numbers, *Adv. Appl. Math.*, 148(2023) Article ID 102535, 15 p.
- [29] Kim T., Kim D.S., Some identities on degenerate hyperharmonic numbers, *Georgian Math. J.*, 30(2) (2023) 255-262.
- [30] Dolgy D.V., Kim D.S., Kim H.K., Kim, T., Degenerate harmonic and hyperharmonic numbers, *Proc. Jangjeon Math. Soc.*, 26(3) (2023) 259-268.
- [31] Kim D.S., Kim T., Normal ordering associated with λ -Whitney numbers of the first kind in λ -shift algebra, *Russ. J. Math. Phys.*, 30(3) (2023) 310-319.
- [32] Kim T., Kim D.S., Some identities on degenerate r -Stirling numbers via boson operators, *Russ. J. Math. Phys.*, 29(4) (2022) 508-517.
- [33] Kim T.K., Kim D.S., Some identities involving degenerate Stirling numbers associated with several degenerate polynomials and numbers, *Russ. J. Math. Phys.*, 30(1) (2023) 62-75.

Dynamics of a Conformable Fractional Order Generalized Richards Growth Model on Star Network with N=20 Nodes

Neriman Kartal ^{1,a,*}

¹ Department of Travel Tourism and Entertainment, Ürgüp Sebhat ve Erol TOKSÖZ Tourism Vocational High School, Nevşehir Hacı Bektaş Veli University, Nevşehir, Türkiye.

*Corresponding author

Research Article

History

Received: 03/11/2023

Accepted: 22/02/2024



This article is licensed under a Creative Commons Attribution-NonCommercial 4.0 International License (CC BY-NC 4.0)

ABSTRACT

In this study, we analyze dynamical behavior of the conformable fractional order Richards growth model. Before examining the analysis of the dynamical behavior of the fractional continuous time model, the model is reduced to the system of difference equations via utilizing piecewise constant functions. An algebraic condition that ensures the stability of the positive fixed point of the system is obtained. With the center manifold theory, the existence of a Neimark-Sacker bifurcation at the fixed point of the discrete-time system is proven and the direction of this bifurcation is determined. In addition, the discrete dynamical system is also studied on the star network with $N = 20$ nodes. Analysis complex dynamics of Richards growth model into coupled dynamical network shows that the complex star network with $N = 20$ nodes also exhibits Neimark-Sacker bifurcation about the fixed point concerning with parameter c . Numerical simulations are performed to demonstrate the stability, bifurcations and dynamic transition of the coupled network.

Keywords: Fractional order model, Star network, Discrete system, Stability, Neimark-Sacker bifurcation.

^a nerimangok@nevsehir.edu.tr

<https://orcid.org/0000-0003-1100-0949>

Introduction

In order to describe physical or biological processes many different types of mathematical models such as Malthus, Logistic, Von Bertalanffy, Richards, Gompertz, Blumberg and Turner are used. The most commonly used of these are the logistic and Richards models. Compared with the logistic equation, Richards equations define for more flexible curves of the S shape where the growth curve is asymmetrical and it can define changes in the initial growth stage, rapid growth stage, and stable growth stage of populations. In the literature, there are many successful applications of the Richards growth model in fields such as forest modelers [1], geology [2], COVID 19 [3,4], Ebola [5], fruit weight [6], microbial growth [7], interaction two-species population [8], traffic [9] and tree growth model [10].

The Richards differential equation has the following form:

$$\frac{dN(t)}{dt} = rN(t) \left(1 - \left(\frac{N(t)}{K} \right)^\beta \right). \quad (1)$$

The more general form of the Richards model, called the generalized Richards growth model, is given as follows.

$$\frac{dN(t)}{dt} = rN^p(t) \left(1 - \left(\frac{N(t)}{K} \right)^\beta \right), \quad (2)$$

where r is the maximum intrinsic rate of increase of N , K is the upper asymptote of N and β is an additional parameter in the Richards equation introduced as a power law so that it can define asymmetric curves and p is known

as the deceleration of growth parameter which captures different early stages of the epidemic.

In recent years, the increasing popularity of fractional order derivatives has led to the increase of using fractional order dynamical systems in literature. Many biological and physical processes are successfully modeled in fields such as biology [11], physics [12], chemistry [13] and complex network [14]. The most important advantage of fractional order differential equations over ordinary differential equations is that they can reflect the long memory and hereditary properties of the systems. There are several kinds of definitions for fractional derivatives such as Caputo-Riemann-Liouville and conformable fractional derivatives. Conformal fractional order derivative has many advantages over other fractional order definitions in practice because it reflects many of the properties which already exist in ordinary differential equations.

For all $t > 0$, $\alpha \in (0,1)$, conformable fractional derivative of $f: [0, \infty) \rightarrow \mathbb{R}$ is defined by

$$({}_T^\alpha f)(t) = \lim_{\varepsilon \rightarrow 0} \frac{f(t+\varepsilon t^{1-\alpha}) - f(t)}{\varepsilon} \quad (3)$$

which has the following properties:

$$({}_T^\alpha f)(t) = (t-a)^{1-\alpha} f'(t), \dots, ({}_b^\alpha Tf)(t) = -(b-t)^{1-\alpha} f'(t), \quad (4)$$

where $({}_T^\alpha f)(t)$ and $({}_b^\alpha Tf)(t)$ are the left and right conformable fractional derivative respectively [15-16].

Busenberg and Cooke [17] introduced a new type of differential equations that is called differential equation with piecewise constant arguments in the early 1980s. Since these equations contain both differential equations

and difference equations, they have some advantages in applications. In particular, the ability to easily transition from these equations to difference equations is extremely important for population dynamics. In this way, many mathematical models for population dynamics that can describe rich dynamic behaviors such as chaos have been created in the literature [18-21].

Complex network is a type of mathematical graph and examines relationships between objects using connectivity. The objects and connectivity are represented nodes and edges respectively and each node is demonstrated by a nonlinear dynamical system in a complex network. Networks are named according to the shape of the connections such as globally coupled network, star network, Erdos-Renyi network and are used to understand the origin and complexity of the dynamical system. Studying on dynamical analysis of different types of complex networks can be found in the studies [22-27].

In study [28], ElRaheem and Salman consider the Caputo fractional-order Logistic differential equation with piecewise constant arguments given by

$$D^\alpha N(t) = \rho x \left(\left\lfloor \frac{t}{h} \right\rfloor h \right) \left(1 - x \left(\left\lfloor \frac{t-h}{h} \right\rfloor h \right) \right), \quad x(0) = x_0. \quad (5)$$

Discretization process gives the system of difference equations as follows:

$$\begin{cases} x(n+1) = x(n) + \rho x(n)(1 - y(n)) \frac{h^\alpha}{\Gamma(\alpha+1)} \\ y(n+1) = x(n). \end{cases} \quad (6)$$

The conformable fractional-order delay Richards growth model can be defined as follows:

$$T^\alpha N(t) = rN^p(t) \left(1 - \left(\frac{N(t-\tau)}{K} \right)^\beta \right). \quad (7)$$

If the piecewise constant arguments are used in the place of the term $t - \tau(t)$ as $\left\lfloor \frac{t-h}{h} \right\rfloor h$ we obtain

$$T^\alpha N(t) = rN^p \left(\left\lfloor \frac{t-h}{h} \right\rfloor h \right) \left(1 - \left(\frac{N \left(\left\lfloor \frac{t-h}{h} \right\rfloor h \right)}{K} \right)^\beta \right), \quad (8)$$

with the initial condition $N(0) = N_0$ where $N(t)$ is a value of a measure of size or density of an organism or population, β is additional shape parameter, p is deceleration of growth parameter, K is the carrying capacity, $\lfloor t \rfloor$ denotes the integer part of $t \in [0, \infty)$ and h is discretization parameter.

The purpose of this study is to examine stability and bifurcation analysis of the conformable fractional order generalized Richards growth model (8).

Local Stability Analysis

We will first apply a discretization procedure to obtain a system of difference equations from the model (8). Let $t \in [0, \infty)$, $n = 0, 1, 2, \dots$. From property (4) one can obtain

$$(t - nh)^{1-\alpha} \frac{dN(t)}{dt} = rN^p(nh - h) \left(1 - \left(\frac{N(nh-h)}{K} \right)^\beta \right) \quad (9)$$

that gives

$$dN(t) = rN^p(nh - h) \left(1 - \left(\frac{N(nh-h)}{K} \right)^\beta \right) (t - nh)^{\alpha-1} dt. \quad (10)$$

By integrating equation (10) with respect to t on $[nh, t)$, one can hold

$$N(t) - N(nh) = rN^p(nh - h) \left(1 - \left(\frac{N(nh-h)}{K} \right)^\beta \right) \frac{(t-nh)^\alpha}{\alpha}. \quad (11)$$

Let $t \rightarrow (n + 1)h$ in equation (11) and obtain

$$\begin{aligned} N((n + 1)h) - N(nh) &= \\ rN^p((n - 1)h) &\left(1 - \left(\frac{N((n-1)h)}{K} \right)^\beta \right) \frac{h^\alpha}{\alpha}. \end{aligned} \quad (12)$$

To use a suitable notation for the representation of difference equations, we replacing $N(nh)$ by $N(n)$.

$$N(n + 1) = N(n) + rN^p(n - 1) \left(1 - \left(\frac{N(n-1)}{K} \right)^\beta \right) \frac{h^\alpha}{\alpha} \quad (13)$$

If we introduce $x(n) = N(n)$ and $y(n) = N(n - 1)$, then we have

$$\begin{cases} x(n + 1) = x(n) + r(y(n))^p \left(1 - \left(\frac{y(n)}{K} \right)^\beta \right) \frac{h^\alpha}{\alpha} \\ y(n + 1) = x(n). \end{cases} \quad (14)$$

Now, we can deal with the stability of the fixed points of model (14). We note that the positive fixed point of the model (14) is $(x^*, y^*) = (K, K)$. Necessary and sufficient algebraic conditions that ensuring the local asymptotic stability of the positive fixed point of the model (14) will be given in the following theorem.

Theorem 1. The fixed point $(x^*, y^*) = (K, K)$ of system (14) is local asymptotically stable if and only if

$$0 < r < \frac{\alpha}{h^\alpha K^{-1+p}\beta}. \quad (15)$$

Proof 1. The Jacobian matrix calculated at positive fixed point $(x^*, y^*) = (K, K)$ of system (14) is

$$J = \begin{pmatrix} 1 & -\frac{h^\alpha K^{-1+p}\beta}{\alpha} \\ 1 & 0 \end{pmatrix}$$

and the corresponding characteristic equation is

$$\lambda^2 + p_1\lambda + p_2 = 0 \quad (16)$$

where

$$p_1 = -1 \quad (17)$$

and

$$p_2 = \frac{h^\alpha K^{-1+p}\beta}{\alpha}. \quad (18)$$

The following conditions that are called Schur-Cohn criterions can be used for the determining asymptotic stability conditions of the fixed point (x^*, y^*) of the system (14).

- i) $1 + p_1 + p_2 > 0$
- ii) $1 - p_1 + p_2 > 0$
- iii) $1 - p_2 > 0$

From i) and ii), we have

$$1 + p_1 + p_2 = \frac{h^\alpha K^{-1+p}\beta}{\alpha} > 0$$

and

$$1 - p_1 + p_2 = 2 + \frac{h^\alpha K^{-1+p}\beta}{\alpha} > 0,$$

respectively. Under the condition $r < \frac{\alpha}{h^{\alpha K^{-1} + p\beta}}$, we hold

$$1 - p_2 = 1 - \frac{h^{\alpha K^{-1} + p\beta}}{\alpha} > 0$$

This completes our proof.

Now we give the topological classification of the fixed point of the model (14).

Theorem 2. Assume that $K > 0$. For the fixed point $(x^*, y^*) = (K, K)$, the following topological classification holds:

- i) The fixed point is sink if $r < \frac{\alpha}{h^{\alpha K^{-1} + p\beta}}$.
- ii) The fixed point is source if $r > \frac{\alpha}{h^{\alpha K^{-1} + p\beta}}$.
- iii) The fixed point is a non-hyperbolic if $r = \frac{\alpha}{h^{\alpha K^{-1} + p\beta}}$.

Neimark Sacker Bifurcation Analysis

In this section, we examine the existence and direction of Neimark-Sacker bifurcation about the positive fixed point for the discrete system (14) in line with the studies [29-31].

Theorem 3: System (14) undergoes Neimark-Sacker bifurcation at the fixed point $(x^*, y^*) = (K, K)$. Moreover, if $k < 0$ then an attracting invariant cycle will appear for $r > r^*$, if $k > 0$ then a repelling invariant cycle will appear for $0 < r < r^*$.

Proof 2. From the characteristic equation of the linearized system at the positive fixed point, the eigenvalues can be calculated as follows.

$$\lambda_{1,2} = \frac{1}{2} \pm i \frac{\sqrt{K\alpha(4h^{\alpha K p r \beta} - K\alpha)}}{2K\alpha}. \tag{19}$$

From the solution of equation $1 - p_2 = 0$ in accordance with parameter r gives the Neimark-Sacker bifurcation point as follows:

$$r = r^* = \frac{\alpha}{h^{\alpha K^{-1} + p\beta}}. \tag{20}$$

For $r = r^*$, these eigenvalues leads to

$$|\lambda_{1,2}| = \left| \frac{1}{2} \pm \frac{i\sqrt{3}}{2} \right| = |a \pm ib| = 1.$$

The transversality condition

$$\frac{d|\lambda_{1,2}(r)|}{dr} \Big|_{r=r^*} = \frac{h^{\alpha K^{-1} + p\beta}}{2\alpha} \neq 0 \tag{21}$$

is always satisfied for all parameter values. In addition, non-resonance conditions is always satisfied for $p_1 \neq 0, 1$.

Let $u = x - x^*$ and $v = y - y^*$, then the system (14) is transformed into

$$\begin{pmatrix} u \\ v \end{pmatrix} \rightarrow \begin{pmatrix} 1 & -1 \\ 1 & 0 \end{pmatrix} \begin{pmatrix} u \\ v \end{pmatrix} + \begin{pmatrix} f_1(u, v) \\ f_2(u, v) \end{pmatrix} \tag{22}$$

where

$$\begin{aligned} f_1(u, v) &= m_{13}u^2 + m_{14}uv + m_{15}v^2 + m_{16}u^3 + m_{17}u^2v + m_{18}uv^2 + m_{19}v^3 + O((|u| + |v|)^4) \\ f_2(u, v) &= m_{23}u^2 + m_{24}uv + m_{25}v^2 + m_{26}u^3 + m_{27}u^2v + m_{28}uv^2 + m_{29}v^3 + O((|u| + |v|)^4) \end{aligned}$$

and

$$\begin{aligned} m_{13} &= m_{14} = m_{16} = m_{17} = m_{18} = m_{23} = m_{24} = m_{25} = m_{26} = m_{27} = m_{28} = m_{29} = 0 \\ m_{15} &= -\frac{-1+2p+\beta}{2K} \\ m_{19} &= -\frac{2+3(-2+p)p-3\beta+3p\beta+\beta^2}{6K^2}. \end{aligned}$$

By using transformation $\begin{pmatrix} u \\ v \end{pmatrix} = T \begin{pmatrix} X \\ Y \end{pmatrix}$, then the map (22) rewritten as the following form

$$\begin{pmatrix} X \\ Y \end{pmatrix} \rightarrow \begin{pmatrix} a & -b \\ b & a \end{pmatrix} \begin{pmatrix} X \\ Y \end{pmatrix} + \begin{pmatrix} F_1(X, Y) \\ F_2(X, Y) \end{pmatrix} \tag{23}$$

where

$$\begin{aligned} T &= \begin{pmatrix} \frac{\sqrt{3}}{2} & 1 \\ 0 & 1 \end{pmatrix} \\ F_1(X, Y) &= -\frac{Y^2(-1+2p+\beta)}{\sqrt{3}K} - \frac{Y^3(2-6p+3p^2-3\beta+3p\beta+\beta^2)}{3\sqrt{3}K^2} + O((|u| + |v|)^4) \\ F_2(X, Y) &= 0. \end{aligned}$$

The constant k , which will determine the direction of the Neimark-Sacker bifurcation, can be calculated using the following equation.

$$k = -\text{Re} \left[\frac{(1-2\lambda)\bar{\lambda}^2}{1-\lambda} \xi_{11} \xi_{20} \right] - \frac{1}{2} |\xi_{11}|^2 - |\xi_{02}|^2 + \text{Re} [\bar{\lambda} \xi_{21}] = \frac{2p-5p^2+\beta-5p\beta-\beta^2}{16K^2} \tag{24}$$

where

$$\begin{aligned} \xi_{20} &= \frac{1}{8} ((F_{1XX} - F_{1YY} + 2F_{2XY}) + i(F_{2XX} - F_{2YY} - 2F_{1XY})) = \frac{-1+2p+\beta}{4\sqrt{3}K} \\ \xi_{11} &= \frac{1}{4} ((F_{1XX} + F_{1YY}) + i(F_{2XX} + F_{2YY})) = -\frac{-1+2p+\beta}{2\sqrt{3}K} \\ \xi_{02} &= \frac{1}{8} ((F_{1XX} - F_{1YY} - 2F_{2XY}) + i(F_{2XX} - F_{2YY} + 2F_{1XY})) = \frac{-1+2p+\beta}{4\sqrt{3}K} \\ \xi_{21} &= \frac{1}{16} ((F_{1XXX} + F_{1XY} + F_{2XXY} + F_{2YY}) + i(F_{2XXX} + F_{2XY} - F_{1XXY} - F_{1YY})) \\ &= \frac{i(2+3p^2+3p(-2+\beta)-3\beta+\beta^2)}{8\sqrt{3}K^2}. \end{aligned}$$

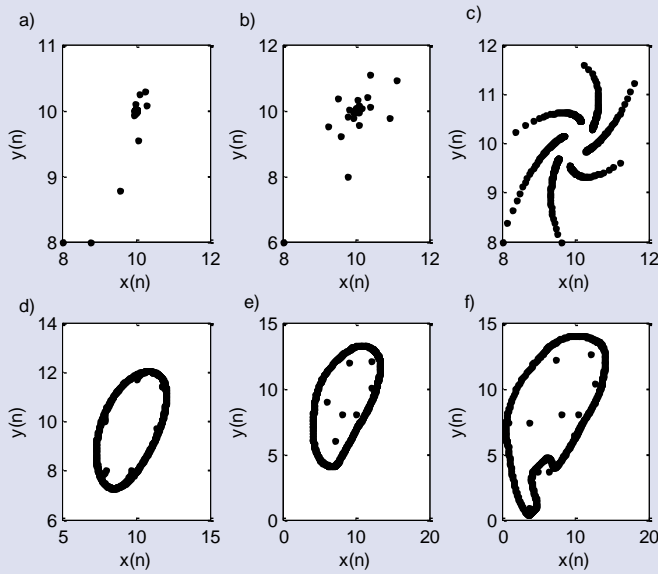


Figure 1. Phase portraits of the discrete model (14) with respect to parameter r for $r = 1$ (a), $r = 1.5$ (b), $r = 2.08295$ (c), $r = 2.3$ (d) $r = 2.6$ (e), $r = 3$ (f) where $\alpha=0.95, \beta=0.7, K=10, h=0.5, p=1.1, x(1)=y(1)=7$.

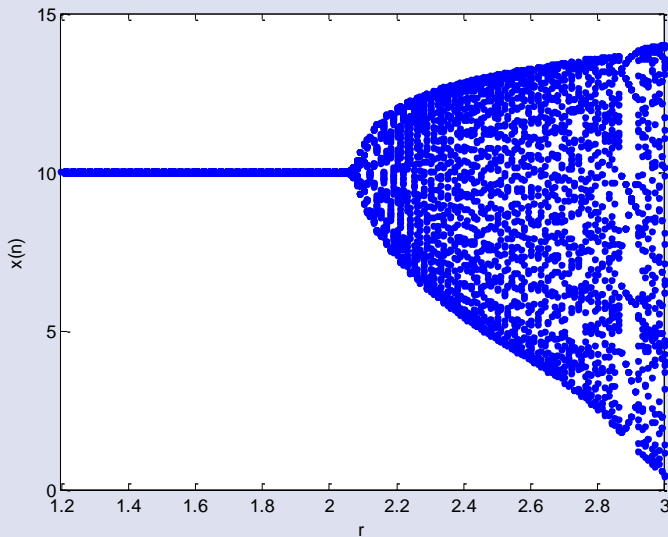
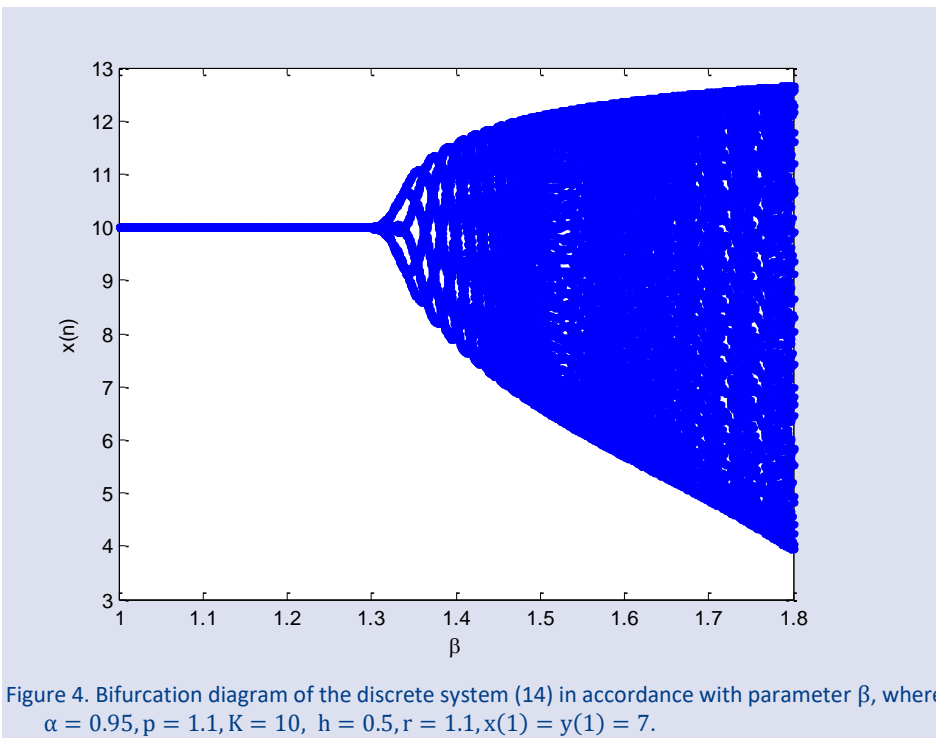
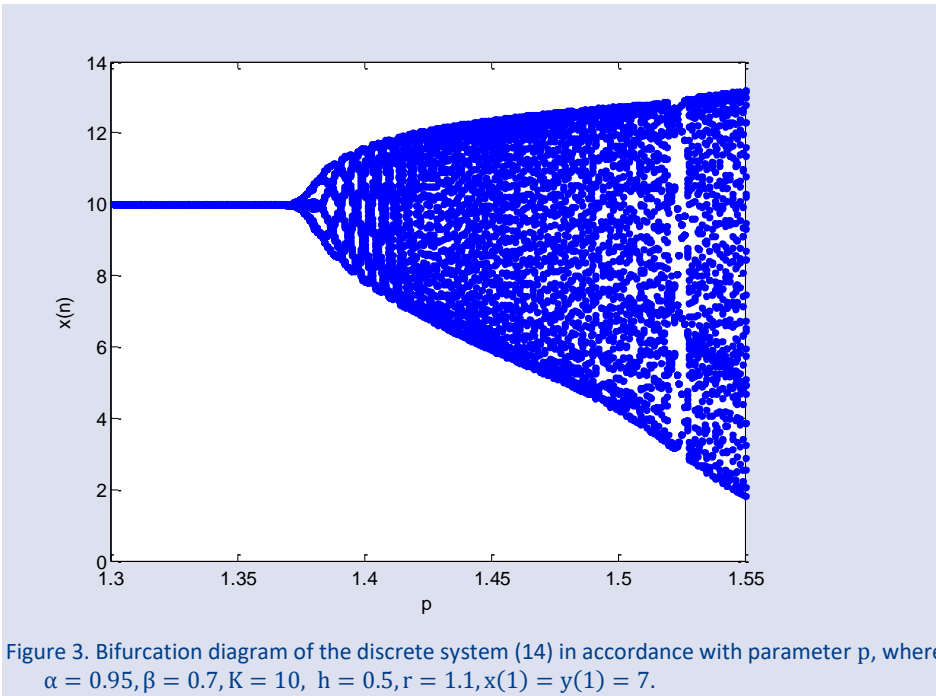


Figure 2. Bifurcation diagram of the discrete system (14) in accordance with parameter r , where $\alpha = 0.95, \beta = 0.7, K = 10, h = 0.5, p = 1.1, x(1) = y(1) = 7$.



Dynamical Analysis of the model on Star Network

Taking into account a dynamical network consisting of N linearly and diffusively coupled nodes, with each node describe a two-dimensional dynamical system defined by discrete system (14). Let's consider the equation (14) as the following form:

$$\begin{cases} x(k+1) = x(k) + r(y(k))^p \left(1 - \left(\frac{y(k)}{K}\right)^\beta\right) \frac{h^\alpha}{\alpha} = f(x(k), y(k)) \\ y(k+1) = x(k) = g(x(k), y(k)). \end{cases} \quad (25)$$

This dynamical network is defined by

$$\begin{cases} x_i(k+1) = f(x_i(k), y_i(k)) - c \sum_{j=1}^N a_{ij} f(x_j(k), y_j(k)) \\ y_i(k+1) = g(x_i(k), y_i(k)) - c \sum_{j=1}^N a_{ij} g(x_j(k), y_j(k)), \end{cases} \quad (26)$$

where i and j are the sequence number of the nodes and c describes the coupling strength of the network. The coupling matrix $A \in \mathbb{R}^{N \times N}$ can be expressed by

$$A = \begin{pmatrix} d_{11} & a_{12} & a_{13} & \dots & a_{1N} \\ a_{12} & d_{22} & a_{23} & \dots & a_{2N} \\ a_{13} & a_{23} & d_{33} & \dots & a_{3N} \\ \vdots & \vdots & \vdots & \ddots & \dots \\ a_{1N} & a_{2N} & a_{3N} & \dots & d_{NN} \end{pmatrix} \quad (27)$$

If there is a connection between node i and j , then $a_{ij} = 1$; otherwise, $a_{ij} = 0$ ($i \neq j$). Let $a_{ii} = d_i$, $i = 1, 2, \dots, N$, where d_i is the degree of node i and can be defined as

$$d_{ii} = -\sum_{j=1, j \neq i}^N a_{ij} = -\sum_{j=1, j \neq i}^N a_{ji}$$

The system (26) can be written in matrix form as follows:

$$\begin{cases} X_{k+1} = (I - cA)f(X(k), Y(k)) \\ Y_{k+1} = (I - cA)g(X(k), Y(k)) \end{cases} \quad (28)$$

where $X_k = (x_1(k), x_2(k), \dots, x_N(k))$, $Y_k = (y_1(k), y_2(k), \dots, y_N(k))$ and $I \in \mathbb{R}^{N \times N}$ identity matrix.

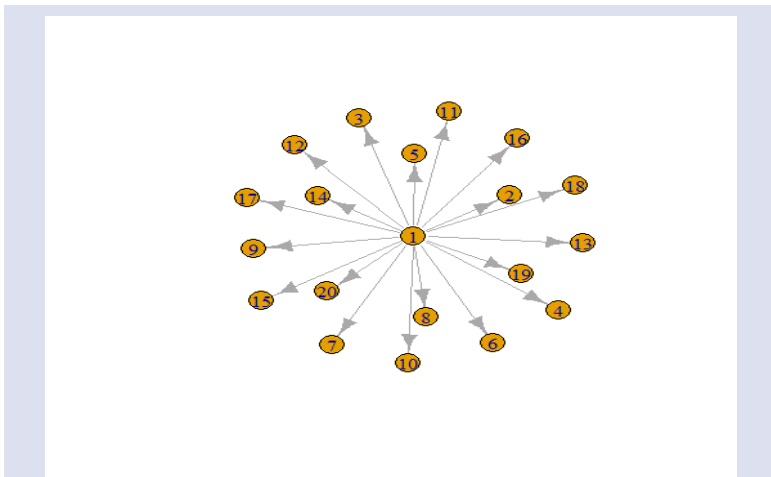


Figure 5. Star network with $N = 20$ nodes.

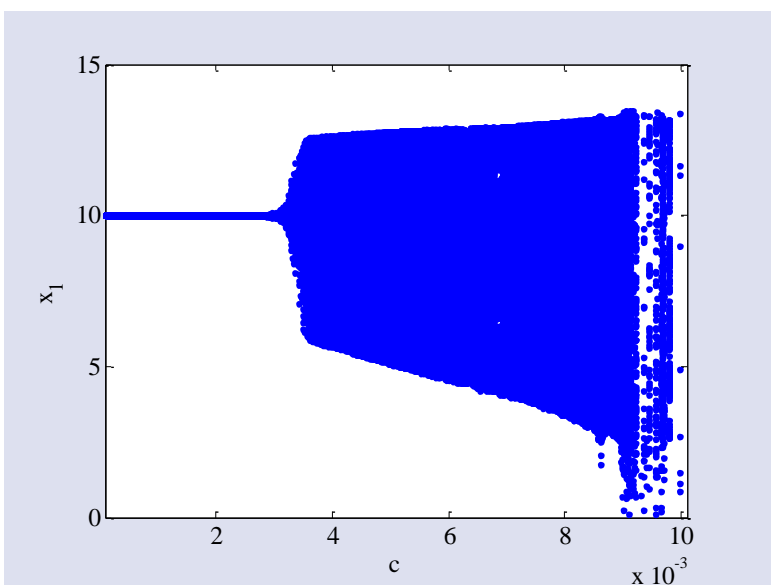


Figure 6. Neimark-Sacker bifurcation in the star network in accordance with parameter c , where $\alpha = 0.95$, $\beta = 0.7$, $p = 1.1$, $K = 10$, $h = 0.5$, $r = 2.07$ and $N = 20$.

Result and Discussion

In this study, we consider the conformable fractional order Richards growth model with piecewise constant arguments. Adding piecewise constant arguments to the model (7) make it possible to transition to the system of difference equation (14). The positive fixed point of the system (14) is obtained as $(x^*, y^*) = (K, K)$ and its stability condition is given in equation (15). To test this algebraic condition based on changing the growth rate parameter r of the population, we select the parameter values as $\alpha = 0.95, \beta = 0.7, K = 10, h = 0.5, p = 1.1$ and $x(1) = y(1) = 7$. The stability region according to the change of the parameter r is obtained as $r < 2.08295$. It can be easily seen in the Figure 1a and 1b that, the fixed point (10,10) of the system (14) is local asymptotically stable.

In bifurcation analysis, we deal with the existence and direction of the Neimark-Sacker bifurcation about the positive fixed point of the system (14). From the solutions of the equation $1 - p_0 = 0$ with respect tom parameter r , the eigenvalue assignment condition can be obtained as $r^* = \frac{\alpha}{h^\alpha K^{-1+p}\beta}$. In addition From the equation (21) and the conditions $p_1 \neq 0,1$, transversality and non-resonance conditions are always satisfied for all of the positive parameter values. Now, all of the conditions for the existence of the Neimark-Sacker bifurcation are satisfied and this bifurcation is shown in Figure 1c and Figure 2. From the equation (24), the value of k that determines the

direction of the Neimark-Sacker bifurcation is calculated as $k = -0.00468125$ which show the existence of supercritical Neimark-Sacker bifurcation. We also deal with the bifurcation analysis for the other parameters such as β and p . The effect of the deceleration of growth parameter p and additional shape parameter β on the dynamic structure of the system is seen in Figures 3 and Figure 4, respectively. From these figures we can also observe the Neimark-Sacker bifurcation for the parameter values $p^* = 1.37721$ and $\beta^* = 1.32529$ and so the model exhibits more unstable dynamics behavior for increased parameters p and β .

Model (12) and model (6) exhibit similar dynamic behaviors such as Neimark-Sacker bifurcation and chaos according to changing the growth rate parameter r and ρ . However, model (12) is a more generalized version of model (6) and includes extra parameters such as β and p . We provide that model (12) also exhibits Neimark-Sacker bifurcation according to changing parameters β and p .

Discrete dynamical system (14) is also considered on the star network with $N = 20$ nodes. In order to investigate the complex dynamics of the model (14) into coupled dynamical network, system (26) is represented the state equations of star network. All simulations have used the same initial condition for all nodes, which are slightly different from the fixed point. Figure 5 shows the star network with $N = 20$ nodes. For the star network with $N = 20$ nodes, the coupling matrix A can be obtained from the equation (27) as follows.

$$A = \begin{pmatrix} -19 & 1 & 1 & 1 & 1 & 1 & 1 & 1 & 1 & 1 & 1 & 1 & 1 & 1 & 1 & 1 & 1 & 1 & 1 & 1 \\ 1 & -1 & 0 & 0 & 0 & 0 & 0 & 0 & 0 & 0 & 0 & 0 & 0 & 0 & 0 & 0 & 0 & 0 & 0 & 0 \\ 1 & 0 & -1 & 0 & 0 & 0 & 0 & 0 & 0 & 0 & 0 & 0 & 0 & 0 & 0 & 0 & 0 & 0 & 0 & 0 \\ 1 & 0 & 0 & -1 & 0 & 0 & 0 & 0 & 0 & 0 & 0 & 0 & 0 & 0 & 0 & 0 & 0 & 0 & 0 & 0 \\ 1 & 0 & 0 & 0 & -1 & 0 & 0 & 0 & 0 & 0 & 0 & 0 & 0 & 0 & 0 & 0 & 0 & 0 & 0 & 0 \\ 1 & 0 & 0 & 0 & 0 & -1 & 0 & 0 & 0 & 0 & 0 & 0 & 0 & 0 & 0 & 0 & 0 & 0 & 0 & 0 \\ 1 & 0 & 0 & 0 & 0 & 0 & -1 & 0 & 0 & 0 & 0 & 0 & 0 & 0 & 0 & 0 & 0 & 0 & 0 & 0 \\ 1 & 0 & 0 & 0 & 0 & 0 & 0 & -1 & 0 & 0 & 0 & 0 & 0 & 0 & 0 & 0 & 0 & 0 & 0 & 0 \\ 1 & 0 & 0 & 0 & 0 & 0 & 0 & 0 & -1 & 0 & 0 & 0 & 0 & 0 & 0 & 0 & 0 & 0 & 0 & 0 \\ 1 & 0 & 0 & 0 & 0 & 0 & 0 & 0 & 0 & -1 & 0 & 0 & 0 & 0 & 0 & 0 & 0 & 0 & 0 & 0 \\ 1 & 0 & 0 & 0 & 0 & 0 & 0 & 0 & 0 & 0 & -1 & 0 & 0 & 0 & 0 & 0 & 0 & 0 & 0 & 0 \\ 1 & 0 & 0 & 0 & 0 & 0 & 0 & 0 & 0 & 0 & 0 & -1 & 0 & 0 & 0 & 0 & 0 & 0 & 0 & 0 \\ 1 & 0 & 0 & 0 & 0 & 0 & 0 & 0 & 0 & 0 & 0 & 0 & -1 & 0 & 0 & 0 & 0 & 0 & 0 & 0 \\ 1 & 0 & 0 & 0 & 0 & 0 & 0 & 0 & 0 & 0 & 0 & 0 & 0 & -1 & 0 & 0 & 0 & 0 & 0 & 0 \\ 1 & 0 & 0 & 0 & 0 & 0 & 0 & 0 & 0 & 0 & 0 & 0 & 0 & 0 & -1 & 0 & 0 & 0 & 0 & 0 \\ 1 & 0 & 0 & 0 & 0 & 0 & 0 & 0 & 0 & 0 & 0 & 0 & 0 & 0 & 0 & -1 & 0 & 0 & 0 & 0 \\ 1 & 0 & 0 & 0 & 0 & 0 & 0 & 0 & 0 & 0 & 0 & 0 & 0 & 0 & 0 & 0 & -1 & 0 & 0 & 0 \\ 1 & 0 & 0 & 0 & 0 & 0 & 0 & 0 & 0 & 0 & 0 & 0 & 0 & 0 & 0 & 0 & 0 & -1 & 0 & 0 \end{pmatrix}$$

Now let's consider the nodes with the highest degree in the star network with $N = 20$ nodes. which for is 1 and . Figure 6 shows that if the coupling parameter c reaches the some critical value where it is interval $c \in [2 \times 10^{-3}, 4 \times 10^{-3}]$, then Neimark-Sacker bifurcation occurs about the positive fixed point.

Acknowledgments

The authors declare that there is no conflict of interest.

Conflicts of interest

There are no conflicts of interest in this work.

References

- [1] Lei Y., Zhang S.Y., Comparison and selection of growth models using the Schnute model, *J. For. Sci.*, 52 (2006) 188-196.
- [2] Yang Y., Fan W., Long L., Xu Z., Zhao Z., Zhang H., Application of the Richards Model in Settlement Prediction of Loess-Filled Foundations, *Appl. Sci.*, 12 (2022) 11350.
- [3] Sharon E.A., Aharoni A., Generalized logistic growth modeling of the COVID-19 pandemic in Asia, *Infect. Dis. Model.*, 5 (2020) 502e509.
- [4] Zreiq R., Kamela S., Boubaker S., Al-Shammary A., Algahtani F.D., Alshammari F., Generalized Richards model for predicting COVID -19 dynamics in Saudi Arabia based on particle swarm optimization algorithm, *Public Health.*, 7 (2020) 828-843.
- [5] Pell B., Kuang Y., Viboud C., Chowell G., Using phenomenological models for forecasting the 2015 Ebola challenge, *Epidemics.*, 22 (2018) 62-70.
- [6] Gerhard D., Moltchanova E., A Richards growth model to predict fruit weight, *Aust. N. Z. J. Stat.*, 64 (2022) 413-421.
- [7] Teleken J.T., Galvao A.C., Robazza W.S., Use of modified Richards model to predict isothermal and non-isothermal microbial growth, *Braz. J. Microbiol.*, 49 (2018) 614-620.
- [8] Cabella B.C.T., Ribeiro F., Martinez A.S., Effective carrying capacity and analytical solution of a particular case of the Richards-like two-species population dynamics model, *Physica A.*, 391 (2012) 1281-1286.
- [9] He J., Mao S., Ng A.K.Y., Neural computing for grey Richards differential equation to forecast traffic parameters with various time granularity, *Neurocomputing.*, 549 (2023) 126394.
- [10] Protazio J.M.B., Souza M.A., Diaz J.C.H., Flores J.G.E., Sanches C.A.P., Parra A.C., Wehenkel C., A Dynamical Model Based on the Chapman–Richards Growth Equation for Fitting Growth Curves for Four Pine Species in Northern Mexico, *Forests.*, 13 (2022) 1866.
- [11] Magin R.L., Fractional calculus models of complex dynamics in biological tissues, *Comput. Math. with Appl.*, 59 (2010) 1586-1593.
- [12] Zhou P., Ma J., Tang J., Clarify the physical process for fractional dynamical systems, *Nonlinear Dyn.*, 100 (2020) 2353-2364.
- [13] Veerasha P., The efficient fractional order based approach to analyze chemical reaction associated with pattern formation, *Chaos. Solit. Fractals.*, 165 (2022) 112862.
- [14] Singh R., Rehman A.U., Masud M., Alhumyani H.A., Mahajan S., Pandit A.K., Agarwal P., Fractional order modeling and analysis of dynamics of stem cell differentiation in complex network, *AIMS math.*, 7 (2022) 5175-5198.
- [15] Khalil R., Horani M.A., Yousef A., Sababheh M., A new definition of fractional derivative, *J. Comput. Appl. Math.*, 264 (2014) 65-70.
- [16] Abdeljawad T., On conformable fractional calculus, *J. Comput. Appl. Math.*, 279 (2015) 57-66.
- [17] Busenberg S., Cooke K.L., Models of vertically transmitted diseases with sequential continuous dynamics, *Nonlinear Phenomena in Mathematical Sciences*, Academic Press, New York (1982).
- [18] Ozturk I., Bozkurt F., Gurcan F., Stability analysis of a mathematical model in a microcosm with piecewise constant arguments, *Math. Biosci.*, 240 (2012) 85-91.
- [19] Bozkurt F., Yousef A., Bilgil H., Baleanu D., A mathematical model with piecewise constant arguments of colorectal cancer with chemo-immunotherapy, *Chaos Soliton Fract.*, 168 (2023) 113207.
- [20] Gurcan F., Kartal S., Ozturk I., Bozkurt F., Stability and bifurcation analysis of a mathematical model for tumor-immune interaction with piecewise constant arguments of delay, *Chaos Soliton. Fract.*, 68 (2014) 169-179.
- [21] Kartal S., Gurcan F., Stability and bifurcations analysis of a competition model with piecewise constant arguments, *Math. Methods. Appl. Sci.*, 38 (2015) 1855-1866.
- [22] Wang Z., Jiang G., Yu W., He W., Cao J., Xiao M., Synchronization of coupled heterogeneous complex networks, *J. Franklin Inst.*, 354 (2017) 4102–4125.
- [23] Huang T., Zhang H., Ma S., Pan G., Wang Z., Huang H., Bifurcations, complex behaviors, and dynamic transition in a coupled network of discrete predator-prey system, *Discrete Dyn. Nat. Soc.*, 2019 (2019) Article ID 2583730.
- [24] Li X., Chen G., Ko K.T., Transition to chaos in complex dynamical networks, *Physica A Stat. Mech. Appl.*, 338 (2004) 367–378.
- [25] Nepomuceno E.G., Perc M., Computational chaos in complex networks, *J. Complex Netw.*, 8 (2020) cnz015.
- [26] Ahmed E., Matouk A.E., Complex dynamics of some models of antimicrobial resistance on complex networks, *Math. Methods Appl. Sci.*, 44 (2021) 1896-1912
- [27] Zhang H.F., Rui X.W., Fu X.C., The emergence of chaos in complex dynamical networks, *Chaos Soliton. Fract.*, 28 (2006) 472-479.
- [28] El Raheem Z.F., Salman S.M., On a discretization process of fractional-order logistic differential equation, *J. Egypt. Math. Soc.*, 22 (2014) 407-412.
- [29] Guckenheimer J., Holmes P., *Nonlinear Oscillations, Dynamical Systems, and Bifurcations of Vector Fields*, Springer, 1983
- [30] Kangalgil F., Neimark–sacker bifurcation and stability analysis of a discrete-time prey–predator model with allee effect in prey, *Adv. Differ. Equ.*, 92 (2019)
- [31] Kangalgil F., Işık S., Controlling chaos and neimark-sacker bifurcation in a discrete-time predator-prey system, *Hacet. J. Math. Stat.*, 49 (2020) 1761 – 1776.

A Note on the Trace of Generalized Permuting Tri-Derivations

Süleyman Zortaç^{1,a}, Hasret Yazarlı^{1,b,*}¹ Department of Mathematics, Faculty of Science, Sivas Cumhuriyet University, Sivas, Türkiye.

*Corresponding author

Research Article

History

Received: 26/07/2023





Accepted: 17/11/2023



This article is licensed under a Creative Commons Attribution-NonCommercial 4.0 International License (CC BY-NC 4.0)

ABSTRACT

Many researchers have studied permuting tri-derivation and generalized derivation in prime or semi-prime rings, BCK-algebras, lattices, d-algebras, MV-algebras and many algebraic structures. Later, they introduced the concept of generalized permuting tri-derivation by combining the concepts of generalized derivation and permuting tri-derivation. In this article, we have examined the properties of generalized permuting tri-derivation by adding conditions on their traces in prime or semi-prime rings. In addition, we examined the properties of two permuting tri-derivation by giving a relation between their traces.

Keywords: Prime ring, Semiprime ring, Permuting tri-derivation, Generalized permuting tri-derivation. zrtsslymn58@gmail.com <https://orcid.org/0000-0002-6079-0695> hyazarli@cumhuriyet.edu.tr <https://orcid.org/0000-0002-9987-2970>

Introduction and Preliminaries

The derivation is one of the important topics of many areas of mathematics. It has also been carried to the ring in algebra. In 1957, Posner defined the derivation in the ring and examined the commutativity of the ring [1]. In 1991, the generalized derivation in rings was introduced by Bresar [2]. Later inspired by partial derivation in analysis, in 1980, the symmetric bi-derivation was defined by Maksa and the permuting tri-derivation by Öztürk in 1999 [3-4]. They investigated the commutativity of prime or semi-prime rings with the help of conditions on these derivations and their traces. After then, many authors studied symmetric bi-derivation and permuting tri-derivation on many kind of algebraic structures as lattice, BCK-algebras, MV-algebras, hyperring, etc. [5-10]. In 2017, Yazarlı defined generalized permuting tri-derivation, combining the concepts of generalized derivation and permuting tri-derivation in the ring [11].

Assume that \mathfrak{A} is a ring and $d: \mathfrak{A} \rightarrow \mathfrak{A}$ is an additive map. If there exists a derivation α of \mathfrak{A} such that $d(ab) = d(a)b + \alpha(a)b$ in \mathfrak{A} , then d is called generalized derivation.

Let \mathfrak{A} is a ring and $F(.,.,.): \mathfrak{A} \times \mathfrak{A} \times \mathfrak{A} \rightarrow \mathfrak{A}$ is a map. If $F(a, b, c) = F(a, c, b) = F(c, a, b) = F(c, b, a) = F(b, c, a) = F(b, a, c)$ is provided in \mathfrak{A} , then F is called permuting and a map $f: \mathfrak{A} \rightarrow \mathfrak{A}$ defined by $f(a) = F(a, a, a)$ is called trace of $F(.,.,.)$. Suppose that $F(.,.,.): \mathfrak{A} \times \mathfrak{A} \times \mathfrak{A} \rightarrow \mathfrak{A}$ is permuting tri-additive, in this case F satisfies the relation $f(a + b) = f(a) + f(b) +$

$3F(a, a, b) + 3F(a, b, b)$ in \mathfrak{A} . A permuting tri-additive map $F(.,.,.): \mathfrak{A} \times \mathfrak{A} \times \mathfrak{A} \rightarrow \mathfrak{A}$ is called permuting tri-derivation if $F(ad, b, c) = F(a, b, c)d + aF(d, b, c)$ in \mathfrak{A} . The trace f is an odd function.

Let \mathfrak{A} be a ring and $\Gamma: \mathfrak{A} \times \mathfrak{A} \times \mathfrak{A} \rightarrow \mathfrak{A}$ be a permuting tri-additive map. Then, $\Gamma: \mathfrak{A} \times \mathfrak{A} \times \mathfrak{A} \rightarrow \mathfrak{A}$ is called generalized permuting tri-derivation of \mathfrak{A} associated with F if

$$\begin{aligned}\Gamma(ad, b, c) &= \Gamma(a, b, c)d + aF(d, b, c) \\ \Gamma(a, bd, c) &= \Gamma(a, b, c)d + bF(a, d, c) \\ \Gamma(a, b, cd) &= \Gamma(a, b, c)d + cF(a, b, d),\end{aligned}$$

in \mathfrak{A} where $F(.,.,.): \mathfrak{A} \times \mathfrak{A} \times \mathfrak{A} \rightarrow \mathfrak{A}$ is a permuting tri-derivation.

Example 1 [11] Let \mathfrak{A} be a ring, F be a tri-derivation of \mathfrak{A} and $\alpha: \mathfrak{A} \times \mathfrak{A} \times \mathfrak{A} \rightarrow \mathfrak{A}$ be a tri-additive map. If $\alpha(a, b, cd) = \alpha(a, b, c)d$, $\alpha(a, bd, c) = \alpha(a, b, c)d$ and $\alpha(ad, b, c) = \alpha(a, b, c)d$ in \mathfrak{A} , then $F + \alpha$ is a generalized F tri-derivation of \mathfrak{A} .

Lemma 1 [13] Let \mathfrak{A} be a prime ring. If there exists a right ideal of \mathfrak{A} which is contained in $\mathfrak{Z}(\mathfrak{A})$, \mathfrak{A} must be commutative where $\mathfrak{Z}(\mathfrak{A})$ be the center of \mathfrak{A}

In this article, we will apply the problems examined for generalized bi-derivations in the article of Ali, Shujat, Khan in 2015 to generalized permuting tri-derivations [12].

Results

In the Theorem 1, Theorem 2 and Theorem 3, we will assume that \mathfrak{A} be a prime ring with 2,3-torsion free, \mathfrak{B} be a non-zero ideal of \mathfrak{A} , $\mathfrak{Z}(\mathfrak{A})$ be the center of \mathfrak{A} , Γ is a generalized permuting tri-derivation with associated permuting tri-derivation F , γ is the trace of Γ and f is the trace of F .

Theorem 1 If $[\gamma(a), a] = 0$ in \mathfrak{B} and \mathfrak{A} is non-commutative then Γ is a left tri-multiplier on \mathfrak{B} .

Proof. Assume that

$$[\gamma(a), a] = 0 \text{ in } \mathfrak{B} \quad (1)$$

Writting $a + b$ instead of a , for $b \in \mathfrak{B}$ in (1), we get

$$\begin{aligned} &[\Gamma(a, a, a), b] + 3[\Gamma(a, a, b), a] + 3[\Gamma(a, a, b), b] \quad (2) \\ &+ 3[\Gamma(a, b, b), a] + 3[\Gamma(a, b, b), b] + [\Gamma(b, b, b), a] = 0. \end{aligned}$$

Substituting $-b$ instead of b in (2) and subtracting from (2), we get

$$[\Gamma(a, a, b), b] + [\Gamma(a, b, b), a] = 0. \quad (3)$$

Writting $a + b$ instead of b , for $b \in \mathfrak{B}$ in (3) and using (1) and (3), we get

$$[\Gamma(a, a, a), b] + 3[\Gamma(a, a, b), a] = 0 \quad (4)$$

Substituting br for b , for $r \in \mathfrak{A}$ in (4) and using (4), we get

$$\begin{aligned} &b[\Gamma(a, a, a), r] + 3\Gamma(a, a, b)[r, a] + 3[b, a]F(a, a, r) \quad (5) \\ &+ 3b[F(a, a, r), a] = 0. \end{aligned}$$

Writting a instead of r , for $a \in \mathfrak{B}$ in (5), we obtain

$$3[b, a]F(a, a, a) + 3b[F(a, a, a), a] = 0. \quad (6)$$

Substituting rb instead of b , for $r \in \mathfrak{A}$ in (6) and using (6), we get

$$[r, a]bF(a, a, a) = 0. \quad (7)$$

Writting rs instead of r , $s \in \mathfrak{A}$ in (7), we get

$$[r, a]sbF(a, a, a) = 0, \quad a, b \in \mathfrak{B} \text{ and } r, s \in \mathfrak{A}.$$

From here, we obtain $[r, a] = 0$ or $bF(a, a, a) = 0$ for all $a, b \in \mathfrak{B}$ and $r \in \mathfrak{A}$, since \mathfrak{A} is prime ring. If $[r, a] = 0$, then $\mathfrak{B} \subseteq Z(\mathfrak{A})$. In this case, \mathfrak{A} is commutative ring. This is a contradiction. Assume that $bF(a, a, a) = 0$ for all $a, b \in \mathfrak{B}$ If we write $a + c$, $c \in \mathfrak{B}$ instead of a , we have

$$bF(a, a, a) + 3bF(a, a, c) + 3bF(a, c, c) + bF(c, c, c) = 0$$

for all $a, b, c \in \mathfrak{B}$. Writting $-c$ instead of c and comparing last two expressions we get $bF(a, c, c) = 0$. Writting $c + d$ instead of c , $d \in \mathfrak{B}$, we get $bF(a, c, c) + 2bF(a, c, d) + bF(a, d, d) = 0$. That is, $bF(a, c, d) = 0$ in \mathfrak{B} . Thus, we obtain that $\Gamma(ad, b, c) = \Gamma(a, b, c)d$ on \mathfrak{B} .

Theorem 2 If $\gamma(a) \circ a = 0$ in \mathfrak{B} and \mathfrak{A} is non-commutative ring, then Γ is a left tri-multiplier on \mathfrak{B} .

Proof. Assume that

$$\gamma(a) \circ a = 0 \text{ in } \mathfrak{B} \quad (8)$$

Writting $a + b$ instead of a , for $b \in \mathfrak{B}$ in (8) and using (8), we get

$$\begin{aligned} &3\Gamma(a, a, b)a + 3\Gamma(a, b, b)a + \Gamma(b, b, b)a + \Gamma(a, a, a)b \\ &+ 3\Gamma(a, a, b)b + 3\Gamma(a, b, b)b + 3a\Gamma(a, a, b) + 3a\Gamma(a, b, b) \\ &+ a\Gamma(b, b, b) + b\Gamma(a, a, a) + 3b\Gamma(a, a, b) + 3b\Gamma(a, b, b) = 0. \quad (9) \end{aligned}$$

Substituting $-b$ for b in (9) and subtracting from (9), we get

$$\Gamma(a, b, b)a + \Gamma(a, a, b)b + a\Gamma(a, b, b) + b\Gamma(a, a, b) = 0. \quad (10)$$

Writting $a + b$ instead of b , for $b \in \mathfrak{B}$ in (10) and using (8) and (10), we obtain

$$0 = \Gamma(a, a, a)b + 3\Gamma(a, a, b)a + 3a\Gamma(a, a, b) + b\Gamma(a, a, a). \quad (11)$$

Substituting bc instead of b , $c \in \mathfrak{B}$ in (11), we get

$$0 = \Gamma(a, a, a)bc + 3\Gamma(a, a, b)ca + 3bF(a, a, c)a + 3a\Gamma(a, a, b)c + 3abF(a, a, c) + bc\Gamma(a, a, a) \quad (12)$$

If we multiply (11) by c on the right side and compare with (12), then we have

$$0 = 3\Gamma(a, a, b)[c, a] + 3bF(a, a, c)a + 3abF(a, a, c) + b[c, \Gamma(a, a, a)]. \quad (13)$$

In (13), witting a instead of c , we get

$$3bf(a)a + 3abf(a) + b[a, \gamma(a)] = 0. \quad (14)$$

Substituting rb instead of b , for $r \in \mathfrak{A}$ in (14), we get

$$3rbf(a)a + 3arbf(a) + rb[a, \gamma(a)] = 0.$$

Multiplying (14) by r on the right side and subtracting from last equation, we have

$$[a, r]bf(a) = 0,$$

since \mathfrak{A} is 3-torsion free.

Since \mathfrak{A} is non-commutative ring, we get $bf(a) = 0$ for all $a, b \in \mathfrak{B}$. Witting $a + c$ instead of a , we get

$$0 = bF(a, a, c) + bF(a, a, c),$$

since \mathfrak{A} is 3-torsion free. Substituting $-c$ instead of c , we get $bF(a, a, c) = 0$ for $a, b, c \in \mathfrak{B}$. From here, $F = 0$ on \mathfrak{B} . Thus, we obtain that $\Gamma(ad, b, c) = \Gamma(a, b, c)d$ on \mathfrak{B} .

Theorem 3 Let \mathfrak{A} be a semiprime ring with 2,3-torsion free and \mathfrak{B} be a non-zero ideal of \mathfrak{A} . If $[\gamma(a), a], [f(a), a] \in \mathfrak{Z}(\mathfrak{A})$ in \mathfrak{B} , then $[\gamma(a), a] = 0$ in \mathfrak{B} .

Proof. Assume that γ is centralizing on \mathfrak{B} . That is,

$$[\gamma(a), a] \in \mathfrak{Z}(\mathfrak{A}) \text{ in } \mathfrak{B} \quad (15)$$

Witting $a + b$ instead of a , for $b \in \mathfrak{B}$ in (15) and using (15), we get

$$[\gamma(a), b] + [\gamma(b), a] + 3[\Gamma(a, a, b), a] + [\Gamma(a, a, b), b] + 3[\Gamma(a, b, b), a] + 3[\Gamma(a, b, b), b] \in \mathfrak{Z}(\mathfrak{A}) \quad (16)$$

Taking $-b$ instead of b in (16) and subtracting from (16), we get

$$[\gamma(a), b] + [\gamma(b), a] + 3[\Gamma(a, a, b), a] + 3[\Gamma(a, b, b), b] \in \mathfrak{Z}(\mathfrak{A}), \quad (17)$$

since \mathfrak{A} is 2,3-torsion free.

Witting $b + c$ instead of b , for $c \in \mathfrak{B}$ in (17) and using (17), we get

$$[\Gamma(b, b, c), a] + [\Gamma(b, c, c), a] + [\Gamma(a, b, b), c] + 2[\Gamma(a, b, c), b] + 2[\Gamma(a, b, c), c] + [\Gamma(a, c, c), b] \in \mathfrak{Z}(\mathfrak{A}), \quad (18)$$

since \mathfrak{A} is 3-torsion free.

Replacing $-b$ by b in (18) and subtracting from (18), we get

$$[\Gamma(b, b, c), a] + [\Gamma(a, b, b), c] + 2[\Gamma(a, b, c), b] \in \mathfrak{Z}(\mathfrak{A}) \quad (19)$$

Taking b instead of c in (19), we get

$$[\gamma(b), a] + 3[\Gamma(a, b, b), b] \in \mathfrak{Z}(\mathfrak{A}) \quad (20)$$

Writting b^2 instead of a and using γ is commuting on \mathfrak{B} ,

$$5[\gamma(b), b]b + 3b[f(b), b] \in \mathfrak{Z}(\mathfrak{A}).$$

Setting $[\gamma(b), b] = s$, $[f(b), b] = t$ and $5[\gamma(b), b]b + 3b[f(b), b] = z$, we get $3bt = z - 5sb$, $b \in \mathfrak{B}$
Now, we calculate

$$\begin{aligned} [\gamma(a^2), a^2] &= [\Gamma(a^2, a^2, a^2), a^2] \\ &= [\gamma(a), a]a^4 + a[\gamma(a), a]a^3 + 3a^2[F(a), a]a^2 \\ &\quad + 3a[F(a), a]a^3 + 3a^3[F(a), a]a + 3a^2[F(a), a]a^2 \\ &\quad + a^4[F(a), a] + a^3[F(a), a]a. \end{aligned} \quad (21)$$

Since $3at = z - 5sa$, we get from (21),

$$-18a^4s + 4a^3z + 2a^4t \in \mathfrak{Z}(\mathfrak{A}). \quad (22)$$

Commuting with $\gamma(a)$, we have

$$\begin{aligned} [\gamma(a), -18a^4s + 4a^3z + 2a^4t] \\ &= -18s[\gamma(a), a^4] + 4z[\gamma(a), a^3] + 2t[\gamma(a), a^4] \\ &= -72a^3s^2 + 12a^2zs + 8a^3st = 0. \end{aligned}$$

Again commuting with $\gamma(a)$, we obtain

$$\begin{aligned} [\gamma(a), -72a^3s^2 + 12a^2zs + 8a^3st] \\ &= -216a^2s^3 + 24s^2az + 24s^2a^2t = 0. \end{aligned}$$

From here, we have

$$\begin{aligned} [\gamma(a), -216a^2s^3 + 24s^2az + 24s^2a^2t = 0] \\ &= -512s^4a + 40s^3z = 0. \end{aligned}$$

Finally,

$$\begin{aligned} [\gamma(a), -512s^4a + 40s^3z] \\ &= -512s^5 = 0. \end{aligned}$$

That is, $s = 0$ from \mathfrak{A} is semiprime ring. Thus, γ is commuting on \mathfrak{B}

Theorem 4 Let Δ and Γ be permuting tri-derivations with δ, γ the traces of Δ and Γ , respectively and \mathfrak{A} is non-commutative prime ring. If $\delta(a)a + a\gamma(a) = 0$ in \mathfrak{B} , then $\Gamma = 0$ and $\Delta = 0$.

Proof. Assume that $\delta(a)a + a\gamma(a) = 0$ for $b \in \mathfrak{B}$. Writting $a + b$ instead of a , for $b \in \mathfrak{B}$, we get

$$\begin{aligned} 0 &= \delta(a + b)(a + b) + (a + b)\gamma(a + b) \\ &= \delta(b)a + 3\Delta(a, a, b)a + 3\Delta(a, b, b)a \\ &\quad + \delta(a)b + 3\Delta(a, a, b)b + 3\Delta(a, b, b)b \\ &\quad + a\gamma(b) + 3a\Gamma(a, a, b) + 3a\Gamma(a, b, b) \\ &\quad + b\gamma(a) + 3b\Gamma(a, a, b) + 3b\Gamma(a, b, b). \end{aligned} \quad (23)$$

Taking $-a$ instead of a in (23) and subtracting from (23), we have

$$\Delta(a, a, b)b + \Delta(a, b, b)a + b\Gamma(a, a, b) + a\Gamma(a, b, b) = 0. \quad (24)$$

Substituting $b + c$ for b , for $c \in \mathfrak{B}$ in (24) and using (24), we get

$$\begin{aligned} \Delta(a, a, b)c + \Delta(a, a, c)b + 2\Delta(a, b, c)a \\ + b\Gamma(a, a, c) + c\Gamma(a, a, b) + 2a\Gamma(a, b, c) = 0. \end{aligned} \quad (25)$$

Writting cd instead of c , $d \in \mathfrak{B}$ in (25), we get

$$0 = \Delta(a, a, b)cd + \Delta(a, a, c)db + c\Delta(a, a, d)b$$

$$+2\Delta(a, b, c)da + 2c\Delta(a, b, d)a + b\Gamma(a, a, c)d + bc\Gamma(a, a, d) + cd\Gamma(a, a, b) + 2ac\Gamma(a, b, d) + 2a\Gamma(a, b, c)d. \quad (26)$$

Multiplying (25) by d on the right side and comparing with (26), we get

$$0 = \Delta(a, a, c)[d, b] + c\Delta(a, a, d)b + 2\Delta(a, b, c)[d, a] + 2c\Delta(a, b, d)a + bc\Gamma(a, a, d) + c[d, \Gamma(a, a, b)] + 2ac\Gamma(a, b, d). \quad (27)$$

In (27), writing rc instead of c, for $r \in \mathfrak{A}$, we get

$$0 = r\Delta(a, a, c)[d, b] + \Delta(a, a, r)c[d, b] + rc\Delta(a, a, d)b + 2r\Delta(a, b, c)[d, a] + 2\Delta(a, b, r)c[d, a] + 2rc\Delta(a, b, d)a + br\Gamma(a, a, d) + rc[d, \Gamma(a, a, b)] + 2arc\Gamma(a, b, d). \quad (28)$$

Multiplying (27) by r on the left side and comparing with (28), we get

$$\Delta(a, a, r)c[d, b] + 2\Delta(a, b, r)c[d, a] + [b, r]c\Gamma(a, a, d) + 2[a, r]c\Gamma(a, b, d) = 0. \quad (29)$$

Writing a instead of b and d in (29), we obtain

$$[a, r]c\gamma(a) = 0.$$

From here, $\mathfrak{B} \subseteq \mathfrak{Z}(\mathfrak{A})$ or $\gamma(a) = 0$ in \mathfrak{B} . Since \mathfrak{A} is non-commutative, we obtain $\gamma(a) = 0$. And so, $\Gamma = 0$ and $\Delta = 0$.

Acknowledgments

This work will be included in master's thesis of Süleyman ZORTAŞ.

Conflicts of interest

There are no conflicts of interest in this work.

References

[1] Posner, E. C., Derivations in prime rings, *Proc. Amer. Math. Soc.* 8 (1957) 1093-1100.
 [2] Bresar, M., On the distance of the compositions of two derivations to generalized derivations, *Glasgow Math. J.* 33 (1991) 89-93.
 [3] Maksa, Gy., A remark on symmetric bi-additive functions having non-negative diagonalization, *Glasnik Mat.*, III. Ser. 15(2) (1980) 279-282.
 [4] Öztürk, M. A., Permuting tri-derivations in prime and semi-prime rings, *East Asian Math. J.* 15 (1999) No. 2, 177-190.
 [5] Durna, H., Symmetric bi-derivation on hyperring, *Cumhuriyet University Faculty of Science Journal*, 37 (4) (2016).
 [6] Yılmaz, D., Orthogonal semiderivations and symmetric bi-semiderivations in semiprime ring, *Cumhuriyet Science Journal*, 43 (1) (2022).
 [7] Çeven, Y., Symmetric bi-derivations of lattices, *Quaestiones Mathematicae*, 32(2009), 241-245.
 [8] Ilbira, S., Firat, A., Jun, Y. B., On symmetric bi-derivations of BCI-algebras, *Applied Mathematical Sciences*, 60 (5) (2011), 2957-2964.
 [9] Öztürk, M. A., Yazarli, H., Kim, K. H., Permuting tri-derivations in lattices, *Quaestiones Mathematicae*, 32 (2009), 415-425.

[10] Yılmaz, D., Davvaz, B., Yazarlı, H., Permuting tri-derivations in MV-algebras, *Malaya Journal of Matematik*, 11 (02) (2022), 142-150.
 [11] Yazarli, H., Permuting triderivations of prime and semiprime rings, *Miskolc Mathematical Notes*, 18 (1) (2017) 489-497.
 [12] Ali, A., Shujat, F., Khan, S., On Commuting Traces of Generalized Biderivations of Prime Rings, *Italian Journal of Pure and Applied Mathematics*, N. 34 (2015) 123-132.
 [13] Mayne, J. H., Ideals and centralizing mappings in prime rings, *Proc. Amer. Math. Soc.*, 86 (2) (1982) 211-212.

Solvability of an Inverse Problem for an Elliptic-Type Equation

Özlem Kaytmaz ^{1,a,*}, Mustafa Yıldız ^{2,b},

¹ Department of Mathematics, Faculty of Sciences, Zonguldak Bülent Ecevit University, Zonguldak, Türkiye.

² Department of Mathematics, Faculty of Sciences, Bartın University, Bartın, Türkiye.

*Corresponding author

Research Article

History

Received: 13/09/2023

Accepted: 26/02/2024





This article is licensed under a Creative Commons Attribution-NonCommercial 4.0 International License (CC BY-NC 4.0)


ABSTRACT


In this study, we consider an inverse problem of determining an unknown source function in the right-hand side of an elliptic equation which is ill-posed in the Hadamard sense. To investigate the solvability of the problem, we reduce it to a Dirichlet problem for a third-order partial differential equation with homogeneous boundary condition. Since the problem is linear, the proof of the uniqueness theorem is based on the Fredholm Alternative Theorem. We prove the existence of the solution to the problem by using the Galerkin method.

Keywords: Elliptic equation, Inverse problem, Solvability of the problem.

 ozlem.kaytmaz@beun.edu.tr

 <https://orcid.org/0000-0003-0420-007X>

 myildiz@bartin.edu.tr

 <https://orcid.org/0000-0003-3367-7176>

Introduction

Elliptic equations are used to describe the behavior of electromagnetic fields, the propagation of waves in a medium and the motion of fluids. They appear in a wide range of applications in various fields of science and technology such as physics, engineering and computer science.

In this paper, we consider the equation

$$\begin{aligned} Pu &\equiv a(x, \bar{y})(u_{xx} + \Delta_y u) + ku_x - b(x, \bar{y})u \\ &= c(x, \bar{y})f(x, \bar{y}) \end{aligned} \quad (1)$$

in the domain

$$Q = \{(x, y) \mid x \in (0,1), y_i \in (0,1), \quad i = 1,2, \dots, n\}$$

where $y = (\bar{y}, y_n)$, $\bar{y} = (y_1, y_2, \dots, y_{n-1})$. The boundary of the domain is defined as

$$\partial Q = \sigma_0 \cup \{y_n = 0\} \cup \{y_n = 1\},$$

$$\sigma_0 = \partial Q / (\{y_n = 0\} \cup \{y_n = 1\}).$$

The coefficients of equation (1) satisfy the following conditions:

$$\begin{aligned} a(x, \bar{y}) &\in C^1(\bar{Q}), \quad b(x, \bar{y}), \quad c(x, \bar{y}) \in C(\bar{Q}), \\ a(x, \bar{y}), \quad b(x, \bar{y}), \quad a'(x, \bar{y}) &> 0, \quad k < 0. \end{aligned}$$

We consider the following problem:

Problem 1. Find the functions $u(x, y)$ and $f(x, \bar{y})$ from equation (1), provided that the following conditions are given:

$$\frac{\partial u}{\partial y_n} \Big|_{y_n=0} = u_0, \quad \frac{\partial u}{\partial y_n} \Big|_{y_n=1} = u_1, \quad u \Big|_{\sigma_0} = u_2, \quad (2)$$

$$u \Big|_{y_n=0} = u_3. \quad (3)$$

A problem is said to be well posed if a unique solution exists which depends continuously on the data. Problem 1 is not a well posed problem. Some of the typical ill-posed problems for partial differential equations are the Cauchy problem for the Laplace equation, the Dirichlet problem for the wave equation and the initial-boundary value problem for the backward heat equation, [1].

The existence, uniqueness and stability of solution of various inverse problems for elliptic, hyperbolic and parabolic equations are studied in [2-5]. As for the solvability results for some ill-posed problems for other type equations, we refer to [6-10].

The first result of this paper is given below:

Theorem 1. Problem 1 has at most one solution (u, f) such that $u \in H^3(Q)$, $f \in H^1(Q)$.

In the proof, we shall use the Fredholm Alternative Theorem and show that the homogeneous problem has only zero solution.

Proof of Theorem 1.

It is sufficient to prove for $u \in C^k(\bar{Q})$, since $C^k(\bar{Q})$ is dense in $H^k(Q)$. Let us assume that $(u^{(1)}, f^{(1)})$, $(u^{(2)}, f^{(2)})$ are two solutions of problem (1)-(3) in the space $C^3(\bar{Q}) \times C^1(\bar{Q})$.

Then we can write

$$a(x, \bar{y})(u_{xx}^{(i)} + \Delta_y u^{(i)}) + ku_x^{(i)} - b(x, \bar{y})u^{(i)} = c(x, \bar{y})f^{(i)}(x, \bar{y}), \tag{4}$$

$$u_{y_n}^{(i)}|_{y_n=0} = u_0, \quad u_{y_n}^{(i)}|_{y_n=1} = u_1, \quad u^{(i)}|_{\sigma_0} = u_2, \tag{5}$$

$$u^{(i)}|_{y_n=0} = u_3, \quad i = 1, 2. \tag{6}$$

For $\tilde{u} = u^{(2)} - u^{(1)}$, $\tilde{f} = f^{(2)} - f^{(1)}$, we have

$$a(x, \bar{y})(\tilde{u}_{xx} + \Delta_y \tilde{u}) + k\tilde{u}_x - b(x, \bar{y})\tilde{u} = c(x, \bar{y})\tilde{f}(x, \bar{y}) \tag{7}$$

$$\tilde{u}_{y_n}|_{y_n=0} = 0, \quad \tilde{u}_{y_n}|_{y_n=1} = 0, \quad \tilde{u}|_{\sigma_0} = 0, \tag{8}$$

$$\tilde{u}|_{y_n=0} = 0, \quad i = 1, 2. \tag{9}$$

Taking the derivative of both sides of equation (7) with respect to y_n yields to

$$P\tilde{u}_{y_n} = 0 \tag{10}$$

and taking $\tilde{u}_{y_n} = \hat{u}$, we obtain

$$P\hat{u} = 0, \tag{11}$$

$$\hat{u}_{y_n}|_{y_n=0} = 0, \quad \hat{u}_{y_n}|_{y_n=1} = 0, \quad \hat{u}|_{\sigma_0} = 0. \tag{12}$$

Dividing both sides of equation (11) by $a(x, \bar{y})$, we get

$$\hat{u}_{xx} + \Delta_y \hat{u} + \frac{k}{a(x, \bar{y})}\hat{u}_x - \frac{b(x, \bar{y})}{a(x, \bar{y})}\hat{u} = 0, \tag{13}$$

$$\hat{u}|_{\partial Q} = 0. \tag{14}$$

Multiplying equation (13) by $-\hat{u}$ and using the equalities

$$\begin{aligned} -\hat{u}_{xx}\hat{u} &= -(\hat{u}_x\hat{u})_x + \hat{u}_x^2, \\ -\hat{u}_{y_i y_i}\hat{u} &= -(\hat{u}_{y_i}\hat{u})_{y_i} + \hat{u}_{y_i}^2, \quad i = 1, 2, \dots, n \\ -\hat{u}\frac{k}{a(x, \bar{y})}\hat{u}_x &= -\frac{1}{2}\left(\frac{k}{a(x, \bar{y})}\hat{u}^2\right)_x - \frac{1}{2}\frac{k}{a'(x, \bar{y})}\hat{u}^2, \end{aligned}$$

we see that

$$\begin{aligned} -\hat{u}P\hat{u} &= \hat{u}_x^2 + \sum_{i=1}^n \hat{u}_{y_i}^2 + \left(\frac{b(x, \bar{y})}{a(x, \bar{y})} - \frac{1}{2}\frac{k}{a'(x, \bar{y})}\right)\hat{u}^2 \\ &\quad - (\hat{u}_x\hat{u})_x - \sum_{i=1}^n (\hat{u}_{y_i}\hat{u})_{y_i} - \frac{1}{2}\left(\frac{k}{a(x, \bar{y})}\hat{u}^2\right)_x. \end{aligned} \tag{15}$$

Since $a(x, \bar{y})$, $b(x, \bar{y})$, $a'(x, \bar{y}) > 0$ and $k < 0$, we have

$$\hat{u}_x^2 + \sum_{i=1}^n \hat{u}_{y_i}^2 + \left(\frac{b(x, \bar{y})}{a(x, \bar{y})} - \frac{1}{2}\frac{k}{a'(x, \bar{y})}\right)\hat{u}^2 > 0.$$

If we integrate equality (15) over Q , we get

$$\int_Q [(\hat{u}_x\hat{u})_x + \sum_{i=1}^n (\hat{u}_{y_i}\hat{u})_{y_i} + \frac{1}{2}\left(\frac{k}{a(x, \bar{y})}\hat{u}^2\right)_x] dQ = \int_Q \left(\hat{u}_x^2 + \sum_{i=1}^n \hat{u}_{y_i}^2 + \left(\frac{b(x, \bar{y})}{a(x, \bar{y})} - \frac{1}{2}\frac{k}{a'(x, \bar{y})}\right)\hat{u}^2\right) dQ. \tag{16}$$

From the Ostrogradsky formula, we can write

$$\int_Q \left(\hat{u}_x^2 + \sum_{i=1}^n \hat{u}_{y_i}^2 + \left(\frac{b(x, \bar{y})}{a(x, \bar{y})} - \frac{1}{2}\frac{k}{a'(x, \bar{y})}\right)\hat{u}^2\right) dQ = \int_Q \left\{ [(\hat{u}_x\hat{u})_x + \frac{1}{2}\left(\frac{k}{a(x, \bar{y})}\hat{u}^2\right)] n_x + \sum_{i=1}^n (\hat{u}_{y_i}\hat{u}) n_{y_i} \right\} dS.$$

By $a(x, \bar{y})$, $b(x, \bar{y})$, $a'(x, \bar{y}) > 0$, $k < 0$ and $\hat{u}|_{\sigma_0} = 0$, we obtain

$$\int_Q \left(\hat{u}_x^2 + \sum_{i=1}^n \hat{u}_{y_i}^2 + \left(\frac{b(x, \bar{y})}{a(x, \bar{y})} - \frac{1}{2}\frac{k}{a'(x, \bar{y})}\right)\hat{u}^2\right) dQ = 0 \tag{17}$$

which means that

$\hat{u}_x = 0, \hat{u}_{y_i} = 0$ and $\hat{u}|_{\sigma_0} = 0$ and thus $\hat{u} = 0$ in the domain Q . Moreover, $\tilde{u} = 0$ in Q from the equality $\tilde{u}_{y_n} = \hat{u}$ and condition (9). On the other hand, we see that $\tilde{f} = 0$ in Q from equation (7). Thus, $\tilde{u} = u^{(2)} - u^{(1)} = 0$ and $\tilde{f} = f^{(2)} - f^{(1)} = 0$ where imply $u^{(1)} = u^{(2)}$ and $f^{(1)} = f^{(2)}$. Therefore, Theorem 1 is proven.

In order to prove the existence of the solution of the problem, we reduce the problem to a homogeneous Dirichlet problem.

Taking the derivative of both sides of equation (1) with respect to y_n , we see that

$$Pu_{y_n} = 0. \tag{18}$$

In conditions (2), if we take $u_{y_n} = \hat{u}$, we can write

$$P\hat{u} = 0, \tag{19}$$

$$\hat{u}|_{y_n=0} = u_0, \hat{u}|_{y_n=1} = u_1, \hat{u}|_{\sigma_0} = u_{2y_n}. \tag{20}$$

Conditions (20) can be written in the form

$$\hat{u}|_{\partial Q} = \tilde{u}_0. \tag{21}$$

Assume that the functions u_0, u_1, u_2 are smooth enough on the boundary of the domain and

$$w \in C^2(\bar{Q}), w|_{\partial Q} = \tilde{u}_0.$$

With the help of the new unknown function $v = \hat{u} - w$, we have

$$-w_{xx} - \Delta_y w - \frac{k}{a(x,\bar{y})}w_x + \frac{b(x,\bar{y})}{a(x,\bar{y})}w = F(x,\bar{y})$$

and problem (19)-(21) becomes

$$Pv \equiv v_{xx} + \Delta_y v + \frac{k}{a(x,\bar{y})}v_x - \frac{b(x,\bar{y})}{a(x,\bar{y})}v = F(x,\bar{y}), \tag{22}$$

$$v|_{\partial Q} = 0. \tag{23}$$

Theorem 2. Assume that $\partial Q \in C^2(\bar{Q})$ and $F \in L^2(Q)$. Then problem (22)-(23) has a generalized solution in the Hilbert space $H_0^1(Q)$.

Proof of Theorem 2.

We first take an a priori estimate for the solution of problem (22)-(23). If we multiply (22) by $-v$, integrate over the domain Q and using the equalities (15)-(16), we obtain

$$\int_Q (v^2_x + \sum_{i=1}^n v^2_{y_i} + (\frac{b(x,\bar{y})}{a(x,\bar{y})} - \frac{1}{2} \frac{k}{a'(x,\bar{y})})v^2) dQ = - \int_Q FvdQ. \tag{24}$$

From the Cauchy-Bunyakovskii inequality, we get

$$- \int_Q FvdQ \leq \int_Q [\beta F \frac{1}{\beta} v] dQ \leq \int_Q \beta^2 F^2 dQ + \int_Q \frac{1}{\beta^2} v^2 dQ.$$

By equality (24), we see that

$$\int_Q (v^2_x + \int_Q (\sum_{i=1}^n v^2_{y_i} + (\frac{b(x,\bar{y})}{a(x,\bar{y})} - \frac{1}{2} \frac{k}{a'(x,\bar{y})})v^2) dQ - \frac{1}{\beta^2} \int_Q v^2 dQ \leq \beta^2 \int_Q F^2 dQ. \tag{25}$$

Moreover, we apply the Rellich-Poincare inequality to the first term on the left side of inequality (25). Since

$$\int_Q v^2_x dQ \geq C \int_Q v^2 dQ, \quad (C = diamQ)$$

and by taking

$$C \int_Q v^2 dQ + \int_Q (\sum_{i=1}^n v^2_{y_i} + (\frac{b(x,\bar{y})}{a(x,\bar{y})} - \frac{1}{2} \frac{k}{a'(x,\bar{y})})v^2) dQ - \frac{1}{\beta^2} \int_Q v^2 dQ \leq \beta^2 \int_Q F^2 dQ,$$

$$(C - \frac{1}{\beta^2}) \int_Q v^2 dQ + \int_Q (\sum_{i=1}^n v^2_{y_i} + (\frac{b(x,\bar{y})}{a(x,\bar{y})} - \frac{1}{2} \frac{k}{a'(x,\bar{y})})v^2) dQ \leq \beta^2 \int_Q F^2 dQ,$$

we have

$$C_1 \int_Q v^2 dQ + \int_Q (\sum_{i=1}^n v^2_{y_i} + (\frac{b(x,\bar{y})}{a(x,\bar{y})} - \frac{1}{2} \frac{k}{a'(x,\bar{y})})v^2) dQ \leq \beta^2 \int_Q F^2 dQ, \tag{26}$$

where $C_1 = C - \frac{1}{\beta^2} > 0$. Inequality (26) is an a priori estimate which we look for.

We apply the Galerkin method to problem (22)-(23). Let the functions $w_1(x, y), w_2(x, y), \dots, w_n(x, y), \dots$ be linearly independent and complete system of functions in $L^2(Q)$.

We assume that $w_i(x, y) = 0$ on ∂Q ($i = 1, 2, \dots$) and $w_i(x, y) \in C^2(\bar{Q})$. There exists a system $\{w_1, w_2, \dots, w_n, \dots\}$ such that

$$u_N(x, y) = \sum_{i=1}^N c_i w_i(x, y).$$

Since $w_i|_{\partial Q} = 0$, then we have $u_N|_{\partial Q} = 0$. Now, let us obtain the function $u_N(x, y)$ from the system of equations

$$\langle u_{Nxx} + \Delta_y u_N + \frac{k}{a(x, \bar{y})} u_{Nx} - \frac{b(x, \bar{y})}{a(x, \bar{y})} u_N, w_j(x, y) \rangle = \langle F(x, \bar{y}), w_j(x, y) \rangle,$$

$$\langle u_{Nxx} + \Delta_y u_N + \frac{k}{a(x, \bar{y})} u_{Nx} - \frac{b(x, \bar{y})}{a(x, \bar{y})} u_N - F, w_j(x, y) \rangle = 0, \quad j = \overline{1, N}. \tag{27}$$

We will show that u_N which is the solution of system (27) converges to the exact solution of problem (22)-(23) when $N \rightarrow \infty$. Then we can write

$$\langle \sum_{i=1}^N (c_i w_i)_{xx} + \Delta_y \sum_{i=1}^N c_i w_i + \frac{k}{a(x, \bar{y})} \sum_{i=1}^N (c_i w_i)_x - \frac{b(x, \bar{y})}{a(x, \bar{y})} \sum_{i=1}^N c_i w_i - F, w_j(x, y) \rangle = 0, \quad j = \overline{1, N}. \tag{28}$$

We will prove the homogeneous system

$$\langle \sum_{i=1}^N (c_i w_i)_{xx} + \Delta_y \sum_{i=1}^N c_i w_i + \frac{k}{a(x, \bar{y})} \sum_{i=1}^N (c_i w_i)_x - \frac{b(x, \bar{y})}{a(x, \bar{y})} \sum_{i=1}^N c_i w_i, w_j \rangle = 0, \quad j = \overline{1, N} \tag{29}$$

has only the zero solution. If we multiply the j th equation of system (29) by $-c_j$ and add from 1 to N , we obtain

$$\langle u_{Nxx} + \Delta_y u_N + \frac{k}{a(x, \bar{y})} u_{Nx} - \frac{b(x, \bar{y})}{a(x, \bar{y})} u_N, -u_N \rangle = 0.$$

Then, from equality (17), we have

$$\int_Q (u_{Nx}^2 + \sum_{i=1}^n u_{Ny_i}^2 + (\frac{b(x, \bar{y})}{a(x, \bar{y})} - \frac{1}{2} \frac{k}{a'(x, \bar{y})}) u_N^2) dQ = 0.$$

In this case, $u_N = 0$ in the domain Q and therefore, we write

$$\sum_{i=1}^N c_i w_i(x, y) = 0.$$

Since $w_i(x, y)$ is linearly independent, we have $c_i = 0, (i = 1, 2, \dots, N)$. Thus, the homogeneous system (28) has only zero solution. Therefore, there is only one solution for every $F(x, y)$ of system (28).

Now, we take an a priori estimate for $u_N(x, y)$. For this, if we multiply the j th equation of system (28) by $-c_j$ and add from 1 to N , we obtain

$$\langle u_{Nxx} + \Delta_y u_N + \frac{k}{a(x, \bar{y})} u_{Nx} - \frac{b(x, \bar{y})}{a(x, \bar{y})} u_N - F, -u_N \rangle = 0,$$

$$\langle u_{Nxx} + \Delta_y u_N + \frac{k}{a(x, \bar{y})} u_{Nx} - \frac{b(x, \bar{y})}{a(x, \bar{y})} u_N, -u_N \rangle = \langle F, -u_N \rangle. \tag{30}$$

By inequality (26), we see that

$$C_1 \int_Q u_N^2 dQ + \int_Q (\sum_{i=1}^n u_{Ny_i}^2 + (\frac{b(x, \bar{y})}{a(x, \bar{y})} - \frac{1}{2} \frac{k}{a'(x, \bar{y})}) u_N^2) dQ \leq \beta^2 \int_Q F^2 dQ,$$

$$C_1 \int_Q u_N^2 dQ \leq \beta^2 \int_Q F^2 dQ \tag{31}$$

and

$$\int_Q (\sum_{i=1}^n u_{Ny_i}^2 + (\frac{b(x, \bar{y})}{a(x, \bar{y})} - \frac{1}{2} \frac{k}{a'(x, \bar{y})}) u_N^2) dQ \leq \beta^2 \int_Q F^2 dQ. \tag{32}$$

Since the right sides of inequalities (31) and (32) are independent of N , there is a constant C_2 independent of N such that

$$\int_Q u_N^2 dQ \leq C_2. \tag{33}$$

Similarly, we get

$$\int_Q \sum_{i=1}^n u_{Ny_i}^2 dQ \leq C_2, \quad \int_Q (\frac{b(x, \bar{y})}{a(x, \bar{y})} - \frac{1}{2} \frac{k}{a'(x, \bar{y})}) u_N^2 dQ \leq C_2. \tag{34}$$

Then, the sequence $\{u_N\}$ is bounded in the Hilbert space $H_0^1(Q)$. Since a bounded set in a Hilbert space is weakly compact, there is a weakly convergent subsequence of $\{u_N\}$. Let this subsequence be $\{u_N\}$ for the sake of simplicity. We can write system (28) in the form

$$\langle u_{Nxx} + \Delta_y u_N + \frac{k}{a(x, \bar{y})} u_{Nx} - \frac{b(x, \bar{y})}{a(x, \bar{y})} u_N, w_j \rangle = \langle F, w_j \rangle, \quad j = \overline{1, N}. \tag{35}$$

By using the equalities

$$\Delta_y u_N \cdot w_j = \int_Q \Delta_y u_N w_j dQ = \int_Q \sum_{i=1}^n u_{Ny_i} w_j dQ,$$

$$\begin{aligned}
 u_{Nxx} \cdot w_j &= (u_{Nx} w_j)_x - u_{Nx} w_{jx}, \\
 u_{Ny_i y_i} \cdot w_j &= (u_{Ny_i} w_j)_{y_i} - u_{Ny_i} w_{j y_i}, \\
 \frac{k}{a(x, \bar{y})} u_{Nx} \cdot w_j &= \left(\frac{k}{a(x, \bar{y})} u_N w_j \right)_x - \frac{k}{a(x, \bar{y})} u_N w_{jx} - \frac{k}{a'(x, \bar{y})} u_N w_j, \\
 \langle u_{Nxx}, w_j \rangle &= - \int_Q u_{Nx} w_{jx} \, dQ, \\
 \langle \Delta_y u_N, w_j \rangle &= - \int_Q \sum_{i=1}^n u_{Ny_i} w_{j y_i} \, dQ, \\
 \langle \frac{k}{a(x, \bar{y})} u_{Nx}, w_j \rangle &= - \int_Q \frac{k}{a(x, \bar{y})} u_N w_{jx} \, dQ - \int_Q \frac{k}{a'(x, \bar{y})} u_N w_j \, dQ
 \end{aligned}$$

in (35), we obtain

$$\begin{aligned}
 &- \int_Q u_{Nx} w_{jx} \, dQ - \int_Q \sum_{i=1}^n u_{Ny_i} w_{j y_i} \, dQ - \int_Q \frac{k}{a(x, \bar{y})} u_N w_{jx} \, dQ \\
 &- \int_Q \frac{k}{a'(x, \bar{y})} u_N w_j \, dQ - \int_Q \frac{k}{a(x, \bar{y})} u_N w_{jx} \, dQ - \int_Q \frac{b(x, \bar{y})}{a(x, \bar{y})} u_N w_j \, dQ \\
 &= \int_Q F w_j \, dQ.
 \end{aligned}$$

Taking the limit for $N \rightarrow \infty$, in the sense of the generalized function ($u_N \rightharpoonup v$ converges), we get

$$\langle v, P^* w_j \rangle = \langle F, w_j \rangle \tag{36}$$

or

$$\langle Pv - F, w_j \rangle = 0. \tag{37}$$

Since the system $\{w_j\}$ in (37) is complete in $L^2(Q)$, we can write

$$Pv - F = 0.$$

Then, v is a solution to equation (22). By $u_N \rightharpoonup v$ and $u_N|_{\sigma_0} = 0$, we have $u|_{\sigma_0} = 0$. Thus, problem

(22)-(23) has a generalized solution in the space $H_0^1(Q)$.

Finally, by (32), we have

$$\int_Q \left(\sum_{i=1}^n v_{y_i}^2 + \left(\frac{b(x, \bar{y})}{a(x, \bar{y})} - \frac{1}{2} \frac{k}{a'(x, \bar{y})} \right) v^2 \right) dQ \leq \beta^2 \int_Q F^2 dQ,$$

as $N \rightarrow \infty$ which show that the solution depends continuously on the data.

Conclusion

In this study, we deal with an inverse problem for an elliptic equation. We prove the uniqueness, existence and stability of the solution of the problem. Our main tools are Fredholm Alternative Theorem and Galerkin method.

Acknowledgments

The authors would like to sincerely thank the editor and the reviewers for the helpful comments and suggestions.

Conflicts of interest

There are no conflicts of interest in this work.

References

- [1] Payne L.E., Improperly Posed Problems in Partial Differential Equations. 1st ed. Philadelphia: Society for Industrial and Applied Mathematics, (1975) 19-42.
- [2] Isakov V., Inverse Problems for Partial Differential Equations. 2nd ed. New York: Springer, (2006) 89-295.
- [3] Kabanikhin S.I., Definitions and Examples of Inverse and Ill-Posed Problems, *J. Inverse Ill-Posed. Probl.*, 16 (4) (2008) 317-357.
- [4] Klivanov M.V., Timonov A.A., Carleman Estimates for Coefficient Inverse Problems and Numerical Applications. 1st ed. The Netherlands: VSP, (2004) 79-145.
- [5] Lavrent'ev M.M., Romanov V.G., Shishatskii S.P., Ill-Posed Problems of Mathematical Physics and Analysis. 1st ed. Providence: American Mathematical Society, (1986) 7-261.
- [6] Amirov A., Gölgeleyen F., Solvability of an Inverse Problem for the Kinetic Equation and a Symbolic Algorithm, *Comput. Model. Eng. Sci.*, 65 (2) (2010) 179-191.
- [7] Bellassoued M., Yamamoto M., Carleman Estimates and Applications to Inverse Problems for Hyperbolic Systems. 1st ed. Tokyo: Springer, (2017) 63-239.
- [8] Gölgeleyen F., Yamamoto M., Uniqueness of Solution of an Inverse Source Problem for Ultrahyperbolic Equations, *Inverse Probl.*, 36 (3) (2020) 035008.
- [9] Gölgeleyen İ., Kaytmaz Ö., Uniqueness for a Cauchy Problem for the Generalized Schrödinger Equation, *AIMS Math.*, 8 (3) (2023) 5703-5724.
- [10] Gölgeleyen İ., Yıldız M., On the Solution an Ill-Posed Boundary Value Problem for Second-Order Evolution Equations, *Cumhuriyet Sci. J.*, 40 (1) (2019) 173-178.

On Almost $C(\alpha)$ - Manifold Satisfying Certain Curvature Conditions

Tuğba Mert ^{1,a,*}, Mehmet Atçeken^{1,b}, Pakize Uygun ^{1,c}

¹ Department of Mathematics, Faculty of Sciences, Sivas Cumhuriyet University, Sivas, Türkiye.

*Corresponding author

Research Article

History

Received: 09/06/2023

Accepted: 21/12/2023



This article is licensed under a Creative Commons Attribution-NonCommercial 4.0 International License (CC BY-NC 4.0)

ABSTRACT

This research article is about the geometry of the almost $C(\alpha)$ - manifold. Some important properties of the almost $C(\alpha)$ - manifold with respect to the W_3 - curvature tensor, such as W_3 -flat and W_3 - semi-symmetry, are investigated. The relationship of W_3 - curvature tensor with Riemann, Ricci, projective, concircular and quasi-conformal curvature tensor is discussed on the almost $C(\alpha)$ - manifold and many important results are obtained. In addition, W_3 - pseudo symmetry and W_3 - Ricci pseudo symmetry are investigated for the almost $C(\alpha)$ - manifold. The results obtained are interesting and give an idea about the geometry of the almost $C(\alpha)$ - manifold.

Keywords: $C(\alpha)$ - Manifold, W_3 - Curvature Tensor, Pseudo-symmetric manifold.

^a tmert@cumhuriyet.edu.tr
^c pakizeuygun@hotmail.com

^b <https://orcid.org/0000-0001-8258-8298>
^d <https://orcid.org/0000-0001-8226-4269>

^e mehmet.atceken382@gmail.com ^f <https://orcid.org/0000-0002-1242-4359>,

Introduction

In recent years, many geometers have defined different curvature tensors on many different manifolds such as Sasakian, para-Sasakian, Lorentzian paracontact, Lorentzian para-Sasakian. The curvature tensor is a very important concept for manifolds. These defined curvature tensors have been characterized in accordance with the properties of the manifold used and their relations with different curvature tensors have been established. Many authors have studied the symmetry case of various manifolds. The flatness of the curvature tensor and the semi-symmetrical curvature conditions revealed interesting properties of manifolds.

Motivated by the work of many geometers using different manifolds and different curvature tensors, this

research paper deals with some curvature properties of the almost $C(\alpha)$ - manifold, which is a subclass of almost contact metric manifolds and the general form of co-Keahler, Kenmotsu, Sasakian manifolds.

The paracontact geometry was studied at first time by Kaneyuki and Williams. And then Zamkovoy gave a characterization of the paracontact metric manifolds and their subclasses [1-2]. Paracontact metric manifolds are studies widely by geometers and they defined a new type of paracontact geometry that is called paracontact metric (k, μ) - spaces [3-8]. And also, semi-symmetric spaces which are generalization of locally symmetric spaces were introduced by some authors [9-10].

A $(1,3)$ -type curvature tensor

$$T(\varpi_1, \varpi_2)\varpi_3 = a_0R(\varpi_1, \varpi_2)\varpi_3 + a_1S(\varpi_2, \varpi_3)\varpi_1 + a_2S(\varpi_1, \varpi_3)\varpi_2 + a_3S(\varpi_1, \varpi_2)\varpi_3 + a_4g(\varpi_2, \varpi_3)Q\varpi_1 + a_5g(\varpi_1, \varpi_3)Q\varpi_2 + a_6g(\varpi_1, \varpi_2)Q\varpi_3 + a_7r[g(\varpi_2, \varpi_3)\varpi_1 - g(\varpi_1, \varpi_3)\varpi_2] \quad (1)$$

on an n -dimensional semi-Riemann manifold was defined by M. Tripathi and P. Gupta [11]. Here a_0, a_1, \dots, a_7 are regular functions; R, S, Q and r are respectively Riemann curvature tensor, Ricci tensor, Ricci operator and scalar curvature. If we specifically choose $a_0 = 1, a_2 = -a_4 = \frac{-1}{2n}, a_1 = a_3 = a_5 = a_6 = a_7 = 0$ in equation (1), the W_3 -curvature tensor of a $(2n + 1)$ -dimensional manifold is obtained as

$$W_3(\varpi_1, \varpi_2)\varpi_3 = R(\varpi_1, \varpi_2)\varpi_3 - \frac{1}{2n}[S(\varpi_1, \varpi_3)\varpi_2 - g(\varpi_2, \varpi_3)Q\varpi_1]. \quad (2)$$

In recent years, many geometers have defined different curvature tensors on many different manifolds such as Sasakian, para-Sasakian, Lorentzian paracontact, Lorentzian para-Sasakian [12-17], [18-19],[23-25]. Based on the many studies mentioned above, in this article, the curvature conditions of almost $C(\alpha)$ -manifold such as $W_3(\varpi_1, \varpi_2)R = 0, R(\varpi_1, \varpi_2)W_3 = 0, W_3(\varpi_1, \varpi_2)P = 0, W_3(\varpi_1, \varpi_2)\tilde{Z} = 0, W_3(\varpi_1, \varpi_2)S = 0$ and $W_3(\varpi_1, \varpi_2)\tilde{C} = 0$ are searched. In addition, W_3 -pseudo symmetry and W_3 -Ricci pseudo symmetry are investigated for the almost $C(\alpha)$ -manifold.

Preliminary

Let M be a differentiable manifold with $(2n + 1)$ -dimensional. If the condition

$$\phi^2\varpi_1 = -\varpi_1 + \eta(\varpi_1)\xi \text{ and } \eta(\xi) = 1 \tag{3}$$

satisfies on M where ϕ is tensor field with type $(1,1)$, ξ is a vector field and η is a 1-form, then we say that (ϕ, ξ, η) is an almost contact structure. Also, we say that (M, ϕ, ξ, η) is an almost contact manifold. Let g be a metric with condition

$$g(\phi\varpi_1, \phi\varpi_2) = g(\varpi_1, \varpi_2) - \eta(\varpi_1)\eta(\varpi_2) \text{ and } g(\varpi_1, \xi) = \eta(\varpi_1), \tag{4}$$

for all $\varpi_1, \varpi_2 \in \chi(M)$ and $\xi \in \chi(M)$. In this case, we say that (ϕ, ξ, η, g) is almost contact metric structure and (M, ϕ, ξ, η, g) is almost contact metric manifold. Moreover, we have the property

$$g(\phi\varpi_1, \varpi_2) = -g(\varpi_1, \phi\varpi_2)$$

for all $\varpi_1, \varpi_2 \in \chi(M)$ on M manifold with $(2n + 1)$ -dimensional. The fundamental 2-form of (ϕ, ξ, η, g) almost contact metric structure is the Φ transformation such that

$$\Phi(\varpi_1, \varpi_2) = g(\varpi_1, \phi\varpi_2), \eta \wedge \Phi^n \neq 0.$$

for all $\varpi_1, \varpi_2 \in \chi(M)$.

Let M be almost contact metric manifold and R be Riemann curvature tensor of it, which provides the following

$$R(\varpi_1, \varpi_2, \varpi_3, \varpi_4) = R(\varpi_1, \varpi_2, \phi\varpi_3, \phi\varpi_4) + \alpha\{-g(\varpi_1, \varpi_3)g(\varpi_2, \varpi_4) + g(\varpi_1, \varpi_4)g(\varpi_2, \varpi_3) + g(\varpi_1, \phi\varpi_3)g(\varpi_2, \phi\varpi_4) - g(\varpi_1, \phi\varpi_4)g(\varpi_2, \phi\varpi_3)\} \tag{5}$$

for all $\varpi_1, \varpi_2, \varpi_3, \varpi_4 \in \chi(M)$, at least one $\alpha \in \mathbb{R}$. In this case, we say that M is almost $C(\alpha)$ -manifold [20]. By the way, we give the Riemann curvature tensor of an almost $C(\alpha)$ -manifold which has c -constant sectional curvature by

$$R(\varpi_1, \varpi_2)\varpi_3 = \left(\frac{c+3\alpha}{4}\right)\{g(\varpi_2, \varpi_3)\varpi_1 - g(\varpi_1, \varpi_3)\varpi_2\} + \left(\frac{c-\alpha}{4}\right)\{g(\varpi_1, \phi\varpi_3)\phi\varpi_2 - g(\varpi_2, \phi\varpi_3)\phi\varpi_1 + 2g(\varpi_1, \phi\varpi_2)\phi\varpi_3 + \eta(\varpi_1)\eta(\varpi_3)\varpi_2 - \eta(\varpi_2)\eta(\varpi_3)\varpi_1 + g(\varpi_1, \varpi_3)\eta(\varpi_2)\xi - g(\varpi_2, \varpi_3)\eta(\varpi_1)\xi\}. \tag{6}$$

So, if we take $\varpi_1 = \xi$ in (6), then we obtain

$$R(\xi, \varpi_2)\varpi_3 = \alpha[g(\varpi_2, \varpi_3)\xi - \eta(\varpi_3)\varpi_2]. \tag{7}$$

If we take $\varpi_3 = \xi$ in (6), then we have

$$R(\varpi_1, \varpi_2)\xi = \alpha[\eta(\varpi_2)\varpi_1 - \eta(\varpi_1)\varpi_2]. \tag{8}$$

Moreover, if we take $\varpi_2 = \xi$ in (8), then we get

$$R(\varpi_1, \xi)\xi = \alpha[\varpi_1 - \eta(\varpi_1)\xi]. \tag{9}$$

Let us take inner product of (6) by $\xi \in \chi(M)$. Then, we get

$$\eta(R(\varpi_1, \varpi_2)\varpi_3) = \alpha[g(\varpi_2, \varpi_3)\eta(\varpi_1) - g(\varpi_1, \varpi_3)\eta(\varpi_2)]. \tag{10}$$

Let M be an almost $C(\alpha)$ -manifold with $(2n + 1)$ dimensional. Then, we have the following equations.

$$S(\varpi_1, \varpi_2) = \left[\frac{\alpha(3n-1)+c(n+1)}{2}\right]g(\varpi_1, \varpi_2) + \frac{(\alpha-c)(n+1)}{2}\eta(\varpi_1)\eta(\varpi_2) \tag{11}$$

$$S(\varpi_1, \xi) = 2n\alpha\eta(\varpi_1) \tag{12}$$

$$Q\varpi_1 = \left[\frac{\alpha(3n-1)+c(n+1)}{2}\right]\varpi_1 + \frac{(\alpha-c)(n+1)}{2}\eta(\varpi_1)\xi \tag{13}$$

$$Q\xi = 2n\alpha\xi \tag{14}$$

$$Q\phi\varpi_2 = \frac{r-2n\alpha}{2n}Q\varpi_2 \tag{15}$$

for each $\varpi_1, \varpi_2, \in \chi(M)$, where Q, S and r are the Ricci operator, Ricci curvature tensor and scalar curvature of manifold M , respectively.

Let M be a $(2n + 1)$ –dimensional Riemannian manifold. Then the \tilde{Z} concircular curvature tensor is defined as

$$\tilde{Z}(\varpi_1, \varpi_2)\varpi_3 = R(\varpi_1, \varpi_2)\varpi_3 - \frac{r}{2n(2n+1)}[g(\varpi_2, \varpi_3)\varpi_1 - g(\varpi_1, \varpi_3)\varpi_2] \tag{16}$$

for each $\varpi_1, \varpi_2, \varpi_3 \in \chi(M)$, where r is the scalar curvature of the manifold [21]. If we choose $\varpi_1 = \xi$ in (16), we get

$$\tilde{Z}(\xi, \varpi_2)\varpi_3 = \left(\alpha - \frac{r}{2n(2n+1)}\right)[g(\varpi_2, \varpi_3)\xi - \eta(\varpi_3)\varpi_2] \tag{17}$$

and if we choose $\varpi_3 = \xi$ in (17), we get

$$\tilde{Z}(\xi, \varpi_2)\xi = \left(\alpha - \frac{r}{2n(2n+1)}\right)[\eta(\varpi_2)\xi - \varpi_2]. \tag{18}$$

The concept of the quasi-conformal curvature tensor was defined by Yano and Sowaki as

$$\begin{aligned} \tilde{C}(\varpi_1, \varpi_2)\varpi_3 &= aR(\varpi_1, \varpi_2)\varpi_3 + b[S(\varpi_2, \varpi_3)\varpi_1 - S(\varpi_1, \varpi_3)\varpi_2 \\ &\quad + g(\varpi_2, \varpi_3)Q\varpi_1 - g(\varpi_1, \varpi_3)Q\varpi_2] \\ &\quad - \frac{r}{2n+1}\left[\frac{a}{2n} + 2b\right][g(\varpi_2, \varpi_3)\varpi_1 - g(\varpi_1, \varpi_3)\varpi_2], \end{aligned} \tag{19}$$

where a and b are constants, Q is the Ricci operator, S is the Ricci tensor and r is the scalar curvature of the manifold [22]. If $\tilde{C} = 0$, then this manifold is called a quasi-conformal flat. If $\varpi_1 = \xi$ is chosen in equation (19),

$$\begin{aligned} \tilde{C}(\xi, \varpi_2)\varpi_3 &= \left[\frac{bc(n+1)+\alpha(2a+7bn-b)}{2} - \frac{r}{2n+1}\left(\frac{a}{2n} + 2b\right)\right] \\ &\quad \otimes [g(\varpi_2, \varpi_3)\xi - \eta(\varpi_3)\varpi_2]. \end{aligned} \tag{20}$$

and if $\varpi_3 = \xi$ is chosen in (20), we reach at

$$\begin{aligned} \tilde{C}(\xi, \varpi_2)\xi &= \left[a\alpha + 2nb\alpha - \frac{r}{2n+1}\left(\frac{a}{2n} + 2b\right) \right][\eta(\varpi_2)\xi - \varpi_2] \\ &\quad + b[2n\alpha\eta(\varpi_2)\xi - Q\varpi_2]. \end{aligned} \tag{21}$$

The projective curvature tensor P is defined as

$$P(\varpi_1, \varpi_2)\varpi_3 = R(\varpi_1, \varpi_2)\varpi_3 - \frac{1}{2n}[S(\varpi_2, \varpi_3)\varpi_1 - S(\varpi_1, \varpi_3)\varpi_2] \tag{22}$$

for all $\varpi_1, \varpi_2, \varpi_3 \in \chi(M)$, by K. Yano and S. Sowaki [22]. If $\varpi_1 = \xi, \varpi_2 = \xi$ and $\varpi_3 = \xi$ are chosen respectively in (22), then we get

$$P(\xi, \varpi_2)\varpi_3 = \alpha g(\varpi_2, \varpi_3)\xi - \frac{1}{2n}S(\varpi_2, \varpi_3)\xi, \tag{23}$$

$$P(\varpi_1, \xi)\varpi_3 = -\alpha g(\varpi_1, \varpi_3)\xi + \frac{1}{2n}S(\varpi_1, \varpi_3)\xi \tag{24}$$

and

$$P(\varpi_1, \varpi_2)\xi = 0. \tag{25}$$

Again, if the inner product of both sides of equation (22) is taken by $\xi \in \chi(M)$, we get

$$\begin{aligned} \eta(P(\varpi_1, \varpi_2)\varpi_3) &= \eta(\varpi_1) \left[\alpha g(\varpi_2, \varpi_3) - \frac{1}{2n}S(\varpi_2, \varpi_3) \right] \\ &\quad - \eta(\varpi_2) \left[\alpha g(\varpi_1, \varpi_3) - \frac{1}{2n}S(\varpi_1, \varpi_3) \right]. \end{aligned} \tag{26}$$

Finally, if we choose $\varpi_1 = \xi$ in the equation (2), then it reduces the form

$$W_3(\xi, \varpi_2)\varpi_3 = 2\alpha[g(\varpi_2, \varpi_3)\xi - \eta(\varpi_3)\varpi_2] \tag{27}$$

and if we choose $\varpi_3 = \xi$ in the same equation, we get

$$\begin{aligned} W_3(\varpi_1, \varpi_2)\xi &= \left(\frac{\alpha(7n-1)+c(n+1)}{4n}\right)\eta(\varpi_2)\varpi_1 - 2\alpha\eta(\varpi_1)\varpi_2 \\ &+ \left(\frac{(\alpha-c)(n+1)}{4n}\right)\eta(\varpi_1)\eta(\varpi_2)\xi. \end{aligned} \tag{28}$$

Similarly, if we choose $\varpi_2 = \xi$ in equation (2), we get

$$W_3(\varpi_1, \xi)\varpi_3 = \left(\frac{(7n-1)\alpha+c(n+1)}{4n}\right)[-g(\varpi_1, \varpi_3)\xi + \eta(\varpi_3)\varpi_1]. \tag{29}$$

Almost $C(\alpha)$ -Manifold Satisfying Some Important Conditions on the W_3 - Curvature Tensor

In this section, let us first examine the case where the $(2n + 1)$ dimensional almost $C(\alpha)$ - manifold is W_3 - flat, and then consider the special curvature conditions. For this, we give the following theorems.

Theorem 1 *If the $(2n + 1)$ dimensional M is an almost $C(\alpha)$ - manifold W_3 -flat, then the manifold M is an η - Einstein manifold.*

Proof. Let us assume that manifold M is W_3 - flat. From (2), we can write

$$W_3(\varpi_1, \varpi_2)\varpi_3 = 0,$$

for each $\varpi_1, \varpi_2, \varpi_3 \in \chi(M)$. Then from (2), we obtain

$$R(\varpi_1, \varpi_2)\varpi_3 = \frac{1}{2n}[S(\varpi_1, \varpi_3)\varpi_2 - g(\varpi_2, \varpi_3)Q\varpi_1] \tag{30}$$

for each $\varpi_1, \varpi_2, \varpi_3 \in \chi(M)$. In (30), if $\varpi_3 = \xi$ is written and (8), (12) are used, we obtain

$$\frac{1}{2n}\eta(\varpi_2)Q\varpi_1 = 2\alpha\eta(\varpi_1)\varpi_2 - \alpha\eta(\varpi_2)\varpi_1. \tag{31}$$

Taking the inner product on both sides of the last equation by $\varpi_3 \in \chi(M)$ and if we choose $\varpi_2 = \xi$, we get

$$S(\varpi_1, \varpi_3) = -2n\alpha g(\varpi_1, \varpi_3) + 4n\alpha\eta(\varpi_1)\eta(\varpi_3).$$

This proves our assertion.

Theorem 2 *Let M be a $(2n + 1)$ dimensional almost $C(\alpha)$ - manifold. Then $W_3 \cdot R = 0$ if and only if M is either co-Kehler manifold or M reduces real space form with constant sectional curvature.*

Proof. Suppose that $W_3(\varpi_1, \varpi_2) \cdot R = 0$. Then, we have

$$\begin{aligned} (W_3(\varpi_1, \varpi_2)R)(\varpi_4, \varpi_5, \varpi_3) &= W_3(\varpi_1, \varpi_2)R(\varpi_4, \varpi_5)\varpi_3 - R(W_3(\varpi_1, \varpi_2)\varpi_4, \varpi_5)\varpi_3 \\ &- R(\varpi_4, W_3(\varpi_1, \varpi_2)\varpi_5)\varpi_3 - R(\varpi_4, \varpi_5)W_3(\varpi_1, \varpi_2)\varpi_3 \\ &= 0. \end{aligned}$$

If we choose $\varpi_1 = \xi$ in here, we get

$$\begin{aligned} (W_3(\xi, \varpi_2)R)(\varpi_4, \varpi_5, \varpi_3) &= W_3(\xi, \varpi_2)R(\varpi_4, \varpi_5)\varpi_3 - R(W_3(\xi, \varpi_2)\varpi_4, \varpi_5)\varpi_3 \\ &- R(\varpi_4, W_3(\xi, \varpi_2)\varpi_5)\varpi_3 - R(\varpi_4, \varpi_5)W_3(\xi, \varpi_2)\varpi_3 \\ &= 0, \end{aligned} \tag{32}$$

for each $\varpi_2, \varpi_3, \varpi_4, \varpi_5 \in \chi(M)$. In (32), using (27), we obtain

$$\begin{aligned} &2\alpha[g(\varpi_2, R(\varpi_4, \varpi_5)\varpi_3)\xi - \eta(R(\varpi_4, \varpi_5)\varpi_3)\varpi_2 \\ &- g(\varpi_2, \varpi_4)R(\xi, \varpi_5)\varpi_3 + \eta(\varpi_4)R(\varpi_2, \varpi_5)\varpi_3 \\ &- g(\varpi_2, \varpi_5)R(\varpi_4, \xi)\varpi_3 + \eta(\varpi_5)R(\varpi_4, \varpi_2)\varpi_3 \\ &- g(\varpi_2, \varpi_3)R(\varpi_4, \varpi_5)\xi + \eta(\varpi_3)R(\varpi_4, \varpi_5)\varpi_2] = 0. \end{aligned} \tag{33}$$

Substituting $\varpi_4 = \xi$ in (33) and using (7), we conclude

$$2\alpha[R(\varpi_2, \varpi_5)\varpi_3 - \alpha(g(\varpi_5, \varpi_3)\varpi_2 - g(\varpi_2, \varpi_3)\varpi_5)] = 0. \tag{34}$$

From (34), we have

$$\alpha = 0$$

or

$$R(\varpi_2, \varpi_5)\varpi_3 = \alpha[g(\varpi_5, \varpi_3)\varpi_2 - g(\varpi_2, \varpi_3)\varpi_5].$$

Thus, M is co-Keahler manifold or M is reduced to the real space form with constant sectional curvature. The converse is obvious, and the proof is complete.

Theorem 3 Let M be a $(2n + 1)$ dimensional almost $C(\alpha)$ - manifold. Then $W_3 \cdot \tilde{Z} = 0$ if and only if M is either co-Keahler manifold or M reduces real space form with constant sectional curvature.

Proof. Suppose that $W_3(\varpi_1, \varpi_2) \cdot \tilde{Z} = 0$. Then we have

$$\begin{aligned} (W_3(\varpi_1, \varpi_2)\tilde{Z})(\varpi_4, \varpi_5, \varpi_3) &= W_3(\varpi_1, \varpi_2)\tilde{Z}(\varpi_4, \varpi_5)\varpi_3 - \tilde{Z}(W_3(\varpi_1, \varpi_2)\varpi_4, \varpi_5)\varpi_3 \\ &\quad - \tilde{Z}(\varpi_4, W_3(\varpi_1, \varpi_2)\varpi_5)\varpi_3 - \tilde{Z}(\varpi_4, \varpi_5)W_3(\varpi_1, \varpi_2)\varpi_3 \\ &= 0. \end{aligned}$$

If we choose $\varpi_1 = \xi$ in here, we get

$$\begin{aligned} (W_3(\xi, \varpi_2)\varpi_3)(\varpi_4, \varpi_5, \varpi_3) &= W_3(\xi, \varpi_2)\varpi_3(\varpi_4, \varpi_5)\varpi_3 - \varpi_3(W_3(\xi, \varpi_2)\varpi_4, \varpi_5)\varpi_3 \\ &\quad - \varpi_3(\varpi_4, W_3(\xi, \varpi_2)\varpi_5)\varpi_3 - \varpi_3(\varpi_4, \varpi_5)W_3(\xi, \varpi_2)\varpi_3 \\ &= 0, \end{aligned} \tag{35}$$

for each $\varpi_2, \varpi_3, \varpi_4, \varpi_5 \in \chi(M)$. In (35), using (27), we obtain

$$\begin{aligned} &2\alpha[g(\varpi_2, \tilde{Z}(\varpi_4, \varpi_5)\varpi_3)\xi - \eta(\tilde{Z}(\varpi_4, \varpi_5)\varpi_3)\varpi_2 \\ &\quad - g(\varpi_2, \varpi_4)\tilde{Z}(\xi, \varpi_5)\varpi_3 + \eta(\varpi_4)\tilde{Z}(\varpi_2, \varpi_5)\varpi_3 - g(\varpi_2, \varpi_5)\tilde{Z}(\varpi_4, \xi)\varpi_3 \\ &\quad + \eta(\varpi_5)\tilde{Z}(\varpi_4, \varpi_2)\varpi_3 - g(\varpi_2, \varpi_3)\tilde{Z}(\varpi_4, \varpi_5)\xi + \eta(\varpi_3)\tilde{Z}(\varpi_4, \varpi_5)\varpi_2] = 0. \end{aligned} \tag{36}$$

Taking $\varpi_4 = \xi$ in (36) and using (17), we obtain

$$2\alpha \left[\tilde{Z}(\varpi_2, \varpi_5)\varpi_3 - \left(\alpha - \frac{r}{2n(2n+1)} \right) (g(\varpi_5, \varpi_3)\varpi_2 - g(\varpi_2, \varpi_3)\varpi_5) \right] = 0. \tag{37}$$

In (37), using (16), we conclude

$$2\alpha[R(\varpi_2, \varpi_5)\varpi_3 - \alpha(g(\varpi_5, \varpi_3)\varpi_2 - g(\varpi_2, \varpi_3)\varpi_5)] = 0. \tag{38}$$

This proves our assertion. The converse obvious.

Theorem 4 Let M be $(2n + 1)$ dimensional an almost $C(\alpha)$ - manifold. Then $W_3 \cdot S = 0$ if and only if M is either co-Keahler manifold or an Einstein manifold.

Proof. Suppose that $W_3 \cdot S = 0$. Then we can easily see that

$$S(W_3(\varpi_1, \varpi_2)\varpi_3, \varpi_4) + S(\varpi_3, W_3(\varpi_1, \varpi_2)\varpi_4) = 0.$$

If we choose $\varpi_1 = \xi$ in here, we get

$$S(W_3(\xi, \varpi_2)\varpi_3, \varpi_4) + S(\varpi_3, W_3(\xi, \varpi_2)\varpi_4) = 0. \tag{39}$$

In (39), using (27), we obtain

$$2\alpha[2n\alpha\eta(\varpi_4)g(\varpi_2, \varpi_3) - \eta(\varpi_3)S(\varpi_2, \varpi_4) + 2n\alpha\eta(\varpi_3)g(\varpi_2, \varpi_4) - \eta(\varpi_4)S(\varpi_3, \varpi_2)] = 0. \tag{40}$$

Substituting $\varpi_3 = \xi$ in (40), we find

$$2\alpha[-S(\varpi_2, \varpi_4) + 2n\alpha g(\varpi_2, \varpi_4)] = 0. \tag{41}$$

From (41), we get

$$\alpha = 0$$

or

$$S(\varpi_2, \varpi_4) = 2n\alpha g(\varpi_2, \varpi_4).$$

This proves our assertion. The converse is obvious.

Theorem 5 Let M be a $(2n + 1)$ dimensional almost $C(\alpha)$ - manifold. Then $W_3 \cdot \tilde{C} = 0$ if and only if M is either co-Kähler manifold or M reduces real space form with constant sectional curvature.

Proof. Suppose that $W_3(\varpi_1, \varpi_2) \cdot \tilde{C} = 0$. Then, we have

$$\begin{aligned} (W_3(\varpi_1, \varpi_2)\tilde{C})(\varpi_3, \varpi_4, \varpi_5) &= W_3(\varpi_1, \varpi_2)\tilde{C}(\varpi_3, \varpi_4)\varpi_5 - \tilde{C}(W_3(\varpi_1, \varpi_2)\varpi_3, \varpi_4)\varpi_5 \\ &\quad - \tilde{C}(\varpi_3, W_3(\varpi_1, \varpi_2)\varpi_4)\varpi_5 - \tilde{C}(\varpi_3, \varpi_4)W_3(\varpi_1, \varpi_2)\varpi_5 \\ &= 0. \end{aligned}$$

If we choose $\varpi_1 = \xi$ in here, we get

$$\begin{aligned} (W_3(\xi, \varpi_2)\tilde{C})(\varpi_3, \varpi_4, \varpi_5) &= W_3(\xi, \varpi_2)\tilde{C}(\varpi_3, \varpi_4)\varpi_5 - \tilde{C}(W_3(\xi, \varpi_2)\varpi_3, \varpi_4)\varpi_5 \\ &\quad - \tilde{C}(\varpi_3, W_3(\xi, \varpi_2)\varpi_4)\varpi_5 - \tilde{C}(\varpi_3, \varpi_4)W_3(\xi, \varpi_2)\varpi_5 \\ &= 0, \end{aligned} \tag{42}$$

for each $\varpi_2, \varpi_3, \varpi_4, \varpi_5 \in \chi(M)$. Using (27) in (42), we get

$$\begin{aligned} 2\alpha[g(\varpi_2, \tilde{C}(\varpi_3, \varpi_4)\varpi_5)\xi - \eta(\tilde{C}(\varpi_3, \varpi_4)\varpi_5)\varpi_2 \\ - g(\varpi_2, \varpi_3)\tilde{C}(\xi, \varpi_4)\varpi_5 + \eta(\varpi_3)\tilde{C}(\varpi_2, \varpi_4)\varpi_5 - g(\varpi_2, \varpi_4)\tilde{C}(\varpi_3, \xi)\varpi_5 \\ + \eta(\varpi_4)\tilde{C}(\varpi_3, \varpi_2)\varpi_5 - g(\varpi_2, \varpi_5)\tilde{C}(\varpi_3, \varpi_4)\xi + \eta(\varpi_5)\tilde{C}(\varpi_3, \varpi_4)\varpi_2] = 0. \end{aligned} \tag{43}$$

Taking $\varpi_3 = \xi$ in (43) and using (20), (21), we obtain

$$\begin{aligned} 2\alpha \left\{ \left[\frac{bc(n+1) + \alpha(2a+7bn-b)}{2} - \frac{r}{2n+1} \left(\frac{a}{2n} + 2b \right) \right] \otimes \right. \\ \left. [g(\varpi_2, \varpi_5)\varpi_4 - g(\varpi_4, \varpi_5)\varpi_2] + \tilde{C}(\varpi_2, \varpi_4)\varpi_5 \right\} = 0. \end{aligned} \tag{44}$$

Substituting $\varpi_2 \rightarrow \phi\varpi_2$ and $\varpi_4 \rightarrow \phi\varpi_4$ in (44), we conclude

$$\begin{aligned} 2\alpha \left\{ \left[\frac{bc(n+1) + \alpha(2a+7bn-b)}{2} - \frac{r}{2n+1} \left(\frac{a}{2n} + 2b \right) \right] \otimes \right. \\ \left. [g(\phi\varpi_2, \varpi_5)\phi\varpi_4 - g(\phi\varpi_4, \varpi_5)\phi\varpi_2] + \tilde{C}(\phi\varpi_2, \phi\varpi_4)\varpi_5 \right\} = 0. \end{aligned} \tag{45}$$

In the last equation, if (19) is written in its place and necessary adjustments are made, we get

$$\alpha = 0 \tag{46}$$

or

$$R(\phi\varpi_2, \phi\varpi_4)\varpi_5 = A[g(\phi\varpi_4, \varpi_5)\phi\varpi_2 - g(\phi\varpi_2, \varpi_5)\phi\varpi_4], \tag{47}$$

where

$$A = \frac{\alpha[(2a+7nb-5b)+b(4r-3n+1)]}{2a} - \frac{r[2(n+1)a+(6n+1)b]}{2n(2n+1)a}$$

It is clear from (46) and (47) that M is either co-Kähler manifold or M reduces real space form with constant sectional curvature. The converse is obvious.

Theorem 6 Let M be a $(2n + 1)$ dimensional almost $C(\alpha)$ - manifold. Then $W_3 \cdot P = 0$ if and only if M is either co-Kähler manifold or η - Einstein manifold.

Proof. Suppose that $W_3 \cdot P = 0$. Then we have

$$\begin{aligned} (W_3(\varpi_1, \varpi_2)P)(\varpi_4, \varpi_5, \varpi_3) &= W_3(\varpi_1, \varpi_2)P(\varpi_4, \varpi_5)\varpi_3 - P(W_3(\varpi_1, \varpi_2)\varpi_4, \varpi_5)\varpi_3 \\ &\quad - P(\varpi_4, W_3(\varpi_1, \varpi_2)\varpi_5)\varpi_3 - P(\varpi_4, \varpi_5)W_3(\varpi_1, \varpi_2)\varpi_3 \\ &= 0. \end{aligned}$$

If we choose $\varpi_1 = \xi$ in here, we get

$$\begin{aligned} (W_3(\xi, \varpi_2)P)(\varpi_4, \varpi_5, \varpi_3) &= W_3(\xi, \varpi_2)P(\varpi_4, \varpi_5)\varpi_3 - P(W_3(\xi, \varpi_2)\varpi_4, \varpi_5)\varpi_3 \\ &\quad - P(\varpi_4, W_3(\xi, \varpi_2)\varpi_5)\varpi_3 - P(\varpi_4, \varpi_5)W_3(\xi, \varpi_2)\varpi_3 \\ &= 0, \end{aligned} \tag{48}$$

for each $\varpi_2, \varpi_3, \varpi_4, \varpi_5 \in \chi(M)$. In (48), using (27), we obtain

$$\begin{aligned} &2\alpha[g(\varpi_2, P(\varpi_4, \varpi_5)\varpi_3)\xi - \eta(P(\varpi_4, \varpi_5)\varpi_3)\varpi_2 \\ &\quad - g(\varpi_2, \varpi_4)P(\xi, \varpi_5)\varpi_3 + \eta(\varpi_4)P(\varpi_2, \varpi_5)\varpi_3 - g(\varpi_2, \varpi_5)P(\varpi_4, \xi)\varpi_3 \\ &\quad + \eta(\varpi_5)P(\varpi_4, \varpi_2)\varpi_3 - g(\varpi_2, \varpi_3)P(\varpi_4, \varpi_5)\xi + \eta(\varpi_3)P(\varpi_4, \varpi_5)\varpi_2] = 0. \end{aligned} \tag{49}$$

If (22) and (23) are used in (49), then we get

$$\begin{aligned} &2\alpha \left\{ g(\varpi_2, R(\varpi_4, \varpi_5)\varpi_3)\xi - \frac{1}{2n}S(\varpi_5, \varpi_3)g(\varpi_2, \varpi_4)\xi \right. \\ &\quad + \frac{1}{2n}S(\varpi_4, \varpi_3)g(\varpi_2, \varpi_5)\xi - \eta(R(\varpi_4, \varpi_5)\varpi_3)\varpi_2 \\ &\quad + \frac{1}{2n}S(\varpi_5, \varpi_3)\eta(\varpi_4)\varpi_2 - \frac{1}{2n}S(\varpi_4, \varpi_3)\eta(\varpi_5)\varpi_2 \\ &\quad - \alpha g(\varpi_2, \varpi_4)g(\varpi_5, \varpi_3)\xi + \frac{1}{2n}g(\varpi_2, \varpi_4)S(\varpi_5, \varpi_3)\xi \\ &\quad + \eta(\varpi_4)R(\varpi_2, \varpi_5)\varpi_3 - \frac{1}{2n}S(\varpi_5, \varpi_3)\eta(\varpi_4)\varpi_2 \\ &\quad + \frac{1}{2n}S(\varpi_2, \varpi_3)\eta(\varpi_4)\varpi_5 + \alpha g(\varpi_2, \varpi_5)g(\varpi_4, \varpi_3)\xi \\ &\quad - \frac{1}{2n}g(\varpi_2, \varpi_5)S(\varpi_4, \varpi_3)\xi + \eta(\varpi_5)R(\varpi_4, \varpi_2)\varpi_3 \\ &\quad - \frac{1}{2n}S(\varpi_2, \varpi_3)\eta(\varpi_5)\varpi_4 + \frac{1}{2n}S(\varpi_4, \varpi_3)\eta(\varpi_5)\varpi_2 \\ &\quad + \eta(\varpi_3)R(\varpi_4, \varpi_5)\varpi_2 - \frac{1}{2n}S(\varpi_5, \varpi_2)\eta(\varpi_3)\varpi_4 \\ &\quad \left. + \frac{1}{2n}S(\varpi_4, \varpi_2)\eta(\varpi_3)\varpi_5 \right\} = 0 \end{aligned} \tag{50}$$

Taking $\varpi_4 = \xi$ in (50) and using (7), we obtain

$$\begin{aligned} &2\alpha \{ \alpha g(\varpi_5, \varpi_3)\eta(\varpi_2)\xi - \alpha g(\varpi_5, \varpi_3)\varpi_2 \\ &\quad + \frac{1}{2n}S(\varpi_5, \varpi_3)\varpi_2 - g(\varpi_5, \varpi_3)\eta(\varpi_2)\xi \\ &\quad + R(\varpi_2, \varpi_5)\varpi_3 - \frac{1}{2n}S(\varpi_5, \varpi_3)\varpi_2 \\ &\quad + \frac{1}{2n}S(\varpi_2, \varpi_3)\varpi_5 + \alpha g(\varpi_2, \varpi_5)\eta(\varpi_3)\xi \\ &\quad + \alpha \eta(\varpi_5)g(\varpi_2, \varpi_3)\xi - \frac{1}{2n}S(\varpi_2, \varpi_3)\eta(\varpi_5)\xi \\ &\quad - \frac{1}{2n}S(\varpi_5, \varpi_2)\eta(\varpi_3)\xi \} = 0. \end{aligned} \tag{51}$$

If we take the inner product of both sides of (51) by $\xi \in \chi(M)$, we have

$$2\alpha\{-g(\varpi_5, \varpi_3)\eta(\varpi_2) + \alpha g(\varpi_5, \varpi_3)\eta(\varpi_2) + \alpha g(\varpi_2, \varpi_5)\eta(\varpi_3) - \frac{1}{2n}S(\varpi_5, \varpi_2)\eta(\varpi_3)\} = 0. \tag{52}$$

If we choose $\varpi_3 = \xi$ in (52), we get

$$2\alpha\left[(\alpha - 1)\eta(\varpi_5)\eta(\varpi_2) + \alpha g(\varpi_2, \varpi_5) - \frac{1}{2n}S(\varpi_5, \varpi_2)\right] = 0. \tag{53}$$

It is clear from (53) that

$$S(\varpi_5, \varpi_2) = 2n\alpha g(\varpi_5, \varpi_2) + 2n(\alpha - 1)\eta(\varpi_5)\eta(\varpi_2)$$

or

$$\alpha = 0.$$

This proves our assertion. The converse obvious.

Definition 1 Let M be a $(2n + 1)$ dimensional almost $C(\alpha)$ - manifold, R be the Riemann curvature tensor of M and S be the Ricci curvature tensor of M . If the pair $R \cdot W_3$ and $Q(g, W_3)$ are linearly dependent, that is, if a λ_1 function can be found on the set $M_1 = \{\varpi_1 \in M | g(\varpi_1) \neq W_3(\varpi_1)\}$ such that

$$R \cdot W_3 = \lambda_1 Q(g, W_3) \tag{54}$$

the M manifold is called a W_3 - pseudo symmetric manifold. Particularly, if $\lambda_1 = 0$, then this manifold is said to be semi-symmetric.

Let us now investigate the case of W_3 - pseudo symmetry.

Theorem 7 Let M be a $(2n + 1)$ dimensional almost $C(\alpha)$ - manifold. M is W_3 - pseudo symmetric if and only if M is either Einstein manifold or $\lambda_1 = \alpha$.

Proof. Let us assume that the manifold M is a W_3 - pseudo symmetric manifold. Then, we can write

$$(R(\varpi_1, \varpi_2) \cdot W_3)(\varpi_3, \varpi_5, \varpi_4) = \lambda_1 Q(g, W_3)(\varpi_3, \varpi_4, \varpi_5; \varpi_1, \varpi_2), \tag{55}$$

for each $\varpi_1, \varpi_2, \varpi_3, \varpi_4, \varpi_5 \in \chi(M)$. In this case, we get

$$\begin{aligned} &R(\varpi_1, \varpi_2)W_3(\varpi_3, \varpi_5)\varpi_4 - W_3(R(\varpi_1, \varpi_2)\varpi_3, \varpi_5)\varpi_4 \\ &- W_3(\varpi_3, R(\varpi_1, \varpi_2)\varpi_5)\varpi_4 - W_3(\varpi_3, \varpi_5)R(\varpi_1, \varpi_2)\varpi_4 \\ &= -\lambda_1 \left\{ W_3\left(\left(\varpi_1 \Lambda_g \varpi_2\right)\varpi_3, \varpi_5, \varpi_4\right) + W_3\left(\varpi_3, \left(\varpi_1 \Lambda_g \varpi_2\right)\varpi_5, \varpi_4\right) \right. \\ &\left. + W_3\left(\varpi_3, \varpi_5, \left(\varpi_1 \Lambda_g \varpi_2\right)\varpi_4\right) \right\}. \end{aligned} \tag{56}$$

If necessary arrangements are made here, we obtain and we choose $\varpi_1 = \xi$ in (56), we get

$$\begin{aligned} &R(\xi, \varpi_2)W_3(\varpi_3, \varpi_5)\varpi_4 - W_3(R(\xi, \varpi_2)\varpi_3, \varpi_5)\varpi_4 \\ &- W_3(\varpi_3, R(\xi, \varpi_2)\varpi_5)\varpi_4 - W_3(\varpi_3, \varpi_5)R(\xi, \varpi_2)\varpi_4 \\ &= -\lambda_1 \{g(\varpi_2, \varpi_3)W_3(\xi, \varpi_5)\varpi_4 - g(\xi, \varpi_3)W_3(\varpi_2, \varpi_5)\varpi_4 \\ &+ g(\varpi_2, \varpi_5)W_3(\varpi_3, \xi)\varpi_4 - g(\xi, \varpi_5)W_3(\varpi_3, \varpi_2)\varpi_4 \\ &+ g(\varpi_2, \varpi_4)W_3(\varpi_3, \varpi_5)\xi - g(\xi, \varpi_4)W_3(\varpi_3, \varpi_5)\varpi_2\}. \end{aligned} \tag{57}$$

Using (7), (27), (28) and (29) in the last equation, we obtain

$$\begin{aligned}
 & \alpha g(\varpi_2, W_3(\varpi_3, \varpi_5)\varpi_4)\xi - \alpha \eta(W_3(\varpi_3, \varpi_5)\varpi_4)\varpi_2 - 2\alpha^2 g(\varpi_2, \varpi_3)g(\varpi_5, \varpi_4)\xi \\
 & + 2\alpha^2 \eta(\varpi_4)g(\varpi_2, \varpi_3)\varpi_5 + \alpha \eta(\varpi_3)W_3(\varpi_2, \varpi_5)\varpi_4 + \\
 & \frac{\alpha[(7n-1)\alpha+c(n+1)]}{4n} g(\varpi_2, \varpi_5)g(\varpi_3, \varpi_4)\xi - \frac{\alpha[(7n-1)\alpha+c(n+1)]}{4n} \eta(\varpi_4)g(\varpi_2, \varpi_5)\varpi_3 \\
 & + \alpha \eta(\varpi_5)W_3(\varpi_3, \varpi_2)\varpi_4 - \frac{\alpha[(7n-1)\alpha+c(n+1)]}{4n} \eta(\varpi_5)g(\varpi_2, \varpi_4)\varpi_3 \\
 & + 2\alpha^2 \eta(\varpi_3)g(\varpi_2, \varpi_4)\varpi_5 - \frac{\alpha(\alpha-c)(n+1)}{4n} g(\varpi_2, \varpi_4)\eta(\varpi_3)\eta(\varpi_5)\xi \\
 & + \alpha \eta(\varpi_4)W_3(\varpi_3, \varpi_5)\varpi_2 = -\lambda_1 \{ 2\alpha g(\varpi_2, \varpi_3)g(\varpi_5, \varpi_4)\xi \\
 & - 2\alpha \eta(\varpi_4)g(\varpi_2, \varpi_3)\varpi_5 - \eta(\varpi_3)W_3(\varpi_2, \varpi_5)\varpi_4 \\
 & - \frac{[(7n-1)\alpha+c(n+1)]}{4n} g(\varpi_2, \varpi_5)g(\varpi_3, \varpi_4)\xi + \frac{[(7n-1)\alpha+c(n+1)]}{4n} \eta(\varpi_4)g(\varpi_2, \varpi_5)\varpi_3 \\
 & - \eta(\varpi_5)W_3(\varpi_3, \varpi_2)\varpi_4 - \eta(\varpi_4)W_3(\varpi_3, \varpi_5)\varpi_2 \\
 & + \frac{[(7n-1)\alpha+c(n+1)]}{4n} g(\varpi_2, \varpi_4)\eta(\varpi_5)\varpi_3 - 2\alpha \eta(\varpi_3)g(\varpi_2, \varpi_4)\varpi_5 \\
 & + \frac{(\alpha-c)(n+1)}{4n} g(\varpi_2, \varpi_4)\eta(\varpi_3)\eta(\varpi_5)\xi \}.
 \end{aligned} \tag{58}$$

If we choose $\varpi_3 = \xi$ in (58), we get

$$\begin{aligned}
 & -2\alpha^2 g(\varpi_5, \varpi_4)\varpi_2 + \alpha W_3(\varpi_2, \varpi_5)\varpi_4 + 2\alpha^2 g(\varpi_2, \varpi_4)\varpi_5 \\
 & = -\lambda_1 \{ 2\alpha g(\varpi_5, \varpi_4)\eta(\varpi_2)\xi - W_3(\varpi_2, \varpi_5)\varpi_4 + 2\alpha \eta(\varpi_5)\eta(\varpi_4)\varpi_2 \\
 & - 2\alpha g(\varpi_5, \varpi_2)\eta(\varpi_4)\xi - 2\alpha g(\varpi_2, \varpi_4)\varpi_5 \}.
 \end{aligned} \tag{59}$$

If we use (2) in (59), we have

$$\begin{aligned}
 & -2\alpha^2 g(\varpi_5, \varpi_4)\varpi_2 + \alpha R(\varpi_2, \varpi_5)\varpi_4 - \frac{\alpha}{2n} S(\varpi_2, \varpi_4)\varpi_5 \\
 & + \frac{\alpha}{2n} g(\varpi_5, \varpi_4)Q\varpi_2 + 2\alpha^2 g(\varpi_2, \varpi_4)\varpi_5 = -\lambda_1 \{ 2\alpha g(\varpi_5, \varpi_4)\eta(\varpi_2)\xi \\
 & - R(\varpi_2, \varpi_5)\varpi_4 + \frac{1}{2n} S(\varpi_2, \varpi_4)\varpi_5 - \frac{1}{2n} g(\varpi_5, \varpi_4)Q\varpi_2 \\
 & + 2\alpha \eta(\varpi_5)\eta(\varpi_4)\varpi_2 - 2\alpha g(\varpi_5, \varpi_2)\eta(\varpi_4)\xi - 2\alpha g(\varpi_2, \varpi_4)\varpi_5 \}.
 \end{aligned} \tag{60}$$

In (60), if we choose $\varpi_4 = \xi$ and we use (8) and (12), we get

$$\begin{aligned}
 & -\alpha^2 \eta(\varpi_5)\varpi_2 + \frac{\alpha}{2n} \eta(\varpi_5)Q\varpi_2 \\
 & = -\lambda_1 \{ 2\alpha \eta(\varpi_2)\eta(\varpi_5)\xi + \alpha \eta(\varpi_5)\varpi_2 \\
 & - \frac{1}{2n} \eta(\varpi_5)Q\varpi_2 - 2\alpha g(\varpi_5, \varpi_2)\xi \}.
 \end{aligned} \tag{61}$$

If $\varpi_5 = \xi$ is chosen in the last equation and we take the inner product of both sides of (61) by $\varpi_4 \in \chi(M)$, then we have

$$(\lambda_1 - \alpha) \left[\alpha g(\varpi_2, \varpi_4) - \frac{1}{2n} S(\varpi_2, \varpi_4) \right] = 0 \tag{62}$$

It is clear from (62) that either

$$\lambda_1 = \alpha$$

or the manifold M is an Einstein manifold. This ends our proof.

Corollary 1 Let M be a $(2n + 1)$ dimensional almost $C(\alpha)$ - manifold. M is a semi-symmetric manifold if and only if M is either a co-Kehler manifold or an Einstein manifold.

Definition 2 Let M be a $(2n + 1)$ dimensional almost $C(\alpha)$ - manifold, R be the Riemann curvature tensor of M and S be the Ricci curvature tensor of M . If the pair $R \cdot W_3$ and $Q(S, W_3)$ are linearly dependent, that is, if a λ_2 function can be found on the set $M_2 = \{\varpi_1 \in M | S(\varpi_1) \neq W_3(\varpi_1)\}$ such that

$$R \cdot W_3 = \lambda_2 Q(S, W_3)$$

the M manifold is called a W_3 –Ricci-pseudo symmetric manifold.

Theorem 8 Let M be a $(2n + 1)$ dimensional almost $C(\alpha)$ - manifold. M is W_3 - Ricci pseudo symmetric if and only if M is an η - Einstein manifold provided $\lambda_2 \neq \frac{1}{2n}$.

Proof. Let us assume that the manifold M is a W_3 - Ricci-pseudo symmetric manifold. Then, we can write

$$(R(\varpi_1, \varpi_2) \cdot W_3)(\varpi_3, \varpi_5, \varpi_4) = \lambda_2 Q(S, W_3)(\varpi_3, \varpi_4, \varpi_5; \varpi_1, \varpi_2), \tag{63}$$

for each $\varpi_1, \varpi_2, \varpi_3, \varpi_4, \varpi_5 \in \chi(M)$. In this case, we get

$$\begin{aligned} &R(\varpi_1, \varpi_2)W_3(\varpi_3, \varpi_5)\varpi_4 - W_3(R(\varpi_1, \varpi_2)\varpi_3, \varpi_5)\varpi_4 \\ &- W_3(\varpi_3, R(\varpi_1, \varpi_2)\varpi_5)\varpi_4 - W_3(\varpi_3, \varpi_5)R(\varpi_1, \varpi_2)\varpi_4 \\ &= -\lambda_2\{W_3((\varpi_1\Lambda_S\varpi_2)\varpi_3, \varpi_5, \varpi_4) + W_3(\varpi_3, (\varpi_1\Lambda_S\varpi_2)\varpi_5, \varpi_4) \\ &+ W_3(\varpi_3, \varpi_5, (\varpi_1\Lambda_S\varpi_2)\varpi_4)\}. \end{aligned} \tag{64}$$

If necessary arrangements are made here, we obtain and we choose $\varpi_1 = \xi$ in (64), we get

$$\begin{aligned} &R(\xi, \varpi_2)W_3(\varpi_3, \varpi_5)\varpi_4 - W_3(R(\xi, \varpi_2)\varpi_3, \varpi_5)\varpi_4 \\ &- W_3(\varpi_3, R(\xi, \varpi_2)\varpi_5)\varpi_4 - W_3(\varpi_3, \varpi_5)R(\xi, \varpi_2)\varpi_4 \\ &= -\lambda_2\{S(\varpi_2, \varpi_3)W_3(\xi, \varpi_5)\varpi_4 - S(\xi, \varpi_3)W_3(\varpi_2, \varpi_5)\varpi_4 \\ &+ S(\varpi_2, \varpi_5)W_3(\varpi_3, \xi)\varpi_4 - S(\xi, \varpi_5)W_3(\varpi_3, \varpi_2)\varpi_4 \\ &+ S(\varpi_2, \varpi_4)W_3(\varpi_3, \varpi_5)\xi - S(\xi, \varpi_4)W_3(\varpi_3, \varpi_5)\varpi_2\}. \end{aligned} \tag{65}$$

Using (7), (27), (28) and (29) in the last equation, we obtain

$$\begin{aligned} &\alpha g(\varpi_2, W_3(\varpi_3, \varpi_5)\varpi_4)\xi - \alpha\eta(W_3(\varpi_3, \varpi_5)\varpi_4)\varpi_2 \\ &- 2\alpha^2 g(\varpi_2, \varpi_3)g(\varpi_5, \varpi_4)\xi + 2\alpha^2\eta(\varpi_4)g(\varpi_2, \varpi_3)\varpi_5 \\ &+ \alpha\eta(\varpi_3)W_3(\varpi_2, \varpi_5)\varpi_4 + \frac{\alpha[(7n-1)\alpha+c(n+1)]}{4n}g(\varpi_2, \varpi_5)g(\varpi_3, \varpi_4)\xi \\ &- \frac{\alpha[(7n-1)\alpha+c(n+1)]}{4n}\eta(\varpi_4)g(\varpi_2, \varpi_5)\varpi_3 + \alpha\eta(\varpi_5)W_3(\varpi_3, \varpi_2)\varpi_4 \\ &- \frac{\alpha[(7n-1)\alpha+c(n+1)]}{4n}\eta(\varpi_5)g(\varpi_2, \varpi_4)\varpi_3 + 2\alpha^2\eta(\varpi_3)g(\varpi_2, \varpi_4)\varpi_5 \\ &- \frac{\alpha(\alpha-c)(n+1)}{4n}g(\varpi_2, \varpi_4)\eta(\varpi_3)\eta(\varpi_5)\xi + \alpha\eta(\varpi_4)W_3(\varpi_3, \varpi_5)\varpi_2 \\ &= -\lambda_2\{2\alpha S(\varpi_2, \varpi_3)g(\varpi_5, \varpi_4)\xi - 2\alpha\eta(\varpi_4)S(\varpi_2, \varpi_3)\varpi_5 \\ &- 2n\alpha\eta(\varpi_3)W_3(\varpi_2, \varpi_5)\varpi_4 - \frac{[(7n-1)\alpha+c(n+1)]}{4n}S(\varpi_2, \varpi_5)g(\varpi_3, \varpi_4)\xi \\ &+ \frac{[(7n-1)\alpha+c(n+1)]}{4n}\eta(\varpi_4)S(\varpi_2, \varpi_5)\varpi_3 - 2n\alpha\eta(\varpi_5)W_3(\varpi_3, \varpi_2)\varpi_4 \\ &- \frac{[(7n-1)\alpha+c(n+1)]}{4n}\eta(\varpi_5)S(\varpi_2, \varpi_4)\varpi_3 - 2n\alpha\eta(\varpi_4)W_3(\varpi_3, \varpi_5)\varpi_2 \\ &- 2\alpha\eta(\varpi_3)S(\varpi_2, \varpi_4)\varpi_5 + \frac{(\alpha-c)(n+1)}{4n}S(\varpi_2, \varpi_4)\eta(\varpi_3)\eta(\varpi_5)\xi\}. \end{aligned} \tag{66}$$

In (66), if we choose $\varpi_3 = \xi$, we get

$$\begin{aligned}
 & -2\alpha^2 g(\varpi_5, \varpi_4)\varpi_2 + \alpha W_3(\varpi_2, \varpi_5)\varpi_4 + 2\alpha^2 g(\varpi_2, \varpi_4)\varpi_5 \\
 & = -\lambda_2\{4n\alpha^2 g(\varpi_5, \varpi_4)\eta(\varpi_2)\xi - 2n\alpha W_3(\varpi_2, \varpi_5)\varpi_4 - 4n\alpha^2 g(\varpi_2, \varpi_4)\eta(\varpi_5)\xi \\
 & \quad + 4n\alpha^2 \eta(\varpi_4)\eta(\varpi_5)\varpi_2 + 2\alpha\eta(\varpi_5)S(\varpi_2, \varpi_4)\xi \\
 & \quad - 2\alpha S(\varpi_2, \varpi_4)\varpi_5 - 4n\alpha^2 g(\varpi_5, \varpi_2)\eta(\varpi_4)\xi\}.
 \end{aligned} \tag{67}$$

If we use (2) in (67), we have

$$\begin{aligned}
 & -2\alpha^2 g(\varpi_5, \varpi_4)\varpi_2 + \alpha R(\varpi_2, \varpi_5)\varpi_4 - \frac{\alpha}{2n}S(\varpi_2, \varpi_4)\varpi_5 \\
 & + \frac{\alpha}{2n}g(\varpi_5, \varpi_4)Q\varpi_2 + 2\alpha^2 g(\varpi_2, \varpi_4)\varpi_5 = -\lambda_2\{4n\alpha^2 g(\varpi_5, \varpi_4)\eta(\varpi_2)\xi \\
 & - 2n\alpha R(\varpi_2, \varpi_5)\varpi_4 + \alpha S(\varpi_2, \varpi_4)\varpi_5 - \alpha g(\varpi_5, \varpi_4)Q\varpi_2 \\
 & - 4n\alpha^2 g(\varpi_2, \varpi_4)\eta(\varpi_5)\xi + 4n\alpha^2 \eta(\varpi_5)\eta(\varpi_4)\varpi_2 + 2\alpha\eta(\varpi_5)S(\varpi_2, \varpi_4)\xi \\
 & - 2\alpha S(\varpi_2, \varpi_4)\varpi_5 - 4n\alpha^2 g(\varpi_5, \varpi_2)\eta(\varpi_4)\xi\}.
 \end{aligned} \tag{68}$$

If we choose $\varpi_4 = \xi$ in (68) and we use (8) and (12), we get

$$\begin{aligned}
 & -\alpha^2 \eta(\varpi_5)\varpi_2 + \frac{\alpha}{2n}\eta(\varpi_5)Q\varpi_2 \\
 & = -\lambda_2\{2n\alpha^2 \eta(\varpi_5)\varpi_2 + 4n\alpha^2 \eta(\varpi_2)\varpi_5 \\
 & - \alpha\eta(\varpi_5)Q\varpi_2\}.
 \end{aligned} \tag{69}$$

If $\varpi_5 = \xi$ is chosen in the last equation and we take the inner product of both sides of (69) by $\varpi_4 \in \chi(M)$, then we have

$$S(\varpi_2, \varpi_4) = \frac{2n\alpha(1-2n)}{(1-2n\lambda_2)}g(\varpi_2, \varpi_4) - \frac{8n^2}{(1-2n\lambda_2)}\eta(\varpi_2)\eta(\varpi_4). \tag{70}$$

It is clear from (70) that the manifold M is an η –Einstein manifold provided $\lambda_2 \neq \frac{1}{2n}$. This ends our proof.

Acknowledgments

The authors declare that there is no conflict of interest.

Conflicts of interest

There are no conflicts of interest in this work.

References

- [1] Kaneyuki, S., Williams, F.L., Almost paracontact and parahodge structures on manifolds, *Nagoya Math. J.*, 99 (1985) 173-187.
- [2] Zamkovoy, S., Canonical connections on paracontact manifolds, *Ann. Global Anal. Geom.*, 36 (2009) 37-60.
- [3] Atçeken, M., Uygun, P., Characterizations for totally geodesic submanifolds of (k, μ) -paracontact metric manifolds, *Korean J. Math.*, 28 (2020) 555-571.
- [4] Atçeken, M., Dirik, S., On the geometry of pseudo-slant submanifolds of a Kenmotsu manifold, *Gulf Journal of Mathematics*, 2 (2014) 51-66.
- [5] Laha, B., Das, B., Bhattacharyya, A., Submanifolds of some indefinite contact and paracontact metric manifolds, *Gulf Journal of Mathematics*, 1 (2013) 180-188.
- [6] Yıldırım, Ü., Atçeken, M., Dirik, S., Generalized B-curvature tensor of normal paracontact metric manifold, *Hagia Sophia Journal of Geometry*, 1 (2009) 1-7.
- [7] Yıldırım, Ü., Atçeken, M., Dirik, S., Pseudo projective curvature tensor satisfying some properties on a normal paracontact metric manifold, *Commun. Fac. Sci. Univ. Ank. Ser. A1, Math. Stat.*, 68 (2019) 997-1006.
- [8] Capelletti-Montano, B., Küpeli Erken, I., Murathan, C., Nullity conditions in paracontact geometry, *Differential Geom. Appl.*, 30 (2012) 665-693.
- [9] Kowalczyk, D., On some subclass of semisymmetric manifolds, *Soochow J. Math.*, 27 (2001) 445-461.
- [10] Szabo, Z.I., Structure theorems on riemannian spaces satisfying $R(\varpi_1, \varpi_2)R=0$, I: The local Version, *J. Differential Geom.*, 17 (1982) 531-582.
- [11] Tripathi, M., Gupta, P., T-Curvature tensor on a semi-Riemannian manifold, *J. Adv. Math. Studies*, 4 (1) (2011) 117-129.
- [12] Yıldız, A., De, U.C., Murathan, C., Arslan K., On the weyl projective curvature tensor of an $N(k)$ -contact metric manifold, *Mathematica Pannonica*, 21 (2010) 1-14.
- [13] De, U.C., Sarkar, A., On the Projective curvature tensor of generalized Sasakian space forms, *Questiones Mathematicae*, 33 (2010) 245-252.
- [14] Atçeken, M., On generalized Sasakian space forms satisfying certain conditions on the concircular curvature tensor, *Bulletin of Mathematical Analysis and Applications*, 6 (2014) 1-8.
- [15] Özgür, C., De, U.C., On the quasi-conformal curvature tensor of a Kenmotsu manifold, *Mathematica Pannonica*, 17 (2006) 221-228.
- [16] Arslan, K., Murathan, C., Özgür, C., On contact manifolds satisfying certain curvature conditions, *An. Univ. Bucuresti Math.*, 49 (2000) 17-26.
- [17] Pokhariyal, G.P., Mishra, R.S., Curvature tensors and their relativistic significance II, *Yokohama Math. J.*, 19 (1971) 97-103.

- [18] Ojha, R., M-projectively flat Sasakian manifolds, *Indian J. Pure Appl. Math.*, 17 (1986) 481-484.
- [19] Uygun, P., Atçeken, M., On (κ, μ) -paracontact metric spaces satisfying some conditions on the W_0 -curvature tensor, *New Trends in Mathematical Sciences*, 9 (2) 2021 26-37.
- [20] Janssens, D., Vanhecke, L., Almost contact structure and curvature tensors, *Kodai Math. J.*, 4 (1981) 1-27.
- [21] Yano, K., Conircular geometry I, Conircular transformations, *Proc. Imp. Acad., Tokyo*, 16 (1940) 195-200.
- [22] Yano, K., Sawaki, S., Riemannian manifolds admitting a conformal transformation group, *J. Diff. Geom.*, 2 (1968) 161-184.
- [23] Mert, T., On a Classification of Almost $C(\alpha)$ -Manifolds, *Journal of Mathematics*, (2022).
- [24] Mert, T., Characterization of Some Special Curvature Tensor on Almost $C(\alpha)$ -Manifold, *Asian Journal of Mathematics and Computer Research*, 29 (1) (2022) 27-41.
- [25] Mert, T., Atçeken, M., Almost $C(\alpha)$ -Manifold on W_0^* -Curvature Tensor, *Applied Mathematical Sciences*, 15 (15) (2021) 693-703.

Kähler Magnetic Curves in Conformally Euclidean Schwarzschild Space

Özgür Kelekçi ^{1,a,*}

¹ *Department of Basic Sciences & Faculty of Engineering, University of Turkish Aeronautical Association Ankara, Türkiye.*

*Corresponding author

Research Article

History

Received: 05/12/2023

Accepted: 04/03/2024



This article is licensed under a Creative Commons Attribution-NonCommercial 4.0 International License (CC BY-NC 4.0)

ABSTRACT

In this paper, we study the magnetic curves on a Kähler manifold which is conformally equivalent to Euclidean Schwarzschild space. We show that Euclidean Schwarzschild space is locally conformally Kähler and transform it into a Kähler space by applying a conformal factor coming from its Lee form. We solve Lorentz equation to find analytical expressions for magnetic curves which are compatible with the almost complex structure of the proposed Kähler manifold. We also calculate the energy of magnetic curves.

Keywords: Magnetic curve, Lorentz equation, Kähler magnetic fields, Euclidean Schwarzschild metric.

^a okelekci@thk.edu.tr

^{id} <https://orcid.org/0000-0001-7617-0231>

Introduction

The path of a charged particle moving on a manifold under the influence of a magnetic field is characterized by a magnetic curve. Generally, a magnetic field is defined by a closed 2-form (B) on a Riemannian manifold (M, g). The magnetic trajectories associated with the magnetic field are the curves γ on M that satisfy the Lorentz equation,

$$\nabla_{\dot{\gamma}} \dot{\gamma} = q\phi\dot{\gamma} \quad (1)$$

where ∇ is the Levi-Civita connection of g, q is a physical constant called charge, and ϕ is an anti-symmetric (1,1) tensor field called the Lorentz force. Magnetic field and Lorentz force are metrically equivalent such that $B(X,Y)=g(\phi(X),Y)$, $\forall X,Y \in \mathfrak{X}$. Note that the Lorentz equation becomes geodesic equation for $B=0$. Anti-symmetric (1,1) tensor field in (1) becomes almost complex structure J for almost complex manifolds. Magnetic curves are generally labelled according to the studied ambient space. If the ambient space is a Kähler manifold the magnetic curves associated with it are called Kähler magnetic curves. Similarly, if the ambient space is a contact manifold, then the magnetic curves on it are called contact magnetic curves. There are also F-planar curves which generalize the magnetic curves and hence, the geodesics [1].

There has been significant amount of research on contact magnetic fields in three-dimensional model spaces of Thurston geometry [2-9]. Studies on Kähler magnetic curves in non-flat Kähler space forms were initiated by works of Adachi [10-12]. Adachi showed that every trajectory associated with a Kähler magnetic field on a complex projective space $\mathbb{C}P^n(c)$, ($c > 0$), is a small circle on a totally geodesic embedded 2-sphere [10]. Same author also obtained explicit expressions for magnetic curves in complex hyperbolic spaces $\mathbb{C}H^n(-c)$, ($c > 0$) [11]. Kalinin studied Kähler magnetic fields and their trajectories on Kähler manifolds of constant holomorphic

sectional curvature [13]. In that study, Kalinin obtained differential equations deduced from Lorentz equation, but he did not provide solutions to those equations. Another line of research was initiated by studying J-trajectories in locally conformally Kähler (lcK) manifolds which are solutions of equation (1) for almost complex manifolds. Ateş, Munteanu and Nistor investigated trajectories in $\mathbb{R} \times S^3$ [14], and the results were extended to arbitrary Vaisman manifolds in [15]. Moreover, Inoguchi showed that J-trajectories in a lcK manifold with parallel anti Lee field are of osculating order at most 3 [16].

Jleli and Munteanu showed that spacelike and timelike magnetic trajectories corresponding to the para-Kähler 2-form on a para-Kähler manifold are circles [17]. Erjavec and Inoguchi studied magnetic curves on $\mathbb{H}^3 \times \mathbb{R}$ with respect to the strictly almost Kähler structure and obtained explicit expressions for magnetic curves which correspond to the almost complex structure compatible with the product metric [18]. Despite the existence of these studies about Kähler magnetic curves, there are few studies which concentrate on explicit construction of Kähler magnetic curves on frequently studied Kähler spaces in physics literature. Our study aims to make a better connection in this sense and potentially provide new research problems. We chose Euclidean Schwarzschild space for this purpose. As will be shown in the next section Euclidean Schwarzschild space is not Kähler but locally conformally Kähler. This fact was briefly mentioned in [19]. Schwarzschild space and its Euclidean version have been studied extensively in physics literature. A recent paper focusing on the detailed analysis of geodesic motion in Euclidean Schwarzschild geometry is more relevant to our study [20]. We refer to the introduction of that paper for a broader literature review on Euclidean Schwarzschild space.

This paper is structured as follows. In Section 2, we give the basic geometric structure of Euclidean

Schwarzschild space, show that it is locally conformally Kähler and obtain its Kähler counterpart. In Section 3, we solve Lorentz equation to find analytical expressions for magnetic curves which are compatible with the almost complex structure of the Kähler space and also calculate

the energy of these magnetic curves. Finally, we summarize the results and give potential research problems in Section 4.

Geometry of Euclidean Schwarzschild Space and Its Conformal Transformation

Euclidean Schwarzschild space is a complete solution to the Euclidean Einstein equations with zero cosmological constant (Λ) and it is characterized by the non-trivial topology of $\mathbb{R}^2 \times S^2$ [21]. Metric for Euclidean Schwarzschild (ES) space is given by

$$\left(1 - \frac{2m}{r}\right) d\tau^2 + \left(1 - \frac{2m}{r}\right)^{-1} dr^2 + r^2(d\theta^2 + \sin^2\theta d\phi^2) \tag{2}$$

It was shown that ES manifold admits a complex Hermitian structure [22]. Hermitian 2-form ω of a complex manifold (M^{2n}, g, J) is an element of Λ^2 (bundle of 2-forms on M) for which self-dual (Ω_+) and anti-self-dual (Ω_-) bases can be defined as

$$\Omega_{\pm} = \{e^1 \wedge e^2 \pm e^3 \wedge e^4, e^1 \wedge e^3 \pm e^4 \wedge e^2, e^1 \wedge e^4 \pm e^2 \wedge e^3\} \tag{3}$$

where e^i 's are orthonormal basis one-forms. We use the following orthonormal frame and the corresponding dual co-frame on ES space to describe its geometric structure .

$$\{e_1, e_2, e_3, e_4\} = \{(1 - 2m/r)^{-1/2} \partial_\tau, (1 - 2m/r)^{1/2} \partial_r, (r \sin\theta)^{-1} \partial_\phi, r^{-1} \partial_\theta\} \tag{4}$$

$$\{e^1, e^2, e^3, e^4\} = \{(1 - 2m/r)^{1/2} d\tau, (1 - 2m/r)^{-1/2} dr, r \sin\theta d\phi, r d\theta\} \tag{5}$$

where $\partial_x \equiv \partial/\partial x$. The fundamental 2-form ω for a Hermitian manifold is given by

$$\omega(X, Y) = g(JX, Y) \quad X, Y \in T_pM$$

We choose the orientation $(e^1 \wedge e^2 \wedge e^3 \wedge e^4)$ and the fundamental 2-form $\omega = e^1 \wedge e^2 + e^3 \wedge e^4$ so that ω becomes self-dual. Almost complex structure that will yield the 2-form ω with respect to the chosen orientation will be:

$$J e^1 = e^2, J e^2 = -e^1, J e^3 = e^4, J e^4 = -e^3 \tag{6}$$

Fundamental 2-form ω and coefficients of almost complex structure J can be written in coordinates as the following.

$$\omega = d\tau \wedge dr + r^2 \sin\theta d\phi \wedge d\theta \tag{7}$$

$$J = \begin{pmatrix} 0 & \frac{r-2m}{r} & 0 & 0 \\ \frac{r}{2m-r} & 0 & 0 & 0 \\ 0 & 0 & 0 & \sin\theta \\ 0 & 0 & -(\sin\theta)^{-1} & 0 \end{pmatrix}$$

It is easy to see that the ω given above and other ω 's formed by elements of Ω_{\pm} are not closed ($d\omega \neq 0$). Hence, ES manifold is not Kähler in its current form. A Hermitian manifold (M^{2n}, g, J) is called locally conformally Kähler (l.c.K) if and only if there exists a globally defined closed 1-form (called Lee form) ξ on M^{2n} so that

$$d\omega = \xi \wedge \omega \tag{8}$$

Furthermore, it was shown that if ξ is exact ($\xi = df$) then there exists a Kähler metric \hat{g} obtained by applying a conformal factor to the original metric g [23]:

$$\hat{g} = e^{-f} g \tag{9}$$

We find that the 1-form $\xi = 2dr/r$ is satisfying (8), hence conclude that ES manifold is locally conformally Kähler. The corresponding Kähler metric is obtained as:

$$\hat{g} = \frac{1}{r^2} \left(1 - \frac{2m}{r}\right) d\tau^2 + \frac{1}{r^2} \left(1 - \frac{2m}{r}\right)^{-1} dr^2 + d\theta^2 + \sin^2\theta d\phi^2 \tag{10}$$

Magnetic curves will be constructed by using this Kähler metric associated to the space which we call conformally Euclidean Schwarzschild space. It will be convenient to use the orthonormal frame and the dual co-frame given in (4)-(5) scaled by r and $1/r$, respectively. We work with the same orientation and fundamental 2-form given in basis 1-forms as

$$\hat{\omega} = \hat{e}^1 \wedge \hat{e}^2 + \hat{e}^3 \wedge \hat{e}^4$$

$$= \frac{1}{r^2} d\tau \wedge dr + \sin\theta d\phi \wedge d\theta \tag{11}$$

This 2-form $\hat{\omega}$ is closed as expected. Therefore, we obtained a Kähler manifold $(\hat{M}^{2n}, \hat{g}, J)$ with the orthonormal frame and the corresponding dual co-frame given as

$$\{\hat{e}_1, \hat{e}_2, \hat{e}_3, \hat{e}_4\} = \{r(1 - 2m/r)^{-1/2} \partial_\tau, r(1 - 2m/r)^{1/2} \partial_r, (\sin\theta)^{-1} \partial_\phi, \partial_\theta\} \tag{12}$$

$$\{\hat{e}^1, \hat{e}^2, \hat{e}^3, \hat{e}^4\} = \{r^{-1}(1 - 2m/r)^{1/2} d\tau, r^{-1}(1 - 2m/r)^{-1/2} dr, \sin\theta d\phi, d\theta\} \tag{13}$$

Following covariant derivatives are obtained by using the orthonormal frame given above

$$\begin{aligned} \nabla_{\hat{e}_1} \hat{e}_1 &= r^{-1}(1 - 2m/r)^{-1/2}(r - 3m)\hat{e}_2, \nabla_{\hat{e}_1} \hat{e}_2 = r^{-1}(1 - 2m/r)^{-1/2}(3m - r)\hat{e}_1 \\ \nabla_{\hat{e}_3} \hat{e}_3 &= -\cot\theta \hat{e}_4, \nabla_{\hat{e}_3} \hat{e}_4 = \cot\theta \hat{e}_3 \end{aligned} \tag{14}$$

consisting of only non-zero $(\nabla_{\hat{e}_i} \hat{e}_j \neq 0)$ derivatives.

Magnetic Curves in Conformally Euclidean Schwarzschild Space

Let us consider a smooth curve $\gamma(s)$ parameterized by its arclength in conformally ES space.

$$\gamma(s) = (\tau(s), r(s), \phi(s), \theta(s))$$

We will be searching for solutions to the Lorentz equation $\nabla_{\dot{\gamma}} \dot{\gamma} = qJ(\dot{\gamma})$, hence $\gamma(s)$ will be a magnetic curve. Note that we consider charged particles with unit mass ($m_p=1$). It is known that a trajectory for a Kähler magnetic field is characterized by the motion of a charged particle with unit mass, maintaining a constant speed under the influence of this magnetic field [12]. The unit tangent vector field can be written as

$$\begin{aligned} \dot{\gamma}(s) &= \dot{\tau}(s)\partial_\tau + \dot{r}(s)\partial_r + \dot{\phi}(s)\partial_\phi + \dot{\theta}(s)\partial_\theta \\ &= \frac{\dot{\tau}(s)\sqrt{1-2m/r(s)}}{r(s)} \hat{e}_1 + \frac{\dot{r}(s)}{r(s)\sqrt{1-2m/r(s)}} \hat{e}_2 + \dot{\phi}(s)\sin(\theta(s)) \hat{e}_3 + \dot{\theta}(s)\hat{e}_4 \end{aligned} \tag{15}$$

Now we can apply J on $\dot{\gamma}$ to compute the right-hand side of Lorentz equation

$$J(\dot{\gamma}) = -\frac{\dot{r}(s)}{r(s)\sqrt{1-2m/r(s)}} \hat{e}_1 + \frac{\dot{\tau}(s)\sqrt{1-2m/r(s)}}{r(s)} \hat{e}_2 - \dot{\theta}(s)\hat{e}_3 + \dot{\phi}(s)\sin(\theta(s)) \hat{e}_4 \tag{16}$$

Then the left-hand side of the Lorentz equation can be computed by using the covariant derivatives given in (14).

$$\begin{aligned} \nabla_{\dot{\gamma}} \dot{\gamma} &= \frac{(2(3m-r(s))\dot{r}(s)\dot{\tau}(s)+r(s)(r(s)-2m)\dot{\tau}(s))}{r(s)^{5/2}(r(s)-2m)^{1/2}} \hat{e}_1 + \\ &\frac{(-12m^3\dot{\tau}(s)^2+16m^2r(s)\dot{\tau}(s)^2+mr(s)^2(\dot{r}(s)^2-7\dot{\tau}(s)^2)+r(s)^3(-2m\dot{r}(s)-\dot{r}(s)^2+\dot{\tau}(s)^2)+r(s)^4\ddot{r}(s))}{r(s)^{7/2}(r(s)-2m)^{3/2}} \hat{e}_2 + (2\cos(\theta(s))\dot{\theta}(s)\dot{\phi}(s) + \\ &\sin(\theta(s))\ddot{\phi}(s))\hat{e}_3 + (\ddot{\theta}(s) - \sin(\theta(s))\cos(\theta(s))\dot{\phi}(s)^2)\hat{e}_4 \end{aligned} \tag{17}$$

The following system of ordinary differential equations are obtained by combining equations (16) and (17) which basically form the Lorentz equation for conformally ES space.

$$\frac{\dot{r}(qr^2+2(3m-r)\dot{\tau})+r(r-2m)\ddot{\tau}}{r^{5/2}(r-2m)^{1/2}} = 0 \tag{18}$$

$$\frac{-12m^3\dot{\tau}^2+16m^2r\dot{\tau}^2-qr^2(r-2m)^2\dot{\tau}+mr^2(\dot{r}^2-7\dot{\tau}^2)+r^3(\dot{\tau}^2-\dot{r}^2-2m\dot{r})+r^4\ddot{r}}{r^{7/2}(r-2m)^{3/2}} = 0 \tag{19}$$

$$\dot{\theta}(q + 2\cos\theta \dot{\phi}) + \sin\theta \ddot{\phi} = 0 \tag{20}$$

$$\ddot{\theta} - \sin\theta \dot{\phi}(q + \cos\theta \dot{\phi}) = 0 \tag{21}$$

Let's rewrite equation (18) as

$$\dot{r}(qr^2 + 4(2m - r)\dot{\tau}) + \partial_s((r^2 - 2mr)\dot{\tau}) \tag{22}$$

Define a function $f(s)$

$$f(s) = (r(s)^2 - 2m r(s))\dot{\tau}(s) \tag{23}$$

Using $f(s)$ in equation (22) gives

$$qr(s)^2\dot{r}(s) - \frac{4f(s)}{r(s)}\dot{r}(s) + \dot{f}(s) = 0 \tag{24}$$

Multiplying both sides of equation (24) by $r(s)^{-4}$

$$qr(s)^{-2}\dot{r}(s) - 4f(s)r(s)^{-5}\dot{r}(s) + \dot{f}(s)r(s)^{-4} = 0$$

which can be written as an exact differential

$$\partial_s(f(s)r(s)^{-4} - qr(s)^{-1}) = 0$$

$$f(s)r(s)^{-4} - qr(s)^{-1} = a \Rightarrow f(s) = qr(s)^3 + ar(s)^4 \tag{25}$$

Then insert this in (23)

$$\dot{\tau}(s) = \frac{f(s)}{r(s)^2 - 2m r(s)} = \frac{qr(s)^2 + ar(s)^3}{r(s)^2 - 2m r(s)} \tag{26}$$

Finally integrating (26) we get

$$\tau(s) = b + \int \frac{r(s)^2(q+ar(s))}{r(s)^2 - 2m r(s)} ds \tag{27}$$

where a and b are arbitrary constants. Inserting this in equation (19) yields:

$$a^2r^5 + ar^4(q - 3am) - 4amqr^3 + r^2(\ddot{r} - mq^2) + m\dot{r}^2 - r(2m\ddot{r} + \dot{r}^2) = 0 \tag{28}$$

We couldn't find analytical solutions to equation (28), so we set $a = 0$ in equation (27) which then gives the following ODE

$$r^2(\ddot{r} - mq^2) + m\dot{r}^2 - r(2m\ddot{r} + \dot{r}^2) = 0 \tag{29}$$

Note that some numerical solutions can be found for equation (28) with a as non-zero constant. But in this study we are interested in exact solutions, so we will concentrate our focus on analytical solutions. It is possible to find some analytical solutions with $a \neq 0$, such as $r = \text{constant}$ and $\tau(s) = cs + d$. However, those are relatively trivial solutions and as will be shown in the proceeding steps they are already included in our more general solution.

Solution to the ODE obtained in (29) is found as

$$r(s) = \frac{m(q^2 + c_1^2)(1 - \cosh(c_1(s + c_2)))}{c_1^2} \tag{30}$$

which leads to $\tau(s)$ by using equation (27) and setting $b = c_3$

$$\tau(s) = -4m \arctan\left(\frac{q \tanh\left(\frac{c_1}{2}(s + c_2)\right)}{c_1}\right) - \frac{mq(q^2 + c_1^2) \sinh(c_1(s + c_2))}{c_1^3} + mq\left(3 + \frac{q^2}{c_1^2}\right)(s + c_2) + c_3 \tag{31}$$

We apply a variable change $\theta(s) \rightarrow \arccos(X(s))$ in order to solve equations (20) and (21) which transform to

$$-\frac{\dot{X}(q + 2X\dot{\phi}) + (X^2 - 1)\ddot{\phi}}{\sqrt{1 - X^2}} = 0 \tag{32}$$

$$\frac{-\dot{\phi}(X^2 - 1)^2(q + X\dot{\phi}) + (X^2 - 1)\ddot{X} - X\dot{X}^2}{(1 - X^2)^{3/2}} = 0 \tag{33}$$

Equation (32) can be rewritten as

$$\partial_s(qX + \dot{\phi}(X^2 - 1)) = 0 \tag{34}$$

Integrating both sides yields

$$qX + \dot{\phi}(X^2 - 1) = c \Rightarrow qX + c_5 = \dot{\phi}(1 - X^2) \Rightarrow \dot{\phi}(s) = \frac{qX(s) + c_5}{1 - X(s)^2} \tag{35}$$

Integrating (35) again gives

$$\phi(s) = c_4 + \int \frac{qX(s) + c_5}{1 - X(s)^2} ds \tag{36}$$

Inserting (36) in (33) yields

$$\frac{X(q^2 + X(qc_5 - \dot{X}) + \dot{X}^2 + c_5^2) + qc_5 + \ddot{X}}{(1 - X^2)^{3/2}} = 0 \tag{37}$$

Solution to (37) is obtained as

$$X(s) = \frac{e^{-c_6(s+c_7)}(c_5^2 + c_6^2)(q^2 + c_6^2) + e^{c_6(s+c_7)} + 2qc_5}{2c_6^2} \tag{38}$$

Inserting $X(s)$ and taking the integral in (36) gives

$$\phi(s) = \arctan\left(\frac{c_6(q + c_5)}{qc_5 + e^{c_6(s+c_7)} - c_6^2}\right) + \arctan\left(\frac{c_6(q - c_5)}{qc_5 + e^{c_6(s+c_7)} + c_6^2}\right) + c_4 \tag{39}$$

Remember that θ was transformed to the variable X by $\theta(s) \rightarrow \arccos(X(s))$. Hence,

$$\theta(s) = \arccos\left(\frac{e^{-c_6(s+c_7)}(c_5^2+c_6^2)(q^2+c_6^2)+e^{c_6(s+c_7)}+2qc_5}{2c_6^2}\right) \tag{40}$$

This concludes the solution of Lorentz equation for the magnetic curve $\gamma(s)$. Note that we fixed only one initial condition in equation (27) and obtained a general solution for the Lorentz equation with seven arbitrary constants out of eight. However, one should be careful when choosing the constants in equation (40) since the domain of inverse cosine function is $[-1, 1]$.

We give a plot of $\gamma(s)$ for $q=m=1$ and all other constants were chosen by respecting the domains of the given functions, particularly fixing $\theta = 0$.

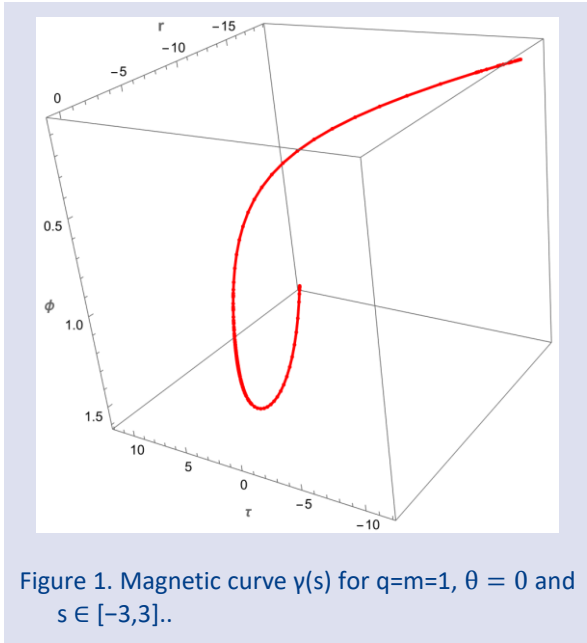


Figure 1. Magnetic curve $\gamma(s)$ for $q=m=1, \theta = 0$ and $s \in [-3,3]$.

It is known that if magnetic field B on M has a global vector potential A , i.e. $B=dA$, then the energy functional of a smooth curve $\gamma : [a, b] \rightarrow M$ can be defined by [12]

$$E_A(\gamma) = \int_a^b \left[\frac{1}{2} \|\dot{\gamma}\|^2 + A(\dot{\gamma}) \right] ds \tag{41}$$

We have given Kähler magnetic field B on ES space in equation (11) as a 2-form which can be written as dA

$$\begin{aligned} \hat{\omega} &= \frac{1}{r^2} d\tau \wedge dr + \sin\theta d\phi \wedge d\theta \\ &= d\left(\frac{d\tau}{r} + \cos\theta d\phi\right) \Rightarrow A = \frac{d\tau}{r} + \cos\theta d\phi \end{aligned} \tag{42}$$

Since there exists a global vector potential A for the magnetic field we can calculate the energy for an interval of magnetic field curve $\gamma(s)$. We first compute the integrand of the integral given in equation (41) by using the metric \hat{g} and $\dot{\gamma}(s)$ given in equation (15) as follows

$$\begin{aligned} \|\dot{\gamma}\|^2 &= \frac{\dot{r}(s)^2}{r(s)(r(s)-2m)} + \frac{(r(s)-2m)\dot{\tau}(s)^2}{r(s)^3} + \dot{\theta}(s)^2 + \sin^2(\theta(s))\dot{\phi}(s)^2 \\ A(\dot{\gamma}) &= \frac{\dot{\tau}(s)}{r(s)} + \cos(\theta(s))\dot{\phi}(s) \end{aligned} \tag{43}$$

which yield the following after inserting the parameterized coordinates $\tau(s), r(s), \phi(s), \theta(s)$ given in equations (30), (31), (39) and (40)

$$\|\dot{\gamma}\|^2 = c_1^2 - c_6^2 \tag{44}$$

$$A(\dot{\gamma}) = c_6^2 e^{c_6(s+c_7)} \left(\frac{q-c_5}{(c_5^2+c_6^2)(q^2+c_6^2)+2(c_5q+c_6^2)e^{c_6(s+c_7)}+e^{2c_6(s+c_7)}} - \frac{q+c_5}{(c_5^2+c_6^2)(q^2+c_6^2)-2(c_6^2-c_5q)e^{c_6(s+c_7)}+e^{2c_6(s+c_7)}} \right) - \frac{2c_1^2q}{(q^2+c_1^2)\cosh(c_1(s+c_2))-q^2+c_1^2}$$

Finally, we take the integral given in (41) and obtain the energy of the magnetic curve associated with the potential A for an interval of $s \in [a, b]$ as

$$\begin{aligned}
 E_A(\gamma) = & \frac{1}{2}(c_1^2 - c_6^2)(b - a) - \arctan\left(\frac{c_6(q+c_5)}{e^{c_6(a+c_7)+c_5q-c_6^2}}\right) + \arctan\left(\frac{c_6(q-c_5)}{e^{c_6(a+c_7)+c_5q+c_6^2}}\right) + \\
 & 2\arctan\left(\frac{q\tanh\left(\frac{1}{2}c_1(a+c_2)\right)}{c_1}\right) + \arctan\left(\frac{c_6(q+c_5)}{e^{c_6(b+c_7)+c_5q-c_6^2}}\right) - \arctan\left(\frac{c_6(q-c_5)}{e^{c_6(b+c_7)+c_5q+c_6^2}}\right) - \\
 & 2\arctan\left(\frac{q\tanh\left(\frac{1}{2}c_1(b+c_2)\right)}{c_1}\right)
 \end{aligned} \tag{45}$$

It is clear that the energy computed in (45) will always be finite for a finite interval [a,b] since the range of arctan function is $(-\pi/2, \pi/2)$. Hence, it is possible to conclude that the proposed magnetic field and the associated magnetic curve solution is physically meaningful.

Conclusions and Outlook

In this study, we showed that Euclidean Schwarzschild space is locally conformally Kähler and transformed it into a Kähler space by applying a conformal factor. Then we solved Lorentz equation to find analytical expressions for magnetic curve which is compatible with the almost complex structure of the newly found Kähler space. Finally, we found a global vector potential A whose exterior derivative gives the magnetic field and calculated the energy of the magnetic curves for this vector potential. We think that the following research problems might be interesting for future study.

- What are the J-trajectories of Euclidean Schwarzschild space?
- J-trajectories of $\mathbb{R} \times S^3$ was already studied in literature. $\mathbb{R} \times S^3$ is also known to be a locally conformally Kähler space. So, can we apply the same procedure that we did in this study and find the Kähler magnetic curves for the Kähler counterpart of $\mathbb{R} \times S^3$?
- More generally, let (M, g, J) be a locally conformally Kähler space and (M', g', J') be its corresponding Kähler space. Can we find a general relationship between J-trajectory γ on M and Kähler magnetic curve γ' on M' ?
- Among the magnetic curves found in literature, which ones can be considered physical, and how can we classify them?

Although there are some studies on Kähler magnetic curves, there are few in the literature that address the explicit construction of these curves, particularly in relation to physics. We expect that this study, along with the proposed problems outlined above, will offer insights for future studies on four-dimensional Kähler magnetic curves.

Acknowledgments

The authors declare that there is no conflict of interest.

Conflicts of interest

There are no conflicts of interest in this work.

References

- [1] Hinterleitner I., Mikes J., On F-planar mappings of spaces with affine connections, *Note Mat.*, 27(1) (2007) 111–118.
- [2] Cabrerizo J.L., Fernandez M., Gomez J., On the existence of almost contact structure and the contact magnetic field, *Acta. Math. Hungar.*, 125 (2009) 191-199.
- [3] Cabrerizo J.L., Fernandez M., Gomez J., The contact magnetic flow in 3D Sasakian manifolds, *J. Phys. A: Math. Theor.*, 42(19) (2009) 195-201.
- [4] Munteanu M. I., Nistor A.I., The classification of Killing magnetic curves in $S^2 \times \mathbb{R}$, *J. Geom. Phys.*, 62(2) (2012) 170-182.
- [5] Druță-Romaniuc S.L., Inoguchi J., Munteanu M.I., Nistor A.I., Magnetic curves in Sasakian manifolds, *J. Nonlinear Math. Phys.*, 22(3) (2015) 428–447.
- [6] Druță-Romaniuc S.L., Inoguchi J., Munteanu M.I., Nistor A.I., Magnetic curves in cosymplectic manifolds, *Rep. Math. Phys.*, 78 (1) (2016) 33-48.
- [7] Erjavec Z., Inoguchi, J., Magnetic curves in Sol₃, *J. Nonlinear Math. Phys.*, 25(2) (2018) 198-210.
- [8] Inoguchi, J., Munteanu, M.I., Magnetic curves in the real special linear group, *Adv. Theor. Math. Phys.*, 23 (8) (2019) 2161-2205.
- [9] Kelekçi Ö., Dündar F.S., Ayar G., Classification of Killing magnetic curves in \mathbb{H}^3 , *Int. J. Geom. Methods Mod. Phys.*, 20 (14) (2023) 2450006.
- [10] Adachi T., Kähler magnetic fields on a complex projective space, *Proc. Japan Acad.*, 70 (1994) 12-13.
- [11] Adachi T., Kähler Magnetic flow for a manifold of constant holomorphic sectional curvature, *Tokyo J. Math.*, 18 (1995) 473-483.
- [12] Adachi T., Kähler magnetic fields on Kähler manifolds of negative curvature, *Differential Geom. Appl.*, 29 (2011) S2-S8.
- [13] Kalinin, D.A., Trajectories of charged particles in Kähler magnetic fields, *Rep. Math. Phys.*, 39(3) (1997) 299-309.
- [14] Ateş O., Munteanu M. I., Periodic J-trajectories on $\mathbb{R} \times S^3$, *J. Geom. Phys.*, 133 (2018) 141-152.
- [15] Inoguchi J., Lee J., J-trajectories in Vaisman manifolds, *Differential Geom. Appl.*, 82(101882) (2022) 1-21.
- [16] Inoguchi J., J-trajectories in Locally Conformal Kahler Manifolds with Parallel Anti Lee Field, *International Electronic Journal of Geometry*, 13(2) (2020) 30-44.
- [17] Jleli M., Munteanu M.I., Magnetic curves on flat para-Kähler manifolds, *Turkish Journal of Mathematics*, 39(6) (2015) 963-969.
- [18] Erjavec Z., Inoguchi J., Magnetic curves in $\mathbb{H}^3 \times \mathbb{R}$, *J. Korean Math. Soc.*, 58(6) (2021) 1501–1511.
- [19] Yau S.T., Einstein manifolds with zero Ricci curvature, *Surveys in differential geometry: essays on Einstein manifolds*, Int. Press, Boston, MA, (1999) 1-14.
- [20] Battista E., Esposito G., Geodesic motion in Euclidean Schwarzschild geometry, *Eur. Phys. J. C*, 82(1088) (2022) 1-13.
- [21] Etesi G., Hausel T., Geometric interpretation of Schwarzschild instantons, *J. Geom. Phys.*, 37 (1–2) (2001) 126-136.
- [22] Rajan D., Complex spacetimes and the Newman–Janis trick, Master thesis, Victoria University of Wellington, School of Mathematics and Statistics, 2015.
- [23] Dragomir S., Ornea L., *Locally Conformal Kähler Geometry*, 1st ed. Birkhäuser Boston, (1998) 1–5.

Evaluation of the Central Copper Contact Pin Effect in High-Energy Region in Gamma-ray Spectrometry

Esra Uyar^{1,2,a,*}

¹ Department of Physics, Faculty of Sciences, Gazi University, Ankara, Türkiye.

² Basic and Engineering Sciences Central Laboratory Application and Research Center (GUTMAM), Gazi University, Ankara, Türkiye.

*Corresponding author

Research Article

History

Received: 18/11/2023

Accepted: 26/02/2024



This article is licensed under a Creative Commons Attribution-NonCommercial 4.0 International License (CC BY-NC 4.0)

ABSTRACT

The detector must be modeled in the most accurate way when Monte Carlo simulation method is used for efficiency calculation in gamma-ray spectrometric studies. This study aims to investigate the effect of the copper contact pin inside the detector on the efficiency of the HPGe detector for high gamma-ray energies. Simulated efficiencies were determined for 6 different energies in the energy range of 1460.8 keV up to 2614.5 keV in point and cylindrical source geometry. According to the modeling using PHITS Monte Carlo simulation code, the presence of copper contact pin at high gamma-ray energies caused a decrease of up to 6% in detector efficiency. It was emphasized that this ignored parameter should be included in the modeling like all other geometric parameters used in detector modeling, by showing the effect on the efficiency.

Keywords: HPGe detector, PHITS, Monte Carlo modeling, Copper contact pin, Full energy peak efficiency.

esrauyar@gazi.edu.tr

<https://orcid.org/0000-0001-7585-9635>

Introduction

Gamma-ray spectrometry is one of the most powerful methods used to determine the amounts of radionuclides in any sample. To quantify the radionuclides, it is necessary to know the full-energy peak efficiency of the detector for the energies of interest [1]. Because the number of detected photons is proportional to the concentration of the isotope, a full-energy peak provides all the data required for identifying and measuring a radioactive isotope in a sample. Since it is always necessary for the analysis of a sample unless a standard with the same features is available, the detector efficiency calibration in gamma-ray spectrometry is a highly significant issue. Monte Carlo (MC) simulation programs, which have been gaining popularity in many areas over the years, help users significantly, especially in the process of determining efficiency in gamma-ray spectrometry [2]. These programs, which work with an algorithm in which random numbers are generated for random variables, physical experiments are simulated on the computer. In gamma-ray spectrometric studies, high purity germanium (HPGe) detectors can be modeled using these programs and efficiency values can be successfully obtained. In detector modeling, the "quality assurance data sheet" in which many geometric dimension information of the detector is given when the detector is first supplied by the manufacturer, is critical [3]. Because detector simulation is mainly based on information provided by the manufacturer [4]. If the manufacturer gives the detector parameters missing, the accuracy of the simulations is directly affected [5–7]. The accuracy of the simulation results depends on adequate input data and the accuracy of the various approaches applied in the physical model

[8]. From the information provided by the manufacturer, for example, dead layer thickness is a time-varying parameter, it is critical to use the existing dead layer thickness determined in the modeling [9, 10]. Otherwise, in the study by Dokania et al. (2014), the physical characteristics of the detector given by the manufacturer were irradiated with the Ge crystal using the radiography method, and they determined that the active detector volume was 20% smaller than the value given by the manufacturer [11]. Therefore, while information is still given about these and similar parameters that need to be tested for accuracy and current status, no manufacturer provides information about the center of the detector is where a copper contact pin is positioned.

The copper contact pin is one of the significant components of the HPGe detector; it is used as both an electrical contact pin and a heat conductor to keep the detector cool (Fig. 1). There are several articles where the presence of this copper contact pin, which reduces the efficiency of the detector, is mentioned, and since its size is not given by the manufacturer, it is included in the modeling with estimated values [12–15].

The research question and purpose of this study is to examine the effect of this copper contact pin, which is located in the middle of the crystal and whose dimensions are not given by any manufacturer, on the detector efficiency at high gamma-ray energies. The necessity of giving the copper contact pin size in the "quality assurance data sheet", which includes the geometric dimension information, is shown with the data obtained from the simulation program.

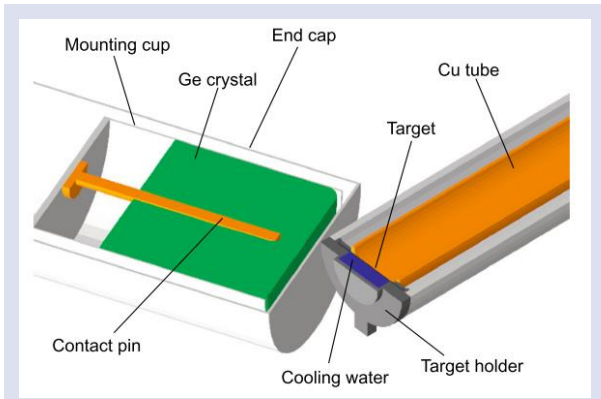


Figure 1. Contact pin in the setup displaying the germanium detector in the investigation by Carson et al. (2010).

Carson et al. assumed that the contact pin design is proprietary information and is not easily given by the manufacturers, estimating as much as possible the geometry of the contact pin inside the crystal hole from a general drawing provided by the manufacturer, as a solid copper rod with a diameter of 6.9 mm [12]. Östlund et al. used 9.2 mm as the contact pin thickness while modeling the detector in Monte Carlo simulations in their study investigating how the peak-to-valley (PTV) ratio is affected by the detector properties. This value is the diameter of the central hole, so they assumed that the contact pin filled the centre hole of the detector. Because they stated that X-ray and computed tomography could not predict the central electrode diameter [16]. Since the X-ray image did not provide sufficient information to obtain the actual dimensions of the contact pin in Dryak and Kovar, they obtained an image of the copper contact pin by taking the gamma-ray radiography with the Ir-192 gamma source and determined its diameter as 3.7 mm [13]. Boson et al., in their study in which they made a detailed examination of the HPGe detector response, showed the copper contact pin in the cross-section of the MCNP detector model [17]. However, this contact pin is ignored in many studies. The lack of information about this contact pin among the information provided by the manufacturer in HPGe detector modeling with Monte Carlo simulation is one of the biggest factors in ignoring this parameter.

As can be seen from these limited studies in the literature, no definite interpretation can be made about the dimensions of the contact pin. Therefore, in this study, the detector was modeled in three different ways using the PHITS Monte Carlo simulation program. It is first modeled without including the contact pin, then with the 3.5 mm contact pin, and finally with the 4.5 mm contact, which is the inner hole diameter of the detector. Also, there is one study in the literature on how this contact pin will have an effect on the detector response and the full energy peak efficiency [18]. In this paper, the effect of the copper contact pin on the detector efficiency was examined in the point source geometry in the energy range of 59.5 keV-1408 keV and it was determined that it

changed of up to 1.9% in the efficiency of the detector. The current study investigates the effect of a copper contact pin on the full energy peak efficiency by calculating efficiency values for higher gamma ray energies up to 2614.5 keV in both cylindrical and point source geometry in the high-energy region where the effect is dominant.

Experimental Details

2.1 PHITS toolkit for Monte Carlo simulations

The PHITS Monte Carlo code (version 3.28) was employed to simulate the transport of radiation to create a model for the HPGe detector. The main reason for using the PHITS MC simulation program in this study is that PHITS is a general-purpose simulation program. Because in such programs (MCNP, GEANT4, EGS4, PENelope, etc.), any desired parameter can be added while modeling the detector. There is no such flexibility in dedicated-purpose simulation programs (GESPECOR, EFFTRAN, etc.) where only geometric dimension information is entered. In PHITS, source files, binary, data libraries, graphic utility, etc. all contents are fully integrated in one package. The latest version of ENDF (Evaluated Nuclear Data File) and JEFF (Joint Evaluated Fission and Fusion), containing more than 1000 γ -ray spectra, are used as nuclear data libraries. PHITS is a general-purpose MC particle transport simulation code that is used in many studies in the fields of accelerator technology, radiotherapy, space radiation, nuclear applications, etc. [19]. Using the EGS5 (Electron Gamma Shower) library in the PHITS MC program, the atomic interactions of electrons and photons in a wide energy range ranging from 1 keV to 1 TeV (depending on the atomic numbers of the target materials) are simulated in the desired geometry. It can also be used successfully used in gamma-ray spectrometry to model and respond to HPGe detector [20]. Many sections such as [parameters], [source], [material], [cell], [surface], [t-deposit] are used when modeling the detector in PHITS. In the first of these sections, the [parameters] section, the total number of histories with maxcas and maxbch, the desired energy range with e_{min} (cut-off energy of photon) and d_{max} (maximum energy of library use for i-th particle), and the library to be used in calculations with file(20) is selected. The capacity of the code is the product of maxcas (number of histories per batch-the upper limit is 2147483647) and maxbch (number of batches-the upper limit is 2147483647) parameters. This is a number like $2 \times 2147483647 = 4294967294 \approx 4.3 \times 10^9$. Therefore, the $1 \times 10^6 - 1 \times 10^7$ particle numbers needed in this study and many similar studies can be easily generated with PHITS and results can be obtained. Since Monte Carlo is a statistical process in which random numbers are used, keeping the number of repetitions as high as possible allows us to obtain more meaningful results. For this reason, one hundred million source particles were used to obtain an uncertainty less than 1% in simulated efficiency in this study.

Source definitions are made in the [source] section. The geometry of the source is determined by the s-type value in this section. s-type=9 is used for point source geometry and s-type=1 is used for volumetric cylinder source geometry. In the [material] section, both the materials that compose the detector and, if the source is volumetric, the density and chemical composition information of the source are defined. The detector was modeled with PHITS computer code using all data provided by the manufacturer. These data are; detector diameter and length, hole diameter and depth, mount cup length and wall thickness, end cap wall and window thicknesses, hole and outside contact layer (dead layer) thicknesses, etc. Such geometric parameters are set in the [surface] section to define the cells in the [cell] section. When determining these surfaces, for example, since the surfaces forming the HPGe detector are cylindrical, they are identified with the symbol RCC. The parameters of RCC

are the coordinates of the center of the bottom of the cylinder, $P(x_0, y_0, z_0)$, a vector from the bottom to the top, $H(H_x, H_y, H_z)$, and the radius of the cylinder, R .

The [t-deposit] tally was used to collect the energy (Pulse Height Distribution) deposited in a given region, per emitted gamma particle. This tally provides the energy distribution of the pulses generated in the active germanium crystal. Accordingly, the full energy peak efficiency values used in the study were obtained using the [t-deposit] tally. In the study, the [t-deposit] tally used to collect the energy deposited in a certain region per emitted gamma particle gives the relative standard error along with the efficiency value. The relative standard errors can be estimated as $1/\sqrt{K}$ where K is the number of histories contributing to the tally result. The number of histories is the product of the maxcas (number of histories per batch) and maxbch (number of batches) parameters.

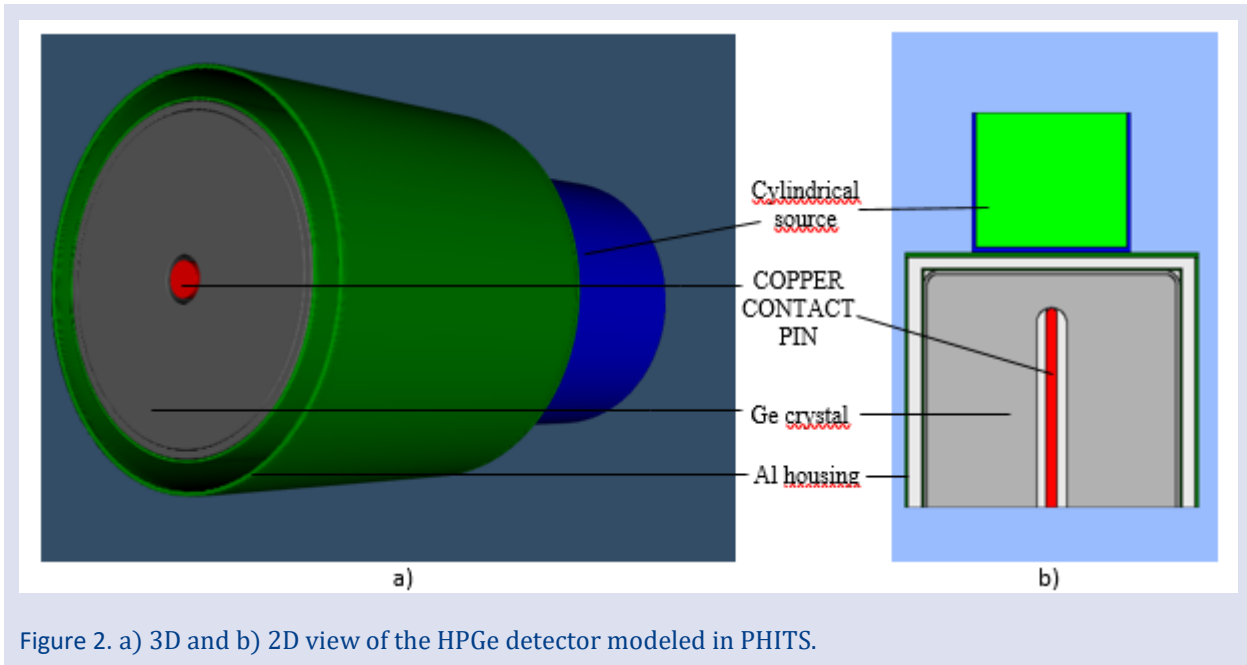


Figure 2. a) 3D and b) 2D view of the HPGe detector modeled in PHITS.

The position of the copper contact pin in the detector system is shown using the PHIG-3D (PHITS Interactive Geometry viewer in 3D), which reads the PHITS input file and visualizes the geometry in 3D and 2D representation of the geometry (Fig. 2).

2.2 Efficiency simulations

The modeled detector is a p-type coaxial HPGe (PGT IGC50195) with a relative efficiency of 54.7% and a full width at half maximum (FWHM) of 3.8 keV at 1332.5 keV (^{60}Co), 1.2 keV at 122.1 keV (^{57}Co). Its peak-to-Compton ratio is 67.2:1 at 1332.5 keV (^{60}Co). The Ge crystal has a 65.8 mm diameter and a 65.8 mm length. The hole of the detector is 9 mm in diameter and 53 mm depth. The detector with 0.5 mm Al window has a crystal to window distance of 5 mm. The dead layer thickness, which changes over time and significantly affects the full energy peak efficiency, is given by the manufacturer as <1 mm.

The dead layer thickness, which was given as <1 mm, was determined as 1.71 mm in our previous study and this value was used in the detector modeling [20].

In the study, efficiency calculations were made for point source geometries counted at certain distances (on the end cap (0 cm), 5 cm, 10 cm, 15 cm and 20 cm) from the detector and cylindrical source geometries counted on the end cap. For this purpose, 1173.2 keV (f_v : 99.85%), and 1332.5 keV (f_v : 99.98%) peaks of ^{60}Co with high gamma-ray energy and 1836.1 keV (f_v : 99.35%), peaks of ^{88}Y were used as point sources. In PHITS, the source information is set in the [source] section. The source type is specified with the number s-type=N. Point source modeling was done by choosing s-type=9, which is the source definition for the sphere or spherical surface. Calculations were made considering the 1460.8 keV (^{40}K - f_v : 10.55%) peak of IAEA-RGK-1, 1764.5 keV ($^{214}\text{Bi}/^{238}\text{U}$ - f_v : 15.31%), peak of IAEA-RGU-1 and 2614.5 keV ($^{208}\text{Tl}/^{232}\text{Th}$ - f_v : 99.76%) peak of IAEA-RGTh-1, which are the most calculated/used in

environmental radioactivity calculations in cylindrical geometry and have high gamma emission probability (f_{γ}). Cylindrical source modeling was done by choosing s-type=1. In s-type=1, the coordinates of the sphere (x_{θ} , y_{θ} , z_{θ}) and its radius, r_{θ} , are defined in cylindrical source modeling. The geometric dimensions of the sample

container consisting of cylinder acrylic material ($\rho=1.19$ g/cm³) were taken as 5 cm inner height, 3 cm inner radius, 0.15 cm wall thickness, and 0.2 cm bottom thickness. Density and elemental compositions given in Table 1 of IAEA-RGK-1, IAEA-RGU-1 and IAEA-RGTh-1 are defined in the [material] section of PHITS.

Table 1.Densities and elemental compositions of the reference materials

Reference material	Density (g/cm ³)	Elemental compositions (%)*
IAEA-RGU-1	1.335	O: 53.4; Si: 46.4; Al: 0.10 ; U: 0.04; Ca: 0.03 Fe: 0.03; Na: 0.02; C: 0.01; Pb: 0.008 ; K: 0.002
IAEA-RGTh-1	1.325	O: 52.8; Si: 45.6; Y: 0.76; Ca: 0.50; Fe: 0.11; P: 0.11 Th: 0.08; K: 0.02; Mg: 0.02; Sr: 0.016; Al: 0.012; Zn: 0.011
IAEA-RGK-1	1.577	K: 44.8; O: 36.7; S: 18.4

*Elemental compositions of the reference material derived from XRF data.

In this study, three approaches were made to model the contact pin thickness. Firstly, without the copper contact pin, then by adding a contact pin with a radius of 3.5 mm, and finally for the 4.5 mm value, where the contact pin is assumed to fill the central hole, as in the work of Östlund et al. [16].

Results and Discussion

In the point source geometry, for 1173.2 keV, 1332.5 keV and 1836.1 keV energies on the detector window (0 cm), at 5 cm, 10 cm, 15 cm and 20 cm distances; in the cylindrical source geometry, efficiency values were obtained for 1460.8 keV, 1764.5 keV and 2614.5 keV energies on the detector window (Table 2). As expected, the efficiency value decreases with the inclusion of the copper contact pin and the increase in its thickness.

Table 2.Simulated efficiencies with PHITS for different contact pin values in point and cylindrical source geometry.

Source geometry	Distance	Nuclide	Energy (keV)	Without contact pin	With 3.5 mm contact pin	With 4.5 mm contact pin
Cylindrical	On the end cap	RGK-1 (⁴⁰ K)	1460.8	1.158E-02	1.119E-02	1.099E-02
		RGU-1 (²³⁸ U)	1764.5	1.033E-02	9.973E-03	9.807E-03
		RGTh-1 (²³² Th)	2614.5	7.452E-03	7.174E-03	7.075E-03
Point	On the end cap (0 cm)	⁶⁰ Co	1173.2	4.700E-02	4.546E-02	4.462E-02
		⁶⁰ Co	1332.5	4.257E-02	4.116E-02	4.051E-02
		⁸⁸ Y	1836.1	3.289E-02	3.174E-02	3.113E-02
	5 cm	⁶⁰ Co	1173.2	7.830E-03	7.604E-03	7.477E-03
		⁶⁰ Co	1332.5	7.135E-03	6.918E-03	6.810E-03
		⁸⁸ Y	1836.1	5.550E-03	5.373E-03	5.281E-03
		⁶⁰ Co	1173.2	3.024E-03	2.943E-03	2.894E-03
		⁶⁰ Co	1332.5	2.761E-03	2.678E-03	2.636E-03
		⁸⁸ Y	1836.1	2.150E-03	2.079E-03	2.040E-03
	10 cm	⁶⁰ Co	1173.2	1.586E-03	1.539E-03	1.515E-03
		⁶⁰ Co	1332.5	1.447E-03	1.401E-03	1.377E-03
		⁸⁸ Y	1836.1	1.146E-03	1.108E-03	1.088E-03
		⁶⁰ Co	1173.2	9.796E-04	9.515E-04	9.355E-04
		⁶⁰ Co	1332.5	8.928E-04	8.643E-04	8.463E-04
		⁸⁸ Y	1836.1	7.030E-04	6.784E-04	6.638E-04
	15 cm	⁶⁰ Co	1173.2	1.447E-03	1.401E-03	1.377E-03
		⁸⁸ Y	1836.1	1.146E-03	1.108E-03	1.088E-03
		⁶⁰ Co	1173.2	9.796E-04	9.515E-04	9.355E-04
⁶⁰ Co		1332.5	8.928E-04	8.643E-04	8.463E-04	
⁸⁸ Y		1836.1	7.030E-04	6.784E-04	6.638E-04	
⁶⁰ Co		1173.2	1.447E-03	1.401E-03	1.377E-03	
20 cm	⁸⁸ Y	1836.1	7.030E-04	6.784E-04	6.638E-04	
	⁶⁰ Co	1173.2	1.447E-03	1.401E-03	1.377E-03	
	⁸⁸ Y	1836.1	7.030E-04	6.784E-04	6.638E-04	
	⁶⁰ Co	1173.2	1.447E-03	1.401E-03	1.377E-03	
	⁸⁸ Y	1836.1	7.030E-04	6.784E-04	6.638E-04	
	⁶⁰ Co	1173.2	1.447E-03	1.401E-03	1.377E-03	

There is true coincidence summing effect in gamma-ray spectrometry, especially in low source-to-detector distance and radionuclides with complex decay scheme that emit more than one gamma-ray [21]. In this study, all radionuclides except ⁴⁰K have this effect. The true coincidence summing factor is an important correction

factor affecting the full energy peak efficiency. However, since the ratios of the full energy peak efficiency values obtained in the study (without contact pin/with 3.5 mm contact pin and without contact pin/with 4.5 mm contact pin) are used, this factor will not have an effect on the results.

The effect of the contact pin was investigated by calculating the % difference between the efficiency values calculated without the contact pin and the efficiency values determined with the 3.5 mm and 4.5 mm contact pin. Accordingly, this effect is given in Fig.3 in point source geometry and in Fig.4 in cylindrical source geometry. In the existence of a copper contact pin with a radius of 3.5

mm, the percent difference in detector efficiency, ie reduction values; 2.7-3.3% at 1173.2 keV; 3.0-3.3% at 1332.5 keV; 3.2-3.5% at 1836.1 keV. In the existence of a copper contact pin with a radius of 4.5 mm, these values are; 4.3-5.1% at 1173.2 keV; 4.5-5.2% at 1332.5 keV; 4.9-5.6% at 1836.1 keV (Fig.3).

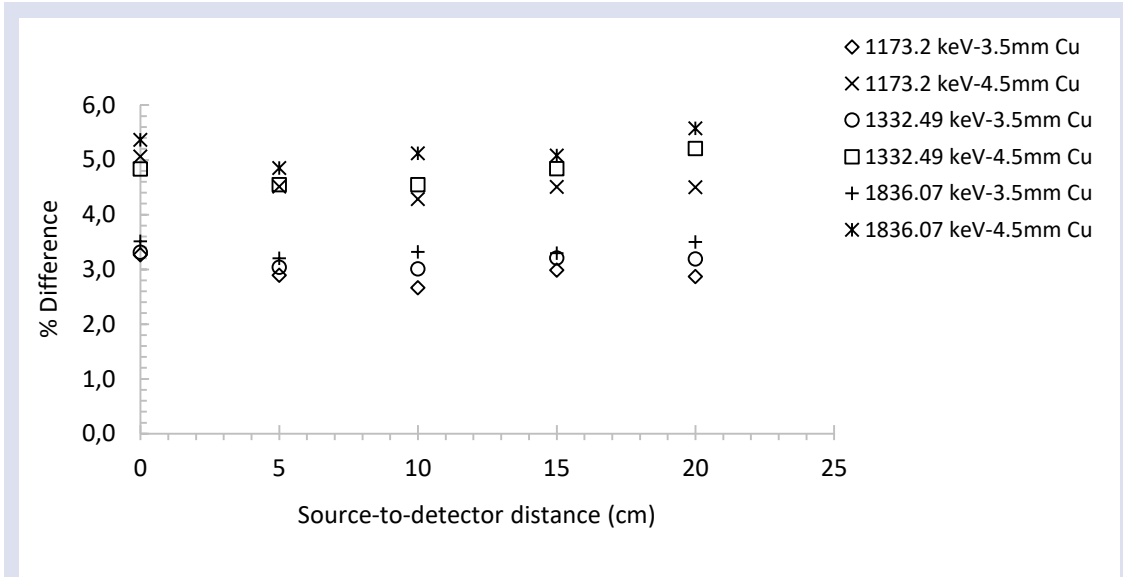


Figure 3. The difference between the efficiency values determined with 3.5 mm and 4.5 mm contact pin at different source-to-detector distances and the efficiency value determined without a contact pin (point source geometry).

In the presence of a 3.5 mm radius copper contact pin, the percent difference in the detector efficiency; 3.4% at 1460.8 keV; 3.4% at 1764.5 keV; 3.7% at 2614.5 keV. In the presence of a copper contact pin with a radius of 4.5 mm, these values are; 5.1% at 1460.8 keV; 5.0% at 1764.5 keV; 5.1% at 2614.5 keV (Fig.4). Similar differences at 1460.8

keV, 1764.5 keV and 2614.5 keV show that the effect does not increase with further increase in energy. Therefore, the biggest difference that can be created in the detector efficiency because of interactions that may occur at high energy is at these levels.

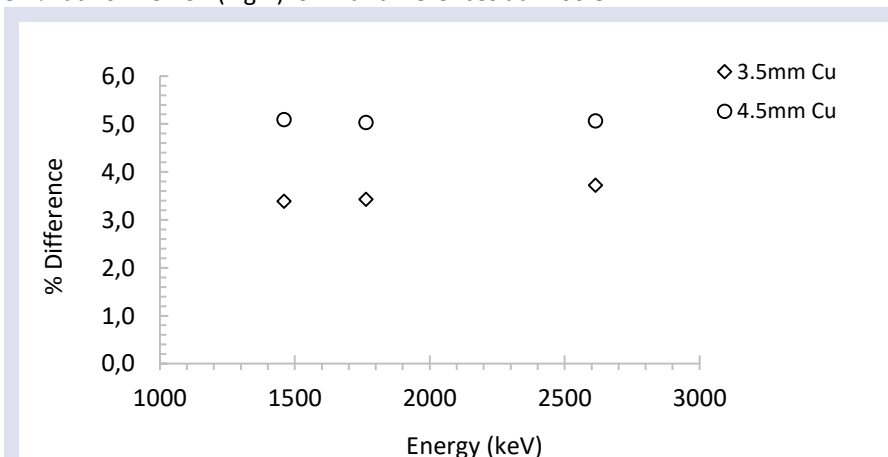


Figure 4. The difference between the efficiency values determined with 3.5 mm and 4.5 mm copper at a fixed source-to-detector distance and the efficiency value determined without copper (cylindrical source geometry).

Compared with the 1836.1 keV peak in the point source geometry, the 1764.5 keV peak in the cylindrical source geometry at close energies, the efficiency change in both energies is $\approx 3.5\%$ at the 3.5 mm contact pin; in 4.5 mm contact pin, it is seen that $\approx 5\%$. Consequently, it can be said that the copper contact pin is independent of the source geometry.

According to the results obtained from both geometries, it was seen that the contact pin affected the efficiency in the modeling of the HPGe detector. Considering the contact pin thickness of 4.5 mm, where the effect is more dominant, it shows that this effect will be even greater as the detector volume and hence crystal diameter increases. Therefore, this parameter is more important in large volume HPGe detectors used in studies such as measurements of the gamma-ray production cross-section from inelastic neutron scattering and time-of-flight measurements.

Conclusion

The manufacturer-provided parameters are critical in simulation calculations where HPGe detectors are modeled. The design of the contact pin is proprietary information and cannot be easily obtained from the manufacturers. While many parameters affecting the efficiency of the detector are investigated in detail in the literature, the effect of the copper contact pin is ignored. The effect of copper contact pin thickness on the detector efficiency in the 1460.8 keV-2614.5 keV energy range was investigated and the decrease in the efficiency increases to approximately 4% when the contact pin thickness is modeled as 3.5 mm, and 6% for 4.5 mm. Since photons with low-energy are absorbed because of photoelectric interaction before they reach that region, only high gamma energy peaks are considered in the study. The peaks in the high-energy region interact with the contact pin, which is the material in the interior of the crystal, due to the Compton scattering and pair production events dominant in this region, decreasing the efficiency values.

There are many sources of uncertainty (such as measurement geometry, decay graph and input data) in determining the efficiency value by simulation in the activity concentration calculation using gamma-ray spectrometry. Therefore, not including a copper contact pin in addition to these uncertainty sources brings extra uncertainty by taking it away from the true value. When modeling the detector in general-purpose Monte Carlo programs, the copper contact pin should be included in the coding so that its center is in the middle of the hole. In dedicated-purpose programs, the developers of the program should add this parameter as a contact pin to the part where the detector parameters are defined. It is also critical to determine the efficiency values to be obtained from the simulation to be used in the activity concentration calculations of the samples containing natural radionuclides such as U, Th, K, which are also considered in this study.

Acknowledgments

The author is thankful to Prof. Emeritus Octavian Sima, University of Bucharest, Physics Department, for his helpful information on the subject.

Conflicts of interest

There are no conflicts of interest in this work.

References

- [1] M. I. Abbas, FEPE Calibration of a HPGe Detector Using Radioactive Sphere Source, *Physics Procedia* 90 (2017) 364-368.
- [2] T. Vidmar, I. Aubineau-Laniece, M. J. Anagnostakis, D. Arnold, R. Brettner-Messler, D. Budjas, M. Capogni, M. S. Dias, L. E. De Geer, et al., An intercomparison of Monte Carlo codes used in gamma-ray spectrometry, *Applied Radiation and Isotopes*, 66 (2008) 764-768.
- [3] M. Travar, J. Nikolov, N. Todorović, A. Vraničar, P. Völgyesi, P. Kirchknopf, I. Čeliković, T. Milanović and D. Joković, Detailed optimization procedure of an HPGe detector using Geant4 toolkit, *Journal of Radioanalytical and Nuclear Chemistry*, 332 (2023) 817-828.
- [4] C. M. Salgado, C. C. Conti and P. H. B. Becker, Determination of HPGe detector response using MCNP5 for 20-150 keV X-rays, *Applied Radiation and Isotopes*, 64 (2006) 700-705.
- [5] W. Khan, Q. Zhang, C. He and M. Saleh, Monte Carlo simulation of the full energy peak efficiency of an HPGe detector, *Applied Radiation and Isotopes*, 131 (2018) 67-70.
- [6] T. Azli and Z. E. A. Chaoui, Performance reevaluation of a N-type coaxial HPGe detector with front edges crystal using MCNPX, *Applied Radiation and Isotopes*, 97 (2015) 106-112.
- [7] I. O. B. Ewa, D. Bodizs, S. Czifrus and Z. Molnar, Monte Carlo determination of full energy peak efficiency for a HPGe detector, *Applied Radiation and Isotopes*, 55 (2001) 103-108.
- [8] E. Stancu, C. Costache and O. Sima, Monte carlo simulation of p-type HPGe detectors – The dead layer problem, *Romanian Reports in Physics*, 67 (2015) 465-473.
- [9] M. H. Bölükdemir, E. Uyar, G. Aksoy, H. Ünlü, H. Dikmen and M. Özgür, Investigation of shape effects and dead layer thicknesses of a coaxial HPGe crystal on detector efficiency by using PHITS Monte Carlo simulation, *Radiation Physics and Chemistry*, 189 (2021) 109746.
- [10] J. G. Guerra, J. G. Rubiano, G. Winter, A. G. Guerra, H. Alonso, M. A. Arnedo, A. Tejera, P. Martel and J. P. Bolivar, Computational characterization of HPGe detectors usable for a wide variety of source geometries by using Monte Carlo simulation and a multi-objective evolutionary algorithm, *Nuclear Instruments and Methods in Physics Research, Section A: Accelerators, Spectrometers, Detectors and Associated Equipment*, 858 (2017) 113-122.
- [11] N. Dokania, V. Singh, S. Mathimalar, V. Nanal, S. Pal and R. G. Pillay, Characterization and modeling of a low background HPGe detector, *Nuclear Instruments and Methods in Physics Research, Section A: Accelerators, Spectrometers, Detectors and Associated Equipment*, 745 (2014) 119-127.

- [12] S. Carson, C. Iliadis, J. Cesaratto, A. Champagne, L. Downen, M. Ivanovic, J. Kelley, R. Longland, J. R. Newton, et al., Ratio of germanium detector peak efficiencies at photon energies of 4.4 and 11.7 MeV: Experiment versus simulation, *Nuclear Instruments and Methods in Physics Research, Section A: Accelerators, Spectrometers, Detectors and Associated Equipment*, 618 (2010) 190-198.
- [13] P. Dryak and P. Kovar, Experimental and MC determination of HPGe detector efficiency in the 40-2754 keV energy range for measuring point source geometry with the source-to-detector distance of 25 cm, *Applied Radiation and Isotopes*, 64 (2006) 1346-1349.
- [14] R. Berndt and P. Mortreau, Monte Carlo modelling of a N-type coaxial high purity germanium detector, *Nuclear Instruments and Methods in Physics Research, Section A: Accelerators, Spectrometers, Detectors and Associated Equipment*, 694 (2012) 341-347.
- [15] S. Sayın, M. Seferinoğlu, E. Yeltepe, B. Çetin and S. Şentürk Lüle, Assessment of the detection efficiency calibration of high-resolution gamma-ray spectrometers by EGSnrc and MCNP6.2 Monte Carlo codes, *Radiation Physics and Chemistry*, 203 (2023) 110601.
- [16] K. Östlund, C. Samuelsson and C. L. Rääf, Experimentally determined vs: Monte Carlo simulated peak-to-valley ratios for a well-characterised n-type HPGe detector, *Applied Radiation and Isotopes*, 95 (2015) 94-100.
- [17] J. Boson, G. Ågren and L. Johansson, A detailed investigation of HPGe detector response for improved Monte Carlo efficiency calculations, *Nuclear Instruments and Methods in Physics Research, Section A: Accelerators, Spectrometers, Detectors and Associated Equipment*, 587 (2008) 304-314.
- [18] E. Uyar, G. Aksoy, H. Ünlü and M. H. Bölükdemir, Investigation of the effect of copper contact pin on efficiency in HPGe detectors using Monte Carlo method, *Journal of Instrumentation*, 16 (2021) T11003.
- [19] T. Sato, Y. Iwamoto, S. Hashimoto, T. Ogawa, T. Furuta, S. ichiro Abe, T. Kai, P. E. Tsai, N. Matsuda, et al., Features of Particle and Heavy Ion Transport code System (PHITS) version 3.02, *Journal of Nuclear Science and Technology*, 55 (2018) 684-690.
- [20] E. Uyar and M. H. Bölükdemir, Characterisation of two p-type HPGe detectors by measurements and Monte Carlo simulations, *Measurement*, 204 (2022) 112092.
- [21] G. Kanisch, T. Vidmar and O. Sima, Testing the equivalence of several algorithms for calculation of coincidence summing corrections, *Applied Radiation and Isotopes*, 67 (2009) 1952-1956.

Machine Learning Based Classification of the Halos in Light Nuclei Region

Serkan Akkoyun ^{1,a,*}¹ Department of Physics, Faculty of Sciences, Sivas Cumhuriyet University, Sivas, Türkiye.

*Corresponding author

Research Article

History

Received: 09/01/2024

Accepted: 27/02/2024



This article is licensed under a Creative Commons Attribution-NonCommercial 4.0 International License (CC BY-NC 4.0)

ABSTRACT

Experimental and theoretical studies on halo nuclei, whose nucleon binding energies are extremely weak, are among the most interesting topics of nuclear physics studies. By better defining and understanding this unusual behavior of these nuclei, our understanding of nuclear structure can be further improved. Although there are already a few experimentally proven halo nuclei in the literature, many others have found their place in the literature as candidate halo nuclei. In this study, the classification of halo nuclei was carried out using an artificial neural network approach. In the light nuclei region, the properties of nuclei, including halo nuclei, were discussed and the existing halo nuclei were classified. The success of the obtained results indicates that machine learning methods can be used for identifying halo nuclei. Thus, these methods are considered as one of the alternative tools to confirm the existence of new or candidate halo nuclei.

Keywords: Nuclear structure, Halo nucleus, Machine-learning, Classification.

sakkoyun@cumhuriyet.edu.tr<https://orcid.org/0000-0002-8996-3385>

Introduction

The halo nucleus has a very weak binding of the last one or two valence nucleons. While the separation energy for stable nuclei is around 6-8 MeV, for halo nuclei this value is much lower (in some cases less than 1 MeV). The main concept of the halo nucleus is a long tail in the density distribution of a nucleus due to the tunnelling of weakly bounded nucleons. It can be understood by the extremely small nucleon separation energy of the halo nucleus compared with that of stable nuclei [1]. The halo can be a proton halo or neutron halo. These are confirmed and considered and has a very long tail of nucleon-density distribution. In 1985, Tanihata et al. [2] discovered ^{11}Li halo nucleus, and Hansen and Jonson [3] validated it. A neutron halo structure was discovered in this nucleus from the series of experiments including the interaction cross-section, the momentum distribution of the ^9Li fragment from ^{11}Li , and enhancement of the Electro-Magnetic Dissociation cross-section. The first halo nucleus ^6He made in the laboratory by using a neutron beam on a ^9Be target. The additional halo nuclei that have undergone experimental confirmation are ^{11}Li , ^{11}Be , ^{14}Be , ^{14}B , ^{15}C , and ^{19}C . Additionally, several potential halo nuclei exist but they are not confirmed experimentally. Some of them are ^8He , ^{12}Be , ^{17}B , ^{16}B , ^{17}C , ^{22}C , ^{22}N , ^{23}O , ^{24}F , ^{26}F , ^{27}F , ^{29}F , and ^{29}Ne [4]. The chart of the confirmed and potential halo nuclei is shown in Figure 1. Neutron halo nuclei are shown by dark green square and candidates of neutron halo are shown by light green. Orange squares show the proton halos. Inside the figure, ^{11}Li halo structure has been shown as an illustration [5].

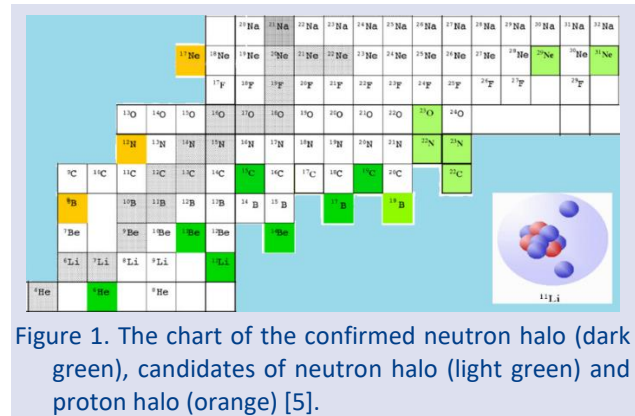


Figure 1. The chart of the confirmed neutron halo (dark green), candidates of neutron halo (light green) and proton halo (orange) [5].

Many theoretical studies exist to explain the properties of halo nuclei, including structure models [6-8] and reaction models [9-12]. To elucidate the structure of halo nuclei, Ryberg et al. [13] used halo effective field theory, in which a field-theoretic approach is used for the construction of the interaction and the calculation of observables. In this study, the classification of halo nuclei was carried out by using the machine learning approach. For this purpose, a feed-forward layered artificial neural network (ANN) model [14] was created and confirmed, and candidate halo nuclei were tried to be identified. Nuclei in the range of $Z=2$ to 10 and $N=2$ to 24 were taken into account and classified as halo or non-halo. 13 different parameters of the nuclei were determined, machine learning was performed with all and some of these parameters and the results were compared. ANN are widely used in the field of nuclear physics. Examples of studies carried out by our working group include: adjustment of non-linear interaction parameters for

relativistic mean field approach [14], time-of-flight discrimination between gamma-rays and neutrons [15], construction of consistent empirical physical formulas for potential energy curves [17], determination of nuclear charge radii [18] and binding energy [19] and estimation of fusion reaction cross-section [20]. According to the results of the present study, machine learning approaches might be possible tool for the determination of the halo nuclei.

Materials and Method

Artificial neural network (ANN) is one of the powerful mathematical tool that mimics the human brain functionality. In the ANN structure, there are neurons in different layers, namely input, hidden, and output layers. Because of this type of structure, ANN is called as layered ANN. The processing units of the ANN are neurons, and they are connected to each other in different layers by adjustable synaptic weights. Input layer neurons receive data and transmit it to hidden layer neurons and then to output layer neurons by adaptive weighted connections. If the data flow forward in one-way, the ANN is named as layered feed-forward ANN. In the present study, layered feed-forward ANN has been used for the classification of the halo nuclei.

The main purpose of the ANN method is to determine the best weight values between neurons by using the given sample data in the training stage of machine-learning. The numbers of neurons in the input and output layers depend on the variety of the data belonging to the problem. Whereas, there is no rule to determine the number of hidden layer and its neurons between input and output layers. The number of hidden layer varies according to the nature of the problem, but generally one hidden layer is sufficient for almost all problems. However, the perfect neuron number in this layer is determined after several trials that give the best results for the problem. In this work, the numbers of hidden layer neuron are either 4 or 12 for different input parameters (Figure 2).

The ANN method is a perfect tool for both linear and nonlinear function approximations. It is composed of two main stages. The entire data belonging to the problem is divided into two separate sets for training and test stages. In the training stage of supervised training procedure, the first part of data is given to the ANN, including both input and desired output values. The weights are modified using the sample data in the training stage. The method generates its own outputs as close as possible to the desired output values. Comparisons between the desired output and the ANN output are made by root mean square error (RMSE) function given by Eq. (1). After an acceptable deviation between the ANN outputs and the desired outputs, the training stage is finally terminated. This means that the ANN is constructed for solving the problem with the modified final weights. However, it is still early to decide whether the constructed ANN is appropriate for the estimation of similar type of another

set of data. The generalization ability of the ANN must be tested using the second set of the data that is never seen by the constructed ANN in the training stage. If the generated outputs in the test stage by using final weights are still close to the desired outputs, it can be confidently concluded that the ANN is appropriate for solving this type of problem. The performance of the results was evaluated by accuracy (AC), certainty (CR), sensitivity (SN) and error rate (ER) indicators. The descriptions of the indicators were given in Table 1 and Eqs.1-4. Here TP, TN, FP and FN are the numbers of true positive, true negative, false positive and false negative events.

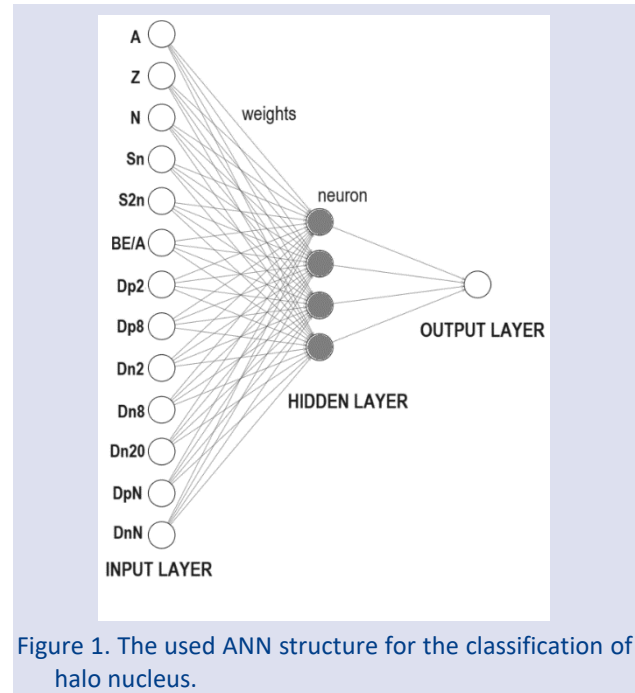


Figure 1. The used ANN structure for the classification of halo nucleus.

Results and Discussions

In order to determine the Halo nuclei for light nuclei region, we have applied artificial neural network method for the classification of the nuclei in the ranges of $Z=2$ to 10 and $N=2$ to 24. Because we have considered one and two neutron halos as ${}^6\text{He}$, ${}^8\text{He}$, ${}^{11}\text{Li}$, ${}^{11}\text{Be}$, ${}^{12}\text{Be}$, ${}^{14}\text{Be}$, ${}^{14}\text{B}$, ${}^{17}\text{B}$, ${}^{19}\text{B}$, ${}^{15}\text{C}$, ${}^{17}\text{C}$, ${}^{19}\text{C}$, ${}^{22}\text{C}$, ${}^{22}\text{N}$, ${}^{23}\text{O}$, ${}^{24}\text{F}$, ${}^{26}\text{F}$, ${}^{27}\text{F}$, ${}^{29}\text{F}$ and ${}^{29}\text{Ne}$, we have interested in this region. These are confirmed and considered halo nuclei available in the literature in p and sd shell regions. Therefore, we have collected the available experimental data of the nuclei for the given range. The collected data parameters are mass number (A), proton number (Z), neutron number (N), one neutron separation energy (S_n), two neutron separation energy (S_{2n}), binding energy per nucleon (BE/A), distance of the proton number of the nucleus from closed core 2 (Dp2), distance of the proton number of the nucleus from closed core 8 (Dp8), distance of the neutron number of the nucleus from closed core 2 (Dn2), distance of the neutron number of the nucleus from closed core 8 (Dn8), distance of the neutron number of the nucleus from closed core 20 (Dn20), distance of the proton number of the nucleus from the closest core (DpN) and distance of the neutron

number of the nucleus from the closest core (DnN). These parameters might be the possible candidates of the inputs of the neural network. The output of the neural network was the 1 or 3 whose correspond to Halo or not Halo nucleus, respectively. In Figure 3, we have presented the correlation between the variables. As can be clearly seen in the figure that the strongest correlation between output and each input parameters are S_n and S_{2n} with the correlation degree of 0.31 and 0.32, respectively. The weakest ones are A and DpN.

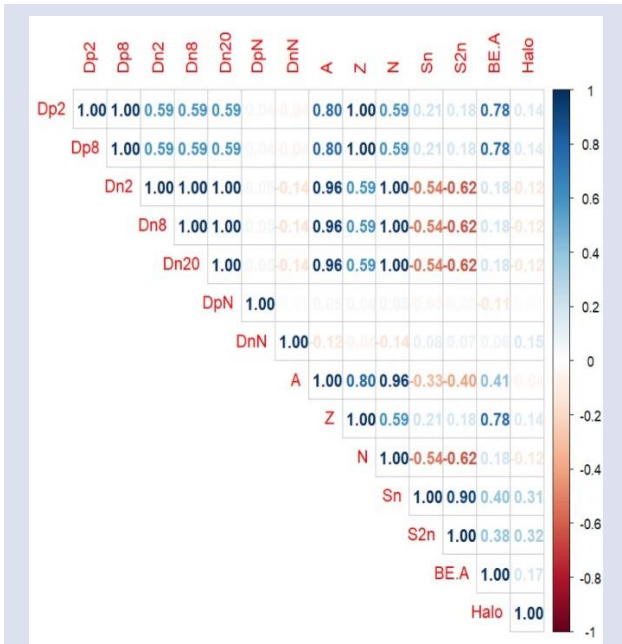


Figure 3. Correlation matrix between potential input and output parameters for the classification of halo nuclei.

In the first step of the classification, we considered all the inputs. The number of the hidden neuron is 4 which gives the best result. According to the results, for the training dataset, the classification performance is obtained very high. In Table 2, we have presented the estimation on the training data of the trained neural network. For the total 87 nuclei, 14 halo nuclei were perfectly assigned as Halo and 73 not halo nuclei was assigned as not halo. The AC, CR, SN and ER values are obtained as 1.00, 1.00, 1.00 and 0, respectively. According to these values obtained from the performance indicators, it is seen that the method has a perfect success on the training data in classifying halo nuclei.

Table 2. The estimation of the machine-learning by all input parameters for the classification of the halo nuclei on the training dataset.

		True	
		Halo	Not Halo
Predicted	Halo	14	0
	Not Halo	0	73

In the training phase, we also performed machine training by limiting the input parameters as a second option. According to the correlation matrix, we only considered S_n and S_{2n} as two inputs, which were most strongly related to the output. The number of hidden layer neurons we used in this ANN structure was 12, which gave the best results. In Table 3, we have presented the estimation on the training data of the trained neural network. All the nuclei was classified correctly. The AC, CR, SN and ER values are obtained as 0.99, 1.00, 0.93 and 0.01, respectively. According to these values obtained from the performance indicators, it is seen that the method has a superior success on the training data in classifying halo nuclei.

Table 3. The estimation of the machine-learning by two input structure of ANN for the classification of the halo nuclei on the training dataset.

		True	
		Halo	Not Halo
Predicted	Halo	13	0
	Not Halo	1	73

In Table 4, we have given the predictions on the test dataset for 26 data points by including all input parameters in the input neurons. Clearly seen in the table that the desired 5 halo nuclei were assigned as halo and desired 19 not halo nuclei were assigned as not halo. Whereas, the desired 2 not halo nuclei were incorrectly assigned as halo nuclei. The AC, CR, SN and ER values are obtained as 0.92, 0.71, 1.00 and 0.08, respectively. According to these values obtained from the performance indicators, it was seen that the method was successful on the test data in classifying halo nuclei and that the method could be an alternative in determining unknown halo nuclei.

Table 4. The predictions of the machine-learning by all input parameters for the classification of the halo nuclei on the test dataset.

		True	
		Halo	Not Halo
Predicted	Halo	5	2
	Not Halo	0	19

In the study where we limited the input parameters to S_n and S_{2n} , the predictions obtained on the test data set are presented in Table 5. The desired 1 halo and 1 not halo nuclei were incorrectly assigned. The AC, CR, SN and ER values are obtained as 0.92, 0.83, 0.83 and 0.08,

respectively. According to these values obtained from the performance indicators, again it was seen that the method was successful on the test data in classifying halo nuclei and that the method could be an alternative in determining unknown halo nuclei.

Table 5. The predictions of the machine-learning by two input structure of ANN for the classification of the halo nuclei on the training dataset.

		True	
		Halo	Not Halo
Predicted	Halo	5	1
	Not Halo	1	19

Conclusions

In this study, ANN, a machine learning approach, was used to classify possible halo nuclei identified in the literature. Parameters that may play a role in determining halo nuclei have been determined. Calculations and classification was made by considering the 13 determined parameters as the input of ANN. Then, the correlation between these parameters and the output value was examined and the number of input parameters was reduced to 2. It has been observed that there is no difference between the results of the calculations performed with the ANN in this structure and the results of the calculations using all input parameters. From this, it was concluded that only S_n and S_{2n} may be sufficient for the classification of the halo nuclei. Additionally, it has been observed that machine learning approaches can be an alternative tool in identifying halo nuclei. Thus, this approach can be considered as an alternative to confirm the existence of new halo nuclei or candidate halo nuclei. In ongoing studies, we will focus on the work on using different machine learning approaches in a wider nuclei region, confirming candidate halo nuclei, and identifying new possible halo nuclei, if any.

Conflicts of interest

There are no conflicts of interest in this work.

References

- [1] Al-Khalili J., An Introduction to Halo Nuclei, *Lect. Notes Phys.* 651 (2004) 77–112.
- [2] Tanihata I., Hamagaki H., Hashimoto O., Shida Y., Yoshikawa N., Sugimoto K., Yamakawa O., Kobayashi T., Takahashi N., Measurements of Interaction Cross Sections and Nuclear Radii in the Light p-Shell Region, *Phys. Rev. Lett.* 55 (1985) 2676.
- [3] Hansen P.G., Jonson B., The Neutron Halo of Extremely Neutron-Rich Nuclei, *Europhys. News* 4 (1987) 409–414.
- [4] Prathapan K., Deneshan P., Damodaran L., Biju R.K., Theoretical study on neutron halo emission from heavy elements, *Nuclear and Particle Physics Proceedings* 336–338 (2023) 45–47.
- [5] Tanihata I., Savajols H., Kanungo R., Recent experimental progress in nuclear halo structure studies, *Progress in Particle and Nuclear Physics* 68 (2013) 215–313.
- [6] Zhukov M.V., Danilin B.V., Fedorov D.V., Bang J.M., Thompson I.J., Vaagen J.S., Bound state properties of Borromean halo nuclei: ^6He and ^{11}Li , *Phys. Rep.* 231 (1993) 151–199.
- [7] Pieper S.C., Wiringa R.B., Quantum Monte Carlo Calculations of Light Nuclei, *Annu. Rev. Nucl. Part. Sci.* 51 (2001) 53–90.
- [8] Dean D.J., Jensen M.H., Pairing in nuclear systems: from neutron stars to finite nuclei, *Red. Mod. Phys.*, 75 (2003) 607–656.
- [9] Sharma Mahesh K., Panda R. N., Sharma Manoj K., Patra S. K., Search for halo structure in ^{37}Mg using the Glauber model and microscopic relativistic mean-field densities, *Phys. Rev. C*, 93 (2016) 014322.
- [10] Kamimura M., Yahiro M., Iseri Y., Sakuragi Y., Kameyama H., Kawai M., Projectile Breakup Processes in Nuclear Reactions, *Prog. Theor. Phys. Suppl.* 89 (1986) 1–10.
- [11] Ono A., Horiuchi H., Maruyama T., Ohnishi A., Fragment formation studied with antisymmetrized version of molecular dynamics with two-nucleon collisions, *Phys. Rev. Lett.*, 68 (1992) 2898–2900.
- [12] Varga V., Suzuki Y., Lovas R.G., Microscopic multicluster description of neutron-halo nuclei with a stochastic variational method, *Nucl. Phys. A* 571 (1994) 447–466.
- [13] Ryberg E., Forssen C., Hammer H.W., Platter L., Range corrections in Proton Halo Nuclei, arXiv:1507.08675v1 [nucl-th] (2015).
- [14] Haykin S., “Neural Networks: a Comprehensive Foundation” Englewood Cliffs, Prentice-Hall, New Jersey, pp.842, 1999.
- [15] Bayram T., Akkoyun S., Şentürk Ş., Adjustment of Non-linear Interaction Parameters for Relativistic Mean Field Approach by Using Artificial Neural Networks, *Physics of Atomic Nuclei*, 81 (2018) 288–295.
- [16] Akkoyun S., Time-of-flight discrimination between gamma-rays and neutrons by neural networks, *Annals of Nuclear Energy*, 55 (2013) 297–301.
- [17] Akkoyun S., Bayram T., Kara S.O., Yildiz N., Consistent empirical physical formulas for potential energy curves of $^{38}\text{--}^{66}\text{Ti}$ isotopes by using neural networks, *Physics of Particles and Nuclei Letters*, 10 (2013) 528–534.
- [18] Akkoyun S., Bayram T., Kara S.O., Sinan A., An artificial neural network application on nuclear charge radii, *Journal of Physics G: Nuclear and Particle Physics*, 40 (2013) 055106.
- [19] Bayram T., Akkoyun S., Kara S.O., A study on ground-state energies of nuclei by using neural networks, *Annals of Nuclear Energy*, 63 (2014) 172–175.
- [20] Akkoyun S., Estimation of fusion reaction cross-sections by artificial neural networks, *Nuclear Instruments and Methods in Physics Research Section B*, 462 (2020) 51–54.

Asymptotic Relative Efficiency Comparison for some Fit Indices in Structural Equation Modeling

İlkay Doğan ^{1,a,*}, İsmet Doğan ^{2,b}, Nurhan Doğan ^{2,c}

¹ Department of Biostatistics, Medical Faculty, Gaziantep University, Gaziantep, Türkiye.

² Department of Biostatistics, Medical Faculty, Afyonkarahisar Health Science University, Afyonkarahisar, Türkiye.

*Corresponding author

Research Article

History

Received: 18/07/2023

Accepted: 12/03/2024



This article is licensed under a Creative Commons Attribution-NonCommercial 4.0 International License (CC BY-NC 4.0)

ABSTRACT

There are many fit statistics used in the structural equation modeling, and new ones are consistently being developed. Because of the variety of fit statistics, it is very important to be able to decide which fit statistics are appropriate to use in studies. When comparing any two statistics, the asymptotic relative efficiency (ARE) between them is used. The ARE can use as a power of the fit indices is one of the familiar optimal criteria. It is frequently more convenient, and also more suggestive, to use a measure of relative merit called the relative efficiency. This study aimed to compare of fit indices using Fraser's asymptotic relative efficiency. The data sets were derived from the multivariate normal distribution using the mean vector and covariance matrix. It was determined that the most efficient fit indices in terms of asymptotic relative efficiency were Z-Test of Wilson & Hilferty (W&H), Root Mean Square Error of Approximation (RMSEA), and Chi-Square indices, respectively.

Keywords: Asymptotic relative efficiency, Structural equation model, Fit indices.

^a ilkay_dgn58@hotmail.com

^b <https://orcid.org/0000-0001-7552-6478>

^c nurhandogan@hotmail.com

^b <https://orcid.org/0000-0001-7224-6091>

^b ismet.dogan@afsu.edu.tr

^b <https://orcid.org/0000-0001-9251-3564>

Introduction

Forecasting is a collaborative effort across a wide range of disciplines, and as a result, the question of how forecasts can best be evaluated is of fundamental importance to much of the scientific community [1]. A good forecast is very important for scientific, economic and administrative purposes. Therefore, it is necessary to know whether the forecaster is skilled enough to predict the future. Due to the increasing dependence on forecasting in various disciplines, forecasting skill indices have been proposed. It is very important to clarify that forecasting skill is not the same as forecasting accuracy. A highly skilled forecaster generally tends to have a high rate of forecast accuracy, but the opposite may not be true [2].

Statisticians, when dealing with specific test problems, often try to take or improve the statistical tests that are most efficient in a certain sense. Therefore, since such tests are not usually available in finite sample cases, the main focus is on efficiency concepts that enable comparison of competing procedures through their specific asymptotic properties [3]. Making a verified selection of the most effective statistical test among the few tests at the statistician's disposal is considered one of Statistics' fundamental problems. This problem became particularly important in the mid-twentieth century when computationally simple but "inefficient" rank tests emerged. Asymptotic relative efficiency (ARE) is a concept that enables the quantitative comparison of two different tests (for example T_1 and T_2) used to test the same statistical hypothesis to be applied in large samples. The

concept of asymptotic efficiency of tests is more complex than the asymptotic efficiency of estimates [4]. The ARE of T_2 relative to T_1 is defined as;

$$ARE_{21} = \lim_{n \rightarrow \infty} \left(\frac{n_1}{n_2} \right) \quad (1)$$

where n_1 and n_2 are sample sizes such that T_1 and T_2 have the same power. The oldest known efficiency is the Pitman efficiency [5]. The most familiar and the classical efficiencies are concepts in this respect are Pitman efficiency, Chernoff efficiency, Hodges-Lehmann efficiency and Bahadur efficiency [5-8]. The four basic types of efficiency mentioned are not easy to calculate. Each type of efficiency statistic has its own advantages and disadvantages. Current studies on ARE mainly focus on two categories. First category, consists of method that compare the efficiency of estimators of the same parameter. The other consists of method that compare test statistics of the same hypothesis. Subsequent studies may assume that the test statistics are asymptotically normal. In the circumstances, the ARE's can be easily calculated. There are also some methods to compare ARE of different test statistics, where the same hypothesis may have different asymptotic distributions. These methods (Pitman efficiency, Hodges-Lehmann efficiency and Bahadur efficiency) suggested different ways to calculate ARE, and are difficult to calculate. Although test statistics have the same asymptotic distribution, ARE can be easily

calculated [9]. A simple statement for the relative efficiency under moderate assumptions has been obtained by Fraser [10]. Under the asymptotic normality assumption of the test statistic the efficacy is given by [10-12].

$$eff = \left(\frac{\mu}{\sigma}\right)^4 \quad (2)$$

Here μ and σ are the mean and standard deviation of the limiting normal distribution. Definition of the ARE of two statistics, T_1 with respect to T_2 is as follows [10, 11];

$$ARE(T_1, T_2) = \frac{eff(T_1)}{eff(T_2)} \quad (3)$$

The value of $ARE(T_1, T_2) > 1$ indicates that T_2 is efficient, $ARE(T_1, T_2) < 1$ indicates that T_1 is efficient. In structural equation modeling (SEM), the fit indices establish whether, overall, the model is acceptable. The model fit evaluating issue in SEM analysis has been at the main topic of theoretical and empirical research for years [13-17]. The simplest model that describes the data well enough and makes the best prediction is the best fit model. Therefore, one of the important goals of scientific theory should be to establish criteria that will enable determining models that produce accurate predictions [18]. Research in this area has focused on various aspects of model fit indices, such as which model fit indices should be used in which situations and how they should be interpreted. Most studies have examined the changing of fit indices under different data conditions, such as estimation methods, sample size, and model misspecification [19].

In this article, we focus our study to the asymptotic relative efficiency via Fraser [10] of the fit indices. We propose an analytic comparison of the some fit indices. To this aim, we introduce Fraser [10] asymptotic relative efficiency, and compare the fit indices' asymptotic relative efficiencies, in the Fraser asymptotic relative efficiency sense.

Material and Methods

Simulation Study

In the study, a model occurred from four latent variables was used. Also each latent variable were explained by four variables. The mean vector and covariance matrix created for this model were obtained from the study of Doğan and Özdamar [15]. The data sets were derived under the assumption of multivariate normal distribution. While the sample sizes were determined as 100, 150, 250, 500, 1000 and 5000 units and the replication number was determined as 1000. The maximum likelihood (ML) was used for parameter estimates. This study was conducted to compare the model fit measures by using Fraser efficiency with different sample sizes. For this purpose, Chi-Square, Goodness of Fit Index (GFI), Root Mean Square Residuals

(RMR), Standardized Root Mean Square Residuals (SRMR), Z-Test of Wilson & Hilferty (W&H), Comparative Fit Index (CFI), Normed Fit Index (NFI), Non-normed Fit Index (NNFI), Incremental Fit Index (IFI), Adjusted Goodness of Fit Index (AGFI), Akaike Information Criterion (AIC), Consistent Akaike Information Criterion (CAIC), Expected Cross Validation Index (ECVI), McDonald's Fit Index (MFI), Root Mean Square Error of Approximation (RMSEA), and Schwarz Bayesian Criterion (SBC) goodness of fit statistics were evaluated. The simulation study was performed in the SAS 9.3 program using the PROC IML and PROC WORK procedures.

There are two aspects to measuring model performance: discriminative capacity and reliability. However, it is generally stated that discrimination capacity is more important than reliability. Discriminative capacity measures a model's ability to distinguish between the presence and absence of the phenomenon in question. Reliability refers to the agreement between predicted values and observed values. Reliability is an important characteristic of the quality of probabilistic forecast models. When the modeling result is continuous, both aspects of model performance (discrimination capacity and reliability) can be evaluated. When the modeling result is binary, only discriminatory capacity can be evaluated. Various indices are used to assess discriminatory capacity and/or reliability. Some of these can only be applied to binary results or to continuous results converted to a binary solution using a specific cut-off value called a threshold. These indices are called threshold-dependent indices. Indices that can be directly applied to continuous cases are called threshold-independent indices [20]. The indices used in this study are non-threshold-dependent measures.

Data Generation

The steps of the simulation study were performed as suggested by Doğan and Özdamar [15] and Fan Xia and Fan Xia [21]. First of all, a 5000-unit data set was generated from the multivariate normal distribution by using the mean vector and covariance matrix of the specified model [15]. Secondly, the covariance matrix of the obtained data set in the first step was calculated to avoid the singular covariance matrix structure. Thirdly, another data set containing 5000 units is generated from the multivariate normal distribution with the help of the covariance matrix calculated in second step. Finally, parameter estimations of the model specified by Doğan and Özdamar [15] were performed with the help of the data set obtained in the third step. The fit statistics of the specified model and the correlation matrix (R) were examined. The correlation coefficients for the variables of each latent variable change $0.30 \leq r \leq 0.90$ intervals.

Results

The comparative summarized table of fit indices based on ARE is given in Table 1. As a result, it was determined that the most efficient fit indices in terms of asymptotic

relative efficiency were W&H, RMSEA, and Chi-Square indices, respectively. The results of the simulation study are same for all sample sizes (n=100, 150, 250, 500, 1000 and 5000). When all fit indices considered in the study are

sorted in terms of efficiency, W&H, RMSEA, Chi-Square, RMR, SRMR, AIC / MFI, ECVI, SBC, CAIC, ACFI, NNFI, IFI, NFI, CFI, and GFI are obtained.

Table 1. The comparisons of the fit indices

	GFI	RMR	SRMR	W&H	CFI	NFI	NNFI	IFI	AGFI	AIC	CAIC	ECVI	MFI	RMSEA	SBC	
Chi-Square	Chi-Square	Chi-Square	Chi-Square	W&H	Chi-Square	Chi-Square	Chi-Square	Chi-Square	Chi-Square	Chi-Square	Chi-Square	Chi-Square	Chi-Square	RMSEA	Chi-Square	
GFI	-	RMR	SRMR	W&H	CFI	NFI	NNFI	IFI	AGFI	AIC	CAIC	ECVI	MFI	RMSEA	SBC	
RMR		-	RMR	W&H	RMR	RMR	RMR	RMR	RMR	RMR	RMR	RMR	RMR	RMSEA	RMR	
SRMR			-	W&H	SRMR	SRMR	SRMR	SRMR	SRMR	SRMR	SRMR	SRMR	SRMR	RMSEA	SRMR	
W&H				-	W&H	W&H	W&H	W&H	W&H	W&H	W&H	W&H	W&H	W&H	W&H	
CFI					-	NFI	NNFI	IFI	AGFI	AIC	CAIC	ECVI	MFI	RMSEA	SBC	
NFI						-	NNFI	IFI	AGFI	AIC	CAIC	ECVI	MFI	RMSEA	SBC	
NNFI							-	NNFI	AGFI	AIC	CAIC	ECVI	MFI	RMSEA	SBC	
IFI								-	AGFI	AIC	CAIC	ECVI	MFI	RMSEA	SBC	
AGFI									-	AIC	CAIC	ECVI	MFI	RMSEA	SBC	
AIC										-	AIC	AIC	AIC/MFI	RMSEA	AIC	
CAIC											-	ECVI	CAIC/MFI	RMSEA	SBC	
ECVI												-	ECVI/MFI	RMSEA	ECVI	
MFI														-	SBC/MFI	
RMSEA															-	RMSEA

Chi-Square, Goodness of Fit Index (GFI), Root Mean Square Residuals (RMR), Standardized Root Mean Square Residuals (SRMR), Z-Test of Wilson & Hilferty (W&H), Comparative Fit Index (CFI), Normed Fit Index (NFI), Non-normed Fit Index (NNFI), Incremental Fit Index (IFI), Adjusted Goodness of Fit Index (AGFI), Akaike Information Criterion (AIC), Consistent Akaike Information Criterion (CAIC), Expected Cross Validation Index (ECVI), McDonald's Fit Index (MFI), Root Mean Square Error of Approximation (RMSEA) and Schwarz Bayesian Criterion (SBC)

Discussion and Conclusion

Structural equation modeling is a very powerful multivariate analysis technique that makes it possible to evaluate hidden structures, while asymptotic relative efficiency is an analysis and testing tool due to its unique properties compared to other techniques. After parameter estimation is made with the appropriate method for the specified model, the model needs to be tested. In testing the model, the compatibility of the data with the specified model is determined. In other words, an answer is sought to the question "to what extent is the theoretical (specified, proposed, and established) model compatible with the sample data" [22]. Compliance is called the ability of a model to reproduce the data, that is, the variance-covariance matrix [23]. There are many fit criteria to evaluate model fit in SEM. Most of these fit measures are based on comparing the covariance matrix of the theoretically proposed model with the sample covariance matrix. The fact that these two matrices are not similar to each other, that is, the difference between the matrices is large, indicates that the data does not fit

the theoretical model, and the fact that the difference between these two matrices is very small indicates that the data fits well with the theoretical model [22, 24, 25]. Evaluating model performance, that is, comparing the predictions produced by the model with observed values, is a fundamental step in model development and use. Once models are obtained, it is necessary to validate some aspects of them. This validation process usually involves a definition of criteria based on mathematical measurements that indicate how well the model's predictions are produced by simulating observed values [26]. The validity of the structural equation model is tested by calculating fit indices based on the collected data.

The results suggest that W&H is the best goodness of fit statistic for all specified assumptions. In the study, the multivariate normality assumption was taken into consideration and the fit indices were compared in terms of their asymptotic relative efficiency for the case where this assumption is valid. Although it is emphasized in the literature [15, 19, 25, 27] that the Chi-Square indices is affected by the sample size and should not be used, its effectiveness was better than the other indices after W&H and RMSEA fit indexes. In future studies, it is recommended to make comparisons for cases where this assumption is violated. Since the W&H fit indices is not calculated in some statistical packages, it is recommended to use the RMSEA fit indices in future studies. Doğan and Doğan [18] emphasize that model selection criteria should be considered as a model comparison or evaluation tool because the term selection includes the idea that something more certain is achieved. In addition, the criteria used in model selection should not be duplicated beyond necessity [18]. As a result, it is more important to decide which one gives better results rather than

duplicating model fit indices. This study shows that the RMSEA fit indices gives better results than others.

Conflicts of interest

There are no conflicts of interest in this work.

References

- [1] Wheatcroft E., Interpreting the skill score form of forecast performance metrics. *Int. J. Forecast.*, 35 (2) (2019) 573-579.
- [2] Sitthiyot T., Holasut K., On the evaluation of skill in binary forecast. *Thailand and The World Economy*, 40 (3) (2022) 33-54.
- [3] Baringhaus L., Gaigall D., On an asymptotic relative efficiency concept based on expected volumes of confidence regions, *Statistics*, 53 (6) (2019) 1396–1436.
- [4] Nikitin Y., Asymptotic Relative Efficiency in Testing, University of Saint-Petersburg, (2010).
- [5] Pitman E.J.G., Mimeographed Lecture Notes on Nonparametric Statistics, Columbia University, New York, (1948) 52-59.
- [6] Chernoff H.A., Measure of asymptotic efficiency for tests of a hypothesis based on the sum of observations, *Ann. Math. Stat.*, 23 (1952) 493–507.
- [7] Hodges J.L., Lehmann E.L., The efficiency of some nonparametric competitors of the t –test, *Ann. Math. Stat.*, 27 (1956) 324–335.
- [8] Bahadur R.R., Stochastic comparison of tests. *Ann. Math. Stat.*, 31 (1960) 276–295.
- [9] Yuan A., Fan R., Xu J., Xue Y., Li Q., Asymptotic relative efficiencies of the score and robust tests in genetic association studies, *The Open Statistics & Probability*, 9 (2018) 26-41.
- [10] Fraser D.A.S., Nonparametric Methods in Statistics, John Wiley & Sons Inc, (1957) 270-276.
- [11] Jammalamadaka S.R., Wells M.T., A test of goodness of fit based on extreme spacings with some efficiency comparisons, *Metrika*, 35 (1988) 223-232.
- [12] Puri M.L., Rao J.S., Yoon Y., A simple test for goodness of fit based on spacings with some efficiency comparisons (Report No.441). University of Wisconsin, (1976) 11-13.
- [13] Anderson J.C., Gerbing D.W., The effect of sampling error on convergence, improper solutions, and goodness-of-fit indices for maximum likelihood confirmatory factor analysis, *Psychometrika*, 49 (1984) 155–173.
- [14] Curran P.J., West, S.G., Finch J.F., The robustness of test statistics to non-normality and specification error in confirmatory factor analysis, *Psychol. Methods*, 1 (1) (1996) 16–29.
- [15] Doğan İ., Özdamar K., The effect of different data structures, sample sizes on model fit measures, *Commun. Stat-Simul. C.*, 46 (9) (2017) 7525-7533.
- [16] Doğan İ., Farklı veri yapısı ve örneklem büyüklüklerinde yapısal eşitlik modellerinin geçerliği ve güvenilirliğinin değerlendirilmesi, PhD Thesis, Eskişehir Osmangazi University, Institute of Health Sciences, (2015).
- [17] Fan X., Thompson B., Wang L., Effects of sample size, estimation methods and model specification on structural equation modeling fit indexes, *Struct. Equ. Modeling*, 6 (1) (1999) 56–83.
- [18] Doğan İ., Doğan, N., Model Performans Kriterlerinin Kronolojisine ve Metodolojik Yönlerine Genel Bir Bakış: Bir Gözden Geçirme, *Türkiye Klinikleri J. Biostat.*, 12 (1) (2020) 114-125.
- [19] Fan X., Sivo S.A., Sensitivity of fit indices to model misspecification and model types, *Multivar. Behav. Res.*, 42 (3) (2007) 509–529.
- [20] Liu C., White M., Newell G., Measuring and comparing the accuracy of species distribution models with presence-absence data. *Ecography*, 34 (2) (2011) 232-243.
- [21] Fan X., Fan X., TEACHER'S CORNER: Using SAS for Monte Carlo Simulation Research in SEM, *Struct. Equ. Modeling*, 12 (2) (2005) 299-333.
- [22] Schumacker R.E., Lomax R.G., A beginner's guide to structural equation modeling (2nd ed.). Mahlah, New Jersey,London: Lawrence Erlbaum Associates. (2004) 79-84.
- [23] Erkorkmaz Ü., Etikan İ., Demir O., Özdamar K., Sanisoğlu S.Y., Doğrulayıcı faktör analizi ve uyum indeksleri, *Türk. Klin. J. Med. Sci.*, 33(1) (2013) 210-223.
- [24] Bollen, K.A. Structural equations with latent variables, New York: John Wiley & Sons, Inc., (1989) 256-289.
- [25] Kline B.R., Principles and practice of structural modeling. New York-London: The Guilford Press, (2011) 189-230.
- [26] Pereira H.R., Meschiatti M.C., Pires R.C.M., Blain G.C., On the performance of three indices of agreement: an easy-to-use r-code for calculating the Willmott indices, *Bragantia*, 77(2) (2018) 394-403.
- [27] Weng L.J., Cheng C.P., Why might relative fit indices differ between estimators?, *Struct. Equ. Modeling*, 4 (2) (1997) 121-128.

Functional Analysis of Variance: An Application to Stock Exchange

Selin Öğütçü ^{1,a,*}, Nuri Çelik ^{1,b}

¹ Department of Mathematics, Faculty of Science, Gebze Technical University, Kocaeli, Türkiye.

*Corresponding author

Research Article

History

Received: 05/10/2023

Accepted: 05/02/2024




This article is licensed under a Creative Commons Attribution-NonCommercial 4.0 International License (CC BY-NC 4.0)

ABSTRACT


The concept of "functional data" allows for the representation of data collected repeatedly over a period of time as a continuous function within a specific range on the time axis, rather than as discrete measurement points. Traditional statistical analysis has been adapted to accommodate functional data. This paper discusses the adaptation of one-way analysis of variance for functional data, covering parameter estimations and obtaining test statistics. As a numerical example, stock exchange values from various countries across different continents are used. The aim is to discern potential differences among countries based on these stock exchange values during the Covid-19 pandemic, utilizing one-way analysis of variance for functional data.

Keywords: Functional data, One-way ANOVA, Covid.

 selinogutcu8@gmail.com

 <https://orcid.org/0000-0003-4568-9254>

 nuricelik@gtu.edu.tr

 0000-0002-4234-2389

Introduction

Functional data analysis (FDA) is a statistical technique employed to infer the features of an underlying function from data collected at multiple time points within the same observation. It facilitates statistical analysis and enables the comparison of entire functions with one another. Furthermore, FDA allows for parameter estimation during the analysis phase, noise reduction through curve smoothing, and the utilization of data collected at different times. The emergence of new technology over the years has underscored the necessity for FDA, which enables the modeling of data collected at various times, eliminating the need for evaluating observations simultaneously, as required in classical repeated measurement analyses.

When data is continuously gathered over a duration and represented as a continuous function on a specific interval on the time axis, rather than as discrete points, it is referred to as "Functional Data." The core concept of functional data analysis is to identify and assess statistical modeling or estimation techniques suitable for these functions. With the aid of advancing technology, computer programs have simplified the execution of this approach, leading to its increased popularity among researchers for analyzing repeated measurements. While several methods for longitudinal data analysis (LDA) exist in the literature for this type of data, functional data analysis holds an advantage over other methods due to its versatility, making it a preferred choice for analyzing repeated measurements.

Although Ramsay [1] and Ramsay & Dalzell [2] coined the term "functional data analysis," the roots of this discipline can be traced back to the works of Grenander [3] and Rao [4], which have a long history [5]. Going even

further back, the evolution of this technique, with broad applications across various fields, can be dated to the 1800s. During this time, Gauss and the French mathematician Legendre endeavored to model and forecast the trajectory of a comet, which follows a curve [6].

Functional ANOVA (Analysis of Variance) is a statistical method employed to assess whether significant differences exist between the mean functions of two or more groups in a functional data set. It serves as an extension of the traditional ANOVA method, typically applied to non-functional data sets. In functional ANOVA, each observation in the data set is a function rather than a scalar value. The method decomposes the total variation in the data into various sources, including between-group and within-group variations. Additionally, the method can test the significance of interactions between different factors, such as time and group membership, on the variation in functional data. With applications in economics, biology, and engineering, Functional ANOVA proves to be a versatile tool in numerous fields.

Functional ANOVA is among the most preferred analysis methods, akin to traditional statistics. It is employed to scrutinize the variation in a set of functional data across various groups or conditions. This statistical approach proves particularly advantageous when data is collected over time and represented as a continuous function within a specific interval on the time axis. The primary objective of functional ANOVA is to identify and assess the sources of variability in the data, determining whether significant differences exist between groups or conditions.

This paper provides a detailed explanation of functional ANOVA, including the calculation of test statistics using the pointwise testing method. The choice of the pointwise testing method is based on its resemblance to traditional statistics and ease of calculation. In the application section, the objective is to investigate the impact on stock markets in different regions worldwide during the Covid-19 pandemic and to determine whether statistically significant differences exist among them. For detailed information, refer to [7].

Functional Analysis of Variance

The problem of one-way ANOVA for functional data can be defined as follows:

Consider k independent samples denoted by $y_{i1}(t), \dots, y_{in_i}(t), i = 1, \dots, k$ (1)

Certain k samples meet the criteria of $y_{ij}(t) = \eta_i(t) + v_{ij}(t), v_{ij}(t) \overset{i.i.d.}{\sim} SP(0, \gamma), j = 1, 2, \dots, n_i; i = 1, 2, \dots, k,$ (2)

where $\eta_1(t), \eta_2(t), \dots, \eta_k(t)$ represent the mean functions of the unidentified groups for the k samples, $v_{ij}(t)$, where $j = 1, 2, \dots, n_i; i = 1, 2, \dots, k$ denote the subject-effect functions, and $\gamma(s, t)$ denotes the shared covariance function for different times for s and t and SP can be described as a stochastic process. Our objective is to perform a one-way ANOVA test on the testing problem of

$$H_0 : \eta_1(t) \equiv \eta_2(t) \equiv \dots \equiv \eta_k(t), \quad t \in \mathcal{T}, \quad (3)$$

where \mathcal{T} is a time period of interest specified as $[a, b]$ with $-\infty < a < b < \infty$, as is often the case. The one-way ANOVA problem mentioned above is recognized as the k -sample problem for functional data, which expands on the two-sample problem for functional data presented in the preceding section.

Frequently, the objective of the one-way ANOVA testing problem (3) is to verify whether the effect of a treatment or factor is statistically significant. This treatment or factor is commonly utilized to divide the individual functions into various groups, categories, or samples. If the treatment or factor has a significant impact on the functional data, then the one-way ANOVA problem (3) will demonstrate statistical significance.

Define $\eta_i(t)$ as $\eta(t)$ added to $\alpha_i(t)$ ($\eta_i(t) = \eta(t) + \alpha_i(t)$) for all values of i ranging from 1 to k ($i = 1, 2, \dots, k$), where $\eta(t)$ represents the mean function across all k samples, and $\alpha_i(t)$ denotes the main-effect function for each value of i . Subsequently, we can express the model (2) as a standard one-way ANOVA model for functional data by representing it as

$$y_{ij}(t) = \eta(t) + \alpha_i(t) + v_{ij}(t), j = 1, 2, \dots, n_i; i = 1, 2, \dots, k. \quad (4)$$

By using this formulation, we can represent the null hypothesis (3) in an equivalent manner as a

$$\alpha_1(t) \equiv \alpha_2(t) \equiv \dots \equiv \alpha_k(t) \equiv 0, t \in \mathcal{T} \quad (5)$$

In other words, the goal is to assess whether the main-effect functions are identical and have a value of zero. Using the k samples (1), we can obtain unbiased estimates for the group mean functions $\eta_i(t)$, where i ranges from 1 to k ($i = 1, 2, \dots, k$), as well as the shared covariance function $\gamma(s, t)$, which can be represented as

$$\hat{\eta}_i(t) = \bar{y}_i(t) = n_i^{-1} \sum_{j=1}^{n_i} y_{ij}(t), i = 1, 2, \dots, k, j = 1, 2, \dots, n_i \quad (6)$$

$$\hat{\gamma}(s, t) = (n - k)^{-1} \sum_{i=1}^k \sum_{j=1}^{n_i} [y_{ij}(s) - \bar{y}_i(s)][y_{ij}(t) - \bar{y}_i(t)]$$

It is worth noting that, in this section, $n = \sum_{i=1}^k n_i$ refers to the total sample size. The approximated covariance function $\hat{\gamma}(s, t)$ is commonly known as the pooled sample covariance function. Keep in mind that $\hat{\eta}_i(t)$, where i takes values from 1 to k ($i = 1, 2, \dots, k$), are independent, and

$$E\hat{\eta}_i(t) = \eta_i(t), \quad cov[\hat{\eta}_i(s), \hat{\eta}_i(t)] = \frac{\hat{\gamma}(s, t)}{n_i}, \quad i = 1, 2, \dots, k, \quad (7)$$

Set $\hat{\eta}(t) = [\hat{\eta}_1(t), \hat{\eta}_2(t), \dots, \hat{\eta}_k(t)]^T$.

This estimator of $\eta(t)$ is impartial. As a result, we obtain $E\hat{\eta}(t) = \eta(t)$ and $Cov[\hat{\eta}(s), \hat{\eta}(t)] = \gamma(s, t)D$, where D is a diagonal matrix with diagonal entries $1/n_i, i = 1, 2, \dots, k$, and $D = diag(1/n_1, 1/n_2, \dots, 1/n_k)$. This implies that the stochastic process $\hat{\eta}(t)$ follows the $SP_k(\eta, \gamma D)$ distribution, where $SP_k(\eta, \Gamma)$ represents a k -dimensional stochastic process with the vector of mean functions $\eta(t)$ and the matrix of covariance functions $\Gamma(s, t)$.

In order to examine techniques for carrying out main-effect, post hoc, it is necessary to explore the characteristics of $\hat{\eta}(t)$ and $\hat{\gamma}(s, t)$ in different scenarios. In pursuit of this objective, we outline the ensuing assumptions:

- i. The k samples (1) are with $\eta_1(t), \eta_2(t), \dots, \eta_k(t) \in \mathcal{L}^2(\mathcal{T})$ and $tr(\gamma) < \infty$.
- ii. The k samples (1) are normal distribution.
- iii. As $n \rightarrow \infty$, the k sample sizes satisfy $n_i/n \rightarrow \tau_i, i = 1, 2, \dots, k$ such that $\tau_1, \tau_2, \dots, \tau_k \in (0, 1)$.
- iv. The subject-effect functions $v_{ij}(t) = y_{ij}(t) - \eta_i(t), j = 1, 2, \dots, n_i; i = 1, 2, \dots, k$ are identically and independently distributed.
- v. The subject-effect function $v_{11}(t)$ satisfies $E \| v_{11} \|^4 < \infty$.
- vi. The maximum variance $\rho = \max_{t \in \mathcal{T}} \gamma(t, t) < \infty$.

vii. The expectation $E[v_{11}^2(s)v_{11}^2(t)]$ is uniformly bounded.

Theorem 2.1

Under above assumptions (i) and (ii), we have

$$D^{-\frac{1}{2}}[\hat{\eta}(t) - \eta(t)] \sim NP_k(0, \gamma I_k), \quad \text{and} \quad (8)$$

$$(n - k)\hat{\gamma}(s, t) \sim WP(n - k, \gamma).$$

The k -dimensional normality process (NP) of $\hat{\eta}(t)$ and the Wishart process (WP) of $(n - k)\hat{\gamma}(s, t)$ are both demonstrated by Theorem 2.1 assuming the normality assumption (ii). It is evident that Theorem 2.1 is fundamental in creating various tests for (3) if the k samples (1) are normal distribution. It's worth noting that even if the sample sizes $\eta_1, \eta_2, \dots, \eta_k$ are finite, Theorem 2.1 remains valid under the normality assumption (ii).

When conducting main-effect, post hoc, there's no requirement to identify the main-effect functions $\alpha_i(t)$, where $i = 1, 2, \dots, k$, as stated in equation (4). In reality, these functions are not identifiable unless certain restrictions are enforced. Suppose we do aim to estimate these main-effect functions; in that case, the most widely employed constraint to ensure their identifiability is

$$\sum_{i=1}^k n_i \alpha_i(t) = 0, \quad (9)$$

which relates to the k sample sizes. Within this constraint, it's straightforward to demonstrate that

$$\hat{\alpha}_i(t) = \bar{y}_i(t) - \bar{y}_..(t), \quad i = 1, 2, \dots, k, \quad (10)$$

provides unbiased estimators of the main-effect functions, where

$$\bar{y}_..(t) = n^{-1} \sum_{i=1}^k \sum_{j=1}^{n_i} y_{ij}(t) = n^{-1} \sum_{i=1}^k n_i \bar{y}_i(t) \quad (11)$$

is the typical sample grand mean function. With constraint (12) enforced, the sample mean function $\bar{y}_..(t)$ becomes an unbiased estimator of the grand mean function $\eta(t)$ defined in equation (4).

$$SSH_n(t) = \sum_{i=1}^k n_i [\bar{y}_i(t) - \bar{y}_..(t)]^2, \text{ and}$$

$$SSE_n(t) = \sum_{i=1}^k \sum_{j=1}^{n_i} [y_{ij}(t) - \bar{y}_i(t)]^2, \quad (12)$$

refer to the pointwise between-subject and within-subject variations, respectively. $\bar{y}_i(t)$, where $i = 1, 2, \dots, k$ as defined in equation (6), and the sample grand mean function $\bar{y}_..(t)$ as defined in equation (11). When constraint (12) is in place, it's clear that

$$SSH_n(t) = \sum_{i=1}^k n_i \hat{\alpha}_i^2(t), \quad (13)$$

where the estimated main-effect functions $\hat{\alpha}_i(t)$, $i = 1, 2, \dots, k$ are given by equation (13), is easy to determine. We observe that when the null hypothesis (3) is true, $SSH_n(t)$ should be minimal, and when it is not valid, it should be substantial. It can be seen from (6) that

$$SSE_n(t) = (n - k)\hat{\gamma}(t, t). \quad (14)$$

The pointwise F -test, pointwise χ^2 -test, and pointwise bootstrap test are all under consideration. Ramsay and Silverman (2005) introduced the pointwise F -test for (3) to extend the classical F -test into the domain of functional data analysis. At each $t \in \mathcal{T}$, the pointwise F -test is implemented for (3) using the pointwise F statistic:

$$F_n(t) = \frac{SSH_n(t)/(k-1)}{SSE_n(t)/(n-k)} \quad (15)$$

It is readily apparent from the classical linear model theory that, assuming the null hypothesis (3),

$$F_n(t) \sim F_{k-1, n-k}, \quad t \in \mathcal{T} \quad (16)$$

is obtained when the k samples (1) are normal distribution.

Application to Stock Exchange

The news of the pandemic caused world stock markets to open with record declines, indicating that the impact of heightened volatility and negative perceptions towards the stock market may exceed expectations. Additionally, the economic repercussions of the coronavirus epidemic have also extended to the stock markets of affected nations. Presently, it is evident that the economic effects of the epidemic are multi-faceted [8]. The apprehension caused by the coronavirus outbreak rapidly spread to global financial markets. The Covid-19 aftermath, which was initially disregarded, has become a significant concern as it continues to spread swiftly beyond China [9].

COVID-19's appearance and subsequent proliferation to over 150 countries within two months have led to the cessation of commercial and economic operations, prompting concerns that it is not solely a health crisis but also harbors the potential for significant and far-reaching consequences for the global economy in the future [10]. The response of the stock markets has elicited significant apprehension, given that the world is presently grappling with the most severe economic downturn since the Great Depression [11]. Furthermore, Ashraf's study [12] discovered a correlation between the number of COVID-19 cases reported in a country and a corresponding decrease in stock market returns. Behavioral finance suggests that the rise in COVID-19 cases may have a substantial impact on global equity markets, making it challenging for individual investors to make informed investment decisions.

The main purpose of this application is to investigate how the stock market movements in different parts of the world move in the Covid-19 pandemic process, how they are affected and whether there is a statistically significant difference between them. For this reason, stock market opening data from various countries between 01/03/2020 – 01/03/2022 were taken from <https://tr.investing.com/indices/world-indices>.

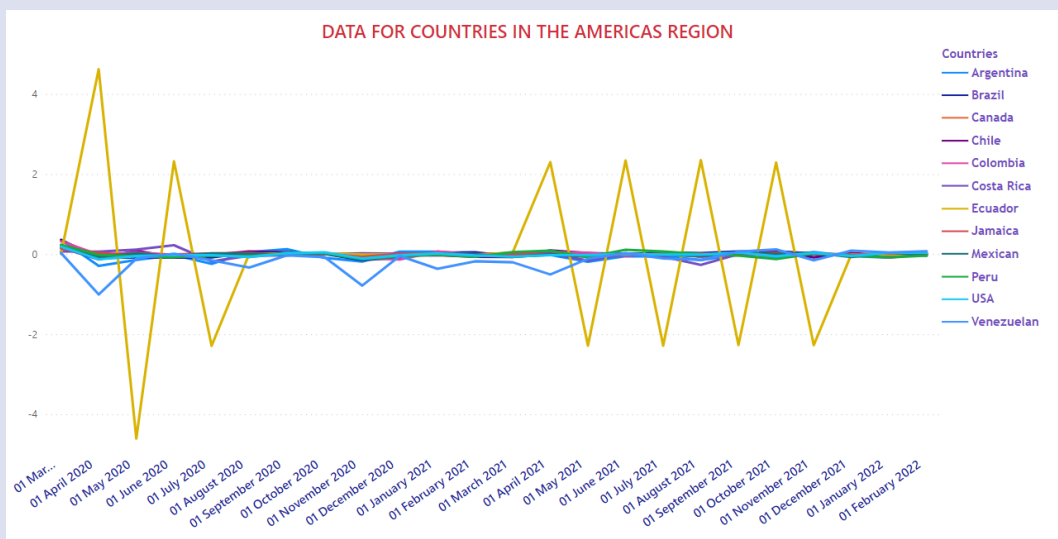


Figure 1. Data for countries in the Americas region.

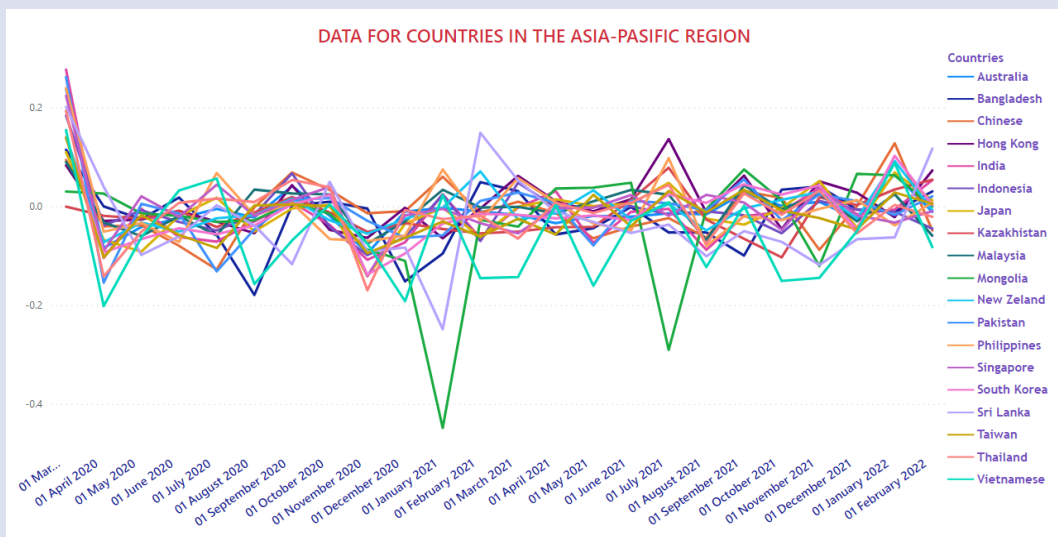


Figure 2. Data for countries in the Asia-Pacific region.

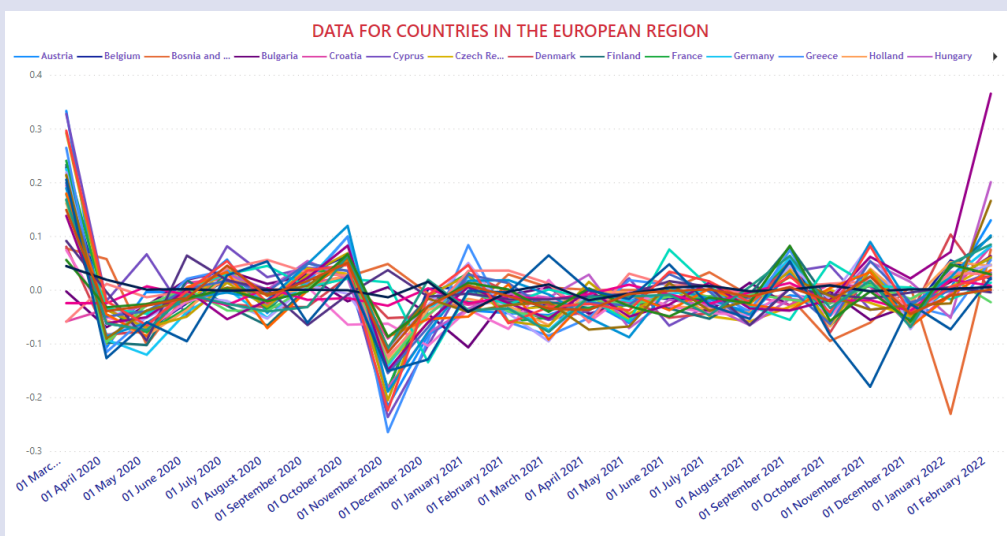


Figure 3. Data for countries in the European region.

By dividing the world geography into three as America, Asia-Pacific and Europe, 12 countries such as Argentina, Brazil, Ecuador, Colombia, Peru, Chile, Venezuela, USA, Canada, Mexico, Jamaica, Costa Rica were taken from the Americas region. In the Asia-Pacific region, 19 countries were included in Australia, Bangladesh, China, Indonesia, Philippines, South Korea, India, Hong Kong, Japan, Kazakhstan, Malaysia, Mongolia, Pakistan, Singapore, Sri Lanka, Thailand, Taiwan, Vietnam, New Zealand. Similarly, a total of 33 countries including Germany, Austria, Belgium, the United Kingdom, Bosnia and Herzegovina, Bulgaria, the Czech Republic, Denmark, Finland, France, Croatia, the Netherlands, Ireland, Spain, Sweden, Switzerland, Italy, Iceland, Montenegro, Cyprus, Hungary, Malta, Norway, Poland, Portugal, Romania, Russia, Serbia, Slovakia, Slovenia, Turkey, Ukraine, and Greece are included from the European region. The African region has

not been taken into account due to its already underdeveloped status and its economic situation not matching that of the other three regions.

Between 01/03/2020 – 01/03/2022, the data were prepared by applying the $\log(P_t/P_{t-1})$ transformation in order to smooth the stock market opening data in different regions and different countries. Figure 1, Figure 2 And Figure 3 show graphs of the transformed data in all three regions.

Before moving on to functional ANOVA, data were tested for normality. The results according to the Shapiro-Wilk test of normality, test statistic is 0.944 and p-value is 0.197 and it has been determined that each data set is normally distributed. ($p - value > 0.05$)

For the functional analysis of variance, firstly the average functions of all three regions were calculated. Figure 4 shows the mean functions.

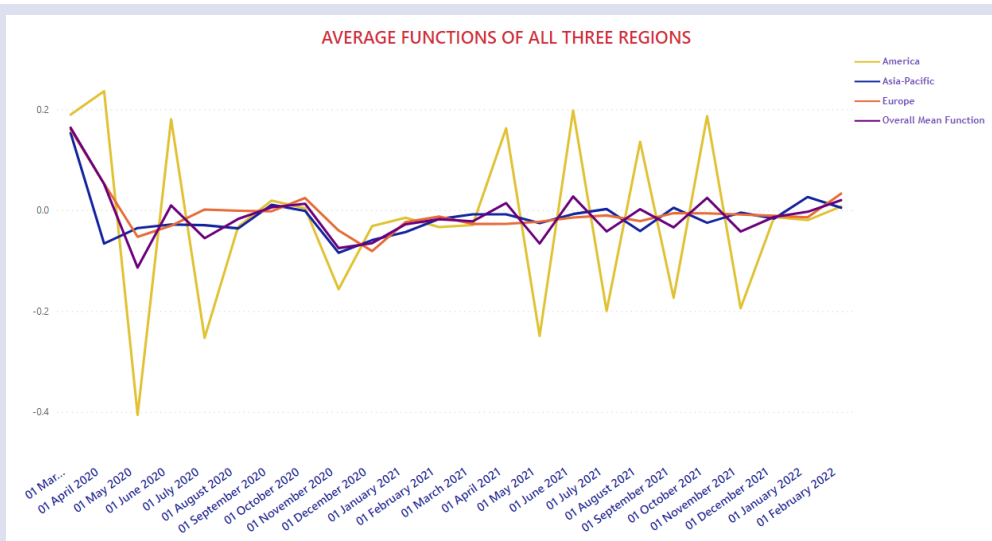


Figure 4. Average functions of all three regions.

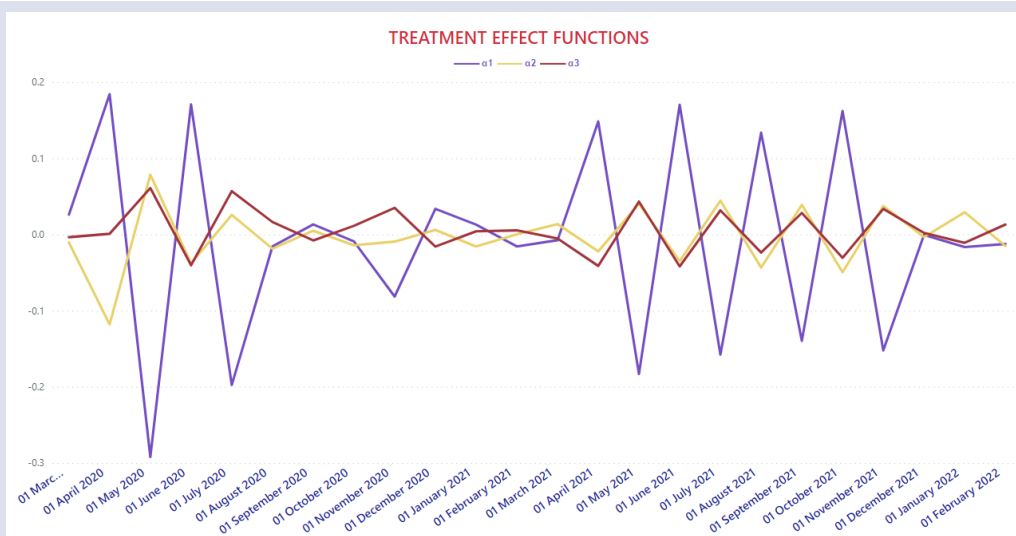


Figure 5. Treatment effects.

Three treatment effect functions were obtained by using these mean functions. Figure 5 shows the treatment effects mentioned.

Finally, using the $SSH_n(t)$ and $SSE_n(t)$ values, the test statistics ($F_n(t)$ values) were calculated as in Figure 6.

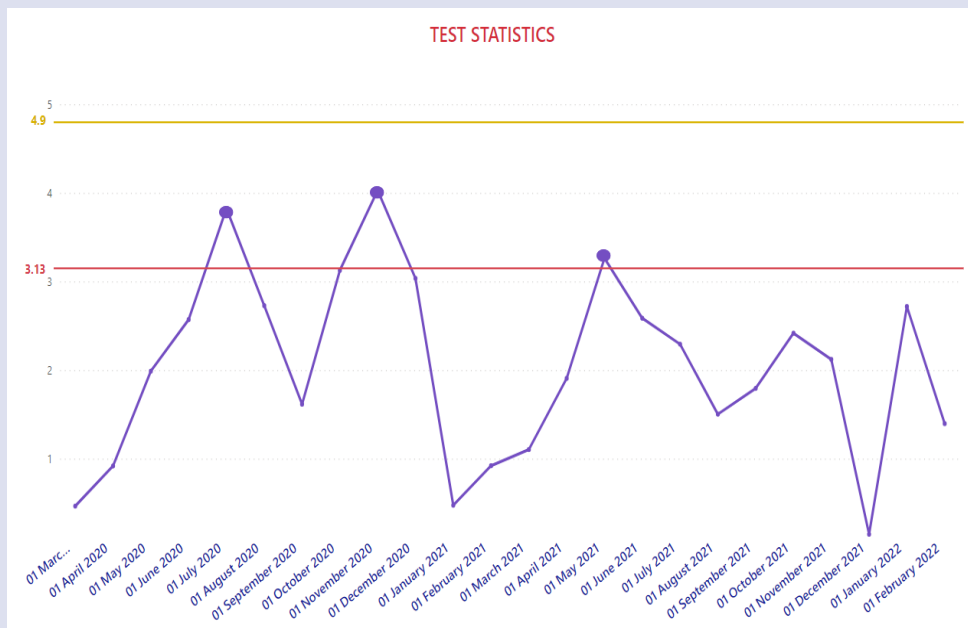


Figure 6. Test statistics ($F_n(t)$ values).

After the critical table value was determined as $F_{2,61} = 3.13$ for $\alpha = 0.05$ and $F_{2,61} = 4.9$ for $\alpha = 0.01$, the analysis result was started.

For $\alpha = 0.01$, stock market data during the Covid-19 process do not differ between continents.

For $\alpha = 0.05$, although we observe that it exceeds $F_{2,61} = 3.13$ on 3 separate dates, 01/07/2020 , 01/11/2020 and 01/05/2021, in the Covid-19 process, stock market data does not generally differ between continents.

According to the Pointwise test, for alpha = 0.05, Table 1 was prepared in order to determine from which regions the difference originated on the said dates, and it was determined that the difference originated from the Americas region. ($p - value < 0.05$)

Table 1. The p-values of the t-tests.

	July/2020	November/2020	May/2021
	America		
Asia-Pacific	0.009	0.014	0.011
Europe	0.002	0.008	0.012

Conclusion

Functional analysis of variance (ANOVA) is a statistical technique used in functional data analysis to investigate the variability in a set of functional data across different groups or conditions. This approach is particularly useful when the data is collected over time and expressed as a continuous function along a specific interval on the time axis. The goal of functional ANOVA is to identify and evaluate the sources of variability in the data and to determine whether there are significant differences between groups or conditions. This method involves decomposing the functional data into a sum of orthogonal

basis functions and then testing the differences between groups or conditions based on the coefficients of these basis functions. Functional ANOVA is a powerful tool for analyzing functional data and can provide valuable insights into the underlying patterns and trends in the data.

In the application part of the paper, it was investigated how the stock market movements in different parts of the world moved during the Covid-19 pandemic process, how they were affected and whether there was a statistically significant difference between them. Adhering to this purpose, stock market opening data recorded by <https://tr.investing.com/indices/world-indices> from various countries between 01/03/2020 and 01/03/2022 were used. By dividing the world geography into three as America, Asia-Pacific and Europe, 12 countries were taken from the Americas region and from the Asia -Pacific region 19 countries and a total of 33 countries from the European region. In addition, the reason for excluding the African region is that it is already considered underdeveloped and its economic situation does not align with the other three regions.

After the necessary statistical analyzes and examinations were completed, the analysis was concluded. For $\alpha = 0.05$, it was observed that there was a significant difference on 3 different dates, 01/07/2020, 01/11/2020 and 01/05/2021, and according to the Pointwise test, it was determined that the difference originated from the Americas region. However, since 3 months is very short for 2 years of data, we conclude that it was concluded that the stock market data in the Covid-19 process did not differ between continents.

Conflicts of interest

There are no conflicts of interest in this work.

References

- [1] Ramsay J., When the data are functions, *Psychometrika*, 47 (4) (1982) 379-396.
- [2] Ramsay J., Dalzell C., Some tools for functional data analysis, *Journal of the Royal Statistical Society, Series B (Statistical Methodology)*, (1991) 539-572.
- [3] Grenander U., Stochastic processes and statistical inference, *Ark. Mat.*, 1 (3) (1950) 195-277.
- [4] Rao C.R., Some statistical methods for comparison of growth curves, *Biometrics*, 14 (1) (1958) 1-17.
- [5] Wang S., Sobel A., Fridlind A., Feng Z., Comstock J.M., Minnis P., and Nordeen M., Simulations of cloud-radiation interaction using large-scale forcing derived from the CINDY/DYNAMO northern sounding array, *J. Adv. Model. Earth Syst.*, 7 (3) (2015) 1472-1498.
- [6] Yaraee K., Functional Data Analysis with Application to MS and Cervical Vertebrae Data, Master thesis, University of Alberta, 2011.
- [7] Ogutcu S., Functional Data Analysis and An Application to Analysis of Variance, Mater thesis, Gebze Technical University, 2023.
- [8] Demirdöğen O., Yorulmaz R., Kovid-19 Salgınının Dünya Ekonomilerine Etkileri, Ortadoğu Araştırmaları Merkezi, Ankara, (2020).
- [9] Albulescu C., Coronavirus and Financial Volatility: 40 Days of Fasting and Fear, *Quantitative Finance*, (2020).
- [10] Khan S., Siddique R., Li H., Ali A., Shereen M.A., Bashir N., Xue M., Impact of coronavirus outbreak on psychological health, *J Glob Health*, 10 (2020) 1-16.
- [11] IMF Blog, The Great Lockdown: Worst Economic Downturn Since the Great Depression, NOS. Available at: <https://www.imf.org/en/Blogs/Articles/2020/04/14/blog-weo-the-great-lockdown-worst-economic-downturn-since-the-great-depression>. Retrieved March 14, 2023.
- [12] Ashraf B.N., Stock Markets Reaction To Covid-19: Cases Or Fatalities?, *Research in International Business and Finance*, (2020).

Row and Column Effects Modelling of Elderly Age Groups and Chronic Health Problem on COVID-19

Gökçen Altun ^{1,a,*}, Serpil Aktaş Altunay ^{2,b}

¹ Department of Econometrics, Ankara Hacı Bayram Veli University 06500, Ankara, Türkiye.

² Department of Statistics, Hacettepe University, 06800, Beytepe, Ankara, Türkiye.

*Corresponding author

Research Article

History

Received: 10/07/2023

Accepted: 27/02/2024



This article is licensed under a Creative Commons Attribution-NonCommercial 4.0 International License (CC BY-NC 4.0)

ABSTRACT

Statistical analysis of COVID-19 data from China and NYC, using log-linear models, helps identifying high-risk groups like those aged over 65 and individuals with chronic health issues. According to the results of row effects model applied to the COVID-19 data set of China, we conclude that when the age group increases by one unit, the risk of getting COVID-19 disease is approximately 8 times higher for the patients having Chronic Obstructive Pulmonary Disease (COPD) than patients having hypertension, 9.37 times higher than patients with coronary heart disease, 13.37 times higher than patients having diabetes and cerebrovascular diseases and 10.16 times higher than patients having other diseases. According to the results of column effects model applied to the COVID-19 data set of NYC, we conclude that when the age group increases by one unit, the risk of death from the COVID-19 disease is approximately 2 times higher for the patients having chronic health problem than the patients not having a chronic health problem. We believe that the empirical findings of the presented study will guide the policymakers to make provision for these disadvantageous groups for COVID-19 disease.

Keywords: Categorical data analysis, Row effects model, Column effects model, COVID-19 data.

gokcenefendioglu@gmail.com

<https://orcid.org/0000-0003-4311-6508>

bspxl@hacettepe.edu.tr

<https://orcid.org/0000-0003-3364-6388>

Introduction

In December 2019, pneumonia caused by the newly identified SARS-CoV-2 factor was identified as coronavirus disease 2019 (COVID-19) in the pneumonia epidemic, which is the center of Wuhan city of China and a large number of people became infected (WHO Report, 2020; CDC (Center for Disease Control) Report, 2020). COVID-19 is caused by a new type of coronavirus which was previously named 2019-nCoV by the World Health Organization (WHO). The transmission characteristics of COVID-19 appear to be similar to those of pandemic influenza. Transmission to human to human have been conformed and structural analysis suggests that SARS-CoV-2 might be able to bind to the angiotensin-converting enzyme 2 receptor in humans [1]. Incubation period was reported between 1 and 19 days [2].

The virus can spread from human to human through respiratory droplets and close contacts [2]. Many clinical studies of hospitalized patients have shown that at onset on COVID-19, patients frequently show symptoms such as fever, cough, sore throat, fatigue, shortness of breath, diarrhea and myalgia [3-6]. The incubation period of COVID-19 could be up to two weeks or longer [7].

COVID-19 morbidity and mortality rates differ from country to country and COVID-19 has been causing a potentially fatal disease as a global public health problem. It is stated that COVID-19 progresses severely in the elderly and comorbid. However, the disease severity was found to be higher in patients under the age of sixty and

without chronic disease compared to influenza pneumonia. Liu et.al [8] found that elderly patients with COVID-19 are more likely to progress to severe disease. Likassa [9] also showed that age variation has a statistical significant associated with COVID-19.

According to CDC, those at high-risk for severe illness from COVID-19 are defined as: 65 years and older age groups; people who live in a nursing home or long-term care facility ; People of all ages with some underlying medical conditions; people with chronic lung disease or moderate to severe asthma, chronic heart disease, diabetes, liver disease; people who are immunocompromised; people with severe obesity; people with chronic kidney disease undergoing dialysis [10].

Sasson [11] investigated the relationship between age and COVID-19-related deaths in conjunction with other causes of mortality. The results obtained from the study, which utilized data from the United States, were employed for the estimation of death counts by age.

In the study by Ahrenfeldt et al. [12] the differences in COVID-19-related survival between genders across age groups and regions in Europe were investigated. According to the study, it was observed that the risk of mortality from COVID-19 was higher for men compared to women in almost all regions and age groups.

COVID-19 is ordinarily diagnosed based on positive SARS-CoV-2 nucleic acid test from respiratory tract specimen or based on clinical diagnosis.

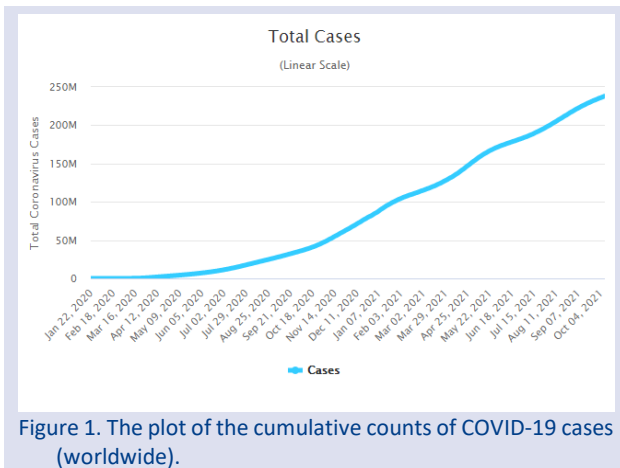


Figure 1. The plot of the cumulative counts of COVID-19 cases (worldwide).

Figure 1 displays the cumulative cases of COVID-19 for all countries as of 4th of October, 2021. This figure shows that there is linear trend in increment of the cases of COVID-19. It is clear that the effects of the pandemic cannot be understood deeply without data and its statistical modeling. This paper consists of two aims: the first is to introduce log-linear models such as row and column effects models which are very powerful to extract the relation between row and column variables. The second aim is to make new inferences using some up-to-date COVID-19 data from the literature. This article addresses the impacts of medical history, age, and underlying diseases on two COVID-19 data set.

The two way cross-classified COVID-19 data are analyzed in the context of ordinal information. First, the row effects model is applied to number of older patients infected positive COVID-19 test according to age and their medical history data set. We secondly analyze the number of deaths patients with positive COVID-19 test according to age and chronic disease status contingency table using the column effects model.

Methods

Row and Column Effects Models

Log-linear models for contingency tables treat all variables as nominal variables. But this situation, meaning that ordinal variables are considered as if they are nominal, yields misleading results. Because treating ordinal variables as nominal variables ignores the ordering information of the ordinal variables. In a $R \times C$ contingency table, consider both the row and column variables are ordinal, linear by linear association and uniform association models in the literature utilize the ordering information of the variables by row and column scores [13,14]. Goodman [15] first proposed the association models and illustrated how the models are applied cross-classification tables.

Row effects models

For the $R \times C$ cross-classification table, let n_{ij} denote the observed frequency in the i th row and j th column of the table ($i = 1, 2, \dots, R; j = 1, 2, \dots, C$), and let E_{ij} denote the corresponding expected frequency under the model,

$$\log(E_{ij}) = u + u_{1(i)} + u_{2(j)} + \mu_i y_j \tag{1}$$

This model is referred to as the Row Effects (RE) model with the following constraints,

$$\sum_{i=1}^R u_{1(i)} = \sum_{j=1}^C u_{2(j)} = \sum_{i=1}^R \mu_i = 0 .$$

The $\{\mu_i\}$ are called as the row effects parameters and the $\{y_j\}$ are the fixed column scores,

The independence model is the special case when $\mu_1 = \mu_2 = \dots = \mu_R$. For analyzing the row effects model, the column scores are assigned to the categories of the column variable as, $y_1 < \dots < y_R$.

The degrees of freedom (df) for testing the goodness of fit test has more $(R - 1)$ than the independence model,

$$df = RC - [1 + (R - 1) + (C - 1) + (R - 1)] = (R - 1)(C - 2) .$$

The general log-odds ratio models are defined as:

$$\ln\theta_{11} = \ln \frac{E_{ij}E_{i+1,j+1}}{E_{i,j+1}E_{i+1,j}} = (\mu_{i+1} - \mu_i)(y_{j+1} - y_j)$$

For instance, for the case $i = 1, j = 1$, the log-odds ratio is

$$\begin{aligned} \ln\theta_{11} &= \ln \frac{E_{11}E_{22}}{E_{21}E_{12}} = \ln E_{11} + \ln E_{22} - \ln E_{12} - \ln E_{21} \\ &= \mu_1 y_1 + \mu_2 y_2 - \mu_1 y_2 - \mu_2 y_1 \\ &= \mu_1(y_1 - y_2) - \mu_2(y_1 - y_2) \\ &= (\mu_1 - \mu_2)(y_1 - y_2) . \end{aligned}$$

Then, the difference between the adjacent row parameters gives the odds ratios,

$$\theta_{ij} = \text{Exp}(\mu_{i+1} - \mu_i) \tag{2}$$

For 2×2 sub-tables formed from adjacent rows, the row effects model satisfies the equality of odds ratios.

Column effects models

Analogously, consider a $R \times C$ cross-classification table in which the row variable has ordinal and the column variable is nominal,

$$\log(E_{ij}) = u + u_{1(i)} + u_{2(j)} + \tau_j x_i \tag{3}$$

This model is referred as the Column Effects (CE) model with constraints,

$$\sum_{i=1}^R u_{1(i)} = \sum_{j=1}^C u_{2(j)} = \sum_{j=1}^C \tau_j = 0 .$$

The column effects model is defined as a simple log-linear model for this situation utilizes the orderings of the row variable. For analyzing the column effects model, the column scores are assigned to the categories of the row variable. $\{\tau_j\}$ is the j th column parameters and, $\{x_i\}$ is the i th row scores, $x_1 < \dots < x_C$. This model has more $(C - 1)$ parameters than the usual independence model, the df for testing the goodness of fit,

$$df = RC - [1 + (R - 1) + (C - 1) + (C - 1)] = (R - 2) (C - 1).$$

Let θ_{ij} denote the corresponding odds-ratio for $i = 1, \dots, R - 1; j = 1, \dots, C - 1$. As in the row effects model, the log-odds ratios are calculated through the adjacent column parameters as,

$$\theta_{ij} = \text{Exp}(\tau_{j+1} - \tau_j) \tag{4}$$

For 2×2 sub-tables formed from adjacent columns, the column effects model satisfies the equality of odds ratios [16].

Although, choice of the row and column scores are assigned as the integer scores in practice, there is a no rule of thumb about choosing the scores for both row effects and column effects models.

Results

Analysis of China Covid-19 data

Countries across the world have been facing an important demographic structure from young to increasingly elderly populations. Unfortunately, elderly people worldwide also have been facing the risk of infected with COVID-19. Particularly, older adults who have severe underlying medical conditions like coronary heart disease, lung disease, diabetes or hypertension seem to be at higher risk for developing more serious complications from COVID-19 illness. It is noted that 8 out of 10 deaths reported in the U.S. have been in adults 65 years old and older.

Data consists of 63 older patients infected with laboratory confirmed COVID-19, described and analyzed the epidemiological and clinical characteristics of the older patients with COVID-19 infection are directly taken from Niu et.al [17]. The authors collected the data on the 63 older patients infected with laboratory confirmed COVID-19, and analyzed the epidemiological and clinical characteristics of the older patients with COVID-19 infection. We only studied on medical history variable among several characteristics. Niu et.al [17] analyzed the data with some frequently used methods.

The row effects model is applied to data in Table 1. The expected frequencies under the row effects model are

given in the square brackets. The aim of applying this model is to estimate how the presence of a medical history increases the likelihood of age groups than others. The odds of being $(i + 1)$ th medical history than i th medical history is θ_{ij} times greater for all age groups.

Table 1. Number of older patients infected positive COVID-19 test according to age and their medical history. (The number in the parentheses of table is the ML fitted values that satisfy the row effects model)

Medical history	Age		
	50-64	65-79	+80
Hypertension	7 (7.369)	12 (11.261)	3 (3.369)
Coronary heart disease	3 (3.019)	4 (3.963)	1 (1.019)
COPD	0 (0.21)	3 (2.58)	6 (6.21)
Diabetes	2 (2.397)	3 (2.205)	0 (0.397)
Cerebrovascular disease	3 (2.397)	1 (2.205)	1 (0.397)
Other	6 (5.608)	6 (6.785)	2 (1.608)

The design matrix for the row effects model contains seven columns where 5 out of 7 columns is represented the row effects parameters. Sum of row effects parameters is set to zero assuming equidistant scores for the categories of the variables [18].

Table 2. Design matrix for the row effects model

Age Groups	Medical history	μ_1	μ_2	μ_3	μ_4	μ_5
1	1	1	0	0	0	0
1	2	2	0	0	0	0
1	3	3	0	0	0	0
2	1	0	1	0	0	0
2	2	0	2	0	0	0
2	3	0	3	0	0	0
3	1	0	0	1	0	0
3	2	0	0	2	0	0
3	3	0	0	3	0	0
4	1	0	0	0	1	0
4	2	0	0	0	2	0
4	3	0	0	0	3	0
5	1	0	0	0	0	1
5	2	0	0	0	0	2
5	3	0	0	0	0	3
6	1	-1	-1	-1	-1	-1
6	2	-2	-2	-2	-2	-2
6	3	-3	-3	-3	-3	-3

Table 3. The goodness of fit statistics, degrees of freedom and p-value of model

Model	G ²	df	p-value
Row effects	3.53	5	0.617

The row effects model holds for data and the model equation would be:

$$\log(E_{ij}) = 1.517 - 0.114RE1 - 0.266RE2 + 1.971RE3 - 0.622RE4 - 0.622RE5 - 0.347RE6 + 0.040Hypertension - 0.701Coronary\ heart\ disease - 5.603COPD - 0.576Diabetes - 0.576Cerebrovascular\ disease + 6.84Other + 0.554age(50 - 64) + 1.092age(65 - 79) - 1.646age(+80).$$

Estimates of the row effects parameters with their standard errors are given in Table 4. Odds ratios over the row effects parameters are illustrated in Table 5.

Table 4. Parameter estimations and odds ratios for the row effects model

Row Effects Parameter	Estimation	Standard Error	Z
μ ₁	-0.114	0.348	-0.328
μ ₂	-0.266	0.494	-0.538
μ ₃	1.971	0.628	3.141
μ ₄	-0.622	0.629	-0.989
μ ₅	-0.622	0.629	-0.989
μ ₆	-0.347	0.799	0.434

Odds ratios calculated over adjacent row effects parameters as in Equation 2.

From the row effects parameters, the odds that an observation will fall in column *j* rather than in column *j*+1, given that it is in row *i* could be calculated. $\theta_{ij} = \text{Exp}(\mu_{i+1} - \mu_i)$ are given in Table 5. For example $i=1; j=2$, the odds ratio is $\theta_{1j} = \text{Exp}(\mu_2 - \mu_1) = \text{Exp}(-0.266 + 0.114) = 0.86$ (1/0.86=1.16).

Table 5. Odds ratios for the row effects

i,j	Odds ratio	i,j	Odds ratio
1-2	1.16	2-6	1.08
1-3	8.04	3-4	13.37
1-4	1.66	3-5	13.37
1-5	1.66	3-6	10.06
1-6	1.26	4-5	1
2-3	9.37	4-6	1.32
2-4	1.43	5-6	1.32
2-5	1.43		

As the age group increases, the risk of incidence does not differ much in those with chronic disease, except for COPD disease.

Table 6. Pairwise comparison of medical history by their odds ratios

Compared medical history	Odds ratio
Hypertension and Coronary heart disease	$\hat{\theta}_1 = \frac{E_{11} \times E_{22}}{E_{12} \times E_{21}} = \frac{E_{12} \times E_{23}}{E_{13} \times E_{22}} = 0.859 \rightarrow \frac{1}{0.859} = 1.16$
Hypertension and COPD	$\hat{\theta}_2 = \frac{E_{11} \times E_{32}}{E_{12} \times E_{31}} = \frac{E_{12} \times E_{33}}{E_{13} \times E_{23}} = 8.04$
Hypertension and Diabetes	$\hat{\theta}_3 = \frac{E_{11} \times E_{42}}{E_{12} \times E_{41}} = \frac{E_{12} \times E_{43}}{E_{13} \times E_{42}} = 0.602 \rightarrow \frac{1}{0.602} = 1.66$
Hypertension and Cerebrovascular disease	$\hat{\theta}_4 = \frac{E_{11} \times E_{52}}{E_{12} \times E_{51}} = \frac{E_{12} \times E_{53}}{E_{13} \times E_{52}} = 0.602 \rightarrow \frac{1}{0.602} = 1.66$
Hypertension and Other	$\hat{\theta}_5 = \frac{E_{11} \times E_{62}}{E_{12} \times E_{61}} = \frac{E_{12} \times E_{63}}{E_{13} \times E_{62}} = 0.792 \rightarrow \frac{1}{0.792} = 1.26$
Coronary heart disease and COPD	$\hat{\theta}_6 = \frac{E_{21} \times E_{32}}{E_{22} \times E_{31}} = \frac{E_{22} \times E_{33}}{E_{23} \times E_{32}} = 9.36$
Coronary heart disease and Diabetes	$\hat{\theta}_7 = \frac{E_{21} \times E_{42}}{E_{22} \times E_{41}} = \frac{E_{22} \times E_{43}}{E_{23} \times E_{42}} = 0.701 \rightarrow \frac{1}{0.701} = 1.43$
Coronary heart disease and Cerebrovascular disease	$\hat{\theta}_8 = \frac{E_{21} \times E_{52}}{E_{22} \times E_{51}} = \frac{E_{22} \times E_{53}}{E_{23} \times E_{52}} = 0.701 \rightarrow \frac{1}{0.701} = 1.43$
Coronary heart disease and other	$\hat{\theta}_9 = \frac{E_{21} \times E_{62}}{E_{22} \times E_{61}} = \frac{E_{22} \times E_{63}}{E_{23} \times E_{62}} = 0.922 \rightarrow \frac{1}{0.922} = 1.08$
COPD and Diabetes	$\hat{\theta}_{10} = \frac{E_{31} \times E_{42}}{E_{32} \times E_{41}} = \frac{E_{32} \times E_{43}}{E_{33} \times E_{42}} = 0.0748 \rightarrow \frac{1}{0.0748} = 13.37$
COPD and Cerebrovascular disease	$\hat{\theta}_{11} = \frac{E_{31} \times E_{52}}{E_{32} \times E_{51}} = \frac{E_{32} \times E_{53}}{E_{33} \times E_{52}} = 0.0748 \rightarrow \frac{1}{0.0748} = 13.37$
COPD and other	$\hat{\theta}_{12} = \frac{E_{31} \times E_{62}}{E_{32} \times E_{61}} = \frac{E_{32} \times E_{63}}{E_{33} \times E_{62}} = 0.09984 \rightarrow \frac{1}{0.09984} = 10.16$
Diabetes and Cerebrovascular disease	$\hat{\theta}_{13} = \frac{E_{41} \times E_{52}}{E_{42} \times E_{51}} = \frac{E_{42} \times E_{53}}{E_{43} \times E_{52}} = 1$
Diabetes and other	$\hat{\theta}_{14} = \frac{E_{41} \times E_{62}}{E_{42} \times E_{61}} = \frac{E_{42} \times E_{63}}{E_{43} \times E_{62}} = 1.32$
Cerebrovascular disease and other	$\hat{\theta}_{15} = \frac{E_{51} \times E_{62}}{E_{52} \times E_{61}} = \frac{E_{52} \times E_{63}}{E_{53} \times E_{62}} = 1.32$

However, as the age group increases, the risk of COVID 19 is 8,04 times higher in patients with COPD disease than in patients with hypertension, 9.37 times higher in patients with coronary heart disease, 13.37 times higher in patients with diabetes and Cerebrovascular disease and 10.16 times more in patients with other diseases. The odds ratio can also be calculated by using the ML fitted values that satisfy the row effects model, given in Table 6.

The odds for Hypertension ($i=1$) and COPD ($i=3$)

For the age groups 50-64 ($j=1$) and 65-79 ($j=2$),

$$\theta_2 = \frac{7.369 \times 2.58}{11.261 \times 0.21} = 8.04$$

For the age groups 65-79 ($j=2$) and ≥ 80 ($j=3$),

$$\theta_2 = \frac{11.261 \times 6.21}{3.369 \times 2.58} = 8.04$$

This calculation can be made through parameter estimates such as:

$$\theta_{ij} = \text{Exp}(\mu_3 - \mu_1) = \text{Exp}(1.971 + 0.114) = 8.04.$$

Note that the adjacent pairs have equal odds ratios. Entire odds ratio calculations under the row effects model is true are given in Table 6.

The pairwise comparison of medical diseases tells us that a patient with diabetes is 13.37 times more likely to get COVID 19 than a patient with COPD disease.

Similarly, a patient with COPD is 13.37 times more likely to have COVID 19 positive than a patient with Cerebrovascular disease in all age groups. The odds ratio equals 1 for Diabetes and Cerebrovascular diseases indicates that these diseases under study are equally likely to occur in entire age groups.

Analysis of NYC Covid-19 data

World case fatality rate of the ongoing COVID-19 pandemic was 7.07 as of May 9, 2020 (<https://ourworldindata.org/mortality-risk-covid#the-case-fatality-rate>). The case fatality rate is the number of confirmed deaths divided by the number of confirmed cases. Mortality rate is extremely higher in country with older-aged population, COVID-19 mortality risk is highly concentrated at older ages, particularly those aged 80+ [19].

We applied the column effects model to number of deaths patients with positive COVID-19 test according to age and chronic disease status data. The data in Table 7 is taken directly from NYC Health and, reflects events and activities as of April 14, 2020. Underlying illnesses include Diabetes, Lung Disease, Cancer, Immunodeficiency, Heart Disease, Hypertension, Asthma, Kidney Disease, and GI/Liver Disease. Distributions of underlying comorbidities of COVID-19 patients will help risk estimates. The concentration to age and chronic disease status in the age groups could be a helpful tool to predict the burden of critical cases and to arrange the hospital and other resources.

Table 7. Number of deaths patients with positive COVID-19 test according to age and chronic disease status. (The numbers in the parentheses of table are the ML fitted values that satisfy the column effects model)

Age	Chronic disease status		
	Underlying illnesses	No underlying illnesses	Underlying illnesses unknown
0-17	1 (0.797)	0 (0.151)	0 (0.052)
18-44	50 (52,659)	5 (4,831)	8 (5,509)
45-64	269 (261,799)	12 (11,638)	36 (43,563)
65-74	254 (261,236)	5 (5,626)	77 (69,137)
75+	458 (455,508)	5 (4,753)	189 (191,738)

The design matrix given in Table 8 is used to specify the column effects model for the 5 x 3 cross-classification of age and chronic disease status. In the design matrix, the third and fifth columns correspond to the column effects parameters. Note that as the chronic disease status variable has three levels, we define (C-1) column effects parameters.

Table 8. Design matrix for the column effects model

Age	Illnesses	τ_1	τ_2
1	1	1	0
1	2	0	1
1	3	-1	-1
2	1	2	0
2	2	0	2
2	3	-2	-2
3	1	3	0
3	2	0	3
3	3	-3	-3
4	1	4	0
4	2	0	4
4	3	-4	-4
5	1	5	0
5	2	0	5
5	3	-5	-5

Table 9. The goodness of fit statistics, degrees of freedom and p-value of model

Model	G ²	df	p-value
Column effects	4.39	6	0.624

As seen in Table 9, the column effects model holds true for the China data set with G² =4.39 and 6 degrees of freedom. Hence, the model equation is,

$$\begin{aligned} \log(E_{ij}) = & 2.502 + 0.087CE1 - 0.638CE2 \\ & + 0.551CE3 - 6.001age1 \\ & - 1.897age2 - 0.38age3 \\ & - 0.469age4 + 8.747age5 \\ & + 3.186illnesses1 + 2.246illnesses2 \\ & - 5.426illnesses3 . \end{aligned}$$

Parameter estimates pertaining the column effects are obtained with their standard errors under the column effects model are given in Table 10.

How the odds ratios are calculated over the expected frequencies is shown in Table 11. The last parameter (τ_3) is estimated so that its total is the sum to zero.

The odds ratio, for instance for $i=1$ and $j=1$:

$\theta_{11} = \text{Exp}(\tau_2 - \tau_1) = \text{Exp}(-0.638 - 0.087) = 0.48$ ($1/0.48=2.06$). They can be reversed to provide more meaningful interpretations, with reference to the odds ratios are smaller than "1".

Table 10. Parameter estimations and odds ratios for column effects model

Parameter	Estimation	St. Error	Z	Odds ratio
τ_1	0.087	0.073	1.195	2.06
τ_2	-0.638	0.134	-4765	3.28
τ_3	0.551	0.56	0.98	1.59

The odds ratio can be calculated by using the ML fitted values that satisfy column effects model, given as follows. These values show that the odds that an observation will fall in the i th row rather than in $i+1$ th row, given that it is in column j . For example, as the age groups tend to increase, the death risk of a patient with chronic disease increases 2.06 times more likely than patients without chronic disease. Similarly, as the age groups tend to increase, the death risk of a patient without chronic disease increases 3.28 times more likely than patients with underlying disease unknown and, the death risk of a patient without chronic disease increases 1,59 times more likely than patients with underlying disease unknown.

Table 11. Age groups comparison in terms of their odds ratios

Compared age groups	Odds ratio
0-17 and 18-44	$\hat{\theta}_1 = \frac{E_{11} \times E_{22}}{E_{12} \times E_{21}} = \frac{0.797 \times 4.831}{0.151 \times 52.659} = 0.484 \rightarrow \frac{1}{0.484} = 2.06$
18-44 and 45-64	$\hat{\theta}_2 = \frac{E_{21} \times E_{32}}{E_{22} \times E_{31}} = \frac{52.659 \times 11.638}{4.831 \times 261.799} = 0.484 \rightarrow \frac{1}{0.484} = 2.06$
45-64 and 65-74	$\hat{\theta}_3 = \frac{E_{31} \times E_{42}}{E_{32} \times E_{41}} = \frac{261.799 \times 5.626}{11.638 \times 261.236} = 0.484 \rightarrow \frac{1}{0.484} = 2.06$
65-74 and 75+	$\hat{\theta}_4 = \frac{E_{41} \times E_{52}}{E_{42} \times E_{51}} = \frac{261.236 \times 4.753}{5.626 \times 455.508} = 0.484 \rightarrow \frac{1}{0.484} = 2.06$

Conclusions

There are several advantages of utilizing efficiently the special models which use the ordinal information. Such models are more parsimonious and have simpler interpretations than the standard models for nominal variables. If at least one of the variables in a two or higher dimensional contingency table, we'd rather some order restricted models. In the fact that researchers prefer to use more conventional statistical methods, we show that when an ordering constraint is imposed on the parameter scores in the row effects model or the column effects model and show how to apply these special models to COVID-19 data sets. The main finding of two modeling approaches is to interpret the odds ratios. Analyzing the number of older patients infected positive COVID-19 test according to age and their medical history in the 50-64; 65-79 and over 80 age groups could be a helpful to arrange the hospital and other resources. Although COVID-19 has been reported from every age group, elderly patients seem to more likely to be more susceptible to infection.

The row effects model indicates that having a particular medical history such as hypertension, diabetes, coronary heart disease, cerebrovascular disease, and other histories gets more likely to have COVID-19. For instance, a patient having COPD is more likely to have COVID-19 than for those who have other diseases.

Different countries have diversely demographic changes, while lower-income countries with high fertility rates and have a very young population, high-income countries have a large elderly population. In NYC data, the chronic disease status was distributed to age groups starting 0-17 towards ≥ 75 . The column effect model explains that the older the age groups, the greater the risk, whereas the odds ratio < 1 indicates a decrease in risk in the exposed group. Higher age groups are "odds ratio" times more likely to meet the COVID-19 compared to smaller age groups. The findings suggest that additional care could be required for elderly people with underlying conditions. Researchers from around the world have been

working to figure out more about the epidemiological and clinical characteristics of COVID 19. In this respects, statistical methods allow us to gain valuable insight into the latest COVID-19 data. Fortunately, the downward trend in curve throughout the world suggests that measures as isolation, hand washing, mask-wearing, social distancing are reducing the spread of coronavirus. The lockdown throughout the world and applying the nationwide control measures efficiently prevented an exponential growth in the number of cases. Coronaviruses are a great threat to world health, there is an urgent need to find strong, long-lasting, and virus-specific immune response safe vaccines effective against these agents. Along with the high morbidity and mortality rates of COVID-19 among older adults, İlgili and Kutsal [20] emphasized in their study that after the pandemic, some permanent problems may arise in elderly people.

Conflicts of interest

There are no conflicts of interest in this work.

References

- [1] Lu, R., Zhao, X., Li, J., Niu, P., Yang, B., Wu, H., ... & Tan, W., Genomic characterisation and epidemiology of 2019 novel coronavirus: implications for virus origins and receptor binding, *The Lancet*, 395(10224) (2020) 565-574.
- [2] Lauer, S. A., Grantz, K. H., Bi, Q., Jones, F. K., Zheng, Q., Meredith, H. R., ... & Lessler, J., The incubation period of coronavirus disease 2019 (COVID-19) from publicly reported confirmed cases: estimation and application, *Annals of Internal Medicine.*, 172(9) (2020) 577-582.
- [3] Chen N, Zhou M, Dong X, et al., Epidemiological and clinical characteristics of 99 cases of 2019 novel coronavirus pneumonia in Wuhan, China: a descriptive study, *Lancet*, 395 (2020) 507–13.
- [4] Guan, W. J., Ni, Z. Y., Hu, Y., Liang, W. H., Ou, C. Q., He, J. X., ... & Zhong, N. S., Clinical characteristics of 2019 novel coronavirus infection in China, *Med. Rxiv*, (2020).
- [5] Guan, W. J., Ni, Z. Y., Hu, Y., Liang, W. H., Ou, C. Q., He, J. X., ... & Zhong, N. S., Clinical characteristics of coronavirus disease 2019 in China, *New England Journal Of Medicine*, 382(18) (2020) 1708-1720.
- [6] Huang, C., Wang, Y., Li, X., Ren, L., Zhao, J., Hu, Y., ... & Cao, B, Clinical features of patients infected with 2019 novel coronavirus in Wuhan, China., *The Lancet*, 395(10223) (2020) 497-506.
- [7] Gomes, C., Report of the WHO-China joint mission on coronavirus disease 2019 (COVID-19), *Brazilian Journal Of Implantology And Health Sciences*, 2(3) (2020).
- [8] Liu, K., Chen, Y., Lin, R., & Han, K., Clinical features of COVID-19 in elderly patients: A comparison with young and middle-aged patients, *Journal of Infection*, 80(6) (2020) e14-e18.
- [9] Likassa, H. T., The impacts of covariates on spatial distribution of corona virus 2019 (COVID-19): what do the data show through ANCOVA and MANCOVA, *EJMO*, 4(2) (2020) 141-148.
- [10] Centers for Disease Control and Prevention. Coronavirus Disease 2019 (COVID-19) Available at: <https://www.cdc.gov/coronavirus/2019-ncov/about/symptoms.htm>
- [11] Sasson, I., Age and COVID-19 mortality, *Demographic Research*, 44 (2021) 379-396.
- [12] Ahrenfeldt, L. J., Otavova, M., Christensen, K., & Lindahl-Jacobsen, R. Sex and age differences in COVID-19 mortality in Europe, *Wiener klinische Wochenschrift*, 133 (2021) 393-398.
- [13] Agresti A., Analysis of Ordinal Categorical Data, 2nd Edition, Wiley and Sons, New York, (2010).
- [14] Davis, C., Estimation of row and column scores in the linear-by-linear association model for two-way ordinal contingency tables, In Proceedings of the 13th Annual SAS Users Group International Conference., (1988) 946-951.
- [15] Goodman, L. A., Simple models for the analysis of association in cross-classifications having ordered categories, *Journal of the American Statistical Association*, 74(367) (1979) 537-552
- [16] Goodman, L.A., The analysis of cross-classified data having ordered and/or unordered categories: association models, correlation models, and asymmetry models for contingency tables with or without missing entries, *The Annals of Statistics*, 13 (1985) 10-69.
- [17] Niu, S., Tian, S., Lou, J., Kang, X., Zhang, L., Lian, H., & Zhang, J., Clinical characteristics of older patients infected with COVID-19: A descriptive study, *Archives of Gerontology and Geriatrics*, 89 (2020) 104058.
- [18] Saraçbaşı T., Aktaş Altunay, S., Kategorik Veri Çözümlemesi, *Hacettepe Üniv. Yayınları*, (2016)
- [19] Dowd, J. B., Andriano, L., Brazel, D. M., Rotondi, V., Block, P., Ding, X., ... & Mills, M. C., Demographic science aids in understanding the spread and fatality rates of COVID-19., *Proceedings of the National Academy of Sciences*, 117(18) (2020) 9696-9698.
- [20] İlgili, Ö., & Kutsal, Y. G., Impact of COVID-19 among the elderly population, *Turkish Journal of Geriatrics*, 23(4) (2020) 419-423.

AUTHOR GUIDELINES

Thank you for choosing to submit your paper to Cumhuriyet Science Journal. The following instructions will ensure we have everything required so your paper can move through pre-evaluating, peer review, production and publication smoothly. Please take the time to read and follow them as closely as possible, as doing so will ensure your paper matches the journal's requirements.

Submission

Cumhuriyet Science Journal is an international, peer-reviewed, free of charge journal covering the full scope of both natural and engineering sciences. Manuscripts should be submitted by one of the authors of the manuscript as online submission after registration to the Cumhuriyet Sciences Journal. Microsoft Word (.doc, .docx, .rtf), files can be submitted. There is no page limit. If there is a problem while uploading the files of manuscript, please try to reduce their file size, especially manuscripts including embedded figures. Submissions by anyone other than one of the authors will not be accepted. The submitting author takes responsibility for the paper during submission and peer review. If for some technical reason submission through the online submission system is not possible, the author can contact csj@cumhuriyet.edu.tr for support.

Submission or processing charges

Cumhuriyet Science Journal does not charge any article submission, processing charges, and printing charge from the authors.

Terms of Submission

Papers must be submitted on the understanding that they have not been published elsewhere (except in the form of an abstract or as part of a published lecture, review, or thesis) and are not currently under consideration by another journal. The submitting author is responsible for ensuring that the article's publication has been approved by all the other coauthors. It is also the authors' responsibility to ensure that the articles emanating from a particular institution are submitted with the approval of the necessary institution. Only an acknowledgment from the editorial office officially establishes the date of receipt. Further correspondence and proofs will be sent to the author(s) before publication unless otherwise indicated. It is a condition of submission of a paper that the corresponding author permit editing of the paper for readability. All enquiries concerning the publication of accepted papers should be addressed to csj@cumhuriyet.edu.tr. Please note that Cumhuriyet Science Journal uses iThenticate software to screen papers for unoriginal material. By submitting your paper to Cumhuriyet Science Journal are agreeing to any necessary originality checks your paper may have to undergo during the peer review and production processes. Upon receiving a new manuscript, the Editorial office conducts initial pre-refereeing checks to ensure the article is legible, complete, correctly formatted, original, within the scope of the journal in question, in the style of a scientific article and written in clear English. Any article that has problems with any of the journal criteria may be rejected at this stage.

Peer Review

This journal operates a single blind review process. All contributions will be initially assessed by the editor for suitability for the journal. Papers deemed suitable are then typically sent to a minimum of two independent expert reviewer to assess the scientific quality of the paper. The author is required to upload the revised article to the system within 15 days by making the corrections suggested by the referee. The article will be rejected if there are no fixes in it. The Editor is responsible for the final decision regarding acceptance or rejection of articles. The Editor's decision is final

Title and Authorship Information

The following information should be included

Paper title

Full author names

Full institutional mailing addresses

Corresponding address

Email address

Abstract

The manuscript should contain an abstract. The researchers who are native speakers of Turkish have to add Turkish title and abstract as well. The abstract should be self-contained and citation-free and should be 250-300 words.

Keywords

Keywords of the scientific articles should be selected from the web address of www.bilimadresleri.com

Introduction

This section should be succinct, with no subheadings.

Materials and Methods

This part should contain sufficient detail so that all procedures can be repeated. It can be divided into subsections if required.

Conflicts of interest

Sample sentence if there is no conflict of interest: The authors stated that did not have conflict of interests.

Acknowledgements

Sample sentences for acknowledgements: The work was supported by grants from CUBAP (T-1111). We would like to acknowledge Prof. Mehmet Sözer, MD, for his precious technical and editorial assistance. We would like to thank

References

References to cited literature should be identified by number in the text in square brackets and grouped at the end of the paper in numerical order of appearance. Each reference must be cited in the text. Always give inclusive page numbers for references to journal articles and a page range or chapter number for books. References should be styled and punctuated according to the following examples

- [1] Karaca E., Ulusoy S., Morgül Ü., Ulusoy H.I., Development of Analytical Method for Sensitive Determination of Streptozotocin based on Solid Phase Extraction, Cumhuriyet Sci. J., 41 (4) (2020) 826-831. (sample reference for journals)
- [2] Keskin B., Ozkan A.S., Inverse Spectral Problems for Dirac Operator with Eigenvalue Dependent Boundary and Jump Conditions, Acta Math. Hungar., 130 (2011) 150-159(sample reference for journals)
- [3] Mazur M.T., Kurman R.J., Dysfunctional Uterine Bleeding. In: Mazur M.T., Kurman R.J., (Eds). Diagnosis of endometrial biopsies and curettings, A practical approach. 2nd ed. Berlin: Springer, (2005) 100-120. (sample reference for book chapters)
- [4] Mazur M.T., Kurman R.J.,Diagnosis of endometrial biopsies and curettings, A practical approach. 2nd ed. Berlin, (2005) 100-120. (sample reference for book)
- [5] National Cancer Institute, Surveillance Epidemiology and End Results. Cancer of the Corpus and Uterus, NOS. Available at: http://seer.cancer.gov/statfacts/html/corp.html?statfacts_page=corp. Retrieved March 2, 2008. (sample reference for websites)
- [6] Surname N., Title of thesis, PD or master thesis, Name of university, name of institue, year. (sample reference for thesis)
- [7] Surname N., Title of fulltext conference paper, name of conference, city, year, pages. (sample reference for Abstratcs in conferences are not accepted as a valid reference except full text)

Preparation of Figures

Each figure can be integrated in the paper body or separately uploaded and should be cited in a consecutive order. Figure widths can be 4-6 inch as 300 dpi. The labels of the figures should be clear and informative. The name and the subtitles of the figures must be 9-point font.

Preparation of Tables

Tables should be cited consecutively in the text. Every table must have a descriptive title and if numerical measurements are given, the units should be included in the column heading. Tables should be simple with simple borders and text written as left text. The name and the subtitle of the tables must be 9-point font

Proofs

Corrected proofs must be returned to the publisher within 2 weeks of receipt. The publisher will do everything possible to ensure prompt publication. It will therefore be appreciated if the manuscripts and figures conform from the outset to the style of the journal.

Copyright

Open Access authors retain the copyrights of their papers, and all open access articles are distributed under the terms of the Creative Commons Attribution license, which permits unrestricted use, distribution and reproduction in any medium, provided that the original work is properly cited.

The use of general descriptive names, trade names, trademarks, and so forth in this publication, even if not specifically identified, does not imply that these names are not protected by the relevant laws and regulations.

While the advice and information in this journal are believed to be true and accurate on the date of its going to press, neither the authors, the editors, nor the publisher can accept any legal responsibility for any errors or omissions that may be made. The publisher makes no warranty, express or implied, with respect to the material contained herein.

Ethical Guidelines

New methods and ethically relevant aspects must be described in detail, bearing in mind the following:

Human Experiments. All work must be conducted in accordance with the Declaration of Helsinki (1964). Papers describing experimental work on human subjects who carry a risk of harm must include:

A statement that the experiment was conducted with the understanding and the consent of the human subject.

A statement that the responsible Ethical Committee has approved the experiments.

Animal Experiments. Papers describing experiments on living animals should provide:

A full description of any anaesthetic and surgical procedure used.

Evidence that all possible steps were taken to avoid animal suffering at each stage of the experiment. Papers describing experiments on isolated tissues must indicate precisely how the donor tissues were obtained.

Submission Preparation Checklist

As part of the submission process, authors are required to check off their submission's compliance with all of the following items, and submissions may be rejected that do not adhere to these guidelines.

The submission has not been previously published, nor is it before another journal for consideration (or an explanation has been provided in Comments to the Editor).

The submission file is in Microsoft Word document file (Times New Roman) format.

Where available, URLs for the references have been provided.

The text is single-spaced; uses a 11-point font; employs italics, rather than underlining (except with URL addresses); and all illustrations, figures, and tables are placed within the text at the appropriate points, rather than at the end.

The text adheres to the stylistic and bibliographic requirements outlined in the Author Guidelines, which is found in About the Journal.

If submitting to a peer-reviewed section of the journal, the instructions in Ensuring a Double-Blind Review have been followed.